UNIVERSITÀ DEGLI STUDI DI MILANO

DOTTORATO DI RICERCA IN SCIENZE DELLA TERRA

Ciclo XXXIII / A.A. 2019-2020

DIPARTIMENTO DI SCIENZE DELLA TERRA

TESI DI DOTTORATO DI RICERCA

"STRUCTURAL AND METAMORPHIC EVOLUTION OF VARISCAN BASEMENT ROCKS OF THE ALPS IN COMPARISON WITH OTHER PORTIONS OF THE EUROPEAN VARISCAN BELT"

GEO/03

MARCO FILIPPI

TUTORI / DIRETTORI DI TESI
Prof. MARIA IOLE SPALLA
Prof. JEAN-MARC LARDEAUX

CO-TUTORE
Prof. DAVIDE ZANONI

COORDINATORE DEL DOTTORATO
Prof. FERNANDO CAMARA ARTIGAS

UNIVERSITÉ FRANCO ITALIENNE | UNIVERSITÀ ITALO FRANCESE

Abstract

The tectonic evolution of the Southern Variscan belt is still poorly understood if compared with that of the central European Variscan belt. That is due to intense late-Variscan to Alpine re-working, in particular in the Alpine axial zone. The Variscan rocks of the external domains of the Alps are instead little affected by Alpine re-equilibration. For this reason, these domains are eligible for constraining the evolution of the Southern Variscan belt, since they well preserve the Variscan record.

This thesis is focused on the Variscan basement rocks in the Argentera-Mercantour Massif (Helvetic domain), Orobic basement (Southalpine domain), and Maures-Tanneron Massif, which is a benchmark for the Variscan belt just outside the Alpine area. The aim is to provide new constrains on the Variscan and Alpine tectonic evolution of the external domains of the Alps and in the Alpine foreland.

This study required structural mapping (1:10.000 to 1:100 scale) integrated by microstructural, chemical, and mineral-chemical analyses. Metamorphic conditions that affected the Variscan basements are estimated in terms of pressure and temperature and constrained in time by relative and absolute ages. By doing so, several stages of the Variscan and Alpine tectonics are addressed, from early Cambrian to Tertiary times, and discussed in light of the geodynamic and paleogeographic reference models for both the Variscan and Alpine belts. The results refer to four main tectonic stages of Southern Variscan belt, from the subduction of the Variscan ocean to the Alpine collision:

First, we constrain the structural and metamorphic evolution of remnants of early Cambrian oceanic lithosphere in the Argentera-Mercantour massif. These rocks experienced prehnite-pumpellyite to eclogite facies conditions (T = 610 – 660°C, P = 1.90 – 2.30 GPa) before exhumation in Carboniferous times. A cold Variscan subduction zone is thus envisaged for the first time in the Helvetic domain of the Alps.

Second, we refine the tectonic evolution of the external domains of the Southern Variscan belt through a comparison between the western Maures-Tanneron Massif and Orobic basement. The western Maures-Tanneron and the Orobic basement retain a similar litho-stratigraphy and tectonic evolution from early-Cambrian to Permian times, with peak metamorphic conditions (T = 550 – 650°C, P = 0.6 – 0.8 GPa) attained during the Variscan collision. A correlation between these two domains, today in opposite position with respect to the subduction complexes of the Southern Variscan belt, is thus proposed.

Third, we decipher the signal of the Permian-Triassic lithospheric thinning on both sides of the Alpine Tethys Ocean, in the Argentera-Mercanotur Massif and Orobic basement. Here, swarms of calc-alkaline and alkaline lamprophyres emplaced at shallow crustal levels in the exhumed Variscan basement. Since the production of mantle-derived melts at the end of the Variscan cycle required forced extension that cannot result from the sole gravitational collapse of the Variscan belt, the emplacement of these mafic magmas is interpreted as marking the beginning of the Alpine cycle in the Alpine portion of the Southern Variscan belt.

Fourth, we quantify the Alpine tectono-metamorphic evolution retained by the Variscan basement rocks in the external domains of the Alps. It follows that similar Alpine peak conditions (T = 420 – 450°C and P = 0.15 – 0.40 GPa) were reached in the Helvetic domain and Southern Alps, on both sides of the Alpine orogenic wedge.

Chapter 0

Introduction

0.1 General introduction

The Variscan belt is the widest European orogeny, which crosses the whole continent only interrupted by the Alps and western Mediterranean. Our understanding of the Variscan belt is indeed limited by the interposition of the Alps that prevents a continuous correlation between the Central and Southern European Variscides. This thesis is aimed at identifying the missing mosaic tiles to complete the Variscan tectonic framework across the Alpine suture.

The tectonic evolution of the European Variscan belt is, nowadays, quite well constrained in space and time and the main tectonic lineaments and litho-tectonic units have been individuated and correlated for more than a century (Stille, 1924; Kossmat, 1927; Weber and Behr, 1983). In more recent times, the thermal evolution of the orogeny has been reconstructed in great detail and solid constrains about plate motions have been defined (Matte, 1998, 2001; Lardeaux et al., 2001, 2014; Stampfli et al., 2002, 2013; Cocks and Torsvik, 2006; Martínez Catalán et al., 2007, 2009; Ballèvre et al., 2009, 2013; Faure et al., 2009; Schulmann et al., 2009, 2014; Torsvik and Cocks, 2009; Berger et al., 2010; Lardeaux, 2014; Domeier, 2016; Franke et al., 2017; Paquette et al., 2017). On the contrary, the tectonic evolution of the Southern Variscan belt is still controversial, just because in the Alpine area difficulties arise from the intense thermo-mechanical re-equilibration and transposition.

Attempts to include the Variscan rocks of the Alps in the Variscan framework have already been made by many authors (e.g. Stampfli et al., 2002, 2013; von Raumer et al., 2002; von Raumer et al., 2009). Most of these correlations only consider the northern external domain of the Alps – the Helvetic domain – since it is poorly affected by Alpine re-equilibration and relatively close to the European Variscan belt. The Variscan rocks of the southern external domain of the Alps – the Southern Alps – have been too poorly considered in this sense, in spite of outstanding preservation of the Variscan record.

The research is focused on three sites of the Southern Variscan belt. Two of them are located in the external domains of the Alps: the Argentera-Mercantour Massif (hereafter referred to as A-M) in the Helvetic domain and the Orobic Basement in the central Southalpine domain. The third site is the Maures-Tanneron Massif (hereafter referred to as M-T) that is in the southern foreland of the Alpine arc. Since this massif was already correlated with other parts of the Variscan belt (Bellot 2005; Corsini and Rolland, 2009; Edel et al., 2014, 2018; Schneider et al., 2014; Simonetti et al., 2020), it is taken as benchmark in the attempt of including the Variscan rocks of the Alps in the Variscan framework.

This work is a collection of new structural, microstructural, mineral-chemical, and geochronological data that are used to constrain the tectono-metmorphic evolution of the Alpine part of the Southern Variscan belt. The study includes i) a new interpretation of superposed Alpine and Variscan structures, which heterogeneously developed in space and time, from the regional to the granular scale, ii) the identification of the mineral assemblages that support Alpine and Variscan structures, and iii) the reconstruction of the polyphasic and polycyclic tectono-metamorphic evolution from Variscan to Alpine times. The results update the correlation of the Southern Variscan belt with the European counterpart and implement the reference model for Alpine tectonics on the two external sides of the Alpine belt.

Investigated sites

The **Maures-Tanneron Massif (**Fig. 0.1**)** is a segment of the southern Variscan Belt in the foreland of the southwestern Alpine arc. Therefore, it is unaffected by significant Alpine deformation and metamorphism. In the western M-T, Variscan rocks pervasively record the Variscan collisional metamorphism under low-grade to amphibolite facies conditions and escaped the late-collisional evolution (Bellot, 2005; Schneider et al., 2014). For these reasons, the western M-T is regarded as an external domain of the Southern Variscan belt. On the contrary, Variscan eclogites located in the eastern M-T indicate that this sector was an internal domain of the Southern Variscan belt. However, the memory of the Variscan subduction has been largely obliterated where the HT-LP collisional to post-collisional re-equilbration was imposed and the boundary of the subduction complex diffusely transposed (Bellot, 2005; Schneider et al., 2014).
The peculiar architecture, rock associations, and tectonic evolution support the correlation of the M-T with other parts of the southern Variscan belt, including Corsica, and Sardinia (e.g.: Bellot et al., 2005; Corsini and Rolland, 2009; Schneider at al., 2014; Edel et al., 2014; 2018). Comparisons with the

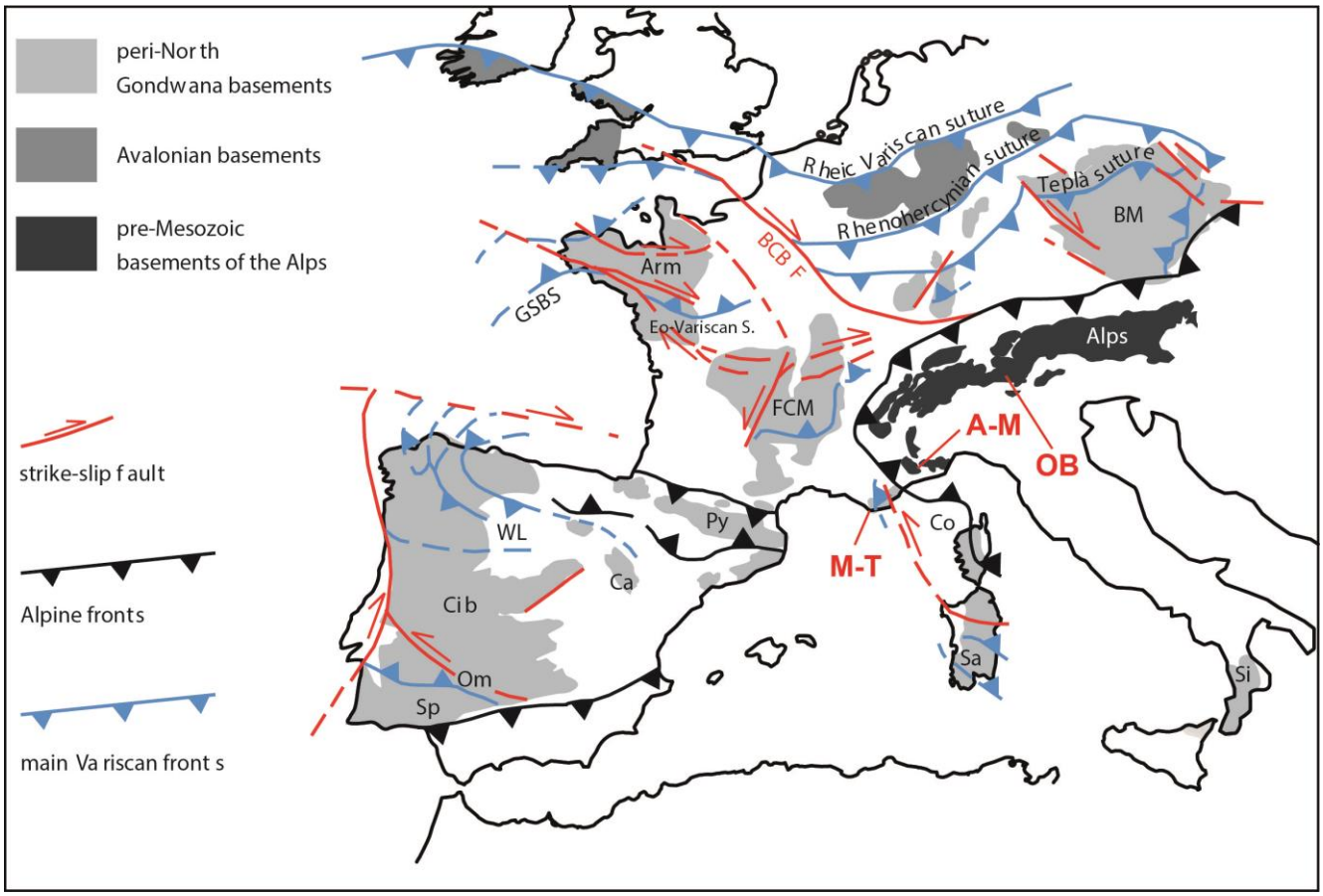

Figure 0.1 - The European Variscan Belt and the Alps (from Regorda et al., 2020 and ref. therein). A-M – Argentera-Mercantour Massif, OB – Orobic basement, M-T – Maures-Tanneron Massif. Other abbreviations: Arm – Armorican Massif, BCBF – Bristol Channel–Bray Fault, BM – Bohemian Massif, Ca – Cantabrian terrane, Cib – Central Iberian, Co – Corsica, FMC – French Massif Central, GSBS – Galicia–Southern Brittany Suture, OM – Ossa Morena, Py – Pyrenees, Sa – Sardinia, Si – Sicilian–Apulian basements, SP – South Portuguese Zone, WL – West Asturian–Leonese.

central European Variscan belt have also been proposed, particularly with the French Central Massif (e.g.: Bellot et al., 2005; Schneider et al., 2015).

The **Argentera-Mercantour Massif (**Fig. 0.1**)** is the southernmost of the external massifs in the Helvetic domain of the Alps, where the effects of the Alpine structural and metamorphic re-working are mostly localized along narrow greenschist facies shear zones (Sanchez et al., 2011; Gosso et al., 2019).

Variscan eclogites in the high-grade Variscan basement rocks of the A-M have been known for over half a century (e.g. Faure-Muret, 1953; Malaroda et al., 1970; Latouche and Bogdanoff, 1987; Paquette et al., 1989; Rubatto et al., 2001). These rocks indicate that the A-M was part of a Variscan subduction complex, as well as the near eastern M-T, to which it is intrinsically correlated by proximity. In the eastern M-T, the subduction complex was affected by widespread partial melting in

late-Variscan times and the memory of the high-pressure evolution is almost entirely lost (Latouche and Bogdanoff, 1987; Paquette et al., 1989; Colombo et al., 1994; Rubatto et al., 2001). The age and thermal state of the Variscan subduction in the A-M is very poorly constrained, so a reliable geodynamic model for this stage is hindered (Rubatto et al., 2010).

Similarly to the A-M, the **Orobic basement** in the central Southern Alps (Fig. 0.1) was partially affected by Alpine structural re-working, manifested by regional-scale folds-and-thrusts belts. The Alpine metamorphic evolution of the whole Orobic basement has not been quantified yet.

Before Alpine history, the Orobic basement pervasively recorded the collisional to post-collisional Variscan evolution, mostly under amphibolite to greenschist facies conditions (Spalla and Gosso, 1999; Spalla et al., 2014). Since Variscan eclogites do not occur in the central Southern Alps, the Orobic basement is considered as an external domain of the Southern Variscan belt, in the same way as the western M-T. However the thermal imprint of the Variscan subduction is envisaged in some parts at low-pressure conditions (Spalla and Gosso, 1999 and ref. therein).

As previously mentioned, remnants of the southern Variscan subduction complex are nowadays evident in the A-M and eastern M-T, as well as in the orogenic wedge of the Alps. In the present configuration, the western M-T and Orobic basement – the external domains of the southern Variscan belt – are characterized by opposed metamorphic field gradients. However, the position of the Orobic basement in the European Variscan belt is puzzling, because of massive reworking and transposition events in late-Variscan time and futher interposition of the Alpine orogenic wedge, which sealed a poorly determined Alpine ocean spreading.

0.2 Method and analytical techniques

Meso-structural analysis

Detailed field mapping and structural analysis is the key to disclose and understand the evolution of crystalline basements. Starting from the outcrop scale, it is effective identifying volumes of rocks that are characterized by different grades of fabric evolution and dividing highly-strained (mylonitic) from medium-strained (tectonitic) and very low-strained (coronitic) domains (Fig. 0.2, Gosso et al., 2015). In this way, it is possible to collect a selection of samples that best retain the tectono-metamorphic history. In fact, in the medium- to low-strained domains, the greatest number of superposed structures and mineral assemblages are preserved, whereas in mylonitic domains the basement rocks are mechanically and chemically re-equilibrated (Passchier et al., 1990 and ref. therein).

The definition of litho-stratigraphic units is an unsuccessful correlation tools in poly-deformed basement rocks, since deformation and transposition are mechanisms capable of completely renovate the litho-stratigraphy and portions of the same litho-stratigraphic unit may have followed different tectonic evolutions and vice-versa (Spalla et al., 2005; Gosso et al., 2015). Similarly, definition of tectonic units based on the dominant metamorphic imprints may lead to misunderstanding. In fact, in most of the cases, the dominant metamorphic imprint is strictly controlled by deformation partitioning at the development of the dominant fabric, which is only a stage of the poly-phasic evolution of the basement rocks and may not even coincide with the peak metamorphic conditions (Fig. 0.3, Spalla et al., 2005).

Micro-structural analysis

Micro-structural analysis is an effective tool for correlating mineral growth and fabric development, through simple geometric criteria (e.g.: Vernon, 2004; Passchier and Trouw, 2005). In this way, it is possible to recognize, in different rock types and under different grade of fabric evolution, sequences of superposed structures that are supported by mineral assemblages developed at equivalent petrogenetic conditions. The combination of meso-structural and micro-structural analyses is a clue for individuating volumes of rocks that experienced coherent tectono-metamorphic evolutions, which represents tectono-metamoprhic units.

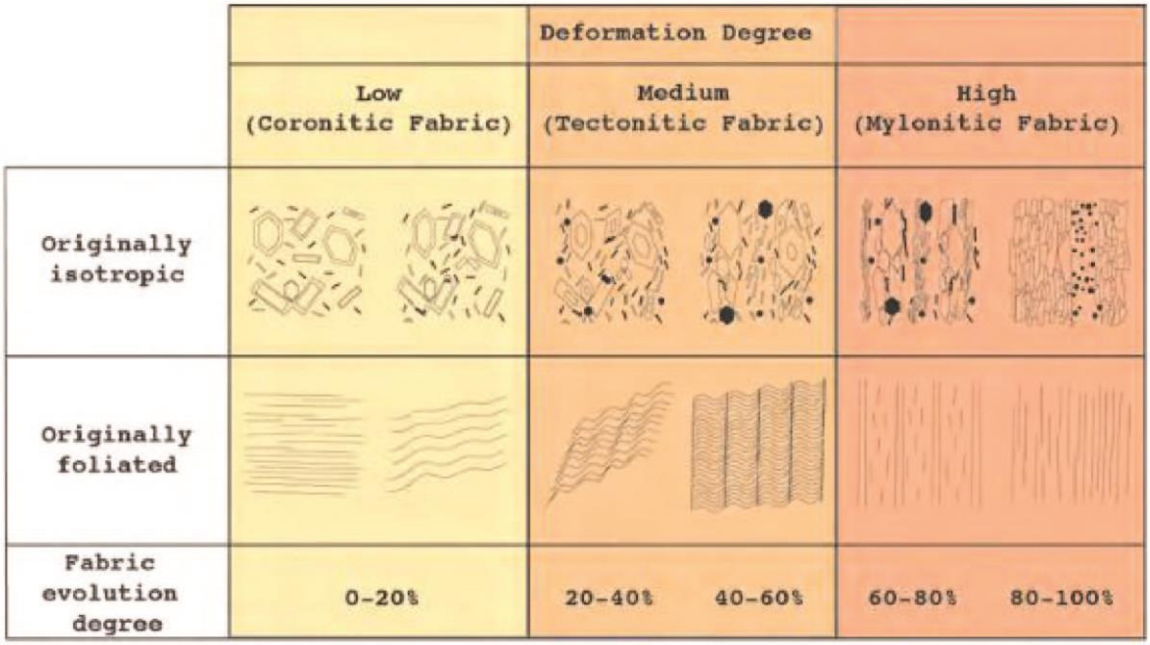

Figure 0.2 - Qualitative estimate of fabric evolution degree during progressive foliation development, starting from originally foliated and initially isotropic rocks (after Salvi et al., 2010 and Gosso et al., 2015 and ref.therein). The volume occupied by newly-oriented fabric elements, including the newly-differentiated mineral layering is used to define the degree of fabric evolution and divided low-, medium-, and high-strained domains.

Whole rock geochemistry

Samples of igneous rocks have been analyzed for bulk composition. The composition of igneous rocks allows speculating on the tectonic setting accountable at the time of their emplacement on the basis of their major, minor, and trace element concentrations (e.g. Pearce, 2008; Saccani, 2015 and ref. therein).

In this study, whole rock analyses have been performed of igneous rocks emplaced in different stages of the Variscan and Alpine tectonic history. Since these intrusive rocks have been deformed and metamorphosed at least during the Alpine event, low-strained and poorly metamorphosed samples best preserving the igneous minerals were considered for this analyses. Homogeneous samples of few kg have been cut to completely remove the surface layer and avoid intersecting veins or altered domains. The samples have been sent to different laboratories, where they were analyzed by ICP-OES and ICP-MS. Moreover, whole rock analyses served as bulk compositions for geochemical and thermodynamic modeling.

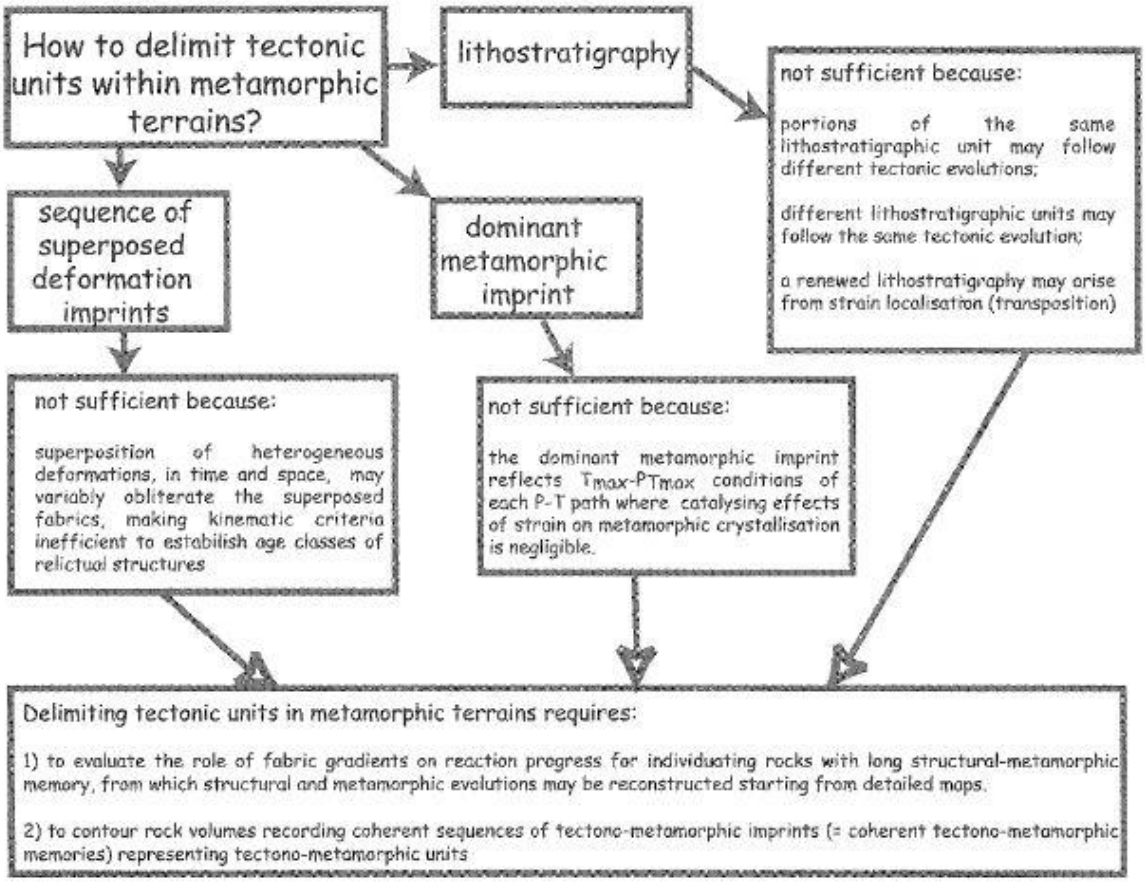

Figure 0.3 - Methodology for tectonic analysis of poly-deformed and poly-metamorphosed basement rocks and for definition of tectonic units (from Spalla et al., 2005).

Mineral-chemical analysis

Mineral chemical analyses were performed on different rock types form all the investigated domains. The measures have been focused on mineral assemblages occupying micro-sites characterized by 1) well constrained relationships between mineral growth and fabric development and 2) of suitable compositions for estimating metamorphic conditions. The aim of the mineral-chemical analysis is to highlight compositional variations in minerals, which are due to transient magmatic and metamorphic conditions. In fact, mineral chemical analysis is the base for quantitative and semi-quantitative estimates of (P-T) metamorphic conditions.

Mineral chemical analysis has been performed at Università degli Studi di Milano, mostly with a JEOL 8200 Super Probe (WDS), working at 15 kV accelerating voltage and a beam current of 5 nA. In few cases, analyses have been acquired by a Cambridge Instruments Stereoscan 360 (EDS) at 15 kV accelerating voltage and with a beam current of 15 nA, and by a JEOL JSM-IT 500 at 20 kV

accelerating voltage and with a current beam of 15 nA. Natural silicates were used as standards. Mineral chemical formulae were re-calculated using the JPT software (Zucali, 2004) at fixed O numbers, except when it is required estimating Fe^{2+} and Fe^{3+} (further specifications are in the text).
In addition, Trace and REE concentrations of igneous minerals from the Orobic basement have been determined by LA-ICP-MS at CNR Pavia. This analysis was aimed at speculating on the source rock nature by partition coefficient modeling (Wood and Blundy, 1997). Finally, trace and REE concentrations in zircon and other minerals from the A-M eclogites have been analyzed at Università degli Studi di Milano by LA-ICP-MS as support for interpreting U-Pb zircon geochronology.

Geochronology

This thesis includes the result of in-situ U-Pb zircon dating performed on the A-M eclogites and Ar/Ar amphibole dating performed on the A-M eclogites and the Orobic basement mafic dykes. Isotopic analyses were performed at Università degli Studi di Milano by LA-ICP-MS and at UMR Géoazur by STMS, respectively. Further details on the adopted techniques are in the text.

Thermobarometry and thermodynamic modeling

Igneous and metamorphic crystallization conditions are estimated by classic thermobarometry, which is based on cation exchange and net transfer reactions between coexisting phases. Information on the adopted calibrations follows in the text. Pseudosections were calculated by the Gibbs free energy minimization program THERIAK-DOMINO (De Capitani and Petrakakis, 2010), using results of WR analyses as starting composition. Two internally consistent thermodynamic dataset were used in this thesis: updated dataset 5 of Holland and Powell (1998), and updated dataset 6 of Holland and Powell (2011).

0.3 Organization of the Thesis

The issues addressed in this thesis are divided by prominent tectonic stage and locality. Tectonic events are here listed and discussed by going backwards from the youngest (the Alpine collision) to the oldest (the Variscan subduction). The paragraphs of this Thesis stand alone as independent papers already published on international peer-reviewed journals, or in the process of being submitted, or in preparation. Final discussions for each chapter collect the syntheses of major results.

The **first chapter** is focused on the post-Variscan and Alpine evolution of the A-M and Orobic basement, in the external domains of the Alps. These issues are intimately linked and actually indivisible since post-Variscan mafic dykes are taken as structural markers for constraining the Alpine tectono-metamorphic evolution of both these domains.

In the eastern A-M, we focused on two different localities, Valscura and Val du Haut Boréon. Here, calc-alkaline mafic dykes have been mapped at different scale and analyzed by whole rocks geochemistry and mineral chemistry. These dykes are of post-early Permian age since they intruded into early Permian granites and were subsequently intersected by Oligocene to Miocene Alpine shear zones (Corsini et al., 2004; Sanchez et al., 2011).
The Alpine foliation is locally observed in the dykes and supported by upper greenschist facies mineral assemblages that developed during Alpine collision. Syn-emplacement and Alpine metamorphic conditions are estimated by thermobarometry and thermodynamic modeling.
The results 1) allowed including the mafic dykes in the record of Permian-Triassic magmatism of the Alps and 2) led to a more accurate quantification of the Alpine metamorphic evolution of the A-M. The two chapters on the A-M mafic dykes are published in *BSGF-Earth Sciences Bulletin* (Filippi et al., 2019, 10.1051/bsgf/2019014) and *Lithos* (Filippi et al., 2020, 10.1016/j.lithos.2020.105653).

Alkaline mafic dykes are widespread in the Aprica and Passo Cavalcafiche tectono-metamorphic units, in the northeastern part of the Orobic basement (central Southern Alps). The dykes crosscut all the Variscan structures and were deformed and foliated during the Alpine convergence, as revealed by structural mapping at different scales. Whole rock geochemistry and mineral chemistry suggest that the alkaline mafic dykes emplaced at shallow crustal levels during continental rifting.
The Alpine foliation in the dykes is supported by upper greenschist to lower epidote-amphibolite facies minerals that may have developed either during on-going Alpine subduction or continental

collision, as suggested by the literature and envisaged by a preliminary numerical model. The alkaline mafic dykes of the Orobic basement are addressed in two paragraphs that will be submitted for publication.

The **second chapter** is focused on the Variscan collision. The Variscan collision is a central issue in the Orobic basement and M-T, where structures supported by Barrovian mineral assemblages are widespread. These two domains are considered external domains of the Southern Variscan belt. In the A-M, the theme of the Variscan collision is instead indirectly addressed in the following chapters by constraining the exhumation path of the mafic eclogites.

In the Orobic basement, and in particular in upper Valcamonica south of the Alpine Gallinera Thrust, Variscan metapelites were pervasively re-equilibrated under thermally perturbed state during late-collisional stages, during which andalusite porphyroblasts developed. Variscan collisional structures, supported by staurolite + garnet + white mica + biotite, as well as Variscan pre-collisional structures, supported by chloritoid + garnet + biotite + white mica, are locally preserved in the metapelites. This research has required detailed field analysis to constrain the relative chronology of superposed fabrics development and accurate P-T estimates to unravel the contrasting tectonic significance of these structures. This part is addressed in one paragraph.

In the Bormes Unit of the western M-T, two deformation events took place under Barrovian metamorphic conditions in the staurolite-kyanite-garnet zone. However, structures and mineral associations relating to previous stages of fabric development may have been found in low-strained domains. The identification of low-strained domains required preliminary structural mapping and microstructural analysis, but more efforts will be needed to fully address this topic. Results are presented in this paragraph including estimates of metamorphic conditions during the collisional and pre-collisional Variscan evolution. A correlation between the Orobic basement and the western M-T is thus proposed on the basis of lithostratigraphic affinity and similar tectonic evolution.

The **third chapter** is focused on the mafic eclogites of the A-M, on their protoliths, and on the tectono-metamorphic evolution the eclogites recorded. In the first paragraph, structural, geochemical, petrological, and geochronological data from different eclogite occurrences in the A-M are presented along with preliminary reconstructions of their Variscan tectono-metamorphic evolution. The re-equilibration under amphibolite facies conditions is constrained in time by Ar/Ar amphibole dating.

The first paragraph is published on the *International Journal of Earth Sciences* (Jouffray et al., 2020, 10.1007/s00531-020-01848-2).

The second paragraph focused on an eclogite boudin from the Tineè Complex, in the eastern A-M. In this rock, high-pressure minerals (garnet + omphacite + clinozoisite + quartz + rutile) are extraordinarily well preserved and allow decipher the thermal state at the time of the Variscan subduction. This eclogite has been analyzed for whole rock composition, mineral chemistry, and U-Pb zircon geochronology. The age and geochemical affinity of the protolith of this eclogite is constrained and discussed in the framework of the European Variscan belt.

0.4 Geological setting

The Central European Variscan belt

The Variscan belt has been the prominent mountain belt of Europe since the Devonian. The Variscan cycle culminated in the Carboniferous with continental collision between Baltica and Laurentia, to the north, and Gondwana, to the south, and the formation of Pangea. At that time, the continental collision was concurrent all over the European Variscan belt, testified by Barrovian metamorphic conditions in basement rocks. Flexural foreland basins developed on both side of the belt, north of the Variscan Front and at its southern termination (e.g. Matte, 1986; Franke and Engel, 1986; Martinez-Catalan et al., 2009; Aretz, 2016).

Many Gondwana-derived continental blocks are included in the Variscan belt (Armorica, Avalonia, etc.). These blocks are rimmed by oceanic units that, in many cases, were affected by Devonian high pressure metamorphism (e.g. Matte, 1998; Lardeaux et al., 2001; Martínez Catalán et al., 2007, 2009; Faure et al., 2009; Ballèvre et al., 2009, 2013; Schulmann et al., 2009, 2014; Berger et al., 2010; Lardeaux, 2014; Lardeaux et al., 2014; Paquette et al., 2017), and that are interpreted as oceanic suture zones. However, there is no consensus on the number of oceanic basins involved in the European Variscan belt and on their ages (Fig. 0.1; Regorda et al., 2020 and ref. therein).

Paleomagnetic and biostratigraphic data suggest that the Rheic Ocean opened at the beginning of the Ordovician time between Avalonia and Gondwana. From that moment, Avalonia rapidly migrated towards north, in response to the closure of the former Iapetus Ocean (Domeir, 2016). South of the Rheic Ocean, other continental blocks (Armorica, Central Iberian Massif, etc.) were separated from Gondwana by one or more oceanic basins. These are the Paleo-Tethys (also known as Middle Euorpean or Galice/Massif Central or Galice/Moldanubian Ocean), to the south, and the Saxo-Thuringian Ocean, to the north. However, the Saxo-Thuringian Ocean is generally considered as a branch of the Rheic Ocean since not clearly identified by paleomagnetic and biostratigraphic data. Finally, the Rheno-Hercynian Ocean opened between Avalonia and Armorica in Lower Devonian to late-Visean times (Edel et al., 2013; Franke et al., 2017, 2020 and ref. therein). The Rheno-Hercynian Ocean is nowadays envisaged by the Lizard Suture in southern Cornwall (e.g. Kirby, 1979; Floyd, 1984; Averbuch and Piromallo, 2012) and by other oceanic remnants in the Rhine Massif and in the Harz (Franke, 2000).

There are three main suture zones of the Variscan belt: first, the Galicia-Southern Brittany Suture, which is located between Gondowana and the Gondwana-derived continental blocks, on the southern

side of the belt (Fig. 0.1). It runs from the central Iberia (Coimbra-Cordoba Shear Zone) to southern Brittany (South Armorican Shear Suture Zone), form the northern French Massif Central to the Southern Bohemian Massif. In the Armorican Massif, the South Armorican Shear Suture Zone is partially superimposed on the former Eo-Variscan Suture (Fig. 0.1). The ophiolitic rocks of the Galicia-Southern Brittany Suture are dated between 490 and 470 Ma (Matte, 2001; Paquette et al., 2017; Lotout et al., 2018; Benmammar et al., 2020; Lotout et al., 2020). Second, the Teplà Suture (i.e. the Saxo-Thuringian Ocean), which runs between the Saxo-Thuringian and Moldanubian domains, and, third, the Rheic Suture between Armorica and Avalonia. Ophiolitic rocks at the northern side of the belt are dated between 500 and 450 Ma (Schulmann et al., 2005; Will et al., 2018).

The Paleo-Tethys and the Rheic Ocean closed by opposite subduction (e.g.: Stampfli et al., 2002, 2013; Regorda et al., 2020 and ref. therein). Old contribution on the northern part of the French Central Massif envisaged oceanic subduction at 430 – 400 Ma (Matte, 2001; Berger et al., 2010; Lardeaux, 2014 and ref. therein). Nowadays, most of the older HP ages are rejected because of out-of-date techniques (Paquette et al., 2017). More recent investigations on the Armorican Massif and southern French Central Massif constrain the HP events related to the Variscan subduction at around 380-355 Ma (Paquette et al., 2017; Lotout et al., 2018; Benmammar et al., 2020; Lotout et al., 2020). Similarly, high-pressure metamorphism on the northern side of the belt is dated between 380 and 330 Ma (Schulmann et al., 2005; Will et al., 2018). Devonian volcanic arcs and retro-arc basins on the continental blocks are further constraints on ages and positions of the oceanic subduction zones (Faure et al, 2008; Edel et al., 2018 and ref. therein).

Structure of the European Variscan belt

The Variscan orogeny is classically divided in four main litho-tectonic domains: the northern Rheno-Hercynian and Saxo-Thuringian domains, i.e. the external domains of the Variscan belt, and the southern Teplà – Barrandian and Moldanubian domains, i.e. the internal domains (Fig. 0.4). However, basement rocks in the Western and Eastern Moldanubian domain are markedly different in protolith ages, structural, metamorphic, and magmatic evolution (Lardeaux et al., 2014).

In the French Massif Central, the Moldanubian domain is in turn divided in Upper Gneiss Units, comprising high pressure rocks including felsic granulites, garnet/spinel peridotites, and eclogites, and the Lower Gneiss Units comprising paragneisses, orthogneisses, and amphibolites (Fig. 0.4, Lardeaux et al., 2014 and ref. therein). These rocks were pervasively re-equilibrated under Barrovian metamorphic conditions during the Variscan collision, between 360 and 325 Ma (Lardeaux et al., 2014 and ref. therein). At the base of the Upper Gneiss Unit, there is the Leptyno-Amphibolitic complex,

which is an important structural marker recognized in many parts of the European Variscan belt. The Leptyno-Amphibolitic complex is an association of mafic, ultramafic and acidic rocks that, in French Central Massif, derived from late Cambrian-Ordovician bimodal magmatic suites (Gebauer et al., 1981; Pin and Lancelot, 1982). According to the old literature, the northern part of the Leptyno-Amphibolitic complex experienced high-pressure metamorphism at around 432-408 Ma (Pin and Lancelot, 1982; Ducrot et al., 1983; Paquette et al., 1995), and subsequent amphibolite facies metamorphism at 345 ± 10 Ma (Pin and Lancelot, 1982). However, the age of the high–pressure event is nowadays comprised between 380 and 360 Ma (Lotout et al., 2018; Benmammar et al., 2020; Lotout et al., 2020). Beneath the Lower Gneiss Units other tectonic units are identified: the Visean-Namurian foreland turbiditic basin, the weakly metamorphosed southern Paleozoic fold-and-thrust belt comprising Cambrian to early Carboniferous sedimentary rocks, and the Parautochtonous Unit with greenschist to epidote-amphibolite facies meta-sediments (Lardeaux et al., 2014 and ref. therein).

In the western part of the Bohemian Massif, the Saxo – Thuringian Zone included Neoproterozoic crystalline basement and its Paleozoic sedimentary sequences which testify the development of a passive margin. Remnants of the Saxo-Thuringian Ocean are found in the Mariánské Lázně Complex and Erbendorf–Vohenstrauss Zone, which include eclogites derived from both passive margin and oceanic crust. The oceanic protholites are up to Cambrian in age (540 Ma, Timmermann et al., 2004) and the eclogite facies re-equilibration is dated at the Devonian (367-377 Ma, Beard et al., 1995). In contrast, Timmermann et al. (2004) envisage in the same rocks a post-eclogitic re-equilibration under upper amphibolite – granulite facies conditions at around 380 Ma. In the eastern Bohemian Massif, the Tepla-Barrandian Unit includes folded Lower Cambrian to Middle Devonian sedimentary sequences (Fig. 0.4; Lardeaux et al., 2014 and ref. therein). Barrovian metamorphism of Devonian age is locally described in the westernmost Tepla-Barrandian Unit (Timmermann et al., 2006). A calk-alkaline magmatic arc of late Devonian to early Carboniferous age, the Central Bohemian Plutonic Complex (346 – 370 Ma, Holub et al., 1997, Janoušek et al., 2006), is interposed between the Tepla-Barrandian Unit and the Moldanubian Units at east.

At top of the Moldanubian Units in the Bohemian Massif there is the Gfohl Unit (Fig. 0.4), which includes felsic granulites with orthogneisses, whose protoliths share Middle Ordovician to Silurian ages (Friedl et al., 2011), and minor mantle peridotites and eclogites. High pressure metamorphism in the Gfohl Unit is dated from late Devonian to early Carboniferous (Becker, 1997; Friedl et al., 2011), in contrast with the Devonian ages of the Mariánské Lázně Complex and Erbendorf–Vohenstrauss Zone to the west. High-K syenites (‘durbachites’) intruded into the Gfohl Unit at 335–348 Ma (Holub, 1997; Kusiak et al., 2010 and ref. therein). Just below the Gfohl Unit, there is the Varied Group that comprises meta-sediments interlayered with amphibolites and leptynites of Early Paleozoic to Late

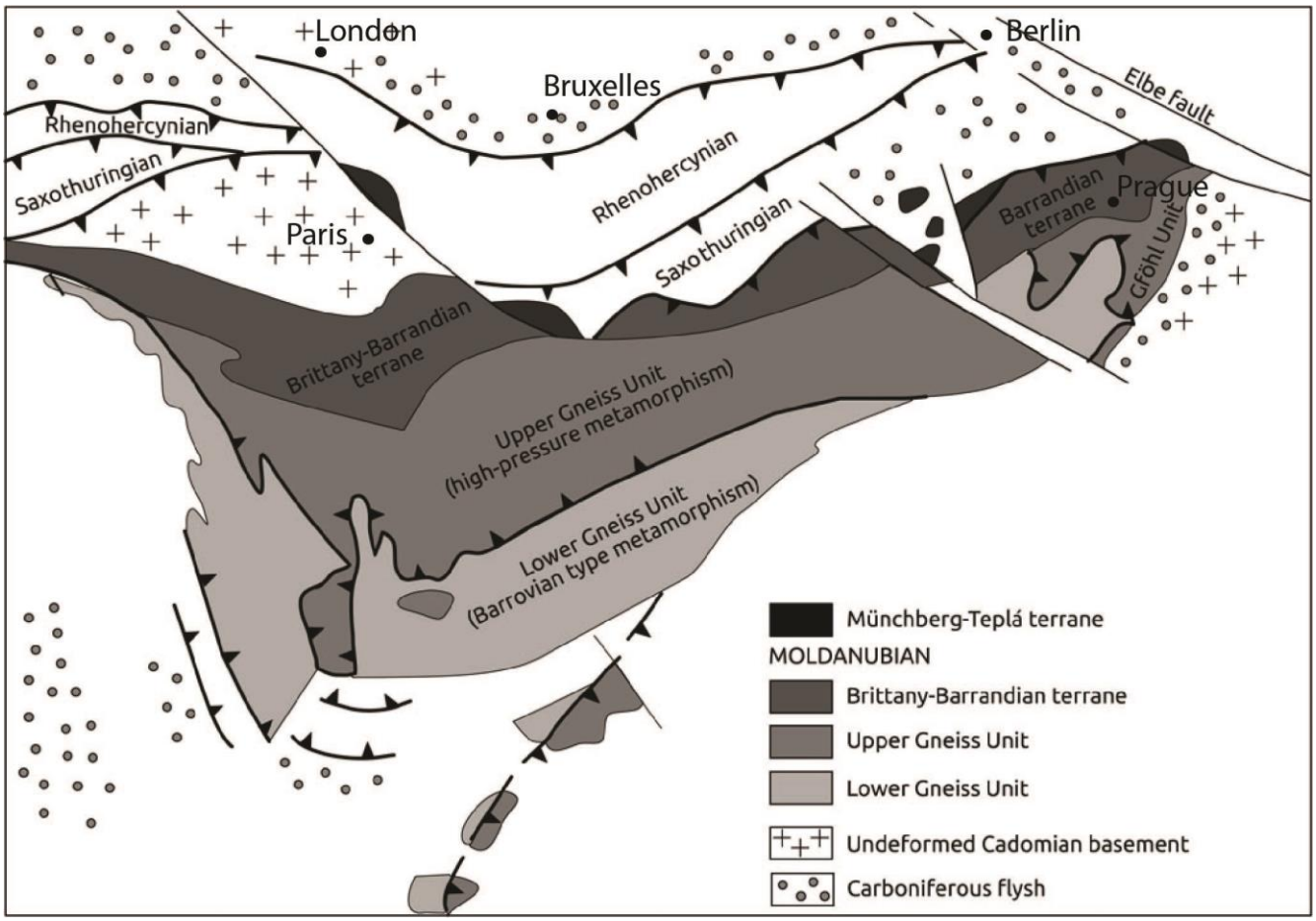

Figure 0.4 – Tectonic scheme of the European Variscan belt and its main litho-tectonic domains (from Lardeaux et al., 2014 and ref. therein).

Ordovician age (Košler et al., 2014), and the Monotonous Group that include paragneisses, orthogneisses, and amphibolites, whose protoliths are dated Proterozoic to Early Palaeozoic (Košler et al., 2014). Both these units pervasively retained Barrovian metamorphism under amphibolite facies conditions at around 350 – 330 Ma (Racek et al., 2006 and ref. therein).

The Southern Variscan belt

The Southern Variscan belt includes Calabria, Sicily, Sardinia, Corsica, and the M-T. The Southern Variscan belt formed a coherent block during the late collisional phase (Edel et al., 2014; 2018). Moreover, the Late-Carboniferous evolution of the southern External Crystalline Massif of the Alps is similar to that of the M-T, in particular in terms of kinematic (e.g. Corsini and Rolland, 2009; Simonetti et al., 2020), and they are considered as part of the Southern Variscan Belt. At odds, little is known about the pre-collisional evolution. Also for these reasons, correlations between the Southern Variscan and the central European Variscan belt are still controversial.

Four main tectonic domains have been distinguished in Sardinia: to the north the poly-metamorphic Migmatite Complex (the axial zone), which include small lenses of mafic eclogites and granulites (Carmignani et al., 1994; Cortesogno et al., 2004; Cruciani et al., 2010); the Internal Nappe Zone, which comprise Grt-St-Ky-bearing metapelites and paragneisses with rare garnet-bearing amphibolites and eclogites (Cortesogno et al., 2004), the External Nappe Zone, and the External Zone, these last units made up of low to very low-grade metamorphic rocks (Conti et al., 2001; Funedda and Oggiano, 2009; Pavanetto et al., 2012). The Asinara-Posada Shear Zone separates the Migmatite Complex and the Internal Nappe Zone (Carmignani et al., 1994; Frassi et al., 2015 and ref. therein), whose Barrovian metamorphic imprint is dated at 350 - 320 Ma (Del Moro et al., 1991; Carosi et al., 2012).
A similar zonation is envisaged in the M-T: low to very low-grade metamorphic rocks outcropping to the west and Grt-St-Ky-bearing metapelites, paragneisses, and orthogneisses to the east in the western M-T, whereas eclogite and granulite facies relics are locally found in the migmatites of eastern M-T (Schneider et al., 2014).
In Corsica, two main domains are distinguished: the Nappe Zone including greenschist to amphibolite facies orthogneisses, amphibolites, and metapelites, and the Migmatite complex, which includes eclogite boudins and a Leptyno-Amphibolite complex (e.g. Palagi et al., 1985; Rossi et al., 2009). Different generations of Carboniferous to Triassic intrusives are intruded in the Southern Variscan Belt. Further details on the late- to post-Variscan magmatism in this area are discussed in the next chapters.

The Variscan eclogites of the Southern Variscan belt have deserved considerable attention in the last years and are a reference to compare our results on the A-M eclogites. Protolith ages of the mafic eclogites in Sardinia are comprised between 460 and 450 Ma (e.g. Cortesogno et al., 2004; Giacomini et al., 2005; Franceschelli et al., 2007). The age of the eclogitic overprinting is poorly constrained at around 400 Ma (Franceschelli et al., 2007), due to pervasive resetting of the U-Pb system in zircon after re-equilibration under granulite to amphibolite facies conditions, likely attained at around 350-330 Ma (Giacomini et al., 2005; Franceschelli et al., 2007).
In Corsica, protolith ages of the Leptyno-Amphibolite complex are dated between 484 and 440 Ma, and experienced high pressure metamorphism likely at 420 – 400 Ma (Rossi et al., 2009 and ref. therein), followed by high-pressure granulite metamorphism at 360 Ma (Li et al., 2014).
The Leptyno-Amphibolite complexes of the eastern M-T are instead markedly older (548 - 507 Ma, Lancelot et al., 1995; Briand et al., 2002; Innocent et al., 2003) and the involvement in the Variscan

subduction is not clear. The age of the eclogite protoliths and of the high-pressure event in the western M-T is still unknown.

Variscan and pre-Variscan basement rocks of the Alps

Little is known about the pre-Variscan history in the Alpine region. Most of the reconstructions on the pre-Variscan history are based on the geochemistry of Neoproterozoic to early Paleozoic intrusive rocks, which were affected by pervasive Variscan and Alpine metamorphism and deep structural re-working. Late-Cadomian (Neoproterozoic – early Cambrian) meta-granitoids in the Alpine area (Penninic and eastern Austroalpine domains) are interpreted as remnants of a volcanic arcs developed at the time of the Cadomian oceanic subduction beneath Gondwana (Stampfli et al., 2002, 2013; Linnemann et al., 2007; Schaltegger and Gebauer, 1999; and ref. therein). The late Cambrian Chamrousse ophiolite (western Belledonne Massif, Helvetic domain) is interpreted as a Cambro-Ordovician back-arc basin precursor of the Rheic Ocean opening at the beginning of the Variscan cycle (Ménot et al., 1988; Stampfli et al., 2002, 2013; Guillot et al., 2009).

Variscan basement rocks are preserved in all the Alpine domains (Spalla et al., 2014 and ref. therein). In the External Crystalline Massifs (Helvetic domain) the Variscan basement comprise eclogites, granulites, amphibolites, and migmatites derived from Ordovician to Carboniferous meta-sediments and meta-granitoids (Paquette et al., 1989; von Raumer et al., 1999, Rubatto et al., 2010, Gosso et al., 2019). Widespread acidic and mafic intrusives testify continental rifting in the Ordovician (Rubatto et al., 2001; Rubatto et al., 2010). Eclogites and high-pressure granulites formed at the time of the Variscan subduction, but the age of the high-pressure peak is poorly constrained at around 340 Ma (Paquette et al., 1989; Colombo et al., 1994; Rubatto et al., 2010; Schulz and von Raumer, 2011). In contrast with these reconstructions, other authors consider the Ordovician magmatism as syn-subductive, in particular in the Gotthard Massif (Helvetic domain) and Strona-Ceneri Zone (western Southern Alps), where widespread Ordovician magmatism is coeval with pre-Variscan eclogite facies metamorphism dated at around 470–450 Ma (e.g. Gebauer et al., 1988; Zurbriggen, 2005; Franz and Romer, 2007).

Variscan basement rocks with Pre-Cambrian to early Palaeozoic protolith ages are widespread in the Penninic domain (Desmons and Mercier, 1993; von Raumer, 1998; Desmons et al., 1999). Variscan eclogites are found in the Grand St. Bernard nappe (Thélin et al., 1993; Desmons et al., 1999; Bergomi et al., 2017), Savona Massif (Messiga et al., 1992; Giacomini et al., 2007), Adula and Suretta nappes

in the Central Alps (Nussbaum et al., 1998; Dale and Holland, 2003; Liati et al., 2009), as well as in the Penninic basement south-east of Tauern window, in the Eastern Alps (Droop, 1983; Zimmermann and Franz, 1989; Droop et al., 1990; von Quadt et al., 1997; Schulz and Bombach, 2003). In the Penninic Unit, the mafic protoliths of the Variscan eclogites are dated from 600 to 470 Ma (Giacomini et al., 2007; Liati et al.,, 2009) and the high-pressure metamorphism from 420 to 330 Ma (von Quadt et al., 1997; Giacomini et al., 2007; Liati et al., 2009). Most of the available ages are referred to the collisional / post-collisional Variscan evolution attained under amphibolite facies conditions (340-320 Ma, Monié, 1990; Bussy et al., 1996; Giacomini et al., 2007).

Variscan metabasites preserving high-pressure assemblages are found in different localities of the Eastern Australpine Domain (Oetzal-Stubai, Silvretta and Languard-Campo nappes, Ulten zone) as small lenses of MORB affinity within metapelites pervasively re-eqilibrated under amphibolite facies conditions (Miller and Thoni, 1995; Godard et al., 1996; Morten et al., 2004; Sassi et al., 2004; Konzett et al., 2005). The mafic protoliths emplaced at 530-520 Ma (Miller and Thöni, 1995), whereas the eclogitic event followed at 360-320 Ma (e.g. Miller and Thöni, 1995; Tumiati et al., 2003; Krenn et al., 2012).

In the Southern Alps, the metamorphic imprint of the Variscan subduction is solely envisaged by epidote-amphibolite facies assemblages supporting syn-subductive Variscan structures (Spalla et al., 1999; Spalla et al., 2014 and ref. therein). The eclogites of the Southern Alps (Borghi, 1991) are considered pre-Variscan in age (Franz and Romer, 2007) like in the Gotthard Massif. In the Southern Alps, the Variscan collision occurred at around 340-330 Ma under amphibolite facies conditions (e.g. Spalla and Gosso, 1999 and ref. therein).

Chapter 1

Alpine evolution of Variscan basement rocks in the external domains of the Alps

The Argentera-Mercantour Massif

1.1 Structure of lamprophyres: a discriminant marker for Variscan and Alpine tectonics in the Argentera-Mercantour Massif, Maritime Alps

Marco Filippi, Davide Zanoni, Guido Gosso, Jean-Marc Lardeaux, Chrystèle Verati, Maria Iole Spalla.
BSGF 2019, 190, 12, 10.1051/bsgf/2019014

Abstract

Structural and microstructural analysis is carried out in two sites of the Argentera-Mercantour Massif, Valscura and Val du Haut Boréon, where swarms of lamprophyres intruded into Variscan migmatites and early Permian granitoids. Efforts aim at defining the structural relationships between lamprophyres and country rocks, and at constraining the structural and metamorphic evolution the dykes record. Mesoscale structural data are synthesised in geologic maps originally surveyed at 1/10 000 scale, supported by form-surface maps at 1/100 scale.

The lamprophyres are magnesian, calc-alkalic to alkali-calcic, and metaluminous; they emplaced at very shallow crustal levels intersecting three generations of ductile structures in the host migmatites (D1, D2, D3). Epidote- and actinolite-bearing mineral assemblages result from late-intrusive hydrothermal circulation that has not affected the host rocks. Mylonitic shear zones of Alpine age (D4) are continuous through migmatites, granites, and lamprophyres: in these latter, they are supported by albite, actinolite, biotite, chlorite, epidote, phengite, and titanite.

This detailed multi-scale structural analysis, coupled with major and trace elements geochemistry, highlights two main results: i) the lamprophyres, which post-date both the late- to post-collisional

"high-Mg" and the "low-Mg" granitoids, reflect the last magmatic event in the Argentera-Mercantour Massif and are related to the Permian-Triassic lithospheric thinning; ii) the metamorphic assemblages that support the Alpine shear zones in the lamprophyres are consistent with the transition between the greenschist and amphibolite facies conditions.

Introduction

Mafic dykes are structural and metamorphic markers of the first order for distinguishing between superposed tectonic and/or metamorphic cycles in orogenic systems, as highlighted in pioneering to recent contributions (e.g. Myers, 1978; Mørk, 1985; Williams, 1985: Spalla et al., 2000; Baletti et al., 2012; Gosso et al., 2015; Zanoni et al., 2016). In the Argentera-Mercantour Massif, a portion of deep Variscan crust reactivated during the Alpine collision, swarms of pre-Alpine lamprophyres have been known for over sixty years (Faure-Muret, 1955; Bortolami and Sacchi, 1968; Malaroda et al., 1970; Compagnoni et al., 2010). Since these lamprophyres intruded into Variscan migmatites and early Permian granitoids and were subsequently deformed and metamorphosed, they are appropriate markers to distinguish between Variscan and Alpine syn-metamorphic structures in the basement rocks of the Argentera-Mercantour Massif.

The purpose of this paper is to present and discuss the multi-scale structural analysis we have carried out in two localities, Valscura and Val du Haut Boréon, where the lamprophyres are widespread. Major and trace element compositions are investigated to frame the Argentera-Mercantour lamprophyres in the record of the Permian and Triassic magmatism of the Southern Variscan belt.

Geological outline

The late- to post-collisional magmatism in the Southern Variscan belt

Two main magmatic cycles of late Carboniferous to Triassic ages are described in the Southern Variscan belt. The first cycle comprises calc-alkaline tonalites, granodiorites, and monzogranites, as well as metaluminous to peraluminous rhyolites and dacites (Cortesogno et al., 1998; Atzori et al., 2000; Paquette et al., 2003; Traversa et al., 2003; Gaggero et al., 2007; Romano et al., 2011; Rossi et al., 2015). The second cycle is of alkaline affinity and includes peralkaline to slightly peraluminous A-type granites and rhyolites, as well as alkaline diorites, andesites, basalts, and minor lamprophyres (Cortesogno et al., 1998; Traversa et al., 2003; Cocherie et al., 2005; Gaggero et al., 2007). Mafic and ultramafic layered complexes and transitional to tholeiitic basalts and andesites are generally ascribed

to the alkaline cycle, although their ages are partially in overlapping with those of the calc-alkaline suites (Paquette et al., 2003; Cocherie et al., 2005).

Field relationships highlight that, in most of the cases, alkaline magmas intruded into the calc-alkaline magmatic suites and bimodal alkaline lavas are the youngest in the volcano-sedimentary sequences (Leroy and Cabanis, 1993; Cortesogno et al., 1998; Traversa et al., 2003; Dallagiovanna et al., 2009; Rossi et al., 2015). Moreover, the alkaline magmatism locally lasted up to Triassic times (Vatin-Pérignon et al., 1972; Vatin-Pérignon et al., 1974; Buffet and Aumaitre, 1979; Gaggero et al., 2007; Barca et al., 2010; Cirrincione et al., 2014; Cirrincione et al., 2016). A mantle contribution in the genesis of these magmatic rocks is undisputed (e.g. Rottura et al., 1998; Traversa et al., 2003; Gaggero et al., 2007; Renna et al., 2007; Duchesne et al., 2013; Cirrincione et al., 2016).

Composite calc-alkaline intrusives emplaced in Corsica at 308-304 Ma (U-Pb zircon dating, Paquette et al., 2003, Rossi et al., 2015) and were followed by calc-alkaline monzogranites, calc-alkaline volcano-sedimentary sequences, and transitional to tholeiitic mafic intrusives, dated between 293 and 279 Ma (U-Pb zircon dating, Rossi et al., 2002, Paquette et al., 2003, Cocherie et al., 2005, Renna et al., 2007; Rossi et al., 2015). Similarly, the A-type granites of Corsica are dated between 290 and 278 Ma (U-Pb zircon dating, Cocherie et al., 2005, Rossi et al., 2015).

In Sardinia, the calc-alkaline cycle started between 321 and 313 Ma, with the apex at 311-307 Ma (U-Pb zircon dating; Casini et al., 2012). Here, calc-alkaline granodiorites and diorites emplaced between 295 to 286 Ma, whereas transitional to alkaline basalts came after at 254 to 248 Ma (hornblende 40Ar/39Ar dating, Gaggero et al., 2007).

Alkali-calcic and calc-alkalic granites emplaced in the Maures-Tanneron Massif at around 300 Ma and were intruded by slightly younger calc-alkaline dolerite dykes (biotite and muscovite 40Ar/39Ar dating, Morillon et al., 2000; U-Pb zircon dating, Duchesne et al., 2013). A-type rhyolites and younger transitional tholeiitic lavas and dykes in the volcano-sedimentary sequence of the adjacent Estrél basin are dated between 278 and 264 Ma (40Ar/39Ar feldspar dating, Zheng et al., 1992; Poitrasson and Pin, 1998; Lapierre et al., 1999); whereas, in the Toulon basin, Middle Permian transitional tholeiitic to alkaline basalts post-date Lower to Middle Permian calc-alkaline rhyolites (Leroy and Cabanis, 1993). Middle to Upper Triassic alkaline to transitional basalts and late Triassic to early Jurassic tholeiites are also reported in Calabria and Sicily (Barca et al., 2010; Cirrincione et al., 2014; Cirrincione et al., 2016).

In the Alpine area, very few lamprophyres intruding ferriferous alkali-calcic granites of late Carboniferous ages are described in the Mont-Blanc and Aiguilles Rouges Massifs (von Raumer, 1987; Bussy et al., 2000). In the Pelvoux Massif, minor swarms of alkaline mafic dykes intersect Carboniferous granites and calc-alkaline diorite dykes, whereas alkaline volcaniclastics are

interlayered in the Triassic sedimentary sequences (Vatin-Pérignon et al., 1972; Vatin-Pérignon et al., 1974; Buffet and Aumaitre, 1979). In the Ligurian basement, calc-alkaline rhyolites, andesites, and rhyodacites of 286 to 272 Ma are post-dated by alkaline rhyolites dated at 258.5 ± 2.8 Ma (Buzzi and Gaggero, 2008; U-Pb zircon dating, Dallagiovanna et al., 2009). Permian and Triassic calc-alkaline to alkaline intrusives and volcanics are also abundant in the Southern Alps (Giobbi Origoni et al., 1988; Sloman, 1989; Rottura et al., 1998; Garuti et al., 2001; Cassinis et al., 2007; Schaltegger and Brack, 2007; Locmelis et al., 2016; Casetta et al., 2018; Zanoni and Spalla, 2018; Storck et al., 2019).

The Argentera-Mercantour Massif

The crystalline basement of the Argentera-Mercantour Massif (Fig. 1.1.1) consists of migmatitic orthogneisses, paragneisses, and amphibolites that include pre-anatectic relics of eclogites, high-pressure mafic granulites, ultramafites and calc-silicates (Faure-Muret, 1955; Malaroda et al., 1970; Blasi, 1971; Bortolami et al., 1974; Bogdanoff and Ploquin, 1980; Bogdanoff, 1986; Latouche and Bogdanoff, 1987; Paquette et al., 1989; Rubatto et al., 2001; Ferrando et al., 2008; Compagnoni et al., 2010; Rubatto et al., 2010). The widespread migmatisation, dated at 323 ± 12 Ma, came after the emplacement of monzonite dykes at 332 ± 3 Ma (U-Pb zircon dating, Rubatto et al., 2001). These monzonites are part of "high-Mg number" suites of the External Crystalline Massifs (Debon and Lemmet, 1999), which are interpreted as products of a late-collisional event that involved melting of an enriched mantle source triggered by slab window or slab break-off (Banzet, 1987; von Raumer et al., 2014).

The late- to post-Variscan exhumation of the migmatitic complex is testified by the structural and metamorphic evolution of the Valletta Shear Zone (VSZ, Fig 1.1.1), a mayor dextral transpressive mylonite that has been active between 330 and 314 Ma during retrograde metamorphism (Faure-Muret, 1955; Musumeci and Colombo, 2002; Corsini et al., 2004; Carosi et al., 2016; Simonetti et al., 2018). The surface exposition of the Argentera-Mercantour Massif is constrained by late Carboniferous to Permian siliciclastic sequences that unconformably rest on the migmatites (Faure-Muret, 1955; Malaroda et al., 1970; Bortolami et al., 1974). At the same time, sets of brittle structures accommodated the emplacement of the Central Granite (Boucarut, 1967; Compagnoni et al., 2010), whose age (292 ± 10 Ma, Rb-Sr muscovite dating, Ferrara and Malaroda, 1969; 299-296 Ma, 40Ar/39Ar muscovite dating, Corsini et al., 2004) and composition match those of late- to post-Variscan "low-Mg number suites" of the External Massifs (Debon and Lemmet, 1999). However, rhyolites, dacites, and basalts in the sedimentary covers testify that magmatic activity in the Argentera-Mercantour Massif lasted, at least, through the Permian (Faure-Muret, 1955; Malaroda et al., 1970;

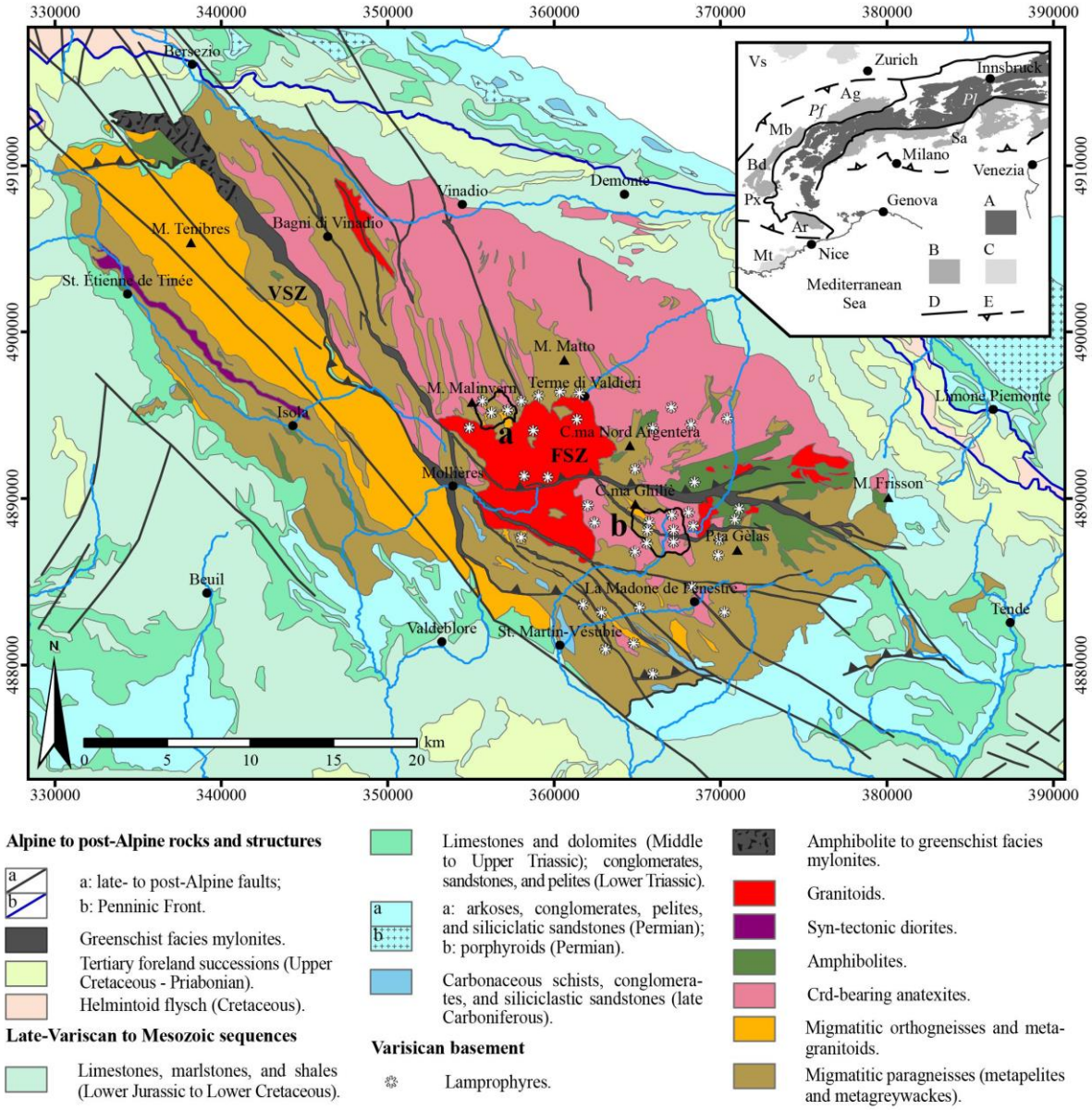

Figure 2.1.1 - Simplified geologic map of the Argentera-Mercantour Massif (after Malaroda et al., 1970, Carosi et al., 2016, Gosso et al., 2019, and refs. therein). Black profiles highlight Valscura (a) and Val du Haut Boréon (b). Abbreviations: FSZ: Fremamorta Shear Zone; VSZ: Valletta Shear Zone (also known as Ferrere-Mollières Shear Zone). Projected coordinate system: WGS 84-UTM32N. Insert: tectonic sketch of the Alps: A: Variscan basement rocks into the axial zone of the Alps; B: Variscan basement rocks at the external margins of the Alps (Ag: Aar-Gothard Massif, Ar: Argentera-Mercantour Massif, Bd: Belledonne Massif, Mb: Mont Blanc Massif, Px: Pelvoux Massif, Sa: Southern Alps); C: Variscan basement rocks external to the Alpine fronts (Mt: Maures-Tanneron Massif, Vs: Vosges); D: lithospheric-scale structures delimiting the axial zone of the Alps (Pf: Penninic Front, Pl: Periadriatic Lineament); E: Alpine fronts.

Romain and Vernet, 1978). In the stratigraphic record, syn-extensional siliciclastic sequences of Permian age (Aicard et al., 1968; Delteil et al., 2003) were firstly followed by Middle to Upper Triassic evaporites and shallow-water limestones, and later by the Lower Jurassic deepening

successions of the European passive margin (Faure-Muret, 1955; Malaroda et al., 1970; Lemoine et al., 1986; Dardeau, 1988).

In the Alpine framework, the Argentera-Mercantour Massif is a segment of thinned European crust shortened during the continental collision (Bogdanoff et al., 2000; Bigot-Cormier et al., 2006; Schwartz et al., 2007; Schreiber et al., 2010; Lardeaux, 2014). The massif attained its maximum burial in the early Oligocene, by overthrusting of internally derived nappes (Kerckhove, 1969; Merle and Brun, 1984; Evans and Elliott, 1999; Ford et al., 1999; Simon-Labric et al., 2009; Sanchez et al., 2010). The VSZ was severely re-activated as a dextral strike-slip mylonite and several inverse shear zones, mainly E-W striking, developed in response to Alpine transpression (Corsini et al., 2004; Sanchez et al., 2011a; Simonetti et al., 2018).

An Alpine metamorphic event affecting Carboniferous covers and early Permian granitoids is described since Boucarut (1967). However, in the lack of structural and/or chronological markers, the Alpine metamorphic overprint in migmatites is hardly distinguishable from that coming along with the late-Variscan exhumation, as Bortolami et al. (1974) point out. 40Ar/39Ar ages of phengite crystals supporting greenschist facies mylonites constrain the Alpine metamorphism between 34 and 20 Ma (Corsini et al., 2004; Sanchez et al., 2011a). In particular, the oldest Alpine shear zones (34 Ma) developed at T = 375 ± 25°C and P = 0.7 - 0.9 GPa, whereas the youngest (22 - 20 Ma) at 375 ± 25°C and 0.4 - 0.6 GPa (Sanchez et al., 2011a). Thermobarometric estimates on Permian-Triassic meta-sedimentary rocks at the southern edge of the Argentera-Mercantour Massif confirm T > 300°C and P > 0.3 GPa for the Alpine metamorphic event (Attal, 2000). The same shear zones, still keeping the same kinematics under brittle-ductile conditions, are accountable for the final exhumation of the basement rocks: exhumation below 150°C occurred at 8 Ma (Apatite FT dating) and this stage was followed by slower exhumation rates driven by the transcurrent tectonic context (Tricart et al., 2004; Bigot-Cormier et al., 2006; Baietto et al., 2009; Sanchez et al., 2010; Sanchez et al., 2011b; Leclère et al., 2014; Bauve et al., 2014).

Principal rocks associations: high-resolution mapping

Valscura site

The basement rocks of Valscura comprise migmatitic paragneisses, meta-granitoids and cordierite-bearing anatexites, with minor migmatitic amphibolites (Fig. 1.1.2). Some outcrops, in which lamprophyres are widely surfacing, are mapped in detail for highlighting structural and petrogenetic relationships with the country rocks (Fig. 1.1.3).

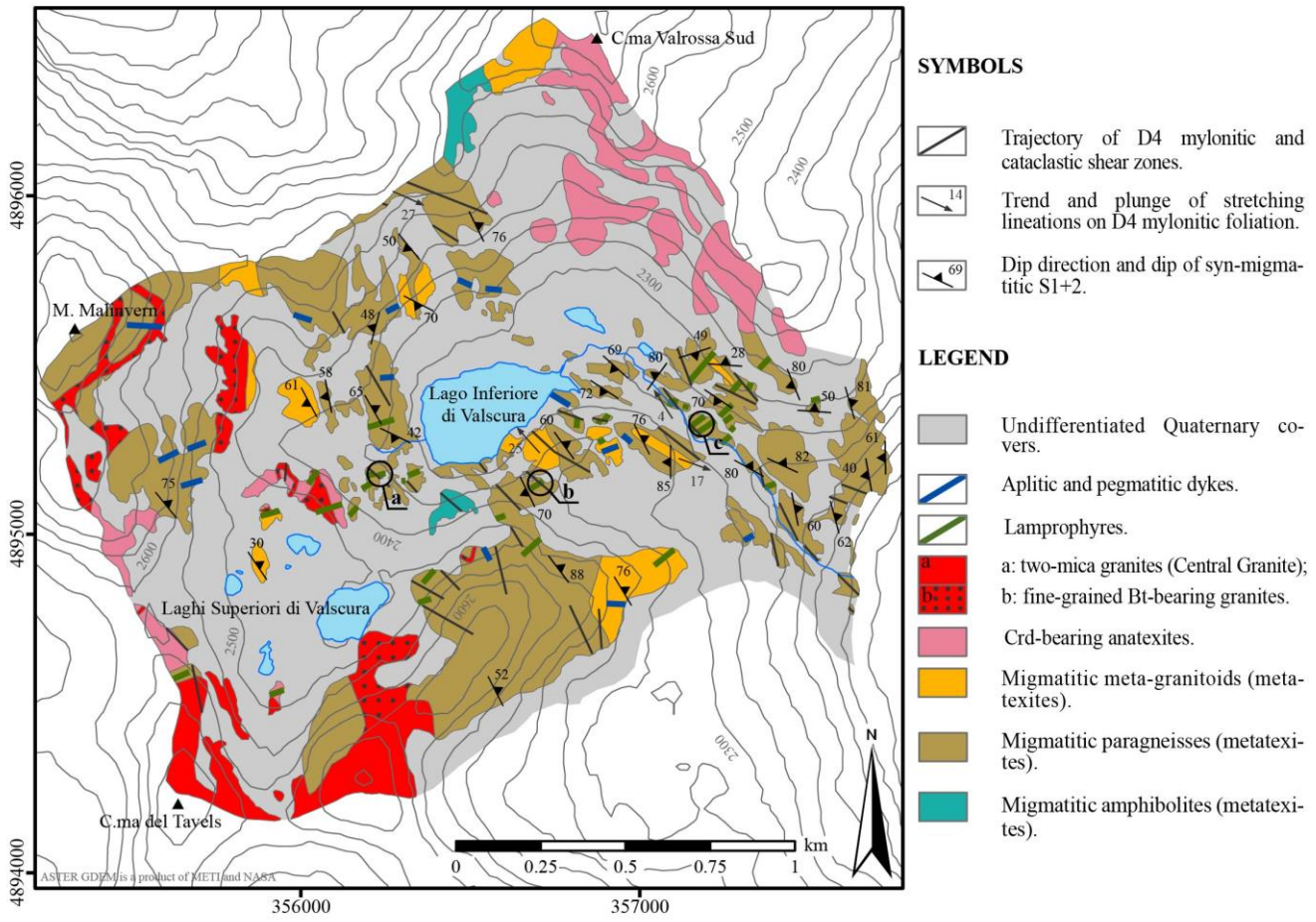

Figure 1.1.2. Geo-structural map of Valscura (cf. Fig. 1.1.1 for location), upgraded after Montani (2004). Projected coordinate system: WGS 84-UTM 32N. Positions of outcrop scale form-surface maps at 1/100 scale are reported (cf. Fig. 1.1.3).

Millimetre-thick films of biotite, fine-grained trails of garnet and sillimanite, and quartz-feldspar leucosomes in centimetre-thick bands outline the migmatitic foliation in paragneisses (Fig. 1.1.4a).

The migmatitic foliation in meta-granitoids is, instead, supported by anastomosing films of biotite, and quartz-feldspar leucosomes occupy microlithons and strain shadow domains around porphyroclasts of igneous K-feldspar. Veins of cordierite-bearing leucosome crosscut the migmatitic foliation in both paragneisses and meta-granitoids. The anatexites are leucocratic rocks mainly composed of quartz + feldspar ± cordierite leucosomes, which result from high degrees of partial melting. Disarticulated and convolute films of biotite support the migmatitic foliation in the anatexites. Chlorite, titanite, white-mica, and rare epidote replace migmatitic mineral assemblages in all the rock types.

Leucosomes and granitoids of different textures and compositions are hosted in the migmatites: fine-grained biotite-bearing granites outcrop between M. Malinvern and Laghi Superiori di Valscura, whereas coarse-grained two-mica-bearing granites (i.e. the Central Granite) surface at C.ma del Tavels

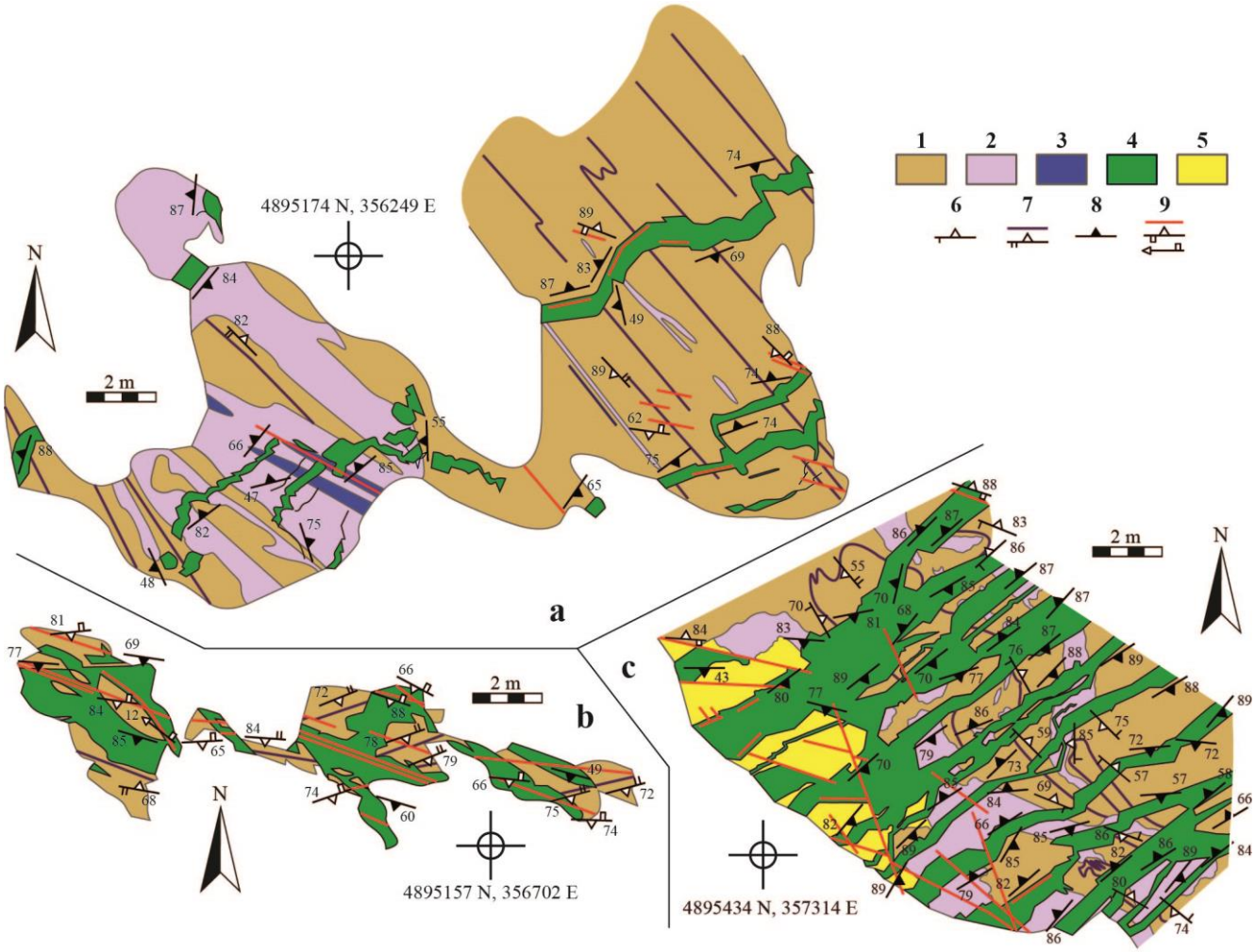

Figure 1.1.3. Form-surface maps of selected outcrops in Valscura, mapped at 1/100 scale (locations are in Fig 1.1.2). Legend: 1: migmatitic paragneisses; 2: leucosome-rich domains; 3: amphibolite relics; 4: lamprophyres; 5: migmatitic paragneisses whose rock forming minerals are pervasively replaced by epidote and chlorite; 6: trajectory, dip direction and dip of S1 foliation; 7: dip direction.

(Fig. 1.1.2). Migmatites and granites were then intruded by aplitic to pegmatitic dykes, consisting of plagioclase, quartz, K-feldspar, white mica with rare biotite and/or garnet, and, lastly, by swarms of lamprophyres.

The intrusive contacts between lamprophyres and country rocks are sharp and outlined by chilled margins (Fig. 1.1.4b). The lamprophyres that are less than a metre-thick are spessartites, with euhedral phenocrysts of amphiboles into a greenish aphanitic groundmass (Fig. 1.1.4c). Amphibole phenocrysts in spessartites may show shape-preferred orientation (SPO) suggesting a magmatic foliation; in other cases, they are randomly oriented, often in glomeroporphyric aggregates. Millimetre-sized vesicles are common in the external parts of the porphyritic dykes, and they can be either empty or filled by aggregates of plagioclase, minor amphibole, or by calcite. The thickest lamprophyres, classified as

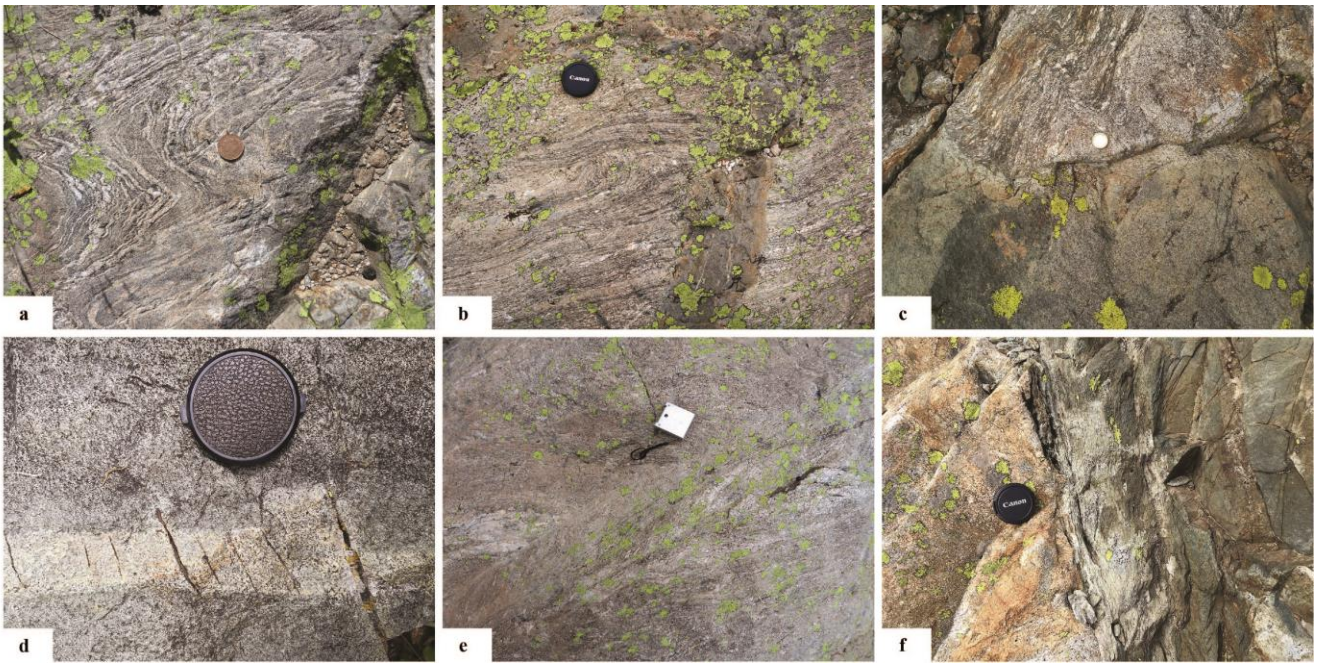

Figure. 1.1.4. Rock types and structures of Valscura: a: D3 folds bending D2 axial planes in migmatitic paragneisses (coin for scale); b: D2 fold hinges transposed into S2 foliation planes. Centimetre-thick lamprophyre with unfoliated chilled margins crosscut S2 (camera cap for scale); c: spessartite dyke with not foliated to slightly foliated chilled margin intersecting D3 folds in migmatitic paragneisses (coin for scale); d: leuco-appinite vein into an appinite dyke; primary igneous minerals are locally replaced by aggregates of epidote and chlorite (yellowish in picture). Millimetre-sized D4 mineralised tensional veins are arranged along the leuco-appinite vein (camera cap for scale); e: D4 mylonitic foliations supported by chlorite and minor biotite interrupting and displacing to the right S1+2 foliation planes (compass for scale); f: spessartite dyke intruding fine-grained biotite-bearing granite. D4 foliation is pervasive along lamprophyre dyke walls (camera cap for scale).

appinites according to IUGS (Le Maitre et al., 2002), are phaneritic, with randomly oriented crystals of amphibole, plagioclase, minor K-feldspar, and rare quartz. Sharp to lobate fragments of appinite may be enclosed into leuco-appinites, which consist of plagioclase, K-feldpsar, quartz, and minor amphibole: such internal structures suggest that mingling and magmatic brecciation occurred during their emplacement. Aggregates of chlorite and epidote extensively replace igneous minerals in the lamprophyres (Fig. 1.1.4d), as well as early formed mineral assemblages in the country rocks close to the dyke walls. Very localised mylonitic shear zones crosscut migmatites, granitoids and lamprophyres. In the migmatites, these structures are supported by chlorite, phengite, minor biotite, and very rare actinolite (Figs. 1.1.2, 1.1.3 and 1.1.4e).

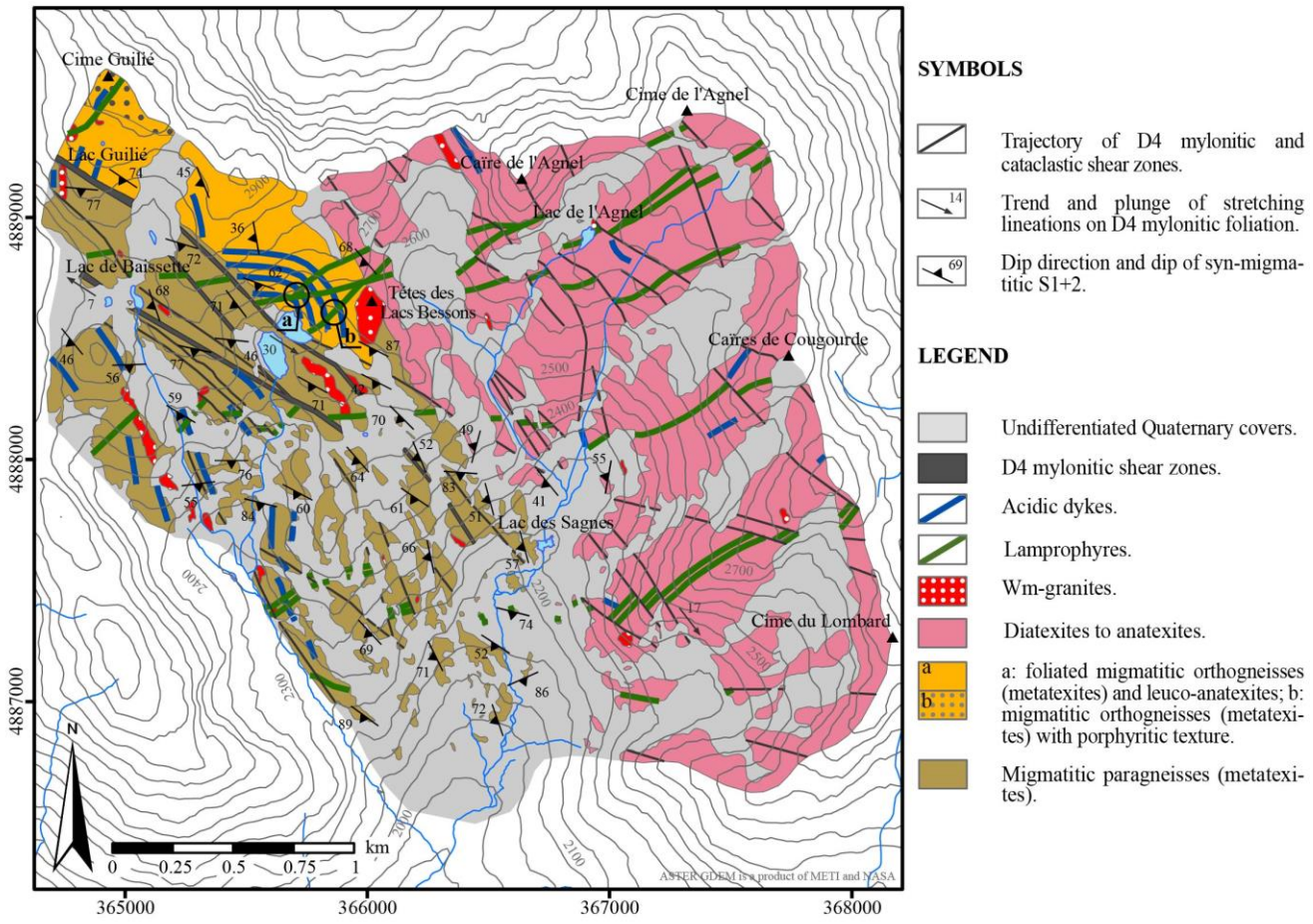

Figure. 1.1.5. Geo-structural map of Val du Haut Boréon (cf. Fig. 1.1.1 to localise), upgraded after Blasi (1968). Projected coordinate system: WGS 84-UTM32N. Lacs Bessons stand at 4888500 N, 365647 E. Positions of outcrop scale form-surface maps are reported (cf. Fig. 1.1.6).

Val du Haut Boréon site

The migmatitic paragneisses of Val du Haut Boréon are locally interlayered with metre-thick layers of amphibolites and grade into diatexites and anatexites towards the eastern edge of the mapped area (Fig. 1.1.5); structures and supporting mineral assemblages are similar to those described in Valscura. Heterogeneously deformed migmatitic orthogneisses with granulite relics, already described as meta-volcanics by Colombo et al. (1993) and Rubatto et al. (2001), outcrop around C.ma Ghilié (Fig. 1.1.5). Cordierite-bearing pegmatites, white mica-bearing granite pockets, and aplite dykes are widespread in the migmatitic complex: all these intrusives are crosscut by the lamprophyres. Structural study of outcrops, where the lamprophyres display clear structural relationships with the country rocks, requests mapping at 1/100 scale (Fig. 1.1.6).

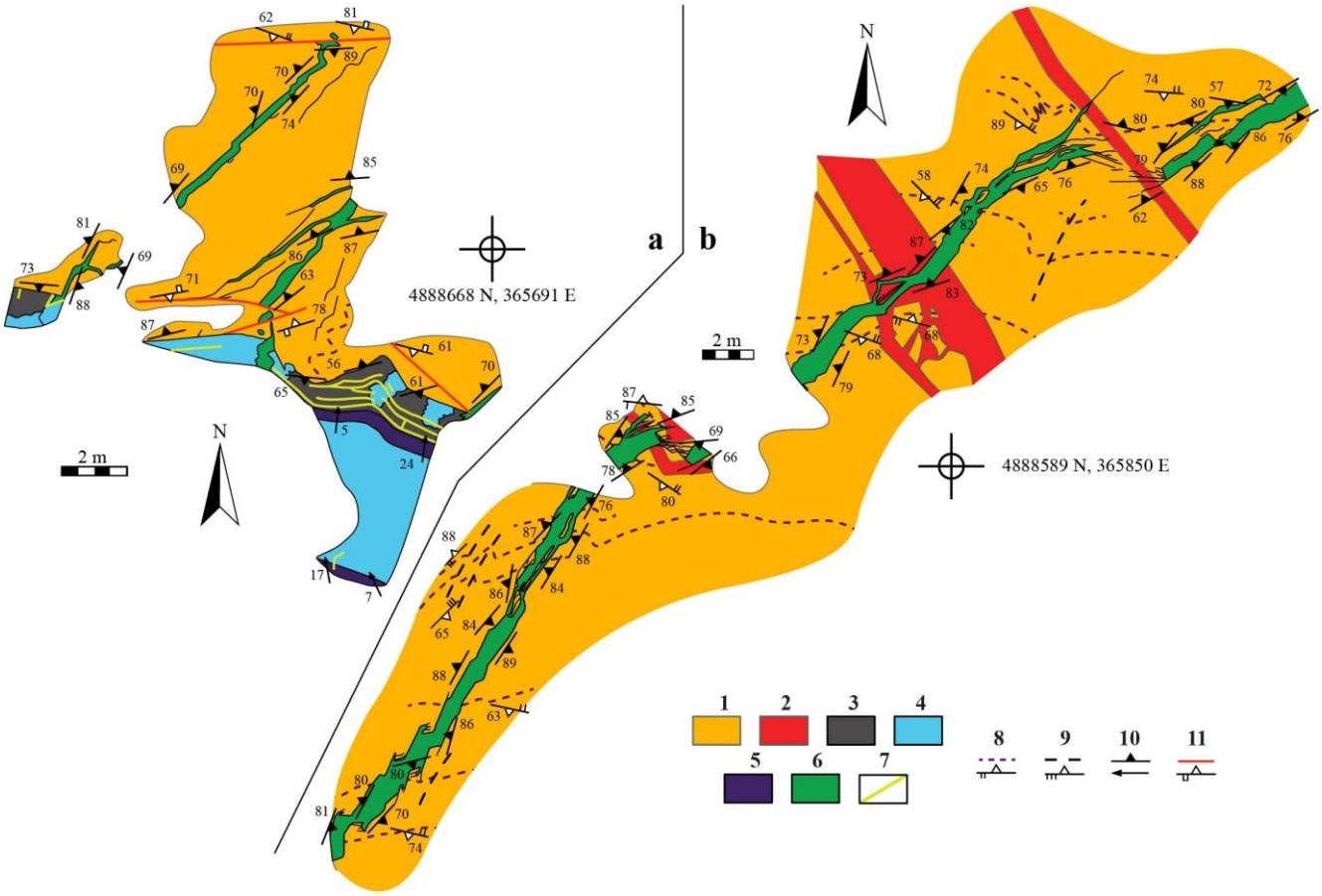

Figure. 1.1.6. Form-surface maps of selected outcrops in Val du Haut Boréon mapped at 1/100 scale (locations in Fig 1.1.5). 5. Legend: 1: leuco-anatexites; 2: white mica-bearing granitic dykes; 3: melanocratic spessartites; 4: mingled appinites and leuco-appinites; 5: comb layered appinites; 6: spessartites; 7: leucocratic veins; 8: trajectory, dip direction, and dip of S1+2 foliation; 9: dip direction and dip of D3 axial plane; 10: dip direction and dip of lamprophyre dyke walls, trend and plunge of amphibole phenocrysts in comb layers; 11: trajectory, dip direction and dip of D4 mylonitic to stylolitic foliation. Scale bars, north arrows, and geo-referenced points are assigned to each outcrop (projected coordinate system: WGS 84-UTM 32N).

In Val du Haut Boréon, the lamprophyres show higher textural and compositional heterogeneities in comparison with those from Valscura, although they are characterised by chilled margins as well (Fig. 1.1.7a). Very rare grains of clinopyroxene, locally in glomeroporphyric aggregates, are found together with phenocrysts of amphibole in up to metre-thick and NW-SE striking spessartites. Vesicles, mainly filled by feldspar, igneous amphibole, or by calcite, are arranged in layers parallel to the dyke walls. A single E-W-striking dyke of 10 metres of thickness runs through all the Val du Haut Boréon from its northwestern edge to Cime de l'Agnel (Fig. 1.1.5): at Lacs Bessons (Figs. 1.1.5 and 1.1.6) it displays a symmetrical structure with two metre-thick bands of melanocratic spessartites along its margins (Fig. 1.1.7a and 1.1.7b) and appinites and leuco-appinites at core (fig. 1.1.7c). Melanocratic spessartites are formed by rounded to angular amphibole-rich domains of millimetre to centimetre size enclosed into a

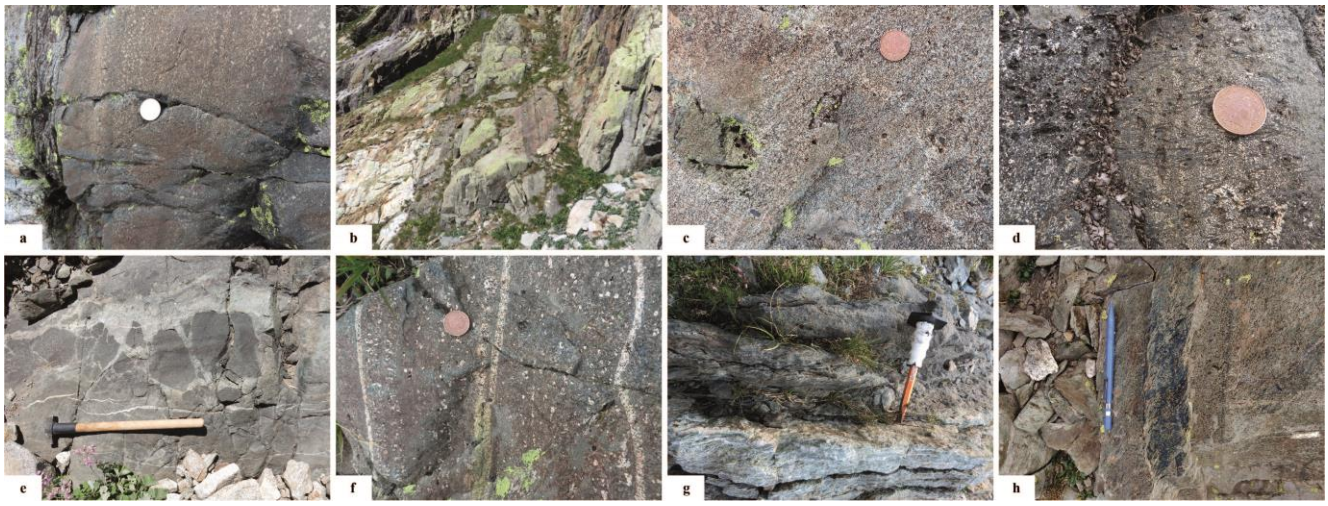

Figure. 1.1.7. Rock types and structures of Val du Haut Boréon: a: foliated chilled margin and vesicle-rich layers running parallel to melanocratic appinite dyke walls (coin for scale); b: the 10-metre-thick mafic dyke of Lacs Bessons and its symmetrical structure; c: appinite enclaves mingled in leuco-appinite at the core of the main mafic dykes of Lacs Bessons. Appinite and leuco-appinite may be pervasively replaced by granoblastic aggregates of epidote and chlorite, i.e. at the left margin (coin for scale); d: comb layered appinite with centimeter-sized amphibole phenocrysts perpendicular to the dyke walls. The fine-grained matrix is locally replaced by greenish aggregates of epidote and chlorite (coin for scale); e: disrupted fragments of melanocratic spessartite into appinite and leuco-appinite groundmass; leucocratic veins crosscut the edges of the fragments (hammer for scale); f: leucocratic veins within melanocratic spessartite characterised by layers of vesicles; at the bottom, the central leucocratic vein is widely replaced by epidote and chlorite (coin for scale); g: mylonitic shear zone of Alpine age crosscutting the dyke of Lacs Bessons. The mafic dyke is affected by a composite foliation where S and C surfaces are mainly supported by biotite and chlorite; S-C structure geometry are consistent with the sense of displacement of the dyke (cf. Fig. 1.1.5) (chisel for scale); h: S-C structures suggesting sinistral sense of shear along the wall of a spessartite dyke (pencil for scale).

mesocratic matrix, and include vesicle-rich layers. In the central part, lobate to angular enclaves of appinites are mingled together with leuco-appinites, as a consequence of different, but concomitant, magmatic pulses (Fig. 1.1.7c). Comb layers, outlined by phenocrysts of amphibole of centimetre size interlayred with fine-grained domains, divide the appinites from the melanocratic spessartites and define two metre-thick bands (Figs. 1.1.6 and 1.1.7d). Amphibole phenocrysts in comb layers are arranged in fan-shaped aggregates, which are almost orthogonal with respect to the dyke walls. Locally, melanocratic spessartites are directly in contact with the appinites: here, fragments of comb layered appinites and melanocratic spessartites, which locally preserve chilled margins, are included in the central part of the dyke (Fig. 1.1.7e). NE-SW striking spessartite dykes intersect the external parts of the main dyke at Lacs Bessons and intrusive contacts are lobate (Fig. 1.1.6); conversely, they seem to be coalescent with appinites and leuco-appinites at its core. Centimetre-thick leucocratic veins follow the margins of the main dyke and crosscut the melanocratic spessartites and, in few cases, the leuco-appinites (Figs. 1.1.7e and 1.1.7f). Similarly to Valscura, igneous minerals are widely replaced

by fine-grained aggregates of epidote and chlorite, which grew in spotted domains, mainly localised in coarse-grained appinite or in and around the leucocratic veins (Figs. 1.1.7c and 1.1.7f): such pervasive pseudomorphosis is not observed in the migmatites away from the dyke walls. Migmatites, granitoids, and lamprophyres are intersected by ductile to cataclastic shear zones (Figs. 1.1.7g and 1.1.7h): the mineral assemblages that support mylonitic and stylolitic foliations in lamprophyres will be the topic of the next paragraphs.

Finite Strain Pattern

Valscura site

The pervasive structure developed in the migmatitic complex of Valscura is the composite fabric S1+2 that defines the boundaries between migmatitic paragneisses and migmatitic meta-granitoids. Relics of S1 and earlier formed veins of leucosome are preserved as hinges of tight to isoclinal D2 folds characterised by sub-horizontal and N- to NW-trending axes (Fig. 1.1.8). S1 and S2 axial plane foliation mainly dip to SW or to NE. S2 is locally affected by grain size reduction, as it occurs between Laghi Inferiori and Laghi Superiori di Valscura (Figs. 1.1.2 and 1.1.4b). Since newly formed cordierite-bearing leucosome veins crosscut D2 fold limbs and leucosomes fill saddle-reefs in D2 fold hinges, D2 developed under migmatitic conditions.

S2 was refolded during D3, which resulted in open to tight folds of metric wavelength (Fig. 1.1.4a), characterised by sub-vertical axes and by steep axial planes dipping NW or N (Fig. 1.1.8). A chlorite and phengite-bearing axial plane foliation (S3), dipping NW or SE (Fig. 1.1.8), is locally coupled with D3 folds. D3 folds are crosscut by granitoids and vertical to sub-vertical, NE-SW striking, lamprophyres (Figs. 1.1.4c and 1.1.8). Local deviation from the average striking likely reflects primary irregularities of the lamprophyre dyke walls (cf. Fig. 1.1.3).

Afterwards, sub-vertical NW-SE and minor E-W striking D4 mylonitic shear zones developed in the basement rocks (Fig. 1.1.8). NW-SE striking D4 mylonites are characterised by strike-slip dextral shearing, as suggested by S-C geometries, by sub-horizontal mineral lineation on shear planes, and by the offset of the lamprophyre dyke walls. The chilled margins were re-activated as shear surfaces during D4 (Fig. 1.1.4f) and stylolitic films, coupled with mineralised tension veins, developed. Field relationships, shear sense indicators, and supporting mineral assemblages allow correlating the D4 shear zones to the regional scale structures of Alpine age (Corsini et al., 2004; Baietto et al., 2009; Sanchez et al., 2011a; Leclère et al., 2014).

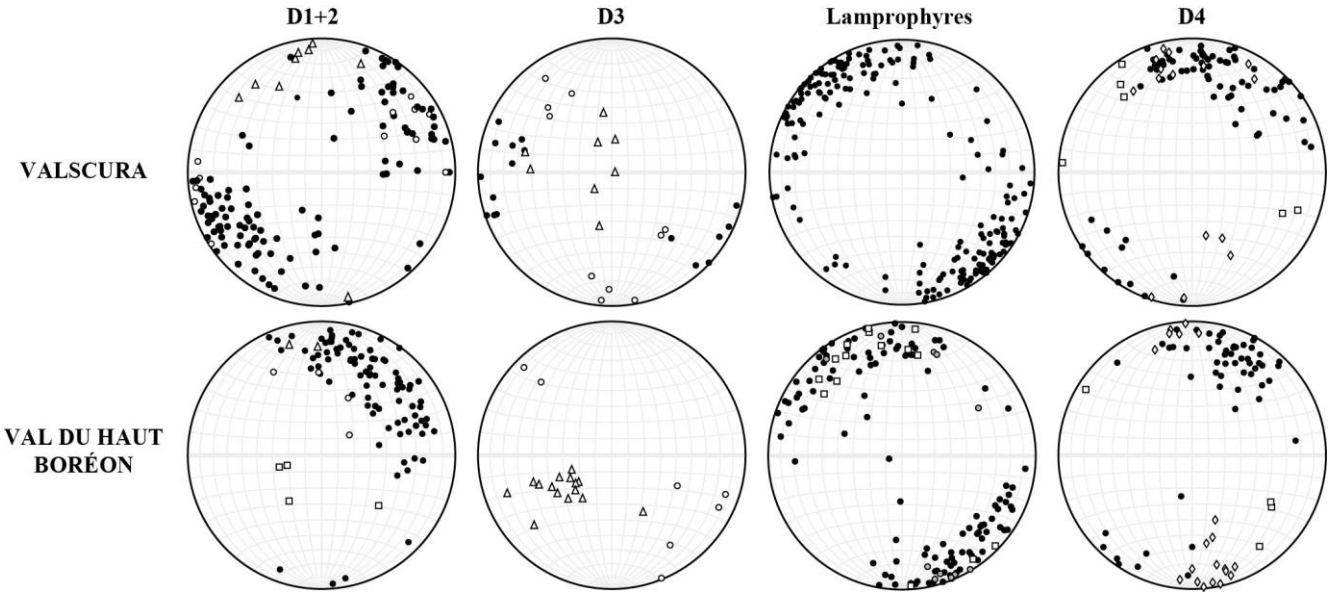

Figure. 1.1.8. Stereographic projections of structural data (equal-area, lower-hemisphere), divided by relative chronology of deformative and intrusive events. Legend: D1+2: circles = poles of S1+2 (111 data from Valscura, 89 data from Val du Haut Boréon); open squares = mineral lineations on S1+2 (4 data from Val du Haut Boréon); open circles = poles of axial planes of D2 folds (12 data from Valscura, 4 data from Val du Haut Boréon); open triangles = axes of D2 folds (9 data from Valscura, 2 data from Val du Haut Boréon). D3: circles = poles of S3 (17 data from Valscura); open circles = poles of axial planes of D3 folds (10 data from Valscura, 7 data from Val du Haut Boréon); open triangles = axes of D3 folds (8 data from Valscura, 15 data from Val du Haut Boréon). Lamprophyres: circles = poles of dyke walls (195 data from Valscura, 116 data from Val du Haut Boréon); grey circles = poles of leucocratic veins (11 data from Val du Haut Boréon); open squares = amphibole-supported lineations in comb layers (15 data from Val du Haut Boréon). D4: circles = poles of mylonitic foliations (76 data from Valscura, 56 data from Val du Haut Boréon); open squares = stretching lineations on D4 shear zones (6 data from Valscura, 4 data from Val du Haut Boréon); open diamonds = poles of D4 stylolitic and mylonitic foliations along lamprophyre dyke walls (15 data from Valscura; 19 data from Val du Haut Boréon).

Val du Haut Boréon site

The dominant structure in the basement rocks of Val du Haut Boréon is the composite fabric S1+2, which results from the superposition of D2 tight to isoclinal folds on S1. Both D1 and D2 structures developed under migmatitic conditions, as suggested by leucosome in microlithons, and by leucosome veins crosscutting D2 hinges and limbs. D2 folds are generally isoclinal and fold limbs are parallel to SW-dipping D2 axial planes (Fig. 1.1.8). D2 stretching lineation in L to S-L syn-migmatitic mylonites in migmatitic orthogneisses between Lac Guillié and Téte du Lacs Bessons, dips 40-70° to SW. S2 is bent by D3 open folds of metric wavelength (Figs. 1.1.6), characterised by axes plunging to SW and axial surfaces dipping either to NW or to SE. D3 folds are intersected by white mica-bearing granite and aplite dykes.

All these rocks and structures are crosscut by sub-vertical NE-SW striking lamprophyres and by the E-W trending dyke of Lacs Bessons. The intrusive contacts between lamprophyres and country rocks are sharp and made angulated by syn-intrusive fracturing. Dykes are locally arranged in en-echelon systems, indicating emplacement contemporaneous to sinistral shearing (Fig. 1.1.6). Migmatites, granites and lamprophyres are, in turn, displaced by the NW-SE striking ductile to cataclastic D4 shear zones, characterized by S-C surfaces and sub-horizontal stretching lineations consistent with dextral sense of shear (Figs. 1.1.5 and 1.1.8). During D4, the intrusive contacts of lamprophyres were locally reactivated as sinistral shear planes, as testified by S-C foliations along the chilled margins (Fig. 1.1.7h).

Whole rock geochemistry

Lamprophyres are analysed for major and trace elements at SARM, "Centre de Recherché Petrographiques et Geochimiques" (CNRS, Vandoeuvre-les-Nancy, France) by ICP-OES and ICP-MS, respectively. Information on the procedure, precision and accuracy is specified by Carignan et al. (2001). Analyses are carried out on 11 unfoliated samples from both the studied sites that do not appear significantly metamorphosed at meso- and micro-scale. Major and trace element compositions are reported in Table 1.1.1.

All the analysed samples share a calc-alkaline high-K character. Silica content of lamprophyres varies from 51 to 60 %wt and the transition to the more silicic magmas is associated with decreasing of MgO, Fe_2O_3 and CaO, as well as increasing of Al_2O_3 and K_2O amount. The MALI indexes plot either in the calc-alkalic or in the alkali-calcic fields (Fig. 1.1.9a); A/CNK ratios from 0.66 to 1.15 correspond to metaluminous to slightly peraluminous melts (Fig. 1.1.9b). Lamprophyres are classified as magnesian in the Fe-number diagram of Frost et al. (2001) (Fig. 1.1.9c), whereas in the Mg-number-B classification scheme of Debon and Le Fort (1988) they plot in close proximity to the "critical line" that divides the "magnesian" from the "ferriferous" field.

The MORB-normalised spider diagram highlights humped patterns: the lamprophyres are markedly enriched in Sr, K, Rb, Ba, and Th, whereas the Ti and Y contents plot close to MORB values (Fig. 1.1.9d). The concentrations of Ni and Cr, which likely testify the mantle influence on the genesis of the melts, widely range from 83 to 6 ppm and from 290 to 15 ppm, respectively, the content of V decreases from 332 to 68 ppm with the increase of the silica content from 50.96 to 56.17 %wt. The geochemical signatures of the Argentera-Mercantour lamprophyres are thus consistent with crustal contamination of mantle-derived magmas.

	Val du Haut Boréon									Valscura	
	sp	sp	mel sp	mel sp	mel sp	c-l ap	ap	ap	leuco ap	sp	ap
	LMA6	**LMC22**	**B168A**	**B168B**	**LMC13**	**LMC8**	**LMC9**	**LMC25**	**B169**	**LMD2**	**LMB26**
SiO_2	54.56	53.28	58.36	53.28	53.16	55.98	60.21	53.05	56.17	50.96	54.24
TiO_2	1.58	1.38	0.83	1.37	1.13	0.93	0.73	1.19	0.80	1.18	1.12
Al_2O_3	15.28	16.31	17.53	15.93	14.73	20.10	17.65	14.41	21.08	13.22	15.97
FeOt	8.08	7.91	5.33	7.16	7.99	5.52	5.38	8.06	5.11	9.65	7.06
MgO	4.83	6.83	2.92	6.35	5.93	2.61	4.15	5.78	2.11	8.31	6.15
CaO	4.28	3.98	5.42	7.11	7.12	4.95	4.94	7.25	5.12	8.41	7.59
Na_2O	4.13	2.75	3.97	4.15	3.98	4.31	2.89	4.08	4.13	1.98	3.08
K_2O	1.82	2.23	2.22	2.26	1.61	1.75	2.19	1.72	2.05	1.26	2.11
P_2O_5	0.72	0.38	0.32	0.57	0.67	0.43	0.21	0.95	0.44	0.96	0.74
MnO	0.15	0.12	0.10	0.11	0.10	0.13	0.08	0.13	0.11	0.15	0.11
LOI	2.85	3.10	1.42	1.10	1.88	1.75	1.45	1.63	1.52	2.21	1.47
total	98.28	98.27	98.42	99.39	98.30	98.46	99.88	98.25	98.64	98.29	99.64
Mg#	0.37	0.46	0.35	0.47	0.43	0.32	0.44	0.42	0.29	0.46	0.47
Rb	100.2	71.8	76.9	75.5	65.5	84.4	81.4	58.4	85.7	54.3	75.2
Ba	258	398.5	1183	1078	875.8	1769	1027	835.3	1889	628	1075
Sr	269	373	772	528	479	1017	436	457	1048	320	494
Pb	21.6	22.8	26.9	25.2	24.2	35.0	8.0	23.6	35.3	13.8	26.1
Th	6.6	5.5	5.4	6.2	6.6	5.3	4.2	4.3	5.2	4.5	5.6
Zr	274	182	193	234	230	357	254	227	381	117	238
Ta	6.8	3.3	3.6	4.3	4.1	4.4	5.2	3.9	3.9	3.7	5.9
Y	43	31	20	34	38	17	15	38	15	47	32
Nb	16	10	12	10	12	10	10	13	10	14	10
Cr	17	20	15	191	94	17	290	92	17	66	185
Ni	33	83	7	64	27	6	26	28	6	14	70
Co	12.8	17.3	12.5	26.1	26.2	6.0	16.5	26.5	5.7	35.2	26.8
V	144	332	111	212	213	70	113	214	68	373	213
Ga	18.7	22.2	21.1	22.2	21.3	24.0	20.1	21.5	24.3	21.4	22.1
Cu	8.7	11.3	5.7	17.9	35.9	8.3	20.2	38.5	8.6	20.5	19.2

Table 1.1.1. Major (wt.%) and trace (ppm) element concentrations of lamprophyres from Valscura and Val du Haut Boréon. Abbreviations: sp: spessartite; mel sp: melanocratic spessartite; c-l ap: comb layered appinite; ap: appinite; leuco ap: leuco-appinite.

Lamprophyre microstructures

Timing of mineral growth inferred by microstructural analysis is indicated by alphanumeric labels, in which capital letters I and M stand for igneous and metamorphic mineral assemblages, associated with progressive numerals related to subsequent igneous and metamorphic stages. Mineral abbreviations are from Whitney and Evans (2010).

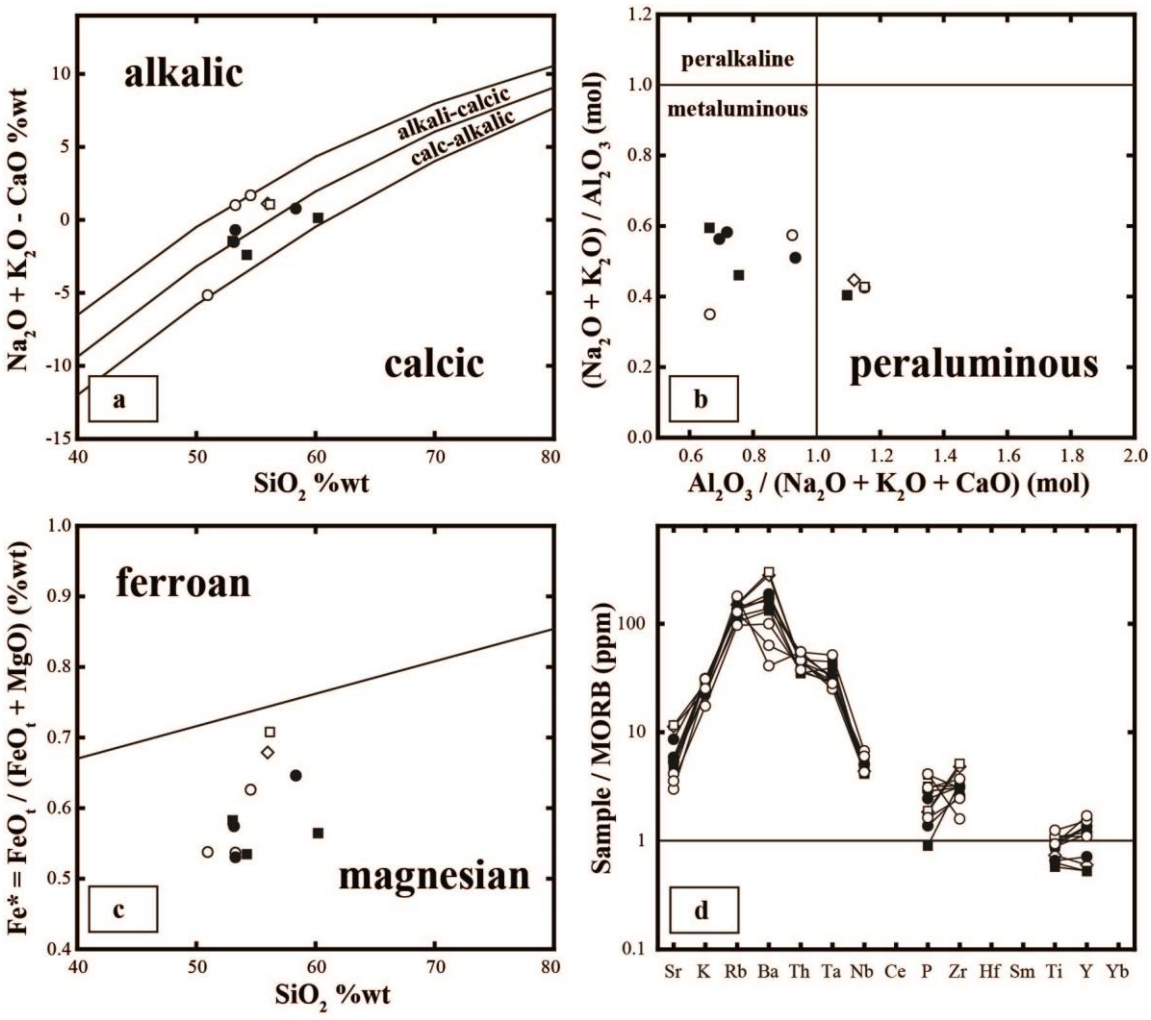

Figure. 1.1.9. Geochemical classification diagrams of igneous rocks (Frost et al., 2001): a: modified alkali-lime index (MALI); b: Al saturation index (ASI); c: Fe-number vs SiO_2 %wt; d: multi-element patterns normalised to MORB values (Sun and McDonough, 1989). Legend: square: appinite; open square: leuco-appinite; circle: melanocratic spessartite; open circle: spessartite; open diamond: comb layered appinite.

Igneous microstructures

Lamprophyres are mainly constituted by igneous amphibole and plagioclase. AmpI1 is brown, euhedral to subhedral, and commonly twinned (mineral abbreviations are from Whitney and Evans, 2010). It displays oscillatory compositional zoning (Fig. 1.1.10a) and, in few cases, preserves dark brown cores with corroded boundaries. PlI1 is in subhedral crystals or small laths, usually forming simple or polysynthetic twins. Glomeroporphyric aggregates of clinopyroxene occur in the spessartites from Val du Haut Boréon (Fig. 1.1.10b), whereas aggregates of chlorite, titanite, and biotite have entirely replaced euhedral crystals likely of igneous biotite or clinopyroxene, in both aphanitic and

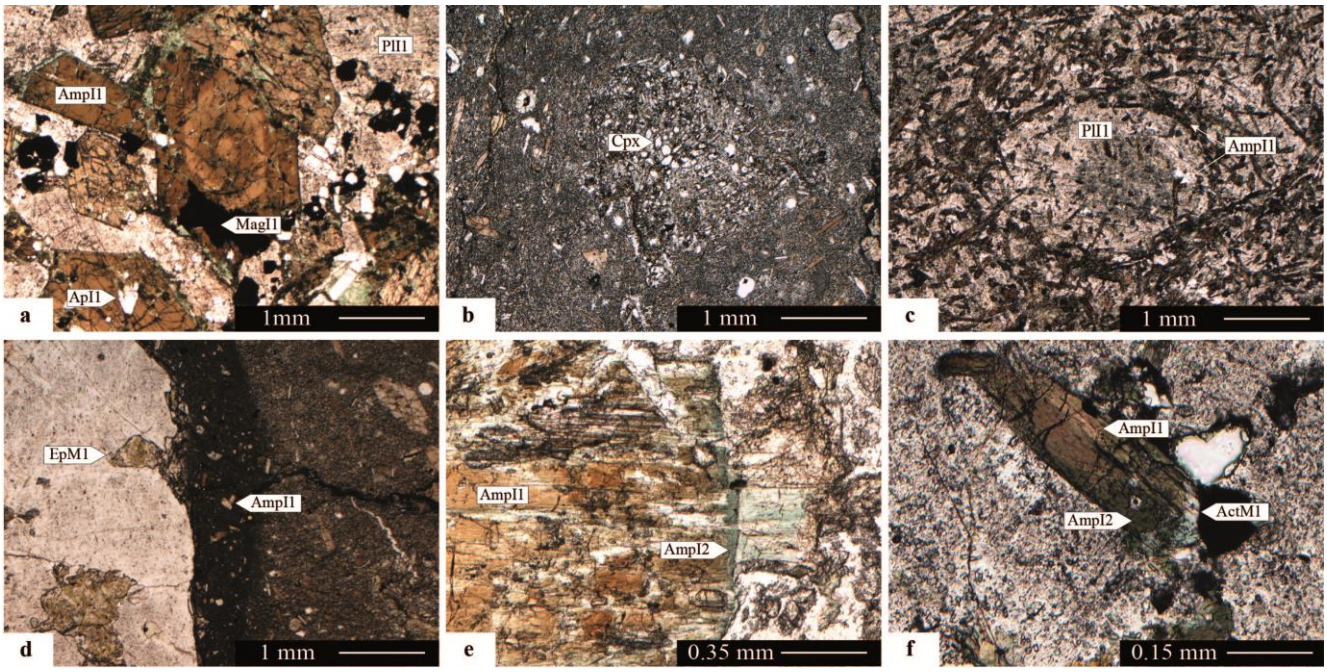

Figure. 1.1.10. Igneous mineral assemblages and microstructures characterising the lamprophyres of Valscura and Val du Haut Boréon: a: euhedral to subhedral crystals of brown AmpI1 and PlI1 partially including ApI1 and MgtI1 in appinite, Val du Haut Boréon. AmpI1 displays oscillatory compositional zoning; b: aggregates of sub-millimetre sized igneous clinopyroxene in spessartite, Val du Haut Boréon; c: vesicles filled by PlI1 and AmpI1 in melanocratic spessartite, Val du Haut Boréon. Phenocrysts of AmpI1 are tangentially oriented around the vescicle; d: chilled margin marking the intrusive contact between a spessartite dyke and the host migmatite in Val du Haut Boréon. Micro-phenocrysts of AmpI1 are within the chilled margin domain; aggregates of EpM1 (see next paragraph) developed in both the rock types close to the intrusive contact; e: zoned crystal of brown AmpI1 rimmed by dark-green AmpI2 in appinite, Valscura; f: leucocratic vein where a phenocryst of AmpI1 is firstly overgrown by dark-green AmpI2 and then by colourless ActM1 (see next paragraph), Val du Haut Boréon. All pictures are taken by plane polarized light.

phaneritic rocks. Accessory apatite, magnetite, and ilmenite are included within AmpI1 and PlI1 in the phaneritic rock types (Fig. 1.1.10a), or lie within the groundmass in the spessartites.

In appinites and leuco-appinites, up to centimetre-sized crystals of AmpI1 are randomly oriented and associated with smaller subhedral to interstitial grains of PlI1, KfsI1, and rare QzI1. Mingling structures between appinites and leuco-appinites are highlighted by modal variations of AmpI1 and PlI1.

Spessartites are highly heterogeneous in term of textures: sub-millimetric phenocrysts of AmpI1 typically occur within a microcrystalline groundmass, or together with twinned laths of PlI1. In few cases, phenocrysts of AmpI1 are partly to entirely enclosed in up to centimetre-sized crystals of PlI1, conveying sub-ophitic to ophitic textures. Strain-free phenocrysts of AmpI1 and laths of PlI1 with SPO support the magmatic foliation in spessartites. Approaching the chilled margins, the SPO of crystals supporting the magmatic foliation is progressively more pervasive and homogeneous.

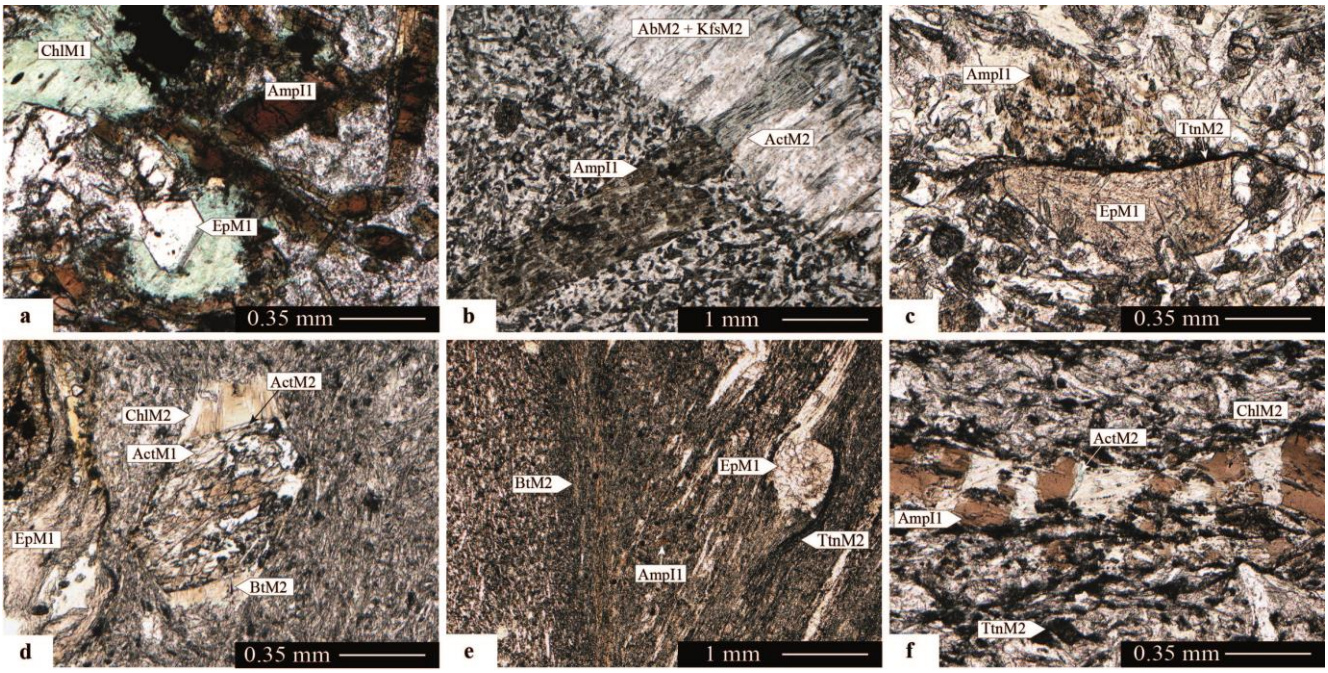

Figure. 1.1.11. Metamorphic mineral assemblages and microstructures characterizing the lamprophyres of Valscura and Val du Haut Boréon: a: granoblastic aggregates of EpM1 + ChlM1 pervasively overgrew igneous crystals in melanocratic spessartite, Val du Haut Boréon; b: mineralised tensional vein filled by elongated crystals of AbM2, ActM2, and KfsM2 in spessartite, Valscura. ActM2 grew in continuity with truncated phenocrysts of AmpI1 already replaced by M1 mineral assemblages; c: stylolitic foliation, supported by fine-grained crystals of TtnM2, which define the contact between a phenocryst of AmpI1 partially replaced by M1 mineral assemblages (at top) and an aggregate of EpM1 (at bottom) in spessartite, Valscura. Stylolitic foliation is cinematically compatible with the opening of mineralised tensional veins in Fig. 1.1.11c; d: spessartite containing a porphyroclast of AmpI1 largely pseudomorphosed by M1 mineral assemblages and wrapped by D4 foliation, Valscura; pressure shadow domains are filled by BtM2, ChlM2 and minor ActM2 at the edges of the AmpI1 porphyroclast; e: aggregates of EpM1 and small phenocrysts of AmpI1 wrapped by D4 foliation in a heterogeneously deformed spessartite dyke, Val du Haut Boréon. Trails of TtnM2 and laminae of BtM2 and ChlM2 are the mineralogical support of D4 S-C surfaces; f: Micro-boudins of AmpI1 in a foliated spessartite dyke, Val du Haut Boréon. Boudin necks are filled by ActM2 and ChlM2; the foliation is mostly defined by trails of fine-grained TtnM2, and minor BtM2 and ChlM2. All pictures are taken by plane polarized light.

In melanocratic spessartites, irregular-shaped amphibole-rich domains of centimetre size are enclosed in a more leucocratic groundmass. Two types of amphibole-rich domains are recognised, both with anhedral to subhedral interstitial PlI1 crystals: in the former, crystals of AmpI1 are dark-brown and highly prolate, whereas, in the latter, AmpI1 occurs in brown stocky grains. AmpI1 crystals in comb layered appinites display a seriate crystal size distribution: centimetre-sized phenocrysts of AmpI1 with interstitial PlI1 are iso-oriented and, locally, in fan-shaped aggregates, whereas millimetre- and sub-millimetre-sized AmpI1 crystals are randomly oriented and completely to partially included in PlI1.

Vesicles, which commonly occur in spessartites and melanocratic spessartites, are tangentially bounded by undeformed crystals of AmpI1 (Fig. 1.1.10c) and locally filled either by PlI1 and AmpI1 radially oriented, by hydrothermal mineral assemblages, or by twinned crystals of calcite. Along the chilled margins, small phenocrysts of AmpI1 are recognisable within the cryptocrystalline groundmass (Fig. 1.1.10d). The igneous mineral assemblages filling leucocratic veins comprise AmpI1, PlI1, KfsI1, and minor QzI1.

Dark-green AmpI2 rims AmpI1 in Valscura lamprophyres (Fig. 1.1.10e) and partially replaces AmpI1 in and around the leucocratic veins in Val du Huat Boréon (Fig. 1.1.10f). AmpI2 is interpreted as late-magmatic phase since it is replaced by hydrothermal mineral assemblages (M1, described below).

Subsolidus microstructures

Microstructures developed under subsolidus conditions and supporting mineral assemblages are similar in both the investigated areas. However, in Val du Boréon, syn-D4 mineral assemblages are significantly developed only in intermediate to high strain domains.

M1 is the earliest post-magmatic mineral assemblage retained by the lamprophyres, which comprises AbM1 + ActM1 + ChlM1 + EpM1 + KfsM1 + TtnM1 ± BtM1 ± CalM1 ± QzM1 in polygonal aggregates with rational grain boundaries and without SPO (Fig. 1.1.11a). Up to millimetre-sized randomly-oriented epidote grains are diagnostic for M1. Rare aggregates of ZoM1 may occupy the same microstructural domains of EpM1, as observed in few samples from Val du Haut Boréon. OpqM1, hematite and pyrite, locally occur. AmpI1 and AmpI2 are partially to totally replaced by aggregates of anhedral and un-twinned AbM1, colourless ActM1, ChlM1, EpM1, TtnM1, and rare QzM1 (Figs. 1.1.10e and 1.1.11b-d); a similar mineral assemblage, but without ActM1, replaced PlI1. BtM1 rims KfsI1.

M2 mineral assemblages support stylolitic and mylonitic D4 foliations in lamprophyres (Figs. 1.1.11c-f). Igneous phenocrysts and aggregates of EpM1 are wrapped by D4 mylonitic foliation marked by SPO of AbM2 + BtM2 + ChlM2 + TtnM2 + PhM2 ± ActM2 ± EpM2 ± OpqM2 ± QzM2 (Fig. 1.1.11d and 1.1.11e), and are partially dissolved at strain caps or along stylolitic films mainly supported by microgranular aggregates of TtnM2 (Figs. 1.1.11c, 1.1.11e and 1.1.11f). Pale-green ActM2 fills pressure shadows and boudin necks of AmpI1 porphyroclasts (Figs. 1.1.11d and 1.1.11f). Newly formed grains of ActM2 rarely mark the D4 mylonitic foliation. KfsM2 exclusively fills tensional veins at dyke margins, where is associated with AbM2 + ActM2 + BtM2 + ChlM2 (Fig. 1.1.11b). In low-strain domains, AmpI1 phenocrysts, partially to totally overgrown by M1 assemblages, are rimmed by discontinuous coronae of ActM2. M2 mineral assemblages, which support D4 structures in

lamprophyres, are consistent with the transition between greenschist and amphibolite facies conditions (Maruyama et al., 1982; Maruyama et al., 1983; Spear, 1993).

Discussion

Structural and metamorphic relationships between lamprophyres, granitoids, and migmatites allow an accurate discrimination between superposed Variscan and Alpine tectono-metamorphic stages in the crystalline basement of the Argentera-Mercantour Massif. During D2, which was coeval with the Variscan migmatisation, deformation was highly heterogeneous, as indicated by D2 mylonites through domains where the dominant fabric is the folded S1 foliation. Late-Variscan D3 event is responsible for folds, subsequently crosscut by acidic dykes and pockets, and by younger NE-SW striking lamprophyres.

The Argentera-Mercantour lamprophyres are spessartites and appinites, formed by AmpI1, PlI1, and minor KfsI1. Igneous clinopyroxene is observed in few spessartite dykes, whereas QzI1 is rare in phaneritic rock types. Rims of late-magmatic AmpI2 may occur, in particular at or near sets of late leucocratic veins. Mingling and magmatic breccia textures are common in spessartites, appinites, and leuco-appinites, which are locally divided by comb layers. These structures point out that the dykes have collected compositionally heterogeneous magmas during their ascent.

Chilled margins and vesicles, the latter interpreted as resulting from degassing (Vernon, 2018), suggest that the Argentera-Mercantour Massif had been already exhumed at shallow depths before the emplacement of the lamprophyres. Furthermore, brittle structures accomodated their emplacement. M1 assemblages (AbM1 + ActM1 + ChlM1 + EpM1 + KfsM1 + TtnM1 ± BtM1 ± CalM1 ± QzM1 ± OpqM1 ± QzM1), which exclusively developed in the lamprophyres and along their margins, reflect localised hydrothermal circulation that took place during the latest emplacement stages, unrelated with the Alpine tectono-metamorphic evolution.

Lamprophyres are crosscut by dextral shear zones of Alpine ages (D4), striking from E-W to NW-SE, the latter of which characterised by sub-horizontal mineral lineations. M2 assemblages (AbM2 + BtM2 + ChlM2 + TtnM2 + PhM2 ± ActM2 ± EpM2 ± KfsM2 ± OpqM2 ± QzM2) support D4 foliation in lamprophyres, fill D4 tensional veins at dyke walls, and rim both igneous and M1 assemblages in low strain domains. Therefore, the lamprophyres of the Argentera-Mercantour Massif retain Alpine metamorphic conditions compatible with the transition between the greenschist and amphibolite facies. Since M2 mineral assemblages are similar in Valscura and Val du Haut Boréon, similar Alpine metamorphic conditions are assumed for the two tectonic slices divided by the Fremamorta Shear Zone (FMZ in Fig. 1.1.1). Furthermore, no changes in dyke attitudes between the two areas imply that

only minor relative rotation has affected these two slices since the lamprophyre emplacement up to the present day, despite of the interposition of the FSZ.

In the Argentera-Mercantour Massif, rapid exhumation of the thickened Variscan crust in late-collisional setting triggered decompression melting at around 323 ± 12 Ma (Rubatto et al., 2001; Ferrando et al., 2008), which culminated with the surface exposure of the lower crust from late Carboniferous times (Faure-Muret 1955; Malaroda et al., 1970; Bortolami et al., 1974). It occurred after the slab break-off (Rubatto et al., 2001; von Raumer et al., 2014) and concurrently with the emplacement of the Central Granite (Boucarut, 1967; Ferrara and Malaroda 1969; Corsini et al., 2004). After tens of million years of migmatisation and successive emplacement of early Permian peraluminous granitoids in the retrogressed and exhumed migmatites, texturally heterogeneous lamprophyres, resulting from crustal contamination of mantle-derived magmas, emplaced at shallow crustal levels. A Permian-Triassic age for the Argentera-Mercantour lamprophyres is suitable for the following reasons: i) the lamprophyres only intruded into Variscan migmatites and early Permian granitoids, but not into the Mesozoic to Tertiary sedimentary sequences (Faure-Muret 1955; Malaroda et al., 1970); ii) the lamprophyres record a prograde metamorphism, reaching metamorphic conditions at the transition between the greenschist and amphibolite facies during the Alpine deformation. Furthermore, dacites and basalts are reported in the Permian siliciclastic sequences (Faure-Muret, 1955; Malaroda et al., 1970; Romain and Vernet, 1978).

The tectonic setting accountable for the Permian-Triassic magmatism in the southern Variscan belt area is controversial. Both the calc-alkaline and the subsequent alkaline cycles, comprising transitional to tholeiitic mafic rocks, have been intepreted either as a result of Variscan collapse, or crustal delamination, or post-orogenic extension (e.g. Lardeaux and Spalla, 1991; Bussy et al., 2000; Cannic et al., 2002; Cocherie et al., 2005; Bussien et al., 2008; Buzzi and Gaggero, 2008; Dallagiovanna et al., 2009; Spalla et al., 2014; Rossi et al., 2015). Numerical models performed to explore the transition from Variscan convergence to Permian-Triassic extension indicate that forced extension (at least 2 cm/yr) is necessary to produce successive pulses of mantle-derived magma in Permian-Triassic times: such a magmatic activity could not result from the gravitational evolution characterising the end of the Variscan subduction-collision (e.g. Marotta et al., 2009; Marotta et al., 2018; Roda et al., 2018). Taking into accounts these model predictions, the Argentera-Mercantour lamprophyres are more easily interpreted as magmatic records of the Permian-Triassic lithospheric thinning, announcing the Jurassic rifting on the European margin, instead of the igneous witness of the late-Variscan collapse.

Conclusion

The multiscale structural analysis carried out in the southeastern portion of the Argentera-Mercantour Massif highlights the following significant steps of its geodynamic evolution, from Variscan to Alpine times:

i) texturally heterogeneous lamprophyres, magnesian, calc-alkalic to alkali-calcic and metaluminous in composition, emplaced at shallow crustal levels crosscutting three generations of superposed Variscan structures in the migmatitic complex and early Permian granitoids;

ii) lamprophyres were place of hydrothermal circulation immediately after their intrusion;

iii) mineral assemblages supporting the strike-slip mylonitic shear zones of Alpine ages are consistent with the transition between the greenschist and amphibolite facies.

Syn-intrusive structures and metamorphic evolution are thus reasonably consistent with the lamprophyres of the Argentera-Mercantour Massif interpreted as evidence of Permian-Triassic lithospheric thinning in the External Crystalline Massifs of Western Alps.

1.2 Evidence of Tethyan continental break-up and Alpine collision in the Argentera-Mercantour Massif, Western Alps

Marco Filippi, Davide Zanoni, Jean-Marc Lardeaux, Maria Iole Spalla, Guido Gosso
Lithos 2020, 372-373, 105653, 10.1016/j.lithos.2020.105653

Abstract

In the Argentera-Mercantour Massif, swarms of high-K calc-alkaline lamprophyres intruded into Carboniferous migmatites and early Permian granites, likely in Permian-Triassic times. The dykes collected multiple magmatic injections, the latest of which of alkaline affinity. Syn-intrusive vesicles and straight chilled margins suggest that the lamprophyres emplaced at a shallow crustal level.
Lower greenschist facies mineral assemblages replaced lamprophyre igneous minerals as a result of late-intrusive hydrothermal circulation that occurred soon after the dyke emplacement. The hydrothermal event is constrained at T = 300 - 350 °C and P < 0.1 GPa by matching thermobarometry and pseudosection results. During the Alpine collision, the lamprophyres were intersected by upper greenschist facies mylonitic shear zones developed at T = 420 - 450°C and P = 0.2 - 0.4 GPa, which are the metamorphic peak conditions of the Argentera-Mercantour Massif in Alpine times.

Introduction

Calc-alkaline to potassium-rich magmatic rocks are widespread in the European Variscan belt where they are insightful markers for estimating the thermal states characterizing plate convergence (see reviews with references therein in Faure et al., 2009; Franke, 2000, 2006; Holub et al., 1997; Janoušek et al., 2000, 2004; Laurent et al., 2017; Rossi et al., 2009; Sabatier, 1991; Schulmann et al., 2009, 2014; von Raumer et al., 2014). That is the case of the External Crystalline Massifs (ECM) of the Alps, where high-K calc-alkaline intrusives emplaced during the late stages of Variscan evolution in late Carboniferous to early Permian times (Bonin et al., 1993; Bussy et al., 2000; Debon and Lemmet, 1999; Rubatto et al., 2001; von Raumer et al., 2013). Afterwards, in the Argentera-Mercantour ECM, swarms of high-K calc-alkaline lamprophyres intruded into migmatites and early Permian granites (Blasi, 1971; Faure-Muret, 1955; Filippi et al., 2019; Malaroda et al., 1970).
This contribution includes new mineralogical and petrological data on the Argentera-Mercantour lamprophyres, obtained through detailed microstructural analysis of lamprophyre dykes sampled

within Alpine finite strain gradients (i.e. poorly-strained to mylonitic domains, e.g. Spalla and Zucali, 2004; Gosso et al., 2015). Because of easy-to-solve structural relationships with respect to the finite strain pattern and suitable chemical composition to record significant metamorphic transitions, the Argentera-Mercantour lamprophyres are the best target for addressing: (i) the transition from the Variscan late collisional stage to continental break-up leading the development of the European passive margin, (ii) the amount of under-thrusting imposed to this segment of passive margin during the Alpine collision. By doing so, we quantify for the first time the prograde Alpine evolution of the Argentera-Mercantour ECM, imposing new constraints on the tectonic significance of the Alpine metamorphism in the ECMs.

Geological outline

The ECMs are amongst those Alpine units that best retain the poly-phasic tectono-metamorphic evolution of the southern Variscan belt, since the Alpine metamorphic overprint is mainly localized within high-strain domains (Guillot et al., 2009; Spalla et al., 2014; von Raumer et al., 2009). The basement rocks of the ECMs largely consist of poly-deformed Variscan migmatites derived from meta-sediments, granitoids, and amphibolites, together with relics of MORBs and ultramafic rocks preserving Variscan eclogite and/or granulite facies imprints (Ferrando et al., 2008; Jouffray et al., 2020; Ménot and Paquette, 1993; Regorda et al., 2020; Rubatto et al., 2001; Rubatto et al., 2010; Spalla and Marotta, 2007; von Raumer, 1984; von Raumer et al., 1993).

The ECMs were affected by long-lasting high-K calc-alkaline magmatism in late to post Variscan times: the "high-Mg-number" intrusives, likely related to late collisional melting triggered by slab break-off or slab window (von Raumer et al., 2014), emplaced in the ECMs between 343 and 332 Ma, and slightly predated the widespread migmatization developed under upper-amphibolite facies conditions (Bonin et al., 1993; Bussy et al., 2000; Debon and Lemmet, 1999; Rubatto et al., 2001). At 305 - 293 Ma, the "low-Mg-number" granites intruded into the exhumed migmatitic complexes (Bonin et al., 1998; Bussy et al., 2000; Debon and Lemmet, 1999). Lastly, minor swarms of mafic to intermediate dykes emplaced in Permian-Triassic times (Aumaitre and Buffet, 1973; Buffet and Aumaitre, 1979; Vatin-Pérignon et al., 1972, 1974). Similar intrusives and dykes are reported in other Alpine domains, where they are interpreted as a signal of Permian-Triassic lithospheric thinning (e.g. Bussien et al., 2008; Cannic et al., 2002; Casetta et al., 2019; De Min et al., 2020; Lustrino et al., 2019; Marotta et al., 2009; Monjoie et al., 2007; Roda et al., 2019; Spalla et al., 2014).

The Argentera-Mercantour ECM

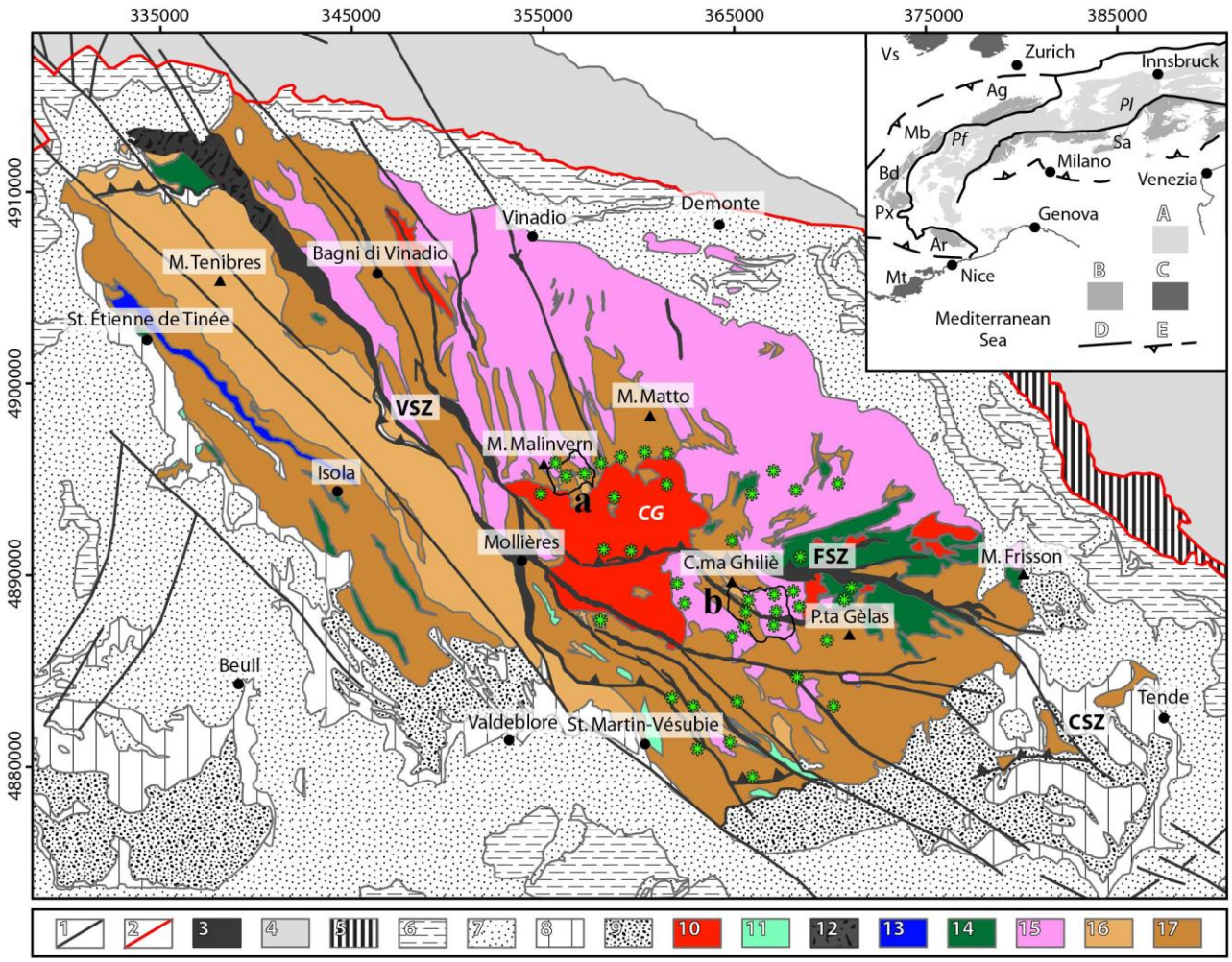

Figure. 1.2.1. Schematic geologic map of the Argentera-Mercantour ECM, modified after Gosso et al. (2019) and refs. therein; lamprophyre occurrences (asterisks) are from Malaroda et al. (1970); a and b contour regions locating the investigated areas of Valscura and Val du Haut Boréon, respectively. Abbreviations: CSZ - Casterino Shear Zone; FSZ - Fremamorta Shear Zone; VSZ - Valletta (or Ferrere-Mollières) Shear Zone; CG - Central Granite. Legend: 1 - late- to post-Alpine faults; 2 - Penninic Front; 3 - Oligocene-Miocene greenschist facies mylonites; 4 - undifferentied Briançonnais units; 5 - undifferentied Sub-Briançonnais units; 6 - Upper Cretaceous to Priabonian foreland successions; 7 - Lower Jurassic to Lower Cretaceous limestones, marlstones, and shales; 8 - Lower Triassic siliciclastic sequences, and Middle to Upper Triassic limestones and dolomites; 9 - Permian siliciclastic sequences and volcanics; 10 - late Carboniferous to early Permian granitoids 11 - late Carboniferous siliciclastic sequences and carbonaceous schists; 12 - Carboniferous amphibolite to greenschist facies mylonites; 13 - syn-tectonic diorites; 14 - migmatitic amphibolites; 15 - diatexites; 16 - migmatitic metagranitoids and orthogneisses; 17 - migmatitic paragneisses. Projected coordinate system: WGS 84-UTM32N (metric grid). Insert: tectonic sketch of the Alps: A - Variscan basement rocks recycled in the Alpine subduction complex; B - Variscan basement rocks of the Helvetic-Dauphinois-Provençal Domains (Ag: Aar-Gotthard Massifs, Ar: Argentera-Mercantour Massif, Bd: Belledonne Massif, Mb: Mont Blanc Massif, Px: Pelvoux Massif) and Southern Alps (Sa); C - Variscan basement rocks external to the Alpine fronts (Mt: Maures-Tanneron Massif); D - lithospheric-scale structures delimiting the axial zone of the Alps (Pf: Penninic Front, Pl: Periadriatic Lineament); E - Alpine fronts.

The basement rocks of the Argentera-Mercantour ECM (Fig. 1.2.1) comprise Variscan migmatites, including diffuse relics of eclogites and HP-granulites, and late to post Variscan granitoids (Blasi, 1971; Bogdanoff, 1986; Bogdanoff and Ploquin, 1980; Bortolami et al., 1974; Boucarut, 1967; Compagnoni et al., 2010; Faure-Muret, 1955; Ferrando et al., 2008; Filippi et al., 2019; Jouffray et al., 2020; Gosso et al., 2019; Latouche and Bogdanoff, 1987; Malaroda et al., 1970; Rubatto et al., 2001). The Variscan basement rocks have been involved into the Alpine collision since the late Eocene to the early Oligocene by overthrusting of internally derived nappes (Bigot-Cormier et al., 2000; Bogdanoff et al., 2000; Corsini et al., 2004; Evans and Elliott, 1999; Ford et al., 1999; Kerckhove, 1969; Merle and Brun, 1984; Sanchez et al., 2010; Sanchez et al., 2011a; Schreiber et al., 2010; Schwartz et al., 2007, Simon-Labric et al., 2009).

The Argentera-Mercantour ECM is divided into "metamorphic complexes" or "terrains" (Bogdanoff, 1986; Compagnoni et al., 2010; Faure-Muret 1955; Malaroda et al. 1970) by the Valletta (or Ferriere-Mollières) Shear Zone (VSZ, Fig. 1.2.1), a major NW-SE striking dextral mylonite that has been active between 341 and 314 Ma under retrograde amphibolite facies conditions (Corsini et al., 2004; Carosi et al., 2016; Faure-Muret, 1955; Musumeci and Colombo, 2002; Simonetti et al., 2018). Anyway, the Variscan P-T evolutions retained by both the western and eastern complexes are similar (Latouche and Bogdanoff, 1987; Ferrando et al., 2008). Migmatites exhumation in late to post Variscan times is constrained by the shallow emplacement level of the main high-K calc-alkaline intrusive stock, the early Permian "Central Granite" (Boucarut, 1967, Corsini et al., 2004; Ferrara and Malaroda, 1969), and by the late Carboniferous to Lower Triassic sedimentary covers (Bortolami et al., 1974; Faure-Muret, 1953; Malaroda et al. 1970).

Magmatism in the Argentera-Mercantour ECM area lasted through the Permian, as suggested by acidic and mafic volcanoclastic strata interlayered in Permian siliciclastic sequences (Malaroda et al., 1970; Romain and Vernet, 1978), and by swarms of high-K calc-alkaline lamprophyres intruded into migmatites and early Permian granites in the eastern complex (Compagnoni et al., 2010; Faure-Muret, 1955; Filippi et al., 2019; Malaroda et al., 1970). The Mesozoic sedimentary record suggests that the Argentera-Mercantour ECM occupied a transition zone between the Helvetic-Provençal reduced sequence and the Dauphinois Zone in the European passive margin framework (Faure-Muret, 1955; Lemoine et al., 1986; Tricart, 1984).

As an effect of the Alpine collision, the VSZ was significantly re-activated as dextral strike-slip shear zone and E-W striking inverse shear zones developed between 34 and 20 Ma (Baietto et al., 2009; Bigot-Cormier et al., 2006; Corsini et al., 2004; Sanchez et al., 2011a; Sanchez et al., 2011b). The metamorphic conditions attained by the Argentera-Mercantour ECM in Alpine times are estimated by fission track ages and sericite formation in Eocene sedimentary sequences at the base of internally

derived nappes (T ~ 200°C, Labaume et al., 2008), as well as by thermobarometric estimates on newly-formed white mica and chlorite in Permian-Mesozoic sedimentary rocks (T > 300°C and P > 0.3 GPa, Attal, 2000) and on mineral assemblages supporting Alpine shear zones in granites, migmatites, and early Triassic quartzites (Corsini et al., 2004; Leclère et al., 2014; Sanchez et al., 2011a). Sanchez et al. (2011a) suggest that a first group of shear zones, active at around 34 Ma, records metamorphic conditions at T = 375 ± 25°C and P between 0.7 and 0.9 GPa, whereas a second group, dated at 22 - 20 Ma, developed at similar temperature, but lower pressure (P = 0.4 - 0.6 GPa).

This research focuses on two sites of the Argentera-Mercantour ECM, Valscura and Val du Haut Boréon, where lamprophyres are widespread. These sites are at the NW and SE edges of the Central Granite, respectively (Fig. 1.2.1). The E-W striking Fremamorta Shear Zone (FSZ), dated at 22 - 23 Ma (Corsini et al., 2004), runs between them.

Lamprophyre field occurrence

In Valscura and Haut Boréon, the lamprophyres are intruded into Variscan basement rocks consisting of migmatitic paragneisses, mainly metatexites grading to diatexites, and minor migmatitic meta-granitoids and amphibolites (Fig. 1.2.2). The dominant structure in the migmatitic complex is the composite foliation S1+2, resulting from superposition of D2 isoclinal folds on S1. NW-SE striking and SW or NE dipping S1+2 developed during migmatization and is parallel to the lithological boundaries. Axial surfaces of D3 folds are steeply dipping to N, NW or SE with sub-vertical to SW plunging axes.

The lamprophyres are in swarms of coalescent dykes (Fig. 1.2.3a), ranging from centimeters up to 10 meters in thickness, with sub-vertical dyke walls that strike at around 60°N (Fig. 1.2.2), with very few exceptions. The lamprophyres crosscut the D3 structures, as well as small granite bodies and dykes and the Central Granite pluton (e.g. Faure-Muret, 1955; Filippi et al., 2019; Malaroda et al., 1970). Intrusive contacts between lamprophyres and host rocks are sharp and angulated as a result of syn-intrusive fracturing; vesicles and centimeter-thick chilled margins are along the dyke margins. These syn-intrusive structures suggest that the dykes emplaced at shallow crustal level.

Lamprophyres of few meters of thickness are spessartites (Le Maitre et al., 2002), with sub-millimetric to millimetric amphibole phenocrysts into a cryptocrystalline to very-fine grained groundmass. Conversely, the thickest dykes are appinites (Le Maitre et al., 2002; Murphy, 2013, 2020), formed by holocrystalline medium- to coarse-grained, locally pegmatitic, aggregates of amphibole, plagioclase, minor K-feldspar, and rare quartz grains. At dyke cores, rounded to angulated appinite xenoliths are enclosed within plagioclase-rich leuco-appinite.

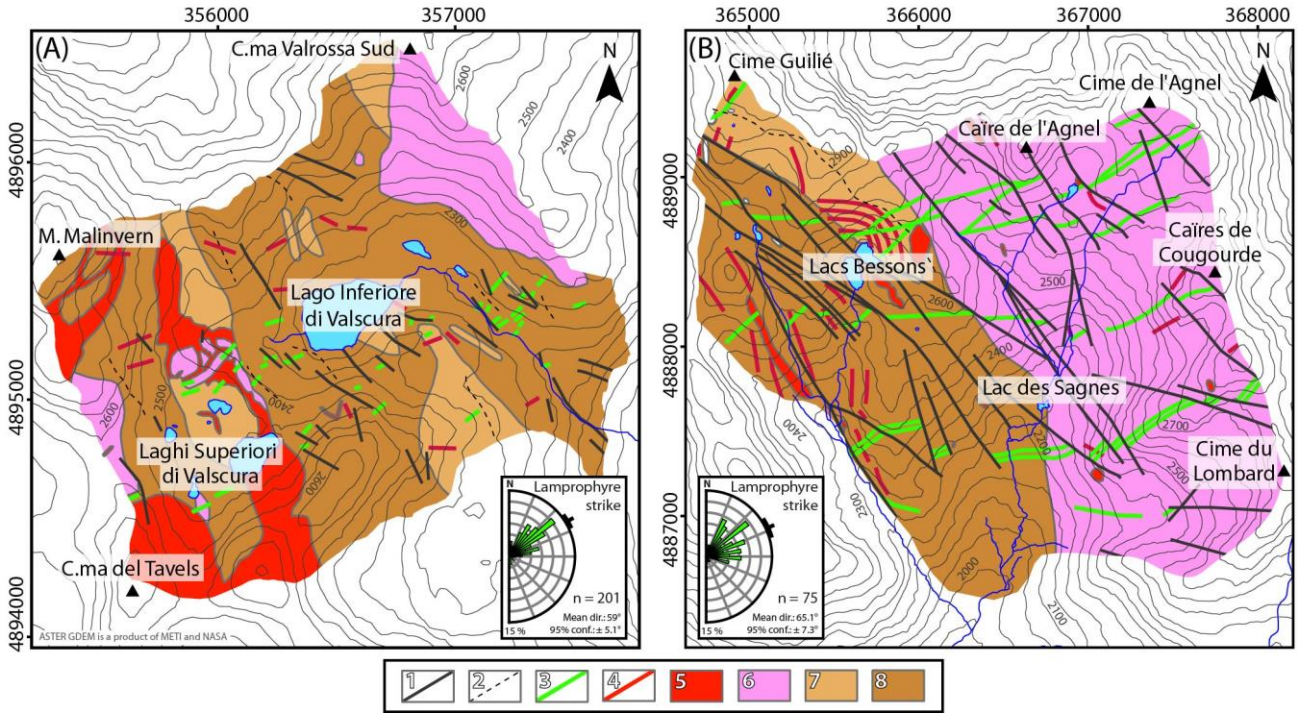

Figure. 1.2.2. Interpretative structural maps of Valscura (A) and Haut Boréon (B), modified after Filippi et al. (2019) and refs. therein. Legend: 1 - trajectory of D4 mylonitic and cataclastic shear zones; 2 – trajectory of S1+2 migmatitic foliation; 3 - lamprophyres; 4 - acidic dykes; 5 - granites; 6 - diatexites; 7 - migmatitic meta-granitoids (metatexites); 8 - migmatitic paragneisses and amphibolites (metatexites). Projected coordinate system: WGS 84-UTM32N (metric grid).

At Lacs Bessons, in Haut Boréon (Fig. 1.2.2), a 10-meter-thick E-W trending dyke displays a symmetrical structure: two bands of melano-spessartite occupy the dyke margins (Fig. 1.2.3b), whereas appinite and leuco-appinite fill the dyke core. Melano-spessartite is a fine-grained phaneritic rock characterized by amphibole-rich domains of centimeter size enclosed within a slightly more leucocratic matrix; chilled margins and trails of up to centimeter-sized vesicles mark the dyke walls. Meter-thick bands of comb layer-textured appinite separate melano-appinite from appinite. Comb layers are outlined by up to 5-centimeter-long amphiboles perpendicular to the dyke walls and included in a groundmass of millimeter-sized amphibole and plagioclase; fine-grained domains are alternating with comb layers. Where appinite is mingled with leuco-appinite, comb layered bands and chilled margins are brecciated (Fig. 1.2.3c, d). Meter-thick spessartite dykes, trending 60°N, intersect the melano-spessartite in the main E-W trending dyke and are coalescent with the leuco-appinite at dyke core. Leucocratic veins, which correspond to the last magmatic pulses, crosscut melano-spessartite (Fig. 1.2.3b) and spessartite at dyke margin, and, locally, appinite and leuco-appinite at dyke core. In most of the cases, the leucocratic veins are parallel to the dyke walls.

In both localities, igneous minerals are often replaced by randomly oriented aggregates of epidote and chlorite, testifying a late-intrusive hydrothermal imprint (M1), with no counterparts in the host

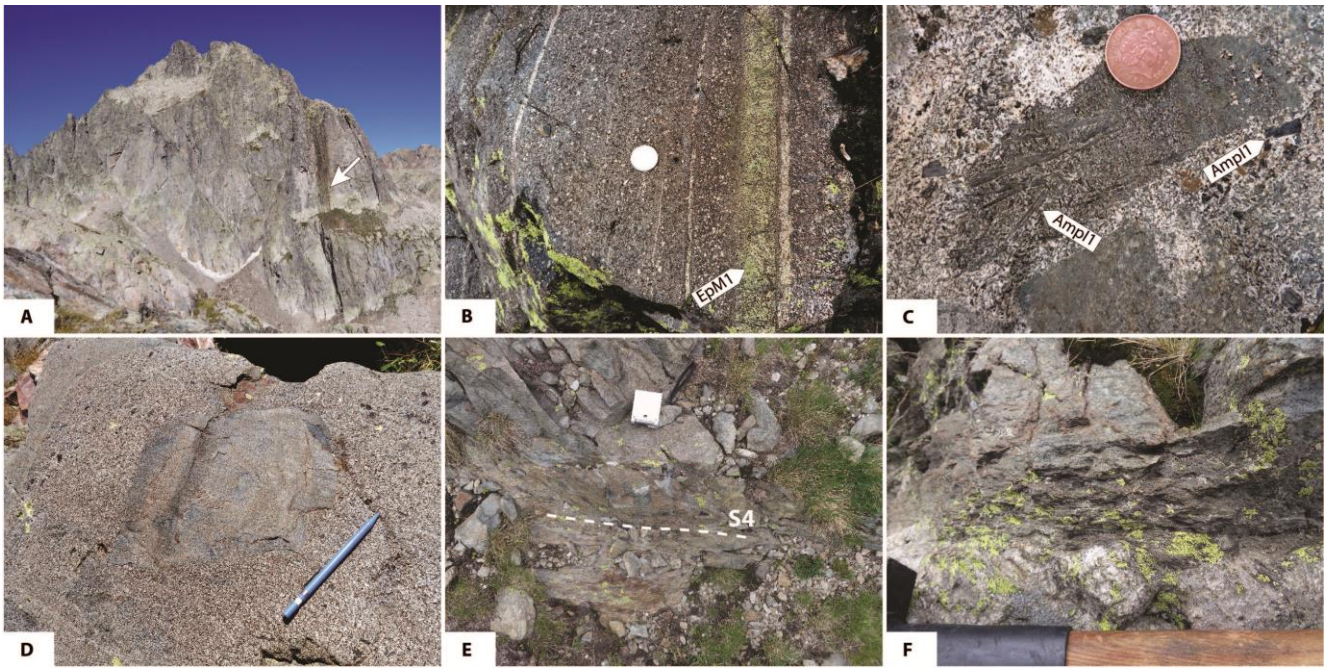

Figure 1.2.3. Argentera-Mercantour ECM lamprophyres: (A) swarms of lamprophyre dykes (white arrow) intruding diatexites on the west slope of Caire de l'Agnel, Haut Boréon; (B) melano-spessartite with vesicles (white dots) occurring in the external parts of the 10-meter thick dyke of Lacs Bessons. Late-intrusive leucocratic veins are parallel to dyke walls. Epidote- and chlorite bearing hydrothermal assemblages are associated with some of these veins (coin for scale); (C) xenolith of comb-layered appinite included in mingled leuco-appinite and appinite in the central part of the lacs Bessons dyke (coin for scale); (D) xenolith of melano-spessartite preserving repeated chilled margins and layers of vesicles in the central part of the lacs Bessons dyke (pencil for scale); (E) 130°N-striking mylonitic foliations (D4) crosscutting spessartite dyke at Valscura (compass for scale). S4 is marked by chlorite, biotite and trails of fine grained titanite; (F) S4 developed along dyke margin in a 60°N-striking spessartite from Valscura (hammer for scale).

migmatites and granites (Fig. 1.2.3b). Dextral strike-slip shear zones of Alpine age (S4), mainly NW-SE striking and with S-C structures (Baietto et al., 2009; Corsini et al., 2004; Filippi et al., 2019; Leclère et al., 2014; Sanchez et al., 2011b), crosscut the lamprophyres and reactivated the intrusive contacts (Fig. 1.2.3e, f).

Microstructure

Timing of mineral growth inferred by microstructural analysis is indicated by alphanumeric labels, in which capital letters I and M stand for igneous and metamorphic mineral assemblages, associated with progressive numerals related to subsequent igneous and metamorphic stages (Tab. 1.2.1). Mineral abbreviations are from Whitney and Evans (2010).

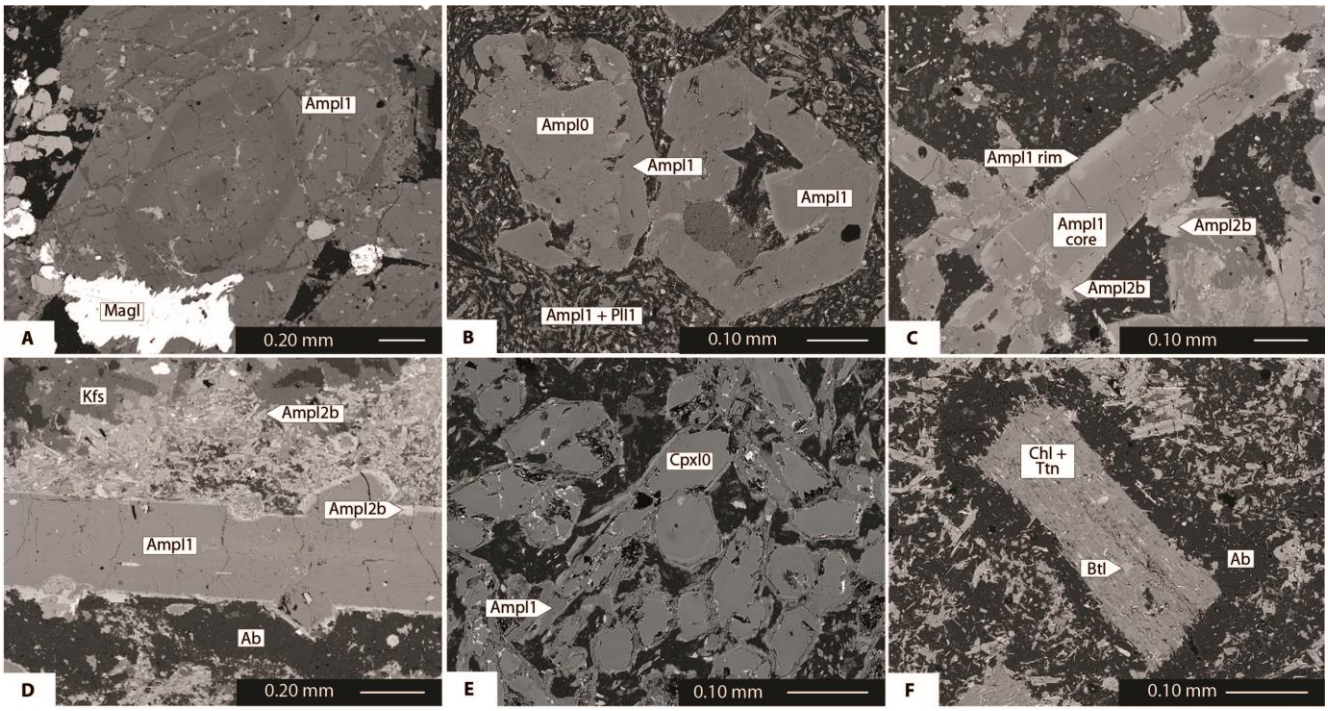

Figure 1.2.4. Igneous mineral assemblages and microstructures characterising the Argentera-Mercantour lamprophyres (BSE images): (A) crystals of AmpI1 including MgtI1 and displaying oscillatory oscillatory compositional zoning in appinite, Haut Boréon; (B) amphibole xenocryst with corroded margins and rimmed by AmpI1 in spessartite from Haut Boréon; (C) AmpI2b rimming AmpI1 in melano-spessartite from Haut Boréon; (D) Rim of AmpI2b developed around AmpI1 and small crystals of AmpI2b filling a leucocratic vein at the contact between melano-spessartite and spessartite, Haut Boréon; (E) igneous clinopyroxene with oscillatory compositional and irregular boundary in spessartite, Haut Boréon; (F) Relic of igneous biotite completely replaced by biotite, chlorite, and titanite during late-intrusive hydrothermalism.

Igneous microstructure

Textures of mafic porphyrites are highly heterogeneous: sub-millimetric phenocrysts of brown igneous amphibole (AmpI1) occur in a microcrystalline groundmass, or together with small laths of igneous plagioclase (PlI1); in few cases, small phenocrysts of AmpI1 are enclosed in crystals of PlI1 (up to centimeter-sized), testifying sub-ophitic and ophitic textures. In all the lamprophyre types, simple twinning and oscillatory compositional zoning are characteristic of euhedral to subhedral crystals of AmpI1 (Fig. 1.2.4a). Locally, AmpI1 encloses dark brown AmpI0 cores with irregular grain boundaries (Fig. 1.2.4b). In Haut Boréon, melano-spessartite contains enclaves enriched in elongated dark brown AmpI1 grains. Rims of dark-green amphibole (AmpI2a) surround AmpI1 in phaneritic and aphanitic Valscura types, whereas green to pale-green amphibole (AmpI2b) rims AmpI1 and occurs as small phenocrysts in the matrix of the Lacs Bessons main dyke, within or nearby the leucocratic veins, together with AbI2b and igneous biotite (Fig. 1.2.4c, d).

STAGE	GENESIS	MINERAL ASSEMBLAGE
I0	igneous	Amp, Cpx
I1 (core, rim)	igneous	Amp, Pl, Qz, Kfs, Mgt, Ilm, Ap, Bt
I2 (a,b)	late-igneous	Ab, Amp
M1	subsolidus, hydrothermal	Ab, Act, Bt, Chl, Ep, Hem, Kfs, Py, Qz, Ttn
M2 (a,b)	subsolidus, syn-D4	Act, Bt, Chl, Ep, Kfs, Pl, Qz, Ttn, Wm

Table 1.2.1. Summary of igneous and metamorphic mineral assemblages in the Argentera-Mercantour lamprophyres.

Subhedral crystals and small laths of PlI, usually with simple or polysynthetic twins, are widely replaced by post magmatic albite, epidote, chlorite, and sericite. In appinite, QzI and KfsI crystals are interstitial with respect to PlI, whereas they occur as subhedral grains in leuco-appinite and leucocratic veins. In Haut Boréon spessartite, xenocrysts of clinopyroxene (CpxI0) form aggregates of submillimetric grains with oscillatory compositional zoning (Fig. 1.2.4e). CpxI0 grain boundaries are irregular and rimmed by AmpI1 (Fig. 1.2.4e). Rare crystals of igneous biotite (BtI) are extensively replaced by hydrothermal chlorite and titanite (Fig. 1.2.4f). Minor magnetite, ilmenite, and apatite are included in AmpI1 and PlI. In spessartite and melano-spessartite, vesicles are rimmed by tangentially oriented AmpI1 and filled by igneous and/or hydrothermal mineral assemblages.

Metamorphic microstructure

Lamprophyre igneous minerals are partially or totally replaced by metamorphic minerals, which formed during different stages of the Argentera-Mercantour ECM tectono-metamorphic evolution. M1 mineral assemblages reflect late-intrusive hydrothermal systems that likely affected the lamprophyres shortly after their emplacement (Filippi et al., 2019). M1 comprises coronitic aggregates of AbM1, ActM1, ChlM1, EpM1, TtnM1, KfsM1, QzM1 replacing igneous amphibole (Fig. 1.2.5a), and AbM1 + EpM1 overgrowing PlI. In BSE images, EpM1 commonly shows patchy, irregular, and sharp zoning. Coronae of BtM1 are around igneous amphibole and K-feldspar (Fig. 1.2.5b). Pyrite and hematite rim MagI1; PlI1 shows K-feldspar exsolutions and sericitization. Anhedral and coarse-grained crystals of calcite fill the vesicles, locally in association with other M1 minerals.

M2 mineral assemblages comprise PlM2, ActM2, BtM2, ChlM2, EpM2, KfsM2, TtnM2, and PhM2 that support S4 foliation and fill syn-kinematic tensional veins (Figs. 1.2.5c, d, e, and f). In high strain domains, S4 wraps porphyroclasts of igneous and M1 hydrothermal minerals. In low-strain domains, igneous and M1 minerals are wrapped by coronae of M2 minerals. EpM2 rims EpM1 (Fig. 1.2.5e).

In Valscura, M2 is subdivided into M2a and M2b, which are related to finite strains increments involving vein opening and growth of coronae during S4 development. AbM2a, ActM2a, and ChlM2a

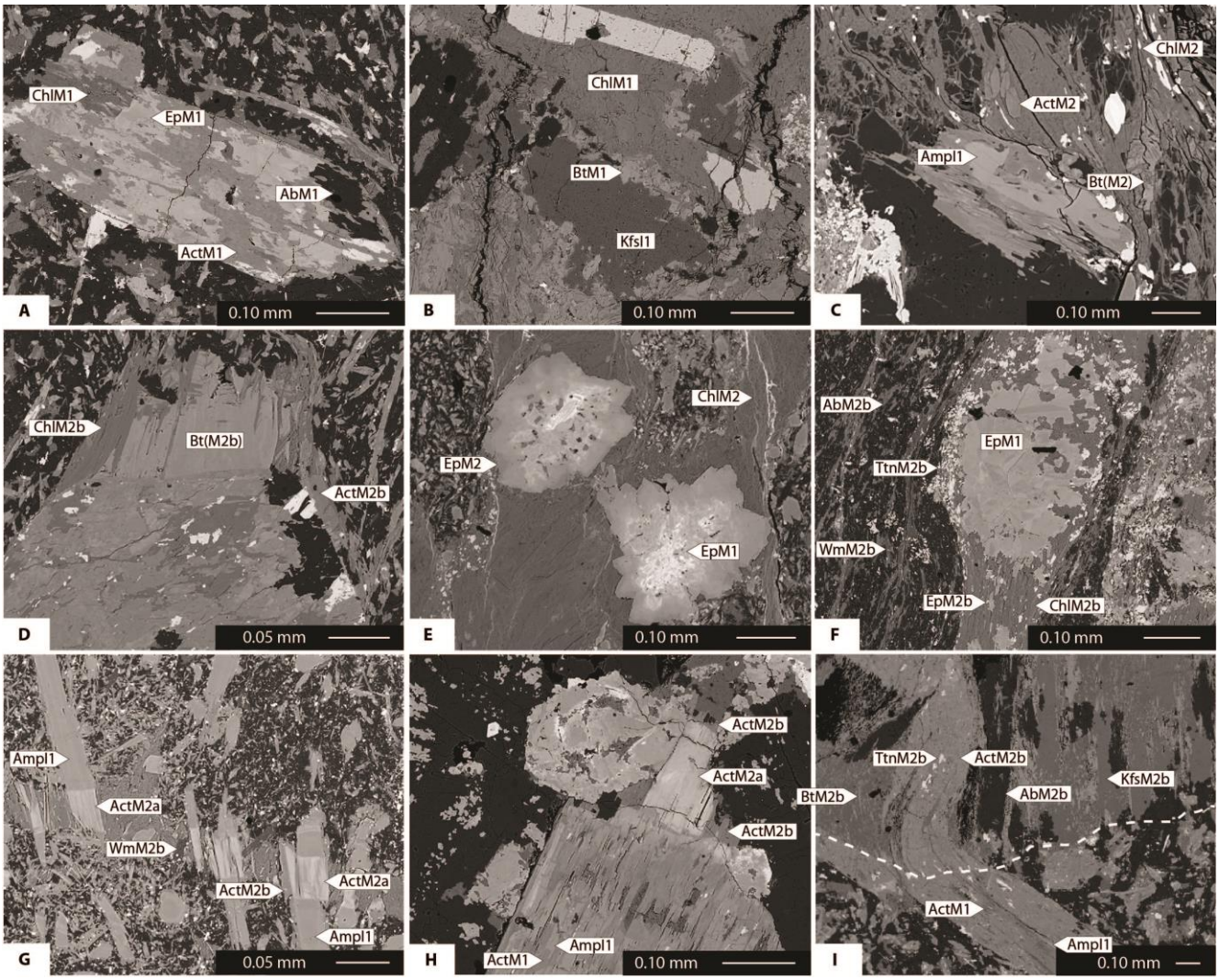

Fig. 1.2.5. Hydrothermal and syn-D4 mineral assemblages (BSE images): (A) AmpI1 phenocryst in spessartite entirely replaced by hydrotermal minerals, Valscura; (B) Hydrothermal BtM1a around a crystal of igneous K-feldspar in appinite, Haut Boréon; (C) AmpI1 crystal wrapped by S4 in an appinite from Haut Boréon. S4 is supported by newly-formed grains of ActM2,ChlM2, and BtM2; other grains of BtM2 are instead relics with respect to S4; (D) Phenocryst of AmpI1 largely replaced by M1 mineral assemblages and wrapped by S4 in a spessartite from Valscura. Pressure shadows are filled by BtM2b, and ActM2b grew at the edges of the AmpI1 phenocryst. BtM2b is partially overgrown by ChlM2; (E) hydrothermal EpM1 crystals wrapped by EpM2 in a foliated spessartite from Haut Boréon; (F) porphyroclast of EpM1 with lobate margins wrapped by S4 foliation in a spessartite from Valscura. EpM1 is characterized by patchy and irregular zoning. S4 foliation is supported by PhM2b and ChlM2b. TtnM2b marks the strain caps. EpM2b fills the pressure shadows; (G) tensional vein mineralized by ActM2a and ChlM2a in spessartite from Valscura. ActM2b wraps ActM2a together with AmpI1; PhM2b intersects the edges of the vein; (H) coarse-grained crystal of AmpI1 locally replaced by ActM1 and ChlM1 in appinite from Valscura. Two highly discontinous coronae of actinolite wrap AmpI1; (I) syn-D4 tensional veins (north of dashed line) filled by ActM2b, AbM2b, BtM2b, KfsM2b, TtnM2b in spessartite from Valscura.

occupy tensional veins along dyke margins coupled with syn-kinematic stylolitic films marked by fine-grained trails of TtnM2a and ChlM2a. In low-strain domains, ActM2a forms coronae around igneous

amphibole crystals, which locally are partially to totally replaced by M1 assemblages (Fig. 1.2.5h). Microcrystals of PlM2b, ActM2b, BtM2b, ChlM2b, EpM2b, TtnM2b, and PhM2b mark S4 (Fig. 1.2.5f). ActM2b occurs together with BtM2b in pressure shadows around igneous amphibole porphyroclasts, and with ChlM2b in syn-kinematic boudin necks. Microcrystalline aggregates of TtnM2b are concentrated in S4 strain caps around igneous- and hydrothermal-derived porphyroclasts (Fig. 1.2.5f). ActM2b rims both igneous amphiboles and ActM2a (Fig. 1.2.5g). AbM2b, ActM2b, and KfsM2b fill tensional veins at dyke margins (Fig. 1.2.5i) and fine-grained aggregates of TtnM2b define D4 stylolites that are orthogonal to the veins. Moreover, ActM2b forms discontinuous rims around ActM2a coronae, which in turn rim igneous amphibole (Fig. 1.2.5h).

In both localities, crystals of BtM2/M2b with SPO parallel to S4 or in AmpI1 pressure shadows are commonly replaced by ChlM2/M2b during S4 development (Fig. 1.2.5c). ActM2, BtM2, and EpM2 supporting S4 are rarely preserved, and their abundance decreases with the increase of chlorite, albite, titanite, and opaque minerals on S4. We interpret the loss of ActM2, BtM2, and EpM2, as well as of igneous and hydrothermal relics, as an effect of the progression of mylonitic deformation during progressive exhumation up to cataclastic and brittle conditions. Hereafter, we focus on samples preserving the most complete mineral record for constraining the prograde Alpine evolution and metamorphic peak.

Mineral chemistry

Mineral analyses were carried out at Università degli Studi di Milano with a JEOL 8200 Super Probe (WDS), working at 15 kV accelerating voltage with a current beam of 5 nA; natural silicates were used as standards. 13 lamprophyre samples (6 from Valscura and 7 from Boréon) were analyzed to constrain the composition of the igneous and metamorphic minerals in different lamprophyre types. Amphibole formulae were calculated checking the most satisfying results of 13, 15, 16 cations, and 23 O normalizations, only considering oxo-component when Ti > 0.5 apfu (Hawthorne et al. 2012, Locock, 2014). Clinopyroxene was recalculated on the basis of 4 cations and 6 O, feldspar of 4 O, epidote of 8 cations and 12.5 O, biotite of 11 O, and chlorite of 7 O. The mineral chemical dataset is available in supplementary data I.

Igneous minerals

In Valscura, AmpI1 is characterized by higher Mg#, Al, Ti, and Na content than in AmpI2a (Tab. 1.2.2, Fig. 1.2.6). AmpI1 in appinite is magnesio-hastingsite, Ti-rich pargasite, pargasite or, in few

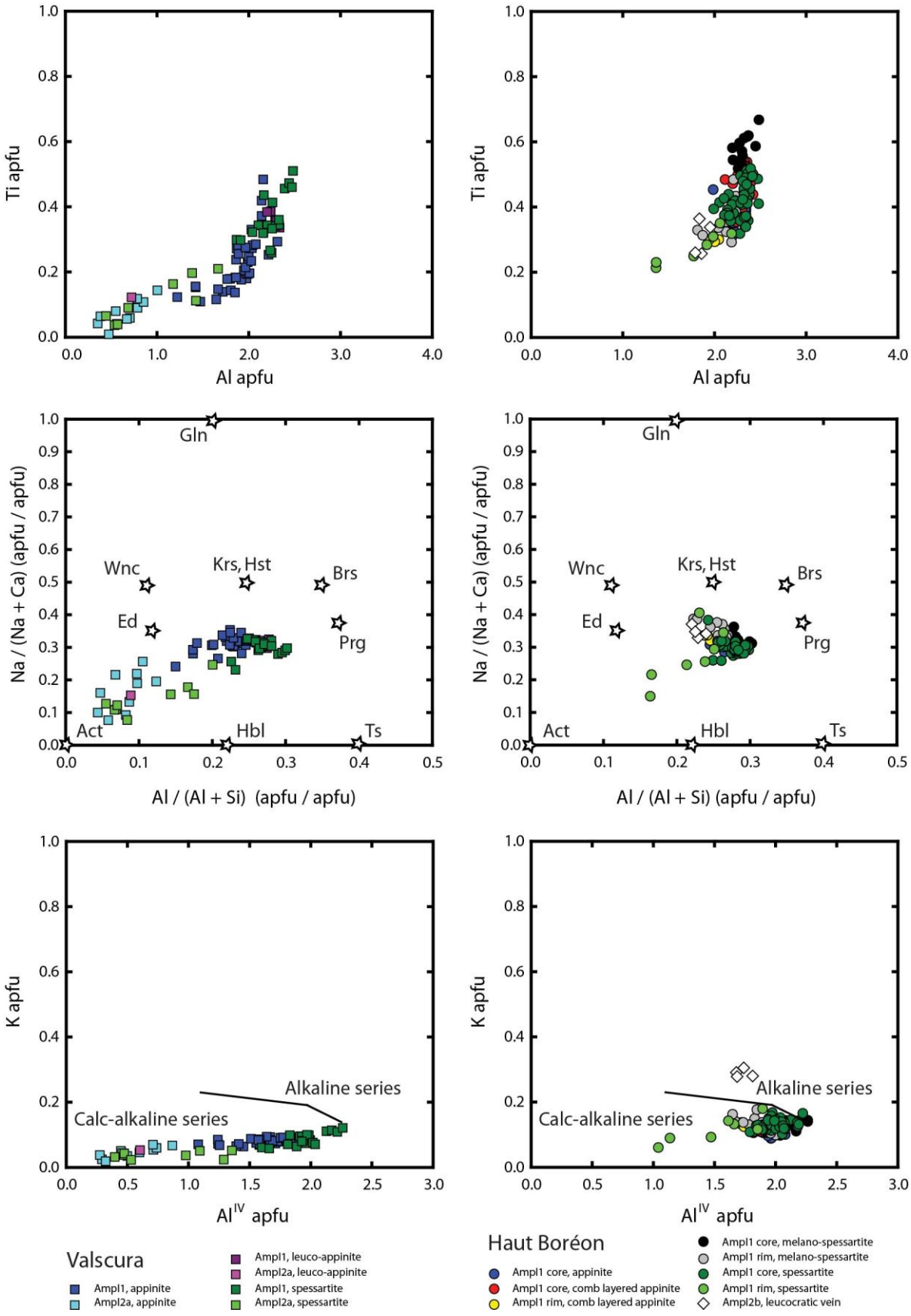

Figure 1.2.6. Compositions of igneous amphiboles in Valscura (left column) and Haut Boréon (right column), as function of microstructural site and lamprophyre rock type. Calc-alkaline and alkaline fields in AlIV vs K diagram are from Ridolfi and Renzulli (2012).

Site	Rock type	Generation	Si	Al^{IV}	Ti	Al^{VI}	Mg#	Ca	Na	K
Valscura	Appinite	AmpI1	**6.00 - 6.92**	**1.08 - 2.00**	**0.11 - 0.48**	**0.14 - 0.38**	**0.56 - 0.71**	**1.57 - 1.88**	**0.51 - 0.91**	**0.07 - 0.11**
		(37 data)	6.36 ± 0.21	1.64 ± 0.21	0.23 ± 0.09	0.26 ± 0.05	0.64 ± 0.04	1.71 ± 0.08	0.79 ± 0.08	0.08 ± 0.01
		AmpI2a	**7.13 - 7.73**	**0.28 - 0.87**	**0.01 - 0.14**	**0.06 - 0.17**	**0.42 - 0.64**	**1.37 - 1.86**	**0.15 - 0.48**	**0.02 - 0.07**
		(10 data)	7.45 ± 0.20	0.55 ± 0.20	0.08 ± 0.04	0.11 ± 0.03	0.55 ± 0.07	1.58 ± 0.16	0.31 ± 0.10	0.05 ± 0.02
	Leuco-appinite	AmpI1	**6.01 - 6.05**	**1.95 - 2.00**	**0.34 - 0.39**	**0.25 - 0.36**	**0.67 - 0.71**	**1.81 - 1.87**	**0.78 - 0.87**	**0.08**
		(5 data)	6.03 ± 0.02	1.97 ± 0.02	0.36 ± 0.02	0.30 ± 0.04	0.69 ± 0.02	1.84 ± 0.02	0.82 ± 0.04	-
		AmpI2a	**7.40**	**0.60**	**0.12**	**0.12**	**0.75**	**1.81**	**0.33**	**0.05**
		(1 data)	-	-	-	-	-	-	-	-
	Spessartite	AmpI1	**5.74 - 6.46**	**1.60 - 2.26**	**0.26 - 0.51**	**0.20 - 0.34**	**0.57 - 0.78**	**1.72 - 1.96**	**0.59 - 0.87**	**0.06 - 0.12**
		(19 data)	6.04 ± 0.16	1.96 ± 0.16	0.36 ± 0.07	0.27 ± 0.04	0.70 ± 0.05	1.86 ± 0.06	0.79 ± 0.07	0.09 ± 0.02
		AmpI2a	**6.65 - 7.60**	**0.40 - 1.36**	**0.04 - 0.21**	**0.05 - 0.31**	**0.53 - 0.70**	**1.23 - 1.94**	**0.16 - 0.58**	**0.02 - 0.05**
		(9 data)	7.22 ± 0.37	0.78 ± 0.37	0.11 ± 0.06	0.15 ± 0.09	0.62 ± 0.07	1.73 ± 0.21	0.29 ± 0.13	0.04 ± 0.01
Haut Boréon	Appinite	AmpI1 core	**5.92 - 6.12**	**1.88 - 2.08**	**0.31 - 0.45**	**0.10 - 0.33**	**0.54 - 0.64**	**1.69 - 1.91**	**0.81 - 0.94**	**0.09 - 0.13**
		(34 data)	6.03 ± 0.05	1.97 ± 0.05	0.38 ± 0.03	0.26 ± 0.04	0.67 ± 0.05	1.87 ± 0.04	0.84 ± 0.03	0.11 ± 0.01
	Melanocratic spessartite	AmpI1 core	**5.74 - 6.06**	**1.94 - 2.26**	**0.41 - 0.67**	**0.19 - 0.37**	**0.55 - 0.68**	**1.84 - 1.94**	**0.79 - 1.05**	**0.10 - 0.14**
		(17 data)	5.94 ± 0.09	2.06 ± 0.09	0.54 ± 0.07	0.25 ± 0.05	0.62 ± 0.03	1.89 ± 0.03	0.89 ± 0.06	0.12 ± 0.01
		AmpI1 rim	**6.03 - 6.41**	**1.59 - 1.97**	**0.23 - 0.48**	**0.15 - 0.35**	**0.41 - 0.62**	**1.73 - 1.88**	**0.85 - 1.10**	**0.10 - 0.18**
		(15 data)	6.16 ± 0.12	1.84 ± 0.12	0.37 ± 0.06	0.28 ± 0.05	0.50 ± 0.05	1.81 ± 0.04	0.98 ± 0.08	0.14 ± 0.02
		AmpI2b	**6.19 - 6.32**	**1.68 - 1.81**	**0.26 - 0.36**	**0.11 - 0.15**	**0.25 - 0.34**	**1.71 - 1.79**	**0.86 - 1.01**	**0.28 - 0.31**
		(4 data)	6.27 ± 0.05	1.73 ± 0.05	0.30 ± 0.05	0.13 ± 0.01	0.28 ± 0.04	1.75 ± 0.03	0.93 ± 0.05	0.29 ± 0.01
	Comb-layered appinite	AmpI1 core	**5.87 - 6.18**	**1.82 - 2.13**	**0.33 - 0.54**	**0.20 - 0.35**	**0.48 - 0.68**	**1.81 - 1.94**	**0.78 - 0.92**	**0.11 - 0.14**
		(27 data)	6.00 ± 0.09	2.00 ± 0.09	0.45 ± 0.06	0.28 ± 0.04	0.60 ± 0.06	1.89 ± 0.04	0.86 ± 0.04	0.12 ± 0.01
		AmpI1 rim	**6.26 - 6.28**	**1.72 - 1.74**	**0.29 - 0.30**	**0.21 - 0.33**	**0.44 - 0.47**	**1.76 - 1.81**	**0.85 - 0.91**	**0.12 - 0.14**
		(3 data)	6.27 ± 0.01	1.73 ± 0.01	-	0.27 ± 0.05	0.45 ± 0.02	1.79 ± 0.02	0.89 ± 0.02	0.13 ± 0.01
	Spessartite	AmpI1 core	**5.78 - 6.21**	**1.79 - 2.22**	**0.32 - 0.52**	**0.13 - 0.38**	**0.51 - 0.75**	**1.79 - 1.96**	**0.66 - 1.11**	**0.10 - 0.17**
		(48 data)	6.00 ± 0.10	2.00 ± 0.10	0.41 ± 0.05	0.27 ± 0.05	0.68 ± 0.05	1.87 ± 0.04	0.80 ± 0.06	0.13 ± 0.01
		AmpI1 rim	**6.10 - 6.96**	**1.04 - 1.90**	**0.21 - 0.35**	**0.21 - 0.32**	**0.37 - 0.71**	**1.70 - 1.90**	**0.31 - 1.16**	**0.06 - 0.18**
		(7 data)	6.47 ± 0.31	1.53 ± 0.31	0.28 ± 0.05	0.28 ± 0.04	0.58 ± 0.10	1.82 ± 0.06	0.72 ± 0.27	0.12 ± 0.04

Table 1.2.2. Compositional ranges and average values (± s.d.) of igneous amphiboles in Argentera-Mercantour lamprophyres.

cases, magnesio-ferri-hornblende; AmpI2a is magnesio-ferri-hornblende, or, rarely, actinolite and ferro-actinolite. In spessartite and leuco-appinite, AmpI1 is Ti-rich pargasite, Ti-rich magnesio-hastingsite, pargasite, or ferri-kaersutite; AmpI2a is magnesio-horneblende, magnesio-ferri-horneblende, or actinolite.

In Haut Boréon, AmpI1 is characterized by decreasing of Mg#, Ti, and Al content from core to rim (Tab. 1.2.2, Fig. 1.2.6). AmpI0 plots amongst the Ti- and Al-richest AmpI1 core, whereas oscillatory zoning in AmpI1 core reflects minor variations in Mg#, Si, Al, and Ti. AmpI1 in appinite is Ti-rich pargasite or Ti-rich magnesio-hastingsite. In melano-spessartite, AmpI1 core is ferri-kaersutite or Ti-rich pargasite, characterized by the highest Ti content; AmpI1 rim is Ti-rich pargasite or ferro-

pargasite. In comb-layered appinite, AmpI1 is ferri-kaersutite, Ti-rich pargasite, or magnesio-hastingsite at core, and Ti-rich ferro-pargasite or ferro-pargasite at rim. In spessartite, AmpI1 core is Ti-rich pargasite or ferri-kaersutite; AmpI1 rim is Ti-rich pargasite, Ti-rich ferro-pargasite, pargasite, or magnesio-hornblende. AmpI2b in the leucocratic veins is Ti-rich hastingsite, hastingsite, or Ti-rich ferro-pargasite, with K content suggesting an alkaline affinity for these late-intrusive veins, in contrast with the calc-alkaline signature of AmpI1 (Fig. 1.2.6).

Simple-twinned euhedral to subhedral plagioclase is An_{1-4} in all the lamprophyre types. However, PlI1 is widely replaced by EpM1 and therefore it may not preserve the primary composition: area analyses on AbM1 + EpM1 domains in Valscura appinites point to An_{28-40}. CpxI0 is characterized by Mg# = 0.66 - 0.75, Ca = 0.88 - 0.91 apfu, Na = 0.03 - 0.04 apfu, and Al lower than 0.09 apfu. BtI shows Mg# = 0.42 - 0.48 and Ti = 0.19 - 0.27 apfu.

Hydrothermal and metamorphic minerals

M1 comprises AbM1 (An_{0-3}), ActM1, ChlM1, EpM1, KfsM1, TtnM1, BtM1, CalM1, HemM1, PyM1. In ChlM1, Si is 2.90 ± 0.08 apfu and Al 2.29 ± 0.10 apfu. ChlM1 in Valscura is Mg richer (Mg# = 0.59 – 0.67) than in Haut Boréon (Mg# = 0.50 - 0.60) (Fig. 1.2.7). BtM1 is characterized by Mg# = 0.40 - 0.52 and Ti = 0.11 ± 0.03 apfu. Epidote (Fig. 1.2.5e) shows decreasing of Fe^{3+} / (Al + Fe^{3+}) ratio from EpM1 at core (0.35) to EpM2 at rim (0.29).

M2 comprises ActM2, BtM2, ChlM2, EpM2, KfsM2, OpqM2, PhM2, PlM2 (An_{3-12}), and TtnM2. In both localities, ActM2 is characterized by higher Al^{IV}, Al^{VI}, ^{B}Na, ^{A}Na and lower Si and ^{B}Ca content than ActM1 (Tab. 1.2.3, Fig. 1.2.8).

In Valscura, ChlM2a shows Si = 2.79 ± 0.05 apfu and Mg# = 0.58 - 0.61, with Al content (2.52 ± 0.05 apfu) higher than in ChlM1 (Fig. 1.2.7). ChlM2b is similar to ChlM2a in Mg# (0.57 - 0.60) and Si content (2.82 ± 0.06 apfu), but Al richer (2.56 ± 0.03 apfu) (Fig. 1.2.7). BtM2b is Ti poorer (0.06 ± 0.02 apfu) than BtM1, with Mg# = 0.53 - 0.62 (Fig. 1.2.7). In PhM2b, Si is 6.51 ± 0.09 apfu, Al is 4.79 ± 0.12 apfu, and Na is lower than 0.04 apfu.

In Haut Boréon, ChlM2 shows Si = 2.78 ± 0.08 apfu and Mg# = 0.49 - 0.60, with Al content (2.52 ± 0.12 apfu) higher than in ChlM1 (Fig. 1.2.7). BtM2 is characterized by Ti = 0.03 - 0.10 apfu and Mg# = 0.57 - 0.60 (Fig. 1.2.7).

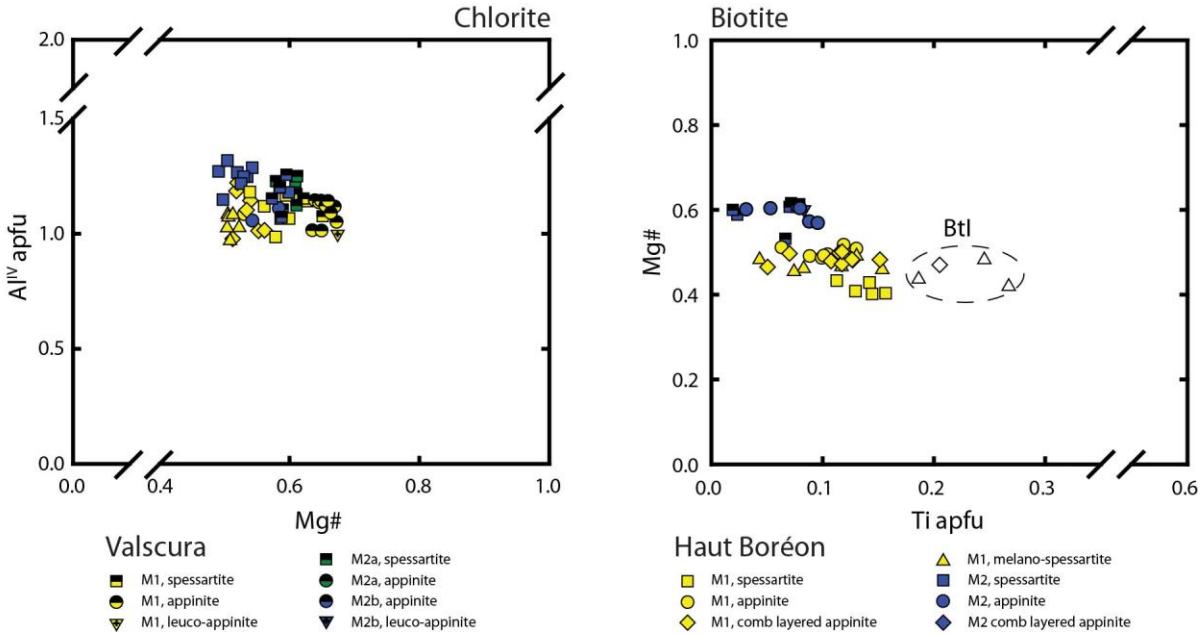

Figure 1.2.7. Compositional variations of hydrothermal (M1) and syn-D4 (M2, M2a, M2b) chlorites and biotites.

Physical conditions of igneous and metamorphic processes

Igneous geo-thermobarometry

Lamprophyre crystallization pressure and temperature are estimated by amphibole thermobarometry. We adopted the formulation of Ridolfi et al. (2010), which is calibrated on mafic to intermediate calc-alkaline rocks. Furthermore, we also apply the Al-in-hornblende barometer of Mutch et al. (2016) calibrated on hornblende-bearing granitoids to better constrain the pressure under which rims of AmpI2a, magnesio-ferri-hornblende, developed. AmpI1 rim in Haut Boréon and AmpI2a in Valscura represent the latest stages of amphibole crystallization and therefore they are used for constraining the maximum emplacement depth.

In Valscura, AmpI1 crystallization conditions are suggested at around 1000°C and 0.1 to 0.7 GPa. AmpI2a records significantly lower temperature, mainly between 700 and 750°C, and pressure lower than 0.1 GPa (Tab. 1.2.4) that corresponds to the emplacement conditions.

A slight decrease in crystallization pressure is also recorded, from core to rim, by AmpI1 in Haut Boréon. Here, AmpI1 core indicates crystallization temperature between 940 and 1050°C and pressure at 0.3 - 0.7 GPa (Tab. 1.2.4). However, AmpI1 core composition may not reflect the crystallization pressure, as suggested by coarse-grained and comb-layer textured AmpI1 indicating directional

Site	Rock type	Generation	Si	Al^{IV}	Ti	Al^{VI}	Mg#	Ca	^{B}Na	^{A}Na	K
Valscura	Appinite	AmpM1	**7.81 - 8.00**	**0.00 - 0.19**	**0.00 - 0.02**	**0.00 - 0.12**	**0.43 - 0.76**	**1.91 - 2.00**	**0.00 - 0.08**	**0.00 - 0.03**	**0.00 - 0.01**
		(35 data)	7.92 ± 0.05	0.08 ± 0.05	-	0.06 ± 0.03	0.70 ± 0.06	1.97 ± 0.02	0.02 ± 0.01	0.01 ± 0.01	-
		AmpM2a	**7.95**	**0.05**	**0.01**	**0.09**	**0.53**	**1.97**	**0.03**	**0.01**	**0.01**
		(1 data)	-	-	-	-	-	-	-	-	-
		AmpM2b	**7.69 - 7.94**	**0.06 - 0.31**	**0.00 - 0.02**	**0.07 - 0.24**	**0.44 - 0.77**	**1.90 - 1.96**	**0.02 - 0.09**	**0.00 - 0.07**	**0.01 - 0.03**
		(14 data)	7.85 ± 0.06	0.15 ± 0.06	-	0.13 ± 0.04	0.67 ± 0.09	1.93 ± 0.02	0.05 ± 0.02	0.02 ± 0.02	-
	Leuco-appinite	AmpM1	**7.93 - 7.96**	**0.04 - 0.07**	**0.00 - 0.01**	**0.01 - 0.07**	**0.71 - 0.72**	**1.96 - 1.98**	**0.00 - 0.04**	**0.00 - 0.00**	**0.00**
		(2 data)	-	-	-	-	-	-	-	-	-
	Spessartite	AmpM1	**7.81 - 7.99**	**0.01 - 0.19**	**0.00 - 0.01**	**0.02 - 0.08**	**0.61 - 0.74**	**1.91 - 1.98**	**0.01 - 0.05**	**0.00 - 0.05**	**0.00 - 0.01**
		(17 data)	7.91 ± 0.05	0.09 ± 0.05	-	0.04 ± 0.02	0.70 ± 0.04	1.96 ± 0.02	0.02 ± 0.01	0.01 ± 0.01	
		AmpM2a	**7.87 - 7.97**	**0.03 - 0.13**	**0.00 - 0.02**	**0.03 - 0.10**	**0.49 - 0.75**	**1.86 - 1.98**	**0.02 - 0.08**	**0.00 - 0.05**	**0.00 - 0.01**
		(9 data)	7.91 ± 0.04	0.09 ± 0.04	-	0.08 ± 0.03	0.66 ± 0.09	1.95 ± 0.04	0.04 ± 0.02	0.01 ± 0.01	-
		AmpM2b	**7.61 - 7.92**	**0.08 - 0.39**	**0.00 - 0.03**	**0.05 - 0.24**	**0.55 - 0.74**	**1.78 - 1.98**	**0.01 - 0.10**	**0.00 - 0.10**	**0.01 - 0.07**
		(21 data)	7.79 ± 0.09	0.21 ± 0.09	-	0.13 ± 0.05	0.68 ± 0.04	1.93 ± 0.05	0.04 ± 0.02	0.03 ± 0.03	0.02 ± 0.01
	All	AmpM1	**7.81 - 8.00**	**0.00 - 0.19**	**0.00 - 0.02**	**0.00 - 0.12**	**0.43 - 0.76**	**1.91 - 2.00**	**0.00 - 0.08**	**0.00 - 0.05**	**0.00 - 0.01**
		(53 data)	7.91 ± 0.06	0.09 ± 0.05	-	0.05 ± 0.03	0.70 ± 0.05	1.97 ± 0.02	0.02 ± 0.01	0.01 ± 0.01	-
	All	AmpM2b	**7.61 - 7.94**	**0.06 - 0.39**	**0.00 - 0.03**	**0.05 - 0.24**	**0.44 - 0.77**	**1.78 - 1.98**	**0.01 - 0.10**	**0.00 - 0.10**	**0.01 - 0.07**
		(35 data)	7.81 ± 0.09	0.19 ± 0.09	-	0.13 ± 0.05	0.68 ± 0.07	1.93 ± 0.04	0.05 ± 0.02	0.03 ± 0.02	0.02 ± 0.01
Haut Boréon	Appinite	AmpM1	**7.89**	**0.11**	**0.00**	**0.06**	**0.58**	**1.97**	**0.03**	**0.04**	**0.01**
		(1 data)	-	-	-	-	-	-	-	-	-
		AmpM2	**7.63 - 7.83**	**0.17 - 0.37**	**0.00 - 0.01**	**0.10 - 0.15**	**0.63 - 0.70**	**1.87 - 1.90**	**0.07 - 0.08**	**0.02 - 0.10**	**0.01 - 0.03**
		(2 data)	-	-	-	-	-	-	-	-	-
	Melanocratic spessartite	AmpM1	**7.92**	**0.08**	**0.01**	**0.05**	**0.63**	**1.95**	**0.03**	**0.01**	**0.01**
		(1 data)	-	-	-	-	-	-	-	-	-
	Comb-layered appinite	AmpM1	**7.94**	**0.06**	**0.00**	**0.08**	**0.65**	**1.87**	**0.10**	**0.02**	**0.01**
		(1 data)	-	-	-	-	-	-	-	-	-
		AmpM2	**7.63**	**0.35**	**0.01**	**0.00**	**0.63**	**1.90**	**0.07**	**0.04**	**0.03**
		(1 data)	-	-	-	-	-	-	-	-	-
	Spessartite	AmpM1	**7.89 - 7.99**	**0.01 - 0.11**	**0.00 - 0.02**	**0.04 - 0.11**	**0.46 - 0.68**	**1.87 - 1.95**	**0.03 - 0.07**	**0.00 - 0.04**	**0.00 - 0.02**
		(6 data)	7.94 ± 0.04	0.06 ± 0.04	-	0.06 ± 0.03	0.56 ± 0.08	1.93 ± 0.03	0.04 ± 0.02	0.01 ± 0.01	-
		AmpM2	**7.59 - 7.88**	**0.12 - 0.41**	**0.00 - 0.02**	**0.09 - 0.26**	**0.52 - 0.70**	**1.90 - 1.97**	**0.03 - 0.08**	**0.02 - 0.09**	**0.01 - 0.07**
		(11 data)	7.75 ± 0.08	0.25 ± 0.08	-	0.16 ± 0.05	0.64 ± 0.05	1.93 ± 0.02	0.05 ± 0.02	0.05 ± 0.02	0.02 ± 0.02
	All	AmpM1	**7.89 - 7.99**	**0.01 - 0.11**	**0.00 - 0.02**	**0.04 - 0.11**	**0.46 - 0.68**	**1.87 - 1.97**	**0.03 - 0.10**	**0.00 - 0.04**	**0.00 - 0.02**
		(9 data)	7.94 ± 0.04	0.06 ± 0.04	-	0.06 ± 0.02	0.58 ± 0.07	1.93 ± 0.03	0.05 ± 0.02	0.01 ± 0.01	-
	All	AmpM2	**7.59 - 7.88**	**0.12 - 0.41**	**0.00 - 0.02**	**0.00 - 0.26**	**0.52 - 0.70**	**1.87 - 1.97**	**0.03 - 0.08**	**0.02 - 0.10**	**0.01 - 0.07**
		(14 data)	7.73 ± 0.08	0.26 ± 0.08	-	0.15 ± 0.06	0.64 ± 0.04	1.92 ± 0.02	0.06 ± 0.02	0.05 ± 0.03	0.02 ± 0.01

Table 1.2.3. Compositional ranges and average values (± s.d.) of hydrothermal (M1) and syn-D4 (M2) amphiboles in Argentera-Mercantour lamprophyres.

crystallization controlled by dyke wall orientation at the final emplacement level. This evidence casts doubts upon the reliability of amphibole barometry at low pressure. Moreover, comb-layered

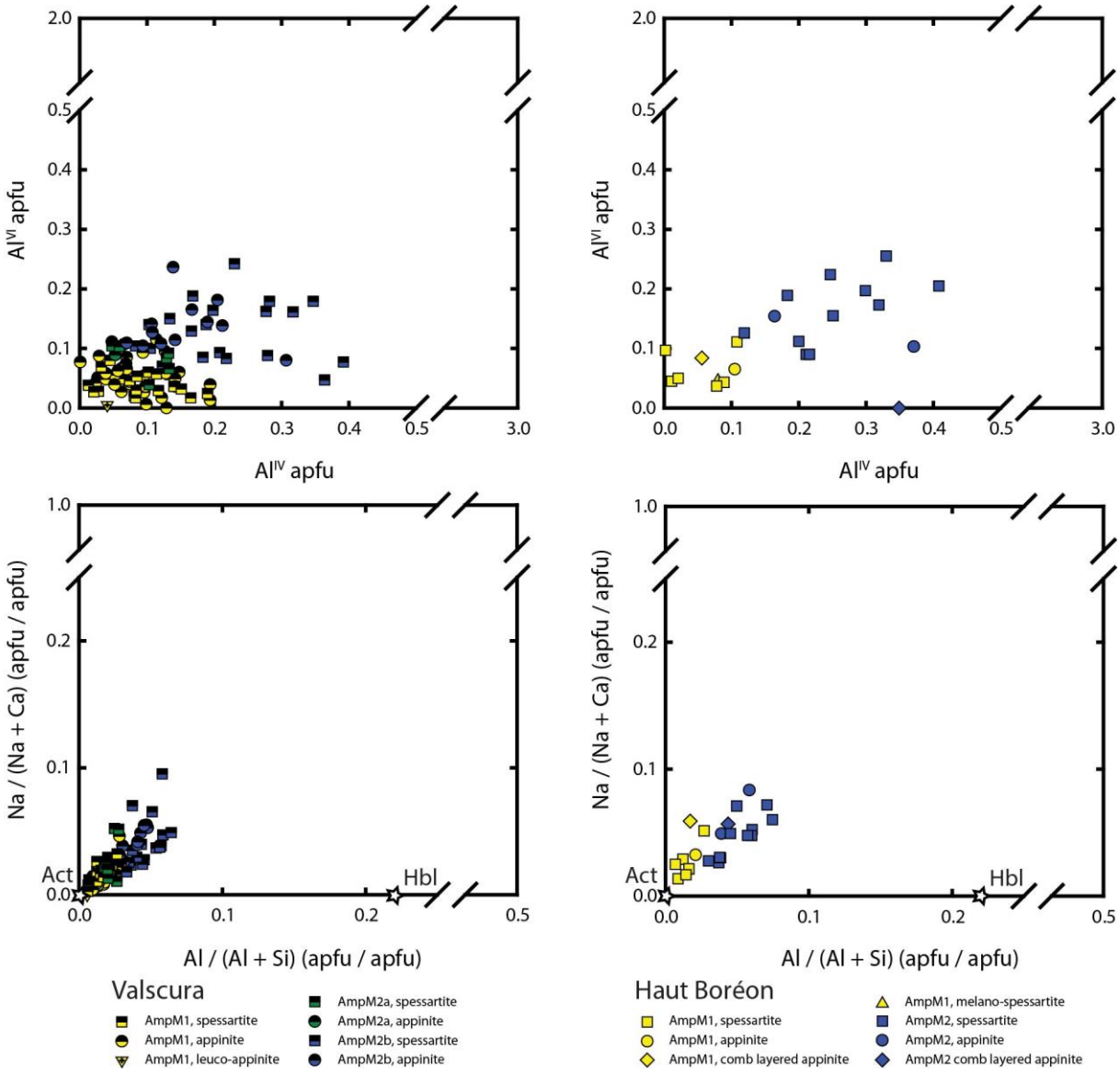

Figure. 1.2.8. Compositional variations of hydrothermal (M1) and syn-D4 (M2, M2a, M2b) amphiboles from Valscura (left column) and Haut Boréon (right column).

amphibole composition is more easily interpreted as function of other parameters, such as temperature, melt composition, water content, and oxygen fugacity (e.g. McCarthy and Müntener, 2016; Pistone et al., 2016). Conversely, compositions of AmpI1 rim in Haut Boréon spessartite suggest emplacement pressure lower than 0.2 GPa (Tab. 1.2.4). Low crystallization pressure for AmpI2a in Valscura and AmpI1 rim in Haut Boréon are thus consistent with shallow-depth emplacement, as confirmed by straight chilled margins and degassing vesicles.

Site	Rock type	Mineral	T (°C)	P (GPa)	
			R10	R10	M16
Valscura	Appinite	AmpI1	**785 - 1009**	**0.11 - 0.52**	
			920 ± 52	0.30 ± 0.09	
		AmpI2a	**666 - 759**	**0.03 - 0.08**	**0.07 - 0.18**
			714 ± 34	0.06 ± 0.02	0.12 ± 0.03
	Leuco-appinite	AmpI1	**1001 - 1021**	**0.44 - 0.54**	
			1009 ± 8	0.49 ± 0.04	
		AmpI2a	**738**	**0.05**	**0.13**
	Spessartite	AmpI1	**927 - 1066**	**0.30 - 0.68**	
			1008 ± 38	0.48 ± 0.11	
		AmpI2a	**665 - 875**	**0.04 - 0.21**	**0.08 - 0.12**
			749 ± 84	0.09 ± 0.06	0.10 ± 0.01
Haut Boréon	Appinite	AmpI1 core	**947 - 1021**	**0.33 - 0.57**	
			1005 ± 14	0.48 ± 0.05	
	Melanocratic spessartite	AmpI1 core	**998 - 1036**	**0.48 - 0.74**	
			1013 ± 12	0.56 ± 0.06	
		AmpI1 rim	**958 - 1001**	**0.40 - 0.48**	
			978 ± 11	0.47 ± 0.02	
	Comb layered appinite	AmpI1 core	**951 - 1034**	**0.40 - 0.64**	
			1002 ± 23	0.53 ± 0.07	
		AmpI1 rim	**929**	**0.31**	
	Spessartite	AmpI1 core	**971 - 1043**	**0.38 - 0.70**	
			1011 ± 18	0.52 ± 0.08	
		AmpI1 rim	**840 - 962**	**0.14 - 0.37**	
			916 ± 45	0.27 ± 0.08	

Table 1.2.4. Thermobarometric estimates on igneous amphiboles (interval and average value ± s.d.). References: R10 - Ridolfi et al. (2010); M16 - Mutch et al. (2016).

P-T constrains on late-intrusive and Alpine metamorphism

Chlorite thermometry (Bourdelle et al., 2013; Cathelineau, 1988; Jowett, 1991) is applied to constrain the temperature of the late-intrusive hydrothermal circulation (M1). Average results from both sites overlap at around T = 300 ± 50°C (Tab. 1.2.5). The Alpine metamorphic peak, recorded by the M2 mineral assemblages, is estimated by amphibole thermobarometry (Gerya et al., 1998). Similarly in Valscura and Haut Boréon, ActM2 records temperature up to 435°C and pressure up to 0.2 GPa (Tab. 1.2.5).

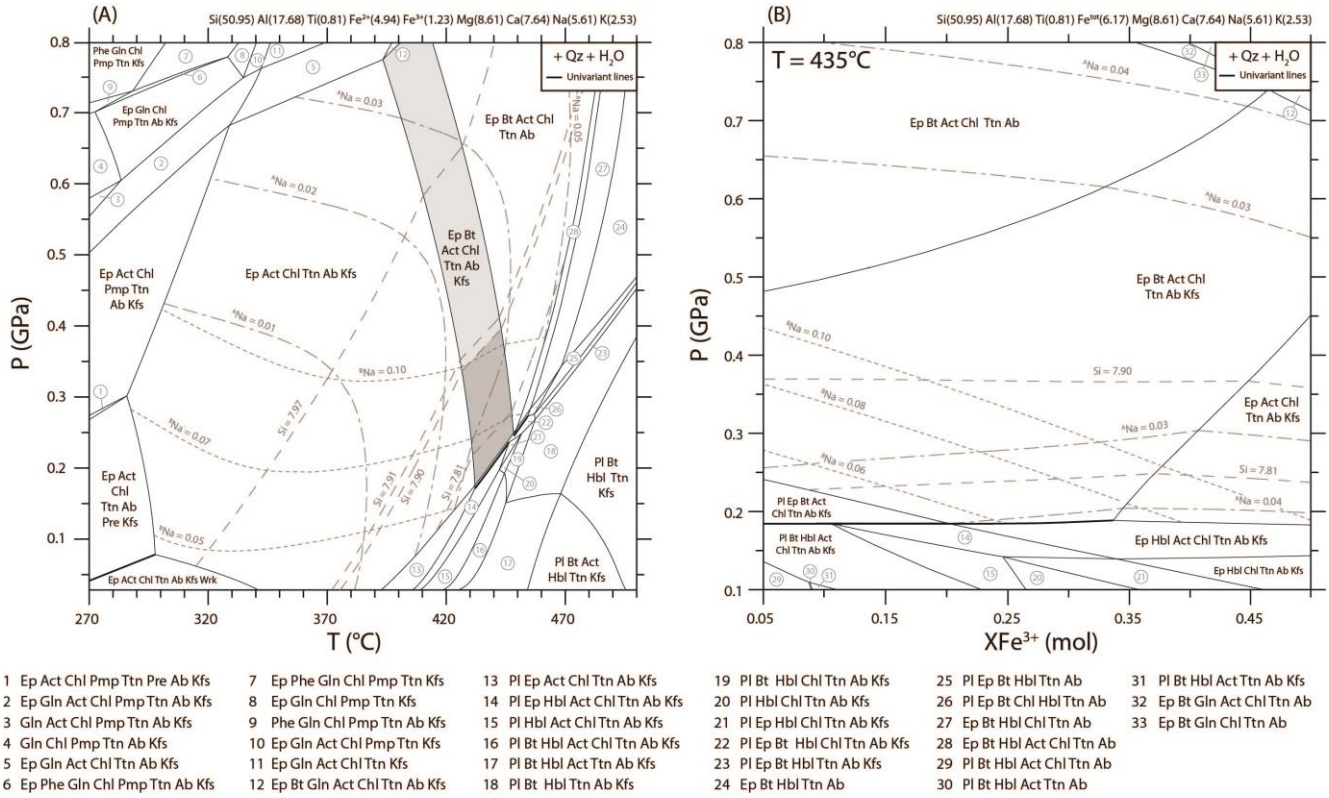

Figure 1.2.9. Pseudosections calculated for the Argentera-Mercantour lamprophyres (sample LMB26: SiO_2 = 54.24, TiO_2 = 1.12, Al_2O_3 = 15.97, FeO_t = 7.06, MgO = 6.15, CaO = 7.59, Na_2O = 3.08, K_2O = 2.11 (%wt), see Filippi et al., 2019) in excess of water. In the picture, bulk composition is converted in cation molar percentage. Details on the adopted thermodynamic database are in the text. Compositional isopleths for actinolite, Si (dashed lines), ^{B}Na (dotted lines) and ^{A}Na (dashed-dotted lines), are added; concentrations are in apfu. A: P-T diagram at X_{Fe}^{3+} = 0.20 (molar ratio). M2b field (Ep + Bt + Act + Chl + Ttn + Ab + Kfs) is colored light grey and further divided by ActM2b compositional isopleths (dark gray). Some very small fields have not been numbered. B: P- X_{Fe}^{3+} diagram at T = 435°C.

Pseudosections are calculated with the free energy minimization program THERIAK-DOMINO (De Capitani & Petrakakis, 2010, version 09/03/2019) for speculating on the stability of M1 and M2 mineral assemblages in the NCKFMASHTO system (Fig. 1.2.9a). The effect of the oxidation state on the stability and preservation of mineral assemblages is evaluated varying the $X_{Fe}^{3+} = Fe^{3+} / (Fe^{2+} + Fe^{3+})$ molar ratio in a P-X diagram at T = 435°C (Fig. 1.2.9b). We adopted a converted version of the thermodynamic database ds62 from Holland and Powell (2011) including a-x relations for epidote, calcic amphibole, white mica, biotite, feldspar, chlorite, and ilmenite (Holland and Powell, 2011; Green et al., 2016; White et al., 2014a; White et al., 2014b). The peristerite gap is modeled including end-member albite in addition to the plagioclase predicted by the solution model.

WR composition of a sample from Valscura (LMB26, Tab. 1.1.1 in Filippi et al. 2019) served as input, in excess of water. We considered the WR composition as reasonable approximation of the reacting

Site	Mineral	T (°C)				P (GPa)
		C88	J91	B13	G98	G98
Valscura	ChlM1	**260 - 371**	**261 - 372**	**251 - 367**		
		297 ± 26	298 ± 27	309 ± 37		
	AmpM2b				**370 - 435**	**0.09 - 0.21**
					394 ± 18	0.15 ± 0.03
Haut Boréon	ChlM1	**250 - 331**	**256 - 336**	**220 - 354**		
		285 ± 23	290 ± 23	300 ± 43		
	AmpM2				**359 - 435**	**0.12 - 0.23**
					405 ± 20	0.17 ± 0.03

Table 1.2.5. Thermobarometric estimates on metamorphic minerals (interval and average value ± s.d.). References : C88 - Cathelineau (1988); J91 - Jowett (1991); B13 - Bourdelle et al. (2013); G98 - Gerya et al. (1998).

volume, because hydrothermal and metamorphic minerals developed in microstructural sites characterized by different finite strain patterns in different rock types (e.g. coronae, differentiated rough and stylolitic films marking S4, porphyroclast rims, strain caps, pressure shadows and/or syn-kinematic extensional veins) are broadly homogeneous in composition.

M1 mineral assemblage (epidote + actinolite + chlorite + titanite + albite + K-feldspar) is constrained between 300 and 400°C at around 0.1 GPa and up to 420°C at 0.4 GPa, assuming $Fe^{3+} / (Fe^{2+} + Fe^{3+}) = 0.2$. Wairakite-in, prehnite-in, and Fe-pumpellyte-in reactions delimit the field at low temperature from low to middle pressure, glaucophane-in at high pressure, plagioclase-in at high temperature and low pressure, biotite-in at high temperature and middle pressure (Fig. 1.2.9a). The lack of biotite in M1 field is expected since BtM1 occurs in K- and likely Ti-rich compositional sub-systems (Fig. 1.2.5b).

The stability field for the M1 assemblage (Fig. 1.2.9a) may be further reduced by considering the compositional isopleths for actinolite Si = 7.91 ± 0.06 apfu and $^{A}Na = 0.01 \pm 0.01$ apfu, representing the average concentrations in AmpM1 in Valscura, and the emplacement pressure determined by igneous barometry (P < 0.1 GPa, Tab. 1.2.4). In this way, the M1 field is delimited between 300 and 400°C. These conditions partially overlap the results of chlorite thermometry on ChlM1 (T = 300 ± 50°C, Tab. 1.2.5): the temperature accountable for the lower greenschist facies M1 stage is constrained between 300 and 350°C.

The stability field of the M2b mineral assemblage (epidote + biotite + actinolite + chlorite + titanite + albite + K-feldspar) is comprised between 390 and 450°C and 0.2 to 0.8 GPa (Fig. 1.2.9a). As expected, phengite is not predicted by the model since it replaces plagioclase. M2b field is delimited by biotite-out reaction at low temperature, by plagioclase-in at low pressure, by K-feldspar-out at high temperature, and by glaucophane-in at high pressure. The hornblende-in reaction at around 460 -

470°C is taken as extreme boundary at higher temperature, since hornblende is never observed in the M2 assemblages. Importantly, volume of chlorite in M2b field abruptly decreases by increasing the temperature of 30°C, whereas biotite increases from 0 to 20 %vol. Relics of BtM2 within S4 and in pressure shadows are overgrown by ChlM2 (Fig. 1.2.5c, d) as result of minimal temperature decrement involving replacement of biotite by chlorite. The P-T interval accountable for the upper greenschist facies M2b stage is better constrained at P = 0.2 - 0.4 GPa and T = 420 - 450°C by compositional isopleths for actinolite Si = 7.81 ± 0.09 apfu and ^{A}Na = 0.03 ± 0.02 apfu (Fig. 1.2.9a). The result well matches the highest thermobarometric estimates (T = 435°C and P = 0.2 GPa, Tab. 1.2.5). Moreover, ^{B}Na compositional isopleths for actinolite are added in Figure 1.2.9. ^{B}Na content is markedly pressure dependent (Fig. 1.2.9a), but significantly shifted towards lower pressure by increasing X_{Fe}^{3+} (Fig. 1.2.9b). In every case, the stability field of ActM1 (^{B}Na = 0.02 ± 0.01 apfu) is restricted to pressure lower than 0.1 GPa, whereas ActM2 (^{B}Na = 0.05 ± 0.02 apfu) is stable in the M2 field at pressure never exceeding 0.4 GPa also for very low X_{Fe}^{3+}.

Discussion

Permian-Triassic lithospheric thinning

Swarms of lamprophyres are widespread in the eastern Argentera-Mercantour ECM. The lamprophyres are heterogeneous in composition and characterized by mingling and magmatic breccia textures that result from multiple magmatic injections. Cores of AmpI1, mainly kaersutite and Ti-rich pargasite, retain crystallization temperature up to 1040°C at 0.3 - 0.6 GPa. However, this pressure does not represent the emplacement condition. Oscillatory compositional zoning at AmpI1 core (Fig. 1.2.4a) reflects complex reaction paths implying interactions of fluid/melt and crystals during ascent of successive magma pulses.

Al^{IV} vs K diagram (Fig. 1.2.6) highlights the calc-alkaline affinity of the lamprophyres. However, the composition of AmpI2b in late-intrusive leucocratic veins suggests an alkaline nature for the last magmatic injection. The transition from Permian calc-alkaline to Permian-Triassic alkaline magmatism is a well-known signature of the Southern Variscan belt (Filippi et al., 2019 and refs. therein).

Conversely, AmpI2a in Valscura and AmpI1 rim Haut Boréon testify a decrease of temperature and pressure during crystallization, confirming that the lamprophyres emplaced at shallow depth, in agreement with field relationships. Pressure estimates on igneous amphibole lower than 0.1 - 0.2 GPa

reflect the maximum pressure of the dyke emplacement, which is consistent with the occurrence of straight chilled margins and degassing vesicles.

The lamprophyres were affected by localized hydrothermal circulation soon after their emplacement. Despite of differences in X_{Fe} in hydrothermal ChlM1 between Valscura and Haut Boréon (Fig. 1.2.7), thermometric estimates are similar (Tab. 1.2.5). The temperature of the hydrothermal fluids associated with M1 mineral assemblages is constrained at 300 - 350°C under lower greenschist facies conditions by combining chlorite thermometry and pseudosection prediction.

The chronological constrains on the emplacement of the lamprophyres in the Argentera-Mercantour ECM are the crosscutting relationships with the Central Granite (Malaroda et al., 1970), dated at 292 ± 10 Ma (Ferrara and Malaroda, 1969) or 299 - 296 Ma (Corsini et al., 2004), and with the Alpine shear zones (34 - 20 Ma, Corsini et al., 2004; Sanchez et al., 2011a) intersecting the dykes. The prograde metamorphic evolution recorded by the lamprophyres confirms that they pre-date the Alpine collision in the Argentera-Mercantour area: a Permian-Triassic age for the lamprophyres appears reasonable (cfr. Filippi et al., 2019).

In late to post Variscan times, decreasing of mantle contribution in high-K calc-alkaline granitoids, from the high- to low-Mg-number suites, is recognized in some of the ECMs (Debon and Lemmet, 1999). After the early Permian, further emplacement of lamprophyres with high crystallization temperatures is consistent with re-enhancing of partial melting of the subcontinental mantle in the Argentera-Mercantour ECM area. This is also characteristic of other segments of the Southern Variscan Belt, in which Permian-Triassic lithospheric thinning triggered mantle melting and led to the Tethys opening in Mesozoic times (e.g. Lardeaux and Spalla, 1991; Lustrino et al., 2019; Marotta et al., 2009; Marotta et al., 2018; Roda et al., 2019, Spalla et al., 2014).

Alpine collision

The Argentera-Mercantour lamprophyres retain the Alpine metamorphic peak at 420 - 450°C and 0.2 - 0.4 GPa (Fig. 1.2.10). Similar dyke orientations and P-T estimates at both sides of FSZ (Fig. 1.2.1 and 1.2.2) point out negligible vertical offset and rotation operated by this Alpine thrust in the eastern Argentera-Mercantour ECM.

The prograde path from lower greenschist facies late-intrusive hydrothermalism towards the transition to the amphibolite facies is reflected by (1) increasing of Ca content in PlM2, (2) relative enrichment in Al^{IV}, Al^{VI}, ^{B}Na, ^{A}Na and depletion in Si in ActM2 with respect to ActM1, (3) Al enrichment in ChlM2, and (4) decreasing of Fe^{3+} / (Al + Fe^{3+}) ratio in EpM2, as expected for mafic systems (Maruyama et al., 1982, 1983; Thompson and Laird, 2005). The occurrence of biotite in the M2

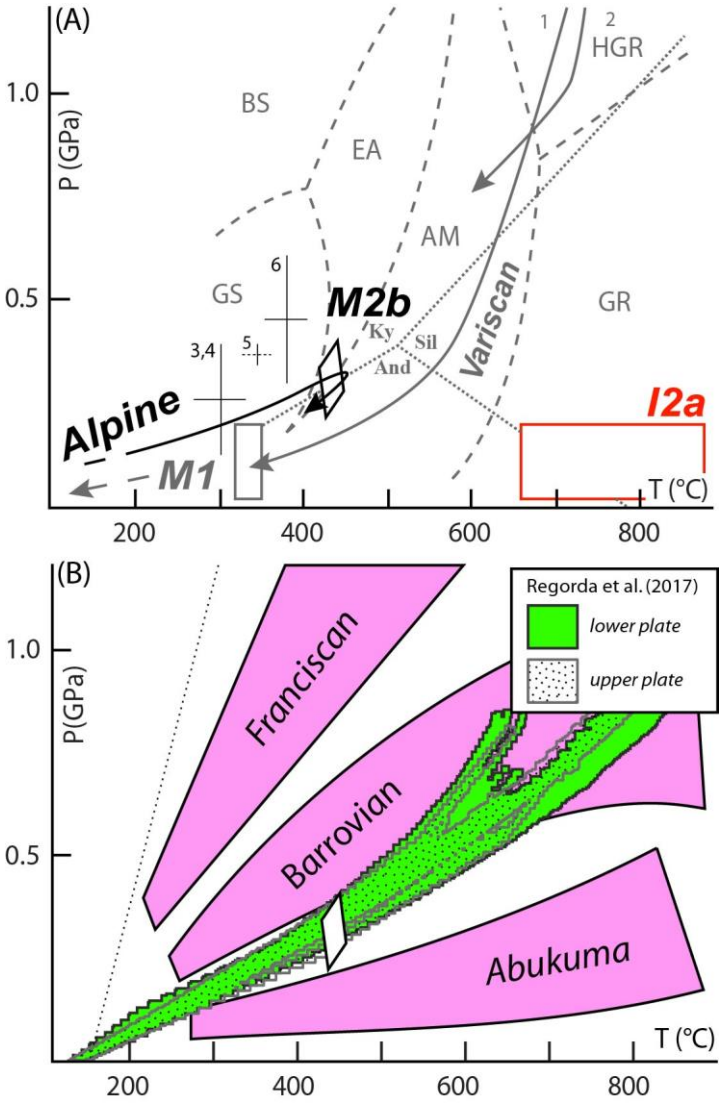

Figure 1.2.10. Metamorphic evolution of Argentera-Mercantour ECM. A: summary of Variscan and Alpine P-T estimates from the literature: 1 - Ferrando et al. (2008); 2 - Latouche & Bogdanoff (1987); 3 - Attal (2000); 4 - Leclère et al. (2014); 5 - Corsini et al. (2004); 6 - Sanchez et al. (2011a) (VSZ); I2a (last stage of igneous crystallization), M1 (hydrothermalism), and M2b (Alpine thermal peak) - this paper. Metamorphic facies are after Ernst & Liou (2008): GS - greenschist; EA - epidote-amphibolite; BS - blueschist; AM - amphibolite; HGR - high-pressure granulite; GR - granulite; aluminosilicate triple point is according to Holland & Powell (1998). B: Comparison between P-T estimates on lamprophyres, classical metamorphic zoning, and numerical model predictions after Regorda et al., (2017); discussion in the text.

assemblage points out upper greenschist facies conditions (Ernst and Liu, 1998) and corroborates the quantitative estimates. Recognizing upper greenschist facies mineral assemblages supporting Alpine structures contrasts with some of the metamorphic maps of the Alps, in which the Alpine metamorphic imprint of the Argentera-Mercantour ECM is labeled as sub-greenschist or lower greenschist facies (Frey et al., 1999; Oberhänsli et al., 2004; Bousquet et., 2012).

However, it should be considered that all over the mapped areas peak mineral assemblages on S4 are only rarely preserved. In fact, in most of the cases, D4 structures are supported by biotite-free assemblages according to decreasing of biotite volume along with temperature (Fig. 1.2.9). The exhumation of the Argentera-Mercantour ECM is in fact accommodated by long-lasting motion and reworking along D4 structures, up to cataclastic and brittle conditions (Baietto et al., 2009; Bigot-Cormier et al., 2006; Corsini et al., 2004; Sanchez et al., 2011a; Sanchez et al., 2011b). Our investigation of the prograde metamorphic evolution has been based on sampling strategies aiming at

selecting mineral fabrics that correspond to the first deformation increments and that escaped the intense retrogression affecting most of the Alpine shear zones. Relics of BtM2 within S4, partially overgrown by ChlM2, testify the beginning of the retrograde path after the Alpine metamorphic peak.
The Alpine P-T peak conditions result in a thermal state of 40°C/km, which is compatible with those expected for crustal thickening (England & Thompson, 1984; Cloos, 1993). This thermal state is comparable with that predicted by the 2-D numerical model of continental collision of Regorda et al. (2017), which considers an Alpine convergence rate in the order of 3 cm/yr (Roda et al., 2012). The thermal state affecting the continental lower plate during the Alpine collision fits well with the record of the Argentera-Mercantour ECM (Fig. 1.2.10).

Conclusion

The lamprophyres of the Argentera-Mercantour ECM, most likely of Permian-Triassic age, are referred the last magmatic event that affected the exhumed Variscan lower crust in the future ECMs of the Western Alps. Since the lamprophyres postdate the early Permian Central Granite intrusion, and consequently the transcurrent motion localized along the VSZ in Carboniferous times (Simonetti et al., 2018), they might well be related to a subsequent tectonic setting, likely the extensional/transtensional phase ancestor of the Tethys ocean opening in Jurassic times (e.g. Roda et al., 2019). The lamprophyres emplaced at very shallow crustal depth and recorded a prograde metamorphic evolution during the Alpine collision, whose peak conditions are now constrained at T = 420 - 450°C and P = 0.2 - 0.4 GPa.

The Orobic Basement

1.3 The Edolo diabase: evidence of continental break-up in the central Southern Alps

Marco Filippi, Jean-Marc Lardeaux, Gisella Rebay, Maria Iole Spalla, Daniele Vergani, Davide Zanoni (paper in preparation)

Abstract

In the northern part of the central Southern Alps (Orobic Alps), a swarm of mafic dykes is historically known as Edolo diabase. The dykes are texturally heterogeneous and display wide compositional variations of igneous mineral phases. On the basis of igneous minerals (clinopyroxene, amphibole, biotite, plagioclase, ilmenite, rare quartz) and WR composition, the Edolo diabase dykes are classified as camptonites, a type of alkaline lamprophyres. WR trace elements concentrations are typical of alkaline within-plate basalts that were emplaced during continental rifting, likely in Triassic times. Thermobarometric estimates on igneous and hydrothermal minerals suggest that the dykes were emplaced at shallow crustal depths (P = 0.09 – 0.16 GPa).

Xenocrysts of igneous clinopyroxene are common in the Edolo diabase dykes: the primitive melt composition at equilibrium with the clinopyroxene xenocrysts is here estimated by REE partition coefficient modelling. A fertile garnet-bearing lherzolitic mantle source is envisaged by batch melting modelling.

Introduction

Permian-Triassic HT metamorphism and mafic magma emplacements in the Variscan basement rocks of the Alps testifies continental rifting that led to the Pangea break-up and Jurassic oceanization (Lardeaux and Spalla, 1991; Diella et al., 1992; Bertotti et al., 1993; Rebay and Spalla 2001; Schuster and Stüwe, 2008; Spalla et al., 2014; Roda et al. 2019). Permian HT metamorphism is well documented in Variscan basement rocks of the Austroalpine domain, in particular in the Sesia Lanzo Zone and Dent-Blanche Nappe (Fig. 1.3.1) (Lardeaux and Spalla, 1991; Rebay and Spalla, 2001; Roda and Zucali, 2011; Manzotti and Zucali, 2013; Manzotti et al., 2014, 2018). In the western Southern Alps, the Variscan basement rocks of the Ivrea Verbano Zone record long lasting thermal relaxation

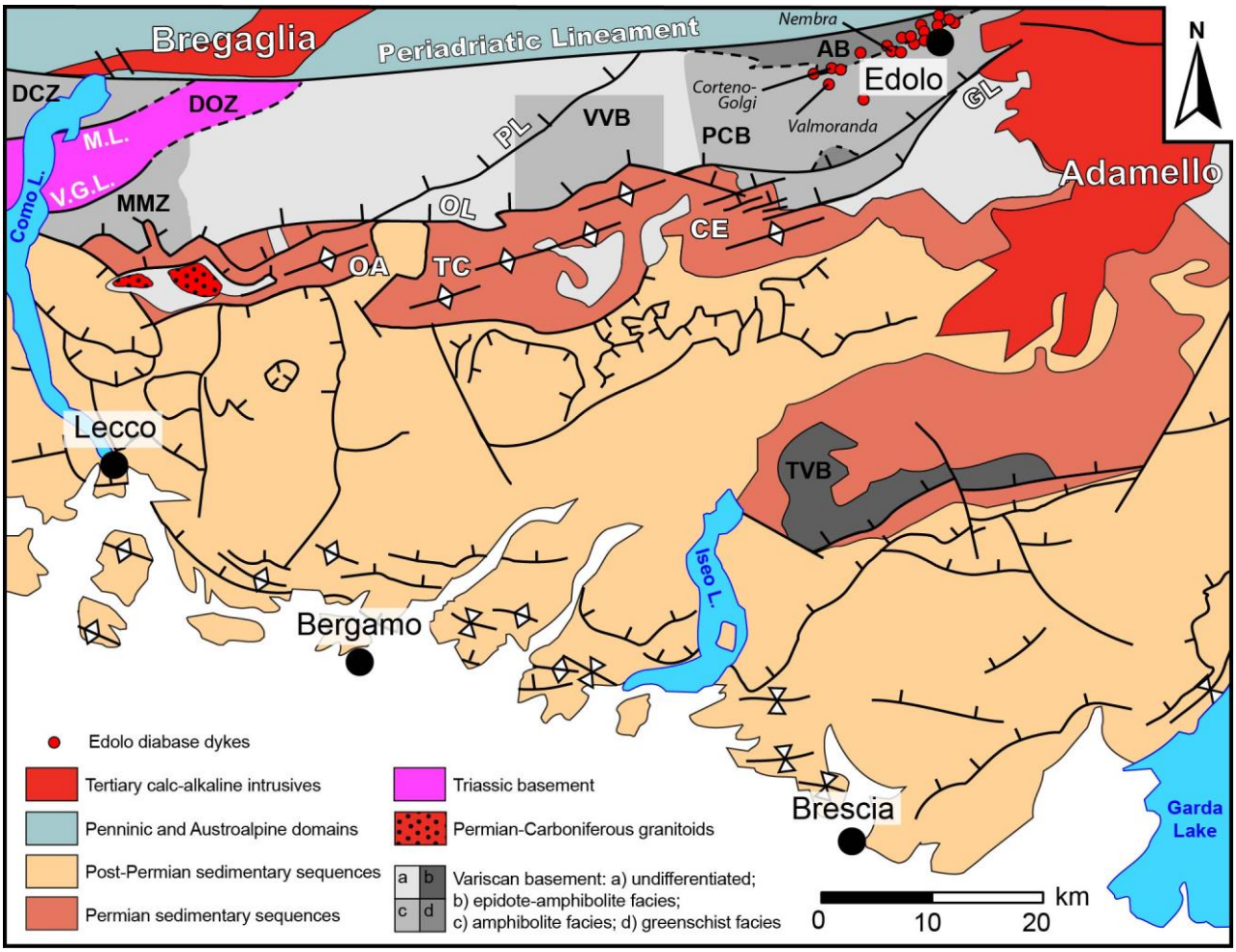

Figure 1.3.1. Geologic sketch of the central Southern Alps and location of Edolo diabase dykes (from Zanoni and Spalla, 2018). Variscan TMUs: AB = Aprica basement; DCZ = Domaso – Cortafò Zone; DOZ = Dervio – Olgiasca Zone; MMZ = Monte Muggio Zone; PCF = Passo Cavalcafiche basement; TVB = Tre Valli Bresciane basement; VVB = Val Vedello basement. GL = Gallinera line; ML = Musso line; OL = Orobic Line; VGL = Val Grande Line. Modified from Zanoni and Spalla (2018) and ref. therein.

from Permian to Triassic times (Henk et al., 1997; Peressini et al., 2007; Klötzli et al., 2014; Guergouz et al., 2018; Smye et al., 2019). In the central Southern Alps, Triassic HT metamorphism is only recorded in the Dervio-Olgiasca (northern Como Lake) tectono-metamorphic unit (TMU) (Fig. 1.3.1) (Diella et al., 1992; Bertotti et al., 1993, 1999; Sanders et al., 1996; di Paola and Spalla, 2000; Spalla et al., 2000).

On the contrary, the HT metamorphic imprint is not retained by those segments of Variscan basement rocks that had already been exhumed and were unconformably overlaid by Permian sedimentary sequences (Zanoni & Spalla, 2018, and ref. therein). In the Southern Alps, the continental rifting and the following break-up may be solely envisaged by transtensional to extensional faults leading the deposition of pre- to syn-rift sequences (De Graciansky et al., 2011; Festa et al., 2020; Zanchi et al.,

2019) and by Permian-Triassic volcaniclastites in sedimentary sequences of the Southern Alps (Cadel et al., 1987; Schaltegger and Brack, 2007; Cassinis et al., 2008; Berra et al., 2015; Beltrán-Triviño et al., 2016). Xenoliths of Permian granulites and migmatites included into Oligocene trachytes are further evidences of Permian-Traissic rifting in the eastern Southern Alps (Sassi et al., 2020).

The continental rifting and break-up come along with mantle- and crustal-derived magma emplacements in the Alpine domains (Spalla et al., 2014, Roda et al. 2019). Mafic intrusives emplaced at different crustal levels and testify asthenosphere upwelling, from the continental rifting to the Thetys Ocean break-up. In the Southern Alps, these rocks are source of information on the composition and transformation of the sub-continental mantle at the end of the Variscan cycle and of its evolution during the subsequent continental rifting (e.g. Casetta et al., 2018a, 2018b, 2019; Lustrino et al., 2019; Storck et al., 2019; De Min et al., 2020).

In this paper, we present a comprehensive petrological and geochemical study of the Edolo diabase, a swarm of alkaline lamprophyres (camptonites) in the northern part of the central Southern Alps. The Edolo diabase has been extensively mapped by Schiavinato (1954) and Rebay et al. (2015a). The dykes are intruded into Variscan basement rocks that do not record the Triassic HT metamorphic event (Aprica and Passo Cavalcafiche Tectono-Metamorphic Units, TMUs). A Triassic age for the Edolo diabase is suggested by the Italian authors of the last century (Schiavinato, 1954 and ref. therein).

Geological setting

The Variscan crust of the central Southern Alps retains contrasting Variscan P-T evolution and different TMUs are here individuated (Spalla and Gosso, 1999). Some of these units, including the Passo Calvalcafiche and Domaso-Cortafò TMUs (Fig. 1.3.1), retain the effects of superposed thermal states compatible with the Variscan subduction and collision (Spalla et al., 1999; di Paola et al., 2001), whereas the Val Vedello, Monte Muggio, and Aprica TMUs (Fig. 1.3.1) only record the Variscan collision, but at different crustal levels (Diella et al. 1992; Siletto et al., 1993; Gosso et al. 1997). Finally, the Tre Valli Bresciane Massif does not record the Barrovian metamorphism related to the Variscan collision, but only the “cooler” imprint of the Variscan subduction (Giobbi Origoni and Gregnanin, 1983; Spalla et al., 2009). The effects of the Triassic HT metamorphism are well documented in the Dervio-Olgiasca TMU (Fig. 1.3.1), where they are subsequent to the Variscan collisional imprint (Diella et al., 1992; Sanders et al., 1996; Spalla and Gosso, 1999; di Paola and Spalla, 2000; Spalla et al., 2000).

The Edolo diabase intruded into the Variscan Aprica and Passo Cavalcafiche TMUs in the northern part of the central Southern Alps, in between the Alpine Gallinera and Insubric lines (Fig. 1.3.1).

These TMUs mostly consist of poly-deformed metapelites and quartzites, in part derived from Ordovician-Silurian sediments (Gansser and Pantic, 1988), with few lenses of orthogneiss. The dominant structure in the Aprica and Passo Cavalcafiche TMUs is the late Variscan foliation S2, which developed during the coupling of these units. S2 is supported by greenschist facies minerals (Qz + Wm + Chl + Ab + Ttn) and dips 30-80° towards NNW at the regional scale (Rebay et al., 2015a). S2 developed under a perturbed thermal state – T < 400-550°C, P < 0.3-0.4 GPa in the Passo Cavalcafiche TMU and T < 300-350°C, P < 0.3 GPa in the Aprica TMU – that is compatible with a late- to post-collisional setting (Spalla et al., 1999; Zanoni et al., 2010; Gosso et al., 2012, Rebay et al., 2015a). The Edolo diabase dykes intersect the late- to post-collisional S2 in both the Passo Cavalcafiche and Aprica TMUs. The dykes are W-SW dipping and characterized by chilled margins.

Pre-S2 foliations are locally preserved as limbs of rootless D2 folds. In the Passo Cavalcafiche TMU, S1a foliation (Bt + Cld + Grt) developed during the Variscan subduction at 480-540°C and 0.75-0.95 GPa, whereas S1b (Bt + St + Grt) during the Variscan collision at 570-660°C and 0.85-1.15 GPa (Spalla et al., 1999; Zanoni et al., 2010; Gosso et al., 2012). Conversely, in the Aprica TMU, S1 foliation (Bt + Grt), developed at T < 450-550°C and P < 0.4-0.6 GPa, (Spalla et al., 1999; Zanoni et al., 2010; Gosso et al., 2012; Rebay et al., 2015a). Clasts of basement rocks ascribable to Aprica and Passo Cavalcafiche TMUs in the Lower Permian siliciclastic sequences of the Southern Alps confirm that parts of these TMUs have been already exhumed before the Triassic HT metamorphic event (Zanoni et al., 2010).

In the northern part of the central Southern Alps, the structural effects of the Alpine convergence are highly heterogeneous in space: in high-strained domains, the Alpine event is testified by chevron folds (D3) coupled with south-verging thrusts, also involving Permian and Mesozoic sedimentary sequences in the adjacent units (Casati and Gnaccolini, 1967; Cadel et al., 1996; Carminati et al., 1997; D'Adda and Zanchetta, 2015; Ghiselli et al., 2015; Rebay et al., 2015a). D3 folds are characterized by sub-horizontal NE-SW trending axes (A3) and axial planes (PA3) steeply dipping towards NW or SE. S3 axial plane foliation is locally developed in metapelites. In low-strained domains, S2 is crenulated at the micro-scale (Rebay et al., 2015a). The Edolo diabase dykes are blandly folded by D3 and S3 is locally developed in the high-strained domains. Mineral assemblages supporting S3 in Nembra area (Fig. 1.3.1) indicate that the Edolo diabase dykes attained upper greenschist facies metamorphic conditions during the Alpine convergence (see next paragraphs).

Field occurrence

The study is focused on three sites, Corteno-Golgi, Valmoranda and Nembra (Fig. 1.3.1), where the Edolo diabase dykes intruded into Variscan metapelites and quartzites of the Variscan Aprica and Passo Cavalcafiche TMUs. The dykes range in thickness from few tens of centimeters up to tens of meters, with sharp margins. The igneous minerals are amphibole, clinopyroxene, biotite, plagioclase, ilmenite, apatite, and rare quartz. In the central part of the dykes, grain size and modal proportion of minerals are widely variable and define texturally heterogeneous enclaves with lobate to blurred contacts (Fig. 1.3.2A). Grain size reduction and chilled margins characterize the dyke margins, where shape preferred orientation of igneous phenocrysts in aphanitic groundmass define a fluidal foliation often wrapping clasts of brecciated host rocks (Fig. 1.3.3A). Albitite veins are characterized by gently lobate to sharp contacts and crosscut the dykes (Fig. 1.3.2B, 1.3.3B).

D3 folds are pervasive in Valmoranda and Nembra, where the Alpine foliation S3 is locally developed within the dykes. S3 is supported by upper greenschist facies mineral assemblages and dips towards SE (see next paragraphs). Conversely, at Corteno-Golgi, Alpine D3 folds are poorly developed: the dykes, blandly to steeply dipping towards W to SW, are crosscut by late cataclastic shear-zones and fractures.

Microstructure

In the Edolo diabase dykes, igneous amphiboles are brown at core (AmpIa), with pale brown – dark green rims (AmpII), which partially to totally include ilmenite and apatite grains. Locally, AmpIa and AmpII are rimmed by blue-green igneous amphibole (AmpIII). AmpIII is also included within igneous biotite grains (Fig. 1.3.3C).

Clinopyroxene is pale-pink at the core (CpxI) and colorless at the rim (CpxII), often showing highly irregular rims. Colorless Amp Ib locally replaces igneous clinopyroxene and, in turn, it is rimmed either by igneous AmpII, AmpIII, or igneous biotite (Fig. 1.3.3D). These textural relationships suggest that some CpxI grains are xenocrysts not in equilibrium with the residual melt. Ilmenite grains are locally included in igneous clinopyroxene.Igneous biotite is dark brown (BtI), locally with pale-brown/green rims (BtII) and interstitial between clinopyroxene and amphibole grains. Crystals of AmpIII, ilmenite, and apatite are included in BtI and BtII.

Igneous plagioclase is subhedral to euhedral, with sharp boundaries at plagioclase-plagioclase interfaces. Plagioclase cores display simple and/or polysynthetic twinning (PlI), whereas plagioclase rims (PlII) are untwinned and show slightly lobate boundaries. Interstices between

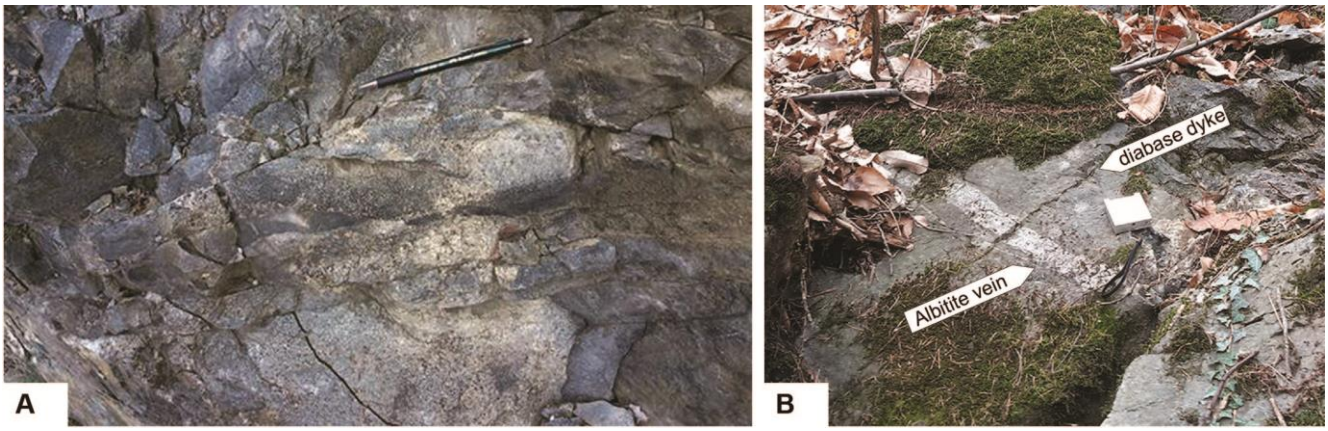

Figure 1.3.2. Mesoscopic characters of Edolo diabase dykes. A: example of textural heterogeneity of the Edolo diabase dykes with dark enclaves (amphibole and clinopyroxene-rich) within a more leucocratic melt. B: an albitite vein crocutting the Edolo diabase dyke.

plagioclase crystals are filled by BtI, BtII, AmpIII, and, more rarely, by quartz or epidote (Fig. 1.3.3E). Apatite is included in igneous plagioclase. Graphic intergrowths between quartz and plagioclase are commonly observed in the interstices.

Albitite veins are composed of abundant sodic plagioclase (PlI) and minor biotite (BtI) and amphibole (Fig. 1.3.3B). At vein margins, clinopyroxene grains show highly irregular grain boundaries and they are always rimmed by amphibole and biotite suggesting disequilibrum with the residual melt (Fig. 1.3.3F). As in the host dykes, igneous amphiboles are euhedral to subhedral with brown cores (AmpIa) and brown/dark green rims (AmpII) (Fig. 1.3.3B). Blue-green AmpIII rims AmpIa and AmpII (Fig. 1.3.3F). Igneous plagioclase is euhedral to subhedral and zoned (Fig. 1.3.3F), with simple and polysynthetic twinning at cores (PlI) and untwinned rims (PlII); biotite (BtI) is from subhedral to interstitial between plagioclase grains.

In the Edolo diabase dykes and albite veins, AmpIa and CpxI are overgrown by colorless AmpIV (Fig. 1.3.3E), whereas pale-green AmpIV replaces them in albitite veins. Chlorite replaces BtI and BtII. AmpIV and chlorite always display coronitic texture. The Alpine foliation S3 is supported by pale-green AmpV, pale-brown biotite, chlorite, epidote, titanite, calcite, and opaque minerals, which wrap igneous and hydrothermal minerals. In low strained domains, AmpV forms coronae around AmpIa and CpxI.

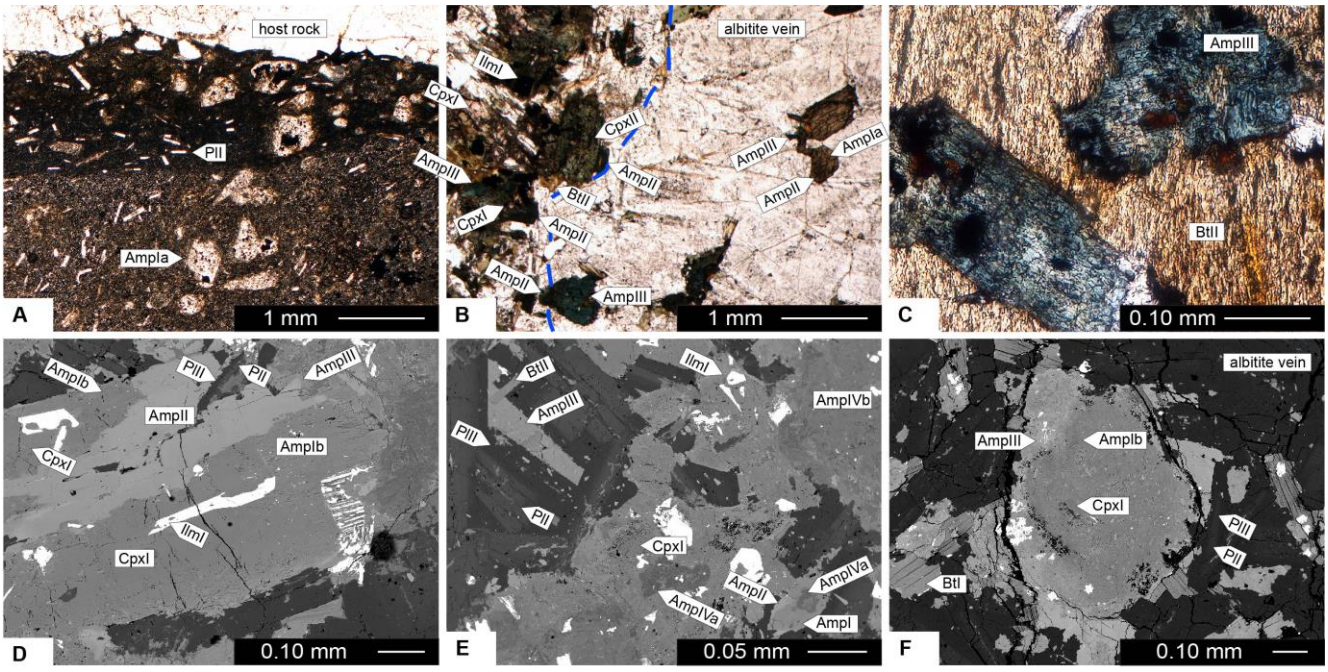

Figure 1.3.3. Microstructural characters of Edolo diabase dykes. A: Intrusive contact between an Edolo diabase dyke and the host meta-quartzite. The dyke is porphyritic and the ground mass shows grain size reduction at the dyke wall. Intrusive contacts are sharp and made angulated by syn-intrusive fracturing. B: An albitite vein intruding into an Edolo diabase dyke; the albitite wall is outlined by a dashed blue line. C: AmpIII (Cl-bearing) included into BtII. D: CpxI rimmed by AmpIb, replaced by AmpII, and in turn rimmed by AmpIII (BSE image). E: AmpIII and BtII interstitial between zoned plagioclase grains. PlI core is lighter than PlII rim (BSE image). F: CpxI xenocrysts replaced by AmpIb and rimmed by AmpIII (BSE image).

Whole rock geochemistry

Whole rock analyses have been performed at Università degli Studi di Genova by XRF and at ACME labs Canada by ICP-OES and ICP-MS. The Edolo diabase is characterized by SiO_2 content ranging from 43.74 to 48.98 %wt, Na_2O from 2.48 to 3.27 %wt, and K_2O from 0.8 to 2.2 %wt (Tab. 1.3.1). Sample 160 is the richest in SiO_2, Al_2O_3, and CaO, and the poorest in FeO, MgO, TiO_2, MnO, Na_2O, K_2O, and P_2O_5. Not accounting for sample 160, Mg# ranges from 47 to 57 and it is mainly controlled by highly varying MgO content from 6.67 to 10.71 %wt. 1 and 2% of CIPW normative nepheline is predicted for samples 76 and 49, respectively, whereas normative quartz (< 1%) only results in sample 160.

The Edolo diabase dykes are alkaline, sodic or potassic (Fig. 1.3.4A and B), with CaO content comprised between 4.59 and 5.87 %wt. In the Nb/Y vs Zr/Ti classification diagram (Winchester and Floyd, 1977), these rocks plot in the alkali-basalt field (Fig. 1.3.4C). Primitive mantle-normalized incompatible elements patterns highlight positive anomalies in P, K, Pb, Zr, Ti and negative anomalies

	Edolo diabase						
sample	**161**	**49**	**76**	**PS**	**151**	**160**	**162**
SiO_2 (wt%)	45.42	44.45	45.04	45.85	46.15	48.98	45.99
TiO_2	2.13	2.74	2.44	2.89	2.98	1.36	2.91
Al_2O_3	13.15	14.29	13.24	13.58	13.53	18.35	13.52
FeOt	14.39	13.72	13.89	13.63	13.22	7.50	13.28
MgO	10.71	9.74	10.52	7.80	6.67	4.88	7.72
MnO	0.30	0.26	0.18	0.22	0.32	0.15	0.24
CaO	5.21	5.70	5.54	4.59	5.87	10.30	5.37
Na_2O	2.76	3.27	3.04	2.64	3.50	2.56	2.86
K_2O	1.18	1.30	1.52	2.24	1.30	0.78	1.84
P_2O_5	0.38	0.56	0.43	0.43	0.45	0.35	0.42
LOI	2.77	2.45	2.61	3.48	3.35	3.84	3.88
Total	98.40	98.48	98.45	97.35	97.34	99.05	98.03
Mg#	0.57	0.56	0.57	0.51	0.47	0.54	0.51
Rb (ppm)	44	47	60	90	30	-	40
Sr	265	325	250	219	339	418	256
Y	28	33	32	33	33	26	32
Zr	135	200	190	160	163	159	161
Nb	14.0	29	27				
Cs				8.5	-	1.9	5.5
Ba	555	270	162	139	483	260	136
La	10	18	20	13.7	12.9	15.2	12.6
Ce	31	41	46	23	22	27	21
Nd	15	22	25	17	12	16	14
Sm				5.1	4.6	4.2	4.6
Eu				1.4	1.2	1.2	1.4
Tb				0.7	0.6	0.6	0.5
Yb				2.2	2.2	1.9	2
Lu				0.3	0.31	0.28	0.3
Th	4		4	1.5	1.3	1.6	1.2
U				-	0.8	-	0.8

Table 1.3.1. WR composition (major, trace, and REE elements) of Edolo diabase dykes from Valmoranda locality.

in Th, Nb, La, Ce, and Sr (Fig. 1.3.4D); primitive-mantle REE patterns are characterized by light REE enrichment and flat middle to heavy REE profile, without Eu anomaly (Fig. 1.3.4E). RRE concentrations in sample 76 are slightly higher than in sample 49, but with similar profiles (Fig. 1.3.4E). La/Yb is 5.86 – 8.00, La/Sm is 2.69 – 3.62, and Sm/Yb is 2.09 – 2.32.

The Edolo diabase dykes plot in the within-plate basalt field of the Zr/Y vs Zr (Fig. 1.3.5A, Pearce and Norry, 1979), Zr/Y vs Ti/Y (Fig. 1.3.5B, Pearce and Gale, 1977), and Nb/Y vs Ti/Y diagrams (Fig. 1.3.5C, Pearce, 1982), as well as the Zr-Nb-Y ternary diagram (Meschede, 1986) (Fig. 1.3.5D).

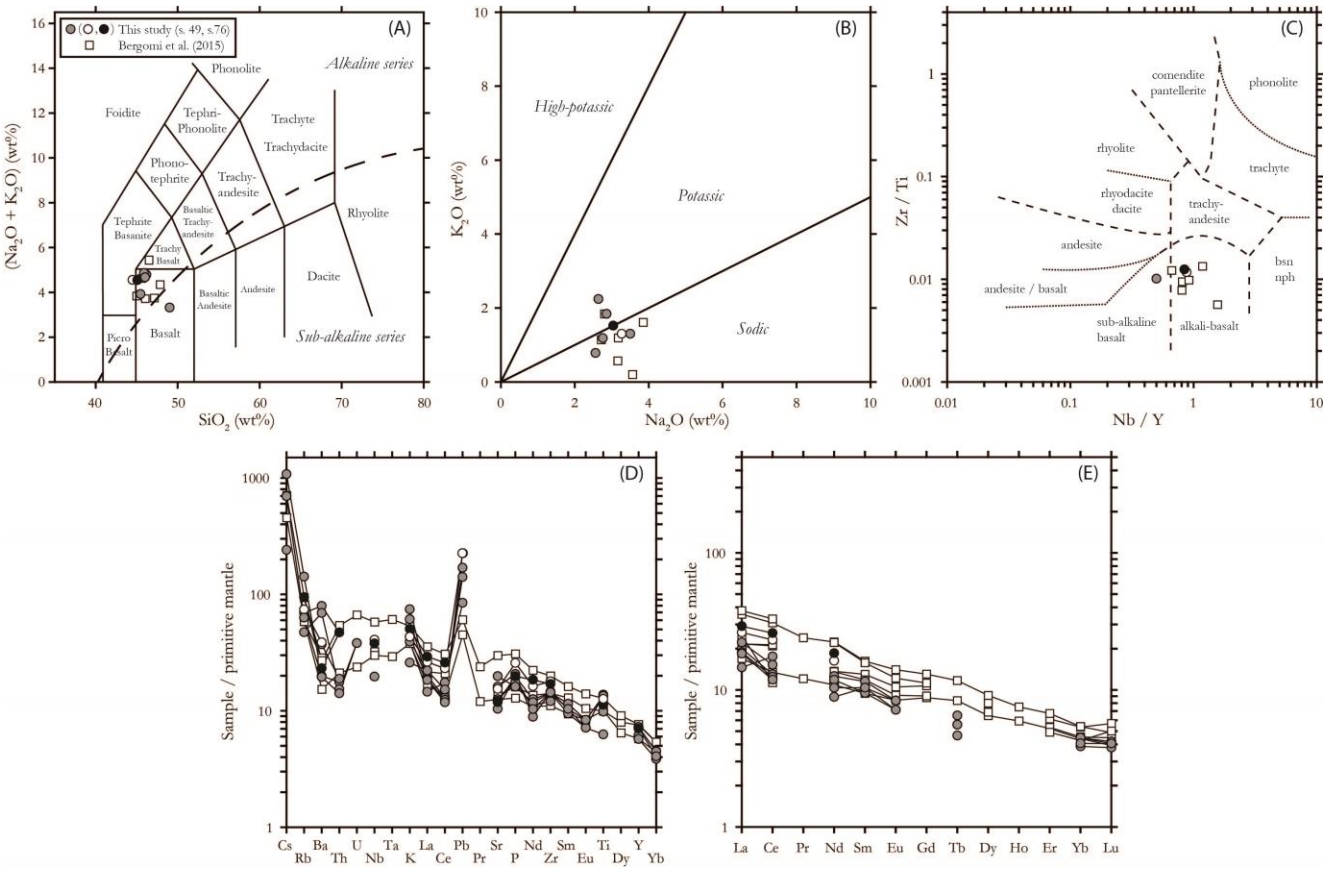

Figure 1.3.4. Edolo diabase WR geochemistry. Legend: gray circle – this study (white circle – sample 49, black circle – sample 76); white square – Bergomi et al. (2015). A: Total Alkali versus Silica diagram. B: K_2O vs Na_2O; C: trace elements classification diagram of Winchester and Floyd (1977). Primitive-mantle (Sun & McDonough, 1989) normalized trace elements (D) and REE (E) patterns.

TiO_2/Yb ratio in the range of 1.31-1.46 indicates OIB affinity, with the sole sample 160 along the MORB array (Pearce, 2008). Th/Yb ratios between 0.60 and 0.84 and Ta/Yb lower than 0.53 suggest OIB affinity (Pearce, 1982). In the Th_N vs Nb_N tectonic discrimination diagram (Saccani, 2015), the Edolo Diabase dykes plot along the MORB-OIB array between E-MORB and alkaline basalts, as proper of oceanic subduction unrelated setting, such as rifted margins and ocean-continent transition zones (Fig. 1.3.5E).

Mineral Chemistry

Minerals from Corteno-Golgi dykes have been analyzed at Università degli Studi di Milano with a JEOL 8200 Super Probe at 15 kV accelerating voltage and with a current beam of 5 nA; minerals from Valmoranda dykes at CGS Università degli Studi di Pavia with a JEOL JXA-840A at 20 kV and 20

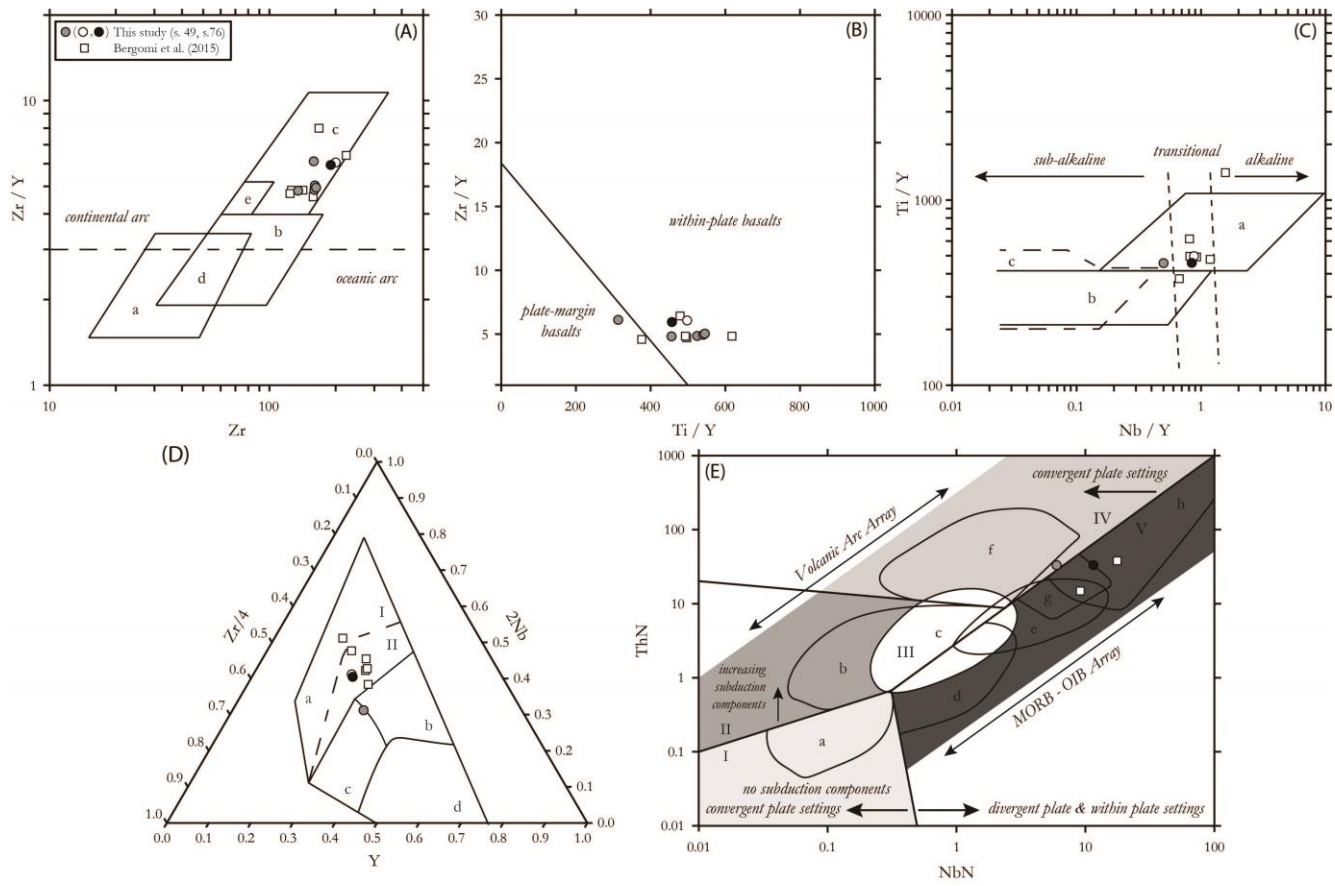

Figure 1.3.5. Classification diagram for the Edolo diabase. Legend: gray circle – this study (white circle – sample 49, black circle – sample 76); white square – Bergomi et al. (2015). A: Zr/Y vs Zr diagram (Pearce & Norry, 1979), legend: a = island arc basalts, b = MORB, c = within-plate basalts, d = overlapping area between a and b, e = overlapping area between b and c. B: Zr/Y vs Ti/Y diagram (Pearce & Gale, 1977). C: Ti/Y vs Nb/Y diagram (Pearce, 1982), legend: a = within plate, b = mid-ocean ridge, c = Volcanic arc. D: diagram of Meschede (1986), legend: aI - aII = within-plate alkaline basalts, aII - c = within-plate tholeiites, b = P-MORB, d = N-MORB, c - d = volcanic arc basalt. E: N-MORB normalized Th vs Nb diagram (Saccani, 2015), legend: A = medium-Ti basalts and supra-subduction zome D-MORB; B = island arc tholeiites and boninites; C = back arc basin basalts, D = N- and G- MORB; E = E-MORB; F = calc-alkaline basalts, G = P-MORB; H = alkaline basalts; I (pale gray) = nascent fore-arcs, II (gray filed) = fore-arcs and intra-arcs, III (white) = back-arcs; IV (light gray) = continental margins, volcanic arcs and polygenetic crust island arcs; V (dark grey) = oceanic subduction unrelated setting and rifted margins, ocean-continent transition zones.

nA. Natural silicates were used as standards. Amphibole formulae are calculated checking the most satisfying results of 13, 15, 16 cations and 23 oxygen normalizations (Locock, 2014) and including oxo-component only for nomenclature (Hawthorne et al. 2012). Clinopyroxene is recalculated at 4 cations and 6 O, feldspar at 4 O, and biotite at 11 O. Mineral chemical analyses are summarized in Table 1.3.2, 1.3.3, and 1.3.4. The mineral-chemical dataset is attached as supplementary data II.

Site	Rock type	Generation	Si	Al^{IV}	Ti	Al^{VI}	Mg#	Ca	Na	K	Cl
Corteno-Golgi	Edolo diabase	AmpIa	**6.13**	**1.87**	**0.46**	**0.17**	**0.46**	**1.75**	**0.90**	**0.22**	**0.00**
		(1 data)	-	-	-	-	-	-	-	-	-
		AmpIb	**7.19 - 7.44**	**0.56 - 0.81**	**0.02 - 0.08**	**0.12 - 0.18**	**0.50 - 0.52**	**1.74 - 1.82**	**0.29 - 0.36**	**0.01 - 0.02**	**0.02 - 0.03**
		(2 data)	-	-	-	-		-	-	-	-
		AmpII	**6.08 - 6.27**	**1.73 - 1.92**	**0.25 - 0.40**	**0.19 - 0.34**	**0.22 - 0.27**	**1.73 - 1.83**	**0.77 - 1.00**	**0.27 - 0.31**	**0.00 - 0.01**
		(3 data)	6.15 ± 0.09	1.85 ± 0.09	0.31 ± 0.06	0.28 ± 0.06	0.25 ± 0.02	1.79 ± 0.05	0.86 ± 0.10	0.29 ± 0.02	-
		AmpIII	**6.57 - 6.89**	**1.11 - 1.43**	**0.01 - 0.08**	**0.23 - 0.46**	**0.26 - 0.33**	**1.73 - 1.80**	**0.42 - 0.58**	**0.02 - 0.05**	**0.02 - 0.03**
		(2 data)	-	-	-	-	-	-	-	-	-
		AmpIV	**7.86 - 7.96**	**0.04 - 0.11**	**0.00 - 0.01**	**0.00 - 0.01**	**0.78 - 0.84**	**1.86 - 1.88**	**0.01 - 0.05**	**0.00 - 0.01**	**0.00 - 0.01**
		(3 data)	7.92 ± 0.04	0.07 ± 0.03	-	-	0.82 ± 0.02	1.87 ± 0.01	0.03 ± 0.02	-	-
		AmpV	**7.45 - 7.81**	**0.19 - 0.55**	**0.02 - 0.06**	**0.06 - 0.11**	**0.55 - 0.56**	**1.86 - 1.92**	**0.05 - 0.21**	**0.01**	**0.00 - 0.01**
		(2 data)	-	-	-	-	-	-	-	-	-
	Albitite vein	AmpIa	**6.25 - 6.47**	**1.53 - 1.75**	**0.43 - 0.44**	**0.15 - 0.20**	**0.37**	**1.72 - 1.75**	**0.51 - 0.83**	**0.23**	**0.00 - 0.01**
		(2 data)	-	-	-	-	-	-	-	-	-
		AmpII	**5.94 - 6.35**	**1.65 - 2.06**	**0.18 - 0.35**	**0.14 - 0.44**	**0.09 - 0.19**	**1.70 - 1.84**	**0.55 - 0.80**	**0.26 - 0.35**	**0.00 - 0.03**
		(4 data)	6.18 ± 0.15	1.82 ± 0.15	0.26 ± 0.06	0.30 ± 0.11	0.15 ± 0.04	1.75 ± 0.07	0.71 ± 0.09	0.32 ± 0.03	-
		AmpIII	**6.06 - 6.66**	**1.34 - 1.95**	**0.04 - 0.12**	**0.16 - 0.66**	**0.16 - 0.23**	**1.80 - 1.90**	**0.39 - 0.73**	**0.08 - 0.22**	**0.10 - 0.24**
		(5 data)	6.28 ± 0.22	1.72 ± 0.22	0.06 ± 0.03	0.43 ± 0.19	0.18 ± 0.03	1.87 ± 0.04	0.58 ± 0.13	0.14 ± 0.05	0.15 ± 0.06
		AmpIV	**7.86 - 7.89**	**0.11 - 0.14**	**0.00 - 0.01**	**0.00 - 0.06**	**0.42 - 0.46**	**1.93**	**0.02 - 0.07**	**0.01**	**0.00 - 0.02**
		(3 data)	7.87 ± 0.01	0.12 ± 0.01	-	0.02 ± 0.03	0.44 ± 0.02	-	0.04 ± 0.02	-	-
Valmoranda	Edolo diabase	AmpIa	**5.95 - 6.31**	**1.69 - 2.05**	**0.34 - 0.69**	**0.00 - 0.38**	**0.48 - 0.54**	**1.77 - 1.84**	**0.74 - 0.90**	**0.20 - 0.24**	**0.00**
	(sample 49)	(7 data)	6.08 ± 0.14	1.92 ± 0.13	0.48 ± 0.10	0.14 ± 0.14	0.51 ± 0.03	1.81 ± 0.02	0.82 ± 0.05	0.22 ± 0.01	-
		AmpIII	**6.80**	**1.2**	**0.03**	**0.31**	**0.40**	**1.91**	**0.31**	**0.22**	**0.08**
		(1 data)	-	-	-	-	-	-	-	-	-
		AmpV	**7.34 - 7.80**	**0.20 - 0.66**	**0.00 - 0.03**	**0.11 - 0.20**	**0.43 - 0.56**	**1.94 - 1.95**	**0.12 - 0.26**	**0.02 - 0.08**	**0.02 - 0.03**
		(3 data)	7.51 ± 0.21	0.49 ± 0.21	-	0.15 ± 0.04	0.49 ± 0.05	-	0.20 ± 0.06	0.04 ± 0.03	-
	Edolo diabase	AmpV	**7.69 - 7.70**	**0.30**	**0.01 - 0.03**	**0.00 - 0,20**	**0.53 - 0.62**	**1.81 - 1.95**	**0.06 - 0.14**	**0.02 - 0.05**	**0.00 - 0.01**
	(sample 76)	(2 data)	-	-	-	-	-	-	-	-	-
Nembra	Edolo diabase	AmpIa	**6.17 - 6.32**	**1.68 - 1.83**	**0.45 - 0.52**	**0.22 - 0.32**	**0.45 - 0.49**	**1.8**	**0.61 - 0.68**	**0.24 - 0.25**	**0.02 - 0.03**
	(sample ge8)	(3 data)	6.22 ± 0.07	1.78 ± 0.07	0.49 ± 0.03	0.26 ± 0.04	0.47 ± 0.02	-	0.63 ± 0.03	-	-
		AmpII	**5.83 - 6.37**	**1.63 - 2.17**	**0.36 - 0.44**	**0.15 - 0.43**	**0.15 - 0.31**	**1.74 - 1.83**	**0.71 - 0.86**	**0.26 - 0.37**	**0.01**
		(6 data)	6.09 ± 0.20	1.91 ± 0.20	0.40 ± 0.03	0.28 ± 0.10	0.22 ± 0.06	1.79 ± 0.03	0.79 ± 0.06	0.31 ± 0.04	-
		AmpIV	**7.86 - 7.91**	**0.09 - 0.14**	**0.00 - 0.02**	**0.05 - 0.08**	**0.53 - 0.64**	**1.90 - 1.99**	**0.04 - 0.07**	**0.01 - 0.02**	**0.00 - 0.01**
		(3 data)	7.89 ± 0.02	0.11 ± 0.02	-	-	0.60 ± 0.05	1.93 ± 0.04	0.05 ± 0.01	-	-
		AmpV	**7.59 - 7.83**	**0.18 - 0.41**	**0.00 - 0.02**	**0.05 - 0.15**	**0.53 - 0.64**	**1.83 - 1.97**	**0.04 - 0.12**	**0.01 - 0.07**	**0.00 - 0.03**
		(13 data)	7.75 ± 0.07	0.25 ± 0.07	-	0.09 ± 0.03	0.59 ± 0.04	1.91 ± 0.04	0.08 ± 0.02	0.03 ± 0.01	-
	Edolo diabase	AmpIa	**5.99 - 6.34**	**1.77 - 2.02**	**0.46 - 0.64**	**0.20 - 0.30**	**0.49 - 0.66**	**1.76 - 1.85**	**0.40 - 0.86**	**0.18 - 0.25**	**0.00 - 0.03**
	(sample ge11)	(8 data)	6.13 ± 0.12	1.87 ± 0.12	0.53 ± 0.07	0.25 ± 0.04	0.57 ± 0.06	1.82 ± 0.03	0.69 ± 0.15	0.22 ± 0.02	-
		AmpII	**5.91 - 6.25**	**1.75 - 2.09**	**0.14 - 0.25**	**0.25 - 0.63**	**0.30 - 0.32**	**1.79 - 1.87**	**0.55 - 0.90**	**0.30 - 0.32**	**0.01 - 0.02**
		(2 data)	-	-	-	-	-	-	-	-	-
		AmpIV	**7.78 - 7.93**	**0.07 - 0.22**	**0.00 - 0.01**	**0.02 - 0.09**	**0.70 - 0.76**	**1.86 - 1.95**	**0.02 - 0.08**	**0.00 - 0.01**	**0.00 - 0.01**
		(9 data)	7.87 ± 0.05	0.13 ± 0.05	-	-	0.72 ± 0.02	1.91 ± 0.02	0.05 ± 0.02	-	-
		AmpV	**7.42 - 7.76**	**0.24 - 0.58**	**0.00 - 0.04**	**0.04 - 0.17**	**0.59 - 0.71**	**1.80 - 1.94**	**0.07 - 0.19**	**0.01 - 0.12**	**0.00 - 0.02**

	(28 data)	7.66 ± 0.09	0.34 ± 0.09	0.01 ± 0.01	0.10 ± 0.04	0.66 ± 0.03	1.88 ± 0.04	0.10 ± 0.03	0.04 ± 0.03	-
Edolo diabase	AmpIa	**6.06 - 6.21**	**1.79 - 1.94**	**0.51 - 0.58**	**0.16 - 0.24**	**0.47 - 0.56**	**1.74 - 1.82**	**0.80 - 0.93**	**0.21 - 0.24**	**0.00 - 0.01**
(sample ge15)	(8 data)	6.14 ± 0.04	1.86 ± 0.04	0.54 ± 0.02	0.19 ± 0.02	0.51 ± 0.03	1.78 ± 0.02	0.85 ± 0.04	0.22 ± 0.01	-
	AmpII	**5.95 - 6.42**	**1.58 - 2.05**	**0.01 - 0.46**	**0.07 - 0.83**	**0.12 - 0.35**	**1.78 - 1.97**	**0.56 - 0.95**	**0.12 - 0.30**	**0.01 - 0.07**
	(5 data)	6.16 ± 0.17	1.84 ± 0.17	0.12 ± 0.17	0.56 ± 0.27	0.24 ± 0.09	1.88 ± 0.06	0.72 ± 0.14	0.20 ± 0.06	0.04 ± 0.02

Table 1.3.2. Compositional range (bold, apfu) and average value (± s.d.) of amphiboles in the Edolo diabase dykes.

Amphibole

AmpIa is Ti-rich ferro-pargasite, kaersutite, ferri-kaersutite, Ti-rich pargasite, Ti-rich magnesio-hastingsite, or Ti-rich magnesio hornblende. AmpIa is characterized by Si = 5.95 – 6.34 pfu, Al = 1.84 – 2.32 pfu, Ti = 0.34 - 0.69 pfu and Na = 0.40 – 0.93 pfu (Tab. 1.3.2, Fig. 1.3.6). The K content of AmpIa (0.18 - 0.25 pfu) is typical of alkaline mafic rocks (Fig. 1.3.6). Fe^{3+} is comprised between 0.00 and 0.23 pfu (Fig. 1.3.6). Variations in AmpIa Mg# occur in different localities. Mg# in AmpIa from Corteno-Golgi dykes (0.46) is slightly lower than in sample 49 from Valmoranda (0.48 – 0.54);
at Nembra, Mg# ranges from 0.45 in sample Ge8 to 0.66 in sample Ge11 (Tab. 1.3.2, Fig. 1.3.6). In albitite veins, AmpIa (Ti-rich ferro-pargasite) is characterized by slightly higher Si (6.25 – 6.47 pfu), and lower Na (0.51 – 0.86 pfu) and Al (1.74 – 1.90 pfu) content than AmpIa in the Edolo diabase, with Ti = 0.43 – 0.44 pfu, K = 0.23 pfu, and Fe^{3+} = 0.07 – 0.14 pfu (Tab. 1.3.2, Fig. 1.3.6). AmpIa in albitite veins displays lower Mg# (0.25 – 0.37) than AmpIa in the Edolo diabase dykes (Tab. 1.3.2, Fig. 1.3.6).
AmpIb (magnesio-ferri hornblende) is Si (7.19 – 7.44 pfu) and Fe^{3+} (0.30 – 0.40 pfu) richer, and Al (0.68 – 0.99 pfu), Ti (0.02 – 0.08 pfu), Na (0.29 – 0.36 pfu), and K (< 0.03 pfu) poorer than AmpIa (Tab. 1.3.2, Fig. 1.3.6). Mg# is 0.50 – 0.52 (Tab. 1.3.2, Fig. 1.3.6).
AmpII (ferro-pargasite or Ti-rich ferro-pargasite) is characterized by Si (5.83 – 6.42 pfu), Al (1.78 – 2.72 pfu), Fe^{3+} (0.00 – 0.44 pfu), and Na (0.55 – 1.00 pfu) content comparable to AmpIa, with higher K (0.12 – 0.37 pfu) and lower Ti (0.01 – 0.46 pfu) content (Tab. 1.3.2, Fig. 1.3.6). Mg# (0.12 – 0.35) is instead makedly lower than in AmpIa (Tab. 1.3.2, Fig. 1.3.6). In the albitite veins, AmpII (Ti-rich ferro-pargasite, ferro-pargasite, or hastingsite) is characterized by Si = 5.94 – 6.35 pfu, Na = 0.55 – 0.80 pfu, and Fe^{3+} = 0.13 – 0.38 pfu (Tab. 1.3.2, Fig. 1.3.6). In comparison with its core (AmpIa), Ti content (0.18 – 0.35 pfu) is lower, whereas Al (1.79 – 2.42) and K (0.26 – 0.35) concentrations are higher (Tab. 1.3.2, Fig. 1.3.6). AmpII Mg# (0.09 – 0.19, Tab. 1.3.2, Fig. 1.3.6) is lower than in AmpIa. In the albitite veins, AmpII is compositionally similar to AmpII in the host Edolo diabase, but Fe richer.

AmpIII (ferro-ferri-hornblende) is characterized by Si = 6.57 – 6.89 pfu, Al = 1.34 – 1.89 pfu, and Ti = 0.01 – 0.08 pfu; Na is 0.32 – 0.58 pfu, K is 0.02 – 0.05 pfu, and Fe^{3+} is 0.40 – 0.63 pfu (Tab. 1.3.2, Fig. 1.3.6). Mg# is comprised between 0.26 – 0.40, with the highest value in sample 49 from Valmoranda (Tab. 1.3.2, Fig. 1.3.6). In the albitite veins, AmpIII (hastingsite or ferro-pargasite) is characterized by Si = 6.06 – 6.66 pfu, Al = 1.61 – 2.56 pfu, Ti = 0.04 – 0.12 pfu, Na = 0.39 – 0.73 pfu, and K = 0.08 – 0.22 pfu, with Fe^{3+} = 0.45 – 0.83 pfu (Tab. 1.3.2, Fig. 1.3.6). Mg# = 0.16 – 0.23 is markedly lower than in Edolo diabase AmpIII (Tab. 1.3.2, Fig. 1.3.6). In the Edolo diabase, AmpIII contains Cl between 0.02 and 0.08 pfu; Amp III in abilitie veins is Cl-rich (0.10 - 0.24 pfu; Tab. 1.3.2, Fig. 1.3.6). The amount of Cl in AmpIII is correlated to the concentration of Fe^{3+} in C-site, which is higher than 0.40 pfu in AmpIII, as well to the K content comprised between 0.02 and 022 pfu (Fig. 1.3.6). The lowest Mg# and highest K content characterizing igneous amphiboles in the albitite veins allows incorporating more Cl in AmpIII (Tab. 1.3.2, Fig. 1.3.6).

AmpIV (actinolite) is characterized by Si = 7.78 – 7.96 pfu and Al = 0.04 – 0.25 pfu, with negligible Ti and K content; Fe^{3+} is 0.00 – 0.16 pfu and Na is 0.00 – 0.08 pfu (Tab. 1.3.2, Fig. 1.3.6). AmpIV is generally characterized by the highest Mg# (0.70 – 0.84), which can be lower when found in Fe-rich microsites (0.53 – 0.64) (Tab. 1.3.2, Fig. 1.3.6). In the Albitite veins, AmpIV (ferro-actinolite) is characterized by Si = 7.86 – 7.89 pfu, Al = 0.11 – 0.20 pfu, Fe^{3+} = 0.07 – 0.12 pfu, Na = 0.02 – 0.07 pfu, and negligible Ti and K content (Tab. 1.3.2, Fig. 1.3.6). AmpIV Mg# in albitite veins (0.42 – 0.48, Tab. 1.3.2) is lower than in the Edolo diabase.

AmpV (actinolite or ferro-actinolite) is characterized by Si = 7.34 – 7.83 pfu, Al = 0.25 – 0.87 pfu, and Ti lower than 0.06 pfu (Tab. 1.3.2, Fig. 1.3.6). Fe^{3+} is 0.01 – 0.46 pfu, Na is 0.04 – 0.26 pfu, and K is

Site	Rock type	Generation	Si	Al^{IV}	Ti	Al^{VI}	Fe	Mg	Mg#	Ca	Na	K
Corteno-Golgi	Edolo diabase	BtII	**5.36 - 5.73**	**2.27 - 2.64**	**0.32 - 0.34**	**0.33 - 0.37**	**2.90 - 2.99**	**2.15 - 2.32**	**0.42 - 0.44**	**0.02 - 0.04**	**0.02 - 0.03**	**1.58 - 1.71**
		(3 data)	5.54 ± 0.15	2.47 ± 0.15	0.33 ± 0.01	0.35 ± 0.01	2.96 ± 0.04	2.21 ± 0.08	0.43 ± 0.01	0.03 ± 0.01	-	1.65 ± 0.05
	Albitite vein	BtI	**5.50 - 5.53**	**2.47 - 2.50**	**0.31 - 0.32**	**0.43 - 0.46**	**3.44 - 3.46**	**1.58 - 1.66**	**0.31 - 0.33**	**0.04 - 0.06**	**0.02**	**1.55 - 1.63**
		(2 data)	-	-	-	-	-	-	-	-	-	-
Valmoranda	Edolo diabase	BtI	**5.40 - 5.47**	**2.53 - 2.60**	**0.53 - 0.76**	**0.03 - 0.17**	**2.89 - 3.13**	**1.65 - 2.24**	**0.34 - 0.44**	**0.00 - 0.01**	**0.00 - 0.21**	**1.62 - 1.65**
	(sample 49)	(3 data)	5.43 ± 0.03	2.57 ± 0.03	0.68 ± 0.10	0.09 ± 0.06	3.02 ± 0.10	1.87 ± 0.26	0.38 ± 0.04	-	0.11 ± 0.09	1.64 ± 0.02
	Edolo diabase	BtI	**5.38 - 3.46**	**2.54 - 2.62**	**0.38 - 0.58**	**0.06 - 0.27**	**2.90 - 3.13**	**1.87 - 2.18**	**0.37 - 0.43**	**0.00 - 0.02**	**0.00 - 0.06**	**2.00 - 2.01**
	(sample 76)	(2 data)	-	-	-	-	-	-	-	-	-	-
Nembra	Edolo diabase	BtI	**5.41 - 5.46**	**2.54 - 2.59**	**0.71 - 0.78**	**0.01 - 0.08**	**2.54 - 2.79**	**1.98 - 2.13**	**0.43 - 0.44**	**0.02 - 0.42**	**0.02 - 0.03**	**1.47 - 1.55**
	(sample ge8)	(2 data)	-	-	-	-	-	-	-	-	-	-
	Edolo diabase	BtI	**5.33 - 5.64**	**2.36 - 2.66**	**0.37 - 0.69**	**0.00 - 0.38**	**2.58 -2.89**	**2.17 - 2.45**	**0.44 - 0.49**	**0.00 - 0.05**	**0.00 - 0.03**	**1.56 - 1.77**
	(sample ge11)	(13 data)	5.47 ± 0.08	2.53 ± 0.08	0.51 ± 0.09	0.19 ± 0.11	2.72 ± 0.08	2.32 ± 0.08	0.46 ± 0.01	0.02 ± 0.01	0.02 ± 0.01	1.72 ± 0.06
	Edolo diabase	BtI	**5.36 - 5.53**	**2.47 - 2.64**	**0.59 - 0.72**	**0.01 - 0.19**	**2.91 - 3.19**	**1.77 - 2.05**	**0.36 - 0.41**	**0.01 - 0.03**	**0.03 - 0.20**	**1.48 - 1.76**
	(sample ge15)	(4 data)	5.44 ± 0.07	2.56 ± 0.07	0.66 ± 0.05	0.08 ± 0.07	3.02 ± 0.10	1.91 ± 0.10	0.39 ± 0.02	0.02 ± 0.01	0.10 ± 0.07	1.62 ± 0.13

Table 1.3.4. Compositional range (bold, apfu) and average value (± s.d.) of biotites in the Edolo diabase dykes.

lower than 0.12 pfu (Tab. 1.3.2, Fig. 1.3.6). Mg# = 0.43 – 0.71 pfu is lower than in AmpIV (Tab. 1.3.2, Fig. 1.3.6).

Clinopyroxene

CpxI xenocrysts (diopside) are characterized by Si = 1.75 – 1.91 pfu, Ti = 0.03 – 0.09 pfu, Al = 0.11 – 0.30 pfu, Ca = 0.82 – 0.87 pfu, and Na = 0.03 – 0.05 pfu (Ca / (Ca + Na) = 0.95 – 0.97) (Tab. 1.3.3, Fig. 1.3.7). Different Mg# is highlighted in different localities: Mg# is 0.67 – 0.69 in Corteno Golgi, 0.70 – 0.75 in sample 49 from Valmoranda, and 0.60 – 0.67 in sample 76 from Valmoranda (Fig. 1.3.7). At Nembra, clinopyroxene Mg# spans over the whole interval (0.66 – 0.76, Fig. 1.3.7). CpxI in sample 49 is silightly Al^{IV} poorer (0.11 – 0.15 pfu) and Na richer (0.04 – 0.05 pfu) than in sample 76 (0.14 – 0.24, and 0.03 pfu, respectively) (Tab. 1.3.3, Fig. 1.3.7).
CpxII (diopside) is characterized by Si = 1.87 – 1.99 pfu, Ti = 0.00 - 0.04 pfu, Al = 0.03 – 0.18 pfu, Ca = 0.84 – 0.94 pfu, and Na = 0.01 – 0.05 pfu (Tab. 1.3.3, Fig. 1.3.7). Mg# in CpxII is 0.70 – 0.72 in Corteno Golgi and Valmoranda, 0.52 – 0.71 in Nembra. Both Ti and Al^{IV} decrease from CpxI to CpxII keeping a constant ratio (Fig. 1.3.7), as characteristic for anorogenic igneous province of alkaline affinity (Loucks, 1990).

Biotite

BtI is characterized by Si = 5.33 – 5.64 pfu, Al^{VI} = 0.00 – 0.38 pfu, and Ti = 0.37 – 0.78 pfu; Mg# is 0.34 – 0.49, with the highest values in sample Ge11 from Nembra (Tab. 1.3.4, Fig. 1.3.7). In the albitite veins, BtI is characterized by Si = 5.50 – 5.53 pfu, Al^{VI} = 0.43 – 0.46 pfu, and Ti = 0.31 – 0.32 pfu, as well as lower Mg# (0.31 – 0.33) than in the Edolo diabase (Tab. 1.3.4, Fig. 1.3.7). BtII is characterized by Si = 5.36 – 5.73 pfu, Al^{VI} = 0.33 – 0.37 pfu, and Ti = 0.32 – 0.34, with Mg# = 0.42 – 0.44 (Tab. 1.3.4, Fig. 1.3.7).

Site	Rock type	Generation	Si	Al^{IV}	Ti	Al^{VI}	Fe^{2+}	Fe^{3+}	Mg	Mg#	Ca	Na
Corteno-Golgi	Edolo diabase	CpxI	**1.81 - 1.90**	**0.10 - 0.19**	**0.03 - 0.06**	**0.01 - 0.04**	**0.24 - 0.31**	**0.03 - 0.08**	**0.67 - 0.74**	**0.67 - 0.69**	**0.82 - 0.85**	**0.03 - 0.04**
		(4 data)	1.86 ± 0.03	0.14 ± 0.03	0.04 ± 0.01	0.02 ± 0.01	0.27 ± 0.02	0.06 ± 0.02	0.71 ± 0.03	0.68 ± 0.01	0.84 ± 0.01	0.04 ± 0.01
		CpxII	**1.98**	**0.02**	**0.01**	**0.04**	**0.28**	**0.00**	**0.71**	**0.72**	**0.94**	**0.02**
		(1 data)	-	-	-	-	-	-	-	-	-	-
Valmoranda	Edolo diabase	CpxI	**1.85 - 1.89**	**0.11 - 0.15**	**0.04 - 0.06**	**0.00 - 0.03**	**0.21 - 0.25**	**0.03 - 0.08**	**0.72 - 0.78**	**0.72 - 0.75**	**0.85 - 0.87**	**0.03**
	(sample 49)	(5 data)	1.87 ± 0.01	0.14 ± 0.01	0.05 ± 0.01	0.02 ± 0.01	0.23 ± 0.01	0.06 ± 0.02	0.76 ± 0.02	0.73 ± 0.01	0.86 ± 0.01	-
		CpxII	**1.90 - 1.91**	**0.09 - 0.10**	**0.03**	**0.00 - 0.01**	**0.25 - 0.26**	**0.06 - 0.07**	**0.74**	**0.70**	**0.86 - 0.87**	**0.03**
		(2 data)	-	-	-	-	-	-	-	-	-	-
	Edolo diabase	CpxI	**1.76 - 1.86**	**0.14 - 0.24**	**0.04 - 0.09**	**0.00 - 0.02**	**0.24 - 0.34**	**0.07 - 0.10**	**0.63 - 0.65**	**0.60 - 0.67**	**0.85 - 0.87**	**0.04 - 0.05**
	(sample 76)	(4 data)	1.81 ± 0.05	0.19 ± 0.05	0.07 ± 0.02	0.01 ± 0.01	0.29 ± 0.04	0.09 ± 0.01	0.63 ± 0.01	0.63 ± 0.03	0.86 ± 0.01	-
Nembra	Edolo diabase	CpxII	**1.89 - 1.96**	**0.04 - 0.11**	**0.00 - 0.02**	**0.01**	**0.35 - 0.37**	**0.04 - 0.09**	**0.62 - 0.63**	**0.57 - 0.62**	**0.85 - 0.94**	**0.01 - 0.02**
	(sample ge8)	(2 data)	-	-	-	-	-	-	-	-	-	-
	Edolo diabase	CpxI	**1.75 - 1.89**	**0.11 - 0.25**	**0.04 - 0.08**	**0.02 - 0.05**	**0.20- 0.30**	**0.04 - 0.09**	**0.66 - 0.76**	**0.66 - 0.74**	**0.85 - 0.87**	**0.03 - 0.04**
	(sample ge11)	(14 data)	1.83 ± 0.04	0.17 ± 0.04	0.05 ± 0.01	0.04 ± 0.01	0.24 ± 0.03	0.06 ± 0.02	0.70 ± 0.04	0.70 ± 0.03	0.86 ± 0.01	-
		CpxII	**1.87 - 1.94**	**0.06 - 0.13**	**0.02 - 0.04**	**0.00 - 0.05**	**0.31 - 0.35**	**0.04 - 0.08**	**0.62 - 0.65**	**0.59 - 0.65**	**0.87 - 0.88**	**0.04**
		(2 data)	-	-	-	-	-	-	-	-	-	-
	Edolo diabase	CpxI	**1.77 - 1.91**	**0.09 - 0.23**	**0.03 - 0.07**	**0.02 - 0.06**	**0.18 - 0.31**	**0.00 - 0.08**	**0.66 - 0.78**	**0.67 - 0.76**	**0.84 - 0.86**	**0.03 - 0.05**
	(sample ge15)	(9 data)	1.87 ± 0.05	0.13 ± 0.05	0.05 ± 0.02	0.04 ± 0.01	0.25 ± 0.04	0.04 ± 0.02	0.73 ± 0.03	0.72 ± 0.03	0.85 ± 0.01	0.04 ± 0.01
		CpxII	**1.91 - 1.99**	**0.01 - 0.09**	**0.01 - 0.03**	**0.02 - 0.05**	**0.30 - 0.46**	**0.00 - 0.04**	**0.52 - 0.74**	**0.52 - 0.71**	**0.84 - 0.91**	**0.03 - 0.05**
		(5 data)	1.96 ± 0.03	0.04 ± 0.03	0.02 ± 0.01	0.03 ± 0.01	0.39 ± 0.07	0.02 ± 0.01	0.61 ± 0.09	0.60 ± 0.08	0.88 ± 0.02	0.04 ± 0.01

Table. 1.3.3. Compositional range (bold, apfu) and average value (± s.d.) of clinopyroxenes in the Edolo diabase dykes.

Plagioclase

In Corteno Golgi, PlI is labradorite (An_{50-53}) and PlII is albite or oligoclase (An_{6-13}). Similar compositions are found in Nembra area, where PlI is labradorite or andesine (An_{44-58}) at core, andesine or oligoclase (An_{10-38}) in intermediate postion between core and rim, and albite (An_{7-8}) at rim. In the albitite veins, PlI and PlII are albite, An_{10} and An_5, respectively.

Clinopyroxene trace and REE elements

CpxI from Valmoranda (sample 49 and sample 76) have been analyzed for minor and trace elements at CNR Pavia by LA-ICP-MS. Representative analyses are proposed in Table 1.3.5.

Figure 1.3.8 shows CpxI trace element and REE patterns from sample 49 (CpxI Mg# = 0.70-0.75) and sample 76 (CpxI Mg# = 0.60 – 0.67) from Valmoranda. Sr is depleted with respect to Nd and Ce in trace element patterns; Gd, Zr, Tb, Dy share similar abundances, whereas Ti is slightly enriched relatively to the neighbouring REEs. Nb and Ta concentrations vary from 1.57 to 61.23 and from 3.49 to 57.07 times the primitive mantle reference (Sun and McDonough, 1989), respectively. CpxI with

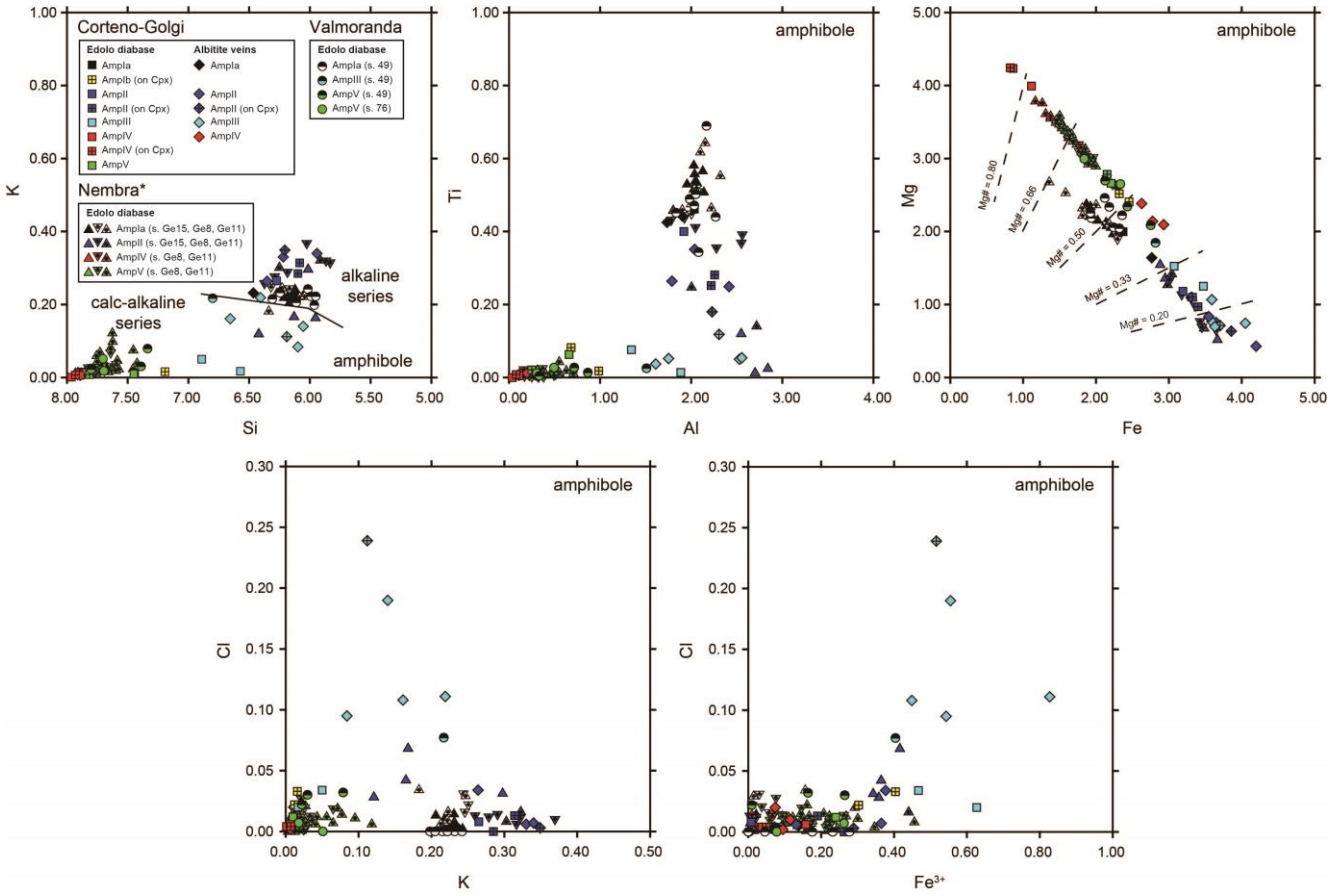

Figure 1.3.6. Composition of amphiboles in the Edolo diabase dykes, divided by locality and microstructural site. Alkaline and calc-alkaline fields are from Ridolfi and Renzulli (2012).

the lowest Nb and Ta concentrations are supposed to have crystallized together with ilmenite and/or amphibole, which preferentially incorporates those two elements (Green and Pearson, 1987). On the other hand, CpxI grains with the highest concentrations of Nb and Ta are also characterized by the highest Fe, Ti, and Eu content, which may indicate that they have crystallized before ilmenite, amphibole, and plagioclase. Trace element patterns are thus a second evidence that some CpxI grains are xenocrysts, as already suggested by microstructural analysis.

However, the exceptionally high concentration of Cs, Rb, and Ba in the analyzed clinopyroxene grains needs further investigation. These concentrations are in fact unlikely in clinopyroxene, as they are typical of K-bearing phases including amphibole. Since coronitic AmpIb, AmpIV, and AmpV commonly replaces from partially to totally the igneous clinopyroxene in the analyzed sample 49 and sample 76, trace and REE element analyses will be repeated on other samples where there is not amphibole replacing igneous clinopyroxene.

The primitive mantle-normalized CpxI REE patterns are similar in shape, with higher values in sample 76 than in sample 49. The patterns show relative depletion in LREE (La_N/Sm_N = 0.36 – 0.59) and

HREE (Gd_N/Yb_N = 1.86 – 3.36) with respect to MREE, at about 11 to 30 times primitive mantle (Sun and McDonough, 1989), with or without Eu anomaly. La_N/Yb_N ratios are in the range of 0.84 – 1.83.

Geothermobarometry

P-T conditions accountable for crystallization of igneous clinopyroxene and amphibole are estimated by single-phase thermometers and barometers. Results are summarized in Table 1.3.6.

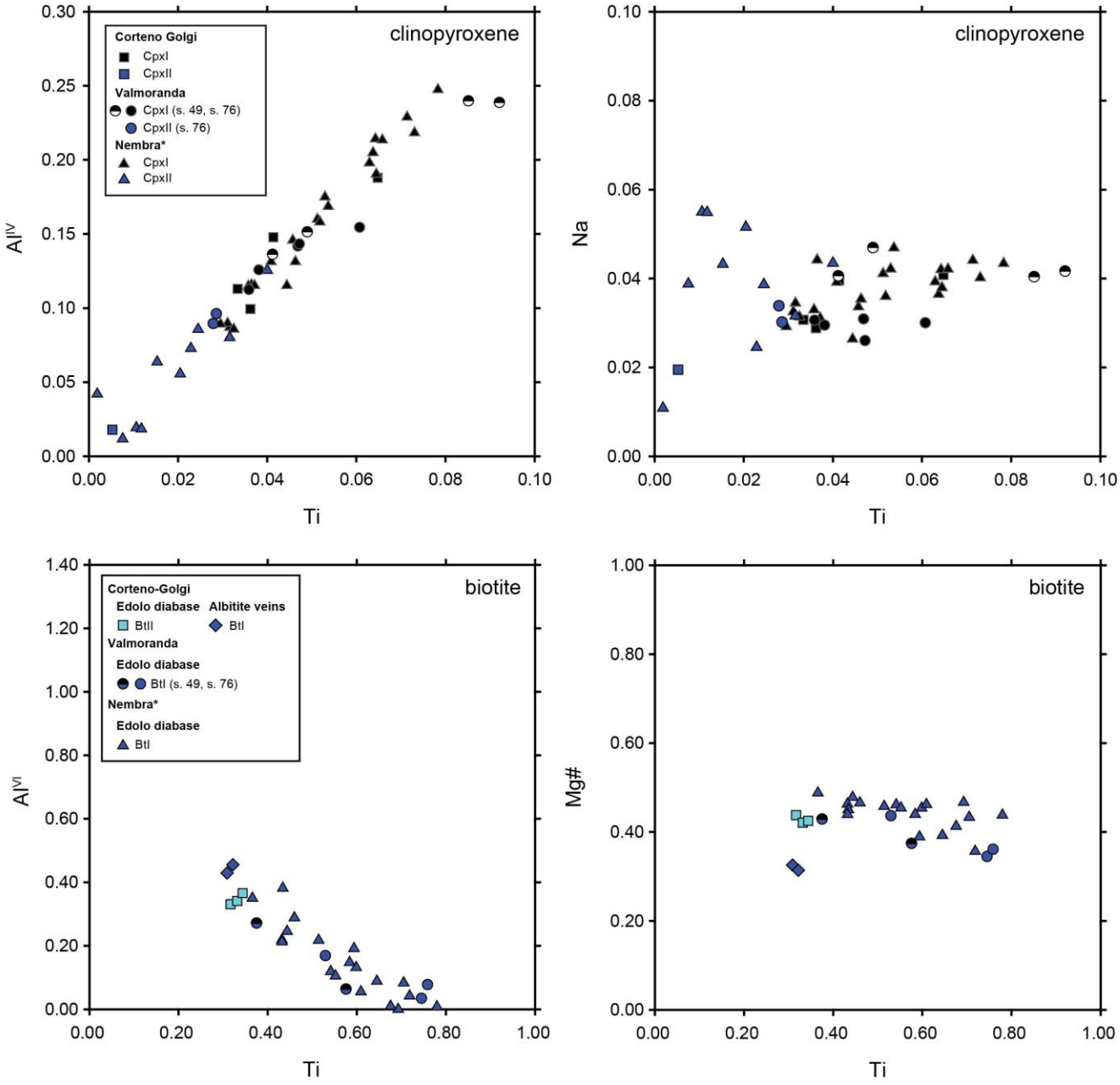

Figure 1.3.7. Composition of igneous clinopyroxene and biotite in the Edolo diabase dykes, distinguished by locality and microstructural site.

Thermometer and barometer established by Putirka (2008) are considered for estimating CpxI crystallization conditions. CpxII is excluded since clinopyroxenes with similar composition are not included within the calibration dataset (Putirka, 2008). In Corteno Golgi area, CpxI crystallized at T = 1129 ± 45°C in two P intervals, 0.14 – 0.26 (± 0.48) and 0.42 – 0.50 (± 0.48) GPa. In Valmoranda, CpxI in sample 49 retains T = 1123 ± 45°C and P = 0.17 – 0.24 (± 0.48) GPa, whereas CpxI in sample 76 crystallized at similar temperature (T = 1097 ± 45°C), but higher pressure (P = 0.29 - 0.39 ± 0.48

	s.49-12	**s.49-14**	**s.76-3**	**s.76-4**	**s.76-5**	**s.76-6**	**s.76-7**	**s.76-8**	**s.76-9**	**s.76-11**
Cs (ppm)	4	1	1	0	1	8	0	0	7	2
Rb	38	12	6	1	6	34	0	1	64	21
Ba	116	23	13	2	4	15	1	5	49	19
Th	0	1	2	0	0	0	0	0	4	1
U	0	0	4	1	3	2	0	2	2	1
Nb	2	3	44	3	1	3	2	2	16	10
Ta	0	0	2	0	0	0	0	0	1	1
Pb	13	9	3	5	3	1	1	1	5	3
Sr	141	43	65	61	56	62	52	53	100	69
Nd	18	22	35	25	22	25	20	22	27	25
Zr	163	136	175	175	124	179	173	170	349	175
Hf	7	8	7	7	5	8	8	7	12	7
Ti	22859	26651	85557	25177	19136	20008	28415	27044	29972	26536
Li	26	28	19	17	14	15	16	15	30	22
Y	32	40	60	41	32	43	41	38	55	43
La (ppm)	5	4	10	6	5	6	5	6	6	8
Ce	15	13	35	21	17	22	20	19	24	25
Pr	2	2	6	4	3	4	4	3	4	4
Nd	18	22	35	25	22	25	20	22	27	25
Sm	8	7	12	9	8	9	9	9	10	9
Eu	2	3	5	2	2	3	2	2	3	3
Gd	7	9	14	11	8	12	10	9	12	11
Tb	1	1	2	2	1	2	2	2	2	2
Dy	7	11	15	10	7	10	10	9	14	11
Ho	1	2	2	2	1	2	1	2	2	2
Er	3	3	6	5	4	5	4	5	7	4
Tm	0	1	1	1	1	1	0	0	1	1
Yb	2	2	5	4	2	3	4	4	5	3
Lu	0	0	1	0	0	0	0	0	1	0

Table 1.3.5. Clinopyroxene trace elements and REE concentrations (samples 49 and 76 from Valmoranda).

GPa) (Tab. 1.3.6). In Nembra area, CpxI crystallized at T = 1134 ± 45°C in two P intervals, 0.22 – 0.39 (± 0.48) and 0.45 – 0.65 (± 0.48) GPa (Tab. 1.3.6).

Thermobarometer of Ridolfi and Renzulli (2012) is considered for estimating temperature and pressure of igneous amphibole crystallization (Tab. 1.3.6). This thermobarometer is regarded as suitable for the Edolo diabase since it is calibrated on alkaline mafic rocks. This calibration requires amphibole Mg# > 0.50 and such a condition is rarely satisfied by the Fe-rich amphibole of the Edolo diabase (cfr. Tab. 1.3.2). However, we have extrapolated this calibration down to Mg# = 0.45. In addition, we applied

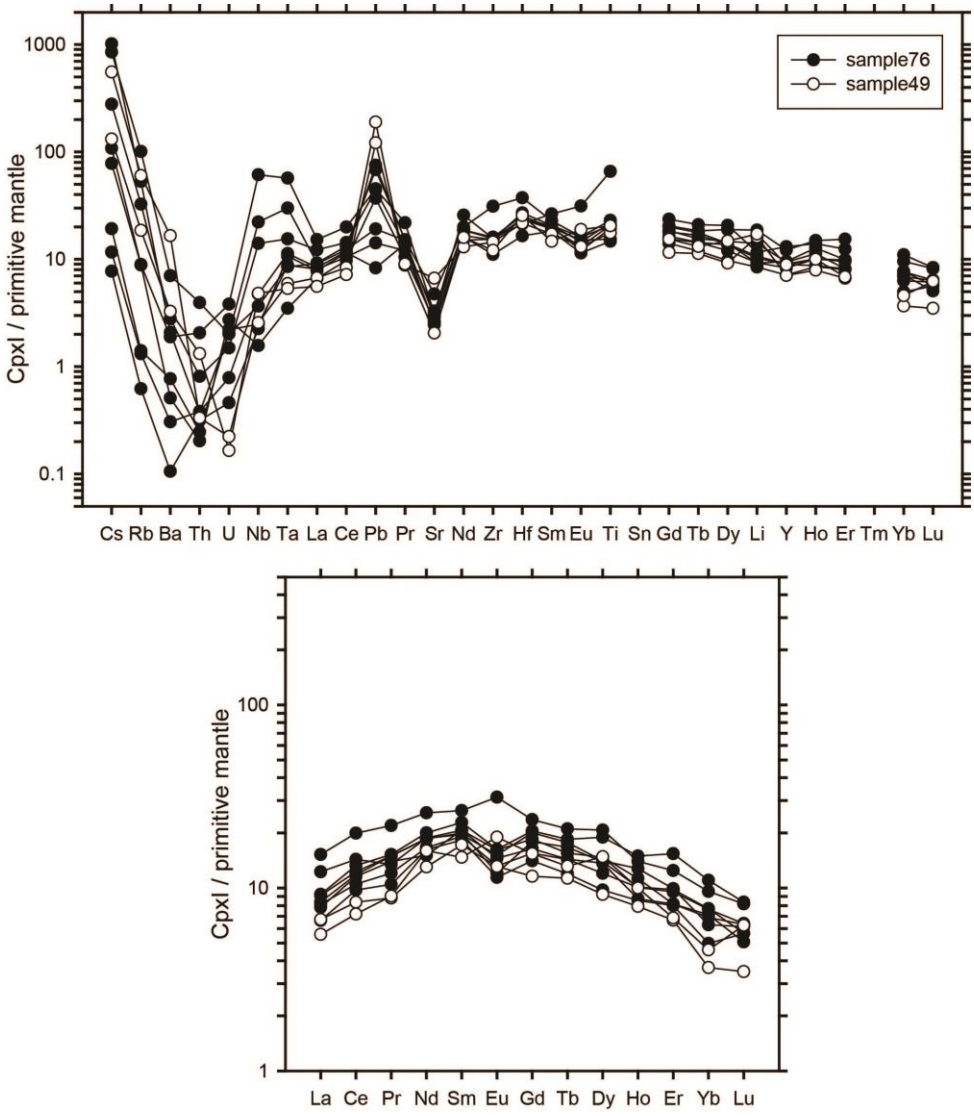

Figure 1.3.8. Primitive-mantle (Sun and McDonough, 1989) normalized race elements and REE patterns of CpxI from Valmoranda. Exceptionally high concentration of Cs, Rb, and Ba suggests that the analyses might have been contaminated by amphibole and will require further investigations.

Site	Rock type	Generation	T (°C) P08	T (°C) RR12	T (°C) P16	T (°C) G97	P (GPa) P08	P (GPa) RR12	P (GPa) G97
Corteno Golgi	Edolo diabase	CpxI	**1123 - 1139**				**0.14 - 0.50**		
		(4 data, Mg# = 0.67 – 0.69)	1129 ± 45				0.33 ± 0.48		
		AmpIa			**948**				
		(1 data, Mg# = 0.46)			± 30				
		AmpIb				**461 - 507**			**0.27 - 0.35**
		(2 data, Mg# = 0.50 - 0.52)				484 ± 40			0.31 ± 0.12
		AmpIII			**744**				
		(1 data, Mg# = 0.33)			± 30				
		AmpIV				**380 - 398**			**0.13 - 0.16**
		(3 data, Mg# = 0.78 - 0.84)				387 ± 40			0.14 ± 0.12
		AmpV				**395 - 460**			**0.14 - 0.25**
		(2 data, Mg# = 0.55 - 0.56)				427 ± 40			0.20 ± 0.12
	Albitite veins	AmpIa			**897**				
		(1 data, Mg# = 0.37)			± 30				
		AmpIV				**374 - 387**			**0.09 - 0.12**
		(3 data, Mg# = 0.42 - 0.46)				380 ± 40			0.11 ± 0.12
Valmoranda	Edolo diabase	CpxI	**1110 - 1126**				**0.17 - 0.24**		
	(sample 49)	(3 data, Mg# = 0.70 – 0.75)	1123 ± 45				0.20 ± 0.48		
		AmpI		**990 - 1034**	**927 - 1019**			**0.50 - 0.63**	
		(4/7 data, Mg# = 0.47 – 0.54)		1009 ± 25	964 ± 30			0.56 ± 0.07	
		AmpIII			**711**				
		(1 data, Mg# = 0.40)			± 30				
		AmpV				**400 - 488**			**0.14 - 0.30**
		(3 data, Mg# = 0.43 - 0.56)				454 ± 40			0.23 ± 0.12
	Edolo diabase	CpxI	**1089 - 1113**				**0.29 - 0.39**		
	(sample 76)	(4 data, Mg# = 0.60 – 0.67)	1097 ± 45				0.33 ± 0.48		
		AmpV				**416 - 421**			**0.16 - 0.22**
		(3 data, Mg# = 0.53 - 0.62)				419 ± 40			0.19 ± 0.12
Nembra*	Edolo diabase	AmpI		**918 ± 25**	**898 - 942**			**0.30 ± 0.03**	
	(sample Ge8)	(1/3 data, Mg# = 0.45 – 0.49)		-	923 ± 30			-	
		AmpIV				**379 - 388**			**0.10 - 0.13**
		(3 data,Mg# = 0.53 - 0.64)				382 ± 40			0.12 ± 0.12
		AmpV				**393- 434**			**0.14 - 0.23**
		(13 data, Mg# = 0.53 - 0.64)				408 ± 40		-	0.17 ± 0.12
	Edolo diabase	CpxI	**1126 - 1144**				**0.22 - 0.63**		
	(sample Ge15)	(9 data, Mg# = 0.67 – 0.76)	1136 ± 45				0.39 ± 0.48		
		AmpI		**977 - 1019**	**957 - 992**			**0.31 - 0.68**	
		(4/8 data, Mg# = 0.47 – 0.56)		1001 ± 25	974 ± 30			0.57 ± 0.07	
	Edolo diabase	CpxI	**1126 - 1139**				**0.25 - 0.57**		
	(sample Ge11)	(14 data, Mg# = 0.66 – 0.74)	1133 ± 45				0.46 ± 0.48		
		AmpI		**866 - 1075**	**940 - 1031**			**0.35 - 0.89**	
		(4/6 data, Mg# = 0.49 – 0.66)		971 ± 75	976 ± 46			0.51 ± 0.20	
		AmpIV				**373 - 409**			**0.10 - 0.17**
		(9 data, Mg# = 0.70 - 0.76)				386 ± 40			0.13 ± 0.12
		AmpV				**404 - 467**			**0.15 - 0.29**
		(28 data, Mg# = 0.59 - 0.71)				425 ± 40			0.20 ± 0.12

Table 1.3.6. Synthesis of thermobarometric estimates, compositional range (bold) and average value ± s.d., on igneous clinopyroxenes (P08 = Putirka, 2008) and amphiboles (RR12 = Ridolfi and Renzulli, 2012, P16 = Putirka, 2016).

the thermometer of Putirka (2016), which is calibrated on a larger amphibole data selection with Mg# comprised between 0.30 and 0.54.

In the Edolo diabase, AmpIa crystallized at around 950 – 1000°C. This result is fully consistent with the amphibole crystallization temperature estimated in Nembra area (Tab. 1.3.6). In the albitite veins, AmpIa retains slightly lower temperature (T = 897 ± 30°C, Tab. 1.3.6). In Valmoranda, selected AmpIa analyses from sample 49 retain P = 0.56 ± 0.07 GPa (Tab. 1.3.6), whereas AmpI in Nembra area crystallized in two pressure intervals, 0.30 – 0.44 and 0.64 – 0.89 GPa. AmpII composition in Corteno Golgi is not suitable for amphibole thermobarometry (Mg# = 0.22 – 0.27). In Nembra area, AmpII crystallized at T = 867 ± 30°C (Putirka, 2016). AmpIII retains T = 727 ± 30°C, which likely represents the last stage of igneous crystallization.

In summary, igneous clinopyroxene retain higher crystallization temperature than amphibole that match the crystallization order suggested by microstructural analysis and CpxI trace element patterns. The crystallization temperature retained by CpxI in different locality is similar (T = 1128 ± 45°C), because of the minimal variation in Mg#, Na content lower than 0.05 pfu, and constant Al^{IV} / Ti ratio. Crystallization temperature for AmpIa falls in a little interval, reflecting small difference in Si content (5.95 – 6.31 pfu) and Mg# = 0.46 – 0.53, which are the most important parameters for amphibole thermometry. Estimates performed by the thermometer of Putirka (2016) are, on average, lower than those determined by the thermometer of Ridolfi and Renzulli (2012). This mismatch is also amplified snce we applied the Putirka's (2016) thermometer on a wider number of data and with higher Fe content. However, the difference is minimal and the crystallization temperature for AmpIa is assumed to be comprised between 960 and 1010°C. AmpIa in albitite veins and AmpIII in both Edolo diabase and albitite veins crystallized at lower temperature (730 – 870°C), in fully agreement with the already constrained crystallization order and field relationships.

On the other hand, comparison between amphibole and clinopyroxene barometric estimates is extremely tricky, first of all since the applied thermometers and barometers come along with a big root mean square error on the calibration dataset, and also because amphibole igneous barometry at lower pressure is problematic (Putirka, 2016). In Valmoranda, CpxI xenocrysts are supposed to have crystallized within the wide range of pressure of 0.13 – 0.65 GPa, with slightly lower pressure in sample 49 (0.17 – 0.24 GPa) than in sample 76 (0.29 – 0.39 GPa). These estimates will be considered for further geochemical modelling in the next paragraphs.

Hydrothermal conditions are estimated by amphibole geothermobarometry which is calibrated on metamorphic hornblende and actinolite (Gerya et al., 1997). AmpIb and AmpIV likely crystallized at sub-solidus conditions during post-intrusive hydrothermal circulation events as suggested by mineral chemical composition and microstructural relationships (Fig. 1.3.3E and D; Tab. 1.3.2). Indeed, AmpIb and AmpIV grew at rims of igneous minerals, without counterparts in the country rocks. In particular, hydrothermal barometric estimates on AmpIV may be helpful to deduce the final

emplacement level for the Edolo diabase. AmpIb, which replaces CpxI xenocrysts and is truncated by AmpII rims and biotite, likely crystallized at T = 460 – 510°C and P = 0.26 – 0.35 GPa (Tab. 1.3.6). These P-T conditions were attained before the crystallization of AmpII and represent a first stage of hydrothermalism, occurred at a crustal depth compatible with the first crystallization of the CpxI xenocrysts. After that, the already hydrothermalized clinopyroxene grains were likely taken in charge by a subsequent magmatic pulse from which AmpII and biotite crystallized. Hydrothermal barometric estimates on AmpIV may be helpful to deduce the final emplacement level for the Edolo diabase, as this is the last hydrothermal amphibole generation.

The results for AmpIV in Edolo diabase dykes and albitite veins at Corteno-Golgi plot in the range of T = 380 – 400 °C and P = 0.09 – 0.16 ± 0.12 GPa (Tab. 1.3.6). Similar hydrothermal conditions (T = 380 ± 40°C and P = 0.12 ± 0.12 GPa) come from AmpIV in Nembra. P = 0.09 – 0.16 GPa is likely ascribable to the final emplacement level of the Edolo diabase dykes, as this pressure matches or is slightly lower than the lowest barometric estimates on the crystallization of the igneous phases.

Finally, composition of AmpV supporting Alpine foliation S3 in Edolo diabase dykes point temperature at around 440 °C and pressure comprised between 0.14 and 0. 30 GPa (Tab. 1.3.6). These results confirm the Alpine metamorphic conditions already estimated in Nembra area (see next paragraphs).

Geochemical modelling

REE concentrations in liquids in equilibrium with the CpxI xenocrysts, i.e. the most primitive parental melts, are calculated by mineral/liquidus partition coefficients (D^i). Only CpxI in sample 76 and 49 without Eu anomaly have been here considered, since they better reflect the parental melt compositions (Fig. 1.3.8). Mineral/liquidus partition coefficients for clinopyroxene are determined according to Wood and Blundy (1997), considering CpxI compositions and thermobarometric estimates performed on sample 49 and sample 76. Partition coefficients for REE elements are determined by solving the Brice equation:

(1) $D^i = D_0 \exp(-4\pi E_{M2} N_a (r_0/2(r_i-r_0)^2+1/3(r_i-r_0)^3)/RT)$

where N_a is the Avogadro's number, E_{M2} is the Young's Modulus of the M2 site, and R is the gas constant. E^{3+}_{M2} is considered pressure and temperature sensitive:

(2) $E^{3+}_{M2} = 318.6 + 6.9P – 0.036T$

R_0 in the Brice equation is the radius of the M2 site in clinopyroxene, which is dependent on the Ca content in M2 and on the Al content in M1:

(3) $R_0 = 0.974 + 0.067\ X^{Ca}_{M2} - 0.051 X^{Al}_{M1}$

It should be noted that the higher Al^{IV} concentration in sample 76 CpxI than in sample 49 has no effect on the modelling, since the Brice equation does not consider the charge effects on REE concentrations of the Al^{IV} / Si substitution. Finally, we consider D_0^{3+} depending on the Mg content in the clinopyroxene M1 site, as well as on the Mg# in the parental melt (Wood and Blundy, 1997):

(4) $D_0^{3+} = Mg\#_{melt} / X^{Mg}_{M1} \exp ((88750 - 65.644T + 7050P - 770T^2) / RT)$

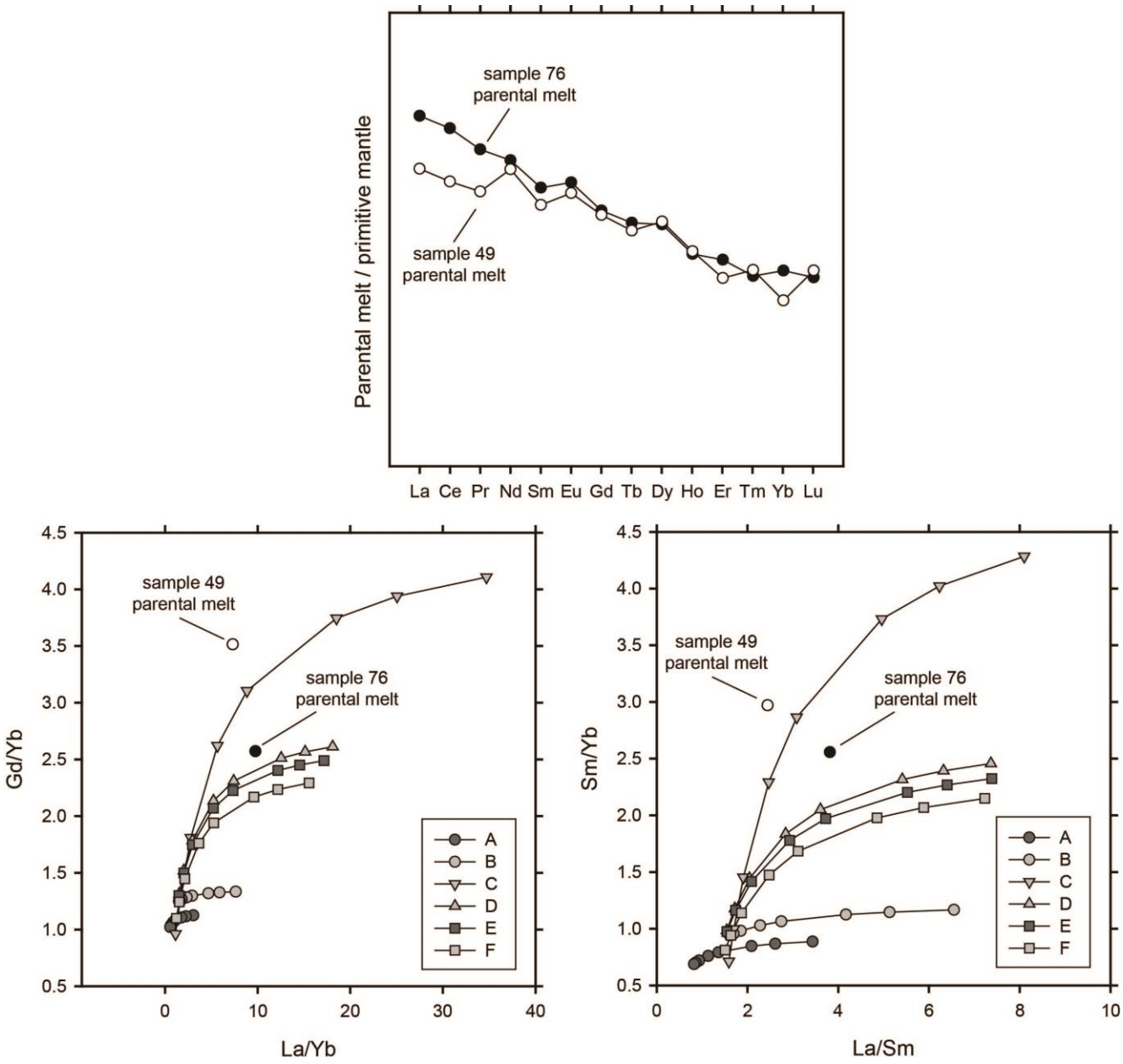

Figure 1.3.9. Parental melt composition inferred by clinopyroxene partition coefficient modelling (Wood and Blundy, 1997). Melting curves modelled by non-modal batch melting (Shaw, 1970). Starting mantle sources, melting proportions, and partition coefficients are listed in Table 1.3.7.

However, different Mg# in the parental melts do not affect the ratio between the REE partition coefficients that are calculated combining (1) to (4). Since the Mg# of the parental melt is unknown, from here on out, we only consider the ratios between REE concentrations in the parental melt. R_0 is calculated for CpxI compositions in sample 49 and sample 76. The determined ratio between partition coefficients are comparable to those proposed by Ubide et al., 2014 for clinopyroxene crystallizing from a camptonite melt under P-T conditions similar to those retained by the Edolo diabase. Our coefficients are used to calculate the parental melt REE patterns for sample 49 and sample 76.

Source Modal Composition

	A	B	C	D	E	F
Ol	0.57	0.55	0.55	0.55	0.55	0.56
Opx	0.28	0.25	0.25	0.19	0.2	0.19
Cpx	0.13	0.15	0.15	0.15	0.15	0.15
Spl	0.02	0.05	0	0.02	0	0
Grt	0	0	0.05	0.04	0.04	0.02
Amp	0	0	0	0.05	0.06	0.02
Phl	0	0	0	0	0	0.06

Source Melting Proportion

	Ol	Opx	Cpx	Spl	Grt	Amp	Phl
A	0.01	0.09	0.6	0.3	0	0	0
B	0.01	0.09	0.6	0.3	0	0	0
C	0.01	0.07	0.6	0	0.32	0	0
D	0.05	0.05	0.1	0.1	0.2	0.5	0
E	0.03	0.05	0.22	0	0.2	0.5	0
F	0.03	0.05	0.1	0	0.15	0.37	0.3

Source REE concentration

	DDM	PM	PM	PM	PM	PM
La	0.192	0.687	0.687	0.687	0.687	0.687
Ce	0.55	1.775	1.775	1.775	1.775	1.775
Pr	0.107	0.276	0.276	0.276	0.276	0.276
Nd	0.581	1.354	1.354	1.354	1.354	1.354
Sm	0.239	0.444	0.444	0.444	0.444	0.444
Eu	0.0096	0.168	0.168	0.168	0.168	0.168
Gd	0.358	0.596	0.596	0.596	0.596	0.596
Tb	0.07	0.108	0.108	0.108	0.108	0.108
Dy	0.505	0.737	0.737	0.737	0.737	0.737
Ho	0.115	0.164	0.164	0.164	0.164	0.164
Er	0.348	0.48	0.48	0.48	0.48	0.48
Tm		0.074	0.074	0.074	0.074	0.074
Yb	0.365	0.493	0.493	0.493	0.493	0.493
Lu	0.058	0.074	0.074	0.074	0.074	0.074

Partition coefficients

	Ol	Opx	Cpx	Spl	Grt	Amp	Phl
La	0.0004	0.002	0.054	0.01	0.01	0.17	0.00002
Ce	0.0005	0.003	0.098	0.01	0.021	0.26	0.0002
Pr	0.0008	0.0048	0.15	0.01	0.054	0.35	0.0002
Nd	0.001	0.0068	0.21	0.01	0.087	0.44	0.0002
Sm	0.0013	0.01	0.26	0.01	0.217	0.76	0.0002
Eu	0.0016	0.013	0.31	0.01	0.32	0.88	0.0218
Gd	0.0015	0.016	0.3	0.01	0.498	0.86	0.0205
Tb	0.0015	0.019	0.31	0.01	0.75	0.83	0.025
Dy	0.0017	0.022	0.33	0.01	1.06	0.78	0.0281
Ho	0.0016	0.026	0.31	0.01	1.53	0.73	0.028
Er	0.0015	0.03	0.29	0.01	2	0.68	0.0303
Tm	0.0015	0.04	0.449	0.01	3	0.64	0.035
Yb	0.0015	0.049	0.28	0.01	4.03	0.59	0.0484
Lu	0.0015	0.06	0.28	0.01	5.5	0.51	0.0471

Table 1.3.7. Parameters adopted for non-modal batch melting geochemical modelling (as in Casetta et al., 2019). Source modal composition: A = Spl-lherzolite; B = Spl-lherzolite; C = Grt-lherzolite; D = Spl–Grt–Amp-lherzolite; E = Grt–Amp-lherzolite; F = Grt–Phl-lherzolite. Considered source REE concentration: DDM (Workman & Hart, 2005); fertile PM (Sun & McDonough, 1989). REE partition coefficients: Ol, Opx, Cpx, Spl, Grt and Amp are from McKenzie & O'Nions (1991) and Schmidt et al. (1999), except for Tm in Cpx (Zack & Brumm, 1998); Phl: La, Ce, Nd and Sm are from Schmidt et al. (1999), Eu, Gd, Dy, Er, Yb and Lu from Fujimaki et al. (1984); Pr, Tb, Ho and Tm were extrapolated

according to Barry et al., (2003).

The computed parental melt REE patterns are characterized by La/Yb = 9.76, La/Sm = 3.82, Gd/Yb = 2.57, and Sm/Yb = 2.56 in sample 76, and by La/Yb = 7.31, La/Sm = 2.46, Gd/Yb = 3.51, and Sm/Yb = 2.97 in sample 49 (Fig. 1.3.9). Similar REE patterns suggest that CpxI in sample 49 and sample 76 likely crystallized by the same parental magma but at different pressure conditions. Moreover, parental melt REE patters are similar in shape to those determined by WR analysis (Fig. 1.3.4): in this way a major contribution of fractionation and assimilation processes is precluded. Since there is evidence of amphibole contamination on igneous clinopyroxene composition, the result should be considered with caution. Further new analyses on well preserved igneous clinopyroxene grains will be soon available.
The composition of the source mantle is further investigated by non-modal batch melting (Shaw, 1970). The modelling considers different source mantle compositions and modal proportion between mantle minerals (Tab. 1.3.7) and is performed by varying the partial melting degree (F) from 0.1% to 20% in the Shaw's (1970) equation:

(5) $C_l^i = C_0^i / (D_0^i + F (1 - P)$

where i is the element of interest, C_0 is the original concentration in the source mantle, C_l is the concentration in the parental melt, D_0^i the averaged partition coefficient for element i in the source mantle at onset of melting, and P the averaged partition coefficient for element i in phases entering melt. Parental melt compositions for sample 49 and sample 76 better approach the melt generated by a garnet bearing lherzolite with a fertile PM composition and F at around 3% (Fig. 1.3.9).

Discussion and Conclusion

In the Alpine area, the Permian-Triassic period is characterized by relaxed thermal state, extension, and mafic magma emplacements (Spalla et al., 2014; Roda et al., 2019). In the central Southern Alps, in the area comprised between the Alpine Gallinera and Insubric lines, alkaline camptonites, historically known as Edolo diabase, intruded into Variscan basement rocks of the Aprica and Passo Cavalcafiche TMUs. The dykes crosscut the late- to post-collisional S2 foliation (greenschist facies) recorded during the Variscan cycle and were subsequently deformed and locally metamorphosed in response to the Alpine convergence.
Igneous phase compositions in Edolo diabase dykes are heterogeneous in terms of major, trace and REE elements. Microstructural evidence for clinopyroxene crystallization predating, in many cases, the other igneous phases is clearly also reflected by clinopyroxene trace elements (high Nb and Ta concentrations) and REE patterns (absence of Eu anomaly). Furthermore, AmpIb (actinolite) replacing

CpxI before crystallization of AmpII (ferro-pargasite) testify cooling before further involvement of clinopyroxene crystals in the dykes as xenocrysts.

Compositions of igneous minerals in the Edolo diabase dykes are widely ranging. For example, AmpI and CpxI in sample 49 from Valmoranda, display the highest Mg# in comparison with the other localities. However, such differences are not reflected by the whole rock compositions, likely due to different modal contribution of biotite, ilmenite, and further generations of Fe-rich amphiboles. AmpI and AmpII in Edolo diabase dykes from Corteno Golgi are broadly similar to AmpI and AmpII in Nembra area, although, in the latter locality, Mg# is up to 0.66. Na-enrichment affects CpxII only in the Nembra area.

Microstructural analysis, trace elements, and REE patterns suggest that CpxI and AmpI are the first igneous phases to crystallize. The lowest barometric estimates on CpxI and AmpI crystallization (0.2 - 0.3 GPa) suggest that the emplacement of the Edolo diabase occurred at shallow depth, as already supported by the presence of straight chilled margins. Moreover, barometric estimates on hydrothermal AmpIV replacing igneous minerals in both the Edolo Diabase and albitite (P = 0.09 – 0.16 GPa) confirm shallow depth emplacements, which reflect the depth of the Aprica and Passo Cavalcafiche TMUs at the time of dyke emplacement.

AmpIII is found in both the Edolo Diabase dykes and albitite veins, but in the latter with lower Mg# and higher K and Cl content. The coexistence of AmpIII in interstitial domains together with BtII constrains its late-igneous origin. AmpIII crystallized at temperature comprised between 700 and 750°C (Tab. 1.3.6). High chlorine concentration in AmpIII is clearly controlled by its chemical composition and, in particular, a correlation with its Fe^{3+} and K content is observed (see Rebay et al., 2015b for a discussion on Cl-rich amphiboles). AmpIII with the highest Cl concentrations (up to 0.24 pfu) is found in the late-intrusive (and Fe-rich) albitite veins, which are supposed to represent the most differentiated melt.

The WR geochemical signature of the Edolo diabase dykes is consistent with alkaline intra-plate magmatism in a continental rifting tectonic setting (Figs. 1.3.4 and 1.3.5). Clinopyroxene REE patterns in different samples are heterogeneous, in particular in terms of REE concentrations. Partition coefficients modelling as function of clinopyroxene composition and thermobarometric estimates indicates that the clinopyroxene xenocrysts crystallized from similar parental magmas but at different P-T conditions. Non-modal batch melting modelling performed on the computed primitive melt for the Edolo diabase suggests a fertile and garnet-bearing lherzolite as source mantle rock, which experienced a 3% of partial melting degree.

1.4 Barrovian metamorphism in the Edolo meta-diabase: first thermodynamic modeling with implications for Alpine tectonics in the central Southern Alps

Marco Filippi, Jean-Marc Lardeaux, Gregorio Pulcini, Gisella Rebay, Manuel Roda, Maria Iole Spalla, Davide Zanoni (paper in preparation)

Introduction

Crustal thickening due to continental collision is documented in the external domains of the Alps since the late Eocene (Schmid et al., 2004; Dal Piaz, 2010; Lardeaux, 2014 and ref. therein). At that time, flysches and molasses filled the Alpine foreland basins (e.g. Ford and Lickorish, 2004 and ref. therein) and collisional structures developed in the Helvetic domain basement under greenschist to upper greenschist facies conditions (e.g. Rolland et al., 2003, Sanchez et al., 2011; Cenki-Tok et al., 2014; Filippi et al., 2019, 2020). At odds, in the central Southern Alps, crustal thickening started as early as the late Cretaceous during active oceanic subduction and lasted through the continental collision in Eocene times (Zanchetta et al., 2011, 2015).

Alpine metamorphic minerals are widely recognized in the central Southern Alps (Crespi et al., 1982; Brack, 1981, 1984; Milano et al., 1988; Albini et al., 1994, Cadel et al., 1996; Gosso et al., 2012; D'Adda and Zanchetta, 2015; Rebay et al., 2015), but a quantification and tectonic interpretation of the Alpine metamorphism in this domain is still missing. In this contribution, we quantify the Alpine metamorphic evolution of the northern part of the central Southern Alps, focusing on the post-Variscan Edolo diabase dykes and combining high-resolution multi-scale structural analysis with mineral chemistry and thermodynamic modeling.

Geological setting

The central Southern Alps west of the Giudicarie Fault consist of Variscan basement rocks and early Permian to Cretaceous sedimentary sequences (Fig. 1.4.1) (Milano et al., 1988; Gosso et al., 2012; Zanoni & Spalla, 2018 and reference therein). They are separated from the axial zone of the Alps – the Austroalpine and Penninic domains – by the Periadriatic Lineament (Fig. 1.4.1), a dominantly strike-slip system that has been active at least since the Oligocene and accommodated the Bregaglia and Adamello calc-alkaline intrusions (Schmid et al., 1989; Müller et al., 2001; Oberli et al., 2004;

Rosemberg, 2004). North of the Periadriatic Lineament, the N-verging Austroalpine and Penninic nappes heterogeneously record Variscan and Alpine metamorphism (e.g. Gazzola et al., 2000; Salvi et al., 2010; Roda et al., 2018; Picazo et al., 2019).

The basement of the central Southern Alps consists of different tectono-metamorphic units (TMUs) that record the Variscan evolution and, nearby the Como Lake, the high thermal signature of the Triassic rifting (Milano et al., 1988; Diella et al., 1992; Bertotti et al., 1993; Spalla et al., 2014). The dominant structure in the Variscan basement in the Adamello area is the greenschist facies S2 foliation, which developed during coupling of basement rocks retaining contrasting tectono-metamorphic evolutions (Spalla & Gosso, 1999; Spalla et al., 2014 and references therein). A minimum age for S2 is constrained by the deposition of Permian siliciclastic sequences, which contain clasts deriving from the Variscan TMUs (Garzanti & Schiunnach, 1997; Spalla et al., 2009; Zanoni et al., 2010; Cassinis et al., 2012; Gosso et al., 2012; Berra et al., 2014; 2016; Zanoni & Spalla 2018). Pre-D2 foliations are marked by epidote amphibolite- and/or amphibolite-facies minerals (Spalla & Gosso, 1999; Zanoni & Spalla 2018 and refs therein).

The main Alpine feature of the central Southern Alps is a south-verging thrust system – i.e. the Orobic-Porcile-Gallinera Thrust (Fig. 1.4.1) – that has brought Variscan basement rocks onto Permian to Mesozoic covers (e.g. Wennekers, 1932; De Sitter, 1963; Cassinis et al., 1986; Schönborn, 1992; Cadel et al., 1996; Carminati et al., 1997; Ghiselli et al., 2015; D'Adda & Zanchetta, 2015). In the footwall, anticlines involving basement and Permian-Mesozoic sequences – i.e. Orobic, Trabuchello-Cabianca, and Cedegolo Anticlines (Fig. 1.4.1) – are interpreted as fault-bend folds formed during on-going southward thrusting in pre-Oligocene times (Brack, 1981; 1984; Zanchetta et al. 2015). In the hanging wall, the most prominent Alpine structures in the Variscan basement rocks are steeply dipping chevron folds (e.g. Milano et al., 1988; Carminati et al., 1997; Rebay et al., 2015). The intrusion of the Adamello calc-alkaline batholith at 43 – 33 Ma (Schaltegger et al., 2019 and ref. therein) post-dates the Orobic-Porcile-Gallinera Thrust and Cedegolo Anticline development (Brack, 1981, 1984) (Fig. 1.4.1). However, reactivation of the Periadriatic Lineament and Orobic-Porcile-Gallinera Thrust, mostly as dextral strike-slip or transpressional faults, has been envisaged since the late Eocene (Zanchetta et al., 2015 and ref. therein).

The age of the syn-subductive Orobic-Porcile Thrust is constrained by Ar/Ar dating of pseudo-tachylytes at 80-43 Ma (Zanchetta et al., 2011 and ref. therein). Cenomanian-Campanian flysches in the southernmost part of the central Southern Alps testify the erosion of both basement and cover units on an active margin propagating southwards (Bersezio et al., 1993). Poorly investigated greenschist facies mylonites are supposed to have accommodated first increments of crustal shortening before Oligocene (e.g. Albini et al. 1994; D'Adda and Zanchetta, 2015). Barometric estimates on

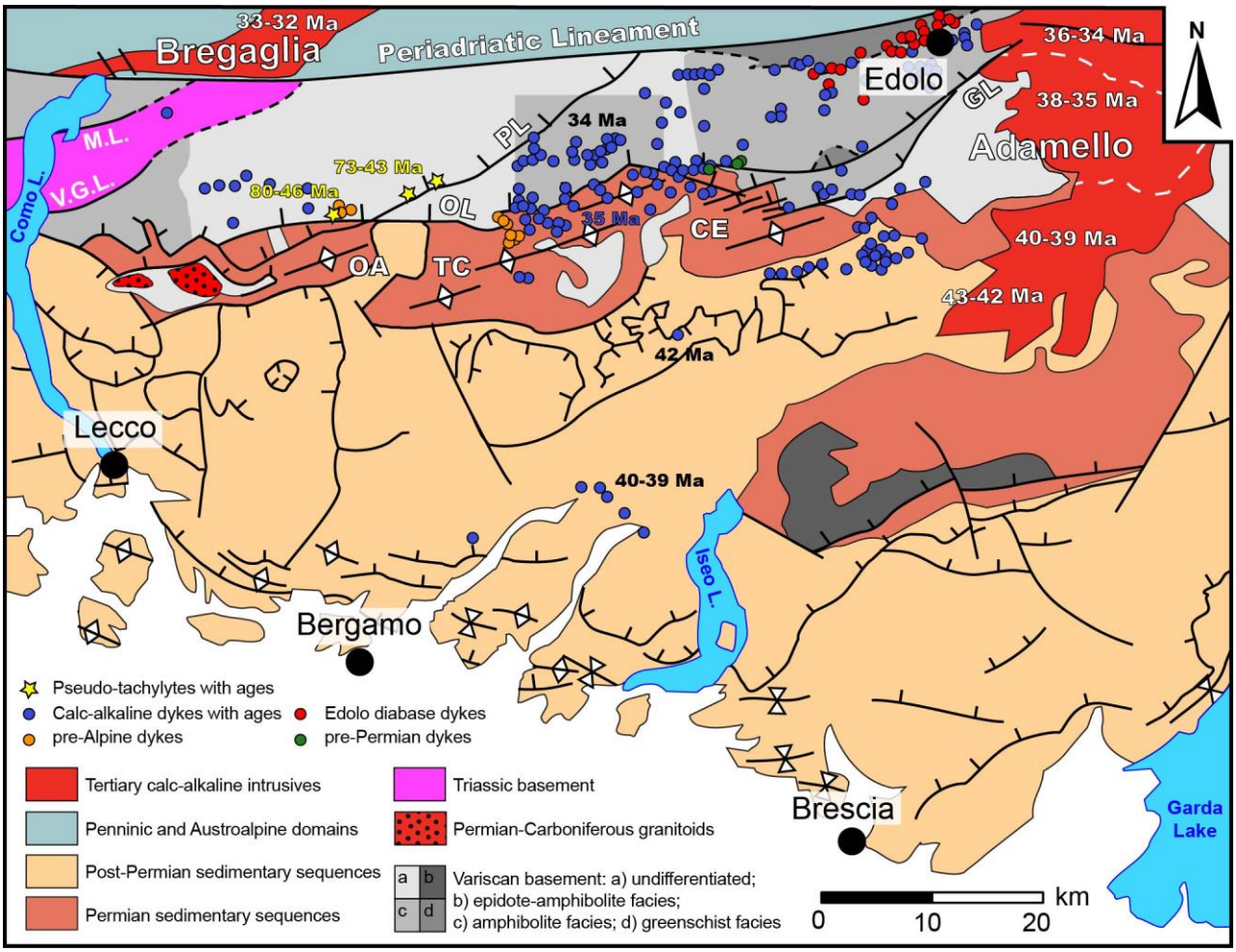

Figure 1.4.1. Tectonic outline of the central Southern Alps (modified after Spalla et al., 2014; Zanchetta et al., 2015; Zanoni & Spalla, 2018 and ref. therein). Abbreviations - OA: Orobic Anticline; TC: Trabuchello-Cabianca Anticline, CE: Cedegolo Anticline, OL: Orobic Line, PL: Porcile Line, GL: Gallinera Line. Adamello ages are from Schaltegger et al. (2019); Bregaglia ages are from Oberli et al. (2004); Alpine pseudo-tachylytes ages are from Zanchetta et al. (2011); the ages of the Tertiary calc-alkaline dykes are from Bergomi et al. (2015).

pseudotachylites in the hanging wall of the Orobic-Porcile Thrust indicate that this unit was buried up to depth equivalent to 0.1 – 0.2 GPa during the Alpine cycle (Viganò et al., 2011).

Calc-alkaline mafic dykes are widespread in the central Sothern Alps (Fig. 1.4.1), where they crosscut regional scale thrusts and folds in the Variscan basement and Permian to Mesozoic sedimentary sequences (D'Adda et al. 2011; Bergomi et al., 2015). The age of these intrusives ranges between 42 and 34 Ma (D'Adda et al., 2011; Bergomi et al., 2015), confirming that most of the central Southern Alps architecture was already accomplished before Oligocene (Zanchetta et al., 2011; Zanchetta et al., 2015).

Other mafic dykes, known as "Edolo diabase" (Schiavinato, 1954), are alkaline and outcrop in the area comprised between the Periadriatic Lineament and Gallinera Thrust (Fig. 1.4.1). The Edolo diabase

dykes pre-date the Adamello intrusion and, for this reason, a Triassic emplacement age was supposed by Italian authors of the past century (Schiavinato et al., 1954 and ref. therein). Igneous minerals are dark brown amphibole and biotite, pale pink clinopyroxene, plagioclase, ilmenite, magnetite, and rare quartz. Mineral assemblages and WR analyses in the previous paragraphs (see also Bergomi et al., 2015) allow classifying the Edolo diabase as camptonite, a type of alkaline lamprophyre (Le Maitre et al., 2002; Casetta et al., 2019). The new meso- and micro-scale structural data here presented reveal that these dykes crosscut the regional scale Variscan S2 foliation in the country rocks and have been deformed and metamorphosed during the Alpine convergence.

Field occurrence

The studied area is comprised between the Gallinera Thrust and the Insubric Line in the northern part of the central Southern Alps (Fig. 1.4.1). This area exclusively comprises basement rocks, such as metapelites and quartzites, where the dominant Variscan S2 foliation is marked by lower greenschist facies minerals. Upper greenschist and amphibolite facies minerals occur as relics within S2 in low strained domains (Gosso et al., 2012; Rebay et al., 2015). South of the Gallinera Thrust, S2 is truncated by the Permian sedimentary sequences (Gosso et al., 2012). The Alpine deformation (D3) in the Variscan basement results in locally schistogenic chevron folds of metric wavelength, which are truncated by the Adamello intrusion towards the east and by calck-alkaline mafic dykes in different localities (Brack, 1981, 1984; Albini et al., 1994; Blom and Passchier, 1997; Carminati et al., 1997; Gosso et al., 2012; Bergomi et al., 2015; Rebay et al., 2015). Biotite- and amphibole-bearing Alpine foliation S3 has been already described in pre-Alpine mafic dykes at the junction between the Porcile and Orobic Thrusts (D'Adda and Zanchetta, 2015).

The Edolo diabase occurs in up to 50 m-thick dykes that are mostly characterized by medium grained phaneritic texture, whereas the thinnest dykes are porphyritic. The intrusive contacts between Edolo diabase dykes and the country rocks are outlined by grain size reduction, and locally, the dykes host albite-rich late-intrusive veins. The Edolo diabase dykes truncate S2 in the host Variscan basement rocks and are weakly folded and intersected by the Alpine foliation S3 (Fig. 1.4.2).

High-resolution mapping

Structural mapping has been performed at 1:1000 scale along the road cut from Nembra to Vico villages, less than 2 kilometers west of Edolo (Fig. 1.4.3). Here, the Edolo meta-diabase dykes are hosted in metapelites and quartzites. S2 is the dominant fabric of the host rocks and is supported by

chlorite, white mica, quartz ribbons, albite, and titanite; in low-strained domains, the older Variscan foliation (S1) is preserved along D2 isoclinal fold limbs; S2 dips towards NNW (Fig. 1.4.3). Alpine D3 folds are chevron-type and metric in wavelength, with sub-horizontal NE-SW trending axes (A3), axial planes (PA3) steeply dipping towards NW or SE (Fig. 1.4.3), and locally associated with an axial plane foliation (S3). The orientation of D2 and D3 structures is consistent with those of D2 and D3 structures in the Orobic-Porcile-Gallinera Thrust hanging wall (Fig. 1.4.3, Milano et al., 1988; Cadel et al., 1996; Carminati et al., 1997; D'Adda and Zanchetta, 2015; Ghiselli et al., 2015; Rebay et al., 2015).

Meter-thick E-W striking Edolo meta-diabase dikes are steeply dipping and truncate S2 (Fig. 1.4.3). Although the limited exposure precludes continuous dyke wall mapping along strike, the detailed structural analysis reveal that the dykes are weakly folded during D3, in contrast with the prominent D3 folds recorded in the country rocks. Despite of gentle folding, S3 is locally developed within the Edolo diabase dykes (Fig. 1.4.3). S3 strike in dykes deviates at least 20° from that of the dyke walls and matches the orientation of PA3 and S3 in the host rocks (Fig. 1.4.3). Moreover, S3 is locally crenulated by late folding (D4a) (Fig. 1.4.3). Kink-bands, and cataclastic shear zones (D4b) intersect all the structures and lithotypes. D4b structures are manly localized along the dyke walls (Fig. 1.4.3).

Microstructure

Edolo diabase dykes are mostly phaneritic, medium grained, and composed of euhedral to subhedral crystals of igneous clinopyroxene (CpxI), amphibole (AmpI), brown biotite (BtI), plagioclase (PlI), and ilmenite (IlmI) (Fig. 1.4.4). The dyke margins are often porphyritic with millimeter-sized phenocrysts of AmpI, CpxI, and BtI in an aphanitic groundmass, very often replaced by coronitic post-igneous assemblages. S3 Alpine foliation in the Edolo diabase dykes is pervasive in centimeter-thick cleavage bands. In the high-strained domains, two post-igneous assemblages, namely M1 and M2, are easily identifiable by microstructural analysis. M1 minerals display coronitic texture and are pre-tectonic with respect to S3. M1 minerals are tentatively interpreted as related to late- to post-intrusive hydrothermal circulation, since there is no way to correlate them with structures developed in the country rocks. On the other hand, M2 minerals support the Alpine S3 foliation, whereas, in low-strained domains, they form coronae around igneous and M1 hydrothermal minerals.

Cores of igneous amphiboles are dark brown (AmpI1), locally with pale brown rims (AmpI2). CpxI is pale pink, zoned core/rim (CpxI1 / CpxI2) and locally rimmed by BtI, AmpI1, or AmpI2. Rare ilmenite grains (IlmI) are included in CpxI, AmpI, and BtI. Igneous plagioclase (PlI) is zoned, with simple to polysynthetic growth-twinning at cores and no twinning at rims. In the phaneritic dykes, the

Figure 1.4.2. Mesotructural characters of foliated Edolo diabase dykes and their Variscan country rocks. A: meter-thick Edolo diabase dyke intruding Variscan basement rocks near Edolo; B-C: detail of Alpine S3 foliation developed within Edolo diabase dykes. D: D3 chevron-type Alpine folds in Variscan metapelites; E: Edolo diabase dykes intersecting S2. S2 is affected by Alpine folding (D3), whereas S3 is developed in the Edolo diabase dyke. The dyke wall (DW) is at low angle with S3.

interstitial domains between PlI are filled by BtI, AmpI2, rare quartz grains, and igneous epidote (EpI) (Fig. 1.4.4), which also wraps BtI. AmpI1, AmpI2, BtI, and CpxI are rimmed by coronitic pale green/colorless amphibole (AmpM1), chlorite (ChlM1), titanite (TtnM1), epidote (EpM1), pyrite, and rare calcite (Fig.1.4.4). S3 in the Edolo diabase dykes is marked by amphibole (AmpM2), biotite (BtM2), chlorite (ChlM2), epidote (EpM2), plagioclase (PlM2), and stylolitic films of titanite (TtnM2) (Fig. 1.4.4). M2 minerals fill D3 syn-kinematic boudin necks and pressure-shadows around igneous and M1 minerals (Fig. 1.4.4). M2 minerals also support micro-shear planes at a low angle with S3, which are in turn crenulated by D4a (Fig. 1.4.4). AmpM1-rich layers are transposed along S3 (Fig. 1.4.4).

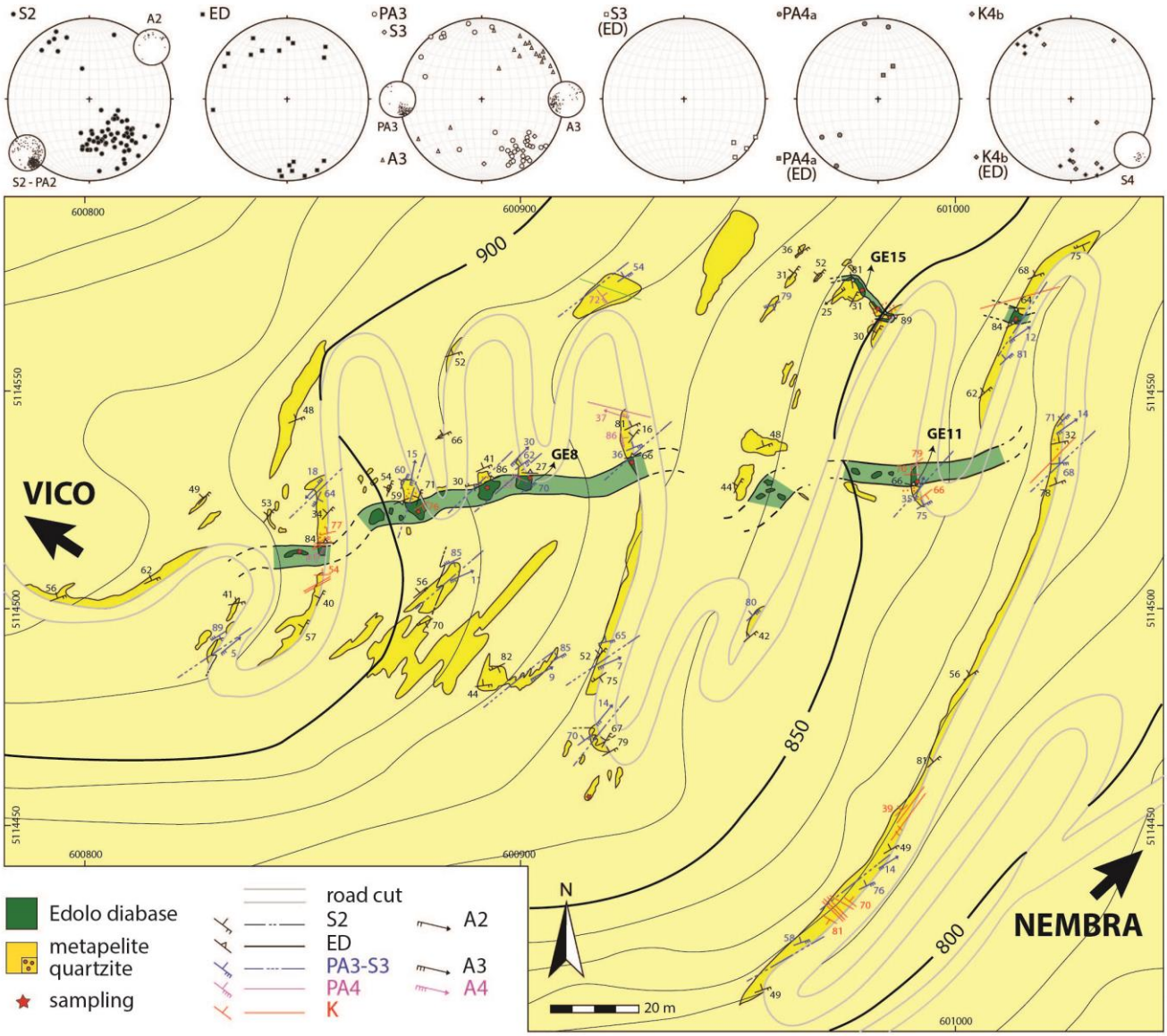

Figure 1.4.3. Structural map at 1:1000 scale along the road cut from Nembra to Vico villages. Sampling localities are indicated by red stars. Projected coordinate system: WGS84-UTM32N. Stereographic projections of structural data (Schmidt equal-area, lower hemisphere) are grouped by relative chronology and rock types (ED: Edolo diabase). Smaller projections represent structural data included for comparison (Rebay et al., 2015).

Mineral chemistry

Edolo diabase dykes (samples Ge8, Ge11, Ge15) were analyzed at Università degli Studi di Milano with a JEOL 8200 Super Probe (WDS) at 15 kV accelerating voltage and with a current beam of 5 nA; natural silicates served as standards. Amphibole formulae are calculated checking the most satisfying results of 13, 15, 16 cations and 23 oxygen normalizations (Locock, 2014) and considering oxo-component only for nomenclature (Hawthorne et al. 2012). Clinopyroxene is recalculated at 4 cations

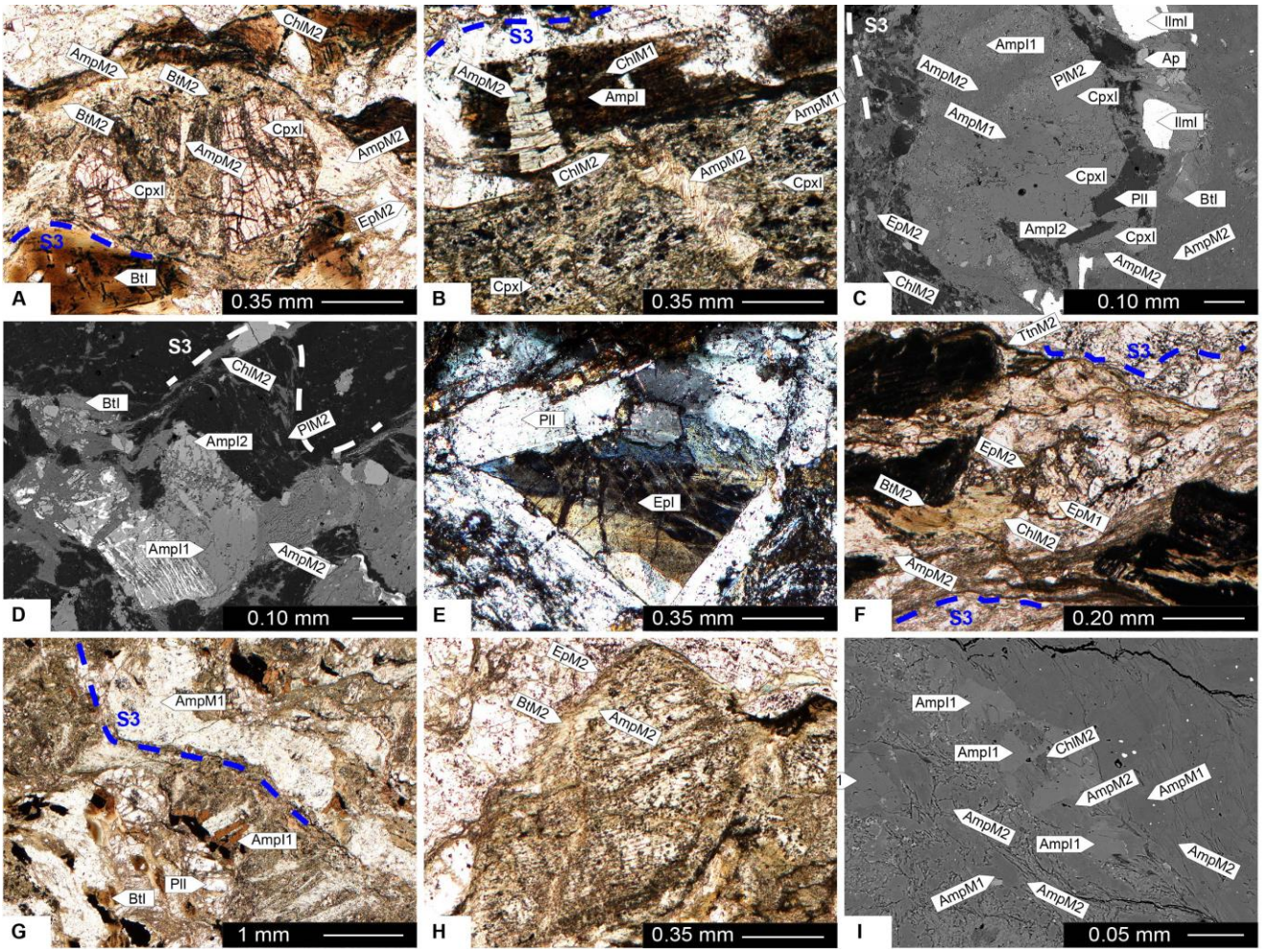

Figure 1.4.4. Micro-structures of Edolo diabase dykes (plane-polarized light and back-scattered electron images). (A): CpxI and BtI wrapped by S3. S3 is marked by AmpM2, BtM2, ChlM2, and trails of EpM2 and TtnM2. BI is parallelized to S3. AmpM2 fills syn-kinematic fractures and pressure shadows around CpxI; (B): CpxI and AmpI are pervasively replaced by ChlM1, AmpM1, and titanite. Fractures in AmpI and CpxI are syn-kinematic with S3 and filled by AmpM2 and ChlM2; (C): AmpI, BtI, IlmI, PlI, and CpxI (rimmed by Amp I2) are wrapped by S3 that is marked by AmpM2, ChlM2, and EpM2. Boudin necks are filled by AmpM2, PlI is rimmed by PlM2; (D): S3 crenulated by D4a. S3 is supported by AmpM2, ChlM2, and PlM2. AmpM2 fills pressure shadows around zoned AmpI; (E) interstitial EpI between PlI laths; (F) relics of EpM1 within S3 marked by AmpM2, BtM2, ChlM2, EpM2, and stylolitic films of TtnM2; (G) Relics of igneous minerals and AmpM1-rich layers within folded S3; (H) relic of CpxI wrapped by S3 supported by AmpM2, BtM2, EpM2 and minor ChlM2; (I): micro-boudins of AmpI aligned in S3 foliation: boudin necks are filled by AmpM2 and ChlM2. In AmpM1-rich layer at right, dark gray core of AmpM1 (Al- and Fe-poorer) are rimmed by light gray AmpM2 (Al- and Fe-richer), which marks S3.

and 6 O, feldspar at 4 O, epidote at 8 cations and 12.5 O. Biotite and chlorite are recalculated at 11 and 7 O, respectively (supplementary data III).

Igneous minerals

Amp I1 is ferri-kaersutite, Ti-rich ferro-pargasite, or Ti-rich magnesio-hornblende, characterized by Si from 5.99 to 6.34 pfu, Ti from 0.45 to 0.64 pfu, Al from 1.90 to 2.32 pfu, and Na from 0.40 to 0.93 pfu (Fig. 1.4.5). Mg and Fe^{2+} range from 1.89 to 2.67 and from 1.11 to 2.29 pfu, respectively (Fig. 1.4.5). K = 0.18 - 0.25 pfu reflects the alkaline affinity of the Edolo diabase (Fig. 1.4.5, supplementary data III). AmpI1 Mg# in sample Ge8 (0.45 – 0.49) is lower than in sample Ge11 (0.49 – 0.66).

AmpI2 is (Ti-rich) ferro-pargasite with Si and Al contents similar to AmpI1 (Si = 5.83 – 6.42 pfu, Al = 1.78 – 2.84 pfu), but Fe^{2+} richer (Fe^{2+} = 2.55 – 3.43 pfu) and Mg and Ti poorer (Mg = 0.52 – 1.42 pfu, Ti = 0.01 – 0.46 pfu) (Fig. 1.4.5). The K content in AmpI2 varies from 0.12 to 0.37 pfu and Na from 0.55 to 0.95 pfu (supplementary data III). AmpI2 is characterized by lower Mg# (0.15 – 0.31) in sample Ge8 than in sample Ge11 (0.30 – 0.32).

CpxI1 is diopside, with Mg = 0.66 – 0.78 pfu, Al = 0.11 – 0.30, Ti = 0.03 – 0.08 pfu, and Na = 0.03 – 0.05 pfu. Cpx I2 is still diopside but characterized by lower Al and Ti content (Al = 0.03 pfu, Ti = 0.01 pfu, supplementary data III) than CpxI1.

In BtI, Si ranges from 5.33 to 5.64 pfu, Al^{VI} from 0.00 to 0.38 pfu, and Ti from 0.37 to 0.78 pfu (Fig. 1.4.5). Mg is 1.77 – 2.45 pfu, Fe is 2.54 – 3.19 pfu, and Mn up to 0.03 pfu (supplementary data III). Mg# in BtI in sample Ge8 (0.43 – 0.44) is lower than in sample Ge11 (0.44 – 0.49) (Fig. 1.4.5).

PlI is An_{44-58} at core, An_{10-38} between core and rim, and An_{7-8} at rim (supplementary data III). Interstitial EpI is characterized by Fe^{3+} = 0.36 – 0.53 pfu and Al^{VI} = 2.47 – 2.64 pfu (Fig. 1.4.5); EpI rimming BtI is slightly Fe^{3+} richer (0.54 – 0.59 pfu) and Al^{VI} poorer (2.41 – 2.46 pfu) than EpI filling interstices between PlI grains (Fig. 1.4.5).

Metamorphic minerals

AmpM1 overgrowing CpxI, AmpI1, and AmpI2, or occurring as porphyroclast within S3, are similarly characterized by Si 7.78 – 7.93 pfu, Al 0.12 – 0.25 pfu, and Ti lower than 0.02 pfu (supplementary data III). Mg ranges from 2.58 to 3.78 pfu, and Fe^{2+} from 1.15 to 2.30 pfu (Fig. 1.4.6). ^{B}Na is 0.01 – 0.05 pfu, ^{A}Na is 0.00 – 0.04 pfu, and K is lower than 0.02 pfu (supplementary data III).

In sample Ge11, AmpM1 is characterized by Mg# comprised between 0.70 and 0.76, with Mg = 3.48 – 3.78 pfu (Fig. 1.4.6). In sample Ge8, AmpM1 overprinting Mg-richer AmpI1, or forming small crystals wrapped by S3, is characterized by Mg# = 0.64, with Mg = 3.15 – 3.18 pfu; whereas AmpM1 overprinting Fe-richer AmpI2 shares similar Si, Al, and Ti content, but lower Mg# (0.53, Mg = 2.58

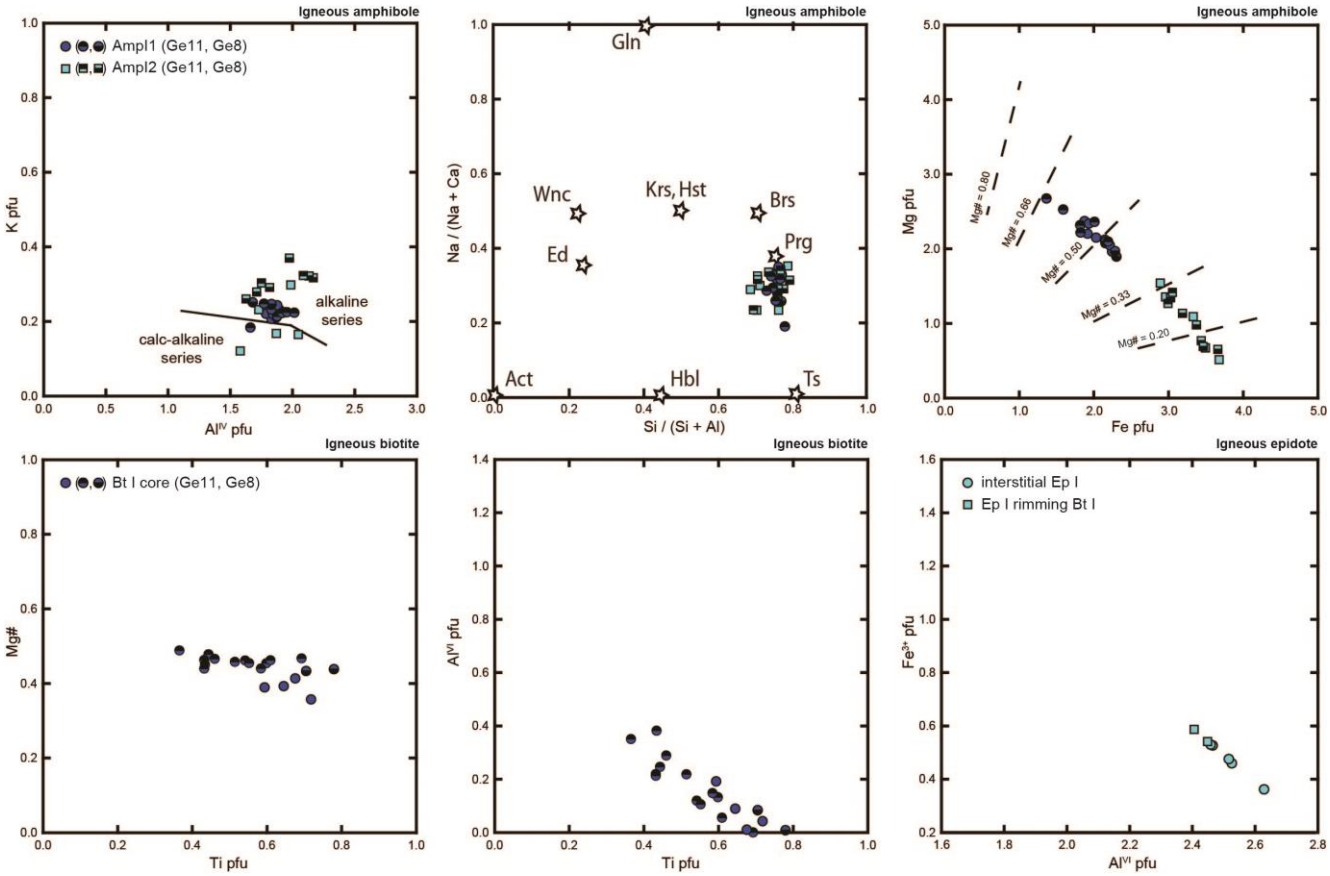

Figure 1.4.5. Compositional variations in igneous minerals from the Edolo diabase dykes.

pfu) (Fig. 1.4.6). ChlM1 replacing AmpI2 is characterized by Al^{IV} = 0.92 pfu and Mg# = 0.46 (Fig. 1.4.6). In EpM1, Al^{VI} is 2.07 – 2.14 pfu and Fe^{3+} is 0.85 – 0.93 pfu (Fig. 1.4.6).

AmpM2 is actinolite or magnesio-ferri-hornblende, with Si from 7.42 to 7.83 pfu, Al from 0.25 to 0.70 pfu, and Ti lower than 0.04 pfu (supplementary data III). Mg ranges from 2.63 to 3.58 pfu, and Fe^{2+} from 1.28 to 2.21 pfu (Fig. 1.4.6). ^{B}Na is 0.02 – 0.10 pfu, ^{A}Na is 0.02 – 0.13 pfu, and K is 0.01 – 0.12 pfu (supplementary data III). In sample Ge11, AmpM2 Mg# is comprised between 0.59 and 0.81 (Mg = 2.89 - 3.58 pfu) (Fig. 1.4.6). In sample Ge8, AmpM2 supporting S3 and filling AmpI1 boudin necks is characterized by Mg# = 0.60 – 0.64, (Mg = 2.95 - 3.19 pfu); AmpM2 replacing AmpI2 is characterized by Mg# = 0.53 – 0.56 (Mg = 2.63 – 2.72 pfu) (Fig. 1.4.6).

BtM2 is characterized by Si = 5.38 – 5.70 pfu, Al^{VI} = 0.46 – 0.61 pfu, and Ti = 0.06 – 0.16 pfu (Fig. 1.4.6). In BtM2, Mg varies between 2.54 and 2.91 pfu, Fe from 2.49 to 2.87, and Mn is lower than 0.02 pfu (Mg# = 0.49 – 0.54, Fig. 1.4.6).

ChlM2 is characterized by Si = 2.63 – 2.91 pfu, Al = 2.24 – 2.79 pfu, Fe = 1.98 – 2.34 pfu, and Mg = 2.24 – 2.83 pfu (supplementary data III). ChlM2 Mg# in sample Ge8 (0.49 – 0.55) is lower than is

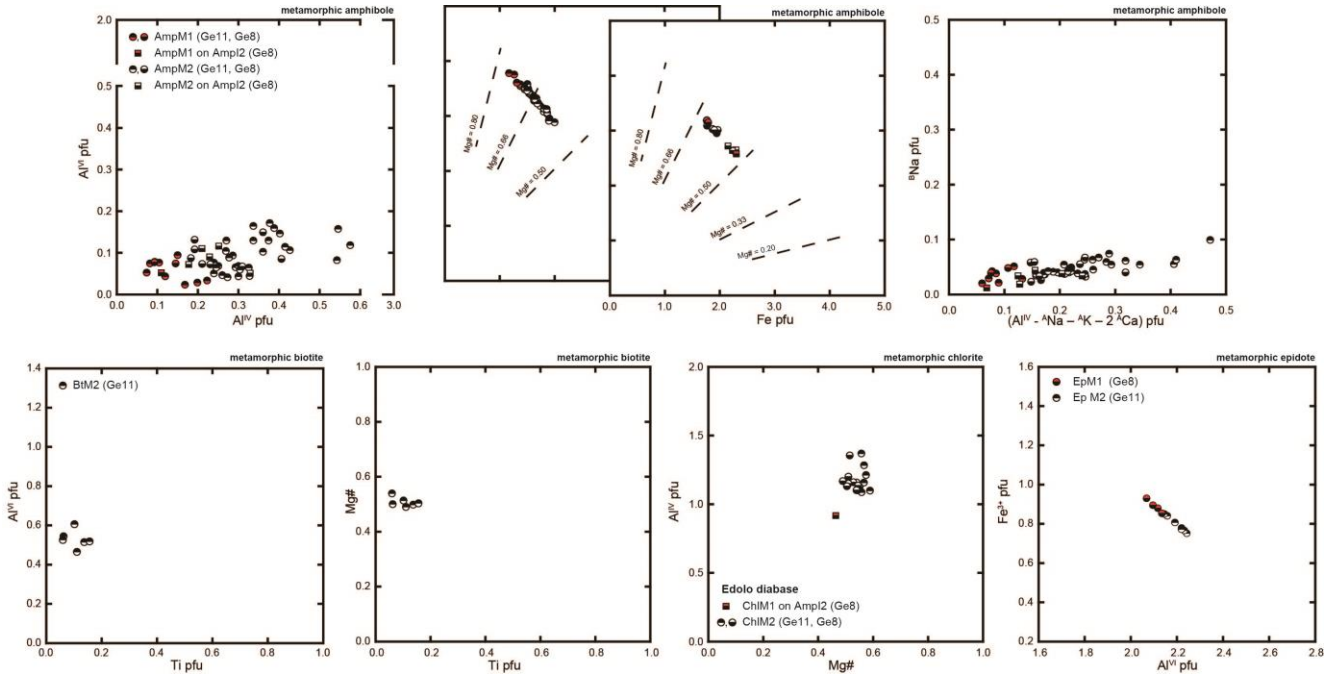

Figure 1.4.6. Compositional variations in metamorphic minerals from the Edolo diabase dykes.

sample Ge11 (0.56 – 0.59). EpM2 is characterized by Fe^{3+} = 0.75 – 0.85 pfu, and Al^{VI} = 2.15 – 2.24 pfu (Fig. 1.4.6). PlM2 is An_{2-7} (supplementary data III).

Even if different Mg# in igneous mineral affect the compositions of the overprinting metamorphic phases, consistent compositional trends are observed and characterized the transition from late- to post-intrusive hydrothermalism to Alpine S3 development: (1) decreasing in Fe^{3+} / (Al^{VI} + Fe^{3+}) ratio from EpM1 (0.31) to EpM2 (0.25), (2) increasing in Al^{IV} content from ChlM1 (0.92 pfu) to ChlM2 (1.37 pfu), (3) increasing of Al content from AmpM1 (0.12 pfu) to AmpM2 (0.70 pfu) (Fig. 1.4.6). Magnitude of AmpM2 composition vectors with respect to tremolite (Schumacher, 2007) point out dominant tschermakite, and minor edenite and glaucophane exchanges (Fig. 1.4.6). These trends are diagnostic of the transition from lower greenschist (M1) to upper greenschist facies (M2) towards epidote amphibolite facies conditions (Maruyama et al. 1983, Thompson and Laird, 2005).

Estimates of metamorphic conditions

Late- to post-intrusive hydrothermal and Alpine metamorphic conditions are firstly constrained by classic thermobarometry. Chlorite thermometry (Bourdelle et al., 2012) on ChlM1 suggest temperatures slightly lower than 300°C, whereas amphibole thermobarometry (Gerya et al., 1997) on AmpM1 returns T = 380 ± 40°C and P = 0.12 ± 0.12 GPa, which are accountable conditions for the late- to post-intrusive hydrothermal circulation. On the other hand, Alpine AmpM2 retains average

crystallization conditions at around T = 420 ± 40°C and P = 0.19 ± 0.12 GPa, with the highest P-T couples at T = 465°± 40°C and P = 0.25 ± 0.12 GPa.

Pseudosections in the NKCFMASHTO system have been calculated with the free energy minimization program THERIAK-DOMINO (de Capitani & Petrakakis, 2010; version 09/03/2019) for better constraining the peak of Alpine metamorphism retained in the Edolo diabase dykes (Fig. 1.4.7). We chose the thermodynamic database ds6.2 from THERMOCALC (Holland & Powell, 2011), including the a-x relations for epidote, amphibole, phengite, biotite, feldspar, chlorite, and ilmenite (Holland & Powell, 2011; Green et al., 2016; White et al., 2014a; White et al., 2014b). The peristerite gap is modeled including end-member albite coexisting with the plagioclase predicted from the solution model. Whole rock composition of Edolo diabase is selected as bulk, with water in excess and after apatite removal. Fe^{3+}/Fe_{tot} molar ratio is set at 0.10 and the effect of its variation is discussed in the text.

The stability fields of M2 mineral assemblages (epidote + biotite + amphibole + chlorite + titanite + albite + quartz) is delimited at low temperature by quartz- and K-feldspar-in reactions, at high pressure by incoming of Na-rich amphibole, and at low pressure by closely-spaced reactions including plagioclase-in, epidote-out, and hornblende-in (Fig. 1.4.7). At high temperature, M2 field is bounded by a very narrow two amphiboles field (i.e. actinolite + hornblende with Si < 6.50 pfu), which marks the transition from the greenschist to epidote amphibolite facies in mafic rocks.

The Si, Al^{VI}, ^{A}Na, and ^{B}Na amphibole compositional isopleths have been computed in order to determine within the wide M2 field the area which could represent the conditions registered by the observed assemblages during Alpine metamorphism. In the model, Si and Al^{VI} content in amphibole mostly increase along with temperature, whereas ^{B}Na concentration is mostly pressure and Fe^{3+} sensitive (Fig. 1.4.7). T = 420 – 450°C and P = 0.15 – 0.35 GPa are thus reliable conditions for AmpM2 crystallization in the Edolo diabase dykes (Fig. 1.4.7). The maximum pressure would be slightly reduced to 0.27 GPa by doubling the Fe^{3+}/Fe_{tot} molar ratio from 0.10 to 0.20.

Discussion and Conclusion

North of the Orobic-Porcile-Gallinera Thrust, the alkaline Edolo diabase dykes are gently folded during D3 Alpine deformation stage and crosscut by S3, which is supported by actinolite/hornblende (Si > 7.40 pfu), biotite, chlorite, epidote, albite and titanite. S3 is also associated with the development of the Orobic-Porcile-Gallinera Thrust (D3) and chevron-type D3 folds in the Variscan basement rocks (Milano et al., 1988; Carminati et al., 1997; D'Adda and Zanchetta, 2015; Ghiselli et al., 2015; Rebay et al., 2015).

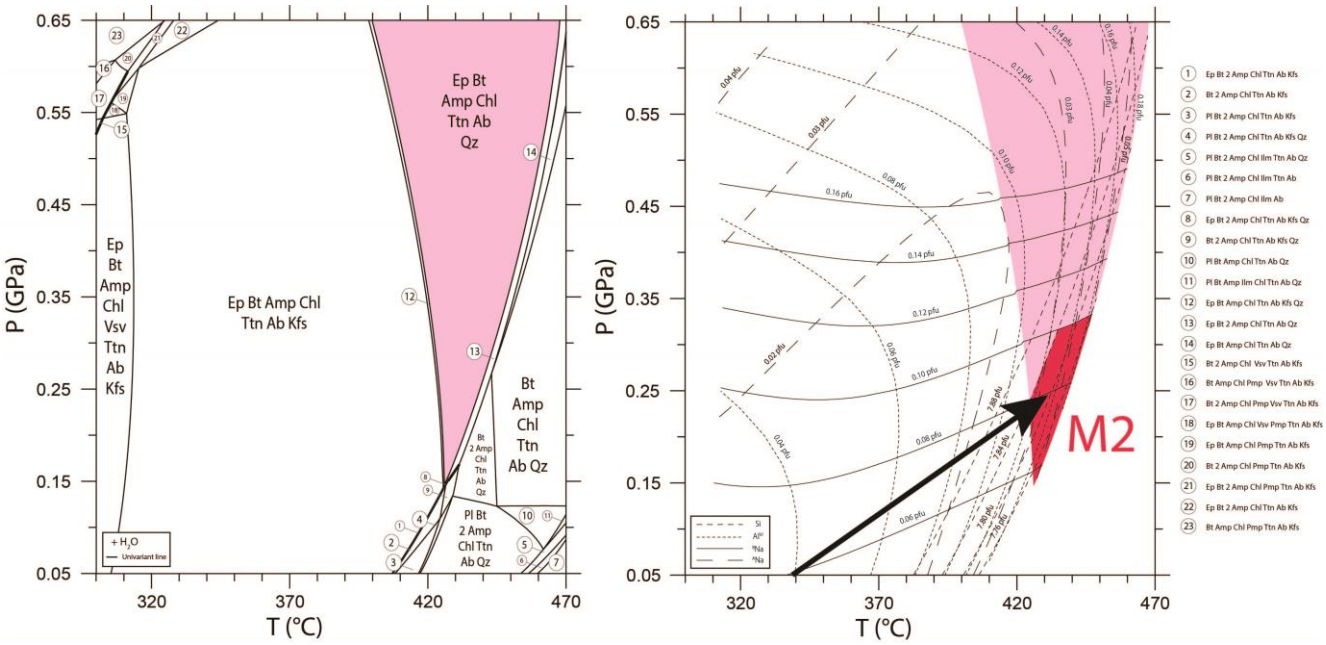

Figure 1.4.7. Pseudosections calculated for Edolo diabase WR composition (%wt), with water in excess, Fe3+/Fetot molar ratio = 0.10, and after apatite removal (SiO_2 = 44.45, TiO_2 = 2.74, Al_2O_3 = 14.29, FeO_T = 13.72, MgO = 9.74, CaO = 5.70, Na_2O = 3.27, K_2O = 1.30, P_2O_5 = 0.56). M2 stability field is colored light pink. Compositional isopleths for amphibole (Si, Al^{VI}, ^{B}Na, ^{A}Na, pfu) allow refining the P-T space at T = 420 – 450°C and P = 0.15 – 0.35 GPa (magenta field) according to AmpM2 composition. These conditions are thus accountable for S3 Alpine foliation development in the Edolo diabase dykes.

The P-T conditions recorded by the Edolo diabase during D3 development (T = 420 – 450°C, P = 0.15 – 0.35 GPa) are the first quantitative estimates of Alpine metamorphic conditions in Southern Alps and the inferred P/T ratio is consistent with Barrovian-type metamorphic gradient. Comparable Alpine mineral association in mafic dykes at the junction between the Orobic and Porcile Thrusts (D'Adda and Zanchetta, 2015) and pressure estimates of 0.1 – 0.2 GPa at the southwestern boundary of the same tectonic unit (Viganò et al., 2011) attribute a regional scale significance to the metamorphic event M2. In orogenic domains, such P-T ratio is compatible with continental collision as indicated by both worldwide geological observations and numerical modeling (see for example England and Richardson, 1977; England and Thompson, 1984; Spear, 1995; Regorda et al. 2017).

On the other hand, the onset of south-verging shortening in the Southern Alps occurred during oceanic subduction, as indicated by the 80 – 43 Ma Ar/Ar ages of the Orobic-Porcile Thrusts (Zanchetta et al., 2011, 2012, 2015). This is taken as maximum age for the upper greenschist facies Alpine metamorphism (M2) recorded by the Edolo diabase during D3. At that time, a perturbed thermal state in the upper-plate of the Alpine subduction system is also envisaged to explain the genesis of syn-subductive magmatism testified in the Veneto volcanic province (~ 40 Ma Bartoli et al., 2013 and ref. therein) and in the southern part of Adamello (43 – 41 Ma, Tiepolo et al., 2011; Ji et al., 2019). A

minimum age of 38-34 Ma for D3 is instead suggested by intersection relationships between the Gallinera Thrust / Cedegolo Anticline and the nearest Adamello intrusive rocks (Schaltegger et al. 2019), at the very onset of the Alpine collision (Brack 1981, 1984).
However, there is evidence of late- to post-collisional reactivation of the Alpine D3 structures along the Orobic-Porcile-Gallinera Thrust (Zanchetta et al., 2015 and ref. therein): in the light of these last observations, the Alpine metamorphic event M2 may be younger than 38-34 Ma, but these metamoprphic stage should also be retained by the younger calc-alkaline rocks, including the Adamello batholith. Further constraints are thus needed to get to a consistent tectonic interpretation of the D3/M2 phase in the central Southern Alps.

Appendix (future development)

This paragraph includes preliminary results obtained by a 2-D numerical model performed to speculate on the Alpine evolution of the central Southern Alps, from syn-subductive to late-collisional stages. The goal is to individuate the most reasonable tectonic setting accountable for the record of M2 event (T = 420 – 450°C and P = 0.15 – 0.35 GPa) in the upper plate of the Alpine subduction system.

Model Setup

The model setup is described by an oceanic lithosphere, representing the Alpine Tethys, and a continental lithosphere, representing the upper Adria plate. A continental lithosphere is included in the left side of the domain after 40 Myr of oceanic subduction, in order to represent the oncoming passive margin (continental allochtonous or European plate). The physics of the crust-mantle system is described by coupled equations for continuity, conservation of momentum, and conservation of energy. Computations were done using the ASPECT code version 2.3.0 (Kronbichler et al., 2012; Heister et al., 2017; Rose et al., 2017; Bangerth et al., 2020), which includes the shear heating. A visco-plastic rheology is assumed for the materials with dislocation creep mechanism. The plasticity limits viscous stresses through a Drucker Prager yield criterion. The model is incompressible. The material and rheological parameters used in the simulation are listed in Table 1.4.1.
An initial continental lithospheric thickness of 100 km, including 30 km of continental crust, is assumed (Fig. 1.4.8) to represent an originally thinned passive margin corresponding to the passive Adria margin (Lardeaux and Spalla, 1991; Dal Piaz, 2001; Manatschal, 2004; Schuster and Stüwe, 2008; Marotta et al., 2018; Roda et al., 2019; Assanelli et al., 2020; Festa et al., 2020; Luoni et al., 2020). An oceanic lithospheric thickness of 95 km with 10 km-thick crust is chosen to represent an age

Parameter	Unit	Upper Continental crust	Lower Continental crust	Upper Oceanic Crust	Lower Oceanic Crust	Mantle
Heat production	Hr (μW m^{-3})	2.43	0.15	0.2	0 2	0.016
Thermal conductivity	K (W m^{-1} K^{-1})	3.2	2.1	1.8	2.6	4.3
Rheology		dry granite	mafic granulite	serpe tine	gabbro	dry olivine
Thermal diffusivitiy	k (m^2 s^{-1})	9.60E-07	8.00E-07	8.60E-07	8.60E 07	1. 4E-06
Heat capacity	Cp (J kg^{-1} K^{-1})	750	670	750	750	1000
Density	rho (kg m^{-3})	2800	2900	3150	3150	3400
Thermal expansivity	a (K^{-1})	3-e5	3-e5	3-e5	3-e5	3-e5
Prefactor dislocation creep	A (Pa^{-n} s^{-1})	1.13E-28	8.83E-22	1.00E-21	1.99E-11	2.41E-16
Stress exponent	n	3.2	4.2	1	3.4	3.5
Activation energy	Q (J mol^{-1} Pa^{-1})	1.23E+05	4.45E+05	0	4.97E+05	5.40E+05
Activation volume	V (m^3 mol^{-1})	0	0	0	0	1.50E-05
Angle of internal friction	f	0	0	0	0	30
Cohesion	MPa	100	100	20	20	20
References		1,2,3	1,4,5	1,2,6,7	1,2,5	1,2,8

Table 1.4.1. Material and rheological parameters used in the simulation. References: (1) Vilà et al., 2010; (2) Schon et al., 2009; (3) Ranalli, 1995; (4) Ramakrishnan et al., 2012; (5) Wilks and Carter, 1990; (6) Hilairet et al., 2007; (7) Petersen and Schiffer, 2016; (8) Karato and Wu, 1993.

of ca. 40 Myr for the Tethys Ocean (Handy et al., 2010; Roda et al., 2012; Assanelli et al., 2020; Luoni et al., 2020; Roda et al., 2020), based on the cooling model of a semi-infinite half-space which accounts for the effects of melt extraction, solid phase transitions, and radioactive thermal conductivity (Korenaga and Korenaga, 2016), and characterized by a slow spreading rate (2.5 cm/yr full spreading).

The upper oceanic crust is generally strongly affected by hydrothermal alteration at mid-ocean ridges, thermal fracturing, and it is covered by oceanic sediments. Furthermore, intense serpentinization affects the oceanic mantle that can be episodically exhumed at ocean floor (Carlson and Miller, 1997; Juteau and Maury, 1999; Christensen, 2004; Malvoisin et al., 2012; Cannat et al., 2013; Balestro et al., 2019; Assanelli et al., 2020). For this reason, the upper oceanic crust is assumed to be composed by a 5 km-thick layer of porous and fractured basalts and serpentinites. Compared to the upper oceanic crust,

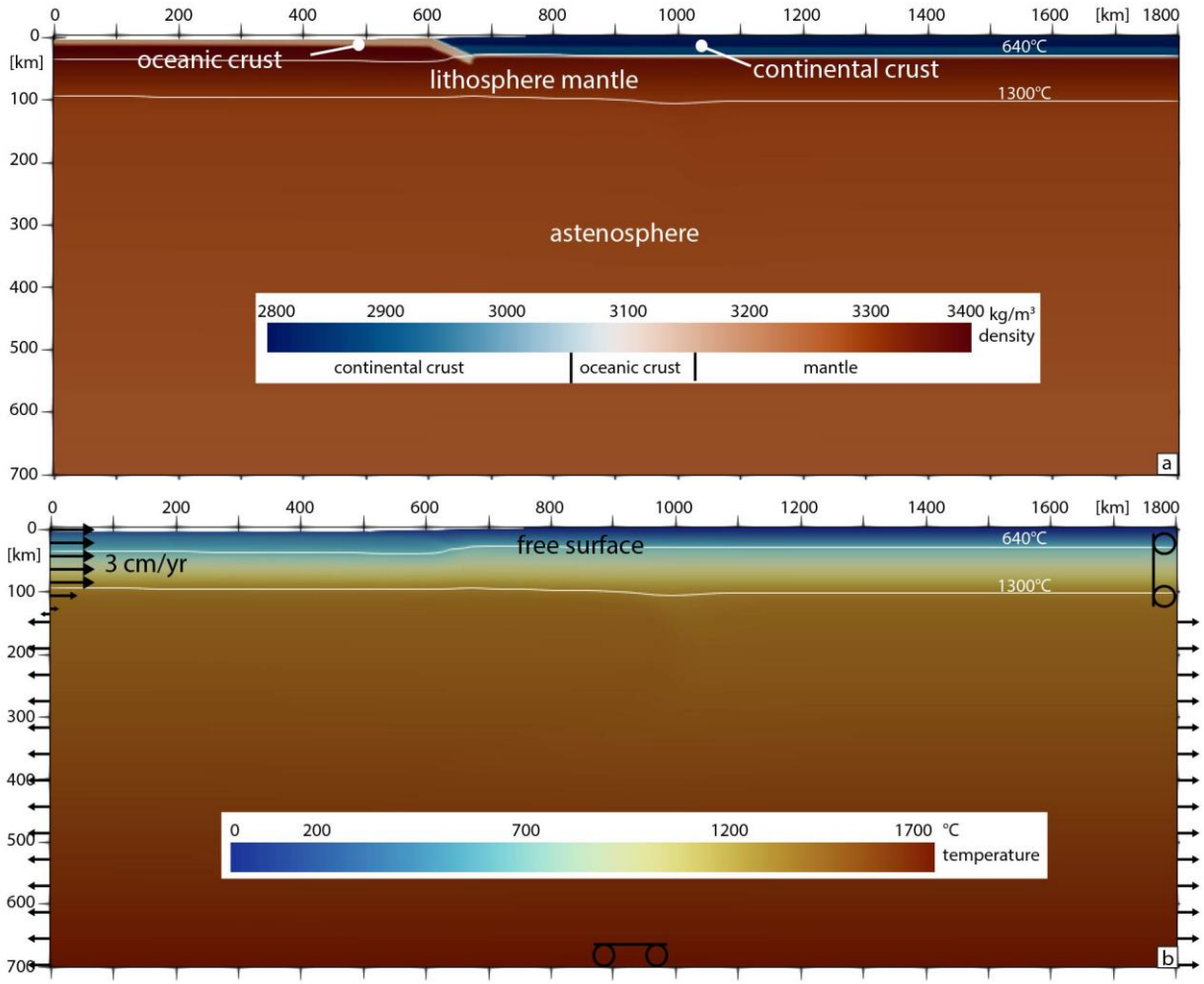

Figure 1.4.8. The model domain is 1800 km wide and 700 km deep. The lithosphere thickness is defined by the 1300◦C isotherm. The velocity boundary conditions correspond to a free-slip condition along the bottom and the right boundaries of the domain. An inflow velocity of 3 cm/yr is fixed along the left boundary throughout the lithosphere and an outflow velocity is fixed up to the bottom to balance the flux. The upper boundary is treated as a free surface. The materials included in the model account for the upper and lower oceanic crust, upper and lower continental crust, and mantle (see Table 1.4.1 for material parameters and rheology).

the lower oceanic crust is considered to be poorly affected by hydrothermal circulation and it is assumed formed by gabbros (Carlson and Miller, 1997; Christensen, 2004; Malvoisin et al., 2012; Cannat et al., 2013; Rüpke and Hasenclever, 2017).

To simulate plate convergence, a horizontal velocity of 3 cm/yr (Roda et al., 2010, 2012) is imposed along the left boundary throughout the oceanic lithosphere (Fig. 1.4.8). To balance the lateral inflow an outflow is prescribed along the left and right boundaries from 130 km depth to the bottom. The bottom and the upper part of the right boundary are free-slip while the top boundary is treated as a free-surface (Fig. 1.4.8). The model runs for 100 Myr. The oceanic subduction lasts 75 Myr, i.e., from 115 to 40 Ma in order to cover the entire range of ophiolite ages synthesized in Assanelli et al. (2020). Continental collision between Adria and Europa plates occurs at 80 Myr (i.e., 35 Ma) and the forced

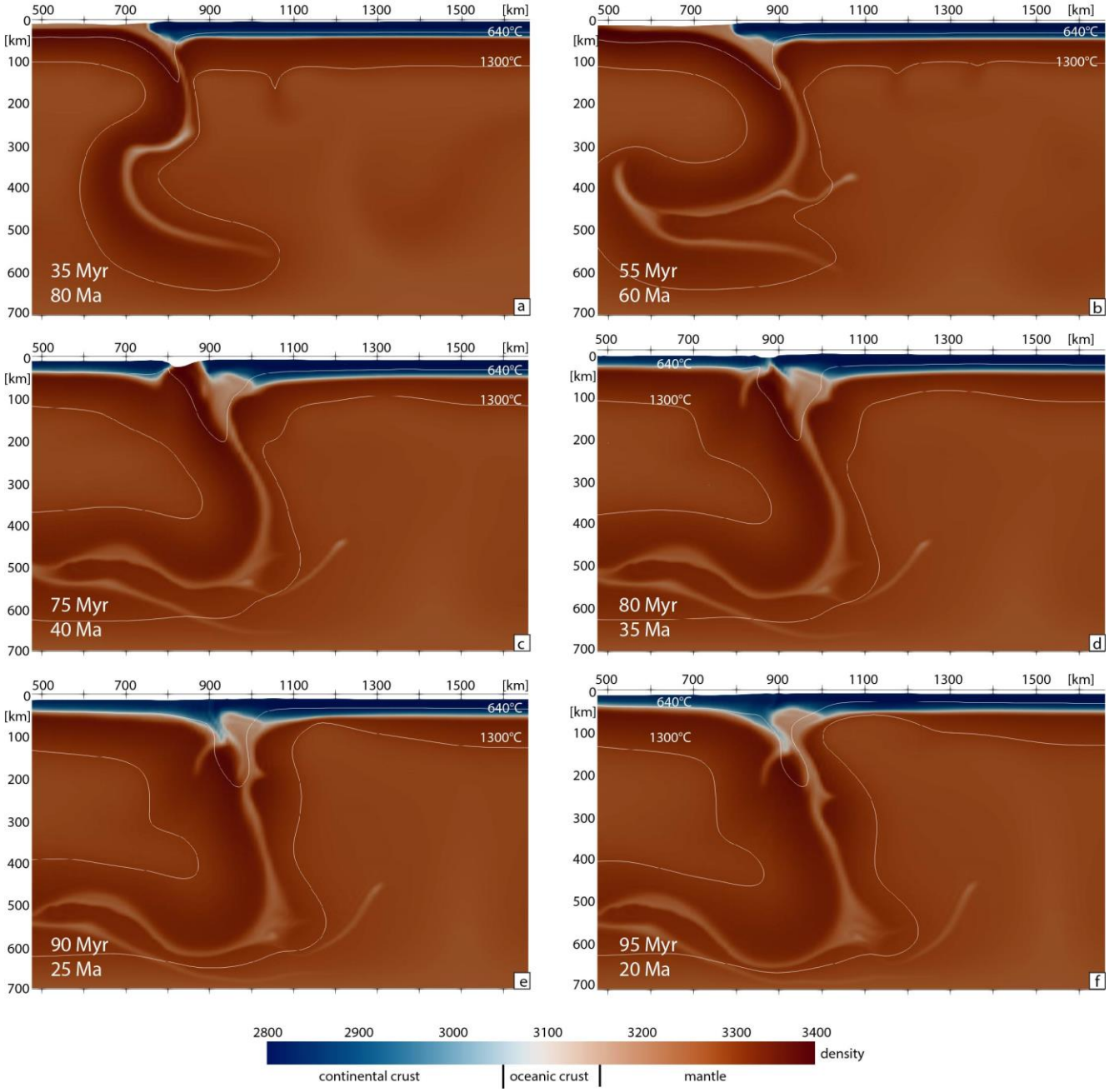

Figure 1.4.9. Results of the simulations in syn-subductive (a-c), collisional (d-e), and post-collisional (f) tectonic settings.

convergence is kept up to 95 Myr (i.e., 20 Ma) (Fig. 1.4.9), in agreement with palaeomagnetic reconstruction of the Mediterranean region (Handy et al., 2015; van Hinsbergen et al., 2020; Le Breton et al., 2020).

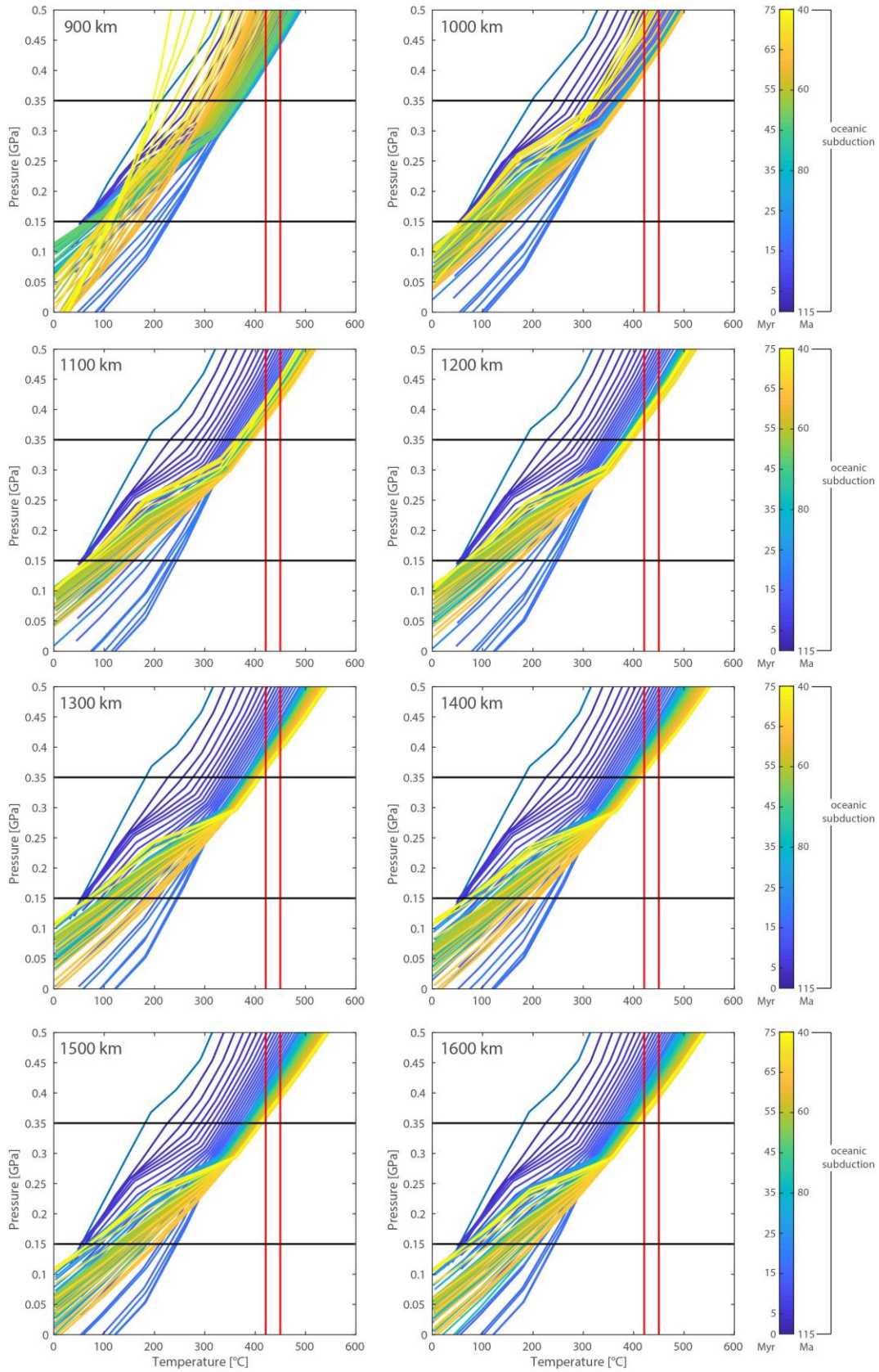

Figure 1.4.10. P-T profiles through the upper Adria plate during active oceanic subduction as a function of time and distance from the left side of the model. Metamoprhic conditions accountable for M2 metamorphic event are delimited by red (T = 420-450°C) and black (P = 0.15-0.35 GPa) lines.

Natural data vs. Model prediction

The subduction system progressively cools down with continuous subduction of oceanic lithosphere, with the maximum deflection of the isotherms just before the onset of the continental collision (75 Myr, 40 Ma, Fig. 1.4.9). During the subduction, the thickness of the continental crust on the upper Adria plate homogeneously increased from 30 to 40 km in response to the Alpine convergence. At that time, Adria is affected by progressive heating, as a result of enhanced mantle activity during active subduction. The syn-subductive thermal peak is attained just before the onset of the continental collision and is diffused all over the Adria plate. However, the determined P-T profiles through the upper plate (Fig. 1.4.10) do not match with the metamorphic record of the Edolo diabase dykes, not even at the end of the subduction. On the contrary, P-T ratios fully compatible with the metamorphic peak conditions for M2 are attained on the Adria plate (x = 1100-1200 km) from 85 to 100 Myr, which means in late- to post-collisional times (30-15 Ma) (Fig. 1.4.11). However, it is unlikely that this metamorphic and deformation event was younger than the non-metamoprhic calc-alkaline mafic dykes and Adamello batolith that sealed the Alpine structures marked by the mineral assemblages used to estimate the metamorphic conditions.

The positioning in the model of mechanical discontinuities that can be correlated with the most prominent Alpine lineaments, the Penninic Front and the Periadriatic Lineament, is highlighted in strain rate vs. horizontal position diagrams (Fig. 1.4.12). They show strain rate intensity as function of the time along a horizontal profile, which was at 15 km of depth at 0 Myr and at 6-8 km of depth at 115 Myr.

During active subduction (0 - 75 Myr), most of the strain is localized within the subduction trench, which migrated towards Adria from 600 to 800 km. Deformation starts to localize on the upper Adria plate at 10 Myr before the continental collision. This event is likely to represent the syn-subductive D3 phase of the central Southern Alps.

At the beginning of the collision, most of the deformation localized in the suture zone, i.e. the Penninic Front, which migrated from 900 to 700 km by time. In addition, from the end of the collision to the post-collisional phase, part of the strain is localized between 1100 and 1000 km where the Periadriatic lineament developed. However, further refinements in the model are required because the model over-estimates the width of the Alps.

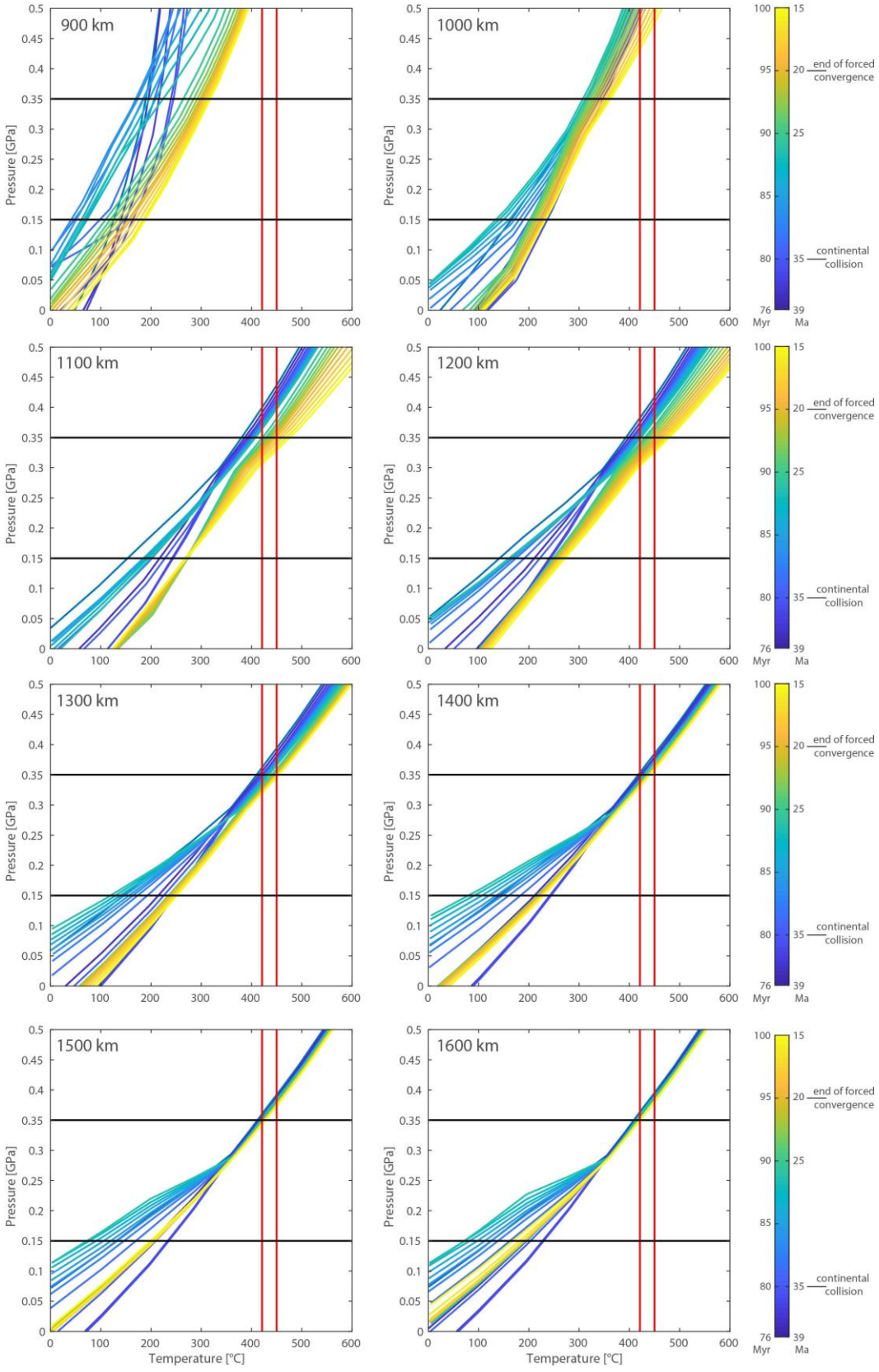

Figure 1.4.10. P-T profiles through the upper Adria plate during and after the continental collision as a function of time and distance from the left side of the model. Metamoprhic conditions accountable for M2 metamorphic event are delimited by red (T = 420-450°C) and black (P = 0.15-0.35 GPa) lines.

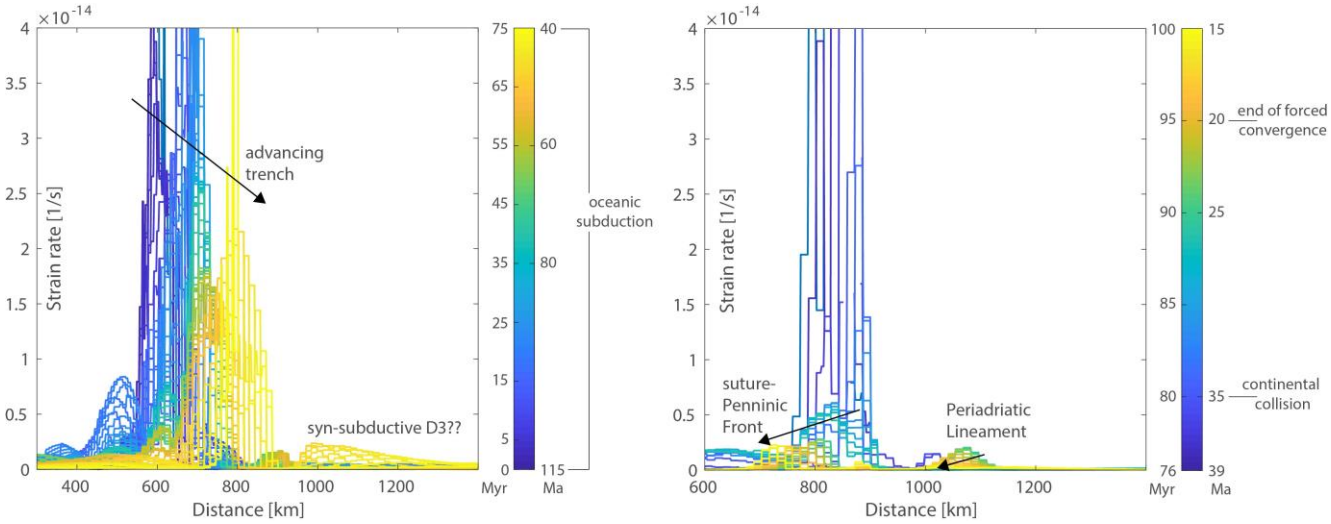

Figure 1.4.11. Strain rate vs. horizontal position diagrams for syn-subductive (left) and collisional to post-collisional (right) tectonic settings. Strain rate discontinuities are interpreted as representing the prominent Alpine tectonic lineaments.

1.5 Discussion Chapter 1

The focus of the first chapter is on post-Variscan lamprophyre dykes that intruded into Variscan basement rocks in both the external domains of the Alps, the Helvetic domain and the central Southern Alps.

The basement of the Argentera-Mercanotur Massif (A-M) comprises high-grade metamorphic rocks, including eclogites and granulites, which pervasively experienced partial melting during the late-Variscan stage at around 323 Ma (Rubatto et al., 2001). In addition, several generations of intermediate to acidic intrusives emplaced in the A-M between 332 Ma (High-Mg number monzonite dykes, Debon and Lemmet, 1999; Rubatto et al., 2001) and 299-292 Ma (Low-Mg number Central Granite, Ferrara and Malaroda, 1969; Corsini et al., 2004). The basement of the central Southern Alps (the Orobic Basement) is mostly composed of metapelites which record Variscan metamorphism under amphibolite facies without partial melting. The Argentera-Mercantour is thus considered an internal zone of the Southern Variscan belt, whereas the Orobic basement represents external domain.

The A-M lamprophyres are spessartites and appinites, mostly composed of Ti-rich amphibole, plagioclase, K-feldspar, magnetite, ilmenite, and rare quartz; those of the Orobic basement are camptonites, with clinopyroxene, Ti-rich amphibole, plagioclase, ilmenite, and rare quartz. The lamprophyres have different geochemical affinity: they are mostly calc-alkaline in the A-M and alkaline in the Orobic basement. However, an alkaline affinity for the last magmatic pulses in the A-M is envisaged by igneous amphibole compositions in late-intrusive veins. The age of the A-M dykes is post-early Permian, because they intruded into the early Permian Central Granite, whereas the age of the Edolo diabase, proposed as Triassic in the literature, is going to be determined by Ar/Ar dating.

The lamprophyres are mafic to intermediate in composition, with crystallization temperature higher than 1000°C. The dykes testify partial melting in the sub-continental mantle after the end of the Variscan cycle. In particular, the dykes emplaced in the Orobic basement were generated by melting a garnet-bearing fertile lherzolite, as suggested by REE concentrations in igneous clinopyroxene. A link with the continental Permian-Triassic rifting is envisaged by the relative age of these dykes in both the Alpine domains and by comparison with numerical model predictions that indicate that forced extension is necessary to produce successive pulses of mantle-derived magmas in Permian-Triassic times (e.g. Roda et al., 2019). Such a magmatic activity cannot be explained by the sole gravitational collapse at the end of the Variscan cycle (Marotta et al., 2009; Marotta et al., 2018; Roda et al., 2019).

In both cases, the dykes intruded into already exhumed basement rocks, according to the estimated low pressures and several field observations including sharp and chilled dyke margins. During emplacement, the dykes experienced localized hydrothermal metamorphism under lower greenschist facies conditions (Argentera-Mercantour: T = 300 – 350°C, P < 0.1 GPa; Orobic Basement: T = 373 – 409°C, P = 0.09 – 0.17 GPa).

The first result of this research is thus to have a complete record of the Permian-Triassic magmatism in the central Southern Alps (e.g. Cadel et al., 1987; Schaltegger and Brack, 2007; Cassinis et al., 2008; Berra et al., 2015; Beltrán-Triviño et al., 2016), and in the External Crystalline Massifs of the Helvetic domain, where Triassic magmatism is only reported in the Pelvoux Massif (Vatin-Pérignon et al., 1972; Vatin-Pérignon et al., 1974; Buffet and Aumaitre, 1979).

The data shown in this part also support a better description and quantification of the Alpine metamorphic conditions in both Argentera-Mercantour Massif and Orobic Basement. The post-Variscan dykes are in fact good structural and metamorphic markers for identifying the effects of the Alpine structural and metamorphic evolution superposed to the poly-deformed and poly-metamorphosed Variscan basement.

In the A-M, the dykes were truncated by syn-metamorphic Alpine shear zones, whose ages range from 34 to 22 Ma (Corsini et al., 2004; Sanchez et al., 2011a). In the lamprophyres, the Alpine shear zones are supported by upper greenschist facies minerals, including Al-rich actinolite, biotite, albite / oligoclase, epidote, chlorite, and K-feldspar that formed at T = 420 – 450 °C, P = 0.20 – 0.40 GPa. The inferred P-T conditions are those typical of a barrovian metamorphic gradient ascribable to the continental collision, according to numerical models (e.g. Regorda et al., 2017). In the Orobic basement, Alpine axial plane foliation S3 is locally developed within lamprophyre dykes. S3 is supported by upper greenschit facies minerals including Al-rich actinolite /magnesio-ferri hornblende, biotite, chlorite, epidote, albite that formed at T = 420 – 450°C and P = 0.15 – 0.35 GPa. Even in this case, the metamorphic conditions are proper of a barrovian metamorphic gradient. Relationships between Tertiary dyke swarms and D3 structures suggest that the latter mostly developed in syn-subductive stages (Zanchetta et al., 2011, 2012, 2015), or at the transition between subduction and continental collision.

Chapter 2

Before and after the Variscan collision in the "external" Variscan domains

2.0 Introduction Chapter 2

The western M-T and the Orobic basement in the Southern Alps represent the external domains of the Southern Variscan belt. Rocks belonging to the internal domains of the Southern Variscan belt are described in the eastern M-T and in the Alpine domains, from Austroalpine to Helvetic and including the A-M. Opposite metamorphic field gradients can be inferred from the present-day location of external and internal zones in the M-T with respect to the Alps: low-grade Variscan rocks (greenschist to amphibolite facies) occur in the western sector of the M-T, whereas high grade Variscan rocks (migmatites and eclogites) in the eastern sector. The configuration is totally reversed in the Alps, where low-grade Variscan rocks (epidote-amphibolite to amphibolite facies) occupy the portion located south and east of the Periadriatic Lineament, i.e. the Southalpine domain, and high grade Variscan rocks (migmatites and eclogites) lay north and west of the Periadriatic Lineament, in the Austroalpine, Penninic, and Helvetic domains.

Three hypotheses may explain this reverse configuration through the Southern Variscan belt. The first is that the western M-T and the Orobic basement are two external domains, symmetrically opposed at margins of the Southern Variscan belt. The second is that they represent the external domains of orogenic belts developed as the result of two subduction systems with opposite vergences, today merged in the Southern Variscan belt. A polycyclic scenario for the Southern Variscan belt is suggested as reliable for the Alpine area by the comparison of natural data with predictions of quantitative geodynamic modeling (Regorda et al., 2020). The third hypothesis is that they are parts of a single external domain that was dismembered and rotated during subsequent late- to post-Variscan tectonic stages, as already suggested by paleogeographic reconstructions based on paleomagnetic data (Edel et al., 2014; 2018).

The clue to choose between the different hypotheses is in highlighting differences and similarities in terms of litho-stratigraphy, magmatic evolution, metamorphic evolution in pre-, syn-, and post-Variscan times. In the next paragraphs, new data are gathered to discuss correlations between the western M-T and the Southern Alps.

The Orobic basement

2.1 Cld-St-And-bearing assemblages in the Central Southalpine basement as markers of evolving thermal regime during Variscan convergence

Marco Filippi, Maria Iole Spalla, Nicola Pigazzini, Valeria Diella, Jean-Marc Lardeaux, Davide Zanoni (paper in preparation)

Abstract

Multi-scale structural analysis and petrologic investigations are carried out to explore the sequence of pre-Alpine chloritoid-, staurolite-, and andalusite-bearing metamorphic assemblages in the poly-deformed crystalline basement of the upper Val Camonica (central Southalpine domain).
The oldest fabric in the Variscan basement of the Upper Val Camonica is the composite S1 foliation. S1 is supported by contrasting mineral assemblages including garnet, chloritoid, and staurolite that developed under intermediate pressure amphibolite facies conditions during the Variscan convergence. S1 is intersected by the dominant late-Variscan greenschist facies foliation S2, which is supported by white mica and chlorite and truncated, in turn, by the base of Permian siliciclastic sequences. The relationship with the sedimentary covers defines a minimum age for the tectono-metamorphic evolution of the pre-Alpine basement.
The special feature of the upper Val Camonica basement in the Southalpine framework is andalusite, which formed in late D1 to early D2 deformation stages. Field relationships and P-T estimates suggest that the Val Camonica andalusite is pre-mid-upper Permian in age and developed during exhumation immediately after the Variscan collision. It follows that the upper Val Camonica andalusite has a different age and tectonic significance with respect to that of other occurrences of pre-Alpine andalusite in the Alps, where andalusite developed during exhumation of Permian – Triassic high-temperature basement rocks.

Introduction

Andalusite-bearing assemblages in metapelites of the continental crust are an indicator of high thermal regimes, such as those characterizing contact metamorphism or regional Buchan/Abukuma-type metamorphism. High T/P ratios accountable for andalusite development are envisaged in various convergent and divergent settings, including late-orogenic thinning and lithospheric unrooting in the mature stages of the continental collision, as well as lithospheric thinning announcing continental rifting in post-orogenic settings.

Andalusite is quite common in the pre-Alpine continental crust of the Alps, even if the age of the andalusite-bearing assemblages and the geological contexts in which they formed are heterogeneous (Fig. 2.1.1, Tab. 2.1.1). Andalusite-bearing rocks are associated with late-Variscan aplites, pegmatites, granitoids, and cordierite-bearing migmatites in the Argentera-Mercantour and Aiguilles Rouges massifs in the Helvetic domain, often confined to the contact-zone of the Permo-Carboniferous intrusives (Ferrara & Malaroda 1969; Compagnoni et al., 1974; Brändlein et al., 1994; Corsini et al., 2004). Similarly, andalusite relics are found in the surroundings of late-Variscan granitoids in the Gran Paradiso massif in the Penninic domain (Compagnoni & Prato, 1969). In other Penninic units, andalusite is instead related to a Permian thermal rise during late-Variscan evolution (e.g. Desmons, 1992 and ref. therein).

Different geological and chronological settings are envisaged in the Austroalpine and Southalpine domains, where numerous andalusite-bearing assemblages testifying Permian-Triassic lithospheric thinning are described together with Permian-Carboniferous andalusite in veins or in the surroundings of late-Variscan intrusives (see references in Tab. 2.1.1). In the Southalpine domain, andalusite has been always found in high-temperature basement rocks that include sillimanite, cordierite, and/or spinel that reflect Buchan/Abukuma-type metamorphism. The upper Val Camonica andalusite is instead the first case in which andalusite is found in chloritoid-, staurolite- and garnet-bearing metapelites, which suggest lower T/P ratios as characteristic of Barrovian/Dalradian metamorphism.

For these reasons, this case study represents an excellent opportunity to improve our understanding of the Variscan basement exhumation path, from the end of the Variscan convergence to the Permian-Triassic lithospheric thinning. To this purpose, we present new multi-scale structural data integrated with a detailed mineral-chemical and petrological analysis aimed at identifying the geodynamic significance of the chloritoid, staurolite, andalusite transition in the upper Val Camonica basement.

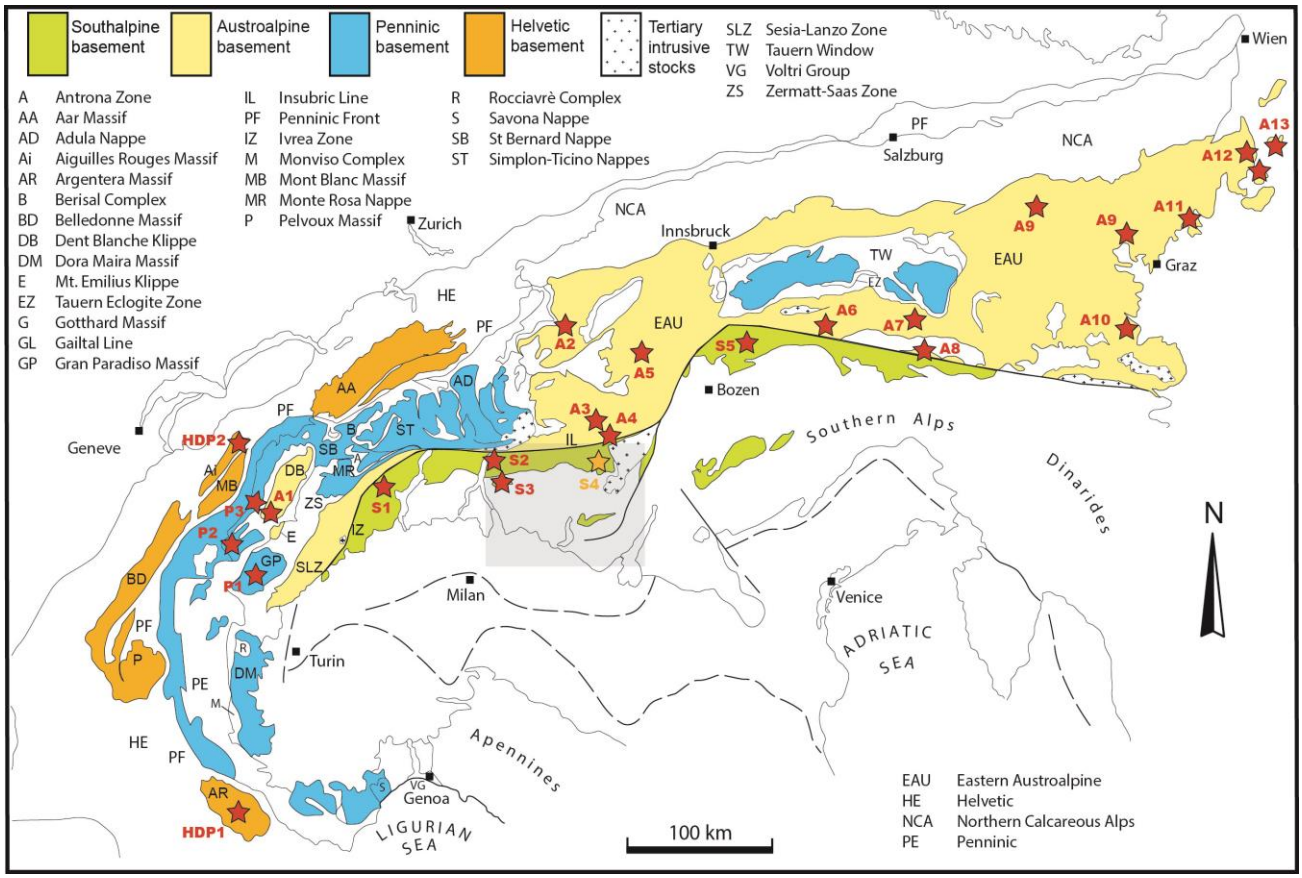

Figure 2.1.1. Tectonic map of the Alps redrawn after Spalla and Marotta (2007), with the location of andalusite-bearing assemblages characterising metapelites from the pre-Alpine continental basements (red stars) and of the andalusite-bearing rocks described in this work (S4 orange star). Keys are coded in Table 2.1.1, where assemblages, inferred P-T conditions and ages are listed with references. The grey shaded area locates the tectonic scheme of central Southalpine domain of Figure 2.1.2.

Geological setting

The Variscan basement of the central Southalpine domain (the Orobic basement) comprises metapelites, gneiss, and quartzites, with minor metagranitoids and amphibolites (Mottana et al., 1985; Siletto et al., 1993; Spalla et al., 2005; Gosso et al., 2012; Zanoni and Spalla, 2018 and refs. therein). Their protoliths mostly derived from Silurian-Ordovician sedimentary sequences and intrusives (Gansser and Pantič, 1988; Milano et al., 1988; Colombo et al., 1994).

The dominant foliation in the basement rocks (S2) is supported by greenschist facies minerals which developed during the late-collisional exhumation of the Variscan basement, with few exceptions (Spalla and Gosso, 1999; Di Paola et al., 2001 and refs. therein). S2 in the Orobic basement is truncated by the base of siliciclastic Permian sequences, including conglomerates, arenites, and volcanicalstites, which are divided by unconformity in two cycles, dated lower and mid-upper

Permian, respectively (Cassinis et al., 1986; Cadel et al., 1996; Gosso et al., 2012; Berra et al., 2016). The basement and sedimentary rocks were subsequently deformed and poorly metamorphosed during Alpine convergence (e.g. Wennekers, 1932; Crespi et al., 1981; Laubscher, 1985), which is associated with the development of D3 and D4 structures (Milano et al., 1988; Albini et al., 1994; Carminati et al., 1997; Rebay et al., 2015).

Mineral assemblages supporting collisional and pre-collisional Variscan structures (D1, D1a, and D1b) are occasionally preserved in the Orobic basement, where five pre-Alpine Tectono-Metamorphic Units (TMUs) are distinguished (Spalla and Gosso, 1999; Spalla et al., 2014):

1) the Val Vedello (VVB) and Monte Muggio (MMB) basements (Fig. 2.1.2), in which kyanite-staurolite-bearing metapelites record the metamorphic peak of the Variscan collision under amphibolite facies conditions (Diella et al. 1992; Siletto et al., 1993; Gosso et al. 1997);
2) the Passo Cavalcafiche basement (PCB) and Domaso-Cortafò zone (DCZ) (Fig. 2.1.2) in which metapelites document a prograde metamorphic evolution. Syn-D1a chloritoid-garnet-bearing assemblages testify pre-collisional piling of cold lithospheric sheets. Syn-D1b staurolite-garnet-bearing assemblages formed during the subsequent Variscan collision (Spalla et al., 1999, di Paola et al., 2001);
3) The Aprica basement (AB) (Fig. 2.1.2), which records two stage of the Variscan tectono-metamorphic evolution both under greenschist facies conditions, but marked by different P/T ratios (Rebay et al., 2015). A similar tectono-metamorphic evolution is also recorded by a small segment of basement rocks immediately north of the Alpine Gallinera Thurst (Gansser and Pantic, 1988; Spalla and Gosso, 1999; Spalla et al., 2009);
4) The Dervio-Olgiasca Zone (DOZ, Fig. 2.1.2), which is the only TMU that records the post-Variscan high thermal state at intermediate crustal depth during D2 (i.e. relatable to the "Tethyan rifting", Diella et al., 1992; Bertotti et al., 1993). Sillimanite-bearing assemblages replaced by andalusite testify exhumation under high T/P ratio (Mottana et al., 1985; Diella et al., 1992; di Paola and Spalla, 2000; Spalla et al., 2000). The Triassic age of these events is constrained by dating syn-D2 pegmatites (Diella et al., 1992; Sanders et al., 1996; Gosso et al., 1997);
5) The Tre Valli Bresciane massif (TVB) (Fig. 2.1.2), which consists of continental crust in which Variscan Barrovian assemblages related to the Variscan collision have not been detected; here, the peak metamorphic conditions in metapelites are testified by chloritoid- and garnet-bearing assemblages that developed under epidote-amphibolite facies conditions (Giobbi Origoni and Gregnanin, 1983; Spalla et al., 2009).

tectonic system	Key	location	assemblage	T (°C)	P (GPa)	age (Ma)	method	refs.
Helvetic-Dauphinois-Provençal	HDP 1	Argentera Massif - Gesso Valley	And + Bt ± Sil ± Pl	-	-	292 ÷ 10 299-296	Rb-Sr Ar/Ar	Ferrara & Malaroda 1969; Compagnoni et al., 1974; Corsini et al., 2004.
"	HDP 2	Aiguilles Rouges - Mieville	And + Ms + Tur ± Tpz ± Crd	-	-	Carboniferous - Permian	-	Brändlein et al., 1994.
Penninic	P1	Gran Paradiso - Pian Teleccio	Bt, Sil, Crn, Qz, Kfs, Pl, And?	-	-	Carboniferous - Permian	-	Compagnoni & Prato, 1969.
Penninic	P2	Briancon basement	And	450-550	0.1-0.3	Permian - Triassic (295-245)	Rb/Sr K/Ar	Bocquet et al., 1974; Desmons, 1992.
Penninic	P3	(Briancon basement) Mont Mort	Grt + Bt + Sil/And	550-600	0.5-0.8	328-332	U/Pb	Bussy et al., 1996; Giorgis et al., 1999.
Austroalpine	A1	Mont Mary Nappe	And + Ms	-	-	Permian	-	Canepa et al., 1990; Dal Piaz, 1993.
Austroalpine	A2	Silvretta (Pischahorn)	Qz + Ms + And	~600	~0.2	353≥ t ≥280 (353-295)	Rb/Sr K/Ar	Brugger, 1994.
Austroalpine	A3	Languard-Campo Sondalo	And + Crd	~540	0.3-0.4	290-260	U/Pb	Gosso et al., 2004; Petri et al., 2016; 2017.
Austroalpine	A4	Languard-Campo	And + Ms	< 500	<0.5	<250	U/Pb	Spalla et al., 2003; Spalla et al., 2005; Salvi et al., 2010; Roda et al., 2018.
Austroalpine	A5	Matsch Nappe	Grt + Sil/And + Bt ± Crd + Pl + Qz	570-640	0.3-0.55	Permian	Rb/Sr U/Pb Sm/Nd	Gregnanin, 1980; Haas, 1985; Habler et al., 2009.
Austroalpine	A6	Jenig Complex	And + Bt + Ms + Chl Qz + Ms + And	450-530	0.24-0.42	254±8	Sm/Nd	Philippitsch et al., 1986; Schuster et al., 2001; Schuster et al., 2015.
Austroalpine	A7	Kreuzeck - Strieden Complex	And + Bt + Qz ± Pl ± Ms	500-570	<0.35	200-230	Ar/Ar	Hoke, 1990; Schuster et al., 2001; Schuster et al., 2004.
Austroalpine	A8	Defereggер Alps Uttenheim	And + Qz	-	-	>260; >190	Rb-Sr 40Ar/39Ar	Stoeckhert, 1987; Schuster et al., 2001.
Austroalpine	A9	Rappold Complex	ex-And	-	-	288 ± 4 262 ± 2	Sm/Nd	Schuster et al., 2001; Schuster et al., 2004.
Austroalpine	A10	Koralpe	ex-And	-	-	Permian - Triassic	-	Schuster et al., 2001; Schuster et al., 2004.
Austroalpine	A11	Stralleg	And + Bt + Qz ± Pl ± Ms	550-600	0.32-0.48	Permian - Triassic	-	Schuster et al., 2001; Schuster et al., 2004.
Austroalpine	A12	Sieggraben	ex-And	-	-	Permian - Triassic	-	Beck-Mannagetta, 1970; Schuster et al., 2001; Schuster et al., 2004.
Austroalpine	A13	Grobgneiss - Sopron	And + Bt ± Spl ± Ilm	575-620	0.18-0.25	320-330	K/Ar	Balogh & Dunkl, 1994; Torok, 1999; Schuster et al., 2001; Schuster et al., 2004.
Southalpine	S1	Strona-Ceneri Zone	Sil, And, Crd	-	-	Permian	-	Boriani and Burlini, 1995; Colombo and Tunesi, 1999.
Southalpine	S2	Dervio Olgiasca Zone	And	<600	<0.3	Triassic	-	Diella et al., 1992; Bertotti et al., 1993; Sanders et al., 1996; Spalla et al., 2005; Spalla et al., 2014.
Southalpine	S3	Val Biandino	And + Crd	500-600	<0.35	312±48 286±20	Rb/Sr K/Ar	De Capitani et al., 1988; Thoeni et al., 1992; Zanoni & Spalla, 2018.
Southalpine	S4	Val Camonica	And + Bt + Qz	-	-	pre-Permian	-	Diella et al., 2001; this work.
Southalpine	S5	Isarco Valley	And + Bt + Crd	<670	0.25-0.35	282 ± 14	Rb/Sr	Del Moro & Visonà, 1982; Visonà, 1995; Benciolini et al., 2006; Wyhlidal et al., 2012.

Table 2.1.1. Pre-Alpine andalusite-bearing assemblages in the metapelites from the continental crust of the Alps. Labels correspond to those of Figure 2.1.1. Mineral abbreviations are after Whitney & Evans, 2010. When the radiometric method is not specified the age is deduced from geological evidence or represents the average from results obtained by different methods.

In addition, P-T trajectories obtained from metamorphic pebbles from conglomerates of the first sedimentary cycle (Lower Permian) have been compared with the P-T evolutions inferred in different units of the Variscan basement (Spalla et al., 2009; Zanoni et al., 2010; Zanoni and Spalla, 2018). In particular, metamorphic conditions inferred from pebbles of basement rocks in the Aga and Vedello (PDC) conglomerates (Fig. 2.1.2) are similar to those characterizing the neighboring VVB and AB TMUs (Zanoni et al., 2010). In the same way, metamorphic conditions retained by pebbles in the Dosso dei Galli (DGC) conglomerate (Fig. 2.1.2) match those of the closest TVB TMU. In the Ponteranica Formation (POC) (Fig. 2) two types of pebbles are distinguished: the first type is similar to those found in the Aga and Vedello conglomerates, whereas, in the second, andalusite-bearing assemblages is interpreted either as developed during late-Variscan contact metamorphism induced by the emplacement of Val Biandino pluton or as during late-orogenic thermal relaxation (Zanoni and Spalla, 2018).

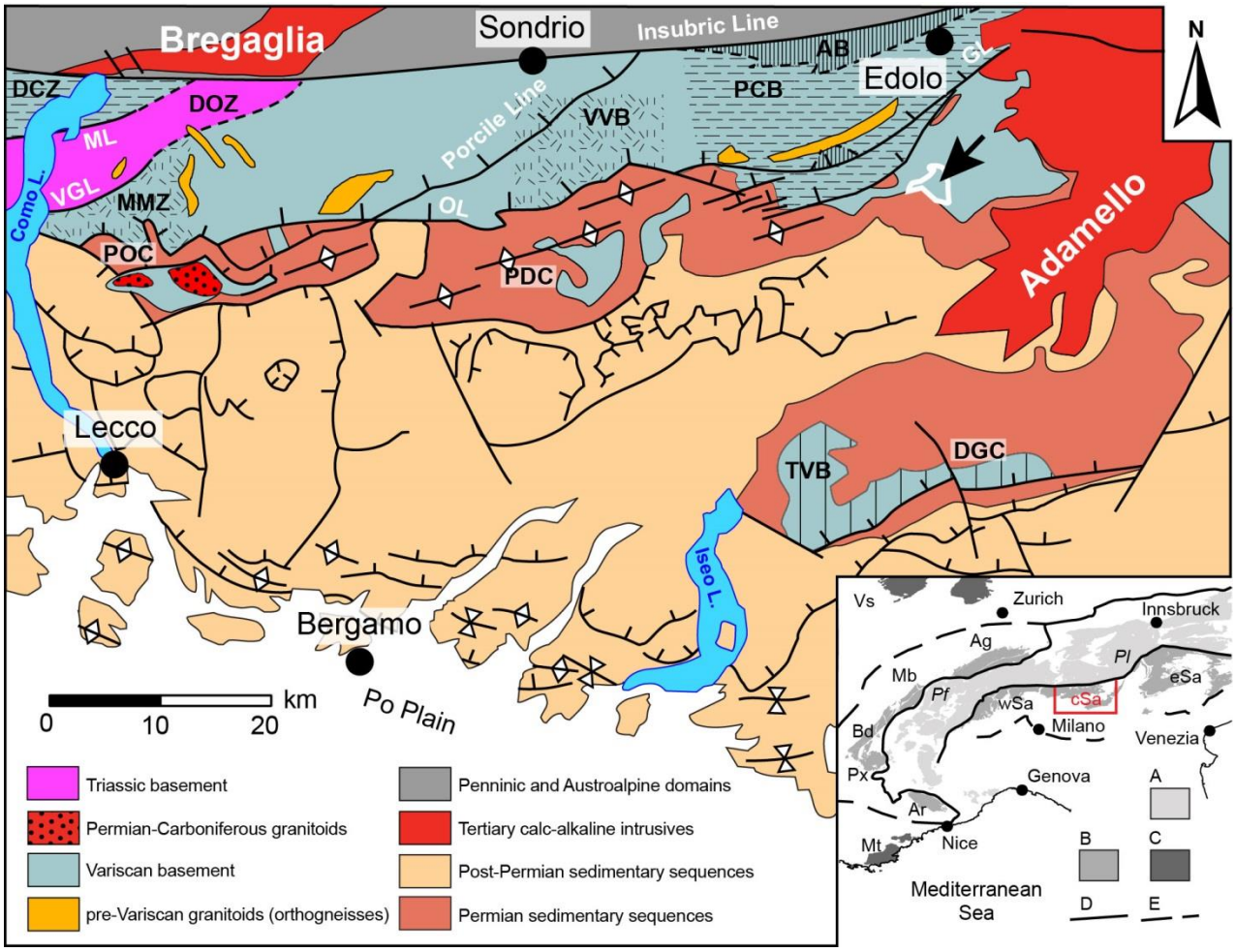

Figure 2.1.2. Geologic sketch of the central Southalpine domain. The mapped area is limited by the white line and indicated by the black arrow. Variscan TMUs: AB = Aprica basement; DCZ = Domaso – Cortafò Zone; DOZ = Dervio – Olgiasca Zone; MMZ = Monte Muggio Zone; PCB = Passo Cavalcafiche basement; TVB = Tre Valli Bresciane basement; VVB = Val Vedello basement. Permian conglomerates with pebbles deriving from the Variscan TMUs: POC = Ponteranica conglomerate; PDC = Aga and Vedello conglomerates; DGC = Dosso dei Galli conglomerate. Main tectonic lines: GL = Gallinera line; ML = Musso Line; OL = Orobic Line; VGL = Val Grande Line. Modified from Zanoni and Spalla (2018) and refs. therein. Inset with the tectonic sketch of the Alps (modified after Filippi et al., 2019). A = Variscan basement rocks in the Alpine subduction complex; B = Variscan basement rocks in the Alpine external domains (Ag: Aar-Gotthard Massif, Ar: Argentera-Mercantour Massif, Bd: Belledonne Massif, Mb: Mont Blanc Massif, Px: Pelvoux Massif, wSa: western Southern Alps, cSa: central Southern Alps, eSa: eastern Southern Alps). C = Variscan basement rocks external to the Alpine fronts (Mt: Maures-Tanneron Massif, Vs: Vosges).

The mid-upper Permian Verrucano Lombardo is part of the second sedimentary cycle capping most of the Orobic basement: it consists of poorly stratified fluvial conglomerates and sandstones (Berra et al., 2016 and ref. therein) that grade into shallow sea deposits (Servino Formation) in early

Triassic times (Sciunnach et al., 1996). This contribution focuses on a segment of Orobic basement just below the Gallinera Thrust footwall (Fig. 2.1.2), where the base of the Verrucano Lombardo truncates the S2 foliation, which is the dominant fabric at regional scale in the exhumed chloritoid-staurolite-andalusite-bearing Variscan basement rocks.

Lithostratigraphy and deformation history

Structural mapping was carried out on the right slope of the Oglio River in Val Camonica, west of Cedegolo and Sellero villages (Fig. 2.1.3), in order to constrain the overprinting relationships of pre-D2 structures in the Variscan basement. The Sellero-Cedegolo basement (SCB) mostly consists of metapelites, with minor lenses of garnet-bearing orthogneisses, paragneisses, and amphibolites, and is capped by the base of Permian siliciclastic sequences. The relevance of this area in the Orobic basement framework is the outstanding occurrence of andalusite in the pre-Permian metapelites (Fig. 2.1.3).

Four generations of superposed structures are distinguished in the SCB. The dominant foliation S2 in the metapelites is supported by white mica, chlorite, and, locally, albite (Fig. 2.1.4). S2 dips from northwest to southeast, due to successive Alpine folding and thrusting (D3), with Alpine D3 folds characterized by southwest trending axes and steeply dipping axial planes (Fig. 2.1.5).

Pre-D2 foliations, S1a and S1b, are occasionally preserved in the SCB, even if mostly parallelized into S2 (Fig. 2.1.5). S1a is supported by white mica, garnet, and biotite, with or without chloritoid, and S1b is supported by white mica, garnet, and biotite, with or without staurolite (Fig. 2.1.4). Overprinting relationships between S1a and S1b are observed only in exceptional cases. As a general rule, the occurrence of chloritoid instead of staurolite supporting S1 has thus been used to discriminate S1a from S1b, and vice-versa. Where both intersection relationships and contrasting assemblages are absent, pre-D2 fabrics have been simply labeled S1, which is, therefore, a composite fabric.

In the orthogneisses, K-feldspar relics are wrapped by two superposed foliations: S1 is supported by biotite, white mica, plagioclase, and quartz and wraps rare garnet porphyroclasts. New white mica, chlorite, and rare plagioclase grains mark S2, which is the dominant foliation at the outcrop scale.

The mid-upper Permian Verrucano Lombardo Formation unconformably covers the basement rocks and cuts S2 at the western boundary of the mapped area (Fig. 2.1.3). D3 folds affect the basement rocks together with the Permian-Mesozoic sedimentary sequences. In both Variscan basement rocks and Verrucano Lombardo D3 folds are characterized by a disgiuntive axial plane foliation S3 and localized shear zones. S3 is marked by chlorite, white mica, and opaque minerals.

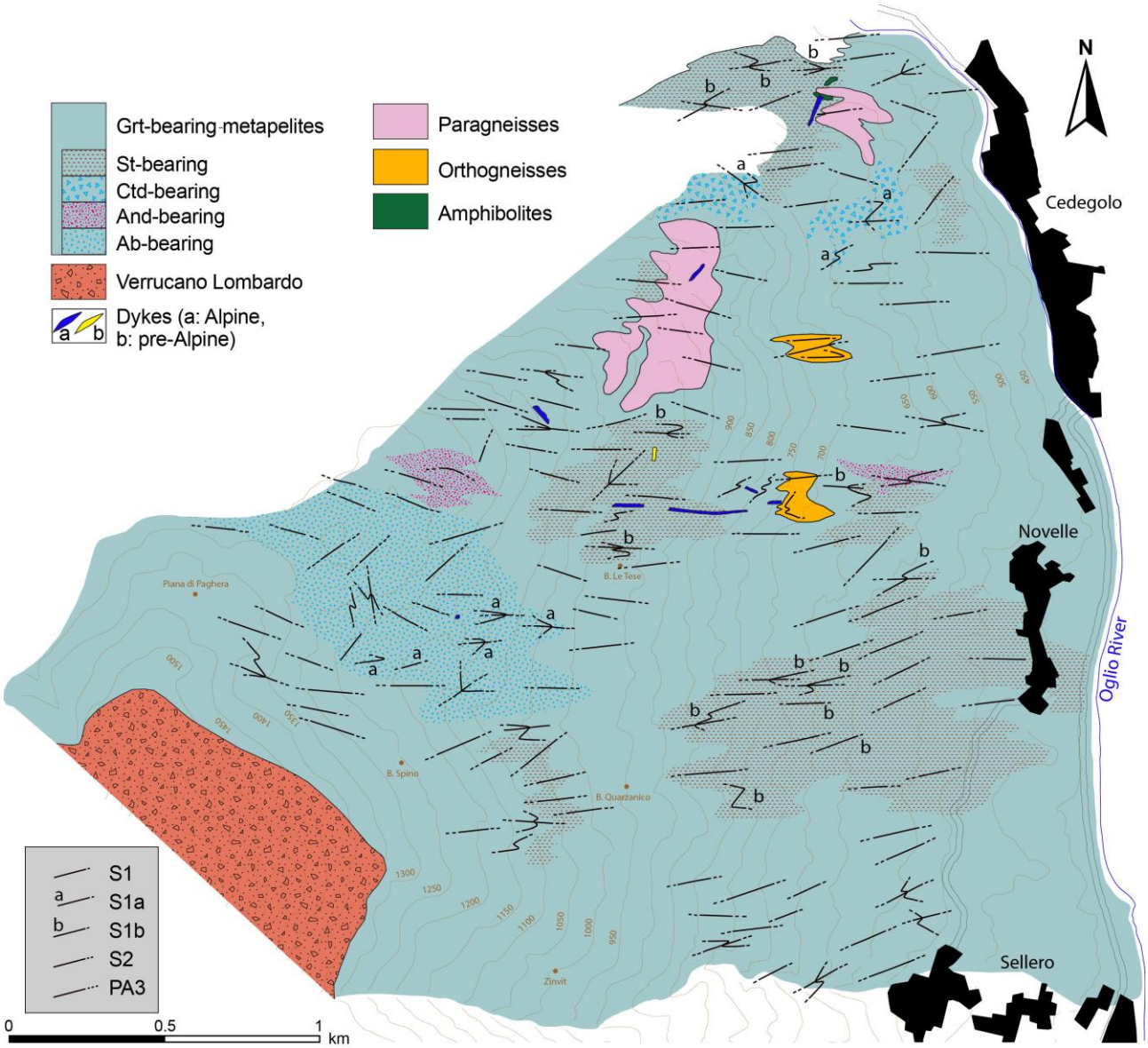

Figure 2.1.3. Interpretative structural map of the area west of Cedegolo and Sellero villages (location in Fig. 2.1.2). Orientations of fabric elements synthesised in this foliation trajectory map are analytically shown in Figure 2.1.5.

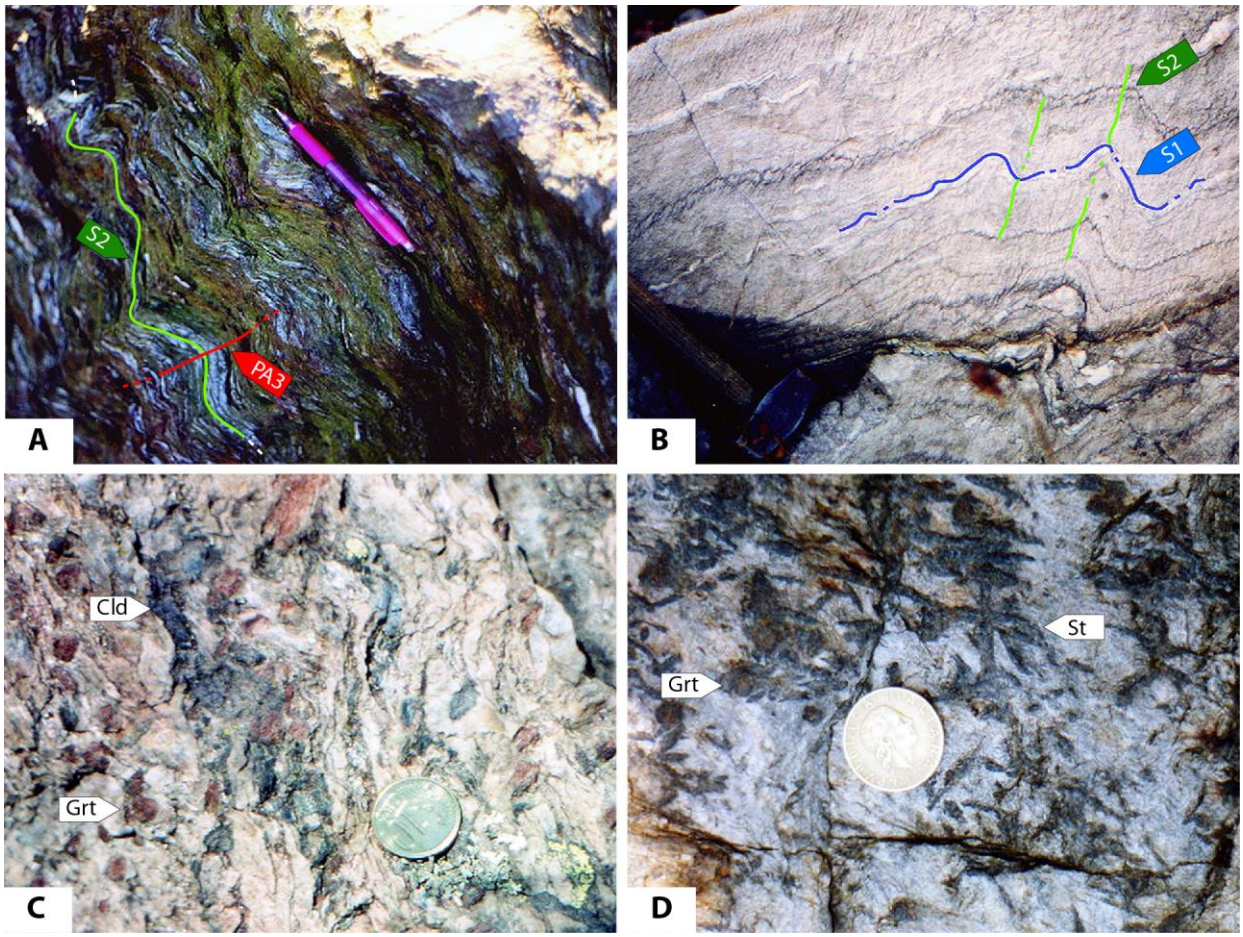

Figure 2.1.4. Meso-scale representative structures and mineral assemblages of Variscan metapelites in the area west to Cedegolo and Sellero villages: A – dominant S2 foliation folded during Alpine D3 stage; B – overprinting relationships between S1 and S2; C – garnet and chloritoid grains supporting S1a foliation; D – aggregates of staurolite grains lying on S1b foliation.

Microstructure and mineral chemistry

Deformation versus mineral growth relationships, synthetized in Table 2.1.2, have been determined for metapelites and orthogneisses that well preserve pre-D2 structures. The aim is to investigate relationships between mineral growth and superposed fabrics and infer a quality P-T-d-t (Pressure-Temperature-deformation-time) path. The above described and regionally valid deformation history has been useful to individuate the site for investigating mineral compositional variations, taking into account: a) the timing of mineral growth with respect to superposed fabric elements; b) deformation mechanisms acting during the same deformation stage (e.g.: Vernon, 2004; Spalla & Zucali, 2004; Passchier & Trouw, 2005; Gosso et al., 2015).

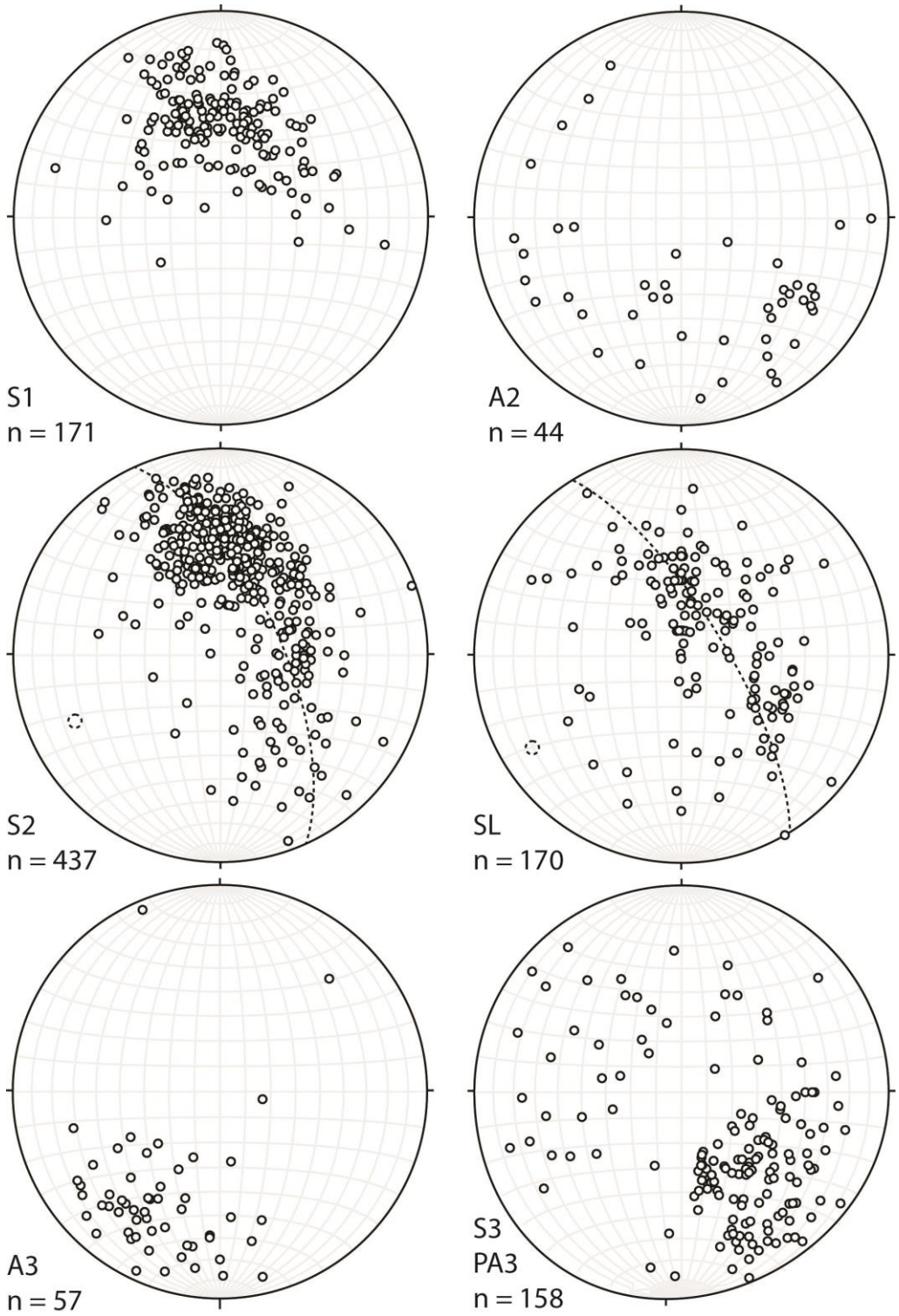

Figure 2.1.5. Schmidt stereographic projections (equal-area, lower hemisphere) of structural data, including Variscan (S1, S2) and Alpine (S3) poles to foliation planes, Variscan (A2) and Alpine (A3) fold axes and axial planes (PA3), and mid-upper Permian strata (SL). Data are distinguished on relative chronology. Dotted lines and poles represent cylindrical best fits.

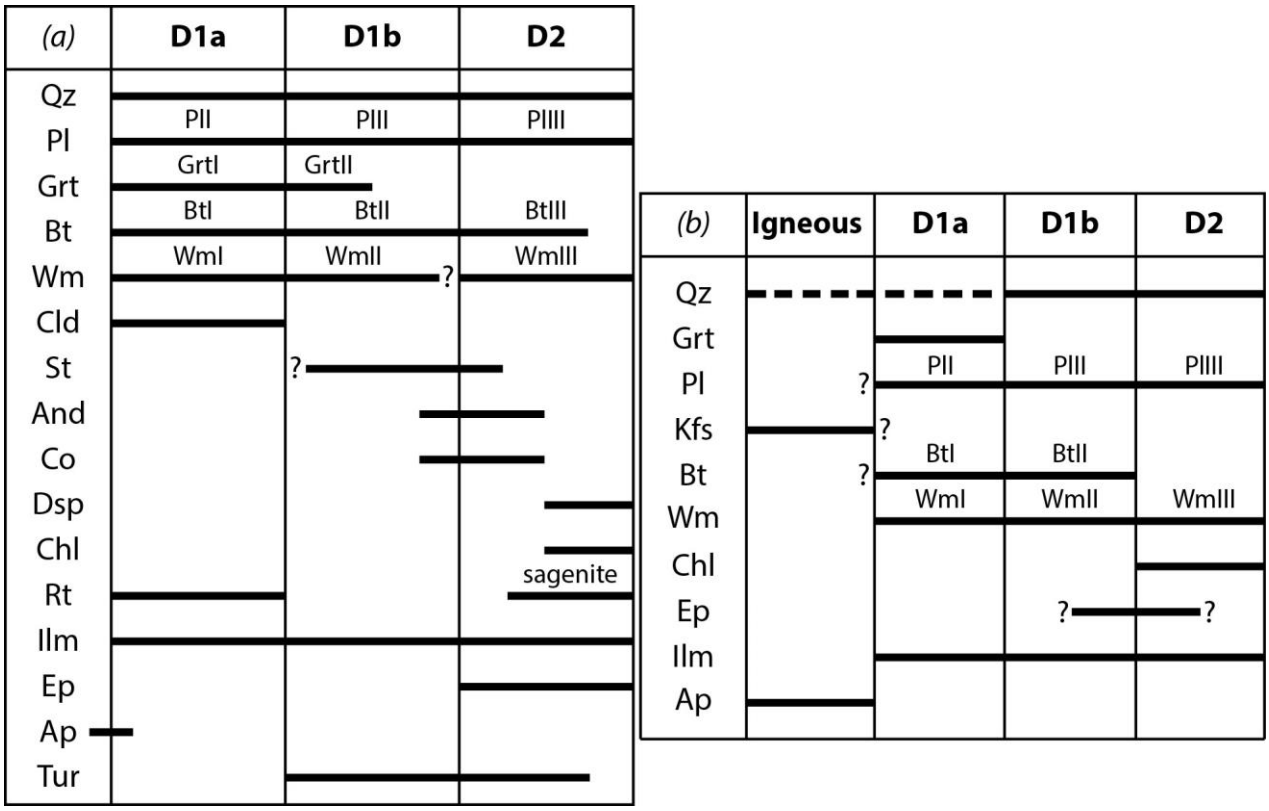

Table 2.1.2. Deformations event versus mineral growth in metapelites (a) and orthogneisses (b).

Mineral chemical analyses are performed at Università degli Studi di Milano with a Cambridge Instruments Stereoscan 360 at 15 kV accelerating voltage and with a beam current of 15 nA. Natural silicates served as standards. Garnet formula is calculated at 8 cations and 12 O, epidote at 8 cations and 12.5 O, biotite and white mica at 22 O, chloritoid at 12 O, staurolite at 46 O, chlorite at 7 O, and plagioclase at 4 O. Compositional parameters in metapelites and orthogneisses are reported in Table 2.1.3. The mineral chemical dataset is attached as Supplementary Data 1. Mineral abbreviations are from Whitney and Evans (2010).

Metapelites

S1a and S1b are well preserved in the selected samples of metapelite. S1a is supported by shape preferred orientation (SPO) of white mica (WmI, Si > 6.20 pfu), chloritoid (Mg# = 0.04 – 0.11), biotite (BtI, Mg# = 0.19 – 0.29), rutile, and ilmenite. The same minerals, together with rare grains of plagioclase (PlI, An_{4-5}), mark the internal foliation in millimeter- to centimeter-sized garnet porphyroblasts (GrtI, $Alm_{81}Grs_{14}Pyr_5$). Inclusion patterns in GrtI are usually straight, slightly curved at

garnet rims, and continuous with S1a outside the porphyroblasts. Similarly, millimeter-sized chloritoid grains include S1a as internal foliation (Fig. 2.1.6A). Quartz and plagioclase are in the microlithons. S1a is crenulated (D1b) and, where S1b is well developed, decussate and plastically deformed WmI and BtI crystals are preserved in microlithons and/or as rotated grains in the cleavage domains. GrtI cores contain an internal foliation, discordant with the external foliation (S1b; Fig. 2.1.6B), and show thin inclusion-free rims (GrtII, $Alm_{89}Grs_6Pyr_4$). S1b is marked by white mica (WmII, $6.10 \leq Si \leq 6.20$ pfu with $Pg < 0.20$), staurolite (Mg# = 0.06 – 0.15), biotite (BtII, Mg# = 0.30 – 0.40), and

Rock type	Stage	Mineral	Alm	Py	Grs	Si	Al	Na/(Na+K)	Fe+Mg	Ti	Mg#	An	Ab	Kfs
Metapelite	**D1a**	GrtI	0.75-0.90	0.01-0.10	0.05-0.20									
			0.81±0.04	0.05±0.02	0.14±0.04									
		WmI				6.21-6.38	5.39-5.72	0.03 - 0.20	0.13-0.43					
		BtI								0.17-0.25	0.19-0.29			
		PlI										4-5	94-96	0-1
		Cld									0.04-0.11			
	D1b	GrtII	0.86-0.94	0.02-0.10	0.02-0.07									
			0.89±0.02	0.6±0.02	0.4±0.01									
		WmII				6.10-6.20	5.67-5.90	0.08-0.28	0.07-0.23					
		BtII								0.10-0.23	0.30-0.40			
		PlII										21-22	77-78	0
		St									0.06-0.15			
	D2	WmIII				5.91-5.94	5.95-6.02	0.09-0.10	0.05-0.06					
		PlIII										1-3	97-98	0
		Chl (And)				2.44-2.53	2.98-3.18				0.36-0.38			
		Chl (Cld)				2.53-2.69	2.90-3.11				0.17-0.29			
		Chl (Grt)				2.44-3.01	2.44-3.05				0.09-0.37			
		Chl (St)				2.49-2.64	2.93-3.05				0.34-0.46			
Orthogneiss	**D1a**	Grt	0.58-0.62	0.03	0.35-0.39									
			0.60±0.01		0.37±0.02									
		WmI				6.11-6.27	5.22-5.38	0.08-0.11	0.34-0.48					
		BtI								0.28-0.38	0.30-0.34			
		PlI										13-42	56-86	1
	D1b	WmII				6.20-6.47	4.88-5.42	0.08-0.12	0.33-0.69					
		BtII								0.21	0.33			
		PlII										2-6	92-97	1-2

Table 2.1.3. Synthesis of mineral chemical analyses.

ilmenite; quartz and plagioclase (PlII, An_{21-22}) occupy the microlithons. Staurolite and GrtII are never in mutual contact; only locally, skeletal GrtII grains are in trails along S1b together with staurolite and thus considered cogenetic. Overprinting of staurolite-bearing S1b on chloritoid-bearing S1a is

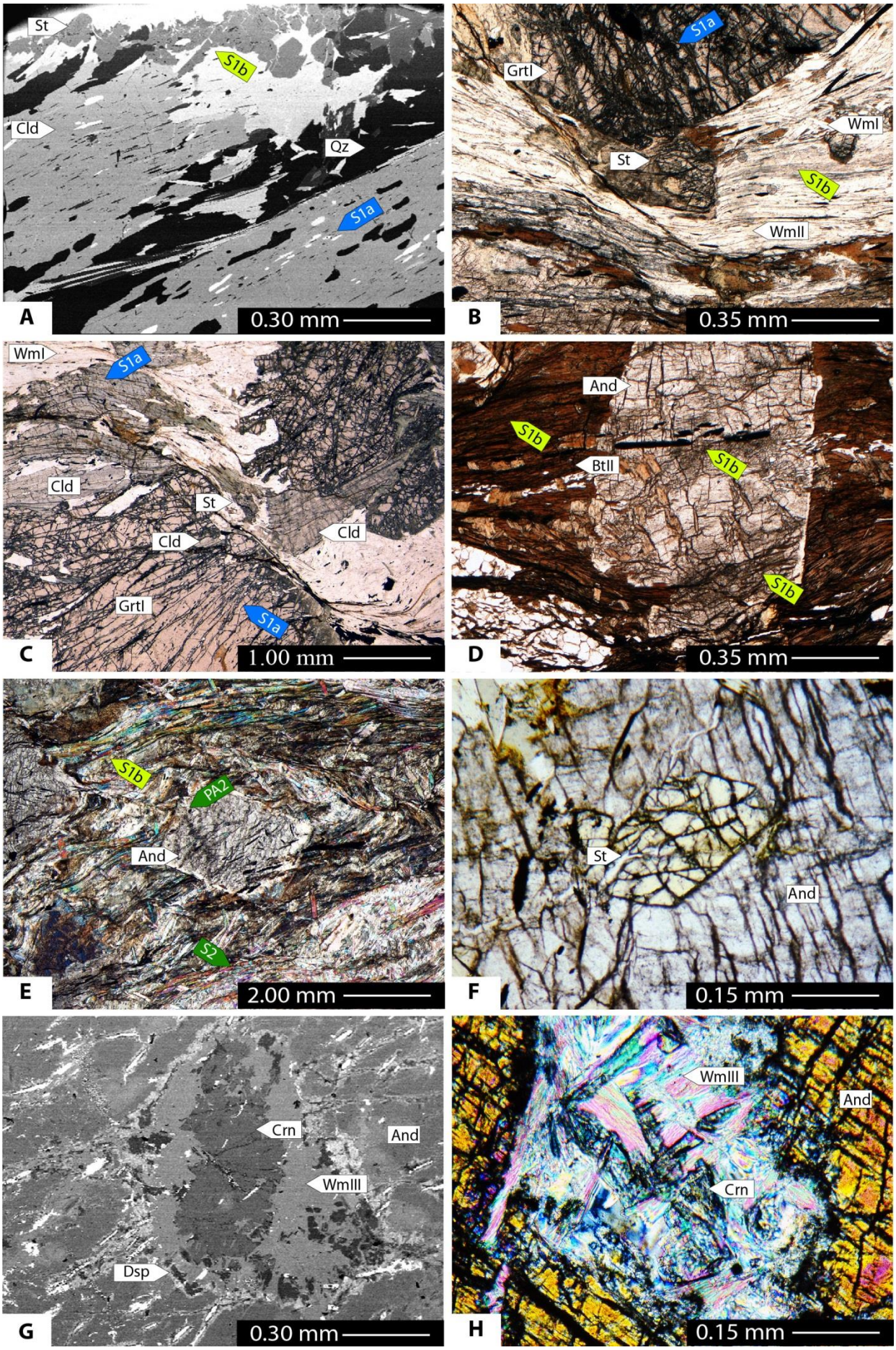
St
S1b
Cld
Qz
S1a
A
0.30 mm
S1a
Grtl
Wml
St
S1b
WmII
B
0.35 mm
Wml
S1a
Cld
St
Cld
Cld
Grtl
S1a
C
1.00 mm
And
S1b
BtII
S1b
S1b
D
0.35 mm
S1b
PA2
And
S2
E
2.00 mm
St
And
F
0.15 mm
Crn
And
WmIII
Dsp
G
0.30 mm
WmIII
And
Crn
H
0.15 mm

Figure 2.1.6. Microphotographs of Variscan metapelites. A – S1a supported by shape preferred orientation of millimeter-sized chloritoid porphyroblasts (BSE image). Internal foliation in chloritoid is continuous with external S1a. S1b is supported by sub-millimetre sized staurolite grains and cuts S1a. B – Porphyroclast of GrtI wrapped by S1b. S1b is supported by WmII and BtII. GrtI retains a straight internal foliation discontinuous with the external one. Staurolite in the strain caps around GrtI encloses deflected S1b. C – S1a supported by chloritoid. Chloritoid is included in GrtI, and the internal foliation in both GrtI and chloritoid is deflected but continuous with the external foliation S1a. Chloritoid grains are boudinaged and staurolite grew in the boudin-neck. D – Andalusite with internal foliation continuous with external S1b: the internal foliation is straight at the grain core and curved at the rim. S1b is supported by BtII. Decussate grains of biotite are preserved in cleavage domains and as inclusions in andalusite. E – Andalusite porphyroblast with internal foliation continuous with the external one, folded by D2. F – Andalusite porphyroblast includes staurolite at equilibrium. G and H – Andalusite porphyroblasts including corundum grains replaced by diaspore and WmIII (BSE and crossed Nicols images, respectively).

exceptionally preserved (Fig. 2.1.6A); in addition, staurolite includes S1b foliation deflected toward grain margins in strain caps around GrtI porphyroclasts (Fig. 2.1.6B), or it fills the necks of micro-boudinaged chloritoid grains (Fig. 2.1.6C).

S1b is crenulated by D2 or micro-faulted along localized shear bands. S2 is outlined by chlorite, white mica (WmIII, Si = 5.91 – 5.94 pfu, Pg = 0.09 – 0.10), ilmenite, tourmaline, and rare biotite (BtIII). Plastically deformed grains of biotite and white mica are re-oriented along S2. Centimeter-sized plagioclase crystals (PlIII, An_{1-3}) retain S2 as internal foliation. Plagioclase porphyroclasts are statically replaced by epidote and sericite, whereas chlorite overgrew garnet, chloritoid, and staurolite.

Andalusite crystals of millimeter to centimeter size include S1b as internal foliation, either straight, curved, or gently folded by D2 (Fig. 2.1.6D, E), but in any case continuous with the external S1b and supported by BtII. Andalusite is micro-boudinaged during D2, with WmIII, BtIII, and chlorite filling the boudin necks, and wrapped by coronae of very fine grained WmIII. All these features suggest that andalusite growth took place during the final stages of S1b development and ceased during early-D2. Staurolite inclusions in andalusite are recurrent and display sharp grain boundaries (Fig. 2.1.6F). Andalusite locally forms aggregates together with small corundum grains. Corundum is in most of the cases rimmed by diaspore (Fig. 2.1.6G and H).

The following mineral compositional evolutions are here summarized and highlighted in Figure 2.1.7 and Table 2.1.3: 1) replacement of Ca by Fe^{2+} from GrtI to GrtII; 2) decresing of Si content from WmI to WmII to WmIII; 3) increasing of Mg# and Ti content from BtI to BtII; 4) increasing of Ca content from PlI to PlII and decreasing from PlII to PlIII.

Chlorite composition seems to be controlled by the microstructural site: chlorite replacing andalusite and staurolite has Mg# = 0.34 – 0.36, chlorite replacing chloritoid has Mg# = 0.17 – 0.29, chlorite rimming garnet has Mg# = 0.09 – 0.37 with the lowest Al content (Fig. 2.1.7).

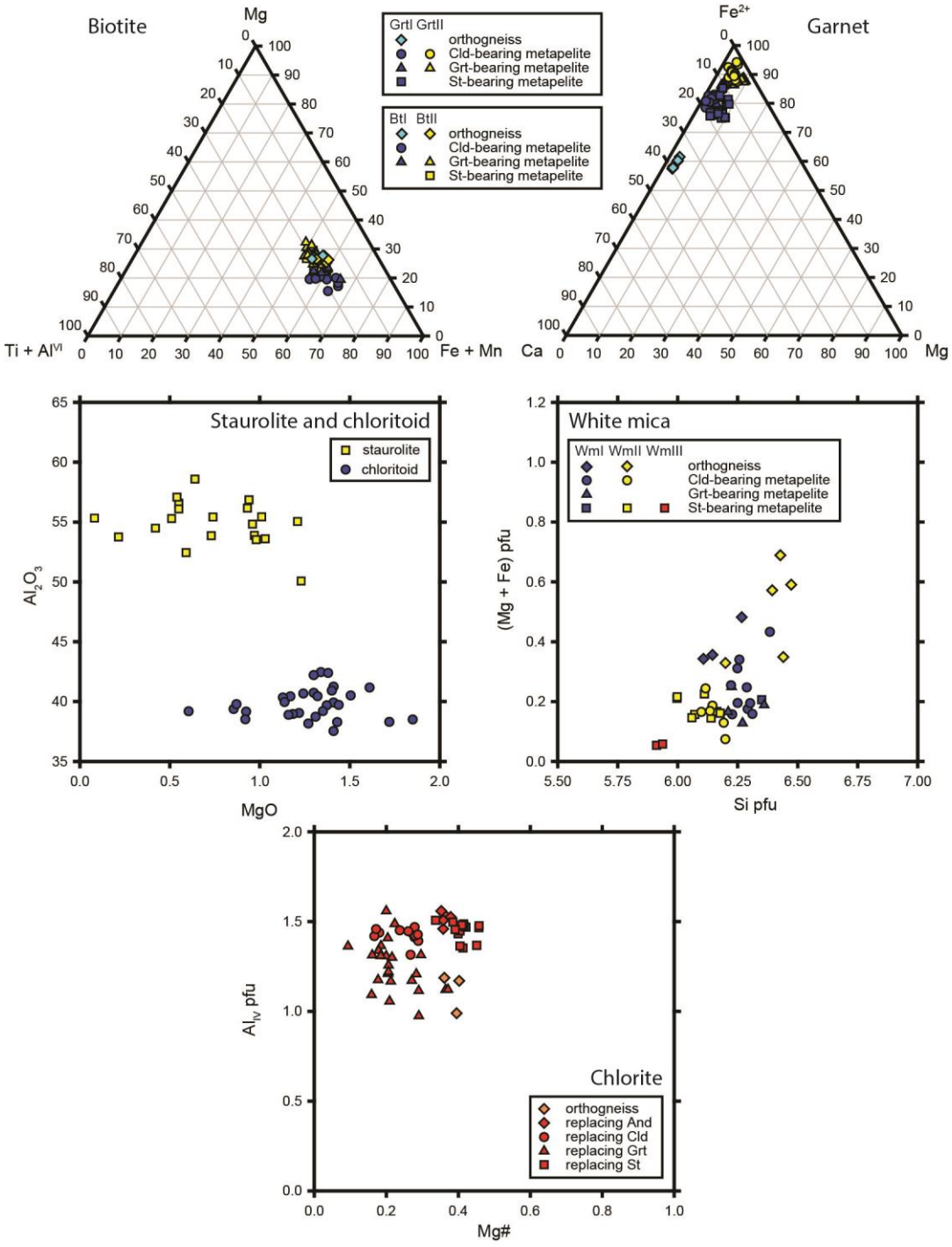

Figure 2.1.7. Compositional variations of the main rock-forming minerals in metapelites and orthogneisses as a function of rock-type (triangle: garnet-bearing metapelites, circle: chloritoid-bearing metapelites, square: staurolite-bearing metapelites) and occupied microstructural site (D1a - blue, D1b - yellow, D2 - red).

Orthogneisses

Despite S2 is the dominant fabric, S1a and S1b are locally preserved in the orthogneisses, where they wrap relics of igneous K-feldspar. S1b is supported by biotite (BtII, Mg# = 0.33, Ti < 0.21 pfu), quartz, plagioclase (PlII, An_{2-5}), ilmenite, and minor white mica (WmII, Si = 6.20 – 6.47 pfu, Pg < 0.12). S1a is internal foliation in skeletal garnet grains ($Alm_{51}Grs_{31}Pyr_{3}Spess_{16}$) and is supported by elongated inclusions of quartz. S1a in the garnet porphyrclasts is discontinuous with respect to the external foliation S1b. Decussate grains of biotite (BtI, Mg# = 0.30 – 0.34, Ti = 0.29 – 0.38 pfu) and white mica (WmI, Si = 6.11 – 6.27 pfu, Pg < 0.11) are found in micro-lithons, together with an early generations of plagioclase (PlI, An_{13-42}) extensively replaced by white mica and epidote (Fe^{3+} / (Al^{VI} + Fe^{3+}) = 0.16 – 0.17). BtI, WmI, PlI, garnet, and quartz are considered stable during S1a development. Finally, S2 is supported by WmIII, ilmenite, and chlorite (Mg# = 0.36 – 0.40), which pervasively replaces biotite and garnet.

Metamorphic evolution vs. deformation history

The aim of this paragraph is constraining the P-T environment in which developed the superposed groups of structures (D1a, D1b, D2) in this portion of the Orobic basement before the deposition of the Verrucano Lombardo, which constrains a minimum mid-upper Permian age for the end of the Variscan evolution of the SCB.

Metamorphic conditions for the subsequent deformation stages recorded in the metapelites are thus estimated by means of thermobarometers and pseudosections. Temperatures have been constrained using different Fe-Mg cationic exchange on mineral pairs in mutual contact. Chloritoid-biotite and chloritoid-garnet thermometry (Perchuck, 1989; 1991) have been applied on mineral grains supporting S1a foliation and give a temperature interval of 490 – 580°C. Staurolite-garnet thermometry (Perchuck, 1991) on minerals marking S1b provides a temperature interval of 580 – 610°C. The result is fully consistent with the upper stability of chloritoid in the FASH system, which reacts to form staurolite and/or almandine by increasing temperature above 550°C (Spear, 1995 and ref. therein). Garnet-biotite thermometry (Holdaway and Lee, 1977; Ferry and Spear, 1978; Perchuck and Lavrent'eva, 1983; Holdaway, 2000) coherently indicates that S1a developed at T = 480 – 540°C and S1b at T = 510 – 630°C. Pressure conditions are then firstly estimated by garnet-plagioclase-biotite-muscovite-quartz (Ghent and Stout, 1981), garnet-plagioclase-muscovite-quartz barometers (Hodges and Crowler, 1985): S1a is supposed to develop at P = 0.8 – 1.0 GPa, S1b at P = 0.4 – 0.6 GPa.

Pseudosections are calculated by the Theriak/Domino program (De Capitani and Petrakakis, 2010) to better constrain the P-T intervals accountable for D1a to early D2 events. We adopted a converted version of the self-consistent ds55 thermodynamic database of Holland and Powell (2003) in the CNKFMASH system, including the following mineral a-x relations: garnet (White et al., 2007), biotite (White et al., 2007), chlorite (Holland and Powell, 1998), white mica (Coggon and Holland, 2002), chloritoid (Holland and Powell, 1998), staurolite (Holland and Powell, 1998), and cordierite (Holland and Powell, 1998). WR analyses of metapelites and orthogneisses from the Orobic basement (Caironi et al. 2004) served as bulk composition, with water in excess and after correction for apatite (Fig. 2.1.8). The selected bulk compositions do not directly refer to the samples analysed by this study, but belong to the same lithostratigraphic units in which the Orobic basement is often subdivided. Mn has been excluded because it is in negligible concentrations in the metapelites and only fractionated in garnet in the orthogneisses.

The syn-D1a assemblage in metapelites plagioclase + garnet + biotite + white mica + chloritoid + quartz is stable at T = 530 – 560°C and P = 0.6 – 0.8 GPa (Fig. 8a). The resulting stability field is delimited at low temperature and high pressure by the chlorite-in and chloritoid-out lines, at high temperature by the chloritoid-out and staurolite-in lines (T = 560 °C), at low-pressure by the garnet-out line. In the D1a field, the garnet composition changes from $Alm_{81}Grs_{16}0Pyr_5$ to $Alm_{87}Grs_8Pyr_5$ increasing the T/P ratio. The Si content in white mica is 6.20 pfu at around P = 0.8 GPa. The computed compositions are fully compatible with those of GrtI ($Alm_{81}Grs_{14}Pyr_5$) and WmI (Si ≥ 6.20 pfu) in the metapelites for T = 530-550°C and P ≃ 0.8 GPa.

The assemblage syn-D1b garnet + biotite + white mica + staurolite + quartz is stable at T = 560 – 650 °C and P = 0.5 – 0.7 GPa. The predicted stability field is delimited at high pressure by the staurolite-out line, at high temperature by the univariant sillimanite-in and staurolite-out line, at low pressure by the garnet-out line. In this field, garnet is characterized by almandine content at around 0.90 and grossular at around 0.05, as in GrtII ($Alm_{89}Grs_6Pyr_4$). This portion of the P-T space likely represents the main stage of S1b development, which was followed by further decompression and exhumation out of the garnet stability field, as suggested by the Si content in WmII (6.10 ≤ Si ≤ 6.20 pfu).

Andalusite is stable together with staurolite at T = 520 – 580°C and P = 0.2 – 0.4 GPa (Fig. 2.1.8b). These metamorphic conditions are most likely those characterizing the transition between D1b and D2 deformation stages. A further exhumation of metapelites towards shallower structural levels is testified by the replacement of corundum by diaspore, which occurs at T ≤ 400°C and P ≤ 0.2 GPa (Holland and Powell, 1998).

In the orthogneisses**,** the stability and composition of garnet is mostly controlled by the amount of water in the system (Fig. 2.1.8c). Increasing water content, garnet is stable towards higher pressure at

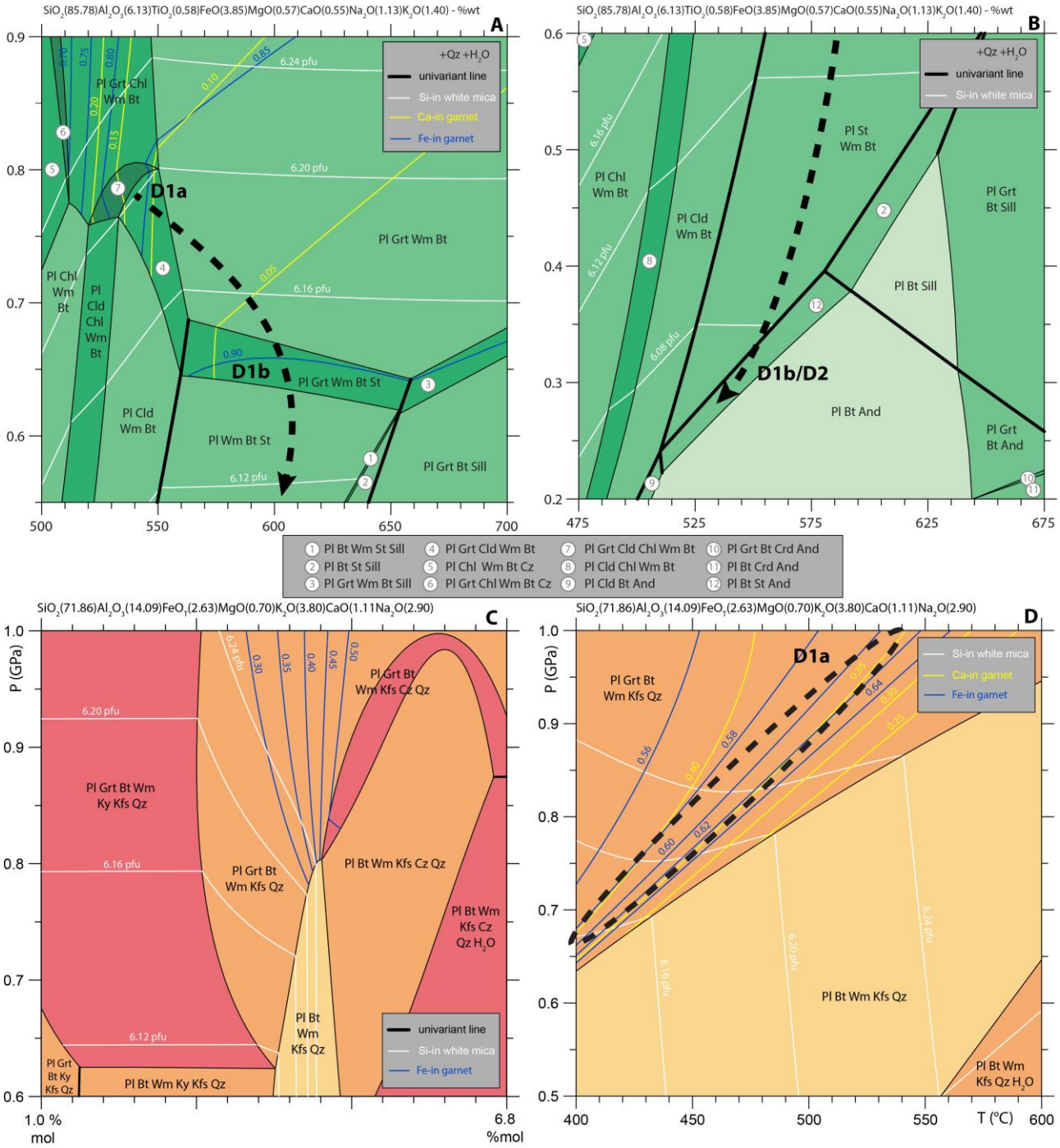

Figure 2.1.8. P-T and P-X pseudosections calculated in the CNKFMASH system for Variscan metapelites (A and B) and orthogneisses (C and D) west of Cedegolo and Sellero villages. Bulk compositions are taken from Caironi et al. (2004). Fields are coloured as function of variance. Si-in white mica, Ca-in garnet, Fe-in garnet isopleths are added. P-T accountable for D1a to D2 deformation stages are highlighted by dotted ellipses and lines.

the same temperature. Garnet with composition similar to the analysed ones ($Alm_{60}Grs_{37}Pyr_3$) is found in the Pl + Grt + Bt + Wm + Kfs + Qz field if considering around 3% mol of H_2O in slightly under-

saturated conditions. The P-T conditions accountable for garnet development vary form 450°C and 0.65 GPa to 530°C and 1.00 GPa (Fig. 2.1.8d). In this wide P-T interval, biotite Mg# (0.30 – 0.38) match with the analysis on Bt I (0.30- 0.34) and the Si content in white mica (6.14 – 6.34 pfu) is comparable to that of Wm I (6.11 – 6.27 pfu). This modelling suggests that garnet stability in the orthogneiss is only possible at P-T conditions (T = 450°C – 530°C, P = 0.7 – 1.0 GPa) that are slightly cooler but comparable with those determined for D1a in the metapelites (T = 520-550 °C, P ≃ 0.8 GPa), and not during D1b.

Discussion and conclusion

Multi-scale structural analysis integrated by petrology on the Southalpine crystalline basement west of Sellero and Cedegolo villages (SCB) allowed the reconstruction of the Variscan P-T-d-t evolution, ending before the Verrucano Lombardo deposition in mid-upper Permian (Figs. 2.1.3 and 2.1.9). The Variscan structural evolution is testified by the superposition of three groups of structures developed under different metamorphic conditions: D1a structures formed at the boundary between epidote amphibolite- and amphibolite-facies conditions (at T = 450 – 570°C and P = 0.7 – 1.0 GPa), D1b under amphibolite-facies conditions, at higher temperature and slightly lower pressure (T = 550 – 650°C and P = 0.4 – 0.7 GPa), whereas D2 structures are marked by mineral assemblages testifying the transition towards greenschist-facies conditions (T ≤ 400°C and P ≤ 0.3 GPa). Overprinting relationships between chloritoid-garnet-bearing S1a and staurolite-garnet-bearing S1b confirm that the development of such contrasting mineral assemblages is controlled by different thermal states in different times, rather than by bulk-related effects.

The textural relationship between staurolite and andalusite in some portion of the SCB basement suggests local equilibrium between these mineral phases. Andalusite-staurolite assemblages developed at T = 520 – 580°C and P = 0.2 – 0.4 GPa, in between late D1 and early D2 stages. This is in contrast with the textural relationships in metamorphic clasts of the Lower Permian Ponteranica Formation that shows andalusite clearly developed at the expenses of staurolite (Zanoni & Spalla, 2018).

The thermal state, suggested by the syn-D1a P-T conditions (Fig. 2.1.9) is characterized by a T/depth ratio of 15 – 18 °C km^{-1}, plots between those of warm subduction zones and plate interior (Cloos, 1993) and is compatible with tectonic piling of cold lithospheric sheets during the Variscan convergence, as already suggested in other portions of the Orobic basement, and interpreted as effect to the Variscan subduction (e.g.: Spalla et al., 1999; Spalla et al., 2009).

D1b structures developed under P-T_{max} conditions, indicating a T/depth ratio of 25-30 °C km^{-1} and suggesting a thermal approaching that of plate interior and spreading ridge or volcanic arc (Cloos,

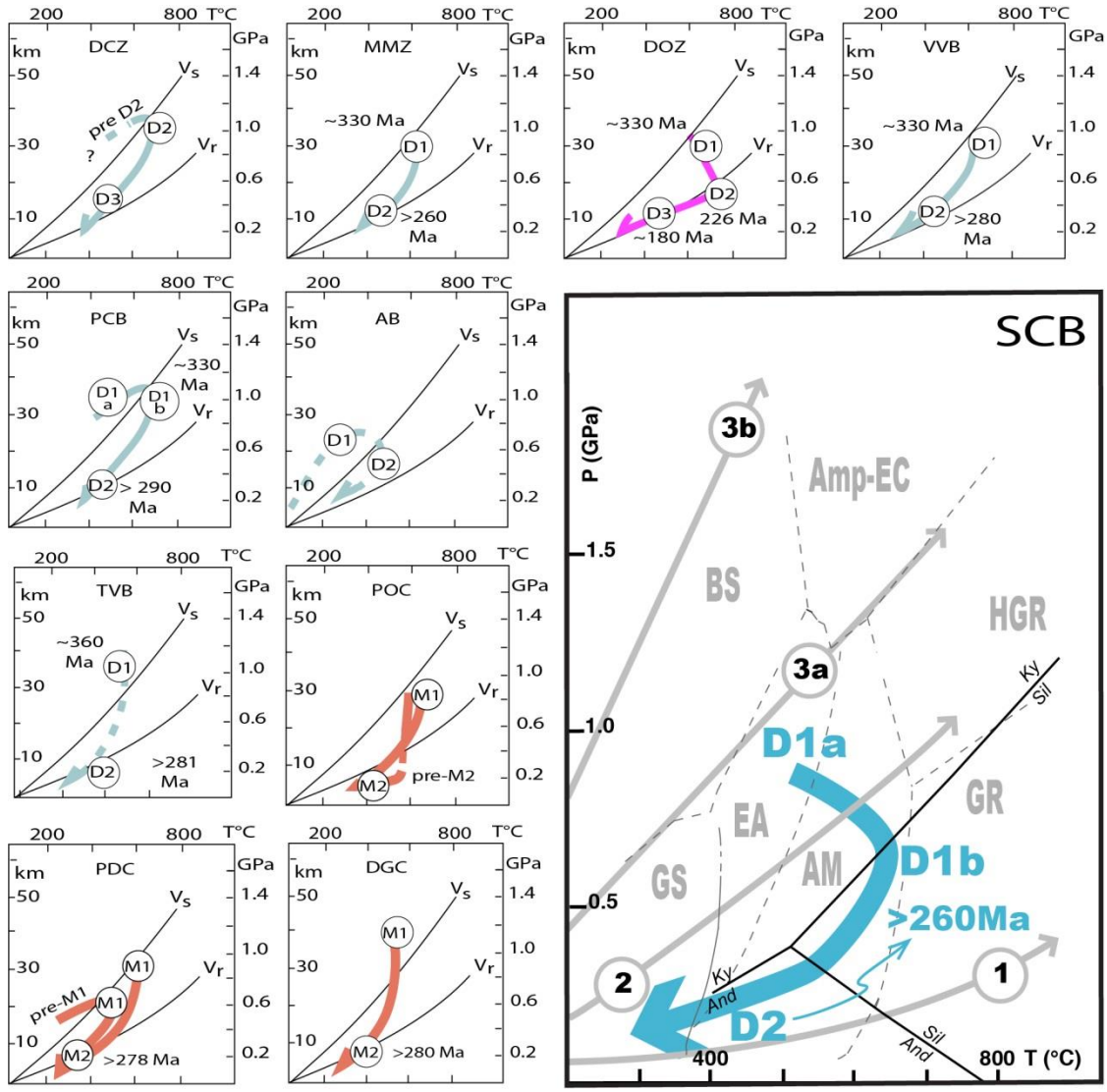

Figure 2.1.9. P-T-d-t paths characterizing Variscan TMUs in the Orobic basement and PT paths recorded in the clasts of Lower Permian conglomerates of the Central Southalpine Domain (references are cited in the text) compared with the P-T-d-t evolution inferred for Sellero and Cedegolo Basement (SCB). Variscan TMUs: AB = Aprica basement; DCZ = Domaso – Cortafò Zone; DOZ = Dervio – Olgiasca Zone; MMZ = Monte Muggio Zone; PCF = Passo Cavalcafiche basement; SCB = Sellero and Cedegolo Basement; TVB = Tre Valli Bresciane basement; VVB = Val Vedello basement; Permian conglomerates: POC = Ponteranica Conglomerate; PDC = Aga and Vedello Conglomerates; DGC = Dosso dei Galli Conglomerate. Metamorphic facies (Ernst and Liou, 2008): GS = greenschist; EA = epidote-amphibolite; BS = blueschist; AM = amphibolite; Amp-EC = amphibole-bearing eclogite; HGR = high-pressure granulite; GR = granulite. Geotherms: 1) near spreading ridge or volcanic arc, 2) normal gradient of old plate interior, 3a) "warm" subduction zones, 3b) cold subduction zones (Cloos, 1993); Vs = stable and Vr = relaxed geotherms for continental crust (England and Thompson, 1984). D2 mid-upper Permian age (>260 Ma) is constrained by the Verrucano Lombardo Fm. capping SCB basement and truncating S2.

1993). This thermal state is compatible with those of the Variscan continental collision, in agreement with other tectono-metamorphic units of Southalpine domain (Diella et al. 1992; Siletto et al., 1993;

Gosso et al. 1997; Spalla et al., 1999; Di Paola et al., 2001; Zanoni et al., 2010; Rebay et al., 2015; Zanoni and Spalla, 2018).

Andalusite-staurolite-bearing assemblages developed under T/depth ratio comprised between 40 and 70 °C km^{-1} in between late-D1 and early-D2 indicate that an anomalous high thermal regime was already effective at the end of the exhumation trajectory of the SCB rocks. The deposition of the Verrucano Lombardo Formation makes the greenschist-facies D2 structures older than the mid-upper Permian (Zanoni & Spalla, 2018 and refs. therein). In this way, any relationship with the Permian-Triassic high thermal state that characterised, for example, the DOZ TMU (Mottana et al., 1985; Diella et al., 1992; Di Paola and Spalla, 2000; Spalla et al., 2000) is precluded, since the SCB was already exhumed at that time. Such a high thermal state likely is supposed to be occurred during a late-orogenic thinning, associated with lithospheric unrooting, during the mature stages of the Variscan collision testified by the garnet-staurolite assemblages supporting S1b in the metapelites.

This makes unique this portion of the Southalpine basement with respect to the others, where the thermal record of the late-collisional evolution is instead recorded at deeper crustal levels, as testified by occurrence of sillimanite and/or cordierite together with andalusite (Boriani et al., 1988; Boriani and Giobbi, 2004; Benciolini et al., 2006; Whylidal et al., 2012; Zanoni and Spalla, 2018).

Appendix

Two zircon grains from orthogneiss and metapelite samples are considered for cathodoluminescence imaging and U-Pb zircon geochronology. The zircon grain in the orthogneiss sample is euhedral, with oscillatory zoning and intermediate resorption surfaces (Fig. 2.1.10a). This zircon is likely of igneous origin. The zircon grain in the metapelite sample is instead anhedral with an altered rim (Fig. 2.1.10b). This zircon is supposed to be detrital.

In-situ U-Pb zircon dating was performed at Università degli Studi di Milano by in-situ ICP-MS using a Thermo Fisher Scientific iCAP RQ quadripole coupled with Teledyne Cetac Tchnologies Analyte Excite 193 nm excimer and equipped with a HelEx 2 volume sample chamber. We used an ablation spot diameter of 20 μm, a repetition rate of 5 Hz, and a fluence of 2 J/cm^2. The 91500 zircon (Wiedenback et al., 1995; Wiedenback et al., 2004) is chosen as standard and the Plesovice Zircon as secondary standard for quality control (Slama et al., 2008). Both the standards were repeatedly measured during the analysis. Back-ground signal has been acquired for 40s and then 60s of analysis with the laser firing. Data have been processed by GLITTER software (Van Achterbergh et al., 2001).

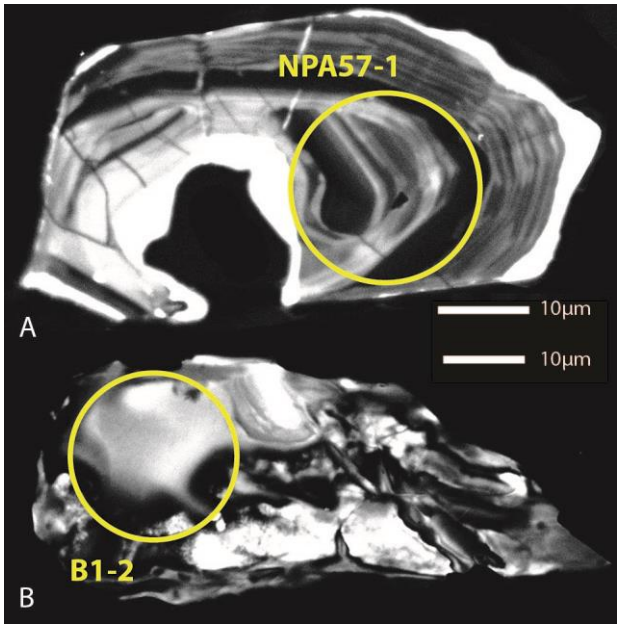

Figure 2.1.10. Cathodoluminescence images of an igneous zircon in orthogneiss (A) and a detrital zircon in metapelite. Spots for in-situ U-Pb dating are colored yellow. Results are in Table 2.1.3.

Sample	Pb207/Pb206	1se	Pb206/U238	1se	Pb207/U235	1se	Pb208/Th232	1se	Conc. Age	2se
NPA57_1	0.693	0.044	0.086	0.002	0.6931	0.04	0.02508	0	531	22
B1_2	0.621	0.057	0.079	0.002	0.62106	0.06	0.02 92	0	492	25

Table 2.1.4. Results of in-situ U-Pb zircon dating.

Results are in Table 2.1.4. An intrusive age of 531 ± 22 Ma is determined for the protolith of the orthogneiss. An age of 492 ± 25 Ma is determined for the detrital zircon grain in the metapelite. This age is interpreted as a minimum age for the sedimentary sequence.

The first data contradicts the assumption of an Ordovician age for all the orthogneiss protoliths in the Southern Alps (e.g. Boriani and Bini, 2012 and ref. therein). Coeval granitoids are found in several parts of the Austroalpine domain, where they are often coupled with mafic intruives (525 ± 5 Ma, Schaltegger et al., 1997, Muller et al., 1995; 532 ± 30 Muller et al., 1996; 530-510 Ma, Poller et al., 1997). These rocks are interpreted as derived from an island arc developed on an active continental margin or from oceanic crust emplaced in a back-arc basin (e.g. Schaltegger et al., 1997; Schaltegger and Gebauer, 1999). The Cambrian-Ordovician age of the detrital zircon in the metapelites is older than the Silurian-Ordovician age determined by Gansser and Pantič (1988) for the protolith of the meta-sedimentary sequences.

The Maures-Tanneron Massif

2.2 Constraints on the Variscan tectono-metamorphic evolution of the Bormes Unit, western Maures Tanneron Massif

Introduction

The Maures-Tanneron Massif (Fig. 2.2.1) is a part of the southern European Variscan belt and consists of a well exposed crustal section of more than 80 km through different Variscan domains that retain contrasting P-T evolutions (Schneider et al., 2014).

In the western Maures-Tanneron Massif (M-T), the continental collision is pervasively recorded under low grade- to amphibolite facies conditions, whereas the late- to post-collisional stage is intermittently recorded under greenschist facies conditions (Schneider et al., 2014). The western M-T is divided in units with a metamorphic field gradient increasing from west to east.

By contrast, Variscan eclogites are preserved in the central-eastern M-T. These rocks were pervasively re-equilibrated during HT-LP late- to post-collisional stages, when the central-eastern M-T experienced widespread partial melting and acidic magma emplacements (Schneider et al., 2014). The central / eastern M-T is thus considered as a Variscan subduction complex, whose boundaries have been deeply transposed by subsequent collisional and late-collisional stages in Carboniferous times (Schenider et al., 2014).

This chapter includes structural and mineral-chemical data aimed at refining the P–T-d-t evolution of the Bormes Unit in the western M-T (Fig. 2.2.1) to compare it with that of the Orobic basement in the central Southern Alps. Variscan metapelites and orthogneisses of the Bormes Unit have been deformed and pervasively re-equilibrated under amphibolite facies conditions during the Variscan collision (Schneider et al., 2014). However, LT-HP pre-collisional relics were locally described (Leyreloup et al., 1996) and suggest that the boundaries of the subduction complex do not coincide with the major collisional to post-collisional tectonic lineaments that divide the western and central-eastern M-T.

In light of this, during the structural and petrological investigation of the Bormes Unit, attention was paid to identify other pre-collisional relics and to discuss the tectonic setting under which they developed. This chapter presents preliminary results, which show the need to extend the petrological-structural analysis undertaken for this sector to the regional scale for inferring a significant tectono-metamorphic outline for the western M-T. The comparison between the western M-T with the Orobic

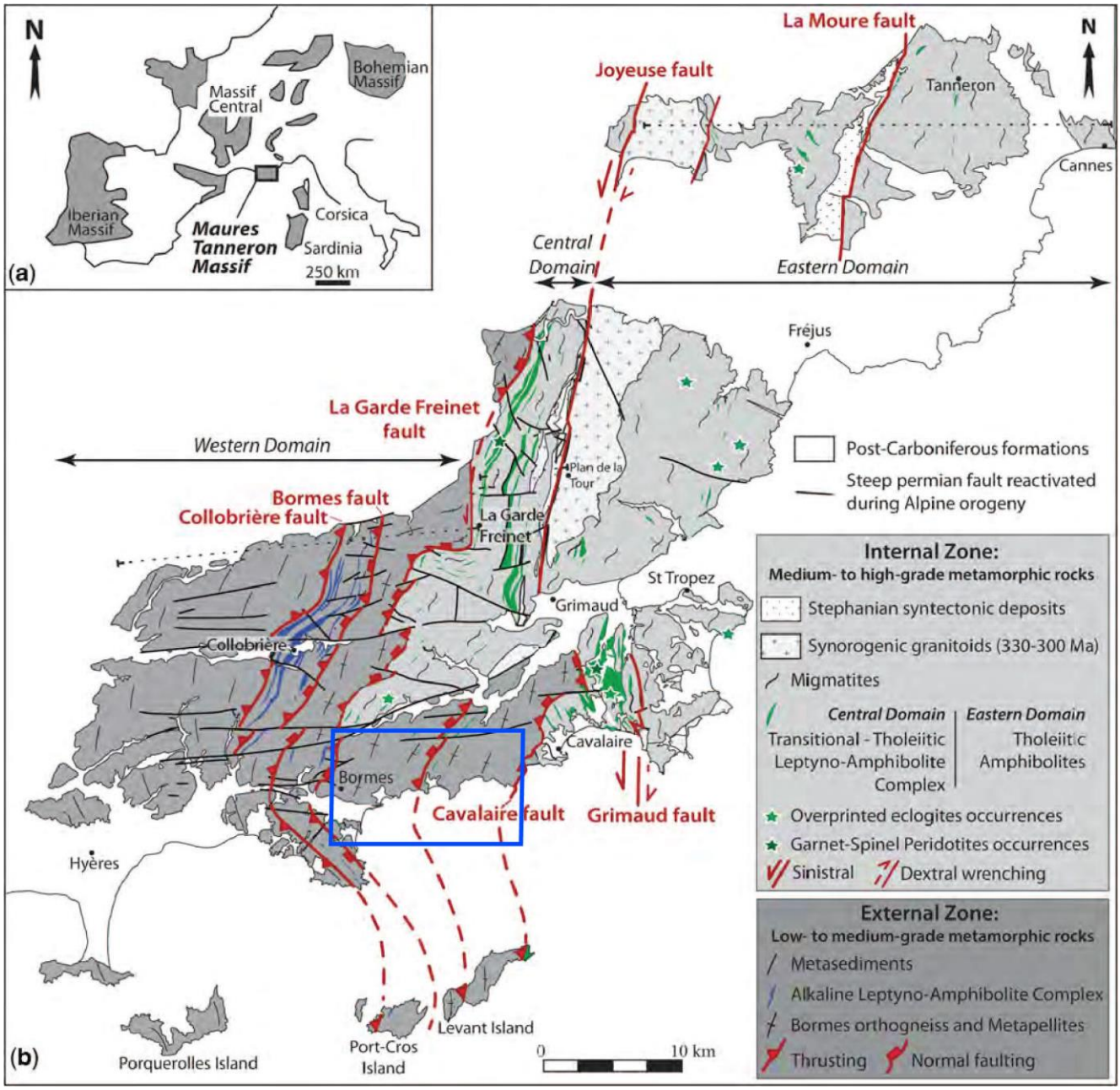

Figure. 2.2.1. The Maures-Tanneron Massif, divided in Western, Central, and Eastern domains (Schneider et al., 2014). The blue rectangle locates the studied area (see also Fig. 2.2.2).

basement of the central Southern Alps (see the previous chapter) is of interest for this thesis because both basements record the Variscan collisional and post-collisional evolution under similar P-T conditions, in similar times (Spalla and Gosso, 1999; Schneider et al., 2014; Oliot et al., 2015), but on opposite sides with respect to the Variscan subduction complex occurring in the eastern M-T (Fig. 2.2.1) and in the Helvetic, Peninic and Austraolpine domains in between.

Geological Setting

The western Maures-Tanneron Massif

The western part of the M-T is mostly composed of poly-deformed and poly-metamorphosed sedimentary sequences (meta-pelites, meta-arenites, quartzites), and orthogneisses (Fig. 2.2.1), which derive from Middle Silurian sedimentary sequences (Gueirard et al., 1970) and pre-Cambrian granites ("the Bormes orthogneiss", Bellot et al., 2005; Schneider et al., 2014 and ref. therein). In the more external parts of the western M-T, the Collobrières complex comprises late Cambrian bimodal alkaline meta-volcanics representing a Leptyno-Amphibolite complex that is a possible marker of the Variscan suture (Briand et al., 2002 and ref. therein). Small amphibolite lenses included in metapelites are described in many parts of the western M-T (Briand et al., 2002). They are interpreted as meta-gabbro and meta-andesite of unknown protolith age, geochemical affinity, and tectonic setting (Bellot et al., 2003).

Transposed compositional layering in meta-sediments allow recognizing the effects of two main folding events (D1 and D2), associated with superposed foliations and developed during the Variscan collision. Folds and foliations are evident in the westernmost part, in which the compositional layering in metasediments (SL) is not completely transposed as in the easternmost part.

D2 is responsible for folds with N30° westward dipping axial surfaces (PA2), axial plane foliations (S2), and sub-horizontal axes (A2). Several syn-D2 mylonitic shear zones are recognized (Collobriere, Bormes, La Garde Freinet, Cavalaire faults) and interpreted as the boundaries between homonymous tectonic units (Schneider et al., 2014). These mylonites dip westward and accommodate top-to-the-SE shearing (Schneider et al., 2014 and ref. therein). These shear zones were reactivated as top-to-the-NW ductile normal faults during the successive D3 stage, which produced folding in the inner parts of the massif during late-to post-collisional stages (Schneider et al., 2014 and ref. therein).

Barrovian metamorphism (M1) affected the western M-T and is supposed to be syn-kinematic with late D1 and lasting until the end of D2. The metamorphic field gradient increases from west to east in the pile of tectonic units, with isograde located in proximity of the main shear zones bounding the main tectonic units (Schneider et al., 2014). West of the Collobrière Fault, Chl + Cld- and Bt + Grt-bearing metapelites and meta-arenites occur, whereas St + Grt + Ky ± Sill- bearing metapelites have been found between the Bormes Fault and the Cavalaire Fault in the Bormes Unit.

Peak metamorphic conditions during D2 are supposed to have increased from west to east from T = 430°C - P = 0.5 GPa to T = 610°C - P = 0.7 GPa, by entering the sillimanite zone in the easternmost

part of the Bormes Unit (Schneider et al., 2014 and ref. therein). The D2/M1 stage, i.e. the Variscan collision, is dated between 352 and 339 Ma (Moussavou, 1998; Oliot et al., 2015).

Thermobarometric estimates on amphibolite lenses at Port-Cros Island in the western M-T suggest that higher peak conditions (T = 700°C and P = 0.7 GPa), were likely reached at the end of D1 (Bellot et al., 2003), in contrast with the observed metamorphic field gradient. In addition, some metapelite lenses included in orthogneiss in the Bormes Unit preserve pre-D2 white-schist assemblages that developed at T = 480-550°C and P = 1.2 – 1.6 GPa (Leyreloup et al., 1996).

The HT-LP late- to post-collisional stages are not testified in the western M-T, except for "a second generation of sillimanite" in rocks near the Cavalaire Fault (Schneider et al., 2014). D3 structures developed under greenschist facies conditions (M3), in contrast with the central and eastern M-T where D3 occurred under HT – LP (M2) and HT – very LP (M3) amphibolite facies conditions (Schneider et al., 2014). Simonetti et al. (2020) group together D2 and D3 as a single deformation event localized along the Cavalaire fault, which started deforming under Barrovian conditions at around 323 Ma and recorded "retro-metamorphism" from amphibolite to greenschist facies conditions.

The central Maures-Tanneron Massif

The central domain east of the Cavalaire fault comprises meta-igneous, meta-sedimentary, and meta-volcanic rocks affected by widespread partial melting and intruded by the Carboniferous Hermitan granite during D3 (Moussavou, 1998; Schneider et al., 2014). The main feature of this segment of the M-T is the occurrence of a second Leptyno-Amphibolite complex, the Les Arcs - Gassin complex, which consist of tholeiitic to transitional amphibolites and alkaline orthogneiss (Fig. 2.2.1). These rocks are interpreted as resulting from bimodal magmatism, characterizing a very late Proterozoic back-arc domain (Briand et al., 2002; Innocent et al., 2003 and ref. therein).

Here, the dominant S2 is affected by north-south trending F3 folds associated with an axial plane foliation S3 N340-N020 directed and steeply dipping, with sub-horizontal stretching lineation.

The occurrence of HP relicts in amphibolitic boudins near to the Leptyno-Amphibolite complex is debated (Bard and Caruba, 1981; Bellot et al., 2010) and syn-subductive high-pressure metamorphism (M0) is constrained in small lenses of spinel and garnet/spinel peridotite (Bellot et al., 2010). The amphibolite facies metamorphism (M1) is dated at 348 Ma (Innocent et al., 2003) and it is followed by syn-D2-D3 granulite facies metamorphic imprint (M2) and syn-D3 HT /very low P re-equilibration (M3) (Schenider et al., 2014). The D3 phase is thus associated with a strong increase of the thermal state, in contrast with the western M-T. In the central M-T, the M2 event has been dated between 332 and 303 Ma (Corsini et al. 2010 and ref. therein).

The eastern Maures-Tanneron Massif

Widespread partial melting affected this sector of the massif during D2 and D3. The Variscan migmatites contain sillimanite, cordierite and garnet, developed at metamorphic peak conditions; HP relics (M0) are locally preserved within the migmatites (Schneider et al., 2014).
The Joyeuse–Grimaud and La Moure faults are the most prominent structures and developed during D3. Syn-tectonic tonalites and calc-alkaline granites dated 338 – 334 Ma emplaced along these shear zones (Moussavou, 1998; Demoux et al., 2008). In the migmatites, PA3 and axial plane foliation (S3) are generally pervasive, N10 trending, and with sub-horizontal stretching lineations. Two Late Carboniferous intra-continental basins are parallel to the Joyeuse–Grimaud and La Moure faults and have been deformed by north–south-trending folds and top-to-the-west thrusts (Rolland et al., 2009 and ref. therein). Lastly, peraluminous granitoids and mafic dykes emplaced between 320 and 295 Ma (Duchesne et al., 2013 and ref. therein).

The Maures-Tanneron Massif in the European Variscan framework

In the last years, many efforts have been made to correlate the M-T with Sardinia, considering that these parts of the Southern Variscan belt were broadly contiguous in pre-Oligocene times (Séranne, 1999). These correlations mostly consider similar rock associations, structural relationships, kinematic interpretations, and geochronological records (e.g. Schneider et al., 2014; Simonetti et al., 2020).
A possible correlation with the Argentera-Mercantour Massif (External Crystalline Massifs of Western Alps) is envisaged by Jouffray et al. (2020) who suggest that both these massifs were part of the same suture zone together with Corsica and Sardinia, highlighting similarities between HP metamorphic rocks in all these domains. Paleomagnetic data confirm a common evolution of the Maures-Estérel-Corsica-Sardinia (MECS) block that coherently moved in the late Carboniferous (Edel et al., 2018 and ref. therein), which likely included the Argentera-Mercantour Massif (Simonetti et al., 2020). On the other hand, possible correlations with the Variscan basement of the Alps out of the External Crystalline Massifs, for example the Southern Alps, are poorly investigated (von Raumer et al., 2013).

Rock types and structural analysis

Field mapping was carried out in the Bormes Unit, from Le Lavandou to the west to Le Canadel to the east, in the western M-T (Fig. 2.2.2). The purpose was unravelling the finite strain pattern of this unit and individuating outcrops preserving the largest number of superposed structures.

In the western sector, the Bormes orthogneiss is the dominant rock type and is mostly composed of plagioclase, quartz, K-feldspar, and biotite and includes deformed mafic enclaves (Fig. 2.2.3A). Biotite- and white mica- bearing gneisses occur between the orthogneisses and metapelites. S2 is the dominant foliation in the Bormes orthogneiss and is supported by biotite, with rare white mica in cleavage domains, and by shape preferred orientation of quartz, plagioclase, and elongated K-feldspar grains in the micro-lihtons (Fig. 2.2.3A). Deformation partitioning during D2 is responsible for the alternance of mylonitic and tectonitic horizons. In the low-strained domains, early S1 planes are locally preserved as rootless F2 fold hinges. Where D2 has not pervasively transposed the previous structures, S1 marks the contact between the Bormes orthogneiss and the metapelites (FIG. 2.2.3B). In the Bormes orthogneiss, S1 is supported by plagioclase, quartz, biotite, and rare white mica.

Metapelites are widespread in the eastern sector of the Bormes Unit, where S2 is the dominant foliation and it is supported by up to centimeter-size crystals of staurolite, kyanite, biotite, white mica and garnet (Fig. 2.2.3C). Fine-grained micaschists, with abundant white mica and minor biotite and tourmaline, are found west of Col du Canadel, near the biotite- and white-mica-bearing gneisses.

Metapelites are compositionally heterogeneous and locally have meter-thick layers of meta-arenites and minor quartzites. Such alternance becomes more evident moving towards the western part of the investigated area. Re-activated and transposed lithological boundaries between metapelites and meta-arenites (SL) are good markers for unraveling the illusory structural simplicity of the metapelites in the high-strain domains. SL is affected by at least 4 superposed groups of folds and foliations (D pre-1, D1, D2, D3). D pre-1 and D1 structures are evident only where S2 is poorly developed.

The key outcrop for observing the structural complexity is Plage de Saint-Claire, in the westernmost sector of the area (Fig. 2.2.2). In this locality, S2 is dominant in meter-thick metapelite layers and supported by up to centimeter-sized kyanite, and millimeter-sized staurolite, biotite, and white mica crystals. Folded and transposed SL defines the boundary between metapelites and voluminous meta-arenite and quartzite layers. Superposition of F1 and F2 on SL (Fig. 2.2.3D) results in Type-2 interference patterns (Ramsay and Huber, 1987), with pre-F1 hinges of sub-centimeter size rarely preserved on F1 flanks (Fig. 2.2.3D). Progressive wavelength reduction of F2 results in very tight Type-2 patterns that could be mistaken for sheath folds.

At Plage Saint-Claire, small volumes of biotite- and garnet-bearing amphibolites are interlayered with meta-arenites and quartzites by transposed SL. In amphibolites, compositional layering of leucocratic and mafic-rich layers of sub-centimeter thickness (Fig. 2.2.3E), is intersected by S2. Similarly, Bellot et al. (2003) described amphibolite lenses in meta-sediments at Port-Cros Island and west of the Grimaud Fault in the northern Bormes Unit (Fig. 2.2.1), but without garnet.

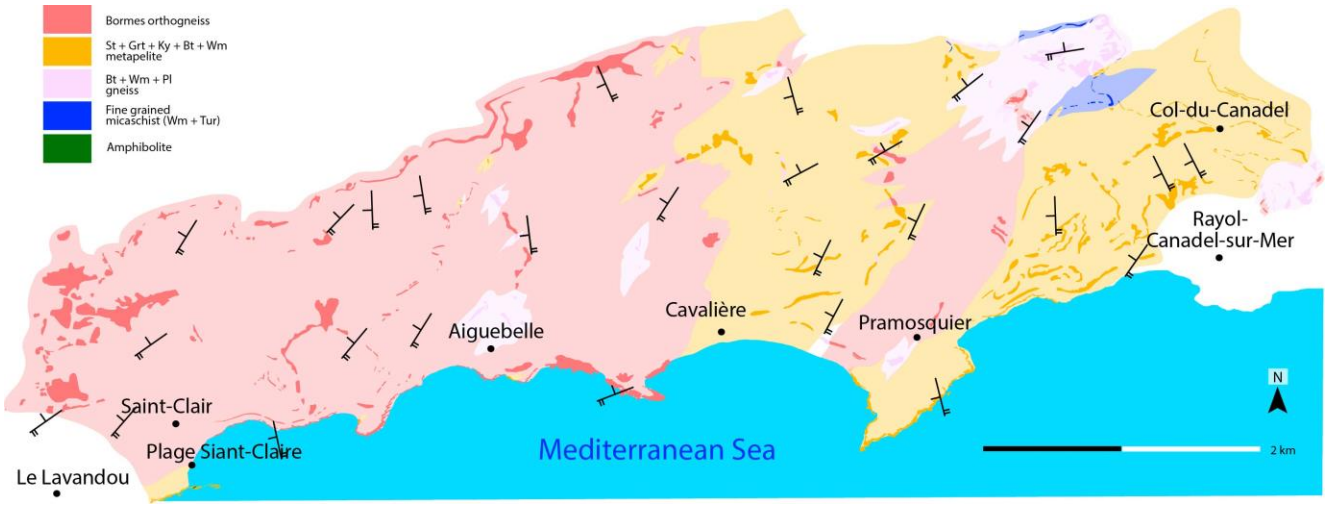

Figure 2.2.2. Geological sketch map of the Bormes Unit in western Maures-Tanneron Massif.

Andalusite-bearing pegmatites are abundant in the metapelites of the eastern Bormes Unit at Col du Canadel and Plage du Rayol, where they are parallel to S2 and they are locally boudinaged in S2 (Fig. 2.2.3F). These pegmatites do not display an internal foliation. Structural relationships between pegmatites and S2 suggested that these pegmatites emplaced before the end of the D2 stage. Field relationships between pegmatites and pre-D2 structures have not been observed.

S2 in both orthogneisses and meta-sedimentary sequences is affected by late D3 folding. D3 folds are of centimeter wavelength and sporadically observed all around the mapped area, mostly localized in the eastern part. A crenulation cleavage supported by chlorite rarely occurs.

In all the investigated area, PA2 and S2 are NE-SW striking, clustering at 310/45 in all the lithotypes, with 240/20 dipping A2 axes (Fig. 2.2.4). D3 folds are characterized by axial planes dipping 60 to 200 with 285/35 plunging axes (Fig. 2.2.4). Usually, SL and S1 are parallelized to S2.

Microstructural analysis

Metapelites at Col du Canadel retain 4 foliations – S pre-1, S1, S2, and S3 – that result from the superposition of Dpre-1, D1, D2, D3 stages (Fig. 2.2.5A, Tab. 2.2.1). S2 is the dominant foliation and it is supported by shape-preferred orientation of staurolite (St II), garnet (Grt II), kyanite, biotite (Bt II), ilmenite, white mica (Wm III), tourmaline, and quartz. S2 is internal foliation in Grt II, St II and kyanite porphyroblasts (Fig. 2.2.5B), as well as in anhedral grains of syn- to post-tectonic plagioclase (Pl II). Internal foliation S2 is supported by Bt II, Wm III, ilmenite, quartz and graphite trails. In rock matrix, S2 is crenulated by D3 (Fig. 2.2.5A) and crosscut by localized shear planes (S3), mostly supported by chlorite.

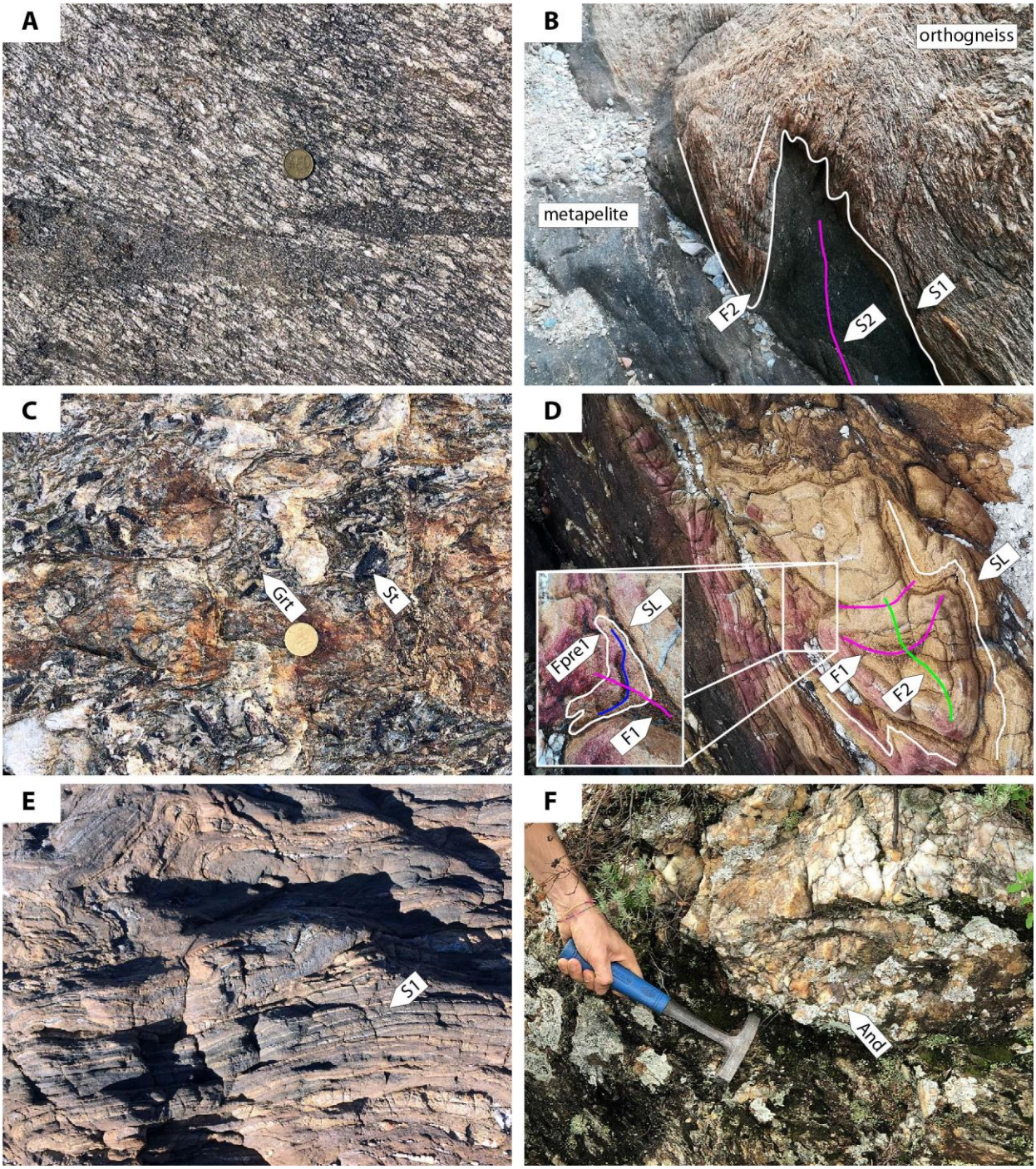

Figure 2.2.3. Photographs of rock types in the Bormes Unit (Western Maures-Tanneron Massif). A: S2 foliation in the Bormes orthogneiss with mafic enclaves. B: Contact between the Bormes orthogneiss and metapelites at Plage de la Fossette. The contact is parallel to S1 foliation and is folded by D2. S1 is preserved only in the orthogneiss, whereas S2 is pervasively developed in metapelites. C: garnet- and staurolite-bearing metapelites at Col du Canadel. D: Type-2 interference patters between F1 and F2 folds in metapelites at Plage Saint Claire. E: garnet-bearing amphibolites at Plage Saint Claire. F: Andalusite-bearing pegmatite in metapelites at Col du Canadel.

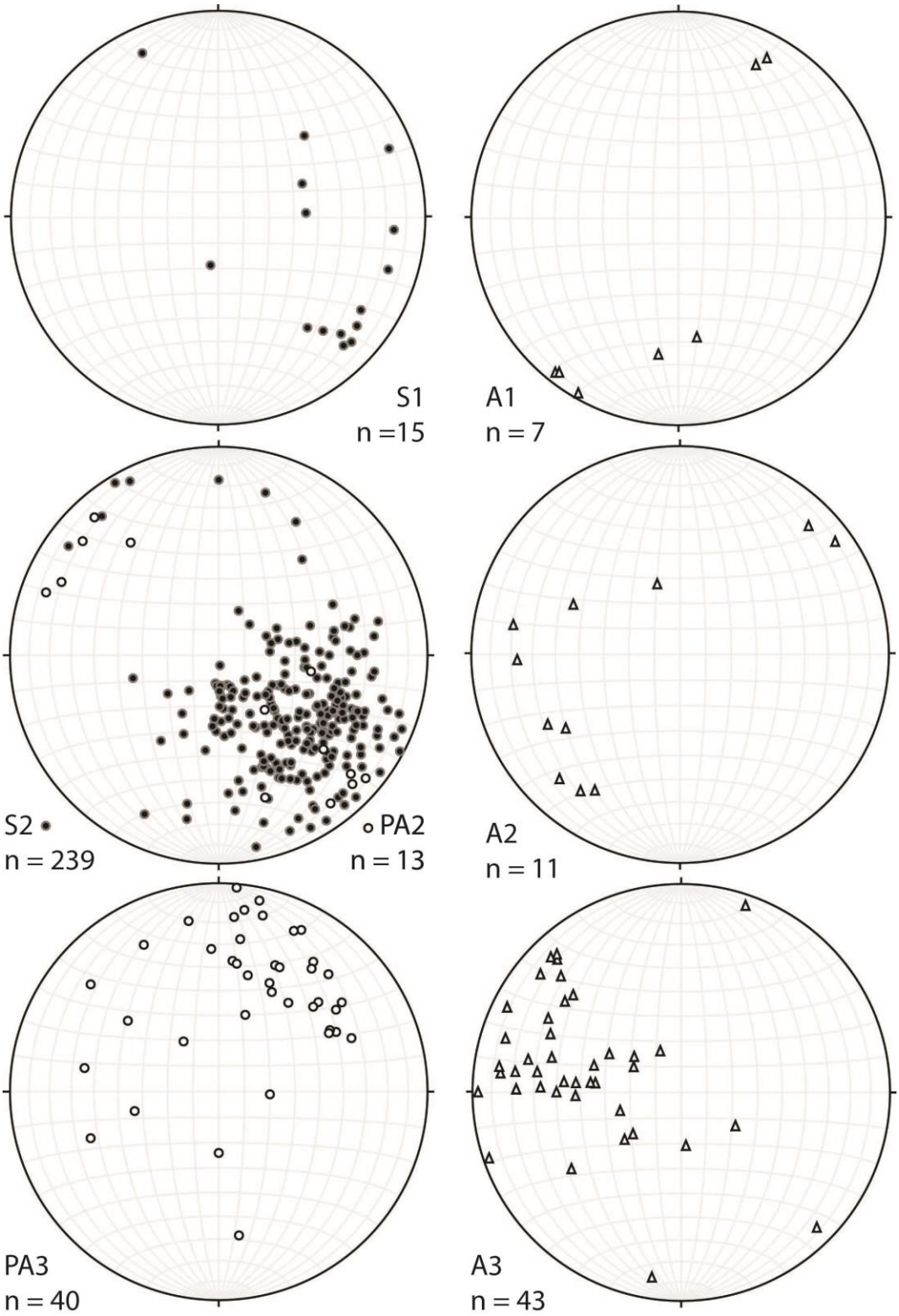

Figure 2.2.4. Stereographic projections (Schmidt equal-area, lower hemisphere) of structural data, including compositional layering (SL) and dominant Variscan foliation (S2), Variscan (A1, A2, A3) fold axes and axial planes (PA2, PA3), grouped by relative chronology.

Porphyroclasts of Grt I, St Ia (Fig. 2.2.5C), and Pl I are wrapped by S2. Bt II, Wm III, and quartz fill pressure-shadows domains around porphyroclasts. Grt II and St II form inclusion-free rims around Grt I and St Ia, respectively. St Ia is boudinaged by S2 and St II rims StIa in boudin necks (Fig. 2.2.5D).
In microlithon domains, crenulated S1 is marked by decussate grains of plastically deformed Bt Ia and Wm II. Straight or gently folded S1 is also preserved as internal foliation in Grt I and St Ia porphyroclasts (Fig. 2.2.5A, C, D, and E). In Grt I, internal S1 is supported by elongated grains of St Ib, Bt Ib, ilmenite, graphite trails and quartz (Fig. 2.2.5E); in St Ia, internal S1 is supported by ilmenite, graphite trails and quartz (Fig. 2.2.5C and D). In both cases, internal S1 is discontinuous with the external S2. In Grt II, St II, and Pl II internal S1 is folded by D2 and crosscut by straight S2, which is continuous with the external S2. In Pl II, internal S1 is supported by tourmaline, rutile, Wm II, and graphite trails (Fig. 2.2.5F). In very rare cases, fibrous sillimanite is found in the rock matrix (Fig. 2.2.5G), or is included in Grt II likely replacing biotite.
S pre-1 is preserved as internal foliation in Grt I and St Ia poprphyroclasts, where it is crenulated by D1 (Fig. 2.2.5C and E). In Grt I, S pre-1 is supported by graphite trails, quartz, ilmenite, and plastically deformed crystals of margarite (Wm I). In St Ia, S pre-1 it is supported by graphite trails, ilmenite and quartz.
Metapelites at Plage Saint-Claire are similar in structure and mineral assemblage to the metapelies at Col du Canadel, even if the D3 folds are poorly developed. Here, two generations of kyanite are observed: the first (Ky I) is relict with respect to the dominant foliation S2 together with garnet (Grt I), biotite (Bt I), white mica (Wm II), staurolite (St I), and ilmenite, whereas the second support S2 together with staurolite (St II), garnet (Grt II), biotite (Bt II), ilmenite, white mica (Wm III), tourmaline, and quartz. Sillimanite does not occur at Plage Saint Claire.
Garnet-bearing amphibolites at Plage Saint-Claire are formed by amphibole, titanite, plagioclase, quartz, epidote, biotite, and rare garnet. These rocks retain superposed S1 and S2 foliation: S1 is supported by compositional layering with amphibole- and biotite-rich layers interposed with plagioclase and epidote rich domains. S2 is supported by amphibole and biotite. Poikioblasts of plagioclase include garnet, biotite, and amphibole grains with shape preferred orientation along S1.

Mineral chemistry

Mineral chemical analyses are performed at Università degli Studi di Milano with a JEOL 8200 Super Probe (WDS) at 15 kV accelerating voltage and with a current beam of 5 nA; natural silicates served as standards. The analyzed samples are metapelites from Col du Canadel, in the westernmost part of the Bormes Unit (Fig. 2.2.2) Garnet formula is calculated at 8 cations and 12 O, biotite and white mica

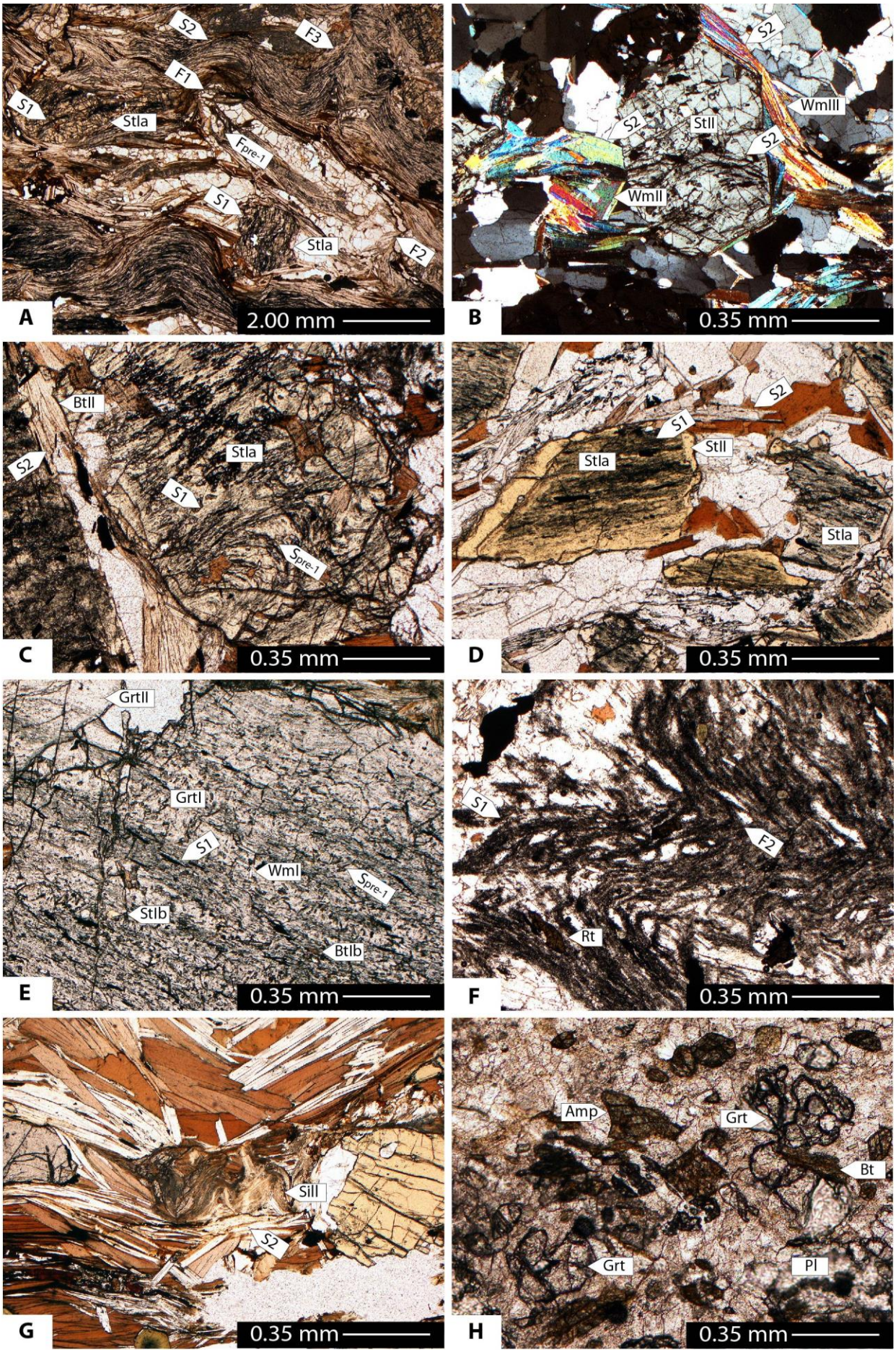
S2
F3
F1
S1
Stla
Fpre-1
S1
Stla
F2
2.00 mm
A
S2
WmIII
S2
StII
S2
WmII
0.35 mm
B
BtII
S2
Stla
S1
Spre-1
0.35 mm
C
S2
S1
StII
Stla
Stla
0.35 mm
D
GrtII
GrtI
S1
WmI
Spre-1
StIb
BtIb
0.35 mm
E
S1
F2
Rt
0.35 mm
F
Sill
S2
0.35 mm
G
Amp
Grt
Bt
Grt
Pl
0.35 mm
H

Figure 2.2.5. Microstructures of metapelites at Col du Canadel (plane polarized light). A: finite strain pattern resulting from superposition of 4 folding events (F pre1, F1, F2, F3). Crenulated S2 is the dominant foliation. S2 wraps pre-tectonic porphyroclasts of St Ia with internal foliation (S1) discontinuous with the external S2. B: syn-S2 St II porphyroblast including early S2 as internal foliation and wrapped by late S2. C: St Ia porphyroclast wrapped by Bt II-beraing S2. The internal foliation in St Ia (S1) is discontinuous with external S2. Microhinges of an older crenulated foliation (S pre-1, mostly supported by graphite trails) are preserved in St Ia. D: inclusion-rich porphyroclasts of St Ia boundinaged in S2. Inclusion-free St II rims St Ia, also in the boudin neck domain. Internal foliation in St Ia is evidenced by graphite trails and ilmenite. E: porphyroclast of Grt I (wrapped by S2) with internal S1 foliation discontinuous with the external one. S1 is supported by St Ib, Bt Ib, ilmenite, quartz and graphite trails. Crenulated S pre-1 is preserved in microlithons and supported by graphite and Wm I. Grt I is rimmed by inclusion-free Grt II. F: Folded S1 as internal foliation in Pl II. S1 is supported by rutile, quartz, biotite, and graphite trails. G: dominant S2 foliation supported by Bt II, Wm III, and St II. Aggregates of fibrous sillimanite resembling folded films mimic an earlier mineral phase. H: poikiloblast of plagioclase including amphibole, garnet, and biotite, in a retrogressed garnet-bearing amphibolite.

at 22 O, staurolite at 46 O, chlorite at 7 O, and plagioclase at 4 O. Compositional parameters are summarized in Figure 2.2.6 and briefly discussed in the text. The mineral chemical dataset is supplementary data V.

Grt I, which includes S1 internal foliation, is $Alm_{68-72}Py_{11-12}Grs_{12-16}Spess_{2-6}Andr_{0-3}$. Grt II, which rims Grt I and forms new grains including S2 as internal foliation, is $Alm_{73-74}Py_{10-12}Grs_{8-11}Spess_{4-6}Andr_{0-2}$. Grt II rims are characterized by the highest Fe^{2+} and lowest Ca content, with minor Mn increasing ($Alm_{75-77}Py_{11-13}Grs_{2-7}Spess_{6-8}Andr_{0}$).

Variations in Al content characterized the different generations of staurolite in different microstructural sites: Al is 17.24 – 17.47 pfu in St Ia, 17.65 – 17.91 in St Ib, and 17.43 – 17.82 pfu in St II. Variations of Mg# (0.10 – 0.19) and Zn content (0 – 0.53 pfu) are likely due to different bulk rock compositions, testified by plagioclase only in some samples. Pl I is An29-37 and Pl II is An24-25.

Bt Ia is characterized by Mg# = 0.41 – 0.49, Ti = 0.16 – 0.23 pfu, and Al^{VI} = 0.90 – 1.12 pfu, Bt Ib by Mg# = 0.36, Ti = 0.16 pfu, and Al^{VI} = 1.15 pfu, and Bt II by Mg# = 0.41 – 0.47, Ti = 0.14 – 0.24 pfu, and Al^{VI} = 0.84 – 1.11 pfu. In plagioclase-bearing metapelites, biotite is Fe-richer than in plagioclase free-samples.

WmI is margarite, with Si = 4.08 – 4.13 pfu, Ca = 1.71 – 1.82 pfu, Fe = 0.09 – 0.11 pfu, and Mg = 0.03 – 0.06 pfu. WmII is characterized by Pg = 0.14 – 0.16, Si = 6.16 – 6.21 pfu, Fe = 0.09 – 0.12 pfu, and Mg = 0.08 – 0.13 pfu. In plagioclase-bearing samples, Wm III is characterized by Pg = 0.11 – 0.17, Si = 6.17 – 6.38 pfu, Fe = 0.09 – 0.13 pfu, Mg = 0.08 – 0.19 pfu; in plagioclase free samples, Wm III is Na-richer (Pg = 0.17 – 0.21) and slightly Si (6.11 – 6.18 pfu), Fe (0.07 – 0.12), and Mg

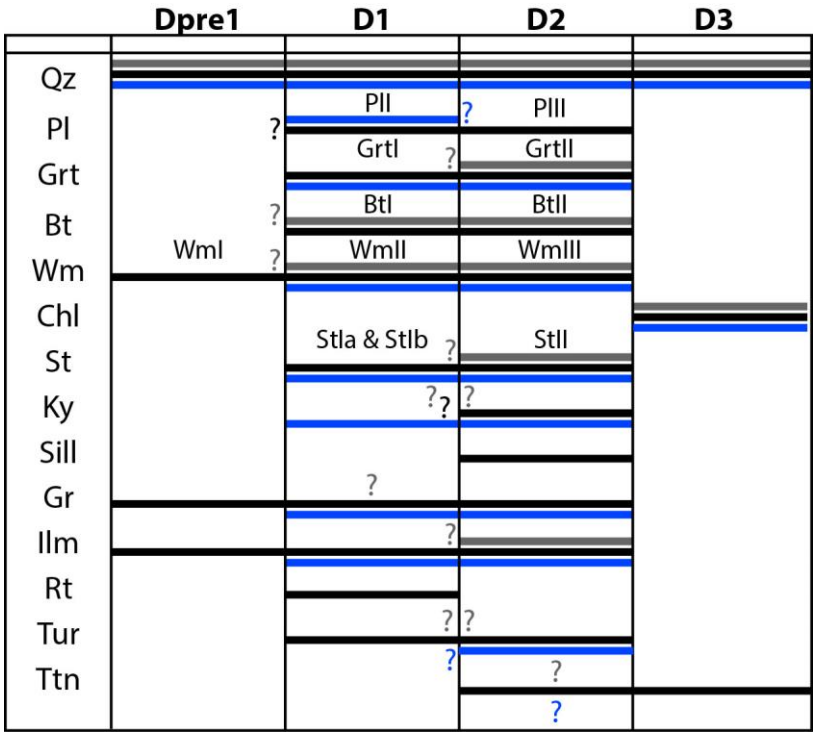

Table 2.2.1. Foliation-forming deformation event versus mineral growth in metapelites of the Bormes Unit, western M-T. Black: plagioclase-bearing metapelites from Col du Canadel; gray: plagioclase-free metapelites from Col du Canadel; Blue: plagioclase-bearing metapelites from Plage Sainte-Claire.

(0.06 – 0.10 pfu) poorer than in plagioclase-bearing samples. Chlorite is characterized by Mg# = 0.38 – 0.50 and Al^{IV} = 1.39 – 1.49 pfu.

Since St Ib and Bt Ib supporting internal S1 in Grt I are richer in Al compared to St Ia and Bt Ia supporting S1 in the rock matrix, we supposed that an association comprising Grt I, St Ib, and Bt Ib has completely overgrown an Al- (and maybe Fe-) rich mineral phase, which likely co-existed with Wm I (margarite). Chloritoid is the main suspect, but it has not been indentified yet. Further investigations are in progress.

M**etamorphic evolution and P-T estimates**

Metamorphic conditions during progressive stages of fabric development at Col du Canadel are estimated by classic thermobarometry. Ti-in biotite thermometry (Henry et al., 2005) gives T = 550 ± 30°C for D1 and T = 580°C ± 30°C for D2. Application at convergence of Ti-in biotite thermometry (Wu and Chen, 2015) and biotite-muscovite barometry (Si-Al in muscovite and Fe-Mg-Al-Ti in biotite, Wu, 2020) led to T = 560 ± 50°C and P = 0.6 ± 0.2 GPa for D1, and T = 590 ± 50°C P = 0.7 ± 0.2 GPa for D2. Staurolite-garnet thermometry (Fe-Mg, Perchuck, 1991) suggests slightly higher

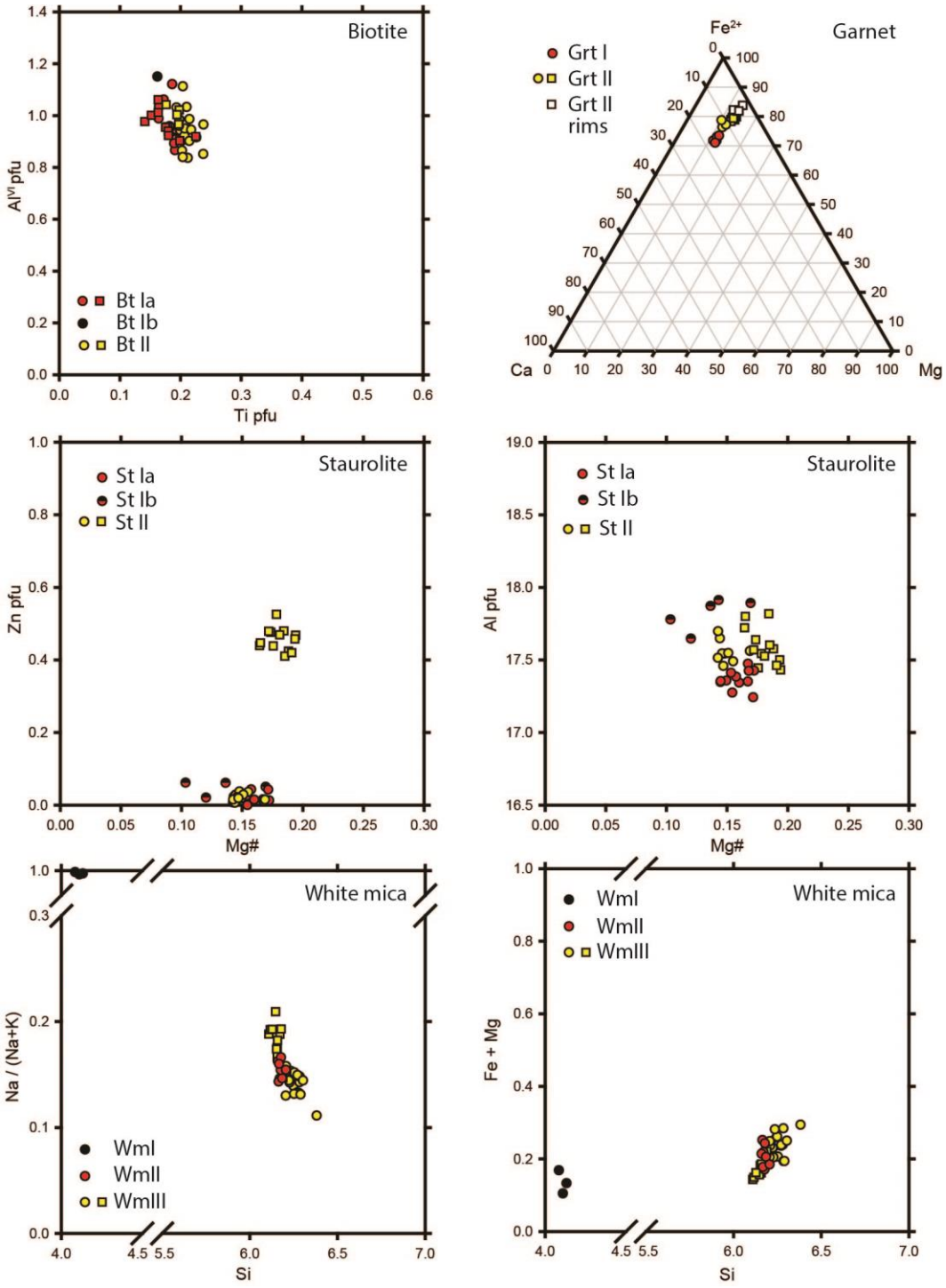

Figure 2.2.6. Composition of minerals in metapelites at Col du Canadel. Circles = plagioclase-bearing samples; squares = plagioclase-free samples.

temperature (T = 600 ± 50°C) during D1, than during D2 (T = 580 ± 50°C). Similarly, biotite-garnet thermometry (Fe-Mg, Perchuck and Lavrent'eva, 1983) indicates T = 630 ± 30°C for D1 at P = 0.6 GPa, and T = 610 ± 30°C for D2 at P = 0.7 GPa. The occurrence of fibrous sillimanite constrains the

metamorphic peak conditions at T > 550 ± 35°C and P > 0.45 ± 0.05 GPa during D2 (Bucher and Frey, 2002 and ref. therein).

On the contrary, there is little constrain on the pre-D1 phase, since pre-D1 mineral assemblages are extremely poorly preserved (quartz + margarite + graphite + ilmenite). In the H_2O – CaO –Al_2O_3 – SiO_2 system, the association margarite + quartz has an upper thermal stability of 635°C and an upper-pressure stability of 0.85 – 1.10 GPa (Jenkins, 1984), which is the main physical constrain on metamorphism during D pre-1. The emplacement of andalusite-bearing pegmatites in the pre-D2 phase requires a re-equilibration step at P < 0.45 ± 0.05 before the metamorphic peak at around 0.7 GPa (Bucher and Frey, 2002 and ref. therein).

Discussion and conclusion

Metapelites from Col du Canadel retain two deformation events (D1 and D2) developed under Barrovian metamorphic conditions. The pre-existing S1 foliation is supported by Grt I, St Ia / St Ib, Bt Ia / Bt Ib, Wm II and Pl I, while the successive S2 foliation is supported by Grt II, St II, Bt II, Wm III, ilmenite, tourmaline, quartz and kyanite. Pl II is from syn- to post-tectonic with respect S2. Both S1 and S2 developed at 550 – 600°C and P = 0.6 – 0.7 GPa (Fig. 2.2.7), confirming the result from the literature (Schneider et al., 2014 and ref. therein). Development of kyanite during D2 and not during D1 may suggest a slight increase of metamorphic conditions from D1 to D2, as also suggested by fibrolitic sillimanite that grew during D2 but after kyanite (Spear, 1995). The pre-D1 stage is poorly constrained due to scarce preservation of S pre-1 as internal foliation in St Ia and Grt I. D pre-1 is constrained at P < 0.85 – 1.10 GPa, T < 635 °C. Andalusite bearing pegmatites predating D2 indicate P < 0.45 ± 0.05 in pre-D2 stages, likely attained during D pre-1 (Fig. 2.2.7) and allow to infer a prograde P-T path never described before.

On the contrary, kyanite grains in both S1 and S2 are found at Plage Saint Claire metapelites. Moreover, in garnet-bearing amphibolites, garnet is syn-tectonic with respect to S1 and relic with respect to S2. Both these evidences suggest that peak P-T conditions may have been reached during D1, and that D2 was attained during retrogression. Further mineral chemical analysis and thermo-barometric will need to refine the metamorphic evolution of metapelites and garnet-bearing amphibolites at Plage Sainte Claire and in other part of the Bormes Unit, and to discuss the tectonic setting compatible with the metamorphic environment under which D1 and Dpre-1 structures developed.

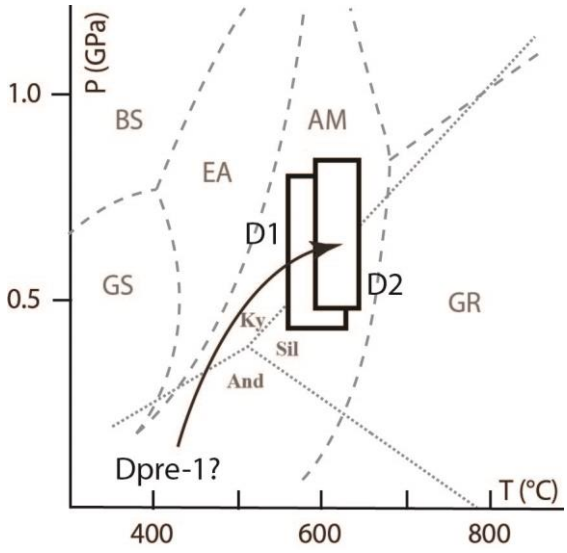

Figure 2.2.7. Variscan P-T path for metapelites at Col du Canadel.

2.3 Discussion Chapter 2

In this chapter, the investigation results on two areas of the Southern Variscan belt are critically presented: the thick-skin fold and thrust belt forming the central Southern Alps, in the core of the Alpine chain hinterland (Orobic basement), and the Bormes Unit, which is part of the western M-T, located in the Alpine foreland. The aim is to upgrade analytical records of pre- to post-Variscan ages in areas opposite with respect of the Alpine chain axis; here we will compare similar elements of the two Variscan geo-histories in order to evaluate correlation possibilities. The Orobic basement and the Bormes Unit are broadly similar in rock associations, since they are mostly composed of metapelites, minor orthogneisses, and rare amphibolites. Lithological, chronological, igneous, metamorphic, and stratigraphic characters of both these domains are summarized in Table 2.3.1.

In the Bormes Unit, the metapelites derive from Middle Silurian sedimentary sequences (Gueirard et al., 1970), the orthogneisses from pre-Cambrian granitoids (Bellot, 2005; Schenider et al., 2014 and ref. therein), and the amphibolites from Cambrian mafic rocks (Innocent et al., 2003). In the Orobic basement, the metapelites derive from Silurian-Ordovician sedimentary sequences (Gansser and Pantič, 1988), whereas the protolihts of the orthogneisses are probably Ordovician in age, but with inherited Ediacaran-early Cambrian ages (Boriani and Bini, 2012; Bergomi et al. 2004; Bergomi and Boriani, 2004). The age of the amphibolite protoliths is instead unknown. U-Pb dating of a detrital zircon grain within the metapelites (492 ± 25 Ma) confirms a minimum late Cambrian age for the sedimentary protoliths of the Orobic basement, whereas U-Pb dating of igneous zircon grains returns an early Cambrian age for the orthogneiss protoliths (531 ± 22 Ma).

In both the domains, the dominant structural and metamorphic imprint is related to collisional to post-collisional settings. In the eastern Bormes Unit, Barrovian amphibolite facies metamorphism (P = 0.6 – 0.7 GPa, T = 550 – 600°C) was attained during D1 and D2. S1 and S2 in metapelites are supported by Grt + Bt + St + Wm ± Ky ± Pl. These conditions match previous results of Bellot et al. (2003) on metabasite lenses all over the western M-T. Syn- to post-D2 sillimanite is only preserved in the eastern part of the Bormes Unit, suggesting that peak metamorphic conditions were reached at the end of D2. However, deeply retrogressed garnet-bearing metapelites have been individuated at Plage Saint-Claire, in the western part of the Bormes Unit. Since garnet grains are pre-tectonic with respect to S2, in this locality, peak metamorphic conditions were likely attained during D1. Consistently, kyanite supports both S1 and S2 in the western part of the Bormes Unit, whereas it is only found as support of S2 in the easternmost part. Finally, S2 was crenulated by D3 under greenschist facies conditions. The

	Orobic Basement	Bormes Unit	References
Lithostratigraphy	1 - Siliciclastic meta-sediments (meta-pelites, meta-arenites, and quartzites). 2 - Orthogneiss. 3 - Rare amphibolites.	1 - Siliciclastic meta-sediments (meta-pelites, meta-arenites, and quartzites). 2 - Orthogneiss. 3 - Rare amphibolites. 4 - Leptyno-amphibolite complexes.	Briand et al. (2002); Bellot et al. (2003); Caironi et al (2004); Bellot (2005); Boriani and Bini (2012); Gosso et al. (2012); Schneider et al. (2014).
Ages of the sedimentary protoliths	Silurian-Ordovician (< 495 ± 25 Ma)	Middle Silurian	Gueirard et al. (1970); Gansser and Pantic (1988).
Ages of acidic intrusives	475-462 Ma (with inherited ages of 600-510 Ma); 531 ± 22 Ma.	605-560 Ma	Bergomi (2004); Bellot (2005) and ref. therein; Boriani and Bini (2012) and ref. therein.
Metamorphic imprint and ages	Amphibolite facies conditions (T = 550-660°C, P = 0.7-1.1 GPa) at 350-330 Ma. Greenschist facies conditions (T = 440°C, P = 0.4 GPa) at 310 Ma.	Amphibolite facies conditions (T = 550-650°C, P = 0.6-0.8 GPa) at 360-330 Ma. Greenschist facies conditions (T = 350-500°C, P = 0.2-0.4 GPa) at 323 Ma.	Bocchio et al. (1981); Mottana et al. (1985); Colombo et al. (1997); Moussavou (1998); Spalla and Gosso (1999) and ref. therein; Bellot et al. (2003); Schneider et al. (2014); Oliot et al. (2015); Simonetti et al. (2020).
post-Variscan basins and sedimentary sequences	Late Carboniferous fault-controlled transpressive basins with continental clastics. Permian extensional continental basins with clastics and bimodal volcanics.	Lower Permian fault-controlled continental basins with clastics, pyroclastic, and lava-flows. Upper Permian alluvial sediments (post-tectonic).	Cadel et al. (1996); Bellot (2005) and ref. therein; Corsini and Rolland (2009) and ref. therein; Berra et al. (2011);

Table 2.3.1. Comparison between the Orobic basement and Bormes Unit, with results from this chapter and literature.

age of D2 has been constrained by U-Pb monazite and zircon dating between 360 and 330 Ma (Moussavou, 1998; Corsini et al., 2010; Schneider et al., 2014; Oliot et al., 2015).

Andalusite-bearing pegmatites are widespread in the eastern part of the Bormes Unit, where they intruded in metapelites. The pegmatites are coarse grained and not foliated. However, they are wrapped by the external foliation S2 and boudinaged. Intersection relationships between andalusite-bearing pegmatites and D1 structures have not been observed. For this reason, the andalusite-bearing pegmatites are considered pre-D2. In addition, since D1 and D2 developed under similar metamorphic

conditions, a pre-D1 age may be reasonably considered. However, this interpretation goes against observations of Buscail (2000), which describes fibrolitic sillimanite and andalusite replacing kyanite in the central part of the M-T, but this could be due to the occurrence of different tectono-metamorphic units in the MTM, mirroring what has been demonstrated in the Sudalpine basement (e.g. Spalla et al., 2014). More field and microstructural analysis integrated by petrology and geochronology is required to properly address this issue.

In the course of this multiscale structural analysis, most of the time has been spent in seeking, pre-D1 structures and pre-D1 mineral associations, to better define the boundaries of the Variscan subduction complex of the M-T and, subsequently, to compare the resulting pre-collisional evolution with that of the Orobic basement. This was addressed by a previous contribution by Leyreloup et al. (1996), which describe lenses of white schists within the Bormes orthogneiss, which preserve mineral associations developed under HP-LT conditions (P = 1.2 – 1.6 GPa, T = 480-550°C). However, none of these rocks was found during this investigation.

Pre-D1 structures are rare in the field, since fold isoclinalization and transposition of litho-stratigraphy during D2 is the rule in most parts of the Bormes Unit. In addition, syn-tectonic growth of centimeter-sized garnet, staurolite, and kyanite porphyroblasts during D1 and D2 obliterated most of the previous fabric. Pre-D1 folds are rarely observed where compositional layering between meta-arenites and metapelites is preserved and D1 and D2 folds are not isoclinal. Centimeter-sized domains preserving pre-D1 folds are found at Plage Saint-Claire. However, even in these domains, S1 and S2 are the dominant foliations in the metapelite layers making the chance of individuating pre-D1 mineral assemblages in rocks with suitable composition to estimate pre-D1 metamorphic conditions very low.

For this reason, the focus was towards the internal foliations preserved in the cores of syn-D1 garnet and staurolite porphyroclasts. In a few rare cases, sub-millimeter grains supporting pre-S1 foliation have been found in metapelites at Col du Canadel, in the eastern Bormes Unit. P-T estimates indicate that pre D1 occurred at P < 0.85 – 1.10 GPa and T < 635°C. At first sight, this result may be in contrast with the P-T estimates of Leyreloup et al. (1996) on pre-D1, and therefore it is not possible to correlate pre-D1 at Col du Canadel (LT – LP) and pre-D1 of Leyreloup et al. (1996) (HP – LT).

In the investigated part of Orobic basement, greenschist facies metamorphism was attained in a post-collisional setting, during which the dominant foliation S2 developed. Andalusite porphroblasts crystallized at the onset of D2, testifying a slightly perturbed thermal state that is interpreted as related to the post-collisional Variscan collapse. The Upper Permian Verrucano Lombardo formation is deposed on the basement rocks and constrains a minimum age for D2.

Pre-D2 foliations, S1a and S1b, are preserved in the metapelites. S1a is supported by Bt + Cld + Wm + Grt + Pl and S1b by Bt + St + Wm + Pl ± Grt. In the orthogneiss, S1b is supported by Wm + Bt + Pl

and wraps garnet prophyroclasts with S1a as internal foliation. Intersection relationships between S1a and S1b constrain the relative chronology between the deformation events. S1a firstly developed at T = 450 – 570°C and P = 0.65 – 1.00 GPa, then S1b at T = 550-640°C and P = 0.40 – 0.65 GPa. In the orthogneiss, garnet is stable at around the same conditions under which S1a developed in the metapelites.

S1b in the Orobic basement developed at around the same P-T conditions of S1 and S2 in the Bormes Unit of the M-T. The age of D1b in the Orobic basement is supposed to be ≥ 330 Ma (Siletto et al., 1993). Age and thermal state indicate that D1b was attained during the Variscan collision, which occurred in late Devonian – Lower Carboniferous time, simultaneously in every part of the European Variscan belt, including the M-T.

However, the age of the D1a event in the Orobic basement is instead an open issue. The only constrain is given by old Rb/Sr geochronological estimates (364 ± 15 Ma, Del Moro in Riklin, 1983). The thermal state attained during former D1a is compatible with continental subduction at lower pressure, as already suggested for other parts of the central Southern Alps (Spalla and Gosso, 1999; Spalla et al., 2014).

Even if the pre-collisional metamorphic evolution in the Bormes Unit is still poorly constrained and likely different from that of the Orobic basement, these two domains are pretty much similar in terms of litho-stratigraphy and tectono-metamorphic evolution, from Cambrian to Permian times. It is reasonable to try to correlate these two domains to propose a geodynamic scenario for the Southern Variscan belt.

The first hypothesis is that Bormes Unit in the western M-T and the Orobic basement of the Southern Alps where two opposed external domains of the Southern Variscan belt. However, this is unlikely because these domains experienced a similar and coeval tectonic evolution from Cambrian to Permian times and are characterized by similar litho-stratigraphy. This symmetrical configuraton would be in contrast with the reference models for subduction-collision orogens that are markedly a-symmetrical.

The second hypothesis is that the Bormes Unit and the Orobic basement were external domains of two different Southern Variscan belt. The poly-cyclic model for the Southern Variscan belt of Regorda et al. (2020) suggests that the Variscan basement rocks of the Alps may have experienced a different tectonic evolution from that of the French Central Massif, the latter correlated to the M-T by some authors (Bellot et al., 2005; Schneider et al., 2015). However, this model assumes that the continental collision occurred in two different time intervals, the first at around 373 Ma, the second at 337 Ma (Regorda et al., 2020). The first collision is testified in the French Central Massif (Lardeaux et al., 2001; Faure et al., 2008), but not in the M-T and neither in the Orobic basement where the continental

collision synchronously occurred at 360 – 330 Ma (Bocchio et al. 1981; Mottana et al. 1985; Bergomi and Boriani, 2004; Schneider et al., 2014; Oliot et al., 2015).

The third hypothesis is that the late- to post-Variscan tectonics might have led to dismemberment and relative rotation between two parts of the same external domain. The highlighted similarities between the Bormes Unit and Orobic Basement support that they were part of the same external domain of the Southern Variscan belt (Tab 2.3.1). There are some paleomagnetic constrains on the Southern Variscan belt, and in particular on the Maures-Tanneron, Estérel, Corsica and Sardinia (MECS) block (Edel et al., 2014, 2018). It is supposed that after the Carboniferous right transcurrence (e.g. Simonetti et al., 2020), the MECS block was affected by a clockwise rotation of 150° (Edel et al., 2014, 2018).

In the early Permian paleogeography, the external domains of the M-T were east of the internal zone (Edel et al., 2014, 2018). In this configuration (Fig. 8 in Edel et al., 2014), the Orobic basement is necessarily placed north of the MECS block including Calabria, and south of the Bohemian Massif. To accommodate the rotation, extension is required at northeast and that matches the ages of the Permian intracontinental basins of the Southern Alps, which rejuvenate from east to west (Zanoni and Spalla, 2018), and to the widespread extensional magmatic activity.

Chapter 3

The Variscan subduction complex in the Alps

The Argentera-Mercantour Massif

3.1 Variscan eclogites from the Argentera–Mercantour Massif (External Crystalline Massifs, SW Alps): a dismembered cryptic suture zone

Fabrice Jouffray, Maria Iole Spalla, Jean-Marc Lardeaux, Marco Filippi, Gisella Rebay, Michel Corsini, Davide Zanoni, Michele Zucali, Guido Gosso

IEJS 2020, 109, 1273-1294, 10.1007/s00531-020-01848-2

Abstract

We document structural, geochemical, petrological and $^{40}Ar/^{39}Ar$ geochronological data performed on Variscan eclogites from the Argentera-Mercantour Massif, southwestern Alps. Based on high-resolution field mapping, we present new eclogite occurrences and discuss the relationships between eclogites and surrounding migmatites. We recognized for the first time in this massif, preserved eclogite facies assemblages. Trace elements and REE patterns establish that eclogites protoliths are MORBs contaminated by continental crust. Standard thermobarometry and thermodynamic modeling are consistent with P-T values of 640-740°C for 1.5 ± 0.25 GPa, coherent with paleo-geotherms predicted for warm subduction of oceanic crust. We interpret these eclogites as a dismembered cryptic suture zone. $^{40}Ar/^{39}Ar$ dating on amphiboles yields an age of 339.7 ± 12 Ma for eclogite retrogression under amphibolite facies conditions. All these data are combined to link the Argentera-Mercantour Massif in the tectonic framework of both pre-Mesozoic Alpine basement and European southern Variscides.

Introduction

Studies on high pressure (HP) and ultra-high pressure (UHP) metamorphic rocks exposed in mountain belts provide first-order constraints for addressing evolution of orogens (Gerya et al., 2002 ; Ernst and Liou, 2008). In orogenic systems, mafic eclogites are of particular interest because, since Miyashiro (1961) and Ernst (1971), they are considered as records of old subduction zones. In the European Variscan belt, HP/UHP metamorphic rocks are widespread (Medaris et al., 1995; Ballèvre et al., 2009; Schulmann et al., 2009; Martinez Catalan et al., 2009; Lardeaux et al., 2014) and have been extensively considered to provide information on pre-continental collision plate tectonics framework (Matte, 2001; Schulmann et al., 2005, 2014; Franke et al., 2017).

Mafic eclogites are also exposed in Variscan basement slices preserved in the Alpine belt (Fig. 3.1.1 and Tab. 3.1.1; Spalla and Marotta, 2007; Spalla et al., 2014; Roda et al., 2019 with references therein). In the External Crystalline Massifs (ECMs) of the western Alps, as a consequence of Alpine reworking, eclogites that retain protolith geochemical signature and pre-alpine HP mineralogy are rare (von Raumer, 1984; Latouche and Bogdanoff, 1987; Bogdanoff et al., 1991; Ferrando et al., 2008; Rubatto et al., 2010). The Argentera-Mercantour Massif (Fig. 3.1.1) is the southernmost of the ECMs, within which the metamorphic evolution of mafic eclogites remains poorly constrained. We document here the discovery of preserved omphacite (jadeite contents up to 42 mol%) within the severely retrogressed eclogites of the Argentera-Mercantour Massif. Thus, the purpose of this paper is to present and discuss structural, geochemical, mineralogical, petrological and $^{40}Ar/^{39}Ar$ geochronological data on these Variscan HP metamorphic rocks.

Geological setting

The ECMs belong to the Helvetic-Dauphinois domain of the Alpine belt (Schmid et al., 2004), within which Alpine tectonic history has not significantly erased Variscan signatures (Von Raumer et al., 1999, 2009, 2013; Guillot et al., 2009; Compagnoni et al., 2010; Spalla et al., 2014; Fréville et al., 2018). The NW-SE elongated Argentera-Mercantour Massif is located at the boundary between France and Italy and covers an area of around 1000 km^2. It is a piece of European continental crust shortened and extruded in response to late Alpine collision (Polino et al., 1990; Bogdanoff et al., 2000; Schwartz et al., 2007; Schreiber et al., 2010).

Following the first geological investigations of Faure-Muret (1955), Malaroda and Schiavinato (1957, 1958, 1960) and Malaroda et al. (1970), the Argentera-Mercantour Massif was systematically divided into two main metamorphic untis (or complexes, or terranes depending on the authors, Bogdanoff et

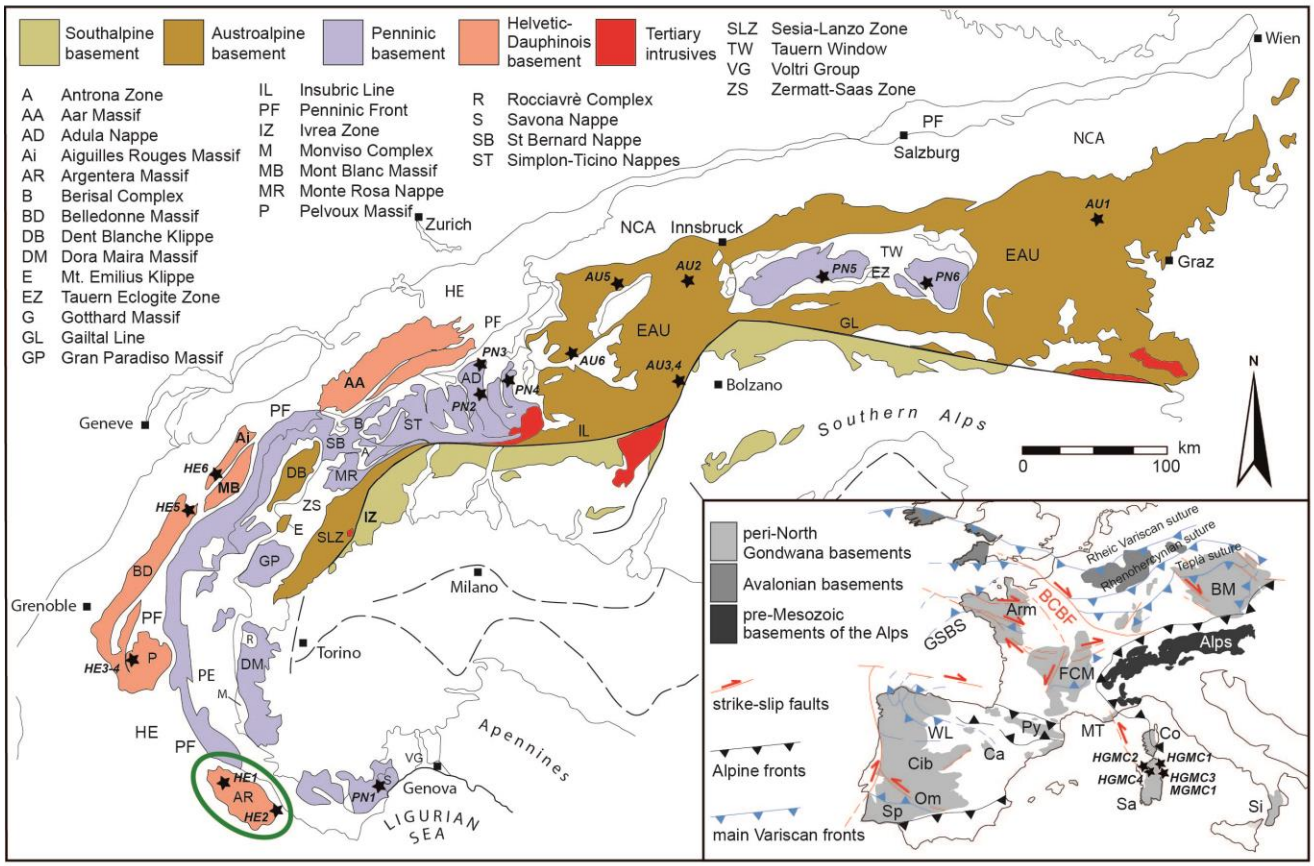

Figure 3.1.1. Location of the Argentera-Mecantour Massif in the Alpine arc (redrawn after Spalla et al., 2014; Regorda et al., 2019). Black stars locate the eclogites known in the pre-Alpine basements from different zones of the Alpine belt; star labels individuate Alpine and Sardinian eclogites as listed in Table 1. Inset shows the location of the Alpine arc in the framework of the European Variscan belt. Inset labels: Arm - Armorican Massif; BCBF - Bristol Channel-Bray Fault; BM - Bohemian Massif; Ca - Cantabrian terrane; Cib - Central Iberian; Co - Corsica; FMC - French Massif Central; GSBS - Galicia-Southern Brittany Suture; MT - Maures-Tanneron Massif; OM - Ossa Morena; Py - Pyrenees; Sa - Sardinia; Si - Sicilian-Apulian basements; SP - South Portuguese Zone; WL - West Asturian-Leonese.

al., 1991; Rubatto et al., 2001; Compagnoni et al., 2010; Carosi et al., 2016) separated by a steeply dipping, NW-SE striking, km-scale shear zone, the « Ferriere-Mollières Shear Zone » (FMSZ, Fig. 3.1.2), also known as « Valletta Shear Zone ». The FMSZ, recognized since Faure-Muret (1955), is a dextral transpressive shear zone active in Late Carboniferous times (i.e. 330-310 Ma, Musumeci and Colombo, 2002; Corsini et al., 2004; Simonetti et al., 2018) and significantly re-activated during Alpine times (i.e. 27-21 Ma, Corsini et al., 2004; Sanchez et al. 2011). HP/HT metamorphic rocks are described in the western and eastern complexes (Faure-Muret, 1955; Malaroda et al., 1970), which consist of Variscan high-grade migmatitic gneisses mainly derived from meta-sediments (Bortolami and Sacchi, 1968; Blasi, 1971; Malaroda, et al., 1970) or from meta-granitoids (Bogdanoff and Ploquin, 1980; Bogdanoff et al., 1991). Upper Ordovician to Lower Silurian ages have been obtained for some magmatic protoliths (Rubatto et al., 2001).

	Key	Location	Lithology	Mineral assemblages	T (°C)	P (GPa)	References
ALPS	**HE1**	AR: Tinèe; Gesso-Stura-Vésubie	Metabasite	Grt + Hbl + Cpx + Pl + Qtz	710-760	1.2-1.4	Latouche and Bogdanoff (1987); Paquette et al. (1989)
	HE2	AR: Frisson	Eclogitc gneiss	Grt + Hbl + Cpx + Pl + Qtz + Ru/Ilm	720-750	1.33-1.43	Ferrando et al. (2008); Rubatto et al. (2010)
	HE3	P: Oisan	Metabasite	Amph + Pl + Opx + Cpx + Grt + Qtz + Ru/Ilm	775-994	0.9-1.7	di Paola (2001)
	HE4	P: La Lavey	Metabasite	Amph + Pl + Cpx + Grt	800-900	1.3-1.5	Le Fort (1973); Guillot et al. (1998)
	HE5	BD: Lac de la Croix; Beaufortin	Metabasite	Grt + Cpx + Pl + Qtz + Ru + Zr Grt + Hbl + Cpx + Qtz + Ru + Zo	610-670	1.1-1.3	Paquette et al. (1989); Guillot et al. (1998)
	HE6	Ai: Lac Cornu	Metabasite	Grt + Cpx + Hbl + Qtz + Ru	725-750	1.5-1.6	Paquette et al. (1989); Liégeois and Duchesne (1981); von Raumer et al. (1999)
	PN1	LB: Savona Massif	Eclogite	Grt + Omp + Zo + Ru + Ky + Qtz + Phe + Pl + Cpx + Ol?	650-750	> 1.7	Messiga et al. (1992); Giacomini et al. (2007); Maino et al. (2012)
	PN2	Ad: Central part	Metabasite	Grt + Omp + Ky + Ms + Amph + Qtz + Dol + Ru Qtz + Ms + Pl + Bt + Grt + Ru	675-825	1.95-2.45	Dale and Holland (2003); Liati et al. (2009)
	PN3	Ad: Northern part	Metabasite	Grt + Omp + Ky + Ru + Ms + Ep + Pl + Qtz Pl + Qtz + Grt + Ms + Amph + Ep + Bt	565-715	1.45-1.95	Dale and Holland (2003); Liati et al. (2009)
	PN4	Su: Suretta	Metabasite	Grt + Hbl + Ep + Qtz + Cpx	617-750	> 2.0	Nussbaum et al. (1998)
	PN5	TW: Frosnitztal	Metabasite	Grt + Omp + Qtz	400-500	0.8-1.2	Zimmermann and Franz (1989); vonQuadt et al. (1997)
	PN6	TW: Doesenertal	Metabasite	Grt + Omp + Qtz	520-720	> 1.2	vonQuadt et al. (1997); Droop (1983)
	AU1	SC: Hochgrossen Massif	Metabasite	Amph + Cpx + Ab + Zo	650-750	1.0-2.2	Faryad et al. (2002); Melcher et al. (2002)
	AU2	Oe: Central Oetztal Stubai	Metabasite	Grt + Omp	700-800	2.5-2.9	Miller and Thöni (1995); Thöni (2002); Konzett et al. (2005)
	AU3	TZ: Ultental	Metabasite	Grt + Omp + Qtz	640-700	1.2-1.6	Herzberg et al. (1977)
	AU4	TZ: Ultental	Ultramafite	Grt- bearing ultramafics	770-810	2.2-2.8	Herzberg et al. (1977); Tumiati et al. (2003); Morten et al. (2004)
	AU5	Sil: Ischgl	Metabasite	Grt + Omp + Qtz + Ru + Phe	620-670	2.3-2.9	Schweinehage and Massonne (1999)
	AU6	Sil: Val Puntota	Metabasite	Grt + Omp + Qtz + Ru + Phe	400-500	2.5-2.7	Schweinehage and Massonne (1999)
SARDINIA	**HGMC1**	Mt Nieddu	Metabasite	Grt + Omp + Ru + Zo $\pm$ Amp $\pm$ Ky + Qtz	550-700	1.3-2.0	Giacomini et al. (2005)
	HGMC2	Giuncana	Metabasite	Grt + Omp $\pm$ Amp + Zo + Ru/Ilm $\pm$ Ms + Qtz	580-660	1.3-1.8	Cruciani et al. (2015)
	HGMC3	Pta Li Turchi	Metabasite	Grt + Omp + Amp + Bt + Ru + Qtz	620-650	1.9-2.1	Cruciani et al. (2011)
	HGMC4	Anglona	Metabasite	Grt + Omp + Amp + Qtz + Ru/Ilm $\pm$ Zo $\pm$ Bt	690-760	>1.3	Cortesogno et al. (2004)
	MGMC1	Posada	Metabasite	Grt + Omp + Amp + Qtz + Ru/Ilm + Czo	610-700	1.3-1.5	Cortesogno et al. (2004)

Table 3.1.1. Tectonic location, mineral assemblages and eclogite-facies P-T conditions of Variscan eclogites from the Alps and Sardinia. Alps: HE - Helvetic Domain, PN - Penninic Domain, AU – Austroalpine Domain; Sardinia: HGMC - high-grade met. compl., MGMC - medium-grade met. compl.). Samples are localized in Figure 3.1.1.

In western and eastern units, the main pre-Alpine structure is a pervasive steeply dipping regional-scale foliation defined by a shape preferred orientation of biotite, feldspar and sillimanite, and by alternating quartz + feldspars + biotite ± garnet-bearing leucosomes and biotite-rich melanosomes. Most leucosomes are parallel to the dominant foliation, and only a few intersect it.

In the eastern unit post-kinematic cordierite-bearing leucocratic diatexites are widespread (Blasi and Schiavinato, 1968; Blasi, 1971). At the regional scale, coarse-grained undeformed cordierite-bearing melts clearly crosscut the main foliation. In both complexes centimeter-scale cordierite-rich leucosomes intersect and progressively erase the main foliation in biotite and sillimanite-bearing migmatites. Therefore two main partial melting events can be inferred: the first syntectonic episode (M1) developed in equilibrium with biotite, garnet and sillimanite, and the second (M2), clearly post kinematic, in equilibrium with cordierite, at lower pressure. The age of 323 ± 12 Ma obtained by U/Pb on zircons dates the last regional migmatitic event (Rubatto et al., 2001).

Within the eastern complex, a large granitic stock (Central Granite, Fig. 3.1.2) intersects the dominant foliation (Boucarut, 1967; Ferrara & Malaroda, 1969). This granite is dated at 292 ± 10 Ma by Ferrara and Malaroda (1969) and in the range 299-296 Ma by Corsini et al (2004), and belongs to the late Carboniferous Fe-rich granitoids (Debon and Lemmet, 1999) in the EMCs of the western Alps.

The exhumation of the Argentera-Mercantour Variscan crust is sealed by impure sandstones and black shales, rich in upper Pennsylvanian vegetal fossils, filling intra-mountain basins bordered by strike-slip faults (Corsin and Faure-Muret, 1946, 1951; Faure-Muret and Fallot, 1955).

During Alpine collision the Argentera-Mercantour Massif was metamorphosed under upper greenschist facies conditions (Corsini et al., 2004; Lardeaux, 2014a; Filippi et al., 2019). Alpine deformation is concentrated in ductile shear zones marked by alternating fine grained recrystallized quartz + albite and muscovite + chlorite ± titanite-rich layers (Sanchez et al., 2010, 2011).

Eclogites in the Argentera-Mercantour Massif: localized or diffuse occurences?

In the Ibero-Armorican arc and French Massif Central, mafic eclogites are localized in specific horizons (Leptyno-Amphibolite Complexes) in association with ultramafic rocks and HP felsic rocks (Martinez Catalan et al., 2007; Ballèvre et al., 2009; Faure et al., 2009; Lardeaux, 2014b). These horizons of UHP/HP rocks are localized at the base of the allochtonous nappes thrusted upon low-pressure units (Matte and Burg, 1981; Ledru et al., 1989, 2001; Lardeaux et al., 2001; Berger et al., 2010). In Sardinia and Maures-Tanneron Massif (southern European Variscides) eclogites are recognized as lenses dispersed within migmatites (Carmignani et al., 1994; Cortesogno et al., 2004; Franceschelli et al., 2007; Cruciani et al., 2011; Schneider et al., 2014).

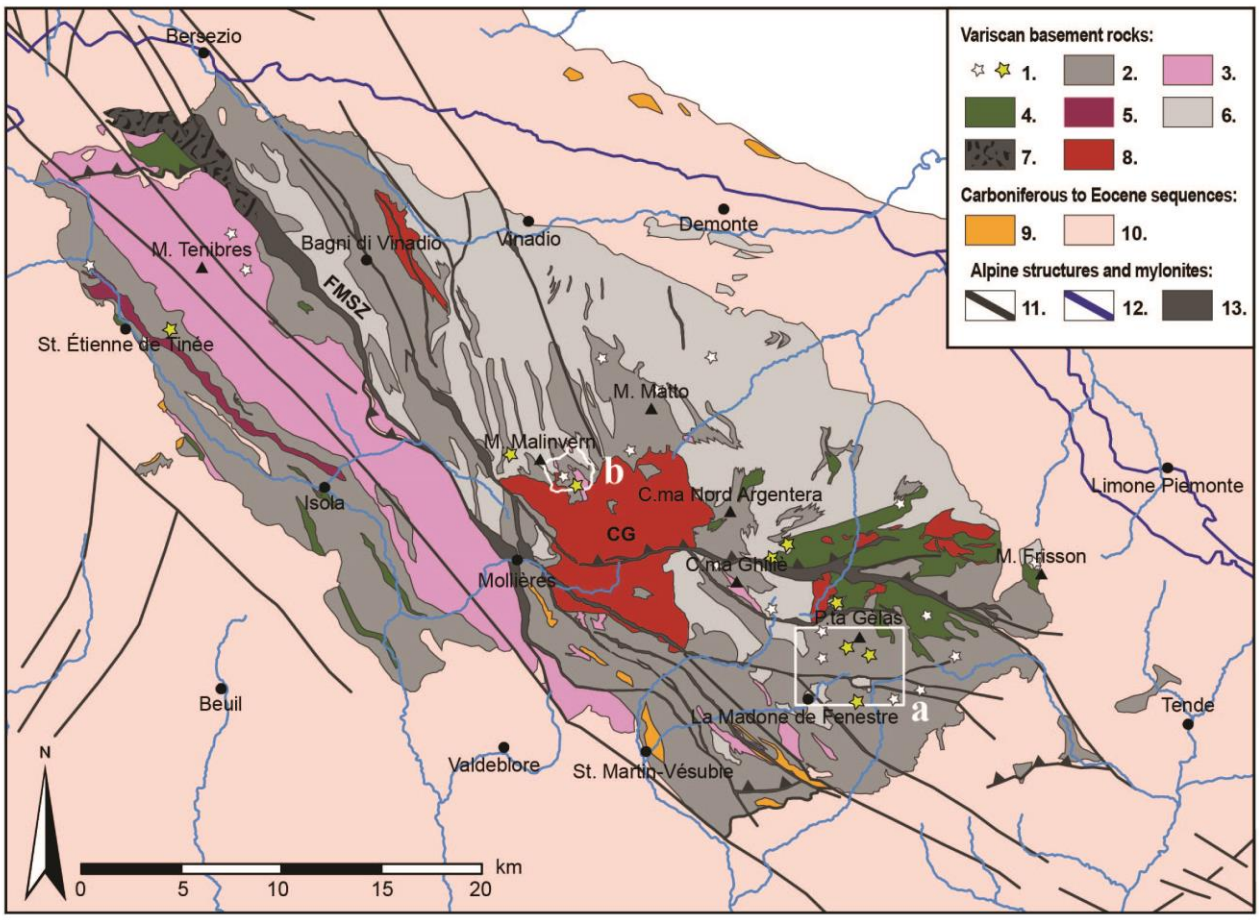

Figure 3.1.2. Geological map of the Argentera-Mercantour Massif (redrawn after Faure- Muret, 1955, Malaroda et al. 1970, Corsini et al., 2004, Carosi et al. 2016 and Gosso et al. 2019). FMSZ - Ferrere-Mollières Shear Zone. CG – Central Granite. 1- Main eclogite occurrences (including our new observations) and sampling localities with yellow stars; 2 - Migmatitic paragneisses 3 - Migmatitic orthogneisses and metavolcanics; 4 - Amphibolites; 5 - Syn-tectonic diorites; 6 - leucocratic cordierite-bearing anatexites; 7 - Amphibolite to greenschistfacies mylonites; 8 - Granitoids; 9 - Carbonaceous schists, conglomerates, and siliciclastic sandstones (late Carboniferous); 10 - Permian to Eocene sequences; 11 - late- to post-Alpine faults; 12 - Penninic Front; 13 - Greenschist-facies mylonites. White contours labelled a and b locate the maps of Figure 3.1.5 and 3.1.6, respectively.

In the Argentera-Mercantour Massif, the presence of rare mafic eclogites was first reported by Faure-Muret (1955) and other limited occurences identified later (Malaroda et al., 1970; Latouche and Bogdanoff, 1987; Colombo et al., 1994; Rubatto et al., 2001). Ages of 459 ± 4 Ma and 486 ± 7 Ma have been obtained by U-Pb dating on zircons for protoliths of HP mafic rocks (Rubatto et al., 2001, 2010). We discovered a significant number of other eclogites occurrences (Fig. 3.1.2) with the following field characters:

- Eclogites occur as lenses of centimetric to metric thickness within surrounding migmatites. They are poorly to undeformed relics within the dominant foliation (Fig. 3.1.3).

Figure 3.1.3. Eclogitic boudins within migmatites. A - Col de Fenestre– Pas des Ladres (France) eclogitic boudin in metatexites; B - Balma Ghiliè valley (Italy) eclogite within biotite-sillimanite paragneisses; C - Monte Matto (Italy) boudin of eclogite in cordierite bearing diatexites; D - Lac Niré (France) eclogite within biotites illimanite paragneisses; E - Lac Long eclogitic boudin in metatexites.

- Boudins of eclogites can be associated with mafic HP granulites and/or serpentinites. Up to now, an association with HP felsic granulites remains unknown.
- Eclogites are in most cases severely retrogressed under amphibolite facies conditions: preserved eclogite facies assemblages are exceptional (Fig. 3.1.4).
- Eclogites occur in both western and eastern units in all types of migmatites, i.e. within biotite-sillimanite-garnet banded M1 migmatites as well as within leucocratic cordierite bearing M2 migmatites, but also within migmatitic orthogneisses and migmatitic amphibolites.

Typical field relationships are illustrated by two lithological and structural maps (Fig. 3.1.5, 3.1. 6).

In this massif, mafic granulites have been studied in detail (Ferrando et al., 2008; Rubatto et al., 2001, 2010), but petrological and structural analyses on eclogites remain scarce, probably because they are severely retrogressed and deciphering preserved eclogite facies assemblages is tricky.

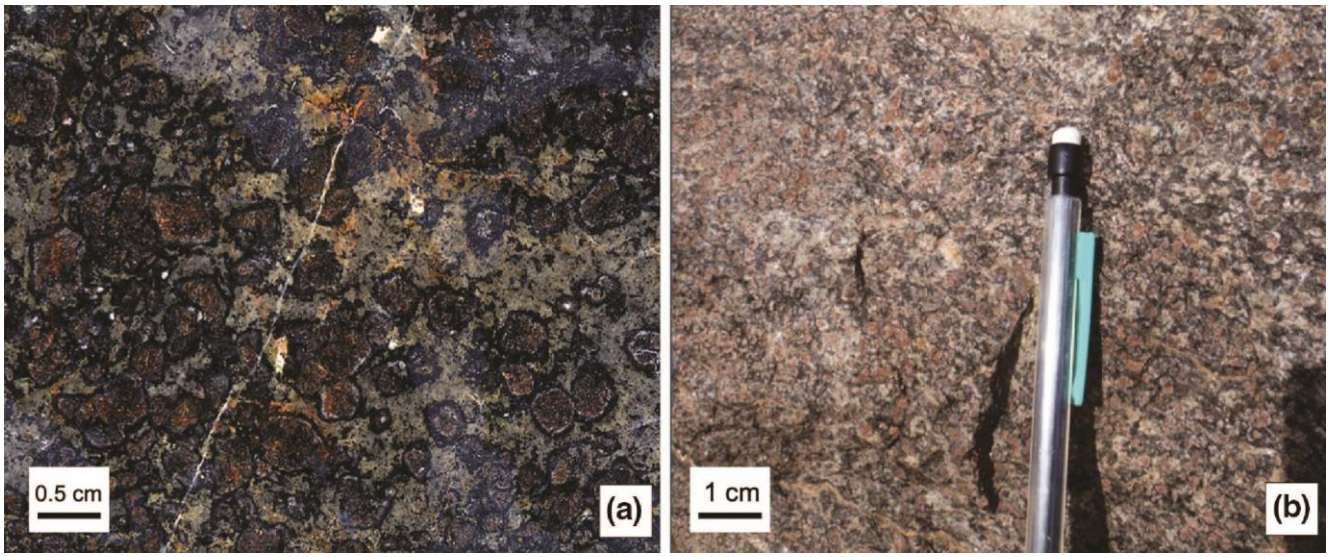

Figure 3.1.4. Retrogressed eclogites. A - Lago Brocan (Italy) eclogite with coronas of amphibole around garnets; B - Lac Niré (France) eclogite with plagioclase around garnets.

Geochemistry of eclogites

Major elements

Our samples, displaying mid ocean ridge basalt (N-MORB) average composition (McKenzie and O'Nions, 1991), show a weak depletion in CaO and TiO_2 and an enrichment in K_2O. On the Al_2O_3 vs. TiO_2 diagram (Konzett et al. 2012), the studied eclogites tend to lie mainly in the basalt field and for a few samples in plagioclase-rich cumulates (Fig. 3.1.7), suggesting that their protoliths were basalts and gabbros.

In the Total Alkali versus Silica diagram, SiO_2 content ranges from 40.51 to 52.01 wt% and our sample compositions are mainly in the field of basalts, while in the AFM diagram, they plot mainly in the fields of tholeiitic, and for a restricted number of samples in the calc-alkaline volcanic series (Fig. 3.1.7).

However, major elements are significantly mobile during metamorphism (Winchester and Floyd, 1977). Taking into account that surrounding migmatites have undergone dehydration reactions coeval with retrogression of eclogites, the latter could have experienced inward fluxes (chemical contamination from outside, see Stipska et al., 2014 for example). Consequently K_2O enrichment from surrounding migmatites is possible. We have therefore to consider the least mobile elements during alteration and metamorphism (i.e. HFS elements such as Sc, Y, Zr, Hf, Ti, Nb and Ta, or REEs) when using chemical diagrams for protoliths characterization.

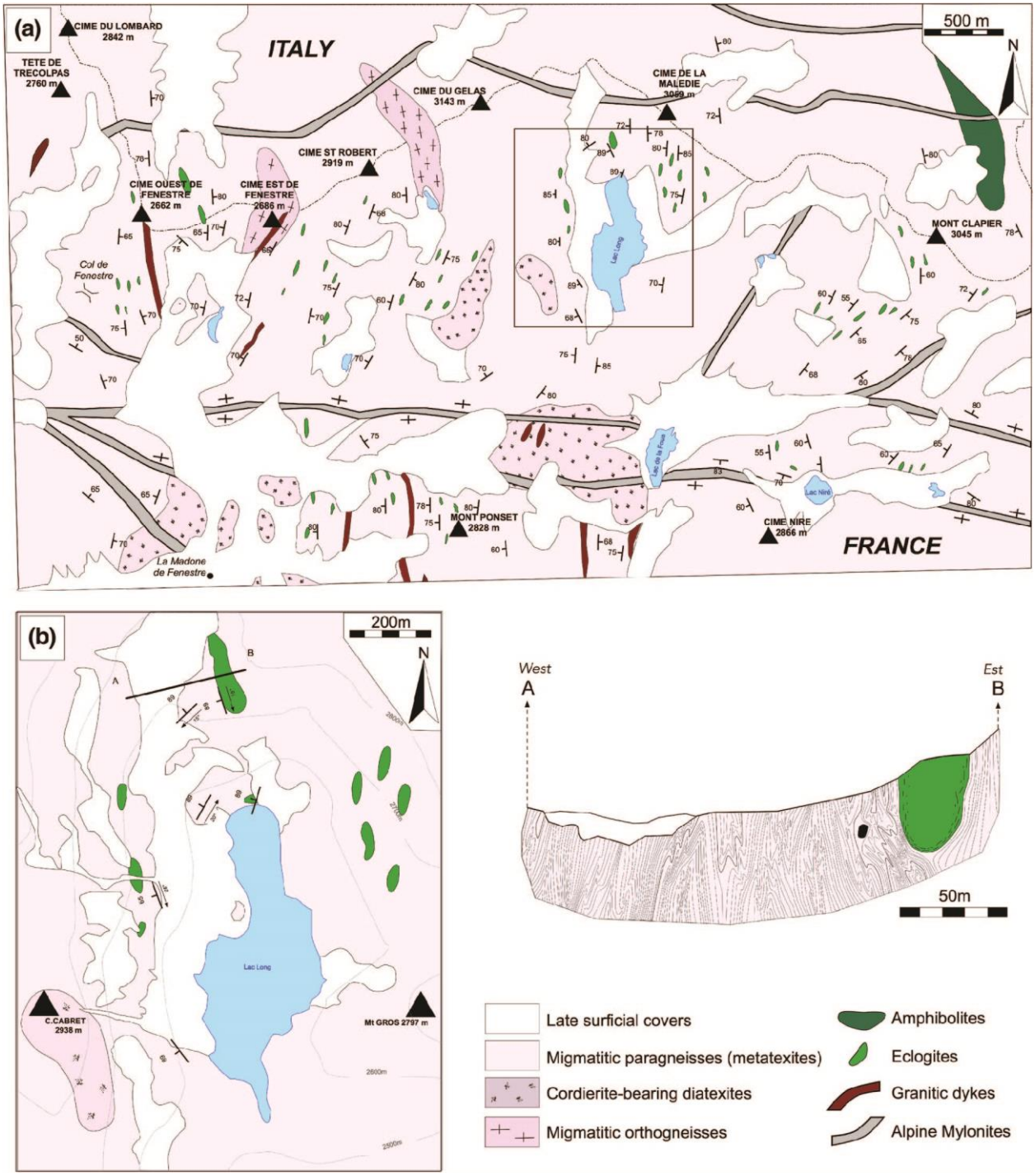

Figure 3.1.5. Geological map of the high Gordolasque valley at the Italian-French border. A - Structural map. B - Detailed map of eclogite boudin outcropping north of the Lac Long and cross-section.

Trace elements and REE

The studied eclogites have typical N-MORB geochemical compositions in the Zr-Ti-Nb-Y (Pearce, 1996) or in the Y-Nb-Zr (Meschede, 1986) diagrams, except for two samples displaying within-plate chemical signatures and corresponding to a foidite and a picrobasalt (Fig. 3.1.8A).

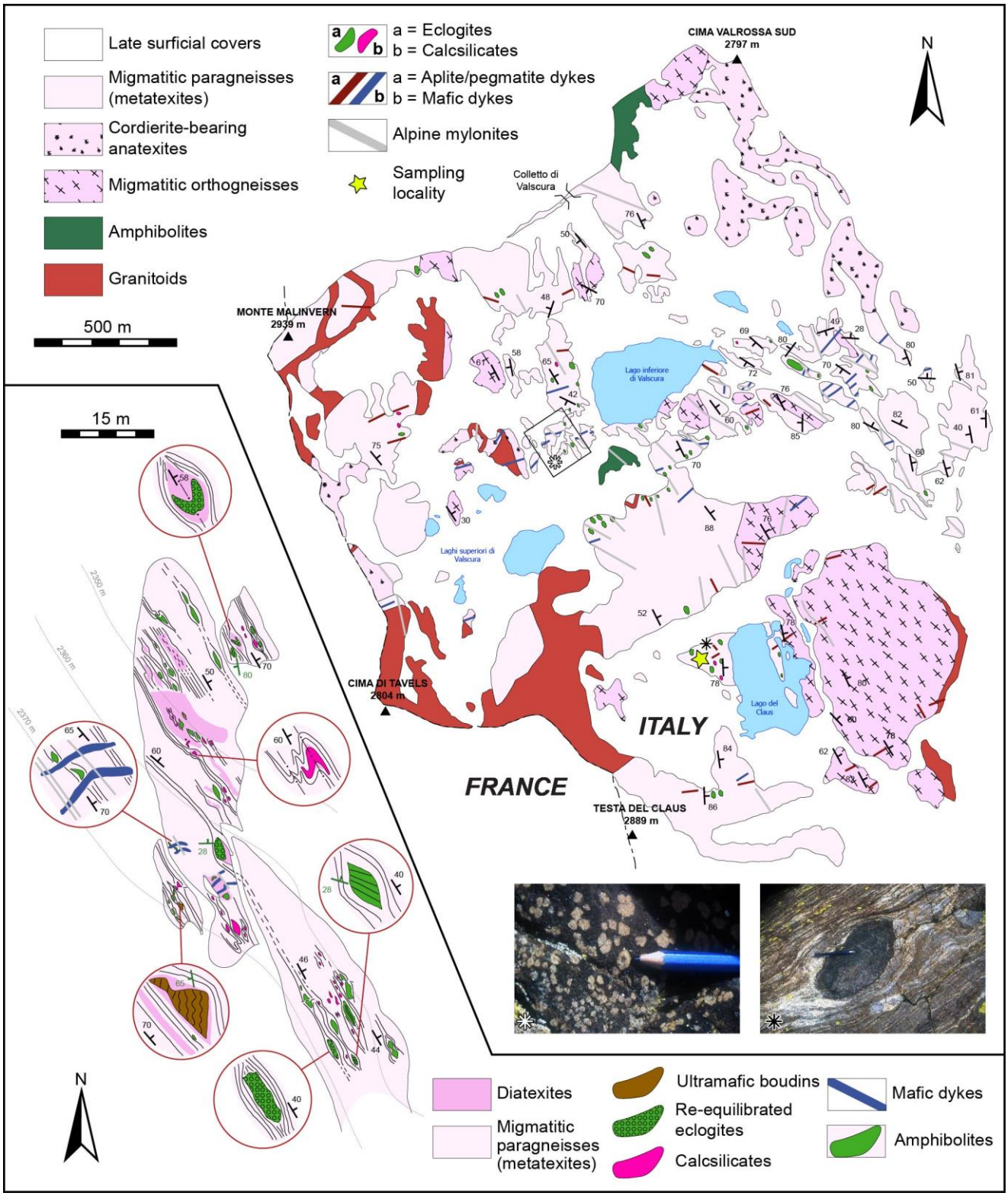

Figure 3.1.6. Structural map of upper Valasco Valley (Italy). In the inset detailed form-surface map located with a black star in the structural map, close to Lago Inferiore di Valscura.

In discriminant diagrams (Fig. 3.1.8B) sample compositions plot in the field of tholeitic basalt and MORB, whereas a few of them show better affinity with calk-alkaline to alkaline basalts. This can be

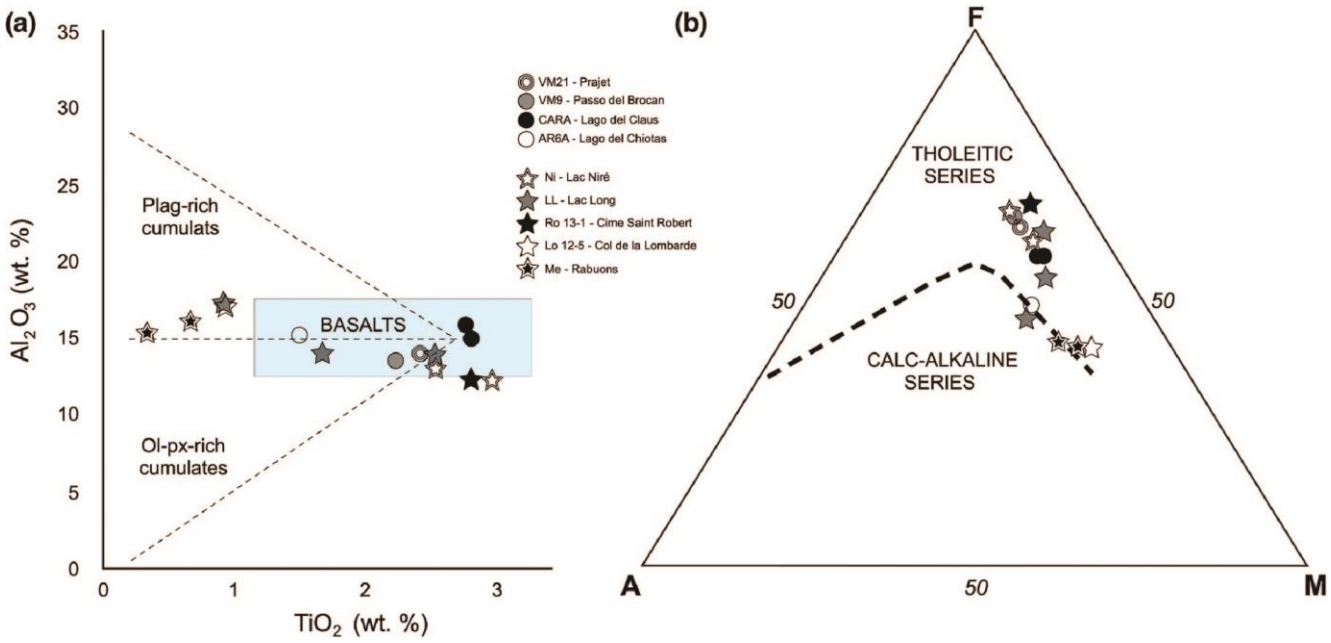

Figure 3.1.7. Geochemistry of Argentera-Mercantour eclogites in the Al2O3 vs. TiO2 diagram after Konzett et al. 2012 (7A) and in the AFM diagram after Irvine and Baragar, 1971 (7B).

interpreted as the consequence of various tectonic contexts of protoliths formation or as the result of chemical contamination during protoliths formation and/or evolution. To face these uncertainties, the best tools are the diagrams proposed by Pearce (2008) or the chondrite normalized Th vs. Nb (normalization according to Sun and McDonough values, 1989) proposed by Saccani (2015), within which the effects of crustal contamination on fractional crystallization and on the MORB-OIB array can be depicted. In these diagrams, a significant number of our samples plot outside the MORB-OIB array suggesting that these rocks have been contaminated by crustal components (Fig. 3.1.8C).

The Nb/La ratio is regarded as an index of crustal contamination of magmas (Thompson et al., 1983). For our eclogites, this ratio ranges between 0.20 and 1.71 with a mean value of 0.7. For comparison, MORB and OIB typically show values of 0.93 and 1.3 respectively (Sun and McDonough, 1989), while continental flood basalts display values of 0.14-1.4 (Thompson et al., 1983). This indicates that our samples have undergone crustal contamination.

Contamination is also suggested by low and variable Zr/Hf ratios (mean value of 34.11) and Nb/Ta ratios (mean value of 12.47) in comparison with those of N- and E-MORB (respectively 36 and 17 according to Sun and McDonough, 1989). Moreover, MORB and OIB uniform value of 25 ± 5 for their Ce/Pb ratio whereas the mean value for continental crust is around 4 (Hofmann et al., 1986). The Ce/Pb value of our samples is in the range of 0.03-15.7 (with a mean value of 5.12) and thus compatible with crustal contamination of MORB basalts.

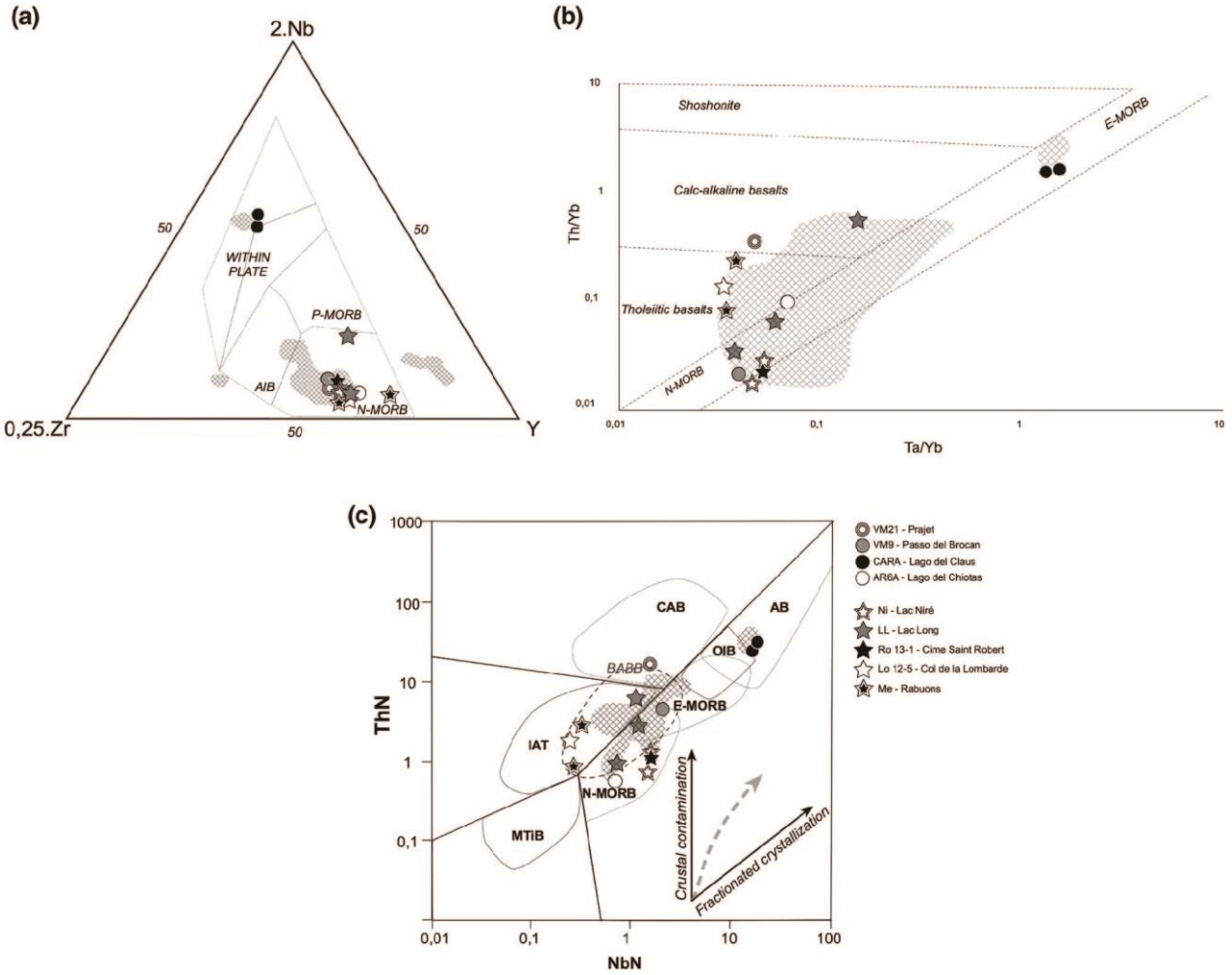

Figure 3.1.8. Chemical compositions of eclogites in the Y-Nb-Zr (8A after Meschede, 1986), the Th/Yb versus Ta/Yb (8B after Pierce, 1982) and in the N-MORB normalized Th-Nb (8C after Saccani, 2015) diagrams. Fields hatched in grey represent available chemical compositions of Sardinian eclogites (see texte for discussion and references).

According to Hofmann (2003), the Nb/U and the Pb/Nd ratios are indicators for crustal contamination. Nb/U ratio of 47 ± 11 is typical for MORBs, while the mean value of continental crust is 8 (Rudnick & Fountain 1995). This ratio varies from 2 to 47.8 with a mean value of 12.6 for the studied eclogites. The Pb/Nd ratios are of 0.04, 0.07, 0.08, and 0.63 for N-MORB, E-MORB, OIB, and continental crust respectively (Hofmann, 2003). Our eclogites present a Pb/Nd ratio ranging between 0.14 and 1.81 with a mean value of 0.41. This confirms the crustal contamination of MORBs.

The total REE content indicates that most samples show an enrichment, 10–40 times greater than average N-MORB.

The REE patterns of the Argentera-Mercantour eclogites are presented in Figure 3.1.9 and the patterns of OIB, N-MORB and E-MORB are shown for comparison.

Primitive mantle normalized trace element pattern shows contrasting trends: a first group of samples show enrichment in LREE with respect to HREE, whereas the second is characterized by slightly

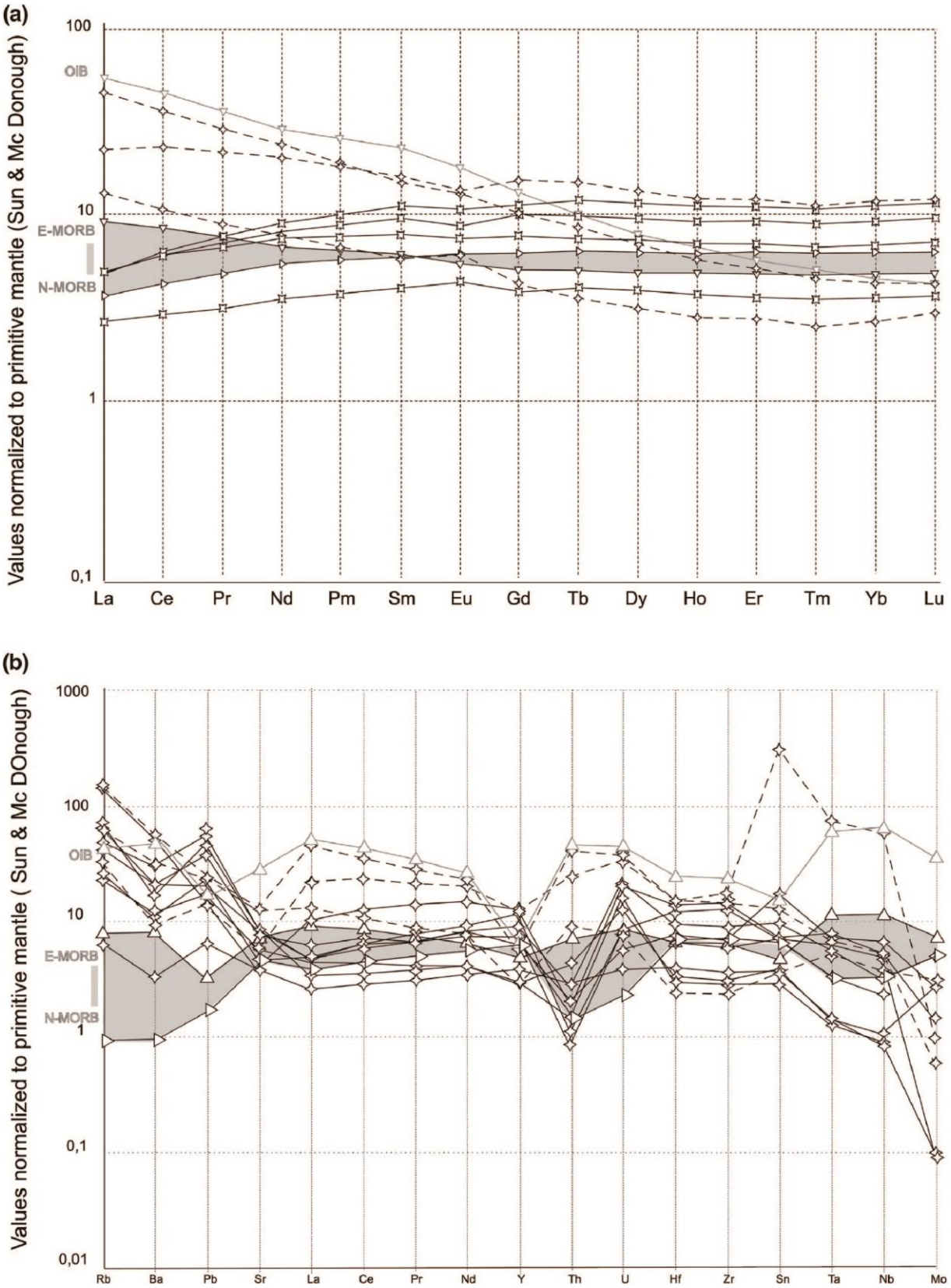

Figure 3.1.9. Primitive mantle normalized REE (A) and LILEs HFSEs (B) patterns of eclogites. N-MORB, E-MORB and OIB compositions after Sun and McDonough (1989).

depletion, compatible with E-MORB and N-MORB trends, respectively. Some samples are characterized by strong Th depletion, similar to average N-MORB values, whereas a few others have Th positive anomaly. All samples show positive Rb, Pb and U anomalies and trends with Sr and Ba depletions, and most of them Nb, Ta and Mo depletions. These trends are relevant markers for contaminated basaltic sources (Donnelly et al. 2004). Finally, the $(La/Sm)_N$ ratio is highly variable (0.42-3.09), indicating various degrees of fractionation (Carlson, 2003) .

Petrography of eclogites

The Argentera-Mercantour eclogites experienced severe retrogression and the peak eclogite facies assemblage is rarely preserved. The cores of the boudins consist of fine-grained rocks with reddish millimeter to centimeter- sized garnets. On the other hand, their margins are totally transformed into garnet-free amphibolites.

The peculiar features of these eclogites are the occurrence of clinopyroxene-plagioclase symplectitic domains and of plagioclase–brown/green amphibole symplectitic coronas around garnets (Fig. 3.1.10A, B, C, D and F). The development of clinopyroxene-plagioclase symplectites is the result of omphacite destabilization (Boland and Van Roermund, 1983; Joanny et al., 1989). It is a discontinuous precipitation explained in terms of decreasing pressure with or without temperature increase (Mysen and Griffin, 1973; Van Roermund and Boland, 1983; Joanny et al., 1991). Some of our samples show an evolution of the symplectite texture, with thinner clinopyroxene lamellae developed at the expense of the coarser ones (Fig. 3.1.10B).

Garnet occurs as fractured grains up to 5 millimeter in size containing inclusions of quartz, amphibole, rutile, zircon and in some samples small sized brown biotite, epidote, ilmenite, apatite and monazite (Fig. 3.1.10E). In one sample (Lac Niré), an inclusion of omphacite associated with amphibole, was observed within garnet.

Amphibole is the most abundant phase in the studied eclogites and occurs in different textural sites: (1) inclusions within garnets, and large green to light-brown amphibole grains in the matrix; (2) dark-brown amphibole rims near the plagioclase-clinopyroxene symplectites, and discontinuous droplets in association with plagioclase within coronas around garnets; (3) large poikiloblastic green-brown grains, in association with biotite, fully replacing the symplectites or invading totally the garnets grains, and 4) pale green amphibole filling late veins or supporting an incipient foliation.

Plagioclase occurs in different micro-sites: 1) together with clinopyroxene in symplectites replacing omphacite; 2) together with the dark-brown amphibole rimming garnet or amphibole 1, close to the

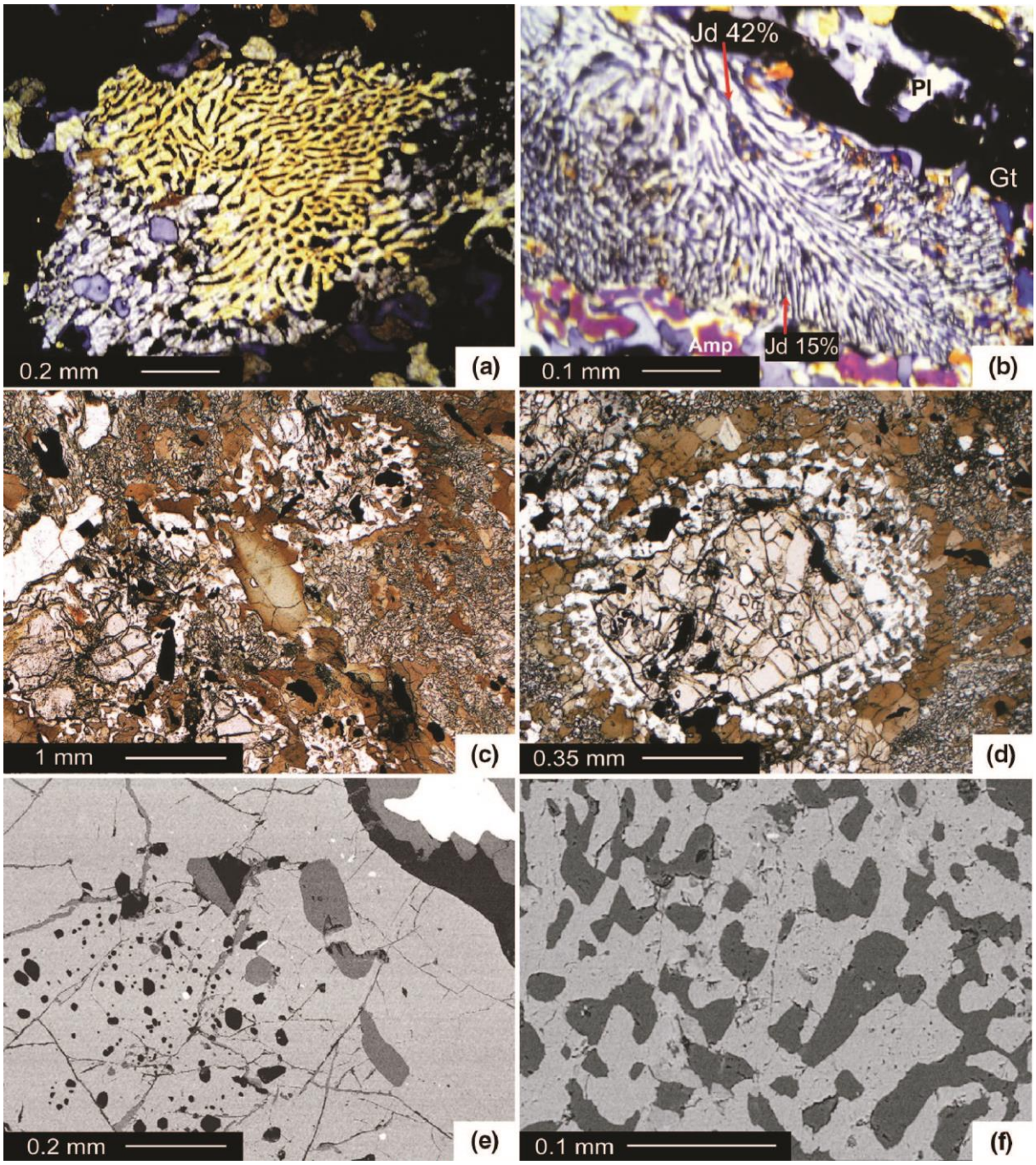

Figure 3.1.10. Photomicrographs of eclogites. A - Clinopyroxene-plagioclase symplectite (crossed polars, lac Niré, France). Note the progressive decrease of lamellae size from center to rim of the symplectite; B - Evolution of the symplectite texture, from coarse clinopyroxene lamellaes (with Jadeite content of 42 mol%) to thinner lamellaes (with jadeite content of 15 mol%), crossed polars, Pas des Ladres (France). Gt - Garnet; Pl - Plagioclase; Amp - Amphibole. C - Microstructure of re-equilibrated eclogites with diopside- plagioclase symplectites replacing original omphacite. Relict amphibole 1 green cores are rimmed by brown Ti rich amphibole 2 that together with plagioclase occurs in coronas around garnets (plane polarised light, Lago Brocan, Italy); D - detail on the plagioclase-amphibole 2 coronas around garnet; E - inclusions of quartz, amphibole 1 and rutile in garnet (BSE image, Brocan Lake, Italy); F - Diopside-plagioclase symplectite replacing omphacite (BSE image, sample 0878, Valasco Valley, Italy).

symplectites and together with droplets of amphibole around garnet; 3) in late veins and cracks associated with titanite, chlorite, white mica, biotite and pale green amphibole.
In the matrix, rutile grains are usually rimmed by ilmenite. Quartz is common and biotite and K-feldspar are generally interstitial with respect to garnet, clinopyroxene and amphibole 1 and 2. In the most retrogressed samples, chlorite is developed at the expense of biotite and amphibole as well as in the fractures of garnet.

Mineral Chemistry

Mineral analyses were performed on three samples (Lac Long, Lac Niré and Pas des Ladres) in the French part of the massif, and 3 samples (upper Valasco Valley) in the Italian part.
Garnet from French samples is almandine-rich (almandine 49-56 mol%) and spessartine-poor with pyrope, grossular contents ranging from 20 to 32 and 17 to 24 mol% respectively. In the diagram of Coleman et al. (1965), garnets are distributed between the fields of B and C eclogite types (Fig. 3.1.11B). The zoning pattern is limited to the mineral rims, with an increase in almandine content correlated to a decrease of pyrope and grossular contents.
In Valasco Valley, garnet is Fe-rich (almandine 61-54 mol%) with low spessartine (3-6 mol% at core, 1-3 mol% at rim), pyrope and grossular contents 8-12 mol% and 21-32 mol%, respectively. They plot in the field of type C eclogites (Fig. 3.1.11B) showing a constant pyrope content and grossular enrichment from core to rim. Indeed Mn and Fe^{2+} decrease from 0.16 to 0.01 and 1.83 to 1.70 apfu, respectively, whereas Ca slightly increases from 0.75 to 0.96 apfu, from core to rim.
Clinopyroxene was identified in different sites. In the Lac Niré sample, the clinopyroxene preserved as an inclusion within garnet is an omphacite with jadeite content around 32 mol%. In Lac Niré as well as in Pas des Ladres eclogites, clinopyroxene 1 microstructural site is replaced by clinopyroxene 2-plagioclase symplectites. In the coarser lamellas, the jadeite component is 42 mol%, while the thinner ones have jadeite contents of 27-15 mol% (Fig. 3.1.11A).
In Valasco Valley, clinopyroxene 1 is not preserved, but its composition has been estimated, by mass balance calculations of symplectite domains, at a jadeite content from 24 to 38 mol%. Pyroxene in symplectite (Cpx 2) is always diopside with jadeite content < 5 mol% in all localities.
Plagioclase lamellae from the symplectites are oligoclase (anorthite 20–32), while plagioclase forming coronitic shells around garnet in equilibrium with amphiboles is andesine (Fig. 3.1.11C). Plagioclase in veins with actinolite is anorthite 8-13.

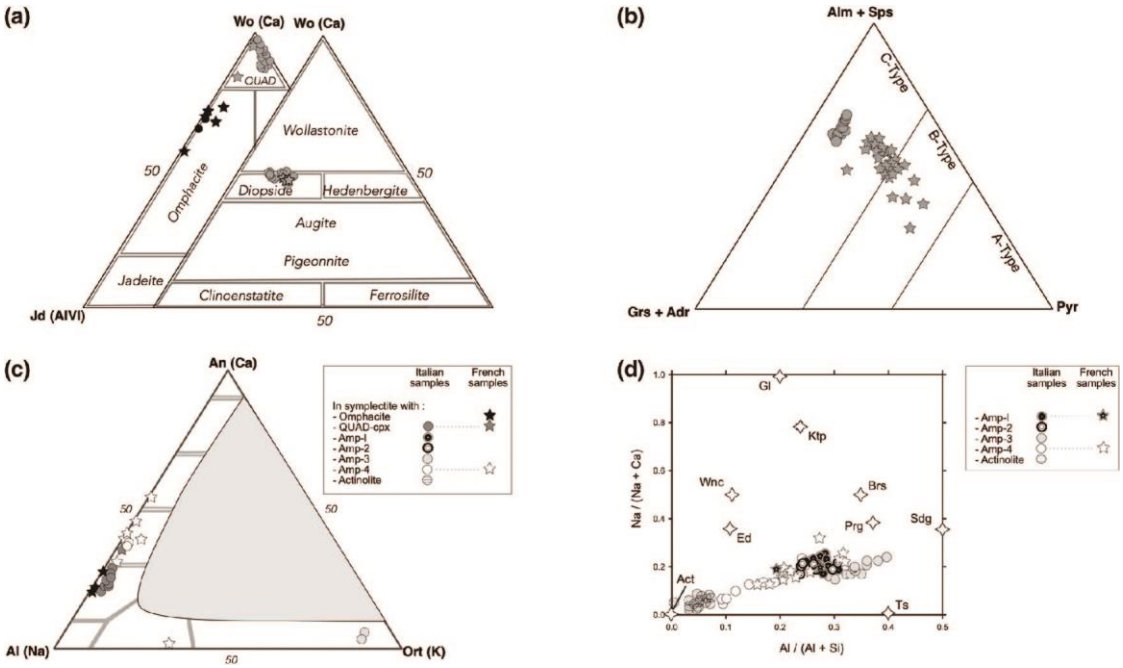

Figure 3.1.11. Composition of clinopyroxenes (A), garnets (B), feldspaths (C) and amphiboles (D) from Argentera eclogites. In all the diagrams minerals from Lac Niré, Lac Long and Pas de Ladres eclogites are represented by stars. Italian eclogites are circles. Different colors have been used for minerals from Valasco Valley: in the diagram 11A of Morimoto (1988) black and grey circles represent the recalculated compositions of omphacites and clinopyroxene 2 respectively. In comparison, omphacite of Lac Nire appears in black stars. In Na/Na+Ca vs Al/Al+Si diagram (11D), stars locate the end-member compositions labelled as follows: ACT - Actinolite, BAR - Barroisite, ED - Edenite, GL - Glaucophane; KTP - Katophorite, PRG - Pargasite, SAD - Sadanagaite, TS - Tschermakite, WIN - Winchite.

Amphiboles from Pas des Ladres and Lac Niré are calcic (Fig. 3.1.11D) according to the classification of Leake et al. (1997; 2004) and Hawthorne et al. (2012). The amphiboles in inclusions within garnets are magnesio-hornblendes with Mg content of about 0.22 to 0.31 apfu. The amphiboles from coronas around garnet as well as the amphibole grains replacing clinopyroxene of the symplectites, or invading garnets are magnesio-hornblendes with Mg content of about 0.30 to 0.38 apfu.

In Valasco Valley, amphibole 1 and 2 are mostly Pargasite. Amphibole 3a is ferro-pargasite, amphibole 3b is mostly ferro-edenite or magnesio-hornblende. Amphibole 4 is actinolite. Amphibole 1 and 2 have Al^{IV} between 1.53 – 2.04 apfu and Al^{VI} between 0.37 and 0.74 apfu. Ti content in amphibole 1 varies between 0.12 and 0.20 whereas amphibole 2 is Ti-richer (from 0.20 to 0.31 apfu). Na content decreases from 0.55 apfu in amphibole 1 to 0.49 apfu in amphibole 2.

Amphibole 3a, in rims around garnet, is particularly Al-rich (Al_{tot} from 2.55 to 3.74 apfu, clustering at 3.06 apfu), with XMg < 0.5 and Ti lower than 0.14 apfu. Amphibole 3b, mainly replacing clinopyroxene, has Al_{tot} between 0.75 and 2.07 apfu and Ti lower than 0.07 apfu. Amphibole 4 has Al_{tot} <0.70 apfu and Ti< 0.04 apfu everywhere.

Metamorphic history and P-T evolution

The Argentera-Mercantour eclogites preserve evidences of a multistage metamorphic history including:

- An eclogitic stage documented by the occurrence of almandine-rich garnet and by the preservation of omphacite (jadeite 42 mol%) within symplectites and as inclusion within garnet (jadeite 32 mol%). Mineral inclusions in garnet suggest that the stable mineral assemblage during this stage was garnet + omphacite + calcic amphibole + quartz + rutile + zircon ± epidote ± biotite.

- A post-eclogitic stage evidenced by the development of (i) clinopyroxene (jadeite 27-5 mol%)-plagioclase symplectites at the expense of omphacites and (ii) plagioclase-calcic amphibole-ilmenite coronas around garnets. This stage is documented by the replacement of rutile by ilmenite in the matrix of eclogites. Garnet rims are in equilibrium with amphibole-plagioclase coronas containaing in some samples also diopside. This last assemblage is typical for granulite-facies conditions.

- An amphibolite-facies stage constrained by the replacement of symplectitic clinopyroxenes by amphiboles, by the development of poikiloblastic amphiboles, in association with biotites and ilmenite, at the expense of all previous minerals.

- A late stage is documented by formation of micro-cracks filled with albite, actinolite, titanite and chlorite as well by replacement of biotites and calcic amphiboles by chlorite. The replacement of ilmenite by titanite can also be related to this late stage (greenschist facies conditions).

A first approach for estimation of eclogitic P-T conditions is the use of experimentally determined domains for the observed main phase association. For our samples with chemical compositions of N-MORB, we can use the grid determined by Schmidt and Poli (1998). With H_2O in excess, the association garnet-omphacite-amphibole-quartz is stable in the range 600-700°C for 1.4-2.4 GPa. This estimation is in agreement with the field of amphibole bearing eclogite facies for basaltic compositions (Ernst and Liou, 2008)

Thermobarometry is a second approach and Fe^{2+}-Mg exchange between garnet and clinopyroxene is particularly well adapted for eclogites. Nowadays, the calibration established by Krogh-Ravna (2000), which integrates the effects of Ca and Mn components and requires clinopyroxene with a sodic content in the range 0-0.51 to work. In our case, because of severe retrogression, this thermometer can be only

applied in the Lac Niré sample using the preserved inclusion of omphacite (Na content of 0.33) within garnet. Application of this geothermometer for pressure range from 1.2 to 1.4 GPa showed temperatures of 710 and 720°C.

The garnet–hornblende Fe–Mg thermometer (Graham and Powell, 1984),

applied to Lac Long samples showing inclusions of magnesio-hornblende with rational grain boundaries with garnet and in equilibrium with quartz and rutile, gives T-range of 640-690 °C.

However, the reliability of Fe-Mg exchange thermometry is dependent on uncertainties in estimation of the Fe^{3+} /Fe^{tot} ratios in minerals (Carswell and Zhang, 1999; Carswell et al., 2000). As established by Stipska and Powell (2005), if Fe^{3+} content is not taken into account for garnet-clinopyroxene thermometry the calculated temperatures are overestimated, therefore the proposed values (720-710°C) are considered as maximum temperatures.

We used also the Zr-in-rutile thermometry (Watson et al. 2006, Thomkins et al., 2007) relevant for quartz and zircon-bearing rocks. In the Lac Niré eclogite, the measured Zr content in rutiles in inclusion within eclogitic garnet is between 221 and 458 ppm. Application of the Zr content in rutile thermometer for pressure of 1.2 and 1.5 GPa showed temperatures of 634-694 and 646-706°C respectively, consistent with the previously estimated T range.

The minimal pressure of the eclogitic stage is estimated at 1.4-1.6 GPa using the maximal values of the jadeite content (32-42 mol%) of omphacites (Gasparik and Lindsley, 1980; Holland, 1990).

Ti-content in amphibole thermometer (Otten, 1984), using the core compositions of in amphibole 1 grains, gives temperatures of 680-715°C in Valasco Valley eclogites. Ernst & Liu (1998) calibration suggests T= 700-740°C, using the same data, for which Al-content indicates P = 1.1-1.7 GPa.

In summary, application of various thermo-barometers, to all the studied samples, yields to a P-T range of 640-740°C and 1.1-1.7 GPa.

Thermodynamic calculations were performed with the free energy minimization program THERIAK/DOMINO (De Capitani and Petrakakis, 2010, version 2015). Pseudosections were calculated for two samples from Valasco Valley and Lac Long, as shown in Figure 3.1.12. Compositions were chosen starting from the whole rock analysis, considering H_2O in excess, and not considering the presence of a melt, as the mafic boudins are enclosed in migmatitic felsic rock, but without evidence of internal melting. For Valasco Valley, we have removed K_2O from the composition, as biotite and K-feldspar occur as interstitial grains or filling late veinlets, mainly affecting the boudin margins. This suggests that boudins were contaminated, during country rocks partial melting post-dating the eclogitic re-equilibration as discussed previously. For Lac Long sample, because biotite was observed in equilibrium with eclogitic garnet, K_2O was considered in the chemical system. Finally, we have evaluated the effect of O and H_2O on our pseudosection, as suggested by

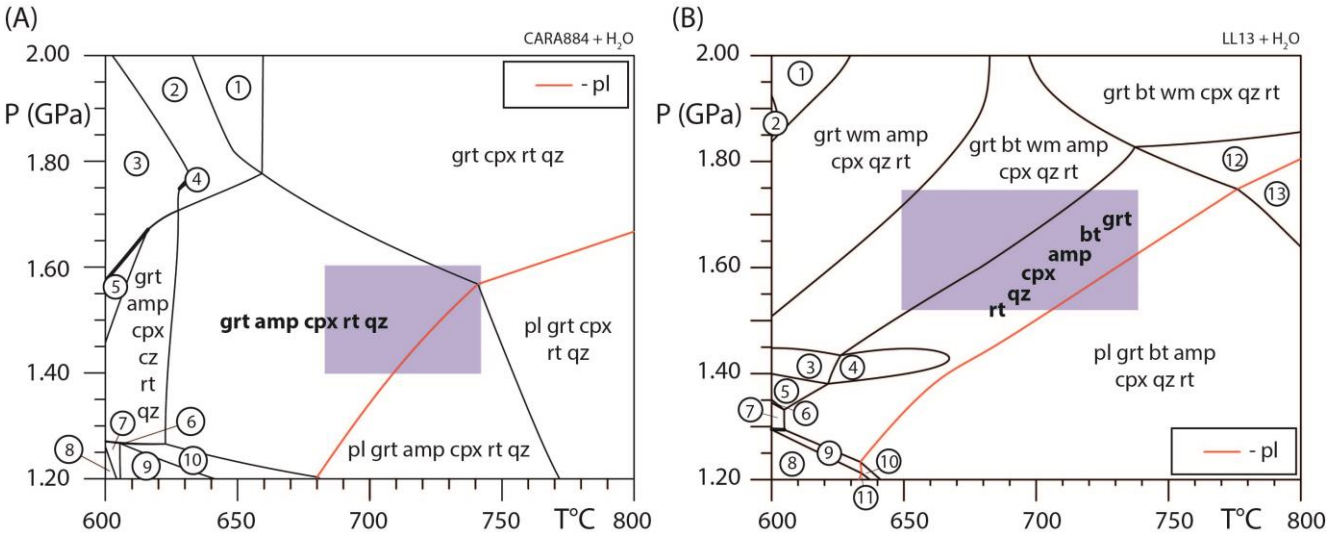

Figure 3.1.12. P-T pseudosections calculated from Valasco Valley (A, sample CARA884) and Lac Long (B, LL13). The red line divides the P-T field of plagioclase bearing assemblages, towards higher temperatures, from assemblages without plagioclase, towards higher pressures. The shaded light blue fields represent the P-T conditions determined using classic geothermobarometry for the eclogite-facies assemblage 1. Univariant lines are thick.

For pseudosection (A), assemblages in the numbered fields are as follow: 1 - garnet, 2 clinopyroxenes, rutile, quartz; 2 - garnet, amphibole, 2 clinopyroxenes, rutile, quartz; 3 - garnet, amphibole, 2 clinopyroxenes, rutile, clinozoisite, quartz; 4 - garnet, 2 amphiboles, 2 clinopyroxenes, rutile, quartz; 5 - garnet, 2 amphiboles, clinopyroxene, clinozoisite, rutile, quartz; 6 - garnet, amphibole, clinopyroxene, titanite, clinozoisite, rutile, quartz; 7 - garnet, amphibole, clinopyroxene, titanite, clinozoisite, quartz; 8 - garnet, amphibole, titanite, clinozoisite, quartz; 9 - garnet, amphibole, clinopyroxene, titanite, quartz; 10 - garnet, amphibole, clinopyroxene, titanite, rutile, quartz. For pseudosection (B), numbered fields match with the following assemblages: 1 - garnet, white mica, 2 amphiboles, clinopyroxene, quartz, rutile; 2 - garnet, white mica, 2 amphiboles, clinopyroxene, quartz, rutile, clinozoisite; 3 - garnet, biotite, white mica, amphibole, 2 clinopyroxenes, quartz, rutile; 4 - garnet, biotite, amphibole, 2 clinopyroxenes, quartz, rutile; 5 - garnet, biotite, white mica, amphibole, clinopyroxene, quartz, rutile; 6 – garnet, biotite, white mica, amphibole, clinopyroxene, quartz, rutile, clinozoisite; 7 - garnet, biotite, amphibole, clinopyroxene, quartz, rutile, titanite; 8 – garnet, biotite, amphibole, quartz, rutile, sphene; 9 - garnet, biotite, amphibole, clinopyroxene, quartz, rutile, clinozoisite; 10 – plaglioclase, garnet, biotite, amphibole, quartz, rutile; 11 - plagioclase, garnet, biotite, amphibole, quartz, rutile, titanite; 12 - garnet, biotite, clinopyroxene, quartz, rutile; 13 – plagioclase,a garnet, biotite, clinopyroxene, quartz, rutile. Some very small fields have not been numbered.

Guiraud et al. (2001) and Rebay et al. (2010) to evaluate the effect of such components on the stability and preservation of assemblages in mafic rocks. We used the following mineral a-x relations: plagioclase (Holland & Powell, 2003), garnet (White et al. 2007), ilmenite (White et al., 2000), amphibole (Diener et al., 2007), clinopyroxene (Green et al., 2007), orthopyroxene (White et al., 2002) and biotite, White et al., 2007; white mica, Coggon and Holland, 2002. The thermodynamic database is ds55 (Holland and Powell, 1998).

Valasco Valley pseudosection is represented in Figure 3.1.12A where the observed HP assemblage, i.e. garnet, amphibole 1, omphacite, rutile and quartz, is predicted to be stable in a field that spans from 625 to 740 °C and 1.2 to 1.75 GPa. This penta-variant field is limited by the appearance of plagioclase towards high temperatures, the disappearence of amphibole towards higher pressure and temperatures, the appearance of a jadeitic pyroxene at higher pressures and lower temperatures, the presence of clinozoisite at lower temperatures and the presence of titanite towards lower temperatures. The compositions of clinopyroxene and amphibole in the field are close to those detected in Valasco Valley eclogites. In addition thermobarometric estimates performed on eclogite facies minerals from Valasco Valley rocks perfectly fit with the HP assemblage stability field. Addition of Fe_2O_3 would shift epidote stability towards higher temperature, up to close the penta-variant field we are interested in for around 10 mol% of FeO_t as F_2O_3. Conversely, plagioclase-in and amphibole-out lines would be affected only by minor shifting towards higher temperatures and pressures, respectively, of the order of four tens of Celsius degrees and less than 0.1 GPa. A similar configuration would result from taking into account zoisite instead of clinozoisite in a Fe_2O_3-free system.

The Lac Long pseudosection is shown in Figure 3.1.12B. The HP assemblage includes amphibole, omphacite, garnet, rutile, quartz and biotite and is predicted to be stable in a P-T range from around 600 to 780°C and 1.25 to 1.80 GPa, in good agreement with thermobarometric estimates established for this sample. The proposed field is bounded by plagioclase at high temperature, amphibole at high pressure, phengite at low temperature, and titanite and clinozoisite at low pressure. If we were to consider zoisite instead of clinozoisite, the lower temperatures field boundary would be shifted to T at around 690°C, still in agreement with other P-T determinations made for this assemblage. Addition of Fe_2O_3 would shift epidote stability towards higher temperature, and phengite towards higher temperature and lower pressure, until the closing of the penta-variant field of interest for slightly more than 10 mol% of FeO_t as Fe_2O_3. The effects on the other field boundaries are negligible.

Geochronological constraints on eclogite facies metamorphism

Ages of eclogite facies metamorphism previously obtained in the eclogites from the ECMs, as well as from other segments of the European Variscan belt, are not well constrained (Von Raumer et al., 2009; Paquette et al., 2017 and Lotout et al., 2018). It seems important to mention that the geochemical signatures of the studied eclogites are totally consistent, particularly regarding multi-elements abundance patterns, with those obtained for HP mafic granulites sampled in the Argentera-Mercantour Massif (Rubatto et al., 2001, 2010) suggesting that these HP mafic granulites could be considered as markers of the incipient stage of eclogites retrogression. In such a case the age of eclogite facies

metamorphism is probably close to that obtained for HP granulite facies, i.e. 340 ± 4 Ma (Rubatto et al., 2010) by U/Pb zircon dating. So far, we have not enough zircons from eclogites to try to get an age of the eclogite facies metamorphism. However, we performed $^{40}Ar/^{39}Ar$ dating on amphiboles from these eclogites. We selected a sample from the Lac Long eclogites. This selected sample (LL09-12J) is closely associated with the (LL13) sample used for the previously presented pseudosection and has a similar geochemistry. However, in this (LL09-12J) sample, magnesio-hornblendes are in textural equilibrium with plagioclase, ilmenite and garnet. The inferred age corresponds thus to the re-equilibration of eclogites under amphibolite facies conditions.

Amphibole single grain of Lac Long sample (LL09-12J) yields a plateau age (Fig. 3.1.13) at 339.7 ± 12 Ma corresponding to 93.77 % Ar released and to four steps. The inverse isochron for the plateau steps gives a concordant age at 339.8 ± 12 Ma (MSWD = 2.17). The plateau-age at 339.7 ± 12 Ma is considered as the best age estimate for the record of amphibolite facies imprint.

Discussion and conclusion

Origin of eclogites protoliths

Trace elements and REE patterns establish that the Argentera-Mercantour eclogites are MORBs contaminated by continental crust components. Crustal contamination can be the consequence of two processes: (i) contamination of basaltic liquids, i.e. eclogite protoliths, prior to HP metamorphism or (ii) contamination of eclogites by surrounding migmatites during or after their emplacement.

In the first hypothesis, the multi-element diagrams of incompatible elements display, in many cases, Pb, U and Large Ion Lithophile Element (LILE) enrichments, and also Nb and Ta depletions. These patterns are characterisric of arc lavas and back-arc basalts (Hofmann, 2003; Labanieh et al., 2012). In that case, the geochemical signatures of the studied eclogites are more compatible with those of supra-subduction zone basalts rather than those of oceanic domains.

Considering the second hypothesis, during high temperature hydrothermalism as well as during high-temperature crustal melts formation and migration, significant K, Pb, U and more generally LILEs influxes by crust-derived fluids migration can be envisaged (Michard and Albarède, 1986; Pattison, 1991; Klinkhammer et al., 1994; Stipska et al., 2014; Burianek et al., 2017). In such a case, the eclogite protoliths could be standard MORBs later contaminated during orogenic processes.

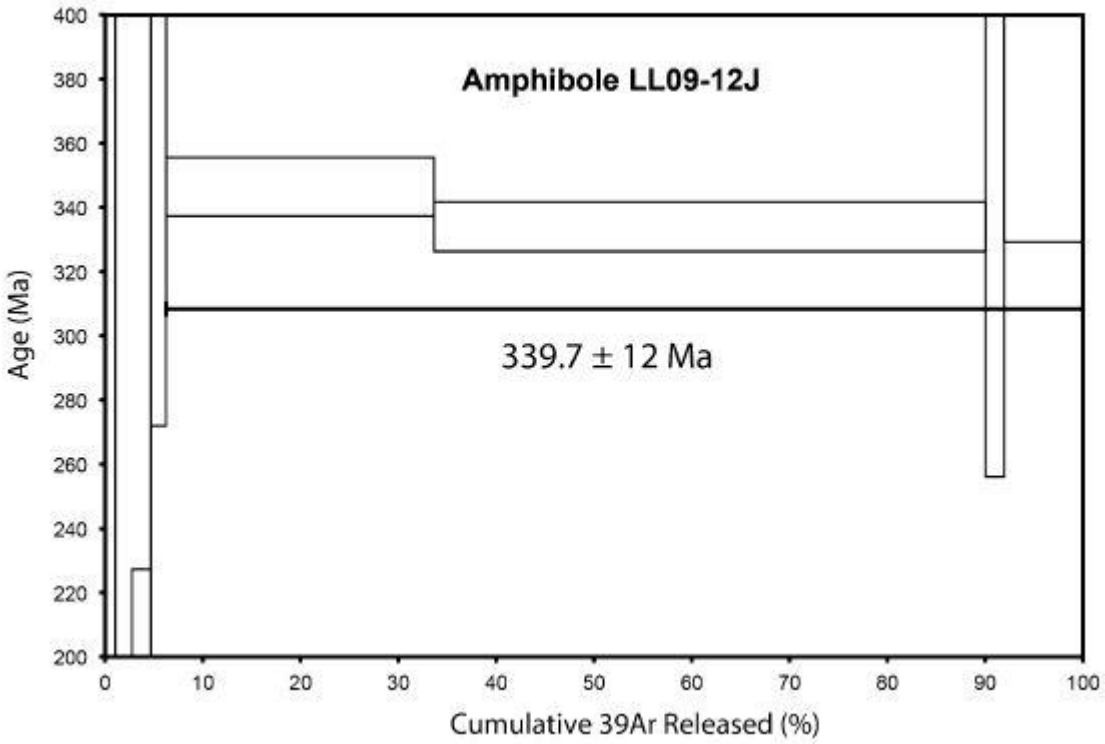

Figure 3.1.13. 40Ar/39Ar age spectrum diagram performed in amphibole from Lac Long sample.

Paleo-gradient and context for eclogites formation

The early metamorphic imprint under eclogite-facies conditions was quantified by independent methods as comparison between natural and experimentally determined mineral assemblages, well calibrated independent thermobarometers and thermodynamic modeling. The obtained results are clearly consistent and allow to propose eclogite facies conditions with temperatures comprised between 640 and 740°C for pressure of 1.5 ± 0.25 GPa.

To infer their geodynamic significance, we compare the proposed P-T estimates with classical metamorphic gradients (Miyashiro, 1961; Ernst, 1971, 1973; Spear, 1993) and with geotherms proposed by Cloos (1993) for cold and warm subduction zones (Fig. 3.1.14).

The eclogitic stage fits the conditions predicted by the the different models calculated for warm subduction of oceanic crust and therefore they represent the traces of a suture zone.

The Argentera-Mercantour Massif: record of a dismembered suture zone

The Argentera-Mercantour eclogites are witnesses of an oceanic crust formed in a back-arc basin or in an oceanic domain. Whatever is the selected pre-orogenic configuration, these rocks are the exhumed

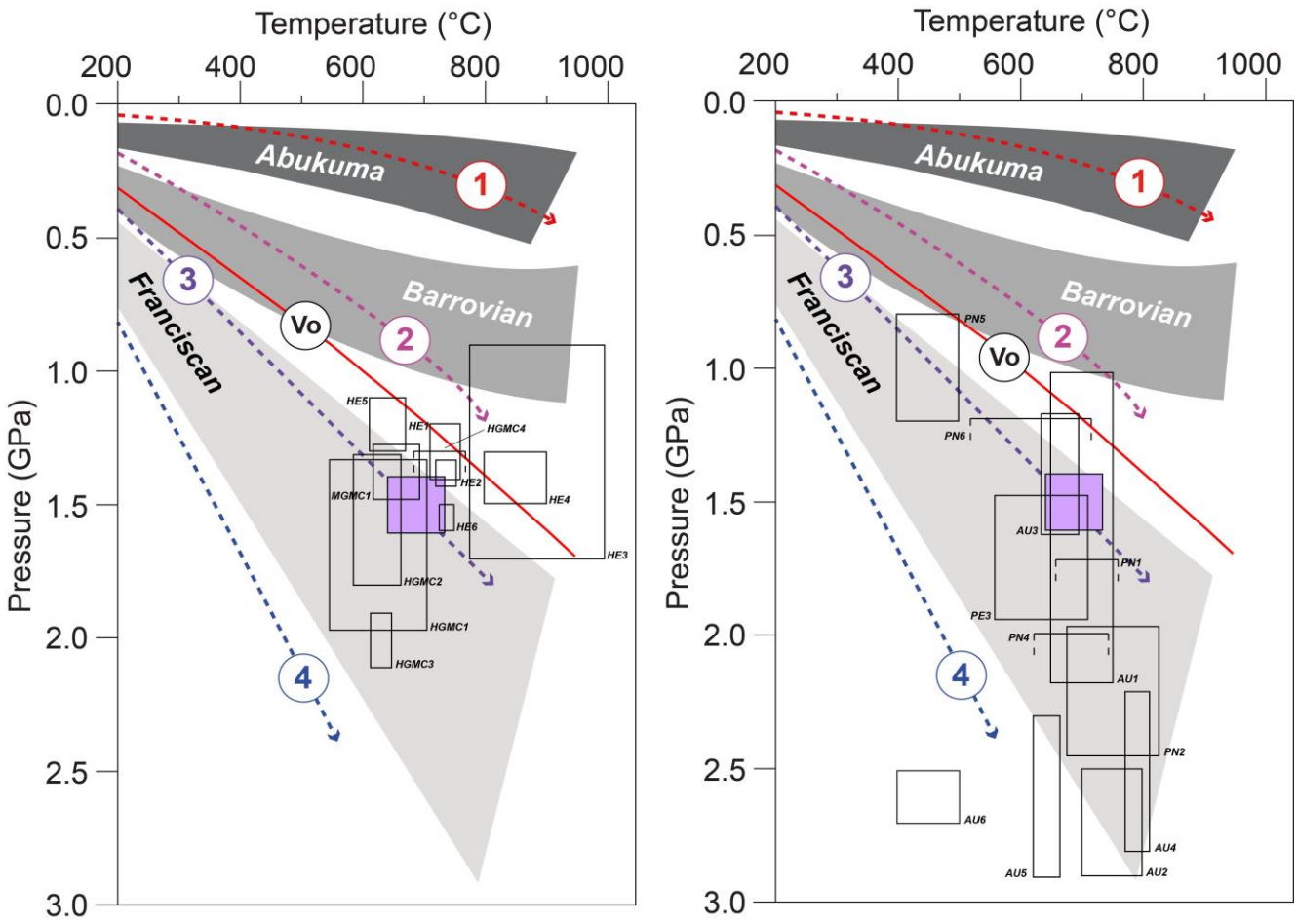

Figure 3.1.14. P-T conditions (violet square) of studied eclogites compared with metamorphic gradients (after Miyashiro, 1961; Ernst, 1971, 1973; Spear, 1993) and geotherms after Cloos (1993): (1) near spreading ridge or volcanic arc, (2) normal gradient of old plate interior, (3) warm subduction zones, and (4) cold subduction zones. Vo represents the initial unperturbed geotherm. A - P-T conditions of Argentera eclogites compared with eclogites from Helvetic-Dauphinois zone and Sardinian eclogites. B - P-T conditions of Argentera eclogites compared with eclogites from Penninic and Austro-Alpines zones. Box labels refer to locations in Figure 3.1.1 and descriptions in Table 3.1.1.

remnants of subducted oceanic crust, therefore localizing the paleo-suture zone transposed after continental collision in a migmatitic complex. However this paleo-suture zone is totally dismembered and eclogites are mixed with various types of migmatites. The original suture is totally overprinted by mass transfer of partially molten continental crust, giving rise to a “diffuse cryptic suture zone” in the sense of Schulmann et al. (2014).

The mechanism leading the extensive dismembering of the suture zone remains unclear and different models can be considered:

- dismembering, during continental collision, of previously stacked ophiolitic unit in response to vertical transfer (i.e. extrusion) of hot partially molten orogenic crust during ongoing shortening. This results in large–scale gravity driven migmatitic dome-like structures favouring mixing of eclogites and

migmatites as proposed in Variscan Bohemian Massif (Stipskà et al., 2004; Schulmann et al., 2005, 2009, 2014) or in the Maures-Tanneron Massif (Schneider et al., 2014, Gerbault et al., 2018);

- dismembering of subducted crust during oceanic subduction and/or incipient collision leading the formation of a "hot subduction channel" composed of subducted, partially molten, upper crustal rocks and lithospheric hydrated mantle rocks as proposed by Gerya et al., (2008). The result is a " hot subduction mélange", localized at the plates interface, producing fast exhumation of mafic HP rocks within molten meta-sediments.

The Argentera-Mercantour eclogites in the southern European Variscides framework

Considering field relationships between eclogites and surrounding migmatites, their geochemistry, and petrological evolutions, the Argentera-Mercantour eclogites show remarkable similarities with Sardinian eclogites (Franceschelli et al., 1998, 2007; Giacomini et al., 2005; Cruciani et al., 2015, 2017; Fig. 3.1.14), with eclogites from the Maures-Tanneron Massif (Bard and Caruba, 1982; Briand et al., 2002; Corsini and Rolland, 2009; Schneider et al., 2014) and finally with Corsican eclogites (Palagi et al., 1985; Lardeaux et al., 1994; Faure et al., 2014).

The European Variscan belt is the result of tectonic accretion of Gondwana derived micro plates ("Armorican Terrane Assemblage"; "European Hunic Terranes"; "Iberian-Armorican Bohemian Microplate", …) colliding with Laurussia during the Devonian (Ziegler, 1986; Matte, 2001; Torsvik et al., 1990, 1996; Tait et al., 1997; Stampfli, 2000, Von Raumer et al., 2002; Stampfli et al., 2013; Von Raumer and Stampfli, 2008; Cocks and Torsvik, 2011). The continuity of this process led to the formation of a huge collision belt and to the amalgamation of the Pangea supercontinent in the late Paleozoic (Franke, 1989, 2000; Matte et al., 1990; McKerrow et al., 2000; Edel et al., 2013; Domeir and Torsvik, 2014). Among the various micro plates involved in this evolution, paleomagnetic constraints combined with geochronological data and regional geologic/tectonic investigations have identified, in the southern Variscides, the so-called Maures-Esterel-Corsica-Sardinia ("MECS") block (see Edel et al., 2013, 2014, 2018). If we consider that the occurrences and the petrochemical characteristics of eclogites (i.e. meta-ophiolites) are critical for deciphering the main suture zones in orogenic systems, the similarities between HP metamorphic rocks recognized in Argentera-Mercantour, Sardinia, Maures-Tanneron and Corsica suggest that the southernmost ECMs possibly linked with the MECS block. Such a link is also consistent with various paleo-plates tectonic reconstructions proposed by Stampfli et al. (2002, 2013). In the framework of Gondwana derived micro-plates these authors distinguish, during upper Devonian times, northern blocks (Iberian Massif,

Armorican Massif, French Massif Central, Bohemian Massif), located close to the Rheic (or Rheno-Hercynian) ocean and southern blocks (Sardinia, Corsica, ECMs,…) located close to the Paleo-Tethys. In such a scheme, the age of eclogite facies metamorphism and the age of first stages of continental collision are different with a decrease of geological ages of HP metamorphism and collision from northern to southern blocks. Geochronological data are therefore first-order constraints to discuss these models.

In the MECS block, Late Cambrian-Ordovician-lower Silurian protolith ages of High-Pressure rocks are well constrained by U/Pb zircon dating (Innocenti et al., 2003; Palmeri et al., 2004; Giacomini et al., 2005, 2008; Rossi et al., 2009; Schneider et al., 2014; Cruciani et al., 2017). This time span is coherent with ages of ages of 459 ± 4 Ma and 486 ± 7 Ma obtained in the Argentera-Mercantour Massif (Rubatto et al., 2001, 2010) but also with all protoliths ages obtained in the ECMs (Von Raumer et al., 2002; Schultz et al., 2004). In the MECS block, the timing of crustal anatexis is constrained in the range 345-310 Ma (Di Vicenzo et al., 2004; Giacomini et al., 2005, 2008; Demoux et al., 2008; Rossi et al., 2009; Corsini et al., 2010; Faure et al., 2014; Li et al., 2014; Cruciani et al., 2015; Oliot et al., 2015). The age of 323 ± 12 Ma obtained for crustal partial melting in the Argentera-Mercantour Massif (Rubatto et al., 2001) as well as our age at 339.7 ± 12 Ma for eclogite re-quilibration under amphibolite facies conditions are in full agreement with these results. A characteristic signature of continental collision in the MECS block is the development of a transpressive regime in the range 330-310 Ma leading the development of ductile strike-slip shear zones in Sardinia (Elter et al., 1990; Cappelli et al., 1992; Carosi and Oggiano, 2002; Carosi et al., 2004, 2009) and Maures-Tanneron Massif (Corsini and Rolland, 2009; Corsini et al., 2010). In the Argentera-Mercantour Massif, the FMSZ transpressive shear zone active in the range 330-310 Ma (Simonetti et al., 2018) is a record of a similar tectonic regime.

However, the ages of eclogite facies metamorphism remains poorly constrained in the MECS block as well as in the ECMs (Von Raumer et al., 2009; Schneider et al., 2014; Cruciani et al., 2015; Spalla et al., 2014; Regorda et al., 2019) and new radiometric datings are necessary to discriminate between the debated paleogeographic and geodynamic scenarios. The U/Pb zircon age obtained on HP granulites in Corsica at ca. 360 Ma is still debated (Li et al., 2014), therefore the only available geochronological constraint is the age of HP mafic granulites at ca. 340 ± 4 Ma (Rubatto et al., 2010) and the retrogression of eclogites under HP granulite facies and re-equilibration under amphibolite facies took place over the time span of 344-330 Ma.

In the framework of the whole Alpine belt, the identification of which and how many Variscan suture zones (e.g. Matte1986, 2001; Franke 2000; Faure et al. 2005; Guillot et al. 2009; Lardeaux et al., 2014) occur in the Alpine chain is still debated (Regorda et al., 2019) mainly because of the Alpine

overprint on the Variscan crust. The evolution of this Palaeozoic lithosphere in terms of geodynamic scenario has been rarely explored (e.g. von Raumer et al. 2003, 2013; Spiess et al. 2010). The discussion on the provenance of the Alpine basement units in terms of both palaeogeography (northern Gondwana margin or Galatian superterrane) and influence of Palaeo-Tethys evolution on the Variscan dynamics is still open. For this purpose, the comparison of the thermo-mechanical evolution of the Argentera-Mercantour eclogites with those of other Variscan eclogites from the Alps is a key starting point to shed light on their geodynamic significance (Tab. 3.1.1 and Fig. 3.1.14). PT conditions inferred from eclogites and HP-granulites of Helvetic Domain indicate a thermal state higher than that of warm subduction zones (Cloos, 1993), mainly compatible with the initial unperturbed geotherm or higher, with the only exception of Valasco Valley and Lac Niré rocks. The P-T conditions of the latter lie on the warm subduction geotherm, fully comprised in the Franciscan metamorphic gradient, like some of the Sardinian eclogites (which plot between the cold and warm subduction zone geotherms), and for the first time indicate that oceanic subduction-related metamorphism developed also in the Helvetic Variscan crust. This makes the investigated rocks more similar to the Variscan eclogites from other Alpine structural domains, which mainly show a thermal state between warm and cold subduction gradients or locally colder, as the case of some Austroalpine eclogites from Oetztal, Tonale and Silvretta nappes.

The previously presented constraints demonstrate the coherence of the Variscan geological signatures depicted in the Argentera-Mercantour Massif and those of the MECS block, which share the same tectono-metamorphic evolution. Hence we envisage that the southernmost ECM is a part of the MECS block in the framework of the European Variscan belt. To test such a hypothesis it will be now critical to obtain high-resolution chronological constraints on the age of eclogite facies metamorphism, particularly in Argentera-Mercantour and Maures-Tanneron Massifs.

3.1 The Saint-Étienne-de-Tinée eclogite: a remnant of early Cambrian oceanic crust involved in the Variscan subduction, western Argentera-Mercantour Massif, southwestern Alps.

Marco Filippi, Fabrice Jouffray, Jean-Marc Lardeaux, Maria Iole Spalla, Massimo Tiepolo (paper in preparation)

Introduction

Ophiolitic rocks in mountain belts are a primary source of information about the opening and closure of the oceans of the past. Most of our understanding of the orogenetic processes, and in particular of the first tectonic stages (i.e. oceanic subduction), is actually based on the study of ophiolite record (e.g. Miyashiro, 1961; Ernst, 1971). However, traces of the earliest tectonic stages is quite rarely preserved, since most of these rocks pervasively re-equilibrated during and after the continental collision.

Variscan ophiolites are scattered along the suture zones of the central European Variscan belt. Despite the re-equilibration attained during the Variscan collision, these rocks may give information about the Variscan oceans and their subduction, where HP/UHP metamorphic records are preserved (Matte, 1998; Lardeaux et al., 2001; Martínez Catalán et al., 2007, 2009; Faure et al., 2009; Ballèvre et al., 2009, 2013; Schulmann et al., 2009, 2014; Berger et al., 2010; Lardeaux, 2014; Lardeaux et al., 2014; Paquette et al., 2017). Distribution of Variscan ophiolites plays primary roles to cast geodynamic models and paleogeographic restorations that constrain, at the first order, the pre-collisional evolution of the central European Variscan belt (Matte, 2001; Stampfli et al., 2002, 2013; Cocks and Torsvik, 2006; Spalla and Marotta, 2007; Torsvik and Cocks, 2009; Domeier, 2016; Franke et al., 2017; Regorda et al., 2020).

Presently, very little is known about the Variscan ophiolites of the southern European Variscan belt, since most of these rocks have been completely re-equilibrated in late Variscan to Alpine times (von Raumer, 1998; Schaltegger and Gebauer, 1999; von Raumer et al., 2013). For these reasons, the pre-collisional evolution of the southern European Variscan belt is very poorly constrained, posing an inconsistency in the full understanding of the Variscan orogeny.

This contribution focuses on the western part of the Argentera-Mercantour Massif (Helvetic domain, Alps), mostly composed of Variscan migmatites that include remnants of subducted oceanic lithospere rocks deeply re-equilibrated during collisional to post-collisional stages (Malaroda et al., 1970; Latouche and Bogdanoff, 1987; Rubatto et al., 2001; Jouffray et al., 2020). At odds, the Saint-Étienne-

de-Tinée eclogite in the western Argentera-Mercantour Massif escaped most of the collisional to post-collisional metamorphic re-equilibration and preserves the record of early Variscan tectonic stages. It thus offers materials that can shed light on the pre-collisional evolution of the southern European Variscan belt.

Geological setting

Since the late Cambrian, several oceanic basins opened along the northern margin of Gondwana, in the future Variscan realm: many crustal blocks were separated from Gondwana and started to migrate northward. In Devonian to Carboniferous times, the closure of the interposed oceanic basins and the collision between the Gondwana-derived continental blocks led to the formation of the European Variscan belt (Franke and Engel, 1986; Matte, 2001; Stampfli et al., 2002, 2013; Martinez-Catalan et al., 2009; Aretz, 2016; Franke et al., 2017).

The evolution of the European Variscan belt is in large part enigmatic, in particular at its southern and eastern boundaries. In late Variscan and Alpine times, severe re-equilibration has indeed erased most of the mineral associations that are traces of the Variscan oceanization and subduction. However, there are a few main widely accepted points, which result from investigations on the better preserved parts of the central European Variscan belt.

It is nowadays clear that the most important actor in the Variscan cycle is the Rheic Ocean (Fig. 3.2.0). The Rheic Ocean opened along the north-western margin of Gondwana in response to south dipping subduction of the Iapetus Ocean (Matte, 2001; Stampfli et al., 2002, 2013; Cocks and Torsvik, 2006; Torsvik and Cocks, 2009; Domeier, 2016; Franke et al., 2017). At its eastern termination, the Rheic Ocean merged with the older Neoproterozoic Ran Sea (Fig. 3.2.0; Hartz and Torsvik, 2002; Domeier, 2016). A first continental block named Avalonia broke away from Gondwana in response to Rheic Ocean opening and rapidly migrated northward (Fig. 3.2.0). As a result, Avalonia collided with Baltica and Laurentia forming Laurussia between the late Ordovician and the early Devonian (i.e. the Caledonian/Acadian orogeny, van Staal et al., 2009; Corfu et al., 2014; Domeier, 2016).

The Rheic Ocean has been firstly envisaged by the distribution of early Paleozoic trilobite and brachiopod populations on opposite Avalonian and Gondwanan shorelines (Cocks and Fortey, 1982; Cocks, 2000; Cocks and Torsvik, 2002) and by paleoclimatic reconstructions (Scotese and Golonka, 1997 and ref. therein). The rifting and northward Avalonia drifting is instead well constrained by paleo-magnetic restorations since the early Ordovician (490-470 Ma, Cocks and Torsvik, 2006; Torsvik and Cocks, 2009; Domeier, 2016). The maximum expansion of the Rheic Ocean is dated late

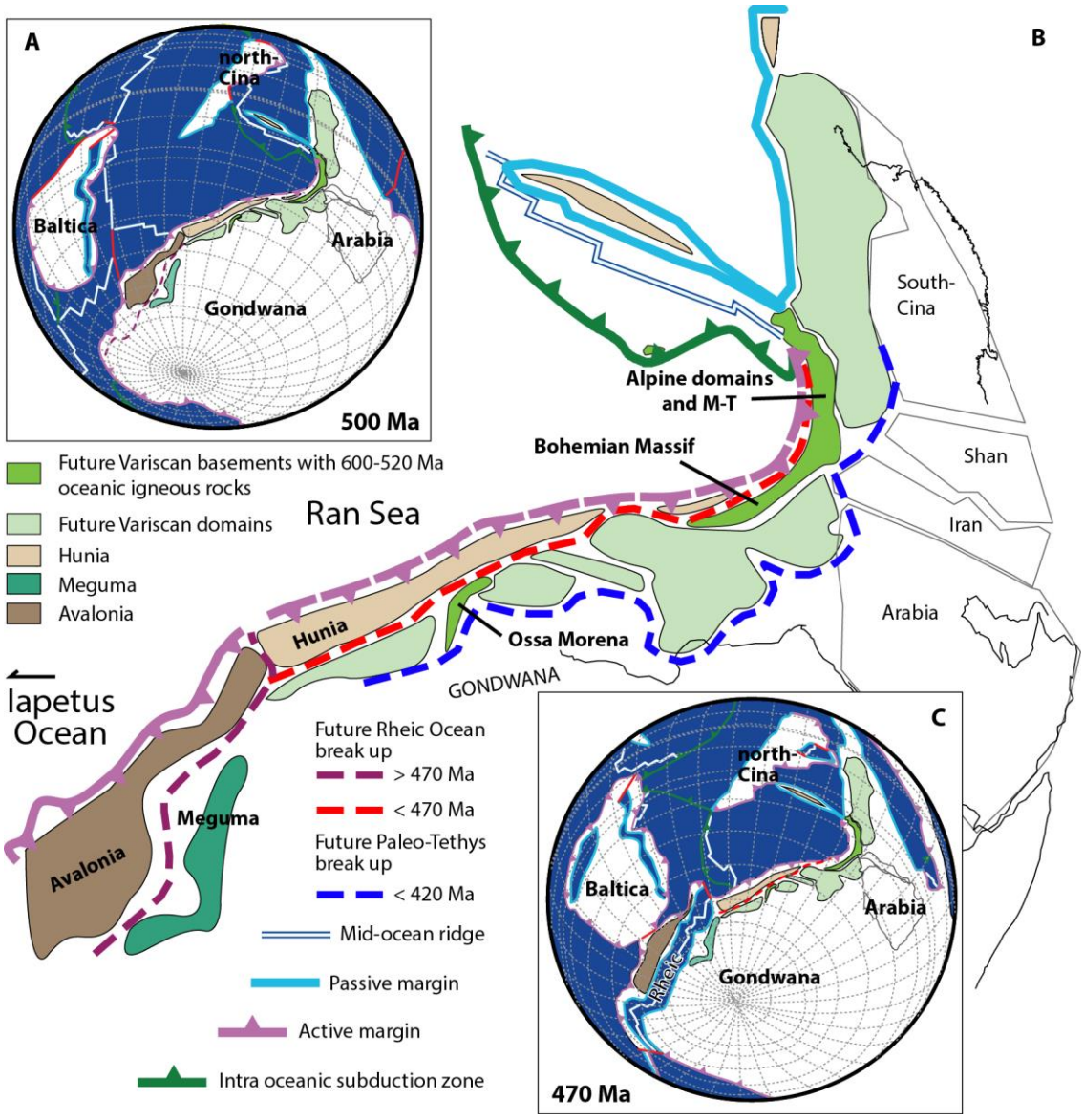

Figure. 3.2.0. Late Cambrian (a) plate configuration with (b) detail on the northern Gondwana margin (after Stampfli et al., 2013; von Raumer et al., 2015; Cocco and Funedda, 2017). Early Ordovician (c) plate configuration (Stampfli et al., 2013). Ran Sea is defined according to Domeier (2016). Since the paleogeographic configuration of Domeier (2016) places a passive margin between the Ran Sea and the future Variscan domains, the eastern part of the northern-Gondwana sudbuction trench is dotted. In this last paleogeography, the Rheic Ocean merged with the Ran Sea at 470 Ma.

Ordovician – early Silurian, at the time of the Caledonian/Acadian orogeny to the North (Cocks and Torsvik, 2002; Stampfli et al., 2002, 2013; Domeier, 2016).

The second actor in the Variscan cycle was the Paleo-Tethys Ocean (Fig. 3.2.0), also known as Middle European or Galice-Massif Central Ocean, which opened between Gondwana and Gondwana derived-crustal blocks at the end of the Silurian (420-400 Ma, Stampfli et al., 2002, 2013; Cocks and Torsvik, 2006; Torsvik and Cocks, 2009; Domeier and Torsvik, 2014; Torsvik and Cocks, 2019). Implication of

the Paleo-Tethys Ocean in the Variscan orogeny is still largely enigmatic due to little field and paleomagnetic evidences.

Other smaller oceanic basins, including the Saxo-Thuringian and Rheno-Hercynian Oceans, are placed in the northern part of the European Variscan belt. The Saxo-Thuringian Ocean is now considered as a branch of the Rheic Ocean after paleomagnetic and biostratigraphic data (Franke et al., 2017). The Rheno-Hercynian Ocean was instead a small oceanic domain of Lower Devonian to late-Visean age testified by the Lizard Suture in southern Cornwall (e.g. Kirby, 1979; Floyd, 1984; Averbuch and Piromallo, 2012), in the Rhine Massif and Harz (Franke, 2000).

Ophiolite remnants of the Variscan oceans are preserved in many suture zones all over the European Variscan belt (Fig. 3.2.1). Here, there is a first group of oceanic rocks dated between 500 and 470 Ma. This time interval well matches with the Rheic Ocean opening. These ophiolites are in the Armorican Massif (Paquette et al., 2017), Galicia (Arenas et al., 2007; Sánchez Martínez et al., 2012), southern Brittany (Paquette et al., 2017), Bohemian Massif (Bowes and Aftalion, 1991; Timmermann et al., 2004), southern French Central Massif (Lotout et al., 2020), and the Alps (Ménot et al., 1988; Giacomini et al., 2007). Likewise, protolith ages of MORB-derived eclogites in Corsica, Sardinia, and Maures-Tanneron Massif are comprised between 490 and 440 (Palmeri et al., 2004; Cortesogno et al., 2004; Bellot, 2005; Giacomini et al., 2005; Franceschelli et al., 2007; Rossi et al., 2009).

A second group of Variscan ophiolites is instead characterized by markedly younger ages, mostly comprised between 400 and 370 Ma. These ophiolites are founded in Galicia (Díaz García et al., 1999; Pin et al., 2002; Sánchez Martínez et al., 2011; Arenas et al., 2014), southern Brittany (Paquette et al., 2017), Vosges (Skrzypek et al., 2012) and Sudetes (Dubińska et al., 2004; Kryza and Pin, 2010). The Rheic Ocean was almost close at that time, as represented in paleogeographic maps (Stampfli et al., 2002; 2013; Franke et al., 2017).

A third group of Variscan MORB-derived metabasites derives protoliths dated Ediacaran to early Cambrian (600 – 520 Ma), which are markedly older than the Rheic Ocean opening. These rocks are found in the Bohemian Massif (Timmermann et al., 2004; Soejono et al., 2010; Tichomirowa and Köhler, 2013; Rötzler and Timmerman, 2020), Maures-Tanneron Massif (Innocent et al., 2003), Ossa-Morena (Sánchez Lorda et al., 2014), and in the Alps (von Quadt, 1992; Miller and Thöni, 1995; Müller et al., 1996; Schaltegger and Gebauer, 1999; Schulz and

Bombach, 2003; Liati et al., 2009; von Raumer et al., 2013 and ref. therein). Since in some localities these MORBs are associated with crustal derived intrusive rocks (Müller et al., 1995; Innocent et al., 2003; Soejono et al., 2010; Tichomirowa and Köhler, 2013), they are considered as formed in a supra-subduction zone or back-arc basin at the time of Iapetus subduction beneath Gondwana (e.g. Schaltegger and Gebauer, 1999; von Raumer et al., 2015; Collett et al., 2020).

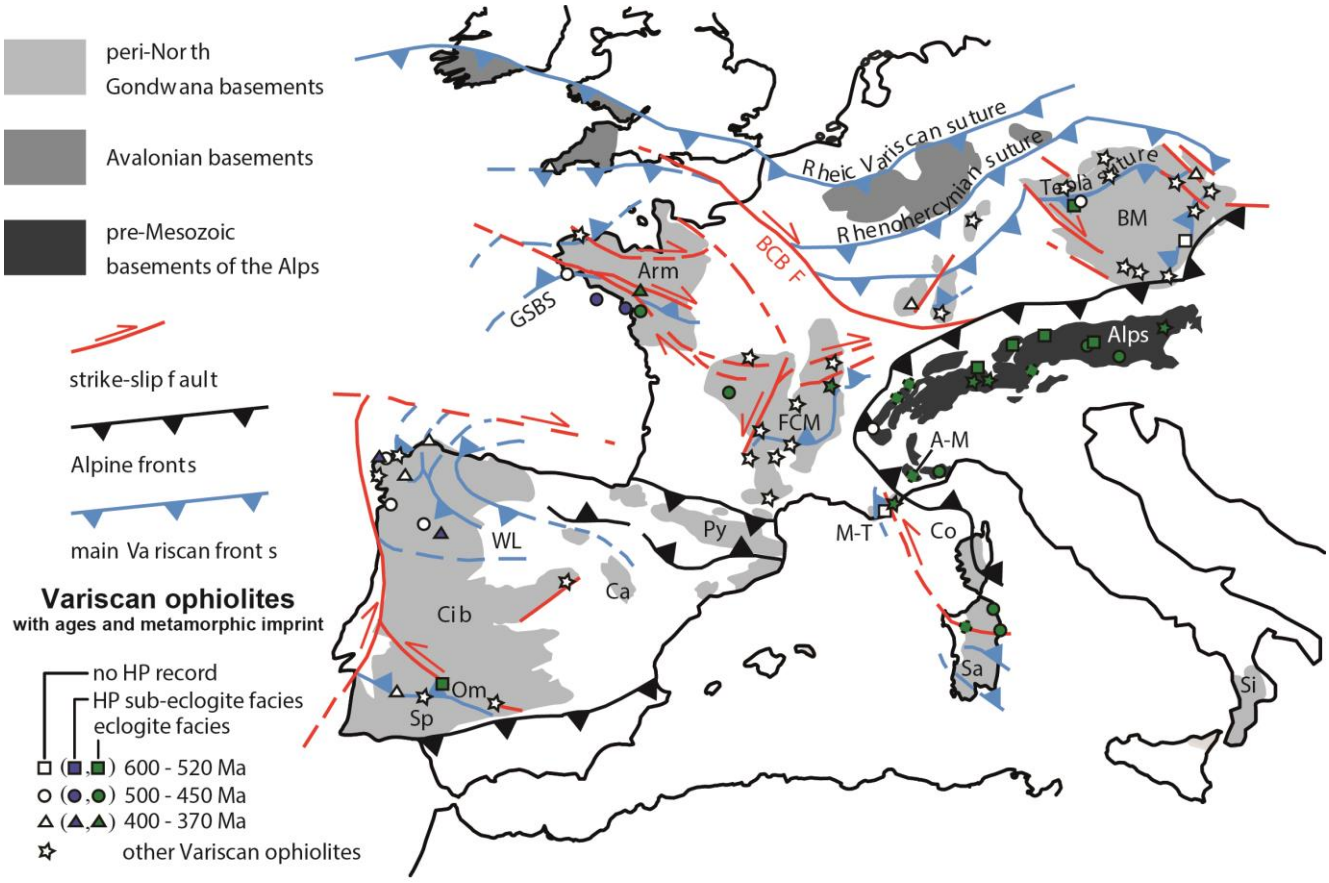

Figure 3.2.1. Simplified tectonic sketch of the Variscan belt (modified after Delleani et al., 2018) with positions of Variscan oceanic relics and eclogitized oceanic relics (ref. are in the text). A-M–Argentera-Mercantour Massif; Arm–Armorican Massif; BCBF–Bristol Channel-Bray Fault; BM–Bohemian Massif; Ca–Cantabrian terrane; Cib–Central Iberian; Co–Corsica; FMC–French Massif Central; M-T–Maures-Tanneron Massif; OM–Ossa Morena; Py–Pyrenees; Sa–Sardinia; Si–Sicilian-Apulian basements; SP–South Portuguese Zone; WL–West Asturian-Leonese.

Most of the Variscan ophiolites experienced HP/UHP metamorphism as a result of the Variscan subduction. However, age and the metamorphic conditions characterizing the Variscan subduction are only constrained in a few points along the European Variscan suture zones, due to pervasive re-equilibration in late-Variscan times. In southern Brittany, blue-schist (P = 1.7 – 2.3 GPa, T = 450 – 525°C) and eclogite-facies conditions (P = 1.6 – 2.5 GPa, T = 550 – 650°C) were attained between 380 and 355 Ma (Godard, 1988; Ballèvre et al., 2003; El Korh et al., 2009; Paquette et al., 2017). In the southern French Central Massif, the high pressure peak (P = 1.5 – 2.3 GPa, T = 560 – 800°C) is dated at around 380 and 360 Ma (Lotout et al., 2018, 2020). In the Bohemian Massif, eclogite facies conditions (P = 1.6 – 1.8 GPa, T = 650 – 720°C) were likely attained at 390-370 Ma (Beard et al., 1995; Timmermann et al., 2004; Faryad, 2012). Similarly, in the Iberian Massif, eclogite facies metamorphism (P = 2.1 – 2.6 GPa, T = 580 – 610 °C) is dated 380-365 Ma (Rodriguéz et al., 2003). In the Southern Variscan belt, eclogites from Sardinia experienced high pressure conditions (P = 1.3 –

2.1, T = 550 – 700°C) likely between 400 and 350 Ma (Palmeri et al., 2004; Giacomini et al., 2005; Franceschelli et al., 2007; Cruciani et al., 2011, Cruciani et al, 2015). In the Alps, radiometric ages interpreted as reflecting the eclogitic peak of the Variscan metamorphism widely span from 400 and 330 Ma (Miller and Thöni, 1995; Faryad et al., 2002; Tumiati et al., 2003; Giacomini et al., 2007; Spalla et al., 2014; Regorda et al., 2020).

The Argentera-Mercantour Massif

In the Argentera-Mercantour Massif (Fig. 3.2.2), Alpine metamorphism under upper greenschist facies conditions is more evident in shear zones dated 34-20 Ma, post-Variscan granites, and mafic dykes (Boucarut, 1967; Corsini et al., 2004; Sanchez et al., 2011; Filippi et al., 2019, 2020).

The Variscan basement of the Argentera-Mercantour Massif mostly comprises Upper Carboniferous migmatites, which derive from sedimentary sequences and mafic and acidic Ordovician (486 - 443 Ma) to Lower Carboniferous (332 ± 3 Ma) continental intrusives (Rubatto et al., 2001; 2010). These rocks have been exhumed in late Carboniferous times (Faure-Muret, 1955; Malaroda et al., 1970; Bortolami et al., 1974) and subsequently intruded by post-collisional granites and mafic dykes (Corsini et al., 2004; Compagnoni et al., 2010; Filippi et al., 2019, 2020).

Mafic boudins and serpentinites deriving from oceanic lithosphere are widespread in the migmatites, as known over decades (Faure-Muret, 1955; Malaroda et al, 1970; Bogdanoff, 1986; Latouche and Bogdanoff, 1987; Paquette et al., 1989; Jouffray et al., 2020). Mafic magma emplacement at 462 ± 6 Ma is supposed to mark the later stages of Ordovician rifting at the dawn of Rheic Ocean opening (Rubatto et al., 2001).

Eclogite facies assemblages are rarely preserved in mafic boudins, often re-equilibrated under HP granulite and amphibolite facies conditions at around 340 Ma (Latouche and Bogdanoff, 1987; Rubatto et al., 2001; 2010; Ferrando et al., 2008; Jouffray et al., 2020). P-T estimates performed on severely retrogressed eclogite samples point metamorphic peak conditions at around P = 1.3-1.8 GPa, T = 640-780°C, which were attained during a warm Variscan subduction (Latouche and Bogdanoff, 1987; Rubatto et al., 2001; Jouffray et al., 2020). Other autors envisage minor differences in P-T conditions between the eclogites and HP granulites (Ferrando et al., 2008; Compagnoni et al., 2010; Rubatto et al., 2010). They interpret the differences in mineral associations between the eclogites and the HP granulites as related to differences in bulk-rock chemical compositions and invoke a tectonic model accountable for the coincidence of pressure and temperature peaks in Argentera-Mercantour Massif.

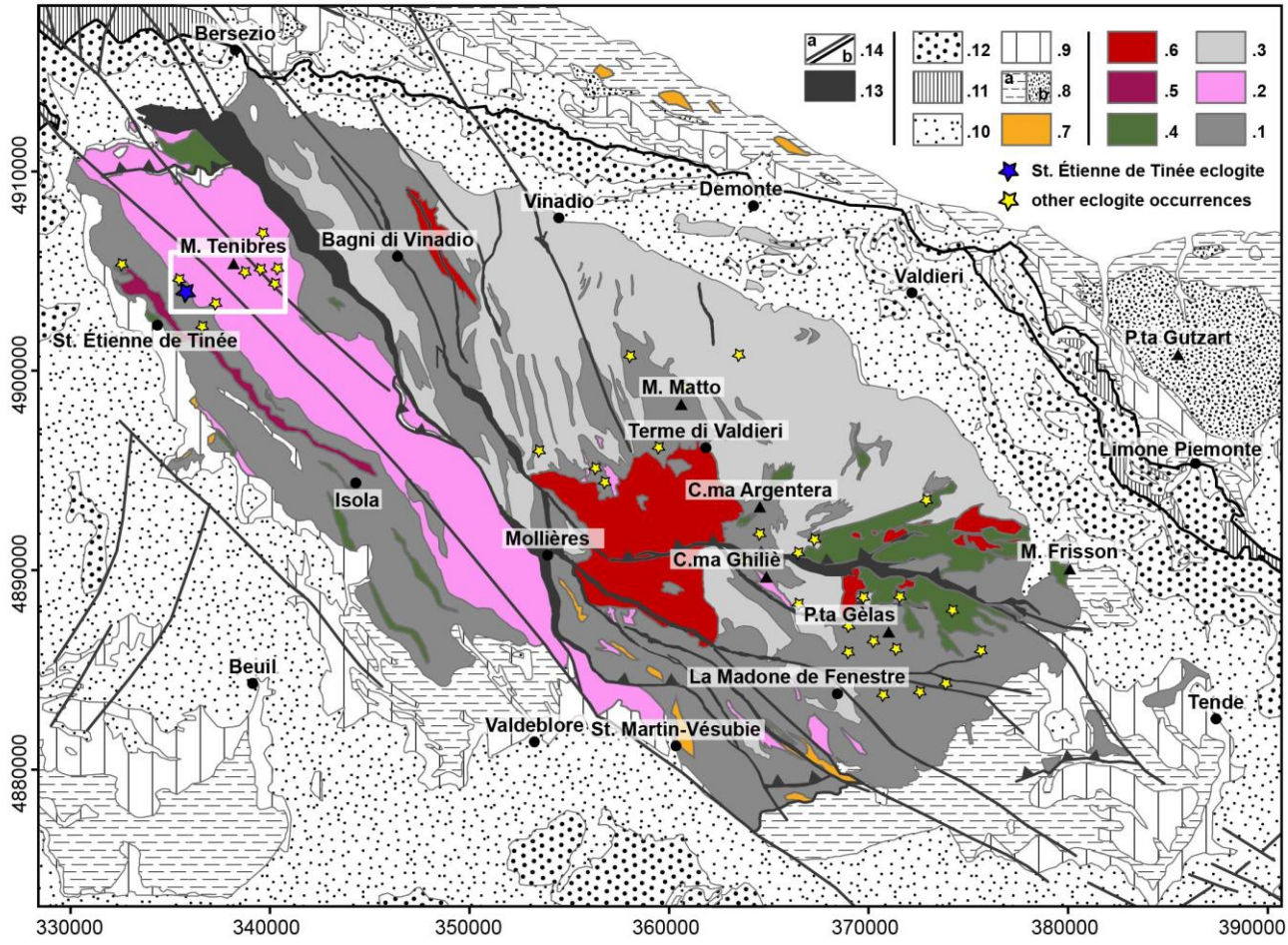

Figure 3.2.2. Simplified Geological map of the Argentera–Mercantour Massif (after Faure-Muret 1955; Malaroda et al. 1970; Gosso et al. 2019). The mapped area is contoured in white (Fig. 3.2.3). Variscan basement rocks (1 - 6): 1 = migmatitic paragneisses, 2 = migmatitic orthogneisses and meta-volcanics, 3 = Crd-bearing anatexites, 4 = Migmatitic amphibolites, 5 = meta-granodiorites, 6 = late carboniferous to early Permian granites. Late Carboniferous to Eocene sedimentary sequences (7 - 12): 7 = late Carboniferous siliciclastic sequences, 8 = Permian siliciclastic sequences (a) and volcanics (b), 9 = Triassic siliciclastic sequences and carbonates, 10 = Jurassic and early Cretaceous deep-sea sediments, 11 = Cretaceous flysches, 12 = late Cretaceous to Oligocene foreland succession. Structures: 13 = Variscan and Alpine amphibolite / greenschist facies shear zones, 14 = late to post-Alpine faults (a), Penninic Front (b).

Eclogite field occurrence

Several mafic eclogite boudins are wrapped by the dominant migmatitic foliation in the paragneisses and orthogneisses of the Tinée complex, in the western part of the Argentera-Mercantour Massif. Most of them pervasively re-equilibrated under amphibolite facies conditions (amphibole + plagioclase + quartz), with few exceptions. The analyzed samples come from a 30-meter sized eclogite boudin

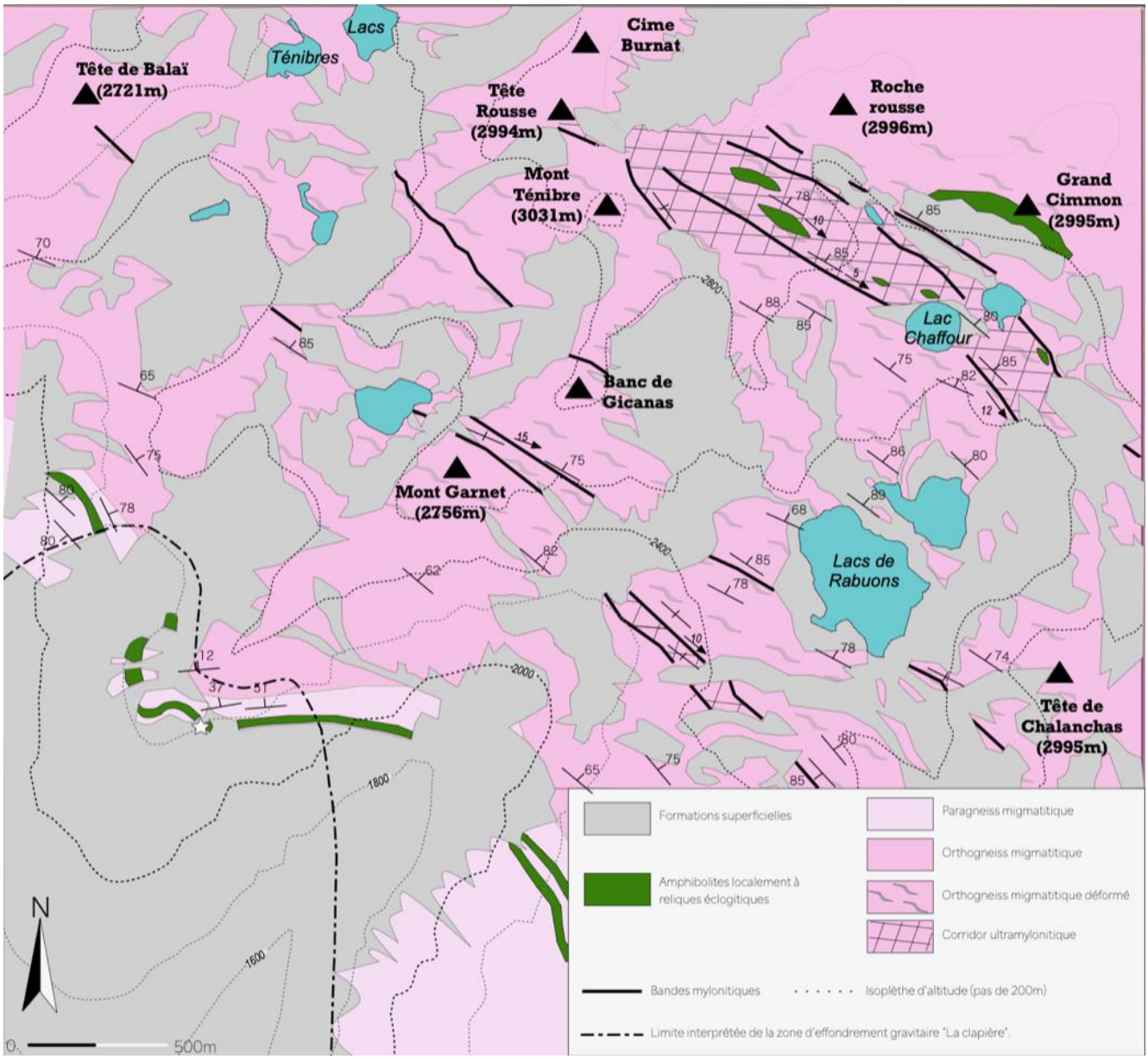

Figure 3.2.3. Geological map of the Mount Ténibre area, east of Saint-Étienne-de-Tinée (cfr. Figure 3.2.2 for location). A white star points the sampling locality for this study.

within migmatitic paragneisses, located a few tens of meters below the contact with the migmatitic orthogneisses, east of Saint Étienne de Tinée (Fig. 3.2.3).

Two superposed foliations are recorded within the eclogite: the youngest foliation is developed at the boudin margins and is parallel to the migmatitic external foliation in paragneisses. This foliation is supported by dark brown amphibole, plagioclase, and quartz (Fig. 3.2.4a). The oldest foliation is retained at boudin core and is truncated by the external foliation at boudin rim. The internal foliation is supported by alternance of garnet and dark-green amphibole rich-layers with plagioclase- and clinopyroxene-rich layers (Fig. 3.2.4b). The internal foliation is generally well developed, but not

Figure. 3.2.4. Mafic boudins in the mapped area (cfr. Fig. 3.2.3). A = re-equilibrated eclogite boudin in migmatitic orthogneiss at lac Chaffour. Internal foliation is supported by amphibole, plagioclase, and quartz and parallel to the external one. B = internal foliation in eclogite boudin supported by plagioclase, clinopyroxene, dark green amphibole, and garnet. C = low-strained core of the sampled eclogite boudin, with millimeter-sized garnet and omphacite.

dominant all over the mafic boudin core. The low-strain domains preserve "true eclogites" (garnet + omphacite > 70%vol, Rebay et al, 2010). Garnet and omphacite are sub-millimeter to centimeter sized, locally displaying a weak shape preferred orientation (Fig. 3.2.4c). The eclogitic assemblage includes garnet, ophacite, quartz, rutile, and rare clinozoisite grains. Garnet is rimmed by deep green amphibole and minor plagioclase coronae, whereas omphacite is partially replaced by lamellar symplectites of clinopyroxene, plagioclase, and minor green amphibole. The following paragraphs focused on the low-strained portions of the mafic boudin, where eclogite minerals are better preserved.

Whole rock geochemistry

One sample of Saint Étienne de Tinée eclogite was analyzed for major, minor, and trace elements at Prague, Centre for Lithospheric Research, Czech Geological Survey, by ICP-MS. Results are in supplementary data VI. The eclogite protolith was likely a sub-alkaline basalt, as envisaged by SiO_2 = 50.02 %wt and $Na_2O + K_2O$ = 3.40 %wt, as well as by Nb / Y = 0.06 and Zr / Ti = 0.01 (Fig. 3.2.5a).The N-MORB normalized spider diagram (Sun and McDonough, 1989) highlights enrichments in some LIL elements (Cs, Rb, Ba, K), U, and Pb with respect to the reference value (Fig. 3.2.5b). Enrichment in LIL elements may point interaction with fluids during the metamorphic evolution. C1-nornmalized REE pattern is flat on the reference N-MORB value (Fig. 3.2.5c), suggesting an oceanic origin for the Saint Étienne de Tinée eclogite.

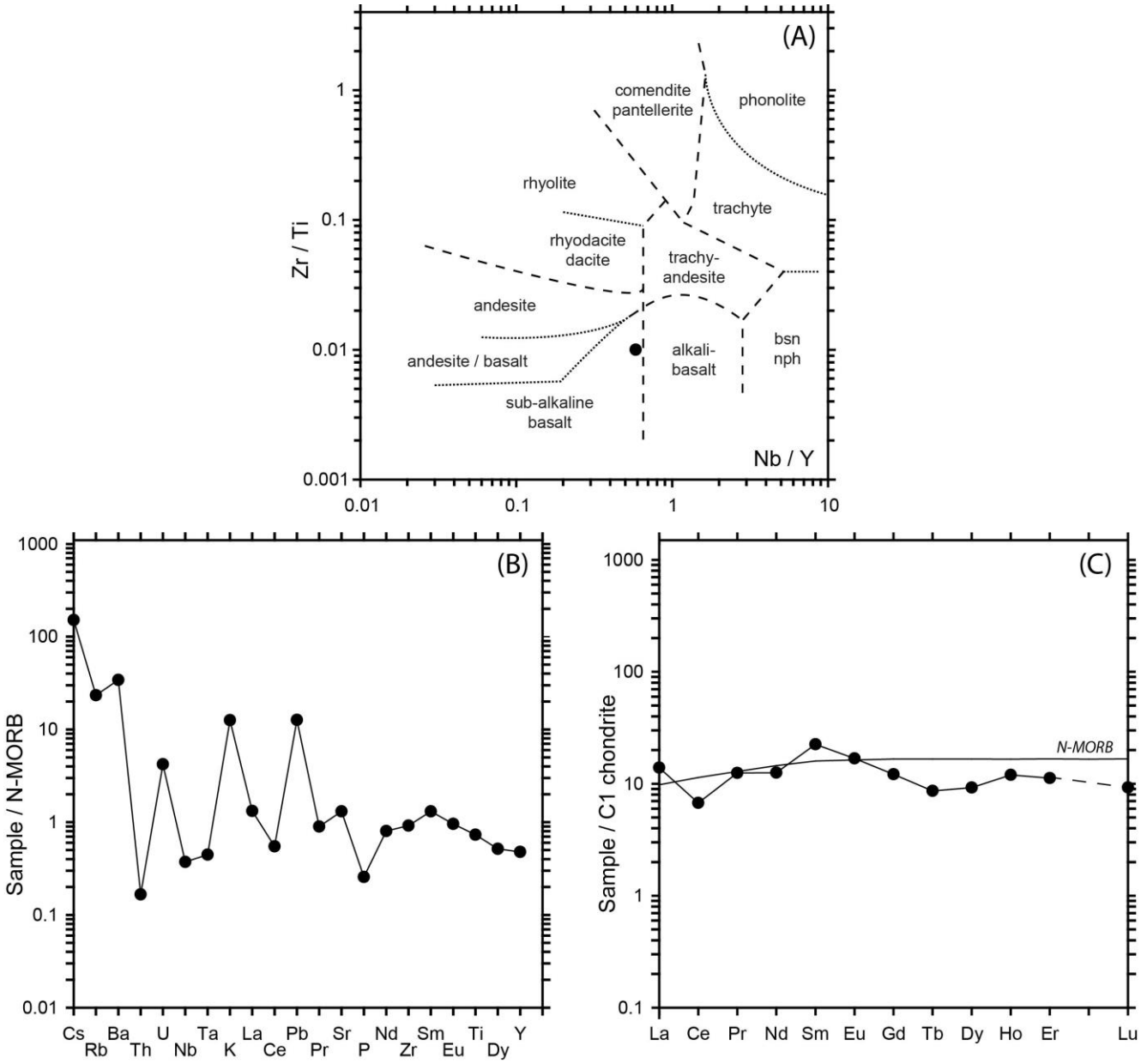

Figure 3.2.5. WR composition and classification of the Saint-Étienne-de-Tinée eclogite. A = Nb / Y versus Zr / Ti diagram (Winchester and Floyd, 1977); B = N-MORB normalized spider diagram (Sun and McDonough, 1989); C = C1 chondrite-normalized REE pattern (Sun and McDonough, 1989). N-MORB pattern is from Sun and McDonough (1989).

Microstructre and mineral chemistry

Microstructural and mineral-chemical analysis were performed at Università degli Studi di Milano with a JEOL 8200 Super Probe (WDS) at 15 kV accelerating voltage and with a beam current of 5 nA; natural silicates served as standards. Amphibole formulae were calculated checking the most satisfying results of 13, 15, 16 cations and 23 O normalizations (Locock, 2014), chlorite at 7 O, clinopyroxene at 4 cations and 6 O, clinozoisite at 8 cations and 12.5 O, feldspar at 4 O, and garnets at 8 cations and 12

O. Abbreviations of mole proportions (%) are: Mg# = Mg / (Mg + Fe_{tot}) (amphibole); Ae = 2 Na / (Ca + Mg + Fe^{2+} + 2 Na) * Fe^{3+} / (Al^{VI} + Fe^{3+}), Q = (Ca + Mg + Fe^{2+}) / (Ca + Mg + Fe^{2+} + 2 Na), Jd = 2 Na / (Ca + Mg + Fe^{2+} + 2 Na) * Al^{VI} / (Al^{VI} + Fe^{3+}), (clinopyroxene); An = Ca / (Ca + Na + K) (plagioclase); Grs = (Ca – 3/2 Fe^{3+}) / (Ca + Mn + Mg + Fe^{2+}), Prp = Mg / (Ca + Mn + Mg + Fe^{2+}), Alm = Fe^{2+} / (Ca + Mn + Mg + Fe^{2+}), Sps = Mn / (Ca + Mn + Mg + Fe^{2+}), Adr = (3/2 Fe^{3+}) / (Ca + Mn + Mg + Fe^{2+}) (garnet). Selected analyses are presented in Table 3.2.1. Compositional variations characterizing eclogitic and post-eclogitic mineral assemblages are summarized in Table 3.2.2 and Figure 3.2.6. The complete dataset is attached in supplementary data VI.

Garnet

Three generations of garnet are distinguished in the Saint Étienne de Tinée eclogite. Grt 1 ($Alm_{50-55}Grs_{24-29}Prp_{13-19}Sps_{2-4}Adr_{1-2}$) is the core of the millimeter-sized garnet grains and is characterized by highly lobate and feathered boundaries (Fig. 3.2.7a). Grt 0 ($Alm_2Grs_{75}Prp_0Sps_0Adr_{23}$) is enclosed together with quartz, albite, chlorite, prehenite, pumpellyite, titanite, rutile, and apatite as small globular grains in Grt 1 (Fig. 3.2.7a and b). Grt 2 ($Alm_{48-55}Grs_{18-28}Prp_{20-27}Sps_{1-4}Adr_{0-3}$) is the main part of the garnet grains. Grt 2 includes omphacite, rutile, ilmenite, albite, oligoclase, and zircon (Fig. 3.2.7c). Lozenge-shaped inclusions completely pseudomorphosed by clinopyroxene and oligoclase, are in between Grt 1 and Grt 2 (Fig. 3.2.7a and b). These inclusions are rimmed by omphacite or amphibole (Fig. 3.2.7a and b).

Omphacite

Two generations of omphacite are distinguished. Small grains of Omp 1 ($Ae_7Q_{38}Jd_{55}$, Al_{VI} = 0.50 pfu) are preserved at the core of Omp 2. Omp 2 is compositionally heterogeneous: Omp 2 core is $Ae_{4-10}Q_{44-53}Jd_{39-48}$ (Al_{VI} = 0.42 – 0.50 pfu), Omp 2 mantle is $Ae_{6-14}Q_{53-64}Jd_{27-38}$ (Al_{VI} = 0.30 – 0.41 pfu), and Omp 2 rim is $Ae_{4-13}Q_{59-70}Jd_{22-33}$ (Al_{VI} = 0.24 – 0.36 pfu). Omp 2 rim with the lowest Al content (Al^{VI} = 0.24 – 0.28 pfu) form intergrowths with oligoclase. Homogeneous grains with compositions similar

Analysis	JM1-C6-188	JM1-C6-189	JM2-C2-47		JM1-C5-153	JM2-C0-9
(wt%)	**Omp2 core**	**Omp2 mantle**	**Omp2 rim**		**Grt1**	**Grt2**
SiO_2	54.35	53.14	54.09	SiO_2	39.15	38.45
TiO_2	0.15	0.19	0.10	TiO_2	0.12	0.13
Al_2O_3	11.50	9.27	6.91	Al_2O_3	22.06	22.51
Cr_2O_3	0.01	0.05	0.00	Cr_2O_3	0.00	0.05
MnO	0.00	0.03	0.04	MnO	0.79	0.45
FeO_T	5.85	6.83	7.38	FeO_T	23.92	23.90
NiO	0.05	0.05	0.06	NiO	0.05	0.03
MgO	7.70	9.03	10.00	MgO	5.04	5.69
CaO	13.38	15.61	15.82	CaO	10.77	10.30
Na_2O	6.87	5.35	5.11	Na_2O	0.00	0.10
K_2O	0.01	0.01	0.00	K_2O	0.01	0.01
Total	**99.88**	**99.57**	**99.51**	**Total**	**101.91**	**101.62**
Si	1.94	1.92	1.96	Si	2.98	2.92
Ti	0.00	0.01	0.00	Ti	0.01	0.01
Al_{IV}	0.06	0.08	0.04	Al_{IV}	0.02	0.08
Al_{VI}	0.42	0.32	0.26	Al_{VI}	1.96	1.94
Cr	0.00	0.00	0.00	Cr	0.00	0.00
Ni	0.00	0.00	0.00	Ni	0.00	0.00
Fe^{2+}	0.07	0.08	0.09	Fe^{2+}	1.49	1.47
Fe^{3+}	0.11	0.12	0.14	Fe^{3+}	0.03	0.05
Mn	0.00	0.00	0.00	Mn	0.05	0.03
Mg	0.41	0.49	0.54	Mg	0.57	0.64
Ca	0.51	0.60	0.61	Ca	0.88	0.84
Na	0.48	0.38	0.36	Na	0.00	0.02
K	0.00	0.00	0.00	K	0.00	0.00
En	0.21	0.24	0.27	Andr	0.02	0.03
Fs	0.03	0.04	0.04	Alm	0.50	0.49
Wo	0.24	0.25	0.30	Pyr	0.19	0.22
Jd	0.42	0.32	0.26	Gr	0.28	0.26
Acm	0.05	0.06	0.10	Spess	0.02	0.01
CaFe-Tsch	0.00	0.06	0.00			
CaTi Tsch	0.00	0.01	0.00			
Ca-Tsch	0.03	0.03	0.02			

Table 3.2.1. Selection of mineral chemical analyses (Part I).

	JM2-C0-6	JM1-C0-1	JM1-C6-190		JM2-C5-91
	Amp1a	**Amp1b**	**Amp1c**		**Pl1c**
	Ti-rich taramite	sadanagaite	pargasite		
SiO_2	41.54	38.28	41.17	SiO_2	65.13
TiO_2	3.60	0.03	0.31	TiO_2	0.06
Al_2O_3	16.74	22.03	16.50	Al_2O_3	22.90
Cr_2O_3	0.00	0.02	0.01	Cr_2O_3	0.00
MnO	0.02	0.14	0.10	MnO	0.00
FeO_T	13.88	17.24	12.14	FeO_T	0.12
NiO	0.00	0.05	0.03	NiO	0.05
MgO	9.08	7.72	12.42	MgO	0.02
CaO	9.44	9.15	11.36	CaO	2.70
Na_2O	4.94	4.26	3.75	Na_2O	10.01
K_2O	0.16	0.20	0.10	K_2O	0.01
Total	**99.42**	**99.13**	**97.89**	**Total**	**101.00**
Si	6.04	5.57	6.00	Si	2.84
Ti	0.39	0.00	0.03	Ti	0.00
Al_{IV}	1.96	2.43	2.00	Al	1.18
Al_{VI}	0.91	1.35	0.84		
Cr	0.00	0.00	0.00	Cr	0.00
Ni	0.00	0.01	0.00	Ni	0.00
Fe^{2+}	1.69	1.29	1.15	Fe	0.00
Fe^{3+}	0.00	0.81	0.33		
Mn	0.00	0.02	0.01	Mn	0.00
Mg	1.97	1.68	2.70	Mg	0.00
Ca	1.47	1.43	1.77	Ca	0.13
Na	1.47	1.45	1.06	Na	0.85
K	0.03	0.04	0.02	K	0.00
				Ab	0.87
				An	0.13
				Kfs	0.00

Table 3.2.1. Selection of mineral chemical analyses (Part II).

Stage	Mineral	X Fe	X Mg	X Ca	Si (pfu)	Al^{VI} (pfu)	Na/ (Ca+Na)	Ti (pfu)	Mg#	Fe^{3+}/ (Al^{VI} + Fe^{3+})	An	Ab
M0	Pl 0										**1 - 9**	**91 - 99**
	(11 data)										4 ± 3	96 ± 3
	Pmp								**0.39 - 0.50**			
	(3 data)								0.44 ± 0.05			
	Chl				**2.76-3.02**	**1.16-1.36**			**0.44 - 0.48**			
	(7 data)				2.86 ± 0.09	1.29 ± 0.07			0.46 ± 0.01			
M1	Omp 1				**1.93**	**0.59**	**0.60**		**0.69**			
	(1 data)											
	Omp 2 core				**1.92 - 1.99**	**0.40 - 0.50**	**0.43 - 0.56**		**0.69 - 0.76**			
	(35 data)				1.96 ± 0.02	0.45 ± 0.02	0.51 ± 0.03		0.72± 0.02			
	Grt 1	**0.51 - 0.57**	**0.14 - 0.19**	**0.27 - 0.32**								
	(7 data)	0.54 ± 0.02	0.17 ± 0.02	0.29 ± 0.02								
	Omp 2 middle				**1.90 - 1.98**	**0.28 - 0.39**	**0.33 - 0.44**		**0.65 - 0.76**			
	(22 data)				1.93 ± 0.02	0.33 ± 0.04	0.39 ± 0.03		0.71± 0.02			
	Omp 2 rim				**1.86 - 1.96**	**0.24 - 0.33**	**0.30 - 0.37**		**0.69 - 0.74**			
	(5 data)				1.92 ± 0.03	0.28 ± 0.03	0.33 ± 0.03		0.71± 0.02			
	Grt 2	**0.50 - 0.55**	**0.20 - 0.28**	**0.18 - 0.29**								
	(61 data)	0.52 ± 0.01	0.23 ± 0.01	0.24 ± 0.02								
	Cz									**0.11 - 0.13**		
	(3 data)									0.12 ± 0.01		
M2	Amp 1a				**5.79 - 6.13**	**0.90 - 1.44**	**0.37 - 0.54**	**0.25 - 0.51**	**0.46 - 0.62**			
	(7 data)				5.97 ± 0.11	1.13 ± 0.19	0.48 ± 0.05	0.36 ± 0.09	0.55 ± 0.05			
	Amp 1b				**5.57 - 5.94**	**1.07 - 1.47**	**0.39 - 0.49**	**0.00 - 0.13**	**0.41 - 0.64**			
	(31 data)				5.71 ± 0.10	1.24 ± 0.09	0.43 ± 0.02	0.02 ± 0.04	0.48 ± 0.05			
	Amp 1c				**5.89 - 6.28**	**0.83 - 1.02**	**0.34 - 0.46**	**0.03 - 0.07**	**0.50 - 0.65**			
	(7 data)				6.03 ± 0.11	0.93 ± 0.07	0.40 ± 0.04	0.05 ± 0.02	0.59 ± 0.05			
	Amp 1d				**6.28 - 6.45**	**0.53 - 0.90**	**0.36 - 0.41**	**0.03 - 0.10**	**0.53 - 0.64**			
	(11 data)				6.24 ± 0.08	0.72 ± 0.09	0.38 ± 0.02	0.07 ± 0.02	0.60 ± 0.03			
	Cpx 1a				**1.96 - 1.97**	**0.01 - 0.06**	**0.05 - 0.06**		**0.52 - 0.79**			
	(4 data)				1.97 ± 0.01	0.04 ± 0.02	0.05 ± 0.00		0.64 ± 0.11			
	Cpx 1b				**1.90 - 1.97**	**0.10 - 0.27**	**0.12 - 0.28**		**0.72 - 0.83**			
	(14 data)				1.94 ± 0.02	0.18 ± 0.05	0.20 ± 0.06		0.76 ± 0.03			
	Pl 1a										**41 -43**	**57 - 59**
	(2 data)										42 ± 0.01	58 ± 0.01
	Pl 1b										**16 - 31**	**69 - 84**
	(6 data)										23 ± 0.06	76 ± 0.06
	Pl 1c										**8 - 22**	**77 - 92**
	(32 data)										13 ± 0.04	86 ± 0.04
M3	Amp 2				**6.03 - 6.08**	**0.62 - 0.82**	**0.39**	**0.07 - 0.09**	**0.52 - 0.54**			
	(2 data)				6.06 ± 0.03	0.72 ± 0.10		0.08 ± 0.01	0.53 ± 0.01			
	Pl 2										**15 - 21**	**79 - 84**
	(3 data)										18 ± 0.02	82 ± 0.02
	Cpx 1				**1.90 - 1.97**	**0.10 - 0.27**	**0.12 - 0.28**		**0.72 - 0.83**			
	(14 data)				1.94 ± 0.02	0.18 ± 0.05	0.20 ± 0.06		0.76 ± 0.03			
M4	Amp 3				**7.88**	**0.33**	**0.02**	**0.01**	**0.45**			
	(1 data)											

Table 3.2.2. Compositonal intervals (bold, apfu) and average values (± s.d.) for minerals of Saint-Étienne-de-Tinée eclogite.

to Omp 2 core or Omp 2 mantle are founded. Omp 2 includes Grt 2, rutile, albite, apatite, and zircon (Fig. 3.2.7d).

Amphibole

Six groups of amphibole are distinguished in the basis of the microstructural site, and divided in three generations on the basis of growth relationships. Amp 1a rims inclusion of rutile, ilmenite, and titanite in Grt 1 and Grt 2 (Fig. 3.2.7a and b). Amp 1a is Ti-rich taramite or Ti-rich sadanagaite, characterized by Si = 5.79 – 6.13 pfu, Al = 2.78 – 3.47 pfu, Ti = 0.25 - 0.51 pfu, Mg# = 0.46 – 0.62, and Na = 0.99 - 1.45 pfu. Amp 1a with the highest Na contents is in contact with the albite inclusions in garnet. Amp 1b forms coronae around Grt 2 together with plagioclase of different composition and ilmenite (Fig. 3.2.7a). More rarely, Amp 1b form rims around omphacite inclusions in garnet (Fig. 3.2.7c). Also Amp 1b is sadanagaite or taramite, with Si = 5.57 – 5.94 pfu, Al = 3.22 – 3.82 pfu, Mg# = 0.41 – 0.64 and Na = 1.07 – 1.26 pfu. Ti in Amp 1b is generally lower than 0.04 pfu, except where it is in contact with ilmenite inclusions (Ti = 0.10 – 0.13 pfu). Amp 1c (pargasite or sadanagaite) forms coarse-grained irregular crystals in the outer part of the coronae around garnet and in the rock matrix, together with oligoclase and ilmenite (Fig. 3.2.7a and d). More rarely, Amp 1c forms symplectites with calcic clinopyroxene and oligoclase. Rims of Amp 1c are developed also around clinozoisite grains in the rock matrix. Amp 1c is characterized by Si = 5.89 – 6.08 pfu, Al = 2.83 – 3.01 pfu (with Al content increasing towards garnet rim), Ti = 0.03 – 0.07 pfu, Mg# = 50 – 65, and Na = 0.90 – 1.18 pfu. Amp 1d (pargasite) rims Omp2 together with oligoclase (Fig. 3.2.7a). Amp 1d is characterized by Si = 6.18 – 6.45 pfu, Al = 2.09 – 2.64 pfu, Ti = 0.03 – 0.10 pfu, Mg# = 53 – 64, and Na = 0.96 – 1.08 pfu. Amp 2 (pargasite) fills late veins together with oligoclase and calcic clinopyroxene. Amp 2 is characterized by Si = 6.03 – 6.08, Al = 2.53 – 2.79 pfu, Ti = 0.07 – 0.09 pfu, Mg# = 52 – 54, and Na = 1.08 – 1.10 pfu. Rare grains of Amp 3 (actinolite) replace previous generations of amphibole or fills small fractures together with chlorite. Amp 3 is characterized by Si = 7.88 pfu, Al = 0.31 pfu, and Ti = 0.01 pfu, (Mg# = 0.45), and Na = 0.04 pfu.

Calcic clinopyroxene

Three generations of calcic clinopyroxene with variable Na content are found in different microstructural sites. Calcic clinopyroxene always occurs with oligoclase, in most of the cases forming

symplectites. Cpx 1a ($Ae_{0-4}Q_{95}Jd_{0-4}$) replaces lozenge-shaped inclusions in between Grt 1 and Grt 2 (Fig. 3.2.7a and b). Cpx 1b and oligoclase form symplectites after omphacite, with or without Amp 1c (Fig. 3.2.7a, c and d). Cpx 1b replacing omphacite cores ($Ae_{4-12}Q_{73-78}Jd_{14-22,}$ Al_{VI} = 0.27 – 0.17 pfu) is Na-richer than Cpx 1b replacing omphacite rims ($Ae_{3-5}Q_{85-88}Jd_{8-12}$, Al_{VI} = 0.10-0.14 pfu). Cpx 2 ($Ae_{5-8}Q_{86-91}Jd_{4-6}$, Al_{VI} = 0.06 – 0.07 pfu) fills late veins together with Amp 2 and oligoclase.

Plagioclase

Five groups of plagioclase are distinguished and grouped in three generations as indicated by microstructural site and growth relationships, respectively. Pl 0 is albite (An_{1-9}) and forms globular inclusion in omphacite and garnet cores (Fig. 3.2.7a and b). Pl 1a is labradorite (An_{57-59}) and is found in the innermost part of the Amp 1b/1c- and ilmenite-bearing coronae around garnet. Pl 1b (An_{16-31}) is oligoclase and is in the middle part of coronae around garnet. Pl 1c is oligoclase (An_{8-19}) and it may form symplectites with Cpx 1b after omphacite, intergrowths with Omp 2 rim or Amp 1d around omphacite grains, intergrowths with Amp 1c in the external part of the coronae around garnet, or replace lozenge-shaped inclusion in garnet with Cpx 1a (Fig. 3.2.7a, c and d). Pl 2 (An_{15-21}) fills late veins together with Amp 2 and Cpx 2.

In summary, the following five stages of metamorphic re-equilibration are identified by microstructural analysis in the mafic eclogite:

1) A first metamorphic re-equilibration M0 is testified by globular inclusions of Pl 0, chlorite, prehenite, pumpellyite, titanite, apatite, quartz, and Grt 0 in Grt 1, and inclusions of Pl 0 in Omp 2. Mutual relationships between these phases are not observed preventing further refinement of pre-eclogitic stages. Prehenite-pumpellyite facies conditions are reasonably supposed.
2) The dominant re-equilibration under eclogite facies conditions (M1), testified by mutual inclusion relationships between Grt 1 and Omp 2 core (M1a) first, and then between Grt 2 and Omp 2 mantle (M1b). Clinozoisite (Fe^{3+} / (Al^{VI} + Fe^{3+}) = 0.11 – 0.13), rutile, and quartz complete the eclogitic assemblage. Lozenge-shaped inclusions between Grt 1 and Grt 2 are remnants of eclogitic and/or pre-eclogitic amphiboles (pre-M1b). Omp 1 likely represents an earlier eclogitic stage.
3) Retrogression in the amphibole and plagioclase stability field (M2), as testified by (a) Omp 2 rim at equilibrium with Pl 1c, (b) coronae of Amp 1b, Pl 1a, Pl 1b, Pl 1c, and ilmenite around

Grt 2, (c) coronae of Amp 1d and Pl 1c around Omp 2, and (d) Cpx 1b + Pl 1c ± Amp 1c symplectites after omphacite. Amp 1a rims around Ti-rich inclusions in garnet probably

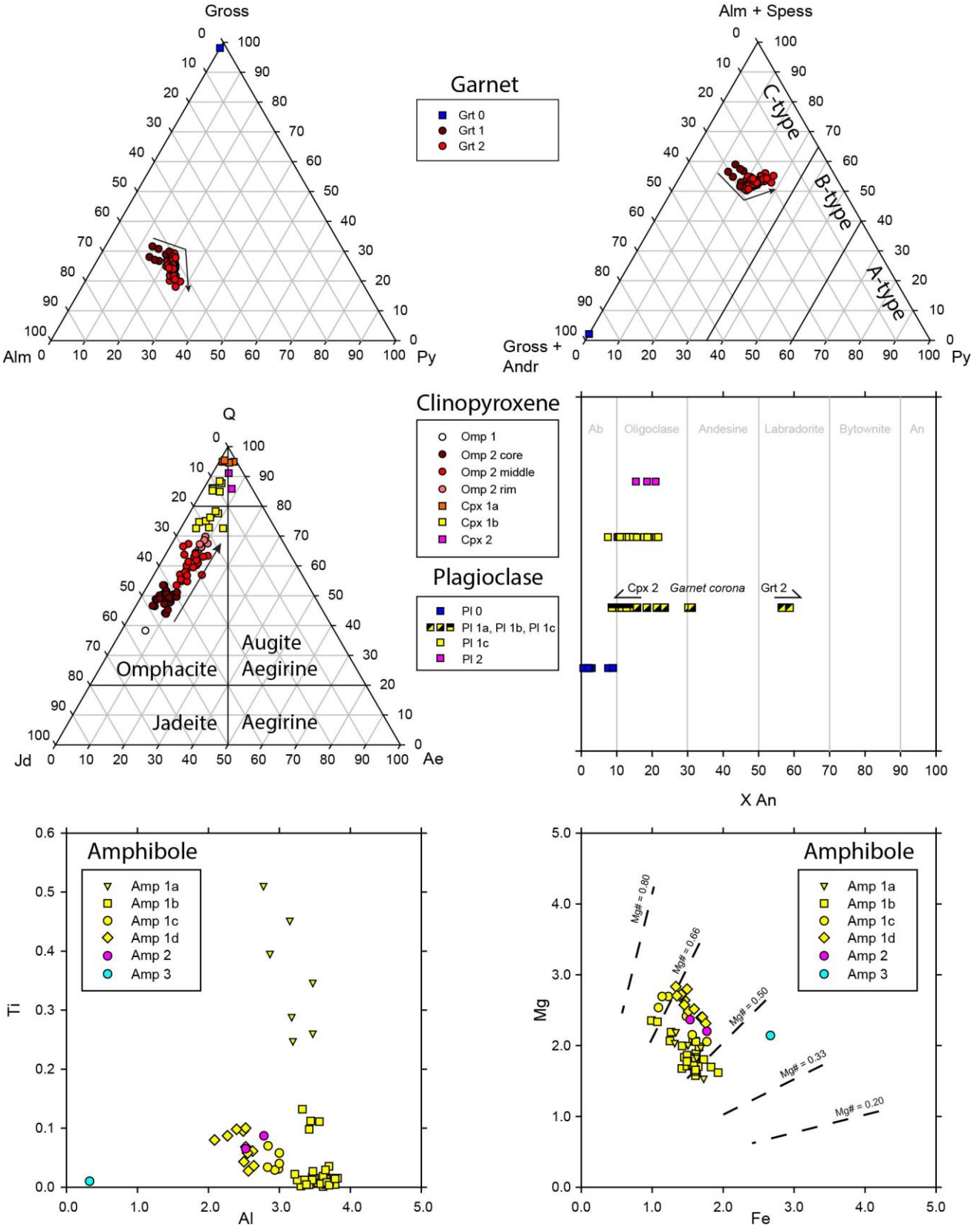

Figure 3.2.6. Compositions of garnet, clinopyroxene, plagioclase, and amphibole in the Saint-Étienne-de-Tinée eclogite.

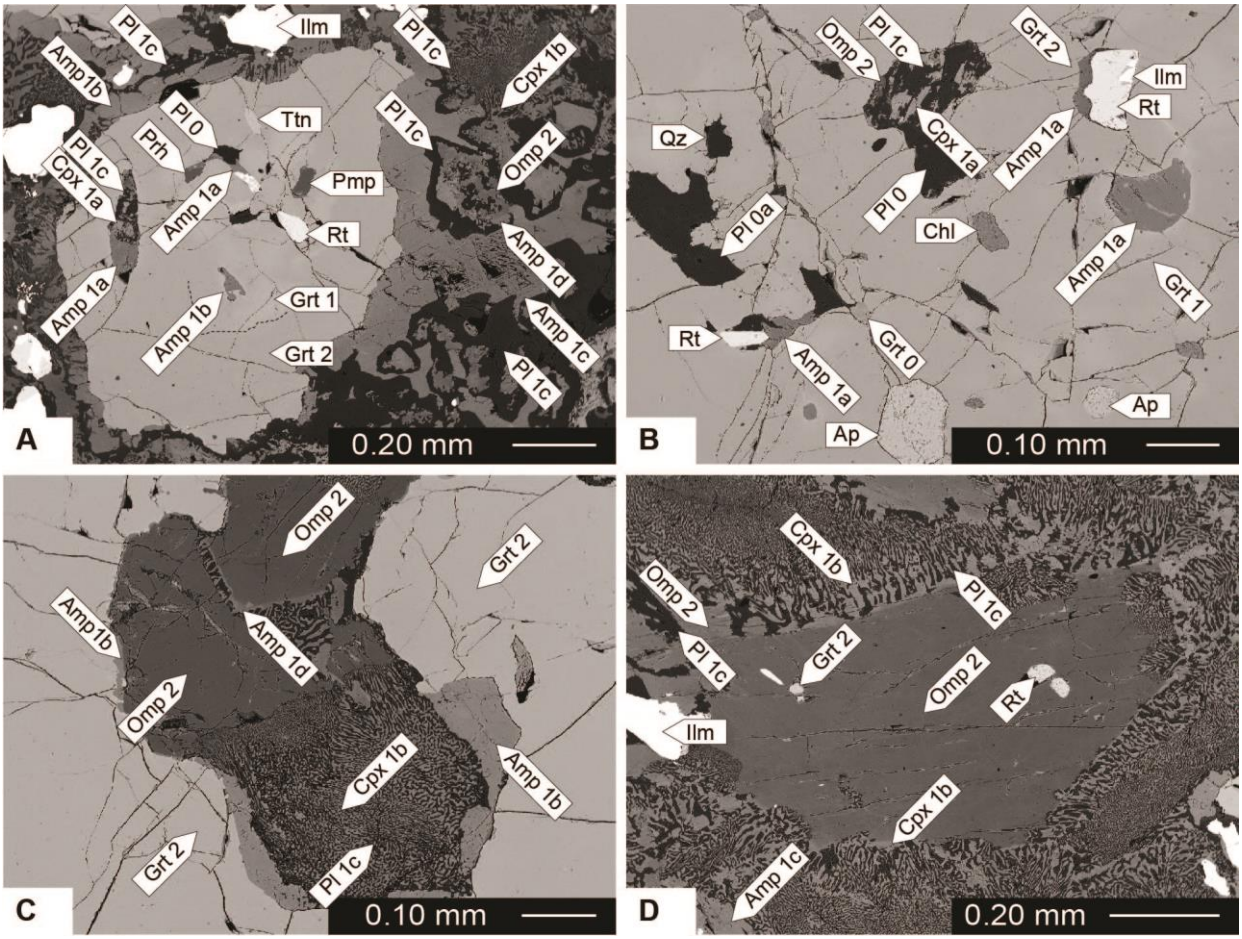

Figure 3.2.7. BSE images of the Saint-Étienne-de-Tinée eclogite. A: millimeter-sized garnet porphyroblast with Grt 1 at core and Grt 2 at rim. Core of Grt 1 includes rutile, titanite, prehnite, pumpellyite, albite, and ilmenite. Grt 2 includes a lozenge-shaped domain completely pseudomorphosed by Pl 1c and Cpx 1a and rimmed by Amp 1a. The garnet porphyroblast is wrapped by a corona of Amp1b, Pl1c and ilmenite. In the rock matrix, a sub-millimeter sized Omp 2 grain is rimmed by Amp 1d and Pl 1c. Symplectites of Pl 1c and Cpx 1b pervasively replace other omphacite grains. B: Grt 1 including Grt 0, Pl 0, quartz, chlorite, rutile and apatite. A lozenge-shaped domain is completely pseudomorphosed by Pl 1c and Cpx 1a. Rutile inclusions are rimmed by Amp 1a and, locally, by ilmenite. C: Omp 2 grains included within Grt 2. Omp 2 is rimmed by Amp 1d and replaced by symplectites of Cpx 1 and Pl 1c. Amp 1b rims Omp 2 and symplectite domains. D: millimeter sized omphacite (Omp 2) porphyroblast including Grt 2 and rutile. Inter-grows between Omp 2 and Pl 1c suggest that the rims of Omp 2 equilibrated together with Pl1c. Symplectites of Cpx 1b and Pl 1c pervasively replaced other omphacite grains.

developed in this phase. The compositional variations for M2 amphibole, plagioclase, and clinopyroxene are better explained in terms of compositional heterogeneities

inherited from previous stages of fabric development than in terms of changing of metamorphic conditions. The high Al-content in both Amp 1a and Amp 1b suggests that they crystallized on

Al-rich microsites and thus after garnet. Stability or metastability of garnet during M2 is hardly assessable, and any further refinement of the M2 phase is precluded in absence of strain-derived microstructures in the analyzed sample. Different Na contents in Cpx 1b seem to be controlled by the composition of the former omphacite.

4) Further retrogression (M3) testified by late-veins filled by Cpx 2, Pl 2, and Amp 2 that crosscut syn-M2 symplectites around Omp 2 and syn-M2 coronae around Grt 2.
5) Late greenschist facies re-equilibration (M4) testified by Amp 3 and chlorite replacement of mafic minerals and filling small fractures.

Physical conditions of metamorphism

Metamorphic conditions for the eclogitic M1 event are firstly estimated by matching clinopyroxene – garnet thermometer (Krogh-Ravna, 2000) and Na-in clinopyroxene barometer (Holland, 1980) on Grt 2 and Omp 2 grains at mutual contact. Results suggest that M1 event took place at $P \geq 1.47 – 1.57$ and $T \leq 650\text{-}700°C$.

Pseudosections have been computed in the NCFMASHTO system with THERIAK-DOMINO (De Capitani and Petrakakis, 2010) considering the thermodynamic database ds55 (Holland and Powell, 1998; 2003) and including a-x relationships for garnet (White et al., 2007), feldspar (Holland and Powell, 2003), amphibole (Diener et al., 2007), clinopyroxene (Green et al., 2007), orthopyroxene (White et al., 2002), chlorite, hercynite-spinel, and talc (Holland and Powell, 1998). The aim of the modeling is to constrain the P-T conditions for the eclogitic M1 event. Since M0 mineral assemblages are rarely preserved as sub-millimetric inclusion within garnet, the WR composition of the sample is considered as reacting volume during M1, with water in excess (supplementary material VI). The bulk rock composition has been corrected for apatite by subtracting from the bulk a molar content of calcium equal to 1.66 of phosphor. In addition, potassium was removed from the bulk because of WR concentration of K_2O lower than 1% and absence of K-bearing minerals, also considering that the adopted amphibole a-x relationship does not include potassium. The only phase in the eclogitic paragenesis including significative Fe^{3+} is epidote. A Fe^{3+} / Fe_{tot} molar ratio = 10 % mol has thus been chosen because it well reproduces the composition of the observed clinozoisite (Fe^{3+} = 0.33 – 039 pfu) at the P-T conditions of interest.

The assemblage garnet + omphacite + clinozoisite + rutile + quartz is not predicted by the model, which always include amphibole and/or kyanite and or talc (Fig. 3.2.8). However, in most of the P-T fields the samples re-equilibrated as “true” eclogite, with omphacite and garnet > 70% vol. The modal amount of additional amphibole, kyanite, and talc is less than 15%vol. The retrogressed character of

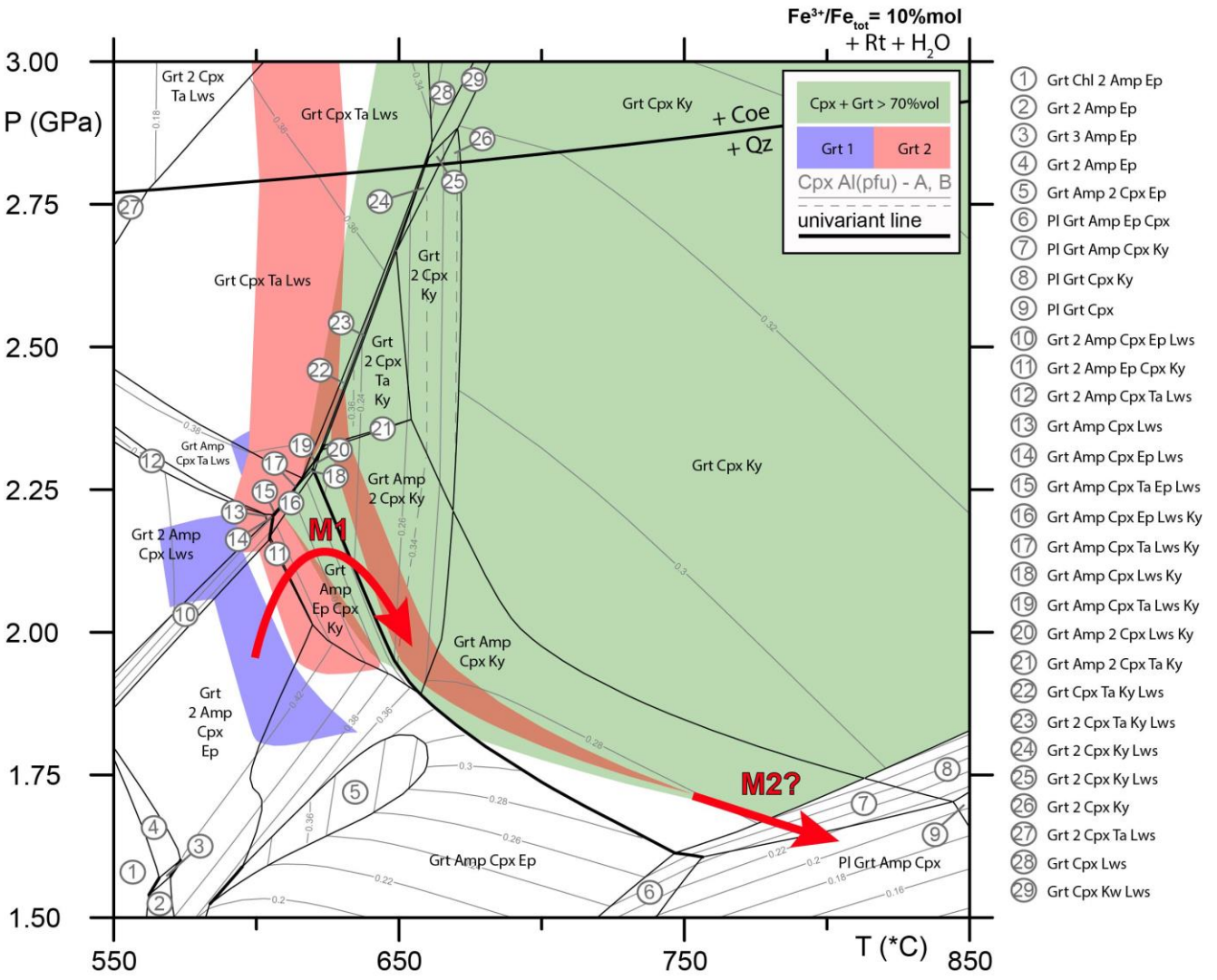

Figure 3.2.8. P-T pseudosection computed for WR composition (supplementary data VI), with water in excess, and corrected by apatite. Molar Fe^{3+}/Fe_{tot} ratio is fixed at 0.10. Rutile, quartz / coesite, and H_2O are present in all fields. Composition of Grt 1 (blue field) and Grt 2 (red field) are determined by intersecting Fe(X), Mg(X), and Ca(X) garnet isopleths in the compositional ranges defined in Table 3.2.2.

the sample may thus have precluded the preservation of these minor phases, as the amphibole inclusions within garnet may suggest.

Compositional isopleths for garnet are added to the pseudosection for discriminating the field of stability of Grt 1 and Grt 2. Grt 1 is stable in the Grt + 2 Amp + Cpx + Lws + Qz + Rt, Grt + 2 Amp + Cpx + Ep + Lws, Grt + 2 Amp + Cpx + Ep + Rt + Qz, and Grt + Amp + Cpx + Ep fields (amphibole eclogite facies) at T =570 – 640°C and P = 1.80 – 2.20 GPa (Fig. 3.2.8). Grt 2 is stable in Grt + Amp + Cpx + Ep + Ky, Grt + Amp + 2 Cpx + Ky, and Grt + Amp + Cpx + Ky fields (kyanite eclogite facies) as well as in Grt + Cpx + Ta + Lws (lawsonite eclogite facies) at T comprised between 660 and 750°C and pressure between 1.70 and 2.80 GPa (Fig. 3.2.8).

Finally, Al^{VI} in clinopyroxene isopleths are added for shrinking the P-T inverval accountable for the eclogitic assemblage development. Omp 2 core is stable with Grt 1 in the amphibole eclogite Grt + 2 Amp + Cpx + Ep field at T = 580 – 620°C and P = 1.8 – 2.1 GPa. Omp 2 middle is stable together with Grt 2 in the Grt + Amp + Cpx + Ep + Ky and Grt + Amp + 2 Cpx + Ky fields at T = 610 – 660 °C and P =1.9 – 2.3 GPa. In the 2 Cpx field, the compositions of the coexisting clinopyroxenes fall in the compositional interval for Omp 2 mantle. Lastly, Omp 2 rim is stable up to the plagioclase-in reaction at T = 750 – 800°C and P = 1.70 GPa, together with a garnet that is characterized by composition similar to those of Grt 2. However, the compositions of M2 mineral assemblages are governed by local equilibria as suggested by microstructural analysis. For this reason, the pseudo-section calculated for bulk rock composition is not appropriate for investigating the retrograde paths.

Trace element mineral chemistry and U-Pb dating

9 zircon grains ranging in size from 50 to 170 μm included in garnet, omphacite, and amphibole were firstly investigated by cathodoluminescence (CL) imaging (Fig. 3.2.9). Zircon grains are anhedral to subhedral: the cores preserve irregular zoning with dark and bright sectors, the rims are discontinuous, bright in the inner part and dark in the external one. Zircon rims are thinner than 20 μm.

In-situ trace element analyses and U-Pb zircon dating were performed at Università degli Studi di Milano by in-situ ICP-MS using a Thermo Fisher Scientific iCAP RQ quadripole coupled with Teledyne Cetac Tchnologies Analyte Excite 193 nm excimer and equipped with a HelEx 2 volume sample chamber. Trace element concentrations were determined with an ablation spot diameter of 20 μm in zircon, a repetition rate of 10 Hz, and a fluence of 2 J/cm^2. Trace element concentrations in garnet, omphacite, and amphibole including zircon were determined with a spot diameter of 40 μm, a repetition rate of 10 Hz, and a fluence of 2 J/cm^2. Back-ground signal has been acquired for 40s and then 60s of analysis with the laser firing. The NIST612 glass was used as standard and the BCR-2G glass as secondary standard for quality control. Standard and quality control glasses were repeatedly measured during the course of the analyses. Si and Ca concentrations were used as internal standard to correct the spread between analyzed silicates and glasses. For zircon U-Pb dating we used an ablation spot diameter of 20 μm, a repetition rate of 5 Hz, and a fluence of 2 J/cm^2, the 91500 zircon (Wiedenback et al., 1995; Wiedenback et al., 2004) was used as standard and the Plesovice Zircon as secondary standard for quality control (Slama et al., 2008), repeatedly measured during the analyses. Back-ground signal has been acquired for 40s and then 60s of analysis with the laser firing. Data have been processed by GLITTER software (Van Achterbergh et al., 2001).

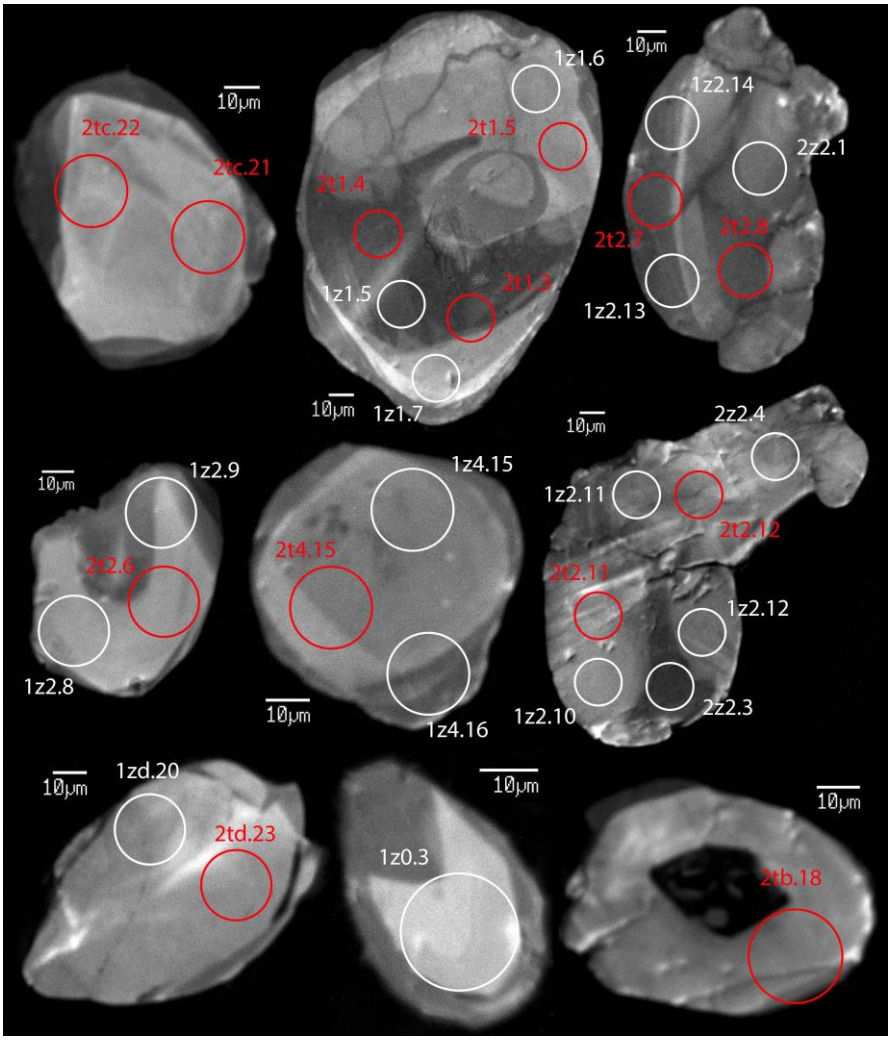

Figure 3.2.9. Cathodoluminescence (CL) images of zircon grains. White circles locate U-Pb analyses and their corresponding analysis number; red circles with number locate REE and trace elements analyses (Cfr. Tab. 3.2.3).

Trace and REE elements

13 analyses of trace and REE elements were performed on 8 zircon grains (Figs. 3.2.9, 3.2.10). The zircons have low Y (193 -710 ppm), Th (1 – 86 ppm), and U (9 - 224 ppm) content. The Th / U ratios (0.03 – 0.40, av. 0.18) are usually higher than expected for metamorphic zircons (i.e. Th / U < 0.1, Rubatto, 2002).

The REE profiles are characterized by HREE-enriched spectra (Lu_N /Sm_N = 45 – 231, av. 125, Yb_N / Gd_N = 12 – 41, av. 22) and display high positive anomaly in Ce (Ce / Ce* = 0.14 – 0.24), low Pr (Pr / Pr* < 0.46), and variable Eu-negative anomaly (Eu / Eu* = 0.17 – 0.77). The determined REE spectra

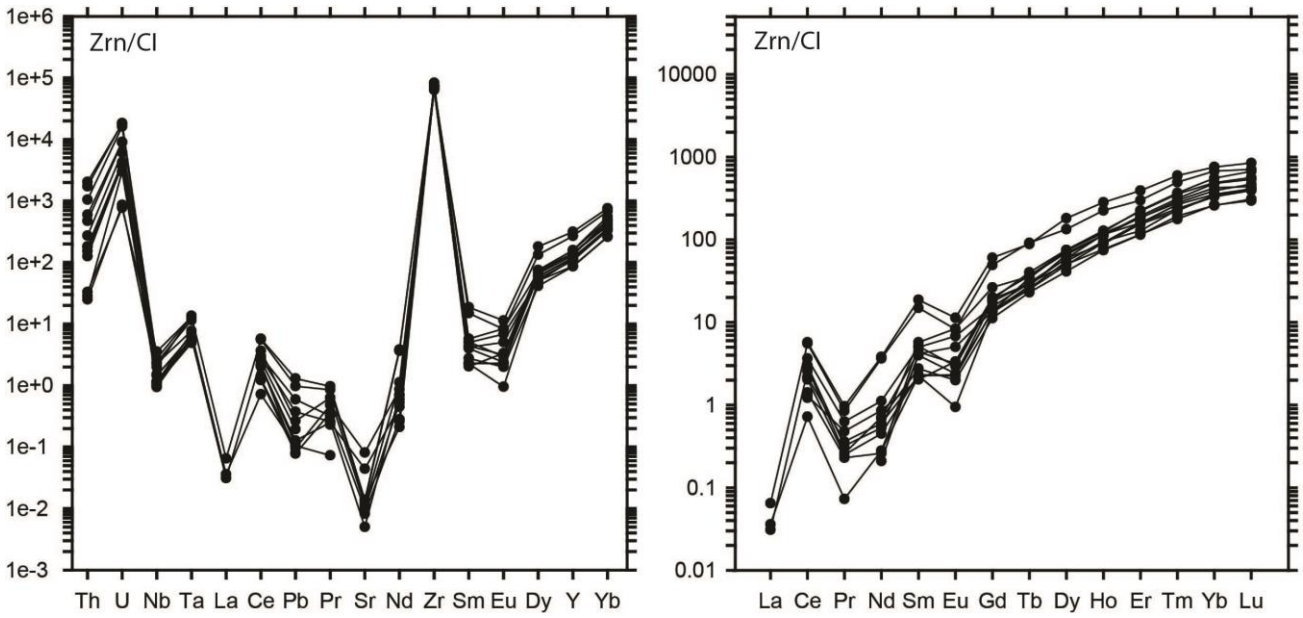

Figure 3.2.10. A: Zircon REE compositions normalized to CI chondrite (Anders and Ebihara, 1982).

are typical of igneous zircons, which usually exhibit a negative Eu anomaly and a strong enrichment in HREE (Rubatto, 2002; Hoskin and Schaltegger, 2003).

REE and trace element concentration are also determined in garnet (Grt 2, 6 data), amphibole (Amp 1b, 2 data), and ompahcite (Omp 1, 4 data) including zircon. Garnet REE-profiles display wide variation in HREE concentrations, with Tb/Lu ratios from to 1.50 to 12.50, as may result from progressive storage of HREE in garnet during the metamorphic evolution (Fig. 3.2.11). Amphibole and omphacite profiles are broadly parallel, with no evidence of interaction with zircon (Fig. 3.2.11). In conclusion, there is no evidence of zircon crystallization during the HP stage.

Zircon U-Pb geochronology

17 analyses were performed on 7 zircon grains already analyzed for trace and REE elements. U-Pb ages widely vary from 536 to 347 Ma. In detail, we found 4 lower Cambrian ages (532 ± 16 Ma, MSWD = 0.09), 3 late Cambrian to Middle Ordovician ages (490 – 463 Ma), 5 Silurian ages (433 – 425 Ma), and 5 Devonian to early Carboniferous ages (401 – 347 Ma) (Tab. 3.2.3, Fig. 3.2.12). Zircon cores are always older than zircon rims. All these ages may be considered as protolith ages in the light of zircon trace and REE patterns. However, a time span of 190 Ma is unlikely for igneous crystallization. We thus argue that solid-state recrystallization could have led to decoupling of the U-

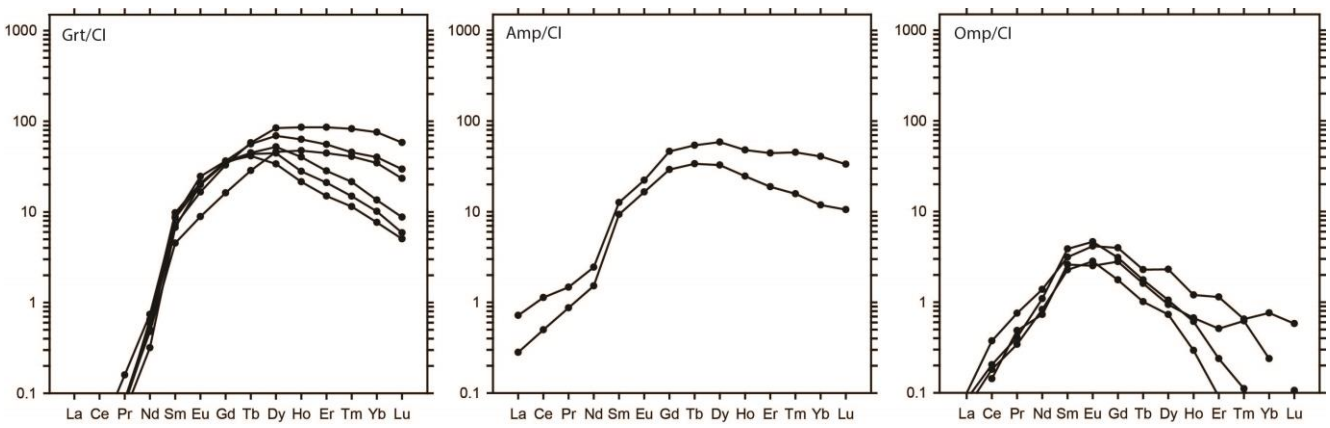

Figure 3.2.11. REE compositions of garnet, omphacite, and amphibole including zircon normalized to CI chondrite (Anders and Ebihara, 1982).

Pb and REE systems, suggesting that partial to total resetting of the U-Pb system occurred leaving the REE system unmodified. In this case, the older age (532 ± 16 Ma) can be considered as protolith age.

Discussion

WR geochemical investigation and in situ U-Pb zircon dating indicate that the Saint-Étienne-de-Tinée eclogite derived from early Cambrian mafic rocks (532 ± 16 Ma) of MORB affinity. This result is not a unicum in the Variscan framework: similar rocks for age and composition are in fact reported in the Bohemian Massif (Timmermann et al., 2004; Soejono et al., 2010; Tichomirowa and Köhler, 2013; Collett et al., 2020; Rötzler and Timmerman, 2020), in Ossa Morena (Sánchez Lorda et al., 2014), in the Alps (Miller and Thöni, 1995; Schaltegger and Gebauer, 1999; Liati et al., 2009), and in the Maures-Tanneron Massif (Innocent et al., 2003). It is interesting to note how these rocks are only founded in the eastern and southern Variscan belt, in and around the Alpine area, in the positon closest to the northern Gondwana margin and rather east with respect to the Iapteus trench and Rheic Ocean position in most of the paleogeographic maps (Cocks and Torsvik, 2006; Torsvik and Cocks, 2009; Domeier, 2016). Surprisingly, in the same domains, there are also Variscan eclogites deriving from late Cambrian to Ordovician oceanic protoliths or relics of obducted Ordovician ophiolites (Ménot et al., 1988; Bowes and Aftalion, 1991; Rubatto et al., 2001, 2010; Timmermann et al., 2004).

As a first result, it is clear that the early Cambrian oceanic crust did not formed in the late-Cambrian-Ordovician Rheic Ocean (Cocks and Torsvik, 2006; Torsvik and Cocks, 2009; Domeier, 2016) and neither in the Silurian Paleo-Thetys (Stampfli et al., 2002, 2013; Cocks and Torsvik, 2006, 2009; Domeir and Torsvik, 2014; Torsvik and Cocks, 2019). A first explanation is that the mafic rocks analyzed in this work may have formed in a

	Pb207/Pb206	1se	Pb206/U238	1se	Pb207/U235	1se	Pb208/Th232	1se	Conc. Age	2se
1z0.3	0.05874	0.01198	0.08666	0.00375	0.699	0.14033	0.04005	0.00542	536	43
1z2.8	0.06463	0.00691	0.086	0.00255	0.76566	0.08042	0.02897	0.00337	536	29
1z1.5	0.05815	0.00656	0.08585	0.00284	0.68676	0.07632	0.0196	0.00195	531	32
1z2.9	0.06211	0.00723	0.08456	0.00259	0.72328	0.08281	0.02551	0.00308	526	30
1z1.7	0.05686	0.00528	0.07894	0.002	0.61856	0.05675	0.02739	0.00232	490	23
2z2.1	0.06187	0.00356	0.07609	0.00139	0.64793	0.03673	0.02565	0.00138	476	16
1z2.10	0.05548	0.00702	0.07458	0.00223	0.57006	0.07113	0.02232	0.00327	463	26
1z4.15	0.05531	0.01101	0.06942	0.00332	0.52884	0.10304	0.02323	0.00405	433	39
1z1.6	0.05558	0.00581	0.06892	0.00195	0.52743	0.05429	0.02181	0.00206	430	23
1z2.14	0.05651	0.00808	0.06868	0.00252	0.53404	0.07483	0.02247	0.0035	429	29
1zd.20	0.05762	0.01161	0.06821	0.0034	0.54103	0.1062	0.02157	0.00456	426	40
1z2.13	0.05531	0.00873	0.06822	0.00259	0.51926	0.08041	0.02336	0.00387	425	30
2z2.3	0.0572	0.00214	0.06377	0.00096	0.50209	0.01877	0.01955	0.00052	401	11
1z4.16	0.05436	0.00963	0.06096	0.00261	0.45619	0.07907	0.01925	0.00368	381	31
1z2.12	0.05153	0.00531	0.05965	0.00163	0.42349	0.04284	0.02064	0.00212	372	19
1z2.11	0.05785	0.00499	0.05606	0.00145	0.44672	0.03788	0.01679	0.00137	354	17
2z2.4	0.05629	0.00374	0.05519	0.00101	0.42771	0.02806	0.02232	0.00174	347	12

Table 3.2.3. In-situ LA-ICP-MS analyses of zircons (cfr. Fig.3.2.9).

supra-subduction zone or in a back-arc basin during Iapetus subduction below the northern margin of Gondwana (Schaltegger and Gebauer, 1999; von Raumer et al., 2015; Collett et al., 2020). This interpretation is also supported by the fact that these rocks are often associated with acidic intrusives of continental affinity (Schaltegger and Gebauer, 1999; Innocent et al., 2003; Tichomirowa and Köhler, 2013; Collett et al., 2020). It is thus reasonable to consider an extension of the Iapetus trench towards the east, as already proposed in some paleogeographic maps (Stampfli et al., 2002, 2013; von Raumer et al., 2015; Collett et al., 2020).

A second explanation is that segments of ancient oceanic basins were preserved on the floor of the Variscan oceans as, today, paleo-oceanic crust is preserved in the eastern Mediterranean Sea (e.g. Stampfli et al., 2001; Stampfli and Borel, 2002; Schettino and Turco, 2011). That was possible at the eastern terminations of the Rheic Ocean, where the northern Gondwana margin faced the Ran Sea (Hartz and Torsvik, 2002; Domeier, 2016; Franke et al., 2017). In this way, the spatial associations with Variscan eclogites deriving from late Cambrian to Ordovician oceanic protoliths would be fully justified.

The second and most remarkable result about the Saint-Étienne-de-Tinée eclogite is that this eclogite exceptionally preserves mineral associations developed in pre-collisional stages. The first metamorphic event M0 likely occurred under prehenite-pumpellyite facies conditions. Prehenite-pumpellyite facies assemblages suggest that the protolith of the Saint-Étienne-de-Tinée was at shallow

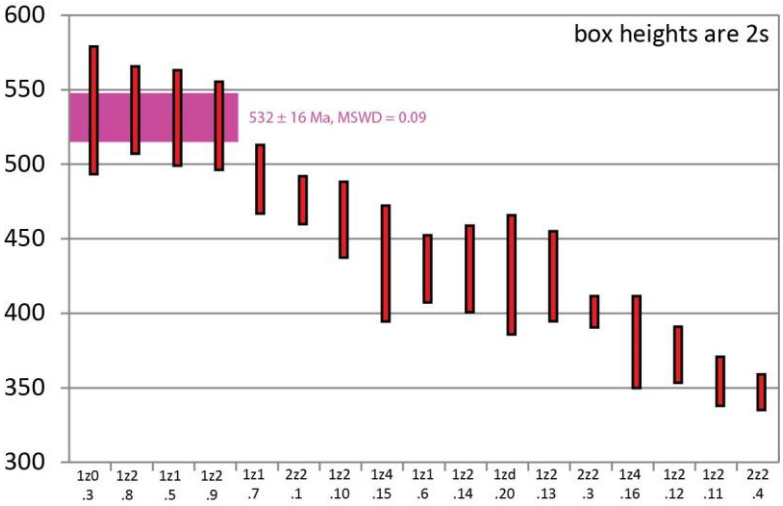

Figure 3.2.12. Results of in-situ LA-ICP-MS analyses of zircons.

structural levels before being involved in the Variscan subduction (T = 200 – 300°C P < 0.6 GPa), i.e. the ocean floor crust. Pre- or non-eclogitic mineral assemblages in the HP rocks of the European Variscan belt are rare (Giraud et al., 1987; Kryza et al., 1990; Smulikowski, 1995; Diaz Garcia et al., 1999; Ballèvre et al., 2003; Patočka and Pin, 2005; Kryza et al., 2011; Faryad and Kachlík, 2013; Majka et al., 2016): form this point of view, the Saint-Étienne-de-Tinée eclogite is probably a unicum in the Southern Variscan belt.

P-T estimates performed on eclogitic mineral assemblages (from T = 580 – 620°C / P = 1.8 – 2.1 GPa to T = 610 – 660°C / P = 1.9 – 2.3 GPa) are proper of a Franciscan metamorphic field gradients, which is typical of oceanic subduction (e.g. Miyashiro, 1961; Ernst, 1971). These P-T conditions are closer to those expected for a cold subduction zone (e.g. Cloos, 1993) with a T/depth ratio of 9-11 °C km^{-1}, lower than what was previously estimated in the much more re-equilibrated eclogites from the Argentera-Mercantour Massif and the other external massifs of the Alps (Liégeois and Duchesne, 1981; Latouche and Bogdanoff, 1987; Guillot et al., 1998; von Raumer et al., 1999; Jouffray et al., 2020). Similar P-T ratios are determined for the Sardinia Variscan eclogites, as well as in the Penninic domain of the Alps (Nussbaum et al., 1998; Schweinehage and Massonne, 1999; Dale and Holland, 2003; Giacomini et al., 2005; Cruciani et al., 2011, 2015).

The discovery of a cold eclogite in the Argentera-Mercantour Massif poses problems to the geodynamic models invoked by previous authors (Rubatto et al., 2001, 2010; Ferrando et al., 2008; Compagnoni et al., 2010) to address the coincidence between metamorphic pressure and thermal peak conditions they envisaged in the eclogites and HP-granulites in other parts of the Argentera-Mercantour Massif.

Conclusion

This work comes to four major results that have consequences on the interpretation of the Variscan rocks in the Helvetic domain of the Alps:

1) the Saint-Étienne-de-Tinée eclogite derived from a MORB protolith, as suggested by trace and REE element patterns (WR);
2) a minimum protolith age for the Saint-Étienne-de-Tinée eclogite is 532 ± 16 Ma. It is interesting to note that the ages of the Variscan ophiolites in the central European Variscan belt (e.g. Paquette et al., 2017) are comprised between 490-390 Ma. Oceanic protoliths of Eadiacaran – early Cambrian ages are instead found in the Bohemian Massif, in the Maures-Tanneron Massif, and in the Alps. Since paleomagnetic reconstructions place the Avalonia drift and Rheic ocean opening at around 490-470 Ma (e.g. Domier, 2016, Torsvik and Cocks, 2019), the mafic eclogite boudins of the western Argentera-Mercantour Massif are not supposed to be formed in the Rheic Ocean and neither in the Silurian Paleo-Tethys;
3) the eclogites preserve very low-grade mineral association likely developed under prehnite-pumpellyite facies conditions, which are relics with respect to the dominant eclogitic paragenesis and represent the P-T prograde metamorphic evolution predating eclogite formation. This demonstrates that these rocks were at shallow crustal levels before being involved in the Variscan subduction system.
4) Eclogitic mineral associations and compositions are extraordinarily preserved. This is the description of the best preserved pre-Alpine eclogitic mineral assemblages in the Helvetic domain of the Alps. P-T estimates on the main eclogitic stage recorded by these rocks (T = 610 – 660°C and P = 1.9 – 2.3) point to oceanic subduction along a cold geotherm (Cloos, 1993).

3.3 Discussion Chapter 3

The tectonic episodes of Variscan oceanization and subduction in the A–M deserve an updated summary. The occurrence of Variscan eclogites preserved in a migmatitic-granulitic complex indicates that the A-M was an internal domain of the Southern Variscan belt, as well as the eastern part of the M-T.

Even if igneous minerals are never preserved in the eclogites and the composition of their protoliths may have been modified during the subsequent metamorphic evolution, trace and REE element concentrations (WR) coherently suggest that they were generated in an oceanic setting. The MORB protolith of Saint-Étienne-de-Tinée (SET in the following) eclogite in the western Argentera-Mercantour Massif is now dated by at 532 ± 16 Ma by in situ ICP-MS U-Pb dating on igneous zircons. This ophiolite is older than the Chamrousse ophiolite of the Belledonne Massif (498 Ma, Ménot et al., 1988), but it is almost coeval with the protoliths of Variscan metabasites in the Alps (Miller and Thöni, 1995; Schaltegger and Gebauer, 1999; Liati et al., 2009; von Raumer et al., 2013 and ref. therein), M-T (Innocent et al., 2003), and Bohemian Massif (Timmermann et al., 2004; Soejono et al., 2010; Tichomirowa and Köhler, 2013; Rötzler and Timmerman, 2020), either characterized by oceanic or continental affinity.

Mafic boudins with alkaline/continental affinity are also reported in the migmatite complex of the A-M (Rubatto et al., 2001, 2010; Ferrando et al., 2008; Jouffray et al., 2020). Differently from the Rabuons protoliths these last are interpreted to have been emplaced in Ordovician time at the initial stages of a Ordovician oceanic rifting (486 – 459 Ma, Paquette et al., 1989; Rubatto et al., 2001, 2010; Ferrando et al., 2008). The dualism between oceanic and continental derived mafic boudins recurs in other parts of the Southern Variscan belt, such as Sardinia (Cruciani et al., 2010), but chronological constrains are missing to discuss it more properly.

As a matter of fact, the MORB protolith of the SET eclogite and all the other Ediacaran-early Cambrian mafic rocks of the eastern and southern Variscan belt did not form in the late Cambrian – Ordovician Rheic Ocean (Domeier, 2016), and neither in the Silurian Paleo-Tethys Ocean (Stampfli et al., 2002, 2013). The tectonic setting reasonably accountable for the Ediacaran-early Cambrian magmatism is a supra-subduction zone / back-arc basin at the time of the Iapetus subduction beneath Gondwana (e.g. Schaltegger and Gebauer, 1999; von Raumer et al., 2015; Collett et al., 2020). As a second, very reasonable hypothesis, these rocks may derive from segments of early oceanic lithosphere preserved on the Variscan ocean floors. This hypothesis would agree with age heterogeneity of

eclogite protoliths in the A-M, ranging from 460-490 Ma in the south-eastern sector (e.g. Paquette et al., 1989; Rubatto et al., 2001; Rubatto et al., 2010) to 532 Ma in the north-west of the massif (this work).

Most of the mafic boudins, oceanic and continental, pervasively re-equilibrated under HP-granulite and amphibolite conditions during the Carboniferous (Rubatto et al., 2001, 2010; Jouffray et al., 2020). Only few of them preserve pre- to early eclogitic mineral assemblages (Latouche and Bogndanoff, 1987; Rubatto et al., 2001; Jouffray et al., 2020).

Pre-eclogitic mineral assemblages developed under prehnite-pumpellyite facies conditions are found in the SET eclogite. Prhenite-pumpellyite facies minerals are preserved as inclusions in eclogite facies garnets. Pumpellyite inclusions in garnet are also found in other re-equilibrated eclogites, in particular at Piano del Praiet (Mt. Gélas group; Montani, 2004), indicating that the vestiges of very low-P mineral assemblages compatible with the physical conditions of oceanic metamorphism are preserved in different A-M eclogites.

After this first metamorphic stage, the mafic boudins re-crystallized under eclogitic facies conditions. Two types of eclogites are distinguished. Eclogites of the first type include amphibole: they are found at Piano del Praiet, Lago di Nasta, Lago del Claus, Pas des Ladres, and Lac Niré (see also Montani, 2004). Eclogites of the second type are “true eclogites” (Garnet + Omphacite > 70%vol) with rare clinozoisite grains. They are found at Lago del Chiotas, Passo del Brocan (Mt. Argentera group), and Saint-Étienne-de-Tinée.

However, very few of the eclogitic mineral assemblages are preserved. The SET eclogite is the most remarkable exception, since it well preserves omphacite and garnet. A few omphacite grains included in garnet are also founded in the Lac Niré eclogite. In all the other cases, omphacite is completely replaced by symplectites of placioclase and clinopyroxene.

The SET eclogite equilibrated at T = 610 – 660°C and P = 1.9 – 2.3 GPa. This is a strong constrain on the Variscan HP metamorphism in the Argentera-Mercantour Massif and confirms that cold oceanic subduction took place in Variscan times. Preliminary estimates on amphibole-bearing eclogites from Valle del Valasco and Lac Long pointed to T = 640-740°C and P 1.1-1.7 GPa, conditions that are proper of warm oceanic subduction. However, a comparison between the two results is not advisable, for the weak preservation of the eclogitic assemblages in the last two localities.

Explaining these differences in terms of contrasting P-T evolution, or artifact of scarce preservation of the eclogite mineral assemblages is premature, even this heterogeneity of igneous and metamorphic ages or geochemical signatures preconizes a complex geodynamic interpretation for the A-M suture zone, which in fact constitutes the whole massif.

The eclogites re-equilibrated under HP-granulite facies conditions as suggested by lamellar symplectites of omphacite and oligoclase after eclogitic omphacite, and by amphibole and plagioclase rims around eclogitic garnets. Accurate P-T estimates on this metamorphic stage are, at this stage, precluded since a determination of the volumes that reacted at equilibrium is needed. Furthermore, there are not a-x models accountable for most of the amphibole compositions at this stage (i.e. sadanagaite).

The tectonic setting accountable for the eclogite re-equilibration under HP-granulite facies conditions is hardly assessable in absence of geochronological constraints. The age of the eclogitic peak is still an open issue. Even if a second cluster of U-Pb zircon age is envisaged at 412 ± 17 Ma, REE and trace element concentrations in zircon still suggest an igneous origin. HP-granulite facies metamorphism in mafic boudins of continental origin at Frisson Lake occurred at around 340 Ma (Ferrando et al., 2008; Rubatto et al., 2010). Such date may be a minimum value for the age of the eclogitic peak, since the eclogites re-equilibrated under HP granulite facies conditions. However, these conditions may have been attained at different times and in different tectonic settings.

In spite of this complex petro-tectonic and chronologic outline, it is a matter of fact that the HP-granulite facies re-equilibration of A-M eclogites, preliminary inferred in SET at T= 750-800 °C and P ~1.7 GPa, is characterized by a T/depth ratio (15 °C km^{-1}) comprised between those of warm subduction zones and plate interior, compatible with the transition between oceanic subduction and continental collision.

Chapter 4

Conclusions

This multi-scale structural study, supported by lithostratigraphy, petrology, geochemistry and geochronology made possible to unveil the first results for identifying the missing mosaic tiles to complete the Variscan tectonic framework across the Alpine suture. The investigated domains are the western M-T, the A-M, and the Orobic basement in the central Southern Alps. The topics refer to the last 500 Ma of tectonic evolution recorded in these domains, from the opening of pre-Variscan oceans to the Alpine collision and late-collisional evolution. Major results are here synthetized according to time and tectonic setting.

Early Cambrian magmatism (results from chapters 2 and 3)

Magmatism of Ediacaran – early Cambrian age is reported in all the three studied areas, even if stronger geochronological constraints are still required. In the metapelites of the Orobic basement, there are small lenses of orthogneiss dated at 531 ± 22 Ma. In the western A-M, the protoliths of MORB-derived eclogites are dated 532 ± 16 Ma.

Rocks similar in age and composition are reported in many other parts of the southern and eastern Variscan belt, where oceanic basalts are often associated to continental-derived acidic rocks (Miller and Thöni, 1995; Innocent et al., 2003; Timmermann et al., 2004; Liati et al., 2009; Soejono et al., 2010; Tichomirowa and Köhler, 2013; Schaltegger and Gebauer, 1999; Collett et al., 2020; Rötzler and Timmerman, 2020). In the M-T, acidic igneous rocks in the central leptyno-amphibolite complex are dated 548 ± 15 Ma (Innocent et al., 2002), and the protolith of the Bormes orthogneiss is dated 600-550 Ma (Bellot, 2005).

The current interpretation is that these rocks emplaced on an active margin, either a supra-subduction zone or a back-arc basin, at the time of Iapetus subduction below the northern Gondwana margin. This interpretation is supported by paleogeographical reconstructions that preclude the hypothesis of an Ediacarian – early Cambrian ocean south of the future Avalonian and Variscan terranes (Matte, 2001; Stampfli et al., 2002, 2013; Cocks and Torsvik, 2006; Torsvik and Cocks, 2009; Domeier, 2016; Franke et al., 2017) and other geochemical arguments (e.g. Schaltegger and Gebauer, 1999; Sánchez Lorda et al., 2014; Collett et al., 2020).

In all the investigated areas, the early Cambrian intrusives are close to younger late Cambrian – Ordovician intrusives, whose tectonic significance has been constrained more precisely. These rocks are interpreted as emplaced in different stages from continental rifting to the Rheic Ocean opening, according to their age and geochemical affinity, in the context of the Ordovician paleogeography.

Most of the Ordovician granitoids in the Southern Alps are interpreted as related to the Ordovician rifting (Boriani and Bini, 2012; Gosso et al., 2012 and ref. therein). However, some of these rocks are interpreted as syn-subductive since they are coeval with the pre-Variscan eclogites of the Aar-Gotthard Massif (e.g. Gebauer et al., 1988; Zurbriggen, 2005; Franz and Romer, 2007). In the A-M, crustal-derived mafic and acidic igneous rocks were emplaced between 486 and 443 Ma (Paquette et al., 1989; Rubatto et al., 2001, 2010). These rocks are linked to the Ordovician rifting by geochemical and geochronological arguments (Rubatto et al., 2001, 2010). The alkaline Leptyno-Amphibolite Complex of the western M-T is similarly supposed to have emplaced during continental rifting (Briand et al., 2002). Coherently, the tholeiitic mafic rocks of oceanic origin, which are the protoliths of the retrogressed eclogites in the eastern part of the massif, are dated Ordovician (452 ± 8 Ma; Bellot, 2005, Schneider et al., 2014 and ref. therein).

The spatial relationship between Ediacaran-early Cambrian and Ordovician intrusives is in large part enigmatic. It may either reflect a pre-Ordovician configuration or have been acquired during the subsequent Variscan evolution. In any case, it is clear that igneous rock of oceanic affinity were emplaced in the Southern and Eastern Variscan belt before the Rheic Ocean opening.

Variscan subduction (results from chapter 3)

In the Southern Variscan belt, HP metamorphism is dated between 400 and 330 Ma (Miller and Thöni, 1995; Faryad et al., 2002; Tumiati et al., 2003; Giacomini et al., 2007). The interpretation of the HP metamorphism is based on ages and thermal states of the eclogitic peak in comparison with the other parts of the European Variscan belt (e.g. Regorda et al., 2020 and ref. therein).

In the A-M, the imprint of the Variscan subduction is retained by the oceanic- and continental-derived mafic eclogites. Amongst them, the SET eclogite record a cold subductive imprint, with the baric peak at T = 610 – 660 °C and P =1.9 – 2.3 GPa (T/depth = 9-11 °C km^{-1}). Similar conditions are also estimated in other parts of the southern Variscan belt, in particular in Sardinia (T = 550 – 700 °C, P = 1.3 – 2.1; Giacomini et al., 2005; Franceschelli et al., 2007; Cruciani et al., 2011, Cruciani et al, 2015). This is an important result for reconstructing the Variscan subduction in the Helvetic domain of the Alps. P-T estimates on the fresh SET eclogite are significantly colder than all the other estimates on

deeply re-equilibrated eclogite samples (Latuche and Bogdanoff, 1987; Guillot et al., 1998; von Ramuer et al., 1999; Rubatto et al., 2001; this study).

These last estimates have been previously compared with those obtained for the HP mafic granulites in the A-M by other authors (Rubatto et al., 2001, 2010 Ferrando et al., 2008; Compagnoni et al., 2010). The leading idea was that the metamorphic conditions of the eclogite peak were not so different from those retained by the HP-granulite, and that eclogites and HP granulites formed during the same tectono-metamorphic event at around 340 Ma (Rubatto et al., 2001, 2010 Ferrando et al., 2008; Compagnoni et al., 2010). However, the geodynamic models proposed to explain these results are no longer valid since cold eclogites have been found by this study.

The age of the eclogitic peak in the A-M is still doubtful. This data is required to make a comparison and correlation with the central European Variscan belt, but also to quantify the time elapsed between the eclogite and HP-granulite-facies metamorphism. By doing so, it will be possible to assess between two contrasting geodynamic hypotheses: the first is that the eclogites formed during oceanic subduction and subsequently re-equilibrated under HP-granulite-facies conditions at the transition to collisional stages; the second is that contrasting thermal states contemporaneously characterized different portion of the same subduction system (e.g. Regorda et al., 2017)

There are no eclogites in the western M-T. Deeply retrogressed eclogites and garnet-bearing peridotites are instead reported in other portions of the M-T, in particular in the central and eastern parts, where a Variscan subduction complex is individuated (Schneider et al., 2014). Nowadays, there are no available P-T quantification of the eclogitic peak and neither of the time of the Variscan subduction.

Variscan eclogites are neither founded in the Orobic basement in the central Southern Alps. The metamorphic imprint of the Variscan subduction is instead observed, but at low pressure, in the metapelites that preserve S1a foliation supported by chloritoid, garnet, white mica, biotite, and rutile. S1a developed at T = 520 – 570°C and P = 0.65 – 0.80 GPa before the Variscan collision, according to a P/T ratio lower than that of plate interior.

Variscan collision (results from chapter 2)

The Variscan basement of the Argentera-Mercantour Massif was already exhumed in the late Carboniferous, when immature intra-mountain basins opened controlled by strike-slip faults (Faure-Muret, 1955; Bortolami et al., 1974). Signals of the Variscan collision may be founded at around 340 Ma when the Variscan eclogites re-crystallized under amphibolite facies conditions. Widespread partial melting affected the Variscan basement rocks at around 323 ± 12 Ma (Rubatto et al., 2001) and

was followed by re-equilibration under greenschist facies conditions (Bortolami et al., 1974), before the emplacement of post-collisional granites (Ferrara and Malaroda 1969; Corsini et al., 2004).

In the metapelites of the western Maures-Tanneron Massif the Variscan collision is recorded under amphibolite faces conditions. During the Variscan collision, these rocks were affected by two deformation stages, during which two superposed foliations supported by garnet, staurolite, kyanite, biotite, and white mica developed at 550 – 600°C and P = 0.6 – 0.7 GPa. The continental collision in the western Maures-Tanneron Massif is dated 352 – 339 Ma (Moussavou, 1998; Oliot et al., 2015). After that, the Variscan basement rocks were deformed under greenschist facies conditions that testify exhumation.

The Variscan collision in the central Southern Alps is dated 330 Ma (Mottana et al., 1985). In the portion of Orobic basement investigated in this thesis, the collision is recorded under amphibolite facies conditions. The collisional S1b foliation is supported by staurolite, biotite, white mica, with or without garnet. The thermal peak of the Variscan collision was at T = 550-670 °C and P = 0.7 GPa.

The Variscan collision is followed by late- to post-collisional re-equilibration in the andalusite stability field at T = 530 – 580 and P = 0.30 – 0.40 GPa. These conditions were attained before the deposition of the Verrucano Lombardo formation in Upper Permian times, when the dominant S2 foliation developed in the basement rocks.

Andalusite-bearing mineral assemblages in the Variscan metapelites of the Southern Alps are often interpreted as products of contact metamorphism around Permian intrusives (e.g. Boriani et al., 1988a; Boriani and Giobbi, 2004; Benciolini et al., 2006; Whylidal et al., 2012; Zanoni and Spalla, 2018) or of the subsequent HT-LP metamorphic event related to the Triassic exhumation (e.g. Mottana et al., 1985; Diella et al., 1992; Schuster et al., 2001; Spalla et al., 2002; Schuster and Stüwe, 2008). In the studied portion of the Orobic basement in Upper Valcamonica, the occurrence of pre-Upper Permian andalusite suggests a perturbed thermal state that was not related to the emplacement of Permian intrusives, which are missing in this area, but rather with a regional significance.

Here, D2 structures developed under the highest T/depth ratio (>60 °C km^{-1}) characterising the Variscan tectono-metamorphic evolution of the SCB basement, indicating that an anomalous high thermal regime was effective only at the end of its exhumation trajectory. Such a high thermal state might have developed during late-orogenic thinning. This is an uniqueness in the context of the Southalpine basement, in which late-Variscan andalusite always developed together with sillimanite and/or cordierite (Boriani et al., 1988; Boriani and Giobbi, 2004; Benciolini et al., 2006; Whylidal et al., 2012; Zanoni and Spalla, 2018).

Permian – Triassic continental rifting (results form chapter 1)

In the Southern and Eastern Variscan belt, post-collisional granitoids were emplaced in early Permian times and were subsequently intruded by Permian – Triassic mantle-derived mafic dykes. The oldest dykes are generally of calc-alkaline affinity (Lower Permian), whereas the youngest (Upper Permian – Triassic) are alkaline. They are described in many parts of the Variscan belt, even outside the Alps.
Calc-alkaline lamprophyres emplaced in the Argentera-Mercantour Massif and intruded into the early Permian Central Granite (Ferrara and Malaroda, 1969; Corsini et al., 2004). Alkaline lamprophyres are instead described in the Orobic basement where they intersect late- to post-collisional Variscan structures. In both cases, the dykes were emplaced at shallow crustal levels ($P < 0.2$ GPa) in the exhumed Variscan basement. Numerical models performed to explore the transition from Variscan convergence to Permian-Triassic extension suggest that forced extension (> 2 cm/yr) is necessary to produce successive pulses of mantle-derived magmas in Permian-Triassic times (Marotta et al., 2009; Marotta et al., 2018; Roda et al., 2018). The lamprophyres of the Argentera-Mercantour Massif and Orobic basement are interpreted as emplaced during diffuse Permian-Triassic lithospheric thinning that led to the localization and subsequent opening of the Alpine Tethys in Jurassic times.

Alpine collision (results from chapter 1)

In the external domains of the Alps, to which the Argentera-Mercantour Massif and the Orobic basement belong, the effect of the Alpine metamorphism is mainly evident along mylonitic shear zones and never exceeding greenschist facies conditions. The Permian-Triassic lamprophyres are reliable markers to quantify the structural and metamorphic effects of the Alpine event on the Variscan basement rocks of the external domains of the Alps, since they post-date all the Variscan evolution.
The Argentera-Mercantour Massif belongs to the lower plate (Europa) of the Alpine subduction system. The peak of the Alpine metamorphism in the Argentera-Mercantour Massif occurred at $T = 420 – 450$°C and $P = 0.2 – 0.4$ GPa. These conditions were likely reached between 34 and 20 Ma, as suggested by the age of the Alpine green-schist facies mylonites of the Argentera-Mercantour Massif (Corsini et al., 2004; Sanchez et al., 2011). Age and thermal state suggest that these conditions were induced by crustal thickening following the Alpine collision.
The Orobic basement belongs to the upper plate (Adria) of the Alpine subduction system. The oldest ages of the Orobic-Porcile Thrust in the Orobic Basement (80 – 73 Ma, Zanchetta et al., 2011) suggest that Alpine crustal thickening started in the Late Cretaceous during active oceanic subduction below Adria. These ages agree with the erosion of basement rocks testified in the Cretaceous sedimentary sequences of the Southern Alps (Zanchetta et al., 2015 and ref. therein). The Alpine deformation

continued up to 38 – 35 Ma, when Alpine D3 structures were truncated by the emplacement of the Adamello intrusive suite, even if a further activation of the Alpine structures of the central Southern Alps is not precluded (Zanchetta et al., 2015).

The peak conditions of the Alpine metamorphism recorded by the lamprophyres intruding the Orobic basement are T = 420 – 450 °C and P = 0.15 – 0.35 GPa. A preliminary numerical model performed to explore the thermal and deformation effects of the Alpine subduction and collision on the Adria plate suggests that Alpine deformation started to localize south of the Periadriatic Lineament since late-subductive stages, and that Adria had started heating up since very late-subductive stages. Future improvements are required to refine the modelling to improve the agreement between the P-T conditions predicted during active oceanic subduction with those inferred by the lamprophyres, at present only showing a poor fit.

Chapter 5

References

Aicard P, Autran A, Gérard J, Lougnon J. 1968. Sur l'âge tertiaire syntectonique et synmétamorphique alpin du gisement plombo-zincifère de Valauria (commune de Tende, Alpes Maritimes). BRGM Bulletin, 1, 5-14.

Albini S., Battaglia D., Bellini G., Bigoni C., Carminati E., Ceriani S., Forcella F., Gosso G., Guizzetti A., Oliva G., Rebay G., Siletto G.B., Spalla M.I. (1994). Alpine deformations and pre-Alpine remnants in the north-eastern Orobic Alps, Southalpine Belt. Quaderni di Geodinamica Alpina e Quaternaria, 2, 25-39.

Arenas R., Martínez Catalán J.R., Sánchez Martínez S., Fernandez-Suarez J., Andonaegui P., Pearce J.A., Corfu F. (2007). The Vila de Cruces ophiolite: a remnant of the early Rheic Ocean in the Variscan suture of Galicia (northwest Iberian Massif). The Journal of Geology, 115(2), 129-148.

Arenas R., Sánchez Martínez S., Gerdes A., Albert R., Fernández R.D., Andonaegui P. (2014). Re-interpreting the Devonian ophiolites involved in the Variscan suture: U–Pb and Lu–Hf zircon data of the Moeche Ophiolite (Cabo Ortegal Complex, NW Iberia). International Journal of Earth Sciences, 103(5), 1385-1402.

Aretz A., Bär K., Götz A.E., Sass I. (2016). Outcrop analogue study of Permocarboniferous geothermal sandstone reservoir formations (northern Upper Rhine Graben, Germany): impact of mineral content, depositional environment and diagenesis on petrophysical properties. International Journal of Earth Sciences, 105(5), 1431-1452.

Aretz M. (2016). The Kulm Facies of the Montagne Noire (Mississippian, southern France). Geologica Belgica.

Assanelli M., Luoni P., Rebay G., Roda M., and Spalla M.I., 2020. Tectono Metamorphic Evolution of Serpentinites from Lanzo Valleys Subduction Complex (Piemonte-Sesia-Lanzo Zone Boundary, Western Italian Alps). Minerals, 10, 985.

Attal M. (2000). Étude tectonique et thermodynamique du tégument permo-triasique du flanc méridional du Massif de l'Argentera. Géologie Alpine 76, 167-170.

Atzori P, Cirrincione R, Del Moro A, Mazzoleni P. (2000). Petrogenesis of late Hercynian calc-alkaline dykes of mid-eastern Sardinia: petrographical and geochemical data constraining hybridization process. European Journal of Mineralogy, 12, 1261-1282.

Aumaitre G., Buffet G. (1973). Minéralogie, pétrographie et géochimie des laves spilitiques et des filons basiques associés du massif des Ecrins-Pelvoux (Alpes françaises occidentales). Géochimie. Phd thesis, Université Scientifique et Medicale, Grenoble.

Averbuch O., Piromallo C. (2012). Is there a remnant Variscan subducted slab in the mantle beneath the Paris basin? Implications for the late Variscan lithospheric delamination process and the Paris basin formation. Tectonophysics, 558, 70-83.

Averbuch O., Piromallo C. (2012). Is there a remnant Variscan subducted slab in the mantle beneath the Paris basin? Implications for the late Variscan lithospheric delamination process and the Paris basin formation. Tectonophysics, 558, 70-83.

Baietto A., Perello P., Cadoppi P., Martinotti G. (2009). Alpine tectonic evolution and thermal water circulations of the Argentera Massif (South-Western Alps). Swiss Journal of Geosciences 102(2), 223-245.

Balestro G., Festa A., Dilek Y. (2019). Structural architecture of the Western Alpine Ophiolites, and the Jurassic seafloor spreading tectonics of the Alpine Tethys. Journal of the Geological Society, 176, 913–930.

Baletti L., Zanoni D., Spalla M.I., Gosso G. (2012). Structural and petrographic map of the Sassa gabbro complex (Dent Blanche nappe, Austroalpine tectonic system, Western Alps, Italy). Journal of Maps, 8, 413-430.

Ballèvre M., Bosse V., Dabard M.P., Ducassou C., Fourcade S., Paquette J.L.,Peucat J.J., Pitra P. (2013). Histoire géologique du Massif armoricain: actualité de la recherche. Bulletin de la Société Géologique et Minéralogique de Bretagne, Société Géologique et Minéralogique de Bretagne, D, 10-11, 5-96.

Ballèvre M., Bosse V., Ducassou C., Pitra P. (2009). Palaeozoic history of the Armorican Massif: models for the tectonic evolution of the suture zones. Compte Rendu Geoscience, 341, 174-201.

Ballèvre, M., Pitra, P., & Bohn, M. (2003). Lawsonite growth in the epidote blueschists from the Ile de Groix (Armorican Massif, France): a potential geobarometer. Journal of metamorphic Geology, 21(7), 723-735.

Balogh K., Dunkl I. (1994). K/Ar dating of metamorphic rocks from the Sopron Mts., Lower Austro-Alpine Unit (Hungary). Mitteilungen der Österreichischen Mineralogischen Gesellschaft, 139, 26-27.

Bangerth W., Dannberg J., Gassmoeller R., Heister T. (2020). ASPECT v2.2.0.

Banzet G. (1987). Interaction croûte-manteaux et genese du plutonisme subalcalin du Haut Dauphiné occidental (Massifs cristallins externs): Vaugnérites, durbachites et granitoides magnésio-potassiques. Géologie Alpine, 63, 95-117.

Barca D., Cirrincione R., De Vuono E., Fiannacca P., Ietto F., Lo Giudice A. (2010). The Triassic rift system in the northern Calabrian-Peloritani Orogen: evidence from basaltic dyke magmatism in the San Donato Unit. Periodico di Mineralogia, 79(2), 61-72.

Bard J.P., Caruba C. (1981). Les sries leptyno-amphiboliques clogites relictuelles et serpentinites des Maures, marqueurs dune palosuture varisque affectant une crote amincie. Comptes rendus de l'Académie des Sciences Paris, 292, 611-614.

Bard J.P., Caruba C. (1982) Texture et minéralogie d'une éclogite à disthène-saphirine-hypersténe-quartz en inclusion dans les gneiss migmatitites des Cavaliéres, massif de Ste Maxime (Maures, Var, France). Comptes Rendus de l'Académie des Sciences, 294, 103-106.

Bartoli O., Meli S., Sassi R., Magaraci D. (2013). Amphiboles and clinopyroxenes from Euganean (NE Italy) cumulus enclaves: evidence of subduction-related melts below Adria microplate. Rendiconti Lincei, 24(2), 151-161.

Bauve V., Plateaux R., Rolland Y., Sanchez G., Bethoux N., Delouis B., Darnault R. (2014). Long-lasting transcurrent tectonics in SW Alps evidenced by Neogene to present-day stress fields. Tectonophysics, 621, 85-100.

Beard B.L., Medaris L.G., Johnson C.M., Jelínek E., Tonika J., Riciputi L.R. (1995). Geochronology and geochemistry of eclogites from the Mariánské Lázně Complex, Czech Republic: implications for Variscan orogenesis. Geologische Rundschau, 84(3), 552-567.

Becker H. (1997). Sm-Nd ages and cooling history of high-temperature garnet peridotite massifs and high-pressure granulites from Lower Austria. Contributions to Mineralogy and Petrology, 127, 224-236.

Beck-Mannagetta P. (1970). Über den geologischen Aufbau der Koralpe. - Verh. Geol. B.-A., 1970, 491-496.

Bellot J.P. (2005). The Palaeozoic evolution of the Maures massif (France) and its potential correlation with others areas of the Variscan belt: a review. Journal of the Virtual Explorer, 19(4), 24.

Bellot J.P., Laverne C., Bronner G. (2010). An early Palaeozoic supra-subduction lithosphere in the Variscides: new evidence from the Maures massif. International Journal of Earth Sciences, 99(3), 473-504.

Bellot J.P., Triboulet C., Laverne C., Bronner, G. (2003). Evidence for two burial/exhumation stages during the evolution of the Variscan belt, as exemplified by P–T–t–d paths of metabasites in distinct allochthonous units of the Maures massif (SE France). International Journal of Earth Sciences, 92(1), 7-26.

Beltrán-Triviño, A., Winkler, W., von Quadt, A., Gallhofer, D. (2016). Triassic magmatism on the transition from Variscan to Alpine cycles: evidence from U–Pb, Hf, and geochemistry of detrital minerals. Swiss Journal of Geosciences, 109(3), 309-328.

Benciolini L., Poli M.E., Visonà D., Zanferrari A. (2006). Looking inside Late Variscan tectonics: structural and metamorphic heterogeneity of the Eastern Southalpine Basement (NE Italy). Geodinamica Acta, 19(1), 17-32.

Benmammar A., Berger J., Triantafyllou A., Duchene S., Bendaoud A., Baele J.M., Bruguier O., Diot H. (2020). Pressure-temperature conditions and significance of Upper Devonian eclogite and amphibolite facies metamorphisms in southern French Massif Central. Bulletin de la Société Géologique de France, 191, 28.

Berger J., Féménias O., Ohnenstetter D., Bruguier O., Plissart G., Mercier J.C., Demaiffe D. (2010) New occurrence of UHP eclogites in Limousin (French Massif Central): age, tectonic setting and fluid–rock interactions. Lithos, 118, 365–382.

Bergomi M.A. (2004). Integrated study of "Gneiss Chiari" in the framework of the Orobic basement of Southern Alps (field relationships, mineral chemistry, geochemistry and geochronology). European Journal of Mineralogy, Plinius, Italian Supplement, 30, 54- 59.

Bergomi M.A., Dal Piaz G.V., Malusà M.G., Monopoli B., Tunesi A. (2017). The Grand St Bernard-Briançonnais nappe system and the Paleozoic inheritance of the Western Alps unraveled by zircon U-Pb dating. Tectonics, 36(12), 2950-2972.

Bergomi M.A., Zanchetta S., Tunesi, A. (2015). The Tertiary dike magmatism in the Southern Alps: geochronological data and geodynamic significance. International Journal of Earth Sciences, 104(2), 449-473.

Berra F., Felletti F., Tessarollo A. (2016). Stratigraphic architecture of a transtensional continental basin in low-altitude semiarid conditions: The Permian succession of the central Orobic basin (Southern Alps, Italy). Journal of Sedimentary Research, 86, 408-429.

Berra F., Tiepolo M., Caironi V., Siletto G. B. (2015). U-Pb zircon geochronology of volcanic deposits from the Permian basin of the Orobic Alps (Southern Alps, Lombardy): chronostratigraphic and geological implications. Geological Magazine, 152, 429-443.

Bersezio R., Fornaciari M., Gelati R., Napolitano A., Valdisturlo, A. (1993). The significance of the Upper Cretaceous to Miocene clastic wedges in the deformation history of the Lombardian southern Alps. Géologie Alpine, 69, 3-20.

Bertotti G., Seward D., Wijbrans J., Ter Voorde M., Hurford A.J. (1999). Crustal thermal regime prior to, during, and after rifting: a geochronological and modeling study of the Mesozoic South Alpine rifted margin. Tectonics, 18(2), 185-200.

Bertotti G., Siletto G.B., Spalla M.I. (1993). Deformation and metamorphism associated with crustal rifting: the Permian to Liassic evolution of the Lake Lugano-Lake Como area (Southern Alps). Tectonophysics, 226(1-4), 271-284.

Bigot-Cormier F., Poupeau G., Sosson M. (2000). Dénudations différentielles du massif cristallin externe alpin de l'Argentera (Sud-Est de la France) révélées par thermochronologie traces de fission (apatites, zircons). Comptes rendus de l'Académie des Sciences 330(5), 363-370.

Bigot-Cormier F., Sosson M., Poupeau G., Stéphan J.F., Larbin E. (2006). The denudation history of the Argentera Alpine External Crystalline Massif (Western Alps, France, Italy): an overview from the analysis of fission tracks in apatites and zircons. Geodinamica Acta, 19(6), 455-473.

Blasi A. (1968). Geo-petrologia della regione del Boréon (settore francese del Massiccio Cristallino dell'Argentera). Università degli Studi di Milano, Master Thesis, p. 165.

Blasi A. (1971). Genesi dei noduli a sillimanite nelle anatessiti del Mt. Pélago (Alpi Marittime) in rapporto ai fenomeni di metamorfismo, piegamento e granitizzazione. Memorie della Società Geologica Italiana, 10, 167-190.

Blasi A., Schiavinato G. (1968). Significato petrologico dei noduli a sillimanite e dei noduli a cordierite diffusi nelle anates-siti biotitiche del M. Pelago (massiccio cristallino dell'Argentera). Bollettino della Società Geologica Italiana, 87, 253-275.

Blom J.C., Passchier, C.W. (1997). Structures along the Orobic thrust, Central Orobic Alps, Italy. Geologische Rundschau, 86(3), 627-636.

Bocchio R., De Capitani L., Liborio G., Mottana A., Nicoletti M., Petrucciani, C. (1981). K-Ar radiometric age determinations of the south-Alpine metamorphic complex, western Orobic Alps (Italy). Neues Jahrbuch fuer Mineralogie, Monatshefte, 289-307.

Bocquet J., Delaloye M., Hunziker J.C., Krummenacher D. (1974). K–Ar and Rb-Sr dating of blue amphiboles, micas and associated minerals from the western Alps. Contributions to Mineralogy and Petrology, 47, 7–26.

Bogdanoff S. (1986). Evolution de la partie occidentale du massif cristallin externe de l'Argentera. Place dans l'arc alpin. Géologie de la France 4, 433-453.

Bogdanoff S., Ménot R.P., Vivier G. (1991). Les massifs cristallins externes des alpes occidentales françaises, un fragment de la zone interne varisque. Sciences Géologiques, bulletins et mémoires, 44(3), 237-285.

Bogdanoff S., Michard A., Mansour M., Poupeau G. (2000) Apatite fission track analysis in the Argentera massif: evidence of contrasting denudation rates in the External Crystalline Massifs of the Western Alps. Terra Nova, 12, 117-125..

Bogdanoff S., Ploquin A. (1980). Les gneiss et migmatites du massif de l'Argentera (Alpes maritimes); apport de deux coupes geochimiques. Bulletin de la Société Géologique de France 7(3), 353-358.

Boland J.N., Van Roermund H.L.M. (1983). Mechanisms of exsolution in omphacites from high temperature, type B, eclogites. Physics and Chemistry of Minerals, 9, 30-37.

Bonin B., Brändlein P., Bussy F., Desmons J., Eggenberger U., Finger F., Graf K., Marro C.H., Mercolli I., Oberhänsli R., Ploquin A., von Quadt A., von Raumer J.F., Schaltegger U., Steyrer H.P., Visonà D., Vivier G. (1993). Late Variscan magmatic evolution of the Alpine basement, in: von Raumer, J.F., Neubauer F. (Eds.), Pre-Mesozoic geology in the Alps. Springer, Berlin, Heidelberg, pp. 171-201.

Borghi, A. (1991). Structural evolution of the northeastern sector of the Serie dei Laghi (Southern Alps). Bollettino della Società Geologica Italiana, 110(3-4), 639-647.

Boriani A., Bini A. (2012). Note Illustrative della Carta Geologica d'Italia alla scala 1:50.000 - foglio 056'SONDRIO', I.S.P.R.A. and Regione Lombardia

Boriani A., Caironi V., Oddone M., Vannucci R. (1988). Some petrological and geochemical constraints on the genesis of the Baveno-Mottarone and Montorfano plutonic bodies. Rendiconti Società Italiana di Mineralogia e Petrologia, 43, 385-393.

Boriani A., Giobbi E. (2004). Does the basement of western southern Alps display a tilted section through the continental crust? A review and discussion. Periodico di Mineralogia, 73(2), 5-22.

Bortolami G., Callegari E., Gosso G. (1974). Caratteri metamorfici nella copertura permocarbonifera e nel basamento cristallino dell'Argentera. Memorie della Società Geologica Italiana 13(1), 257-267.

Bortolami G., Sacchi R. (1968) Osservazioni geologico-petrografiche sui medi valloni di S.Anna e Rio Freddo (Massiccio Cristallino dell'Argentera). Memorie della Società Geologica Italiana 7,37-64.

Boucarut M. (1967). Structure du granite de l'Argentera et style tectonique de l'ensemble de ce massif. Comptes Rendus de l'Académie des sciences 264, 1573-1576.

Bourdelle F., Parra T., Chopin C., Beyssac O. (2013). A new chlorite geothermometer for diagenetic to low-grade metamorphic conditions. Contributions to Mineralogy and Petrology, 165(4), 723-735.

Bousquet R., Oberhänsli R., Schmid S.M., Berger A., Wiederkher M., Robert C., Möller; A., Rosemberg C., Zeilinger G., Molli G., Koller F. (2012). Metamorphic Framework of the Alps. CCGM (Commission of the Geological Maps of the World), Paris.

Bowes D.R., Aftalion M. (1991). U-Pb zircon isotopic evidence for early Ordovician and late Proterozoic units in the Marianske Lazne complex, Central European Hercynides. Neues Jahrbuch für Mineralogie Monatshefte, (7), 315-326.

Brack P. (1981). Structures in the Southwestern border of the Adamello intrusion (Alpi Bresciane, Italy). Schweizerische Mineralogische und Petrographische Mitteilungen, 61, 37-50.

Brack P. (1984). Geologie der Itrusiva und Rahmengesteine des Südwest-Adamello (Nord-Italien). PhD thesis. Zurich, ETH, pp. 253.

Brändlein P., Nollau G., Sharp Z., von Raumer J. (1994). Petrography and geochemistry of the Vallorcine granite (Aiguilles Rouges massif, Western Alps). Schweizerische Mineralogische und Petrographische Mitteilungen, 74, 227-243

Briand B., Bouchardon J.L., Capiez P., Piboule M. (2002). Felsic (A-type)–basic (plume-induced) Early Palaeozoic bimodal magmatism in the Maures Massif (southeastern France). Geological Magazine, 139(3), 291-311.

Brugger J. (1994). Les veines à andalousite du Pischahorn (Grisons, Suisse). Schweizerische Mineralogische und Petrographische Mitteilungen, 74, 191–202.

Bucher K., Frey M. (2002). Petrogenesis of metamorphic rocks. Springer-Verlag Berlin Heidelberg, Germany, pp. 334.

Buffet G., Aumaitre R. (1979). Implications tectoniques possibles des directions des filons carbonifères et triasiques de la partie Sud et Ouest du massif cristallin des Ecrins-Pelvoux. Géologie Alpine 55, 35-43.

Buriánek D., Houzar S., Krimicek L., Smerda J. (2017). Origin of the pegmatite veins within the skarn body at Vevčice near Znojmo (Gföhl Unit, Moldanubian Zone). Journal of Geosciences, 62, 11-23.

Bussien D., Bussy F., Masson H., Magna T., Rodionov N. (2008). Variscan lamprophyres in the Lower Penninic domain (Central Alps): age and tectonic significance. Bulletin de la Société géologique de France, 179(4), 369-381.

Bussy F., Hernandez J., Von Raumer J., 2000. Bimodal magmatism as a consequence of the post-collisional readjustment of the thickened Variscan continental lithosphere (Aiguilles Rouges-Mont Blanc Massifs, Western Alps). Earth and Environmental Science Transactions of the Royal Society of Edinburgh 91(1-2), 221-233.

Bussy F., Sartori M., Thélin P. (1996). U-Pb zircon dating in the middle Penninic basement of the Western Alps (Valais, Switzerland). Schweizerische Mineralogische und Petrographische Mitteilungen, 76, 81-84.

Buzzi L, Gaggero L. (2008). Petrogenesis of post–orogenic Lower Permian andesites in southern Europe: insights into the collapse of the Variscan range. Geodinamica Acta, 21(5-6), 273-290.

Cadel G., Cosi M., Pennacchioni G., Spalla M.I. (1996). A new map of the Permo-Carboniferous cover and Variscan metamorphic basement in the Central Orobic Alps, Southern Alps - Italy. Memorie di Scienze Geologiche, Padova, 48, 1-53.

Caironi V., Colombo A., Tunesi A. (2004). Geochemical approach to characterization and source identification of the protoliths of metasedimentary rocks: an example from the Southern Alps. Periodico di Mineralogia, 73, 109-118.

Canepa M., Castelletto M., Cesare B., Martin S., Zaggia L. (1990). The Austroalpine Mont Mary nappe (Italian Western Alps). Memorie di Scienze Geologiche, Padova, 42, 1-17.

Cannat M., Fontaine F., Escartín J. (2013). Serpentinization and Associated Hydrogen And Methane Fluxes at Slow Spreading Ridges, in Diversity Of Hydrothermal Systems On Slow Spreading Ocean Ridges, American Geophysical Union (AGU), 241–264.

Cannic S., Lapierre H., Monié P., Briqueu L., Basile C. (2002). Late orogenic evolution of the Variscan lithosphere: Nd isotopic constraints from the western Alps. Schweizerische mineralogische und petrographische Mitteilungen, 82, 77-99.

Cappelli B., Carmignani L., Castorina F., Dipisa A., Oggiano G., Petrini R. (1992) A Variscan suture zone in Sardinia: geological and geochemical evidence. Geodinamica Acta, 5, 101-118.

Carignan J., Hild P., Mevelle G., Morel J., Yeghicheyan D. (2001). Routine analyses of trace elements in geological samples using flow injection and low pressure on-line liquid chromatography coupled to ICP-MS: A study of geochemical reference materials BR, DR-N, UB-N, AN-G and GH. Geostandards Newsletter, 25(2-3), 187-198.

Carlson R.L., Miller D.J. (1997). A new assessment of the abundance of serpentinite in the oceanic crust. Geophysical Research Letters, 24, 457–460.

Carmignani L., Carosi R., Di Pisa A., Gattiglio M., Musumeci G., Oggiano G., Pertusati P.C. (1994). The Hercynianchain in Sardinia (Italy). Geodinamica Acta, 7, 31-47.

Carminati E., Siletto G.B., Battaglia D. (1997). Thrust kinematics and internal deformation in basement involved foreland fold and thrust belts: the Eastern Orobic Alps case (Central Southern Alps, Northern Italy). Tectonics, 16, 259-271.

Carosi R., D'Addario E., Mammoliti E., Montomoli C., Simonetti M. (2016). Geology of the northwestern portion of the Ferriere-Mollieres Shear Zone, Argentera Massif, Italy. Journal of Maps 12, sup1, 466-475.

Carosi R., D'Addario E., Mammoliti E., Montomoli C., Simonetti M. (2016). Geology of the northwestern portion of the Ferriere-Mollieres Shear Zone, Argentera Massif, Italy. Journal of Maps 12sup1, 466-475.

Carosi R., Di Pisa A., Iacopini D., Montomoli C., Oggiano G. (2004). The structural evolution of the Asinara Island (NW Sardinia, Italy). Geodinamica Acta, 17, 309-329.

Carosi R., Frassi C., Montomoli C. (2009). Deformation during exhumation of medium-and high-grade metamorphic rocks in the Variscan chain in northern Sardinia (Italy). Geological Journal, 44, 280-305.

Carosi R., Montomoli C., Tiepolo M., Frassi C. (2012). Geochronological constraints on post-collisional shear zones in the Variscides of Sardinia (Italy). Terra Nova, 24, 42–51.

Carosi R., Oggiano G. (2002). Transpressional deformation in NW Sardinia (Italy): insights on the tectonic evolution of the Variscan belt. Compte Rendu Geosciences, 334, 273-278.

Carswell D.A., Wilson R.N., Zhai M. (2000). Metamorphic evolution, mineral chemistry and thermobarometry of schists and orthogneisses hosting ultra-high pressure eclogites in the Dabieshan of central China. Lithos, 52, 121-155.

Carswell D.A., Zhang R.Y. (1999). Petrographic characteristics and metamorphic evolution of ultra high-pressure eclogites in plate-collision belts. International Geology Review, 4, 781-798.

Casati P., Gnaccolini M. (1967). Geologia delle Alpi Orobie occidentali. Rivista Italiana di Paleontologia e Stratigrafia, 73, 25-172.

Casetta F., Coltorti M., Ickert R.B., Bonadiman C., Giacomoni P.P., Ntaflos T. (2018). Intrusion of shoshonitic magmas at shallow crustal depth: T–P path, H 2 O estimates, and AFC modeling of the Middle Triassic Predazzo Intrusive Complex (Southern Alps, Italy). Contributions to Mineralogy and Petrology, 173(7), 57.

Casetta F., Coltorti M., Marrocchino E. (2018). Petrological evolution of the Middle Triassic Predazzo Intrusive Complex, Italian Alps. International Geology Review, 60(8), 977-997.

Casetta F., Ickert R.B., Mark D.F., Bonadiman C., Giacomoni P.P., Ntaflos T., Coltorti M. (2019). The alkaline lamprophyres of the Dolomitic Area (Southern Alps, Italy): markers of the Late Triassic change from orogenic-like to anorogenic magmatism. Journal of Petrology, 60(6), 1263-1298.

Casini L., Cuccuru S., Maino M., Oggiano G., Tiepolo M. (2012). Emplacement of the Arzachena Pluton (Corsica–Sardinia Batholith) and the geodynamics of incoming Pangaea. Tectonophysics, 544, 31-49.

Cassinis G., Cortesogno L., Gaggero L., Perotti C., Ronchi A. (2007). Volcanic products from the Early Permian Collio Basin (southern Alps) and their geodynamic implications. Periodico di Mineralogia, 76, 25-47.

Cassinis G., Cortesogno L., Gaggero L., Perotti C.R., Buzzi L. (2008). Permian to Triassic geodynamic and magmatic evolution of the Brescian Prealps (eastern Lombardy, Italy). Bollettino della Società Geologica Italiana, 127(3), 501-518.

Cassinis G., Dal Piaz G.V., Eusebio A., Gosso G., Martinotti G., Massari. F., Milano P.F., Pennacchioni G., Perello M., Pessina C.M., Roman. E., Spalla. M.I.., Tosetto. S., Zerbato M. (1986). Report on a structural and sedimentological analysis in the Uranium Province of the Orobic Alps - Uranium 2, 241-260.

Cassinis G., Perotti C.R., Ronchi A. (2012) - Permian continental basins in the Southern Alps (Italy) and peri-mediterranean correlations. International Journal of Earth Sciences, 101, 129-157.

Cathelineau M. (1988). Cation site occupancy in chlorites and illites as a function of temperature. Clay minerals, 23(4), 471-485.

Cenki-Tok B., Darling J.R., Rolland Y., Dhuime B., Storey C.D. (2014). Direct dating of mid-crustal shear zones with synkinematic allanite: new in situ U-Th-Pb geochronological approaches applied to the Mont Blanc massif. Terra Nova, 26(1), 29-37.

Christensen N.I. (2004). Serpentinites, Peridotites, and Seismology. International Geology Review, 46, 795–816.

Cirrincione R., Fiannacca P., Lustrino M., Romano V., Tranchina A., Villa I.M. (2016). Enriched asthenosphere melting beneath the nascent North African margin: trace element and Nd isotope evidence in middle-late Triassic alkali basalts from central Sicily (Italy). International Journal of Earth Sciences, 105(2), 595-609.

Cirrincione R., Fiannacca P., Lustrino M., Romano V., Tranchina A. (2014). Late Triassic tholeiitic magmatism in Western Sicily: A possible extension of the Central Atlantic Magmatic Province (CAMP) in the Central Mediterranean area? Lithos 188: 60-71.

Cloos M., (1993). Lithospheric buoyancy and collisional orogenesis: Subduction of oceanic plateaus, continental margins, island arcs, spreading ridges, and seamounts. Geological Society of America Bulletin, 105(6), 715-737.

Cocco F., Funedda A. (2017). The Sardic phase: field evidence of Ordovician tectonics in SE Sardinia, Italy. Geological Magazine, 156(1), 25-38.

Cocherie A., Rossi P., Fanning C.M., Guerrot C., (2005). Comparative use of TIMS and SHRIMP for U–Pb zircon dating of A-type granites and mafic tholeiitic layered complexes and dykes from the Corsican Batholith (France). Lithos, 82(1-2), 185-219.

Cocks L.R.M. (2000). The early Palaeozoic geography of Europe. Journal of the Geological Society, 157(1), 1-10.

Cocks L.R.M., Fortey R.A. (1982). Faunal evidence for oceanic separations in the Palaeozoic of Britain. Journal of the Geological Society, 139(4), 465-478.

Cocks L.R.M., Torsvik T.H. (2002). Earth geography from 500 to 400 million years ago: a faunal and palaeomagnetic review. Journal of the Geological Society, 159(6), 631-644.

Cocks L.R.M., Torsvik T.H. (2006). European geography in a global context from the Vendian to the end of the Palaeozoic. Geological Society, London, Memoirs,32, 83–9.

Cocks L.R.M., Torsvik T.H. (2011) The Palaeozoic geography of Laurentia and western Laurussia: a stable craton with mobile margins. Earth Sciences Review, 106, 1-51.

Coggon R., Holland T.J.B., (2002). Mixing properties of phengitic micas and revised garnet-phengite thermobarometers. Journal of Metamorphic Geology, 20(7), 683-696.

Coleman R.G., Lee D.E., Beatty L.B., Brannock W.W. (1965). Eclogites and eclogites - their differences and similarities. Geological Society of America Bulletin, 76, 483-508.

Collett S., Schulmann K., Štípská P., Míková J. (2020). Chronological and geochemical constraints on the pre-variscan tectonic history of the Erzgebirge, Saxothuringian Zone. Gondwana Research, 79, 27-48.

Colombo A., Caironi V., Tunesi A. (1997). The ortogneisses in the Southalpine basement: new geochemical data and zircon typology of the M.Fioraro magmatic complex and Gneiss Chiari (Central-Western Alps-Italy) Quaderni di Geodinamica Alpina e Quaternaria, 4, 167-169.

Colombo A., Siletto G.B., Tunesi A. (1994). Pre-Variscan magmatism in the central Southern Alps: the Monte Fioraro magmatic complex. Schweizerische Mineralogische und Petrographische Mitteilungen, 74(1), 127-135.

Colombo A., Tunesi A. (1999). Pre-Alpine metamorphism of the Southern Alps west of the Giudicarie Line. Schweizerische Mineralogische und Petrographische Mitteilungen, 79, 63-77.

Colombo F., Compagnoni R., Lombardo B. (1994). Le rocce eclogitiche dei Laghi del Frisson (Argentera sud-orientale, Alpi Marittime). Atti Ticinesi Scienze della Terra serie speciale, 1, 75-82.

Colombo F., Ghiglione G., Compagnoni R.. (1993). Relitti di porfidi granitici a xenoliti granulitici nelle migmatiti dell'Argentera (Alpi Marittime). Plinius, 10, 113-116.

Compagnoni R., Ferrando S., Lombardo B., Radulesco N., Rubatto D. (2010). Paleo-European crust of the Italian western Alps: Geological history of the Argentera Massif and comparison with Mont Blanc-Aiguilles Rouges and Maures-Tanneron Massifs. In : Beltrando M, Peccerillo A, Mattei M, Conticelli S, Doglioni C, Eds. Journal of the Virtual Explorer 36, paper 3, 1-32.

Compagnoni R., Lombardo B., Prato R. (1974). Andalousite et sillimanite aux contacts du Granite Central de l 'argentera (Alpes Maritimes). Rendiconti della Società Italiana di Mineralogia e Petrologia, 39(1), 31-54.

Compagnoni R., Prato R. (1969). Paramorfosi di cianite su sillimanite in scisti pregranitici del Massiccio del Gran Paradiso. Bollettino della Società Geologica Italiana, 88, 537–549.

Conti P., Carmignani L., Funedda A. (2001). Change of nappe transport direction during the Variscan collisional evolution of central-southern Sardinia (Italy). Tectonophysics, 332(1-2), 255-273.

Corfu F., Andersen T.B., Gasser D. (2014). The Scandinavian Caledonides: main features, conceptual advances and critical questions. Geological Society, London, Special Publications, 390(1), 9-43.

Corsin P., Faure-Muret A. (1946). Découverte d'une florule stéphanienne au cirque de Férisson près de Saint-Martin Vésubie (Alpes Maritimes). Compte Rendu Sommaires de la Société géologique de France, 256-257.

Corsin P., Faure-Muret A. (1951). Nouvelle flore du Stéphanien à l'est de Saint-Martin Vésubie (Alpes Maritimes), Compte Rendu Sommaires de la Société géologique de France, 57-58.

Corsini M., Bosse V., Féraud G., Demoux A., Crevola G. (2010). Exhumation processes during post-collisional stage in the Variscan belt revealed by detailed 40Ar/39Ar study (Tanneron massif, SE France). International Journal of Earth Sciences, 96, 1-9.

Corsini M., Bosse V., Féraud G., Demoux A., Crevola G. (2010). Exhumation processes during post-collisional stage in the Variscan belt revealed by detailed 40 Ar/39 Ar study (Tanneron Massif, SE France). International Journal of Earth Sciences, 99(2), 327-341.

Corsini M., Rolland Y. (2009). Late evolution of the southern European Variscan belt: exhumation of the lower crust in a context of oblique convergence. Compte Rendu Geosciences, 341, 214–223.

Corsini M., Rolland Y. (2009). Late evolution of the southern European Variscan belt: Exhumation of the lower crust in a context of oblique convergence. Comptes Rendus Geoscience, 341(2-3), 214-223.

Corsini M., Ruffet G., Caby R. (2004). Alpine and late-hercynian geochronological constrains in the Argentera Massif (Western Alps). Eclogae Geologicae Helvetiae, 97, 3-15.

Cortesogno L, Cassinis G, Dallagiovanna G, Gaggero L, Oggiano G, Ronchi A, Seno S., Vanossi M. (1998). The Variscan post-collisional volcanism in late Carboniferous–Permian sequences of Ligurian Alps, southern Alps and Sardinia (Italy): A synthesis. Lithos 45(1-4): 305-328.

Cortesogno L., Gaggero L., Oggiano G., Paquette J.L. (2004). Different tectono-thermal evolutionary paths in eclogitic rocks from the axial zone of the Variscan chain in Sardinia (Italy) compared with the Ligurian Alps. Ofioliti, 29(2), 125-144.

Cortesogno L., Gaggero L., Oggiano G., Paquette J.L. (2004). Different tectono-thermal evolutionary paths in eclogitic rocks from the axial zone of the Variscan chain in Sardinia (Italy) compared with the Ligurian Alps. Ofioliti, 29(2), 125-144.

Crespi, R., Liborio, G., Mottana, A. (1982). On a widespread occurrence of stilpnomelane to the South of the Insubric line, Central Alps, Italy. Neues Jahrbuch für Mineralogie Monatshefte, 6, 265-271.

Cruciani G., Dini A., Franceschelli M., Puxeddu M., Utzeri D. (2010). Metabasite from the Variscan belt in NE Sardinia, Italy: within-plate OIB-like melts with very high Sr and low Nd isotope ratios. European Journal of Mineralogy, 22(4), 509-523.

Cruciani G., Franceschelli M., Groppo C. (2011). P–T evolution of eclogite-facies metabasite from NE Sardinia, Italy: insights into the prograde evolution of Variscan eclogites. Lithos 121:135–150.

Cruciani G., Franceschelli M., Groppo C., Oggiano G., Spano M.E. (2015). Re-equilibration history and P–T path of eclogites from Variscan Sardinia, Italy: A case study from the medium-grade metamorphic complex. International Journal of Earth Sciences, 104, 797–814.

Cruciani G., Franceschelli M., Langone A., Puxedd M., Scodina M. (2017). Nature and age of pre-Variscan eclogite protoliths from the Low- to Medium-Grade Metamorphic Complex of north–central Sardinia (Italy) and comparisons with coeval Sardinian eclogites in the northern Gondwana context. Journal of Geological Society, 172, 792-807.

D'Adda P., Zanchi A., Bergomi M., Berra F., Malusà M.G., Tunesi A., Zanchetta S. (2011). Polyphase thrusting and dyke emplacement in the central Southern Alps (Northern Italy). International Journal of Earth Sciences, 100(5), 1095-1113.

D'Adda P., Zanchetta S. (2015). Geological-structural map of the Orobic and Porcile thrust junction, central southern Alps (N Italy). Journal of Maps, 11(1), 25-38.

Dal Piaz G.V. (1993). Evolution of Austroalpine and Upper Penninic basement in the Northwestern Alps from Variscan convergence to post-Variscan extension. In: von Raumer J. & Neubauer F. (eds), Pre- Mesozoic Geology in the Alps. Springer, Heidelberg, 325–342.

Dal Piaz G.V. (2001). History of tectonic interpretations of the Alps. Journal of Geodynamics, 32, 99–114.

Dal Piaz G.V. (2010). The Italian Alps: A journey across two centuries of Alpine geology. Journal of the Virtual Explorer, 36, paper 8.

Dale J., Holland T.J.B. (2003). Geothermobarometry, P–T paths and metamorphic field gradients of high-pressure rocks from the Adula Nappe, Central Alps. Journal of Metamorphic Geology, 21(8), 813-829.

Dallagiovanna G, Gaggero L, Maino M, Seno S, Tiepolo M. (2009). U–Pb zircon ages for post-Variscan volcanism in the Ligurian Alps (Northern Italy). Journal of the Geological Society, 166(1), 101-114.

Dardeau G. (1988). Tethyan evolution and Alpine reactivation of Jurassic extensional structures in the French "Alpes Maritimes". Bulletin de la Sociéte géologique de France, 4(4), 651-657.

de Capitani C., Petrakakis K. (2010). The computation of equilibrium assemblage diagrams with Theriak/Domino software. American Mineralogist, 95(7), 1006-1016.

De Capitani L., Delitala M.C., Liborio G., Mottana A., Nicoletti M., Petrucciani C. (1988). K–Ar dating of the Val Biandino plutonic complex (Orobic Alps, Italy). Memorie di Scienze Geologiche, Padova, 40, 285–294.

De Graciansky P.C., Roberts D.G., Tricart P. (2011). The Western Alps, from rift to passive margin to orogenic belt: an integrated geoscience overview. Elsevier, Amsterdam, The Netherlands, pp. 397.

De Min A., Velicogna M., Ziberna L., Chiaradia M., Alberti A., Marzoli A. (2020). Triassic magmatism in the European Southern Alps as an early phase of Pangea break-up. Geological Magazine, 157(11), 1800-1822.

De Sitter L.U. (1963). La structure des Alpes Lombardes. In: Livre à la mémoire du Prof. P. Fallot consacré à l'évolution paléogéographique et structurale des domaines méditerranéens et Alpin d'Europe. Societe géologique France 2, 243-256.

Debon F, Lemmet M. (1999). Evolution of Mg/Fe ratios in late Variscan plutonic rocks from the external crystalline massifs of the Alps (France, Italy, Switzerland). Journal of Petrology, 40(7), 1151-1185.

Debon F., Le Fort P. (1988). A cationic classification of common plutonic rocks and their magmatic associations: principles, method, applications. Bulletin de Minéralogie, 111(5), 493-510.

Del Moro A., Di Pisa A., Oggiano G., Villa I.M. (1991). Isotopic ages of two contrasting tectono metamorphic episodes in the Variscan chain in northern Sardinia. Geologia del basamento Italiano. 21–22 marzo 1991, Siena, 33–35.

Del Moro A., Visonà D. (1982). The epiplutonic Hercynian Complex of Brixen (Bressanone, Eastern Alps, Italy). Petrologic and radiometric data, N. Jahrb. Mineral. Abh., 145, 66-85.

Delleani F., Rebay G., Zucali M., Tiepolo M., Spalla M.I. (2018). Insights on Variscan geodynamics from the structural and geochemical characterization of a Devonian-Carboniferous gabbro from the Austroalpine domain (Western Alps). Ofioliti, 43(1), 23-39.

Delteil J., Stephan J.F., Attal M. (2003). Control of Permian and Triassic faults on Alpine basement deformation in the Argentera massif (external southern French Alps). Bulletin de la Société géologique de France, 174(5), 481-496.

Demoux A., Schärer U., Corsini M. (2008). Variscan evolution of the Tanneron massif, SE-France, examined through U–Pb monazite ages. Journal of Geological Society of London, 165, 467-478.

Desmons J. (1992). The Briancon basement (Pennine Western Alps): mineral composition and polymetamorphic evolution. Schweizerische Mineralogische und Petrographische Mitteilungen, 72, 37-55.

Desmons J., Compagnoni R., Cortesogno L., Frey M., Gaggero L. (1999). Pre-Alpine metamorphism of the internal zones of the Western Alps. Schweizerische Mineralogische und Petrographische Mitteilungen, 79(1), 23-39.

Desmons J., Mercier D. (1993). Passing through the Briançon zone. In Pre-Mesozoic geology in the Alps (pp. 279-295). Springer, Berlin, Heidelberg.

di Paola S. (2001) Eredità litostratigrafica, strutturale e metamorfica paleozoica nel margine interno Europeo (Grandes Rousses e Argentera), ristrutturato durante l'orogenesi Alpina. Ph.D. Thesis, Università degli Studi di Milano and Université Claude Bernard Lyon.

di Paola S., Spalla M.I. (2000). Contrasting tectonic records in pre-Alpine metabasites of the Southern Alps (Lake Como, Italy). Journal of Geodynamics, 30(1-2), 167-189.

di Paola, S., Spalla, M. I., Gosso, G. (2001). New structural mapping and metamorphic evolution of the Domaso CortafoZone (Southern Alps—Lake Como). Memorie di Scienze Geologiche, Padova, 53, 1-14.

Di Vincenzo G., Carosi R., Palmeri R. (2004). The relationship between tectono-metamorphic evolution and argon isotope records in white mica: constraints from in situ 40Ar–39Ar laser analysis of the Variscan basement of Sardinia. Journal of Petrology, 45(5), 1013-1043.

Díaz García F., Arenas R., Martínez Catalán J.R., González del Tánago J., Dunning G.R. (1999). Tectonic evolution of the Careón ophiolite (Northwest Spain): a remnant of oceanic lithosphere in the Variscan belt. The Journal of geology, 107(5), 587-605.

Diella V., Pigazzini N., Gosso G., Siletto G.B., Spalla M.I. (2001). New occurrence of Cld- And-bearing metapelites in the Southalpine basement of the upper Val Camonica. Geol. Paläont. Mitt. Innsbruck, 25, 68-69.

Diella V., Spalla M.I., Tunesi A. (1992). Contrasting thermomechanical evolutions in the Southalpine metamorphic basement of the Orobic Alps (Central Alps, Italy). Journal of Metamorphic Geology, 10(2), 203-219.

Diener J.F.A., Powell R., White R.W., Holland T.J.B. (2007). A new thermodynamic model for clino- and orthoamphiboles in the system Na2O–CaO–FeO–MgO–Al2O3–SiO2–H2O–O. Journal of Metamorphic Geology, 25, 631-656.

Domeier M. (2016). A plate tectonic scenario for the Iapetus and Rheic oceans. Gondwana Research, 36, 275-295.

Domeier M., Torsvik T.H. (2014). Plate tectonics in the Late Paleozoic. Geoscience Frontiers, 5, 303-350.

Donnelly K.E., Goldstein S.L., Langmuir C.H., Spiegelman M. (2004). Origin of enriched ocean ridge basalts and implications for mantle dynamics. Earth and Planetary Science Letters, 226, 347-366.

Droop G.T.R. (1983). Pre-Alpine eclogites in the Pennine Basement Complex of the Eastern Alps. Journal of Metamorphic Geology, 1(1), 3-12.

Droop G.T.R., Lombardo B., Pognante U. (1990). Formation and distribution of eclogite facies rocks in the Alps. In: Carswell, D.A. (Ed.), Eclogite Facies Rocks. Blackie and Son Ltd, London, pp. 225–256.

Dubińska E., Bylina P., Kozłowski A., Dörr W., Nejbert K., Schastok J., Kulicki C. (2004). U–Pb dating of serpentinization: hydrothermal zircon from a metasomatic rodingite shell (Sudetic ophiolite, SW Poland). Chemical Geology, 203(3-4), 183-203.

Duchesne J.C., Liégeois J.P., Bolle O., Vander Auwera J., Bruguier O., Matukov D.I., Sergeev S.A. (2013). The fast evolution of a crustal hot zone at the end of a transpressional regime: The Saint-Tropez peninsula granites and related dykes (Maures Massif, SE France). Lithos, 162, 195-220.

Ducrot J., Lancelot J.R., Marchand, J. (1983). Datation U-Pb sur zircons de l'eclogite de la Borie (Haut-Allier, France) et consequences sur l'evolution ante-hercynienne de l'Europe occidentale. Earth and Planetary Science Letters, 62(3), 385-394.

Edel J.B., Casini L., Oggiano G., Rossi P., Schulmann K. (2014). Early Permian 90° clockwise rotation of the Maures–Estérel–Corsica–Sardinia block confirmed by new palaeomagnetic data and followed by a Triassic 60° clockwise rotation. In: Schulmann K., Martìnez Catalàn J.R., Lardeaux J.M., Janousek V., Oggiano G. (Eds). TheVariscan Orogeny: Extent, Timescale and the Formation of the European Crust. Geological Society of London, Special Publications, 405, 333-361.

Edel J.B., Schulman K., Skrzypek E., Cocherie A. (2013). Tectonic evolution of the European Variscan belt constrained by palaeomagnetic, structural and anisotropy of magnetic susceptibility data from the Northern Vosges magmatic arc (eastern France). Journal of the Geological Society, 170(5), 785–804.

Edel J.B., Schulmann K., Lexa O., Lardeaux J.M. (2018). Late Palaeozoic palaeomagnetic and tectonic constraints for amalgamation of Pangea supercontinent in the European Variscan belt. Earth-science reviews, 177, 589-612.

El Korh A., Schmidt S.T., Ulianov A., Potel S. (2009). Trace element partitioning in HP–LT metamorphic assemblages during subduction-related metamorphism, Ile de Groix, France: a detailed LA-ICPMS study. Journal of Petrology, 50(6), 1107-1148.

Elter F.M., Musumeci G., Pertusati, P.C. (1990). Late Hercynian shear zones in Sardinia. Tectonophysics, 176:387-404.

England P.C, Richardson, S.W. (1977). The influence of erosion upon the mineral fades of rocks from different metamorphic enviroments. Journal of Geological Society, 134(2), 201-213.

England P.C., Thompson A.B. (1984). Pressure-temperature-time paths of regional metamorphism I. Heat transfer during the evolution of regions of thickened continental crust. Journal of Petrology, 25(4), 894-928.

Ernst W.G. (1971). Metamorphic zonations on presumably subducted lithospheric plates from Japan, California, and the Alps. Contributions to Mineralogy and Petrology, 34, 43-59.

Ernst W.G. (1973). Blueschist metamorphism and P-T regimes in active subduction zones, Tectonophysics, 17, 255–272.

Ernst W.G., Liou J.G. (2008). High- and ultrahigh-498 pressure metamorphism: Past results and future prospects. American Mineralogist 93(11-12), 1771-1786.

Ernst W.G., Liu J. (1998). Experimental study of Al- and Ti-contents of calcic amphibole in MORB - A semiquantitative thermobarometer. American Mineralogist 83(9-10), 952-969.

Evans M.J., Elliott T. (1999). Evolution of a thrust-sheet-top basin: The Tertiary Barreme basin, Alpes-de-Haute-Provence, France. Geological Society of America Bulletin 111(11), 1617-1643.

Faryad S.W. (2012). High-pressure polymetamorphic garnet growth in eclogites from the Mariánské Lázně Complex (Bohemian Massif). European Journal of Mineralogy, 24(3), 483-497.

Faryad S.W., Kachlík V. (2013). New evidence of blueschist facies rocks and their geotectonic implication for Variscan suture(s) in the Bohemian Massif. Journal of Metamorphic Geology 31, 63-82.

Faryad S.W., Melcher F., Hoinkes G., Puhl J., Meisel T., Frank W. (2002). Relics of eclogite facies metamorphism in the Austroalpine basement, Hochgrössen (Speik complex), Austria. Mineralogy and Petrology, 74(1), 49-73.

Faure M., Rossi P., Gaché J., Melleton J., Frei D., Li X., Lin W. (2014). Variscan orogeny in Corsica: new structural and geochronological insights, and its place in the Variscan geodynamic framework. International Journal of Earth Sciences, 103, 1533-1551.

Faure M., Bé Mézème E., Cocherie A., Rossi P., Chemenda A., Boutelier D. (2008). Devonian geodynamic evolution of the Variscan Belt, insights from the French Massif Central and Massif Armoricain. Tectonics, 27(2).

Faure M., Bé Mézème E., Duguet M., Cartier C., Talbot J.Y. (2005). Paleozoic tectonic evolution of medio-Europa from the example of the French Massif Central and Massif Armoricain. Journal of the Virtual Explorer, 19(5), 1-26.

Faure M., Lardeaux J.M., Ledru P. (2009). A review of the pre-Permian geology of the Variscan French Massif Central. Compte Rendu Geosciences, 341, 202-213.

Faure-Muret A. (1955). Etudes géologiques sur le Massif de l'Argentera-Mercantour et sur ses enveloppes sédimentaires. Mémoire pour servir à l'explication de la Carte géologique détaillée de la France, Paris, pp. 336.

Faure-Muret A., Fallot P. (1955). Carte géologique de la France au 1/50000. Notice de la feuille de St Etienne de Tinée. XXXVI-40. BRGM.

Ferrando S., Lombardo B., Compagnoni R. (2008). Metamorphic history of HP mafic granulites from the Gesso-Stura Terrain (Argentera Massif, Western Alps, Italy). European Journal of Mineralogy 20, 777-790.

Ferrara G., Malaroda R. (1969). Radiometric age of granitic rocks from the Argentera Massif (Maritime Alps). Bollettino della Società Geologica Italiana 88, 311-320.

Ferry J.T., Spear F.S. (1978). Experimental calibration of the partitioning of Fe and Mg between biotite and garnet. Contributions to mineralogy and petrology, 66(2), 113-117.

Festa A., Balestro G., Borghi A., De Caroli S., Succo A. (2020). The role of structural inheritance in continental break-up and exhumation of Alpine Tethyan mantle (Canavese Zone, Western Alps). Geoscience Frontiers, 11(1), 167-188.

Filippi M., Zanoni D., Gosso G., Lardeaux J.M., Verati C., Spalla M.I. (2019). Structure of lamprophyres: a discriminant marker for Variscan and Alpine tectonics in the Argentera-Mercantour Massif, Maritime Alps. BSGF-Earth Sciences Bulletin, 190, 12.

Filippi M., Zanoni D., Lardeaux J.M., Spalla M.I., Gosso, G. (2020). Evidence of Tethyan continental break-up and Alpine collision in the Argentera-Mercantour Massif, Western Alps. Lithos, 372, 105653.

Floyd P. A. (1984). Geochemical characteristics and comparison of the basic rocks of the Lizard Complex and the basaltic lavas within the Hercynian troughs of SW England. Journal of the Geological Society, 141(1), 61-70.

Ford M., Lickorish W.H., Kusznir N.J. (1999). Tertiary foreland sedimentation in the Southern Subalpine Chains, SE France: a geodynamic appraisal. Basin Research 11(4), 315-336.

Franceschelli M., Eltrudis A., Memmi I., Palmeri R., Carcangiu G. (1998). Multi-stage metamorphic re-equilibration in eclogitic rocks from the Hercynian basement of NE Sardinia (Italy). Mineralogy and Petrology, 62, 167-193.

Franceschelli M., Puxeddu M., Cruciani G., Utzeri D. (2007). Metabasites with eclogite facies relics from Variscides in Sardinia, Italy: a review. International Journal of Earth Sciences, 96(5), 795-815.

Franke W. (1989). Variscan plate tectonics in Central Europe – current ideas and open questions. Tectonophysics, 169, 221–228.

Franke W. (2000). The mid-European segment of the Variscides: tectonostratigraphic units, terrane boundaries and plate tectonic evolution. Geological Society, London, Special Publications, 179(1), 35-61.

Franke W. (2006). The Variscan orogen in Central Europe: construction and collapse. Geological Society, London, Memoirs, 32(1), 333-343.

Franke W., Ballevre M., Cocks L.R.M., Torsvik T.H., Żelaźniewicz A. (2020). Variscan orogeny. Reference Module in Earth Systems and Environmental Sciences.

Franke W., Cocks L.R.M., Torsvik, T.H. (2017). The Palaeozoic Variscan oceans revisited. Gondwana Research, 48, 257-284.

Franke W., Engel W. (1986). Synorogenic sedimentation in the Variscan Belt of Europe. Bulletin de la Société géologique de France, 2(1), 25-33.

Franz L., Romer R.L. (2007). Caledonian high-pressure metamorphism in the Strona-Ceneri Zone (Southern Alps of southern Switzerland and northern Italy). Swiss Journal of Geosciences, 100(3), 457-467.

Frassi C. (2015). Structure of the Variscan metamorphic complexes in the central transect of the Posada-Asinara Line (SW Gallura region, Northern Sardinia, Italy). Journal of Maps, 11(1), 136-145.

Fréville K., Trap P., Faure M., Melleton J., Li X.H., Lin W., Blein O., Bruguiere O., Poujol M. (2018) Structural, metamorphic and geochronological insights on the Variscan evolution of the Alpine basement in the Belledonne Massif (France). Tectonophysics 726:14–42.

Frey M., Desmons J., Neubauer F. (1999). The new metamorphic maps of the Alps: Introduction. Schweizerische Mineralogische und Petrographische Mitteilungen, (79), 1-4.

Friedl G., Cooke R.A., Finger F., McNaughton N.J., Fletcher I.R. (2011). Timing of Variscan HP-HT metamorphism in the Moldanubian Zone of the Bohemian Massif: U-Pb SHRIMP dating on multiply zoned zircons from a granulite from the Dunkelsteiner Wald Massif, Lower Austria. Mineralogy and Petrology, 102(1-4), 63.

Frost B.R., Barnes C.G., Collins W.J., Arculus R.J., Ellis D.J., Frost C.D. (2001). A geochemical classification for granitic rocks. Journal of Petrology, 42(11), 2033-2048.

Fujimaki H., Tatsumoto M., Aoki K.I. (1984). Partition coefficients of Hf, Zr, and REE between phenocrysts and groundmasses. Journal of Geophysical Research: Solid Earth, 89(S02), B662-B672.

Funedda A., Oggiano G. (2009). Outline of the Variscan basement of Sardinia. Rendiconti della Società Paleontologica Italiana, 3(1), 23-35.

Gaggero L., Oggiano G., Buzzi L., Slejko F., Cortesogno L. (2007). Post-Variscan mafic dykes from the late orogenic collapse to the Tethyan rift: evidence from Sardinia. Ofioliti, 32(1), 15-37.

Gansser A., Pantic N. (1988). Prealpine events along the Eastern Insubric Line (Tonale Line, northern Italy). Eclogae Geologicae Helveticae, 81, 567–577.

Garuti G., Bea F., Zaccarini F., Montero P. (2001). Age, geochemistry and petrogenesis of the ultramafic pipes in the Ivrea Zone, NW Italy. Journal of Petrology, 42(2), 433-457.

Garzanti E., Sciunnach D. (1997). International ophiolite symposium field excursion guide-continental rifting to ocean floor metamorphism (21st-23rd September 1995): First day - Permo-Triassic evolution - constraints from the sedimentary records. Ofioliti, 22, 147-152.

Gasparik T., Lindsley D.H. (1980). Phase equilibria at high pressure of pyroxenes containing monovalent and trivalent ions. In: Prewitt CT (Ed) Pyroxenes. Reviews in mineralogy 7. Mineralogical Society of America, 309-339.

Gazzola D., Gosso G., Pulcrano E., Spalla M.I. (2000). Eo-Alpine HP metamorphism in the Permian intrusives from the steep belt of the central Alps (Languard-Campo nappe and Tonale Series). Geodinamica Acta, 13(2-3), 149-167.

Gebauer D., Bernard-Griffiths J., Grünenfelder M. (1981). U-Pb zircon and monazite dating of a mafic-ultramafic complex and its country rocks. Contributions to Mineralogy and Petrology, 76(3), 292-300.

Gebauer D., Quadt A.V., Compston W., Williams I.S., Grünenfelder M. (1988). Archaean zircons in a retrograded, Caledonian eclogite of the Gotthard Massif (Central Alps, Switzerland). Schweizerische Mineralogische und Petrographische Mitteilungen, 68(3), 485-490.

Genier F., Bussy F., Epard J.L., Baumgartner L. (2008). Water-assisted migmatization of metagraywackes in a Variscan shear zone, Aiguilles-Rouges massif, western Alps. Lithos, 102(3-4), 575-597.

Gerbault M., Schneider J., Reverso-Peila A., Corsini M. (2018). Crustal exhumation during ongoing compression in the Variscan Maures-Tanneron Massif, France-Geological and thermo-mechanical aspects. Tectonophysics, 746, 439-458.

Gerya T.V., Perchuk L.L., Burg J.P. (2008). Transient hot channels: Perpetrating and regurgitating ultrahigh-pressure, high-temperature crust–mantle associations in collision belts. Lithos 103:236–256.

Gerya T.V., Perchuk L.L., Triboulet C., Audren C., Sez'Ko A.I., 1997. Petrology of the Tumanshet zonal metamorphic complex, eastern Sayan. Petrology, 5(6), 503-533.

Gerya T.V., Stöckhert B., Perchuk A.L. (2002). Exhumation of high-pressure metamorphic rocks in a subduction channel: A numerical simulation. Tectonics, 21, 6.

Ghiselli A., Zucali M., Bini A. (2015). Structural and geomorphological map of the Passo San Marco–Pizzo di Trona area (western Orobic Alps, southern Alps, Italy). Journal of Maps, 11(1), 56-65.

Giacomini F., Bomparola R.M., Ghezzo C. (2005). Petrology and geochronology of metabasites with eclogite facies relics from NE Sardinia: constraints for the Palaeozoic evolution of Southern Europe. Lithos, 82, 221-248.

Giacomini F., Bomparola R.M., Ghezzo C. (2005). Petrology and geochronology of metabasites with eclogite facies relics from NE Sardinia: constraints for the Palaeozoic evolution of Southern Europe. Lithos, 82(1-2), 221-248.

Giacomini F., Braga R., Tiepolo M., Tribuzio R. (2007). New constraints on the origin and age of Variscan eclogitic rocks (Ligurian Alps, Italy). Contributions to Mineralogy and Petrology 153(1), 29–53.

Giacomini F., Dallai L., Carminati E., Tiepolo M., Ghezzo C. (2008). Exhumation of a Variscan orogenic complex: insights from the composite granulitic-amphibolitic metamorphic basement of South-East Corsica (France). Journal of Metamorphic Geology, 26, 403-436.

Giobbi Origoni E., Bocchio R., Boriani A., Carmine M., De Capitani L. (1988). Late-Hercynian mafic and intermediate intrusives of Serie dei Laghi (N-Italy). Rendiconti della Società Italiana di Mineralogia e Petrologia, 43, 395-410.

Giobbi Origoni, E., Gregnanin, A. (1983). The crystalline basement of the "Massiccio delle Tre Valli Bresciane": new petrographic and chemical data. Memorie della Società Geologica Italiana, 26(1), 133–144.

Giorgis D., Thélin P., Stampfli G., Bussy F. (1999). The Mont-Mort metapelites: Variscan metamorphism and geodynamic context (Brianconnais basement, western Alps, Switzerland). Schweizerische Mineralogische und Petrographische Mitteilungen, 79, 381–198.

Godard G. (1988). Petrology of some eclogites in the Hercynides: the eclogites from the southern Armorican massif, France. In Eclogites and eclogites-facies rocks (pp. 451-519).

Gosso G., Engi M., Koller F., Lardeaux J.M., Oberhaensli R., Spalla M.I. (2004). Thermo-mechanical evolution of the Alpine Belt, from the Engadine Window to the Matterhorn. 32nd IGC Field Trip Guidebook - APAT (Roma), B29, 1 – 52.

Gosso G., Lardeaux J.M., Zanoni D., Volante S., Corsini M., Bersezio R., Mascle J., Spaggiari L., Spalla M.I., Zucali M., Giannerini G., Camera L. (2019) Mapping the progressive geologic history at the junction of the Alpine mountain belt and the western Mediterranean ocean. Ofioliti, 44, 97-110.

Gosso G., Rebay G., Roda M., Spalla M.I., Tarallo M., Zanoni D., Zucali M. (2015). Taking advantage of petrostructural heterogeneities in subduction-collisional orogens and effect on the scale of analysis. Periodico di Mineralogia 84 (3B Special Issue), 779–825.

Gosso G., Siletto G.B., Spalla M.I. (1997). International ophiolite symposium field excursion guide—continental rifting to ocean floor metamorphism (21st–23rd September 1995): First day: HT/LP metamorphism and structures in the South-Alpine basement near Lake Como, Orobic Alps; intracontinental imprints of the Permo-Triassic rifting. Ofioliti, 22, 133-145.

Gosso G., Spalla M.I., Bini A., Siletto G.B., Berra F., Forcella F., 2012. Note Illustrative della Carta Geologica d 'Italia alla scala 1: 50.000, Foglio 057 Malonno. ISPRA and Regione Lombardia.

Graham C.M., Powell R. (1984) A garnet–hornblende geo-thermometer: calibration testing and application to the Pelona schist, southern California. Journal of Metamorphic Geology, 2, 13-31.

Green E.C., Holland T.J.B., Powell R (2007). An order– disorder model for omphacitic pyroxenes in the system jadeite– diopside hedenbergite–acmite, with applications to eclogitic rocks. American Mineralogist, 92, 1181-1189.

Green E.C.R., White R.W., Diener J.F.A., Powell R., Holland T.J.B., Palin R.M. (2016). Activity–composition relations for the calculation of partial melting equilibria in metabasic rocks. Journal of Metamorphic Geology, 34(9), 845-869.

Green T.H., Pearson N.J. (1987). An experimental study of Nb and Ta partitioning between Ti-rich minerals and silicate liquids at high pressure and temperature. Geochimica et Cosmochimica Acta, 51(1), 55-62.

Gregnanin A. (1980). Metamorphism and magmatism in the western Italian Tyrol. Rendiconti della Società Italiana di Mineralogia e Petrologia, 36, 49–64.

Grimes C.B., John B.E., Cheadle M.J., Mazdab F.K., Wooden J.L., Swapp S., Schwartz, J.J. (2009). On the occurrence, trace element geochemistry, and crystallization history of zircon from in situ ocean lithosphere. Contributions to Mineralogy and Petrology, 158(6), 757.

Grimes C.B., John B.E., Kelemen P.B., Mazdab F.K., Wooden J.L., Cheadle, M.J., Hanghøj K., Schwartz J.J. (2007). Trace element chemistry of zircons from oceanic crust: A method for distinguishing detrital zircon provenance. Geology, 35(7), 643-646.

Gueirard S., Waterlot G., Samat M., and Gherzi A. (1970). Nouvelles précisions sur l'âge des schistes à graptolites du Fenouillet (massif des Maures, Var). Comptes Rendus del'Académie des Sciences, Paris. 270, 661–662.

Guergouz C., Martin L., Vanderhaeghe O., Thébaud N., Fiorentini M. (2018). Zircon and monazite petrochronologic record of prolonged amphibolite to granulite facies metamorphism in the Ivrea-Verbano and Strona-Ceneri Zones, NW Italy. Lithos, 308, 1-18.

Guillot S., Di Paola S., Ménot R.P., Ledru P., Spalla M.I., Gosso G., Schwartz S. (2009). Suture zones and importance of strike-slip faulting for Variscan geodynamic reconstructions of the External Crystalline Massifs of the western Alps. Bulletin de la Société géologique de France, 6, 483-500.

Guillot S., Ménot R.P. (2009). Paleozoic evolution of the external crystalline massifs of the Western Alps. Compte Rendu Géoscience, 341, 253-265.

Guillot S., Ménot R.P., Fernandez A. (1998). Paleozoic evolution of the external crystalline massifs along the Belledonne-Oisans transect (Western Alps). Acta Universitatis Carolinae Geologica, 42, 257–258.

Guiraud M., Powell R., Rebay G. (2001). H2O in metamorphism and unexpected behaviour in the preservation of metamorphic assemblages. Journal of Metamorphic Geology, 19, 445-454.

Guiraud, M., Burg J.P., Powell, R. (1987). Evidence for a Variscan suture zone in the Vendée, France: a petrological study of blueschist facies rocks from Bois de Cené. Journal of Metamorphic Geology, 5(2), 225-237.

Haas R. (1985). Zur metamorphose des suedlichen Oetztalkristallins unter besonderer Beruecksichtigung der Matscher Einheit (Vintschgau/Suedtirol). PhD thesis, Innsbruck.

Habler G., Thoeni M., Grasemann B. (2009). Cretaceous metamorphism in the Austroalpine Matsch Unit (Eastern Alps): The interrelation between deformation and chemical equilibration processes. Mineralogy and Petrology, 97, 149-171.

Handy M.R., Schmid S.M., Bousquet R., Kissling E., Bernoulli D. (2010). Reconciling plate-tectonic reconstructions of Alpine Tethys with the geological--geophysical record of spreading and subduction in the Alps. Earth-Science Reviews, 102, 121–158.

Handy M.R., Ustaszewski K., Kissling, E. (2015). Reconstructing the Alps–Carpathians Dinarides as a key to understanding switches in subduction polarity, slab gaps and surface motion. International Journal of Earth Sciences, 104, 1-26.

Hartz E.H., Torsvik T.H. (2002). Baltica upside down: a new plate tectonic model for Rodinia and the Iapetus Ocean. Geology, 30(3), 255-258.

Hawthorne F.C., Oberti R., Harlow G.E., Maresch W.V., Martin R.F., Schumacher J.C., Welch M.D. (2012). Nomenclature of the amphibole supergroup. American Mineralogist, 97(11-12), 2031-2048.

Heister T., Dannberg J., Gassmöller R., Bangerth W. (2017). High accuracy mantle convection simulation through modern numerical methods – II: realistic models and problems. Geophysical Journal International, 210, 833–851.

Henk A., Franz L., Teufel S., Oncken O. (1997). Magmatic underplating, extension, and crustal reequilibration: Insights from a cross-section through the Ivrea Zone and Strona-Ceneri Zone, northern Italy. The Journal of Geology, 105(3), 367-378.

Henry D.J., Guidotti C.V., Thomson J.A. (2005) The Ti-saturation surface for low-to-medium pressure metapelitic biotites: implications for geothermometry and Ti-substitution mechanisms. American Mineralogist, 90, 316–328.

Hermann J., Müntener O., Günther D. (2001). Differentiation of mafic magma in a continental crust-to-mantle transition zone. Journal of Petrology, 42(1), 189-206.

Herzberg C., Riccio L., Chiesa A., Fornoni A., Gatto G.O., Gregnanin A., Piccirillo E.M., Scolari, A. (1977). Petrogenetic evolution of a spinelgarnet-lherzolite in the austridic crystalline basement from Val Clapa

(Alto Adige, northeastern Italy). Memorie degli Istituti di Geologia e Mineralogia dell'Università di Padova XXX, 6–23.

Hilairet N., Reynard B., Wang Y., Daniel I., Merkel S., Nishiyama N., Petitgirard S. (2007). High-Pressure Creep of Serpentine, Interseismic Deformation, and Initiation of Subduction. Science, 318, 1910–1912.

Hofmann A.W. (2003). Sampling mantle heterogeneity through oceanic basalts isotopes and trace elements. In: Carlson RW (Ed) The Mantle and Core. Treatise on Geochemistry 2. Elsevier, New York, 61-101.

Hofmann A.W., Jochum K.P., Seufert M., White W.M. (1986). Nb and Pb in oceanic basalts: new constrains on mantle evolution. Earth and Planetary Science Letters, 80, 299-313.

Hoke L. (1990). The Altkristallin of the Kreuzeck Mountains, SE Tauern Window, Eastern Alps - Basement Crust in a Convergent Plate Boundary Zone. Jahrbuch des Geologischen Bundesantall, 133, 5-87.

Holdaway M.J. (2000). Application of new experimental and garnet Margules data to the garnet-biotite geothermometer. American Mineralogist, 85(7-8), 881-892.

Holdaway M.J., Lee S.M. (1977). Fe-Mg cordierite stability in high-grade pelitic rocks based on experimental, theoretical, and natural observations. Contributions to Mineralogy and Petrology, 63(2), 175-198.

Holland T.J. (1980). The reaction albite = jadeite + quartz determined experimentally in the range 600–1200 °C. American Mineralogist, 65(1-2), 129-134.

Holland T.J.B. (1990). Activities of components in omphacite solid solutions. Contributions to Mineralogy and Petrology, 105, 446–453.

Holland T.J.B., Powell R (2003). Activity-composition relations for phases in petrological calculations: an asymmetric multicomponent formulation. Contributions to Mineralogy and Petrology, 145, 492-501.

Holland T.J.B., Powell R. (1998). An internally consistent thermodynamic dataset for phases of petrological interest. Journal of Metamorphic Geology, 16, 309-343.

Holland T.J.B., Powell R. (2011). An improved and extended internally consistent thermodynamic dataset for phases of petrological interest, involving a new equation of state for solids. Journal of Metamorphic Geology, 29(3), 333-383.

Holub F.V. (1997). Ultrapotassic plutonic rocks of the durbachite series in the Bohemian Massif: petrology, geochemistry and petrogenetic interpretation. Sbornik geologickych ved, Loziskova geologie–mineralogie, 31, 5-26.

Holub F.V., Cocherie A., Rossi, P. (1997). Radiometric dating of granitic rocks from the Central Bohemian Plutonic Complex (Czech Republic): constraints on the chronology of the thermal and tectonic events along the Moldanubian–Barrandian boundary. Comptes Rendus de l'Académie des Sciences, Series IIA, Earth and Planetary Sciences, 325, 19–26.

Hoskin P.W., Schaltegger U. (2003). The composition of zircon and igneous and metamorphic petrogenesis. Reviews in Mineralogy and Geochemistry, 53(1), 27-62.

Innocent C., Michard A., Guerrot C., Hamelin B. (2003). Datation U-Pb sur zircons à 548 Ma de leptynites des Maures centrales. Signification géodynamique des complexes leptyno-amphibolitiques de l'Europe varisque. Bulletin de la Société géologique de France, 174(6), 585-594.

Irvine T.N.J., Baragar W.R.A. (1971). A guide to the chemical classification of the common volcanic rocks. Canadian Journal of Earth Sciences, 8, 523-548.

Janoušek V., Bowes D.R., Braithwaite C.J., Rogers G. (2000). Micro structural and mineralogical evidence for limited involvement of magma mixing in the petrogenesis of a Hercynian high-K calc-alkaline intrusion: the Kozárovice granodiorite, Central Bohemian Pluton, Czech Republic. Earth and Environmental Science Transactions of the Royal Society of Edinburgh, 91(1-2), 15-26.

Janoušek V., Braithwaite C.J., Bowes D.R., Gerdes A. (2004). Magma-mixing in the genesis of Hercynian calc-alkaline granitoids: an integrated petrographic and geochemical study of the Sázava intrusion, Central Bohemian Pluton, Czech Republic. Lithos, 78(1-2), 67-99.

Janoušek V., Gerdes A., Vrána S., Finger F., Erban V., Friedl G., Braithwaite C.J. (2006). Low-pressure granulites of the Lišov Massif, Southern Bohemia: Viséan metamorphism of Late Devonian plutonic arc rocks. Journal of Petrology, 47(4), 705-744.

Jenkins D.M. (1984). Upper-pressure stability of synthetic margarite plus quartz. Contributions to Mineralogy and Petrology, 88(4), 332-339.

Ji W.Q., Malusà M.G., Tiepolo M., Langone A., Zhao L., Wu F.Y. (2019). Synchronous Periadriatic magmatism in the Western and Central Alps in the absence of slab breakoff. Terra Nova, 31(2), 120-128.

Joanny V., Lardeaux J.M., Trolliard G., Boudeulle M. (1989). La transition omphacite => diopside + plagioclase dans les éclogites du Rouergue (Massif central français): un exemple de précipitation discontinue. Compte Rendu Académie des Sciénces, Paris, 309, 1929-1930.

Joanny V., van Roermund H., Lardeaux J.M. (1991). The clinopyroxene/plagioclase symplectite in retrograde eclogites: a potential geothermometer. Geologische Rundschau, 80, 303–320.

Jouffray F., Spalla M.I., Lardeaux J.M., Filippi M., Rebay, G., Corsini, M., Zanoni D., Zucali M, Gosso, G. (2020). Variscan eclogites from the Argentera–Mercantour Massif (External Crystalline Massifs, SW Alps): a dismembered cryptic suture zone. International Journal of Earth Sciences, 109, 1273-1294.

Jourdan F., Renne P.R. (2007). Age calibration of the Fish Canyon sanidine 40Ar/39Ar dating standard using primary K–Ar standards. Geochimica et Cosmochimica Acta, 71(2), 387-402.

Jowett E.C. (1991). Fitting iron and magnesium into the hydrothermal chlorite geothermometer. In GAC/MAC/SEG Joint Annual Meeting, Toronto, May 27-29, 1991, Program with Abstracts 16.

Juteau T., Maury R. (1999). The Oceanic Crust, from Accrection to Mantle Recycling: London, United Kingdom, Praxis Springer, p. 402.

Karato S.I.., Wu P. (1993). Rheology of the Upper Mantle: A Synthesis. Science, 260, 771–778.

Kerckhove C. (1969). La Zone du flysch dans les nappes de l'Embrunais-Ubaye (Alpes occidentales). Géologie Alpine, 45, 5-204.

Kirby G.A. (1979). The Lizard Complex as an ophiolite. Nature, 282(5734), 58-61.

Klinkhammer G.P., Elderfield H., Edmond J.M., Mitra A. (1994). Geochemical implications of rare earth element patterns in hydrothermal fluids from mid-ocean ridges. Geochimical and Cosmochimical Acta, 58, 5105–5113.

Klötzli U.S., Sinigoi S., Quick J.E., Demarchi G., Tassinari C.C., Sato K., Günes Z. (2014). Duration of igneous activity in the Sesia Magmatic System and implications for high-temperature metamorphism in the Ivrea–Verbano deep crust. Lithos, 206, 19-33.

Konzett J., Krenn K., Hauzenberge C., Whitehouse M., Hoinkes G. (2012). High pressure tourmaline formation and fluid activity in Fe–Ti-rich eclogites from the Kreuzeck Mountains, Eastern Alps, Austria. Journal of Petroligy, 53, 99-125.

Korenaga T., Korenaga J. (2016). Evolution of young oceanic lithosphere and the meaning of seafloor subsidence rate. Journal of Geophysical Research: Solid Earth, 121, 6315–6332.

Košler J., Konopásek J., Sláma J., Vrána S. (2014). U–Pb zircon provenance of Moldanubian metasediments in the Bohemian Massif. Journal of the Geological Society, 171(1), 83-95.

Kossmat F. (1927). Gliederung des varistischen Gebirgsbaues: Abhandlungen Sächsischen Geologischen Landesamts, 1.

Krenn E., Schulz B., Finger F. (2012). Three generations of monazite in Austroalpine basement rocks to the south of the Tauern Window: evidence for Variscan, Permian and Eo-Alpine metamorphic events. Swiss Journal of Geosciences, 105(3), 343-360.

Krogh-Ravna E. (2000). The garnet-clinopyroxene Fe^{2+}-Mg geothermometer: an updated calibration. Journal of Metamorphic Geology, 18, 211-219.

Kronbichler M., Heister T., Bangerth W. (2012). High accuracy mantle convection simulation through modern numerical methods. Geophysical Journal International, 191, 12–29.

Kryza R., Muszyński A., Vielzeuf D. (1990). Glaucophane-bearing assembalges overprinted by greenschist-facies metamorphism in the Variscan Kaczawa complex, Sudetes, Poland. Journal of Metamorphic Geology 8, 345-355.

Kryza R., Pin, C. (2010). The Central-Sudetic ophiolites (SW Poland): petrogenetic issues, geochronology and palaeotectonic implications. Gondwana Research, 17(2-3), 292-305.

Kusiak M.A., Dunkley D.J., Suzuki K., Kachlík V., Kędzior A., Lekki J., Opluštil S. (2010). Chemical (non-isotopic) and isotopic dating of Phanerozoic zircon-A case study of durbachite from the Třebíč Pluton, Bohemian Massif. Gondwana Research, 17(1), 153-161.

Labanieh S., Chauvel C., Germa A., Quidelleur X. (2012). Martinique: a clear case for sediment melting and slab dehydration as a function of distance to the trench. Journal of Petrology, 53, 2441–2464.

Labaume P., Jolivet M., Souquière F., Chauvet A. (2008). Tectonic control on diagenesis in a foreland basin: combined petrologic and thermochronologic approaches in the Grès d'Annot basin (Late Eocene–Early Oligocene, French–Italian external Alps). Terra Nova 20(2), 95-101.

Laubscher H.P. (1985). Large scale thin-skin thrusting in the Southern Alps. GSA Bulletin, 96, 710-718.

Ladenhauf C., Armstrong R., Konzett J., Miller C. (2001). The timing of pre-Alpine high-pressure metamorphism in the Eastern Alps: constraints from U-Pb SHRIMP dating of zircons from the Austroalpine Silvretta nappe. Conmference Abstract EUG XI, 600.

Lancelot J., Moussavou M., Pupin J.P., Seyler, M. (1995). Témoins-clés de l'évolution anté-Hercynienne et anté-Cambrienne des Maures. In Magmatismes dans le sud-est de la France, p. 12. Séance spécialisée de la Société Géologique de France et de l'Association des géologues du Sud Est.

Lapierre H., Basile C., Dupuis V. (1999). Basaltes et trachytes permiens de l'Esterel (SE France); une serie tholeiitique transitionnelle epanchee pendant l'amincissement lithospherique. Bulletin de la Société géolgique de France, 170(2), 253-265.

Lardeaux J. M., Spalla M.I. (1991). From granulites to eclogites in the Sesia zone (Italian Western Alps): a record of the opening and closure of the Piedmont ocean. Journal of Metamorphic Geology, 9(1), 35-59.

Lardeaux J.M. (2014). Deciphering orogeny: a metamorphic perspective. Examples from European Alpine and Variscan belts. Part I: Alpine metamorphism in the western Alps. A review. Bulletin de la Société Géologique de France, 185, 93-114.

Lardeaux J.M. (2014). Deciphering orogeny: a metamorphic perspective Examples from European Alpine and Variscan belts: Part II: Variscan metamorphism in the French Massif Central–A review. Bulletin de la Société Géologique de France, 185(5), 281-310.

Lardeaux J.M., Ledru P., Daniel I., Duchêne S. (2001). The Variscan French Massif Central—a new addition to the ultra-high pressure metamorphic 'club': exhumation processes and geodynamic consequences. Tectonophysics 332:143-167.

Lardeaux J.M., Ménot R.P., Orsini J.B., Rossi P., Naud G., Libourel G. (1994) Corsica and Sardinia in the Variscan chain. In: Keppie JD (Ed) Pre- Mesozoic Geology in France and Related Areas. Springer, Berlin, 467-479.

Lardeaux J.M., Schulmann K., Faure M., Janoušek V., Lexa O., Skrzypek E., Edel J.B., Štípská, P. (2014). The Moldanubian zone in the French Massif Central, Vosges/Schwarzwald and Bohemian Massif revisited: differences and similarities. Geological Society, London, Special Publications, 405(1), 7-44.

Latouche L., Bogdanoff S. (1987). Evolution précoce du massif de l'Argentera: apport des eclogites et des granulites. Géologie Alpine, 63, 151-164.

Laurent O., Couzinié S., Zeh A., Vanderhaeghe O., Moyen J.F., Villaros A., Gardien V., Chelle-Michou, C. (2017). Protracted, coeval crust and mantle melting during Variscan late-orogenic evolution: U–Pb dating in the eastern French Massif Central. International Journal of Earth Sciences, 106(2), 421-451.

Le Breton E., Brune S., Ustaszewski K., Zahirovic S., Seton M., Müller R.D. (2020). Kinematics and extent of the Piemont-Liguria Basin -- implications for subduction processes in the Alps. Solid Earth Discussions, 2020, 1–42.

Le Fort P. (1973). Geologie du Haut-Dauphine cristallin (Alpes Francaise): Etudes petrologique et structurale de la partie occidentale. Ph.D. thesis, Université Nancy.

Le Maitre R.W., Streckeisen A., Zanettin B., Le Bas M.J., Bonin B., Bateman P., eds. 2002. Igneous rocks: a classification and glossary of terms: recommendations of the International Union of Geological Sciences Subcommission on the Systematics of Igneous Rocks. Cambridge: Cambridge University Press, p. 236.

Leake B.E., Woolley A.R., Arps C., Birch W., Gilbert C., Grice J., Hawthorne F. (1997). Nomenclature of amphiboles: report of the subcommittee on amphiboles of the international mineralogical association, commission on new minerals and mineral names. Canadian Mineralogist, 35, 219-246.

Leake B.E., Woolley A.R., Birch W.D., Burke E.A.J., Ferraris G., Grice J.D., Hawthorne F.C., Kisch H.J., Krivovichev V.G., Schumacher J.C., Stephenson N.C.N., Whittaker E.J.W. (2004). Nomenclature of amphiboles: additions and revisions to the International Mineralogical Association's amphibole nomenclature. European Journal of Mineralogy, 16, 191-196.

Leclère H., Lacroix B., Fabbri O., (2014). Fault mechanics at the base of the continental seismogenic zone: Insights from geochemical and mechanical analyses of a crustal-scale transpressional fault from the Argentera crystalline massif, French-Italian Alps. Journal of Structural Geology 66, 115-128.

Ledru P., Courrioux G., Dallain C., Lardeaux J.M., Montel J.M., Vanderhaeghe O., Vitel G. (2001) The Velay dome (French Massif Central): melt generation and granite emplacement during orogenic evolution. Tectonophysics, 342, 207–237.

Ledru P., Lardeaux J.M., Santallier D., Autran A., Quenardel J.M., Floc'h J.P., Lerouge G., Maillet N., Marchand J., Ploquin A. (1989). Où sont les nappes dans le Massif central français? Bulletin de la Société géologique de France, 8, 605-618.

Lemoine M., Bas T., Arnaud-Vanneau A., Arnaud H., Dumont T., Gidon M., Bourbon M., de Graciansky P.C., Rudkiewicz J.L., Megard-Galli J., Tricart P. (1986). The continental margin of the Mesozoic Tethys in the Western Alps. Marine and Petroleum Geology 3(3), 179-199.

Leroy S, Cabanis B. (1993). Le volcanisme permien du bassin de Toulon: Un jalon septentrional du volcanisme permien de l'Ouest méditerranéen. Geologie de France, 2, 57-66.

Leyreloup A., Buscail F., Motard C., Ciancaleoni L., Dumoulin C., Lavigne J.-F., Monié P., Brunel M. (1996). Découvertede paragenèses de type schistes blancs dans les Maures occidentales. Chemin PTt. Implications géodynamiques. RST meeting, Orléans, France, p. 55.

Li X.H., Faure M., Lin, W. (2014). From crustal anatexis to mantle melting in the Variscan orogen of Corsica (France): SIMS U–Pb zircon age constraints. Tectonophysics, 634, 19-30.

Liati A., Gebauer D., Fanning C.M. (2009). Geochronological evolution of HP metamorphic rocks of the Adula nappe, Central Alps, in pre-Alpine and Alpine subduction cycles. Journal of the Geological Society, 166(4), 797-810.

Liégeois J.P., Duchesne J.C. (1981). The Lac Cornu retrograded eclogites (Aiguilles Rouges massif, Western Alps, France): evidence of crustal origin and metasomatic alteration. Lithos 14(1), 35–48.

Linnemann U., Gerdes A., Drost K., Buschmann B. (2007). The continuum between Cadomian orogenesis and opening of the Rheic Ocean: Constraints from LA-ICP-MS U-Pb zircon dating and analysis of plate-tectonic setting (Saxo-Thuringian zone, northeastern Bohemian Massif, Germany). Special Papers Geological Society of America, 423, 61.

Locmelis M., Fiorentini M.L., Rushmer T., Arevalo Jr R., Adam J., Denyszyn S.W. (2016). Sulfur and metal fertilization of the lower continental crust. Lithos, 244, 74-93.

Locock A.J. (2014). An Excel spreadsheet to classify chemical analyses of amphiboles following the IMA 2012 recommendations. Computers & Geosciences, 62, 1-11.

Lotout C., Pitra P., Poujol M., Anczkiewicz R., Van Den Driessche J. (2018). Timing and duration of Variscan high-pressure metamorphism in the French Massif Central: A multimethod geochronological study from the Najac Massif. Lithos, 308, 381-394.

Lotout C., Poujol M., Pitra P., Anczkiewicz R., Van Den Driessche J. (2020). From burial to exhumation: emplacement and metamorphism of mafic eclogitic terranes constrained through multimethod petrochronology: a case study from the Lévézou massif (French Massif Central, Variscan belt). Journal of Petrology, 61(4).

Loucks R.R. (1990). Discrimination of ophiolitic from nonophiolitic ultramafic-mafic allochthons in orogenic belts by the Al/Ti ratio in clinopyroxene. Geology, 18(4), 346-349.

Luoni P., Rebay G., Roda M., Zanoni D., Spalla M.I. (2020). Tectono-metamorphic evolution of UHP Zermatt-Saas serpentinites: a tool for vertical palaeogeographic restoration: International Geology Review, 1–26.

Lustrino M., Abbas H., Agostini S., Caggiati M., Carminati E., Gianolla P. (2019). Origin of Triassic magmatism of the Southern Alps (Italy): Constraints from geochemistry and Sr-Nd-Pb isotopic ratios. Gondwana Research, 75, 218-238.

Maino M., Dallagiovanna G., Gaggero L., Seno S., Tiepolo M. (2012). U-Pb zircon geochronological and petrographic constraints on late to post-collisional Variscan magmatism and metamorphism in the Ligurian Alps, Italy. Geological Journal 47(6), 632–652.

Maino M., Gaggero L., Langone A., Seno S., Fanning M. (2019). Cambro-Silurian magmatisms at the northern Gondwana margin (Penninic basement of the Ligurian Alps). Geoscience Frontiers, 10(1), 315-330.

Majka J., Mazur S., Kośmińska K., Dudek K., Klonowska I. (2016). Pressure-temperature estimates of the blueschists from the Kopina Mt., northern Bohemian Massif, Poland – constraints on subduction of the Saxothuringian continental margin. European Journal of Mineralogy, 28(6), 1047-1057.

Malaroda R., Carraro F., Dal Piaz G.V., Franceschetti B., Sturani C., Zanella E. (1970). Carta geologica del Massiccio dell'Argentera alla scala 1:50.000 e note illustrative. Memorie della Società Geologica Italiana, 9, 557-663.

Malaroda R., Schiavinato G. (1957). Osservazioni preliminari sui fenomeni di anatessi nel settore italiano del Massiccio dell'Argentera (Alpi Marittime). Bollettino della Società Geologica Italiana 76-97.

Malaroda R., Schiavinato G. (1958). Le anatessiti dell'Argentera. Rendiconti Socità Mineralogica Italiana, 14, 249-274.

Malaroda R., Schiavinato G. (1960). Agmatiti e migmatiti anfiboliche omogenee nel settore meridionale del Massiccio dell'Argentera. Rendiconti Socità Mineralogica Italiana,14, 335-346.

Malvoisin B., Carlut J., Brunet F. (2012). Serpentinization of oceanic peridotites: 1. A high-sensitivity method to monitor magnetite production in hydrothermal experiments. Journal of Geophysical Research: Solid Earth, 117.

Manatschal G. (2004). New models for evolution of magma-poor rifted margins based on a review of data and concepts from West Iberia and the Alps: International Journal of Earth Sciences, 93, 432–466.

Manzotti P., Ballèvre M., Pitra P., Müntener O., Putlitz B., Robyr M. (2020). The growth of sodic amphibole at the greenschist-to blueschist-facies transition (Dent Blanche, Western Alps): bulk-rock chemical control and thermodynamic modelling. Journal of Petrology, 61(4).

Manzotti P., Ballèvre M., Zucali M., Robyr M., Engi M. (2014). The tectonometamorphic evolution of the Sesia–Dent Blanche nappes (internal Western Alps): review and synthesis. Swiss Journal of Geosciences, 107(2-3), 309-336.

Manzotti P., Rubatto D., Zucali M., El Korh A., Cenki-Tok B., Ballèvre M., Engi M. (2018). Permian magmatism and metamorphism in the Dent Blanche nappe: constraints from field observations and geochronology. Swiss Journal of Geosciences, 111(1-2), 79-97.

Manzotti P., Zucali M. (2013). The pre-Alpine tectonic history of the Austroalpine continental basement in the Valpelline unit (Western Italian Alps). Geological Magazine, 150(1), 153-172.

Marotta A.M., Roda M., Conte K., Spalla M.I., (2018). Thermo-mechanical numerical model of the transition from continental rifting to oceanic spreading: the case of study of the Alpine Tethys. Geological Magazine 155(2), 250-279.

Marotta A.M., Spalla M.I., Gosso G. (2009). Upper and lower crustal evolution during lithospheric extension: numerical modelling and natural footprints from the European Alps. Geological Society of London, Special Publications, 321, 33-72.

Martinez Catalán J. R., Arenas R., Abati J., Martínez S.S., García F.D., Suárez J.F., Clavijo E.G. (2009). A rootless suture and the loss of the roots of a mountain chain: the Variscan belt of NW Iberia. Comptes Rendus Geoscience, 341(2-3), 114-126.

Martínez Catalán J.R., Arena R., Abat J., SánchezMartínez S., Díaz García F., Fernández- Suárez J., González Cuadra P., Castiñeiras P., Gómez Barreiro J., Díez Montes A., González Clavijo E., Rubio Pascual F.J., Andonaegui P., Jeffries T.E., Alcock J.E., Díez Fernández R., López Carmona A. (2009). A rootless suture and the loss of the roots of a mountain chain: the Variscan belt of NW Iberia. Compte Rrendu Geosciences, 341, 114-126.

Martínez Catalán J.R., Arenas R., Díaz García F., González Cuadra P., Gómez-Barreiro J., Abati J., Castiñeiras P., Fernández-Suárez J., Sánchez Martínez S., Andonaegui P., González Clavijo E., Díez Montes A., Rubio Pascual F.J., and Valle Aguado B. (2007). Space and time in the tectonic evolution of the north-western Iberian Massif: Implications for the Variscan belt. Geological Society of America Memoir, 200, 403–423.

Martínez S.S., Gerdes A., Arenas R., Abati J. (2012). The Bazar Ophiolite of NW Iberia: a relic of the Iapetus–Tornquist Ocean in the Variscan suture. Terra Nova, 24(4), 283-294.

Maruyama S., Liou J.G., Suzuki K., (1982). The peristerite gap in low-grade metamorphic rocks. Contributions to Mineralogy and Petrology 81(4), 268-276.

Maruyama S., Suzuki K., Liou J.G. (1983). Greenschist–amphibolite transition equilibria at low pressures. Journal of Petrology 24(4), 583-604.

Matte P. (1986). Tectonics and plate tectonics model for the Variscan belt of Europe. Tectonophysics, 126(2-4), 329-374.

Matte P. (1998). Continental subduction and exhumation of HP rocks in Paleozoic orogenic belts: Uralides and Variscides. Gff, 120(2), 209-222.

Matte P. (2001). The Variscan collage and orogeny (480–290 Ma) and the tectonic definition of the Armorica microplate: a review. Terra Nova, 13(2), 122-128.

Matte P., Burg J.P. (1981). Sutures, thrusts and nappes in the Variscan arc of western Europe. Plate tectonics interpretation. Geological Society of London, Special Publications, 8, 353-358.

Matte P., Maluski H., Rajlich P., Franke W. (1990). Terrane boundaries in the Bohemian Massif: result of large-scale Variscan shearing. Tectonophysics 177, 151-170.

Mattioli M., Lustrino M., Ronca S., Bianchini G. (2012). Alpine subduction imprint in Apennine volcaniclastic rocks. Geochemical–petrographic constraints and geodynamic implications from Early Oligocene Aveto-Petrignacola Formation (N Italy). Lithos, 134, 201-220.

McCarthy A., Müntener O. (2016). Comb layering monitors decompressing and fractionating hydrous mafic magmas in subvolcanic plumbing systems (Fisher Lake, Sierra Nevada, USA). Journal of Geophysical Research: Solid Earth, 121(12), 8595-8621.

McKenzie D.A.N., O'Nions R.K. (1991). Partial melt distributions from inversion of rare earth element concentrations. Journal of Petrology, 32(5), 1021-1091.

McKerrow W.S., Mac Niocaill C., Ahlberg P., Clayton G., Cleal C.J., Eagar R.M.C. (2000). The Late Palaeozoic relations between Gondwana and Laurussia. Geological Society of London Special Publications, 179, 9-20.

Medaris L.G., Jelinek E., Misar Z. (1995). Czech eclogites: terrane settings and implications for Variscan tectonic evolution of the Bohemian Massif. European J ournal of Mineralogy, 7, 7-28.

Melcher F., Meisel T., Puhl J., Koller F. (2002). Petrogenesis and geotectonic setting of ultramafic rocks in the Eastern Alps: constraints from geochemistry. Lithos 65(1-2), 69-112.

Ménot R.P., Paquette J.L. (1993). Geodynamic significance of basic and bimodal magmatism in the external domain, in: von Raumer, J.F., Neubauer F. (Eds.), Pre-Mesozoic geology in the Alps. Springer, Berlin, Heidelberg, pp. 241-254.

Ménot R.P., Peucat J.J., Scarenzi D., Piboule M. (1988). 496 My age of plagiogranites in the Chamrousse ophiolite complex (external crystalline massifs in the French Alps): evidence of a Lower Paleozoic oceanization. Earth and Planetary Science Letters, 88(1-2), 82-92.

Merle O., Brun J.P. (1984). The curved translation path of the Parpaillon Nappe (French Alps). Journal of Structural Geology 6(6), 711-719.

Meschede M. (1986). A method of discriminating between different types of mid-ocean ridge basalts and continental tholeiites with the 2Nb - Zr/4 - Y diagram. Chemical geology, 56(3-4), 207-218.

Messiga B., Tribuzio R., Caucia F. (1992). Amphibole evolution in Variscan eclogite-amphibolites from the Savona crystalline massif (Western Ligurian Alps, Italy): controls on the decompressional P-T-t path. Lithos, 27, 215–230.

Messiga B., Tribuzio R., Scambelluri M. (1992). Mafic eclogites from the Valosio crystalline massif (Ligurian Alps, Italy). Schweizerische Mineralogische und Petrographische Mitteilungen, 72(3), 365-377.

Michard A., Albarède F. (1986). The REE content of some hydrothermal fluids. Chemical Geology, 55, 51-60.

Milano P.F., Pennacchioni G., Spalla M.I. (1988). Alpine and pre-Alpine tectonics in the Central Orobic Alps (Southern Alps). Eclogae Geologicae Helvetiae 81, 273-293.

Miller C., Thöni M. (1995). Origin of eclogites from the Austroalpine Ötztal basement (Tirol, Austria): geochemistry and Sm/Nd vs. Rb/Sr isotope systematics. Chemical Geology, 122(1-4), 199-225.

Miller C., Thöni M. (1997). Eo-Alpine eclogitisation of Permian MORB-type gabbros in the Koralpe (Eastern Alps, Austria): new geochronological, geochemical and petrological data. Chemical Geology 137, 283–310.

Miyashiro A. (1961). Evolution of Metamorphic Belts. Journal of Petrology, 2, 277-311.

Monie P. (1990). Preservation of Hercynian 40Ar/39Ar ages through high-pressure low-temperature Alpine metamorphism in the Western Alps. European Journal of Mineralogy, 343-361.

Monjoie P., Bussy F., Schaltegger U., Mulch A., Lapierre H., Pfeifer H.R. (2007). Contrasting magma types and timing of intrusion in the Permian layered mafic complex of Mont Collon (Western Alps, Valais, Switzerland): evidence from U/Pb zircon and 40 Ar/39 Ar amphibole dating. Swiss Journal of Geosciences, 100(1), 125-135.

Montani V. 2004. Studio meso e microstrutturale dei boudin di metabasiti del complesso Malinvern-Argentera: resti dell'Oceano Reico nel Dominio Provenzale delle Alpi Marittime. Università degli Studi di Milano, Master Thesis, p. 181.

Morillon A.C., Féraud G., Sosson M., Ruffet G., Crevola G., Lerouge G. (2000). Diachronous cooling on both sides of a major strike slip fault in the Variscan Maures Massif (south-east France), as deduced from a detailed 40Ar/39Ar study. Tectonophysics, 321(1), 103-126.

Morimoto N. (1988). Nomenclature of pyroxenes. Mineralogy and Petrology, 39, 55-76.

Mørk MBE. (1985). A gabbro to eclogite transition on Flemsøy, Sunnmøre, western Norway. Chemical Geology, 50(1-3), 283-310.

Morten L., Nimis P., Rampone E. (2004). Records of mantle–crust exchange processes during continental subduction–exhumation in the Nonsberg-Ultental garnet peridotites (eastern Alps). A review. Periodico di Mineralogia 73, 119–129.

Mottana A., Nicoletti M., Petrucciani C., Liborio G., De Capitani L., Bocchio R. (1985). Pre-alpine and alpine evolution of the Southalpine basement of the Orobic Alps. Geologische Rundschau 74, 353-366.

Moussavou M. (1998). Contribution a` l'histoire thermotectonique Varisque du Massif des Maures, par la typologie du zircon et la géochronologie U/Pb sur minéraux accessoires. Unpublished Thesis, University of Montpellier, France.

Müller B., Klötzli U.S., Flisch M. (1995). U-Pb and Pb-Pb zircon dating of the older orthogneiss suite in the Silvretta nappe, eastern Alps: Cadomian magmatism in the upper Austro-Alpine realm. Geologische Rundschau, 84(3), 457-465.

Müller B., Schaltegger U., Klötzli U., Flisch M. (1996). Early Cambrian oceanic plagiogranite in the Silvretta nappe, eastern Alps: Geochemical, zircon U-Pb and Rb-Sr data from garnet-hornblende-plagioclase gneisses. Geologische Rundschau, 85(4), 822-831.

Müller W., Prosser G., Mancktelow N.S., Villa I.M., Kelley S.P., Viola G., Oberli F. (2001). Geochronological constraints on the evolution of the Periadriatic Fault System (Alps). International Journal of Earth Sciences, 90, 623-653.

Murphy J.B. (2013). Appinite suites: A record of the role of water in the genesis, transport, emplacement and crystallization of magma. Earth-Science Reviews, 119, 35-59.

Murphy J.B. (2020). Appinite suites and their genetic relationship with coeval voluminous granitoid batholiths, International Geology Review, 62(6), 683-713.

Musumeci G., Colombo F. (2002). Late Visean mylonitic granitoids in the Argentera Massif (western Alps, Italy): age and kinematic constraints on the Ferrière–Mollières shear zone. Comptes Rendus Geoscience 334(3), 213-220.

Mutch E.J.F., Blundy J.D., Tattitch B.C., Cooper F.J., Brooker R.A., (2016). An experimental study of amphibole stability in low-pressure granitic magmas and a revised Al-in-hornblende geobarometer. Contributions to Mineralogy and Petrology, 171(10), 85.

Myers J.S. (1978). Formation of banded gneisses by deformation of igneous rocks. Precambrian Res earch, 6(1), 43-64.

Mysen B., Griffin W.L. (1973). Pyroxene stoichiometry and breakdown of omphacite. American Mineralogist, 58, 60-63.

Nussbaum C., Marquer D., Biino G.G. (1998). Two subduction events in a polycyclic basement: Alpine and pre-Alpine high-pressure metamorphism in the Suretta nappe, Swiss Eastern Alps. Journal of Metamorphic Geology, 16(5), 591-605.

Oberhänsli R., Bousquet R.., Engi M., Goffé B., Gosso G., Handy M.R., Höck V., Koller F., Lardeaux J.M., Polino R., Rossi P., Schuster R., Schwartz S., Spalla M.I., 2004. Metamorphic Structure of the Alps. CCGM (Commission of the Geological Maps of the World), Paris.

Oberli F., Meier M., Berger A., Rosenberg C.L., Gieré R. (2004). U-Th-Pb and 230Th/238U disequilibrium isotope systematics: Precise accessory mineral chronology and melt evolution tracing in the Alpine Bergell intrusion. Geochimica et Cosmochimica Acta, 68(11), 2543-2560.

Oliot E., Melleton J., Schneider J., Corsini M., Gardien V., Rolland Y. (2015). Variscan crustal thickening in the Maures-Tanneron massif (South Variscan belt, France): new in situ monazite U-Th-Pb chemical dating of high-grade rocks. Bulletin de la Société Géologique de France, 186(2-3), 145-169.

Otten M.T. (1984). Metamorphism and deformation during and after cooling of the Artfjallet gabbro. Journal of the Geological Society, 141, 189-190.

Palagi P., Laporte D., Lardeaux J.M., Menot R.P., Orsini J.B. (1985). Identification d'un complexe leptyno-amphibolique au sein des "gneiss de Belgodère" (Corse occidentale). Comptes Rendus de l'Académie des sciences, Paris, 301, 1047–1052.

Palmeri R., Fanning M., Franceschelli M., Memmi I., Ricci C.A. (2004). SHRIMP dating of zircons in eclogite from the Variscan basement in north-eastern Sardinia (Italy). Neues Jahrbuch für Mineralogie-Monatshefte, 2004(6), 275-288.

Paquette J.L., Ménot R.P., Peucat J.J. (1989). REE, SM-Nd and U-Pb zircon study of eclogites from the Alpine External Massifs (western Alps): evidence for crustal contamination. –Earth and Planetary Science Letters, 96, 181-189.

Paquette J.L., Ballèvre M., Peucat J.J., Cornen, G. (2017). From opening to subduction of an oceanic domain constrained by LA-ICP-MS U-Pb zircon dating (Variscan belt, Southern Armorican Massif, France). Lithos, 294, 418-437.

Paquette J.L., Ménot R.P., Pin C., Orsini J.B. (2003). Episodic and short-lived granitic pulses in a post-collisional setting: evidence from precise U–Pb zircon dating through a crustal cross-section in Corsica. Chemical Geology, 198(1-2), 1-20.

Paquette J.L., Monchoux P., Couturier M. (1995). Geochemical and isotopic study of a norite-eclogite transition in the European Variscan belt: Implications for U / Pb zircon systematics in metabasic rocks. Geochimica et Cosmochimica Acta, 59(8), 1611-1622.

Passchier C.W. (1990). Reconstruction of deformation and flow parameters from deformed vein sets. Tectonophysics, 180(2-4), 185-199.

Passchier C.W., Trouw R.A. (2005). Microtectonics. Springer-Verlag Berlin Heidelberg.

Patočka F., Pin C. (2005). Sm-Nd isotope and trace element evidence for heterogeneous igneous protoliths of Variscan mafic blueschists in the East Krkonoše Complex (West Sudetes, NE Bohemian Massif, Czech Republic). Geodinamica Acta 18, 363-374.

Pattison D.R.M. (1991). Infiltration-driven anatexis in granulite facies metagabbro, Grenville Province, Ontario, Canada. Journal of Metamorphic Geology, 9, 315-332.

Pavanetto P., Funedda A., Northrup C.J., Schmitz M., Crowley J., Loi A. (2012). Structure and U–Pb zircon geochronology in the Variscan foreland of SW Sardinia, Italy. Geological Journal, 47(4), 426-445.

Pearce J.A. (1982). Trace element characteristics of lavas from destructive plate boundaries. Andesites, 8, 525-548.

Pearce J.A. (1996). A user's guide to basalt discrimination diagrams. In: Wyman D.A. (Ed) Trace Element Geochemistry of Volcanic Rocks: Applications for Massive Sulphide Exploration. Geol Ass Canada, Short Course Notes, 12, 79-113.

Pearce J.A. (2008). Geochemical fingerprinting of oceanic basalts with applications to ophiolite classification and the search for Archean oceanic crust. Lithos, 100(1-4), 14-48.

Pearce J.A., Gale G.H. (1977). Identification of ore-deposition environment from trace-element geochemistry of associated igneous host rocks. Geological Society, London, Special Publications, 7(1), 14-24.

Pearce J.A., Norry M.J. (1979). Petrogenetic implications of Ti, Zr, Y, and Nb variations in volcanic rocks. Contributions to Mineralogy and Petrology, 69(1), 33-47.

Perchuck L.L. (1991). Derivation of thermodynamically consistent set of geothermometers and geobarometers for metamorphic and magmatic rocks. In: Progress in metamorphic and magmatic petrology. A memorial volume in honor of D.S. Korzhinskiy. University Press Cambridge, United Kingdom, pp. 93-112.

Perchuck L.L., Lavrent'eva I.V. (1983). Experimental investigation of exchange equilibria in the system cordierite-garnet-biotite. In: Saxena S.K. (Ed), Kinetics and equilibrium in mineral reactions. Advances in physical geochemistry, vol. 3, Springer, Berlin Hiedelberg New York, pp. 199- 239.

Perchuk L.L. (1989). PT-fluid regimes of metamorphism and related magmatism with specific reference to the granulite-facies Sharyzhalgay complex of Lake Baikal. Geological Society, London, Special Publications, 43(1), 275-291.

Peressini G., Quick J.E., Sinigoi S., Hofmann A.W., Fanning, M. (2007). Duration of a large mafic intrusion and heat transfer in the lower crust: a SHRIMP U–Pb zircon study in the Ivrea–Verbano Zone (Western Alps, Italy). Journal of Petrology, 48(6), 1185-1218.

Petersen K.D., Schiffer C. (2016). Wilson cycle passive margins: Control of orogenic inheritance on continental breakup. Gondwana Research, 39, 131–144.

Petri B., Mohn G., Skrzypek E., Mateeva T., Galster F., Manatschal G. (2017). U-Pb geochronology of the Sondalo Gabbroic Complex (Central Alps) and its position within the Permian post-Variscan extension. International Journal of Earth Sciences, 106(8), 2873-2893.

Petri, B., Mohn, G., Štípská, P., Schulmann, K., Manatschal G. (2016). The Sondalo Gabbro contact aureole (Campo Unit, Eastern Alps): implications for mid-crustal mafic magma emplacement. Contributions to Mineralogy and Petrology 171 (5), 52.

Philippitsch R., Malecki G., Heinz H. (1986). Andalusit-Granat-Staurolith-Glimmerschiefer im Gailtalkristallin (Kärnten). Jahrbuch der Geologischen Bundesanstalt, 129(1), 93-98.

Picazo, S.M., Ewing, T.A., Müntener, O. (2019). Paleocene metamorphism along the Pennine–Austroalpine suture constrained by U–Pb dating of titanite and rutile (Malenco, Alps). Swiss Journal of Geosciences, 112(2-3), 517-542.

Pin C., Lancelot J. (1982). U-Pb dating of an early Paleozoic bimodal magmatism in the French Massif Central and of its further metamorphic evolution. Contributions to Mineralogy and Petrology, 79(1), 1-12.

Pin C., Paquette J.L., Zalduegui J.S., Ibarguchi J.G. (2002). Early Devonian supra subduction-zone ophiolite related to incipient collisional processes in the Western Variscan Belt: The Sierra de Careón unit, Ordenes Complex, Galicia. Geological Society of America, Special Papers, 364, 57-72.

Pistone M., Blundy J.D., Brooker R.A. (2016). Textural and chemical consequences of interaction between hydrous mafic and felsic magmas: an experimental study. Contributions to Mineralogy and Petrology, 171(1), 8.

Poitrasson F., Pin C. (1998). Extreme Nd isotope homogeneity in a large rhyolitic province: the Estérel massif, southeast France. Bulletin of Volcanology, 60(3), 213-223.

Polino R., Dal Piaz G.V., Gosso G. (1990). Tectonic erosion at the Adria margin and accretionary processes for the Cretaceous orogeny of the Alps. Memoire de la Société géologique de France, 156, 345-367.

Poller U., Liebetrau V., Todt W. (1997). U-Pb single-zircon dating under cathodoluminescence control (CLC-method): application to polymetamorphic orthogneisses. Chemical Geology, 139(1-4), 287-297.

Putirka K. (2016). Amphibole thermometers and barometers for igneous systems and some implications for eruption mechanisms of felsic magmas at arc volcanoes. American Mineralogist, 101(4), 841-858.

Putirka K.D. (2008). Thermometers and barometers for volcanic systems. Reviews in mineralogy and geochemistry, 69(1), 61-120.

Quick J.E., Sinigoi S., Mayer A. (1994). Emplacement dynamics of a large mafic intrusion in the lower crust, Ivrea-Verbano Zone, northern Italy. Journal of Geophysical Research: Solid Earth, 99(B11), 21559-21573.

Racek M., Štípská P., Pitra P., Schulmann K., Lexa O. (2006). Metamorphic record of burial and exhumation of orogenic lower and middle crust: a new tectonothermal model for the Drosendorf window (Bohemian Massif, Austria). Mineralogy and Petrology, 86(3-4), 221-251.

Ramakrishnan D., Bharti R., Nithya M., Kusuma K.N., Singh, K.D. (2012). Measurement of thermal properties of select intact and weathered granulites and their relationship to rock properties: Geophysics, 77, D63–D73.

Ramsay J.G., Huber M. I. (1987). The techniques of modern structural geology: Folds and fractures (Vol. 2). Academic Press, London.

Ranalli G. (1995). Rheology of the Earth. Springer Netherlands, p. 414.

Rebay G., Maroni M., Siletto G.B., Spalla M.I. (2015). Superposed syn-metamorphic structures of the Alpine and pre-Alpine convergent cycles in the Southalpine basement of the Orobic Alps (Northern Italy). Journal of Maps, 11(1), 168-180.

Rebay G., Powell R., Diener J. (2010). Calculated phase equilibria for a MORB composition in a P T window, 450–650°C and 18–28 kbar: the stability of eclogite. Journal of Metamorphic Geology, 28, 635-645.

Rebay G., Riccarci M.P., Spalla M.I. (2015). Fluid rock interactions as recorded by Cl-rich amphiboles from continental and oceanic crust of Italian orogenic belts. Periodico di Mineralogia, 84, 3B (Special Issue), 751-777.

Rebay G., Spalla M.I. (2001). Emplacement at granulite facies conditions of the Sesia–Lanzo metagabbros: an early record of Permian rifting? Lithos, 58(3-4), 85-104.

Rebay, G., Powell, R., Diener, J.F.A. (2010). Calculated phase equilibria for a MORB composition in a P–T range, 450–650 C and 18–28 kbar: the stability of eclogite. Journal of Metamorphic Geology, 28(6), 635-645.

Regorda A., Lardeaux J.M., Roda M., Marotta A.M., Spalla, M.I. (2020). How many subductions in the Variscan orogeny? Insights from numerical models. Geoscience Frontiers, 11(3), 1025-1052.

Regorda A., Roda M., Marotta A.M., Spalla M.I. (2017). 2-D numerical study of hydrated wedge dynamics from subduction to post-collisional phases. Geophysical Journal International 211(2), 952-978.

Renna M.R., Tribuzio R., Tiepolo M. (2007). Origin and timing of the post-Variscan gabbro–granite complex of Porto (Western Corsica). Contribution to Mineralogy and Petrology, 154(5), 493-517.

Ridolfi F., Renzulli A. (2012). Calcic amphiboles in calc-alkaline and alkaline magmas: thermobarometric and chemometric empirical equations valid up to 1,130° C and 2.2 GPa. Contributions to Mineralogy and Petrology 163(5), 877-895.

Ridolfi F., Renzulli A., Puerini M. (2010). Stability and chemical equilibrium of amphibole in calc-alkaline magmas: an overview, new thermobarometric formulations and application to subduction-related volcanoes. Contributions to Mineralogy and Petrology, 160(1), 45-66.

Roda M., Marotta A.M., Spalla M.I. (2010). Numerical simulations of an ocean-continent convergent system: Influence of subduction geometry and mantle wedge hydration on crustal recycling. Geochemistry, Geophysics, Geosystems, 11, 1–21.

Roda M., Regorda A., Spalla M.I., Marotta A.M. (2019). What drives Alpine Tethys opening? Clues from the review of geological data and model predictions. Geological Journal, 54, 2646–2664.

Roda M., Spalla M.I., Marotta A.M. (2012). Integration of natural data within a numerical model of ablative subduction: a possible interpretation for the Alpine dynamics of the Austroalpine crust. Journal of Metamorphic Geology, 30, 973–996.

Roda M., Zucali M. (2011). Tectono-metamorphic map of the Mont Morion Permian metaintrusives (Mont Morion—Mont Collon—Matterhorn Complex, Dent Blanche Unit), Valpelline—Western Italian Alps. Journal of Maps, 7(1), 519-535.

Roda M., Zucali M., Li Z.X., Spalla M.I., Yao W. (2018). Pre-alpine contrasting tectono-metamorphic evolutions within the Southern Steep Belt, Central Alps. Lithos, 310, 31-49.

Roda M., Zucali M., Regorda A., Spalla M.I. (2020). Formation and evolution of a subduction-related mélange: The example of the Rocca Canavese Thrust Sheets (Western Alps). GSA Bulletin, 132, 884–896.

Rodrıguez J., Cosca M.A., Ibarguchi J.G., Dallmeyer R.D. (2003). Strain partitioning and preservation of 40Ar/39Ar ages during Variscan exhumation of a subducted crust (Malpica–Tui complex, NW Spain). Lithos, 70(3-4), 111-139.

Rolland Y., Cox S., Boullier A.M., Pennacchioni G., Mancktelow N. (2003). Rare earth and trace element mobility in mid-crustal shear zones: insights from the Mont Blanc Massif (Western Alps). Earth and Planetary Science Letters, 214(1-2), 203-219.

Romain J., Vernet J. (1978). Decouverte d'un volcanisme basique d'age permien dans la vallee de la Gordolasque (Sud-Ouest du massif de l'Argentera-Mercantour, Alpes-Maritimes, France). Bulletin de la Societé géologique de France S7-XX(6), 929-933.

Romano V., Cirrincione R., Fiannacca P., Lustrino M., Tranchina A. (2011). Late-Hercynian post-collisional dyke magmatism in central Calabria (Serre Massif, southern Italy). Periodico di Mineralogia, 80(3Special Issue), 489-515.

Rose I., Buffett B., Heister T. (2017). Stability and accuracy of free surface time integration in viscous flows. Physics of the Earth and Planetary Interiors, 262, 90–100.

Rosenberg C.L. (2004). Shear zones and magma ascent: a model based on a review of the Tertiary magmatism in the Alps. Tectonics, 23.

Rossi P., Cocherie A., Fanning C.M. (2015). Evidence in Variscan Corsica of a brief and voluminous Late Carboniferous to Early Permian volcanic-plutonic event contemporaneous with a high-temperature/low-pressure metamorphic peak in the lower crust. Bulletin Société géologique de France, 186(2-3), 171-192.

Rossi P., Cocherie A., Lahondère D., Fanning C.M. (2002). The European margin of the Jurassic Tethys in Corsica: dating of Balagne trondhjemites and evidence to support a continental crust beneath the Balagne-Ligurian domain. Comptes Rendus Geoscience, 334(5), 313-322.

Rossi P., Oggiano G., Cocherie A. (2009). A restored section of the “southern Variscan realm” across the Corsica–Sardinia microcontinent. Comptes Rendus Geoscience, 341(2-3), 224-238.

Rottura A., Bargossi G.M., Caggianelli A., Del Moro A., Visona D., Tranne C.A. 1998. Origin and significance of the Permian high-K calc-alkaline magmatism in the central-eastern Southern Alps, Italy. Lithos, 45(1-4), 329-348.

Rötzler J., Timmerman M.J., (2020). Geochronological and petrological constraints from the evolution in the Saxon Granulite Massif, Germany, on the Variscan continental collision orogeny. Journal of Metamorphic Geology.

Rubatto D. (2002). Zircon trace element geochemistry: partitioning with garnet and the link between U–Pb ages and metamorphism. Chemical geology, 184(1-2), 123-138.

Rubatto D., Ferrando S., Compagnoni R., Lombardo B. (2010) Carboniferous high-pressure metamorphism of Ordovician protoliths in the Argentera Massif (Italy), Southern European Variscan belt. Lithos, 116, 65-76.

Rubatto D., Schaltegger U., Lombardo D., Colombo F., Compagnoni R. (2001). Complex Paleozoic magmatic and metamorphic evolution in the Argentera massif (Western Alps), resolved with U-Pb dating. Schweizerische Mineralogische und Petrographische Mitteilungen, 81, 213-228.

Rubatto, D. (2002). Zircon trace element geochemistry: partitioning with garnet and the link between U–Pb ages and metamorphism. Chemical Geology, 184(1-2), 123-138.

Rudnick R.L., Fountain D.M. (1995). Nature and composition of the continental crust: a lower crustal perspective. Reviews of geophysics, 33(3), 267-309.

Rüpke L.H., Hasenclever J. (2017). Global rates of mantle serpentinizationand H 2 productionat oceanic transform faultsin 3-D geodynamic models. Geophysical Research Letters, 44(13), 6726-6734.

Sabatier H. (1991). Vaugnerites: special lamprophyre-derived mafic enclaves in some Hercynian granites from Western and Central Europe, in: Didier J., Barbarin B., eds. Enclaves and granite petrology. Elsevier, Amsterdam, pp. 63-81.

Saccani E. (2015). A new method of discriminating different types of post-Archean ophiolitic basalts and their tectonic significance using Th-Nb and Ce-Dy-Yb systematics. Geoscience Frontiers, 6, 481-501.

Salvi F., Spalla M.I., Zucali M., Gosso G. (2010). Three-dimensional evaluation of fabric evolution and metamorphic reaction progress in polycyclic and polymetamorphic terrains: a case from the Central Italian Alps. Geological Society of London, Special Publications, 332, 173-187.

Sanchez G., Rolland Y., Jolivet M., Brichau S., Corsini M., Carter A. (2011). Exhumation controlled by transcurrent tectonics: the Argentera-Mercantour massif (SW Alps). Terra Nova, 23(2), 116-126.

Sanchez G., Rolland Y., Schneider J., Corsini M., Oliot E., Goncalves P., Verati C., Lardeaux J.M., Marquer D. (2011). Dating low-temperature deformation by 40Ar/39Ar on white mica, insights from the Argentera-Mercantour Massif (SW Alps). Lithos 125(1): 521-536.

Sanchez G., Rolland Y., Schreiber D., Giannerini G., Corsini M., Lardeaux J.M. (2010). The active fault system of SW Alps. Journal of Geodynamics 49(5), 296-302.

Sánchez Lorda M., Sarrionandia F., Ábalos B., Carrracedo M., Eguíluz L., Ibarguchi J.G. (2014). Geochemistry and paleotectonic setting of Ediacaran metabasites from the Ossa-Morena Zone (SW Iberia). International Journal of Earth Sciences, 103(5), 1263-1286.

Sánchez Martínez S., Arenas R., Gerdes A., Castiñeiras P., Potrel A., Fernández-Suárez, J. (2011). Isotope geochemistry and revised geochronology of the Purrido Ophiolite (Cabo Ortegal Complex, NW Iberian Massif): Devonian magmatism with mixed sources and involved Mesoproterozoic basement. Journal of the Geological Society, 168(3), 733-750.

Sanders C.A., Bertotti G., Tommasini S., Davies G.R., Wijbrans J.R. (1996). Triassic pegmatites in the Mesozoic middle crust of the Southern Alps (Italy): Fluid inclusions, radiometric dating and tectonic implications. Eclogae Geologicae Helvetiae, 89(1), 505-526.

Sassi R., Mazzoli C., Merle R., Brombin V., Chiaradia M., Dunkley D.J., Marzoli A. (2020). HT-LP crustal syntectonic anatexis as a source of the Permian magmatism in the Eastern Southern Alps: evidence from xenoliths in the Euganean trachytes (NE Italy). Journal of the Geological Society.

Sassi R., Mazzoli C., Miller C., Konzett J. (2004). Geochemistry and metamorphic evolution of the Pohorje Mountain eclogites from the easternmost Austroalpine basement of the Eastern Alps (Northern Slovenia). Lithos, 78(3), 235-261.

Schaltegger U., Brack P. (2007). Crustal-scale magmatic systems during intracontinental strike-slip tectonics: U, Pb and Hf isotopic constraints from Permian magmatic rocks of the Southern Alps. International Journal of Earth Sciences, 96(6), 1131-1151.

Schaltegger U., Gebauer D. (1999). Pre-Alpine geochronology of the central, western and southern Alps. Schweizerische Mineralogische und Petrographische Mitteilungen, 79, 79-87.

Schaltegger U., Nägler T., Corfu F., Maggetti M., Galetti G., Stosch H.G. (1997). A Cambrian island arc in the Silvretta nappe: constraints from geochemistry and geochronology. Schweizerische Mineralogische und Petrographische Mitteilungen, 77(3), 337-350.

Schaltegger U., Nowak A., Ulianov A., Fisher C.M., Gerdes A., Spikings R., Whitehouse M.J., Bindeman I., Hanchar J.M., Duff J., Vervoort J.D., Sheldrake T., Caricchi L., Brack P., Müntener O. (2019). Zircon Petrochronology and 40Ar/39Ar Thermochronology of the Adamello Intrusive Suite, N. Italy: Monitoring the Growth and Decay of an Incrementally Assembled Magmatic System. Journal of Petrology, 60(4), 701-722.

Schettino A., Turco, E. (2011). Tectonic history of the western Tethys since the Late Triassic. GSA Bulletin, 123(1-2), 89-105.

Schiavinato G. (1954). Sulle rocce diabasiche comprese negli Scisti di Edolo in Val Camonica (Lombardia). Rendiconti della Società Mineralogica Italiana, 11, 233-261.

Schmid S.M., Aebli H.R., Heller F., Zingg A. (1989). The role of the Periadriatic Line in the tectonic evolution of the Alps. Geological Society, London, Special Publications, 45(1), 153-171.

Schmid S.M., Fügenschuh B., Kissling E., Schuster R. (2004). Tectonic map and overall architecture of the Alpine orogen. Eclogae Geologicae Helvetiae, 97, 93-117.

Schmidt K.H., Bottazzi P., Vannucci R., Mengel K. (1999). Trace element partitioning between phlogopite, clinopyroxene and leucite lamproite melt. Earth and Planetary Science Letters, 168(3-4), 287-299.

Schmidt M.W., Poli S. (1998). Experimentally based water budgets for dehydrating slabs and consequences for arc magma generation. Earth and Planetary Science Letters, 163, 361-379.

Schneider J., Corsini M., Reverso-Peila A., Lardeaux J.M. (2014). Thermal and mechanical evolution of an orogenic wedge during Variscan collision: an example in the Maures–Tanneron Massif (SE France). Geological Society, London, Special Publications, 405(1), 313-331.

Schon S.C., Head J.W., Fassett C.I. (2009). Unique chronostratigraphic marker in depositional fan stratigraphy on Mars: Evidence for ca. 1.25 Ma gully activity and surficial meltwater origin. Geology, 37, 207–210.

Schönborm G. (1992). Alpine tectonics and kinematic models of the central Southern Alps. Memorie di Scienze Geologiche, Padova, 44, 229-393.

Schreiber D., Lardeaux J.M., Martelet G., Courrioux G., Guillen A. (2010). 3-D modelling of Alpine Mohos in Southwestern Alps. Geophysical Journal International 180, 961-975.

Schulmann K., Konopásek J., Janoušek V., Lexa O., Lardeaux J.M., Edel J.B., Štípská P., Ulrich S., 2009. An Andean type Palaeozoic convergence in the Bohemian massif. Comptes Rendus Geoscience, 341(2-3), 266-286.

Schulmann K., Lexa O., Janoušek V., Lardeaux J.M., Edel J.B. (2014). Anatomy of a diffuse cryptic suture zone: an example from the Bohemian Massif, European Variscides. Geology, 42(4), 275-278.

Schulmann K.., Kröner A.., Hegner E.., Wendt I.., Konopásek J., Lexa O., Štípská, P. (2005). Chronological constraints on the pre-orogenic history, burial and exhumation of deep-seated rocks along the eastern margin of the Variscan Orogen, Bohemian Massif, Czech Republic. American Journal of Science, 305(5), 407-448.

Schulz B., Bombach K. (2003). Single zircon Pb-Pb geochronology of the early-Palaeozoic magmatic evolution in the Austroalpine basement to the south of the Tauern Window. Jahrbuch der Geologischen Bundesanstalt, 143, 303-321.

Schultz B., Bombach K., Pawlig S., Brätz H. (2004). Neoproterozoic to Early-Palaeozoic magmatic evolution in the Gondwana-derived Austroalpine basement to the south of the Tauern Window (Eastern Alps). International Journal of Earth Sciences, 93, 824–843.

Schumacher J.C. (2007). Metamorphic amphiboles: composition and coexistence. Reviews in Mineralogy and Geochemistry, 67(1), 359-416.

Schuster R., Koller F., Hoeck V., Hoinkes G. and Bousquet R. (2004). Metamorphic evolution of the Eastern Alps. Mitteilungen der Österreichischen Mineralogischen Gesellschaft, 149, 175-199.

Schuster R., Scharbert S., Abart R., Frank W. (2001). Permo-Triassic extension and related HT/ LP metamorphism in the Austroalpine- Southalpine realm. Mitt. Ges. Geol. Bergbaustud. Oesterr. 45, 111-141.

Schuster R., Stüwe K. (2008). Permian metamorphic event in the Alps. Geology, 36(8), 603-606.

Schuster R., Tropper P., Krenn E., Finger F., Frank W., Philippitsch R. (2015). Prograde Permo-Triassic metamorphic HT/LP assemblages from the Austroalpine Jenig Complex (Carinthia, Austria). Austrian Journal of Earth Sciences 108, 73-90.

Schwartz S., Lardeaux J.M., Tricart P., Guillot S., Labrin E. (2007). Diachronous exhumation of HP-LT metamorphic rocks from south-western Alps: evidence from fission track analysis. Terra Nova 19(2), 133-140.

Schweinehage R., Massonne H. (1999). Geochemistry and metamorphic evolution of metabasites from the Silvretta nappe, Eastern Alps. Memorie Scienze Geologiche 51(1), 191– 203.

Sciunnach D., Garzanti E., Confalonieri M.P. (1996). Stratigraphy and petrography of Upper Permian to Anisian terrigenous wedges (Verrucano Lombardo, Servino and Bellano formations; western southern Alps). Rivista Italiana di Paleontologia e Stratigrafia, 102(1), 27-48.

Scotese C.R., Golonka J. (1997). Paleogeographic atlas (pp. 1-45). Arlington: PALEOMAP Project, University of Texas at Arlington.

Séranne M. (1999). The Gulf of Lion continental margin (NW Mediterranean) revisited by IBS: an overview. Geological Society, London, Special Publications, 156(1), 15-36.

Shaw D.M. (1970). Trace element fractionation during anatexis. Geochimica et Cosmochimica Acta, 34(2), 237-243.

Shervais J.W. (1982). Ti-V plots and the petrogenesis of modern and ophiolitic lavas. Earth and Planetary Science Letters, 59, 101-118.

Siletto, G.B., Spalla, M.I., Tunesi, A., Lardeaux, J.M., Colombo, A. (1993). Pre-Alpine structural and metamorphic histories in the Orobic southern Alps, Italy. In: von Raumer, J., Neubauer, F. (eds). The pre-Mesozoic geology in the Alps. Springer, Berlin Heidelberg New York, pp. 585–598.

Simonetti M., Carosi R., Montomoli C., Langone A., D'Addario E., Mammoliti E. (2018). Kinematic and geochronological constraints on shear deformation in the Ferriere-Mollières shear zone (Argentera-Mercantour Massif, Western Alps): implications for the evolution of the Southern European Variscan Belt. International Journal of Earth Sciences, 107, 2163-2189.

Simonetti, M., Carosi, R., Montomoli, C., Corsini, M., Petroccia, A., Cottle, J.M., Iaccarino, S. (2020). Timing and kinematics of flow in a transpressive dextral shear zone, Maures Massif (Southern France). International Journal of Earth Sciences, 109(7), 2261-2285.

Simon-Labric T, Rolland Y, Dumont T, Heymes T, Authemayou C, Corsini M, Fornari M. (2009). 40Ar/39Ar dating of Penninic Front tectonic displacement (W Alps) during the Lower Oligocene (31–34 Ma). Terra Nova, 21(2), 127-136.

Skrzypek E., Štípská P., Cocherie A. (2012). The origin of zircon and the significance of U–Pb ages in high-grade metamorphic rocks: a case study from the Variscan orogenic root (Vosges Mountains, NE France). Contributions to Mineralogy and Petrology, 164(6), 935-957.

Sláma J., Košler J., Condon D.J., Crowley J.L., Gerdes A., Hanchar J.M., et al., (2008). Plešovice zircon - a new natural reference material for U–Pb and Hf isotopic microanalysis. Chemical Geology, 249(1-2), 1-35.

Sloman L.E. (1989). Triassic shoshonites from the dolomites, northern Italy: Alkaline arc rocks in a strike-slip setting. Journal of Geophysical Research: Solid Earth 94(B4), 4655-4666.

Smulikowski W. (1995). Evidence of glaucophane-schist facies metamorphism in the East Karkonosze complex, west Sudetes, Poland. Geologische Rundschau 84, 720-737.

Smye A.J., Lavier L.L., Zack T., Stockli D.F. (2019). Episodic heating of continental lower crust during extension: A thermal modeling investigation of the Ivrea-Verbano Zone. Earth and Planetary Science Letters, 521, 158-168.

Soejono I., Žáčková E., Janoušek V., Machek M., Košler J. (2010). Vestige of an Early Cambrian incipient oceanic crust incorporated in the Variscan orogen: Letovice Complex, Bohemian Massif. Journal of the Geological Society, 167(6), 1113-1130.

Spalla M.I., Carminati E., Ceriani S., Oliva A., Battaglia D. (1999). Influence of deformation partitioning and metamorphicre-equilibration on P–T path reconstruction in the pre-Alpine basement of central Southern Alps (Northern Italy). Journal of Metamorphic Geology, 17, 319-336.

Spalla M.I., Gosso G. (1999). Pre-Alpine tectonometamorphic units in the central Southern Alps: structural and metamorphic memory. Memorie di Scienze Geologiche, Padova, 51, 221–229.

Spalla M.I., Marotta A.M. (2007). P-T evolutions vs. numerical modelling: a key to unravel the Paleozoic to early-Mesozoic tectonic evolution of the Alpine area. Periodico di Mineralogia, 76, 267-308.

Spalla M.I., Siletto G.B., di Paola S., Gosso G. (2000). The role of structural and metamorphic memory in the distinction of tectono-metamorphic units: the basement of the Como lake in the Southern Alps. Journal of Geodynamics, 30(1-2), 191-204.

Spalla M.I., Zanoni D., Gosso G., Zucali M. (2009). Deciphering the geologic memory of a Permian conglomerate of the Southern Alps by pebble P–T estimates. International Journal of Earth Sciences, 98(1), 203-226.

Spalla M.I., Zanoni D., Marotta A.M., Rebay G., Roda M., Zucali M., Gosso G. (2014). The transition from Variscan collision to continental break-up in the Alps: insights from the comparison between natural data and numerical model predictions. Geological Society, London, Special Publications, 405(1), 363-400.

Spalla M.I., Zucali M. (2004). Deformation vs. metamorphic reequilibration heterogeneities in polymetamorphic rocks: a key to infer quality P-T-d-t path. Periodico di Mineralogia, 73, 249–257.

Spalla M.I., Zucali M., Di Paola S., Gosso G. (2005). A critical assessment of the tectono-thermal memory of rocks and definition of tectono-metamorphic units: evidence from fabric and degree of metamorphic transformations. Geological Society, London, Special Publications, 243(1), 227-247.

Spalla M.I., Zucali M., Salvi F., Gosso G., Gazzola D. (2003). Tectono-metamorphic map of the Languard-Campo, Serie del Tonale Nappes between Upper Val Camonica and Valtellina (Central Italian Alps, Austroalpine domain). Memorie di Scienze Geologiche, Padova, 55, 105–118.

Spear F.S. (1995). Metamorphic phase equilibria and pressure-temperature-time paths. Mineralogical Society of America Monograph, pp. 799.

Spiess R, Cesare B., Mazzoli C., Sassi R., Sassi F.P. (2010). The crystalline basement of the Adria microplate in the eastern Alps: a review of the palaeo- structural evolution from the Neoproterozoic to the Cenozoic. Rendiconti Lincei Scienze Fisiche e Naturali, 21, 31-50.

Stampfli G. (2000). Tethyan oceans. In: Boxkurt E., Winchester J.A., Piper J.D. (Eds) Tectonics and magmatism in Turkey and the surrounding area. Geological Society, London, Special Publications, 173, 1-23.

Stampfli G.M., Borel G.D. (2002). A plate tectonic model for the Paleozoic and Mesozoic constrained by dynamic plate boundaries and restored synthetic oceanic isochrons. Earth and Planetary Science Letters, 196(1-2), 17-33.

Stampfli G.M., Hochard C., Vérard C., Wilhem C., von Raumer J. (2013). The formation of Pangea. Tectonophysics, 593, 1-19.

Stampfli G.M., Von Raumer J.F., Borel G. (2002). The Paleozoic evolution of pre-Variscan terranes: from Gondwana to the Variscan collision. In: Martinez Catalan J.R., Hatcher Jr R.D., Arenas R., Diaz Garcia F. (Eds) Variscan–Appalachian Dynamics: The Building of the Late Paleozoic Basement. Geological Society of Amererica Special Papers, 364, 263-280.

Stille H. (1924). Grundfragen der vergleichenden Tektonik. Borntraeger, Berlin, pp 1–443.

Stipskà P., Powell R., (2005). Constraining the P–T path of a MORB-type eclogite using pseudosections, garnet zoning and garnet-clinopyroxene thermometry: an example from the Bohemian Massif. Journal of Metamorphic Geology, 23, 725-743.

Stipskà P., Powell R., Racek M., Lexa O. (2014). Intermediate granulite produced by transformation of eclogite at a felsic granulite contact, in Blansky les, Bohemian Massif. Journal of Metamorphic Geology, 32, 347-370.

Stipskà P., Schulmann K., Kröner A. (2004). Vertical extrusion and middle crustal spreading of omphacite granulite: a model of syn-convergent exhumation (Bohemian Massif, Czech Republic). Journal of Metamorphic Geology, 22, 179-198.

Stoeckhert, B., 1987. Das Uttenheimer Pegmatitfeld (Ostalpines Altkristallin, Südtirol). Genese und alpine Überprägung. Erlanger geol. Abh., 114, 83-106

Storck J.C., Brack P., Wotzlaw J F., Ulmer P. (2019). Timing and evolution of Middle Triassic magmatism in the Southern Alps (northern Italy). Journal of the Geological Society, 176(2), 253-268.

Sun S.S., Mc Donough W.F. (1989). Chemical and isotopic systematics of oceanic basalts: implications for mantle composition and processes. Geological Society, London, Special Publications, 42(1), 313-345.

Tait J.A., Bachtadse V., Franke W., Soffel H.C. (1997). Geodynamic evolution of the European Variscan fold belt: palaeomagnetic and geological constraints. Geologische Rundschau, 86, 585-598.

Thélin P., Sartori M., Burri M., Gouffon Y., Chessex R. (1993). The pre-Alpine basement of the briançonnais (Wallis, Switzerland). In: von Raumer J.F., Neubauer F. (Eds.), Pre-Mesozoic Geology in the Alps. Springer-Verlag, Heidelberg, pp. 297–315.

Thompson A.B., Laird J. (2005). Calibrations of modal space for metamorphism of mafic schist. American Mineralogist, 90(5-6), 843-856.

Thompson R., Morrison M.A., Dickin A., Hendry G.L. (1983). Continental flood basalts arachnids rule OK? In: Hawkesworth CJ, Norry MJ (Eds) Continental Basalts and Mantle Xenoliths. Shiva Publications, India, 158-185.

Thöni M., Mottana A., Delitala M.C., De Capitani L., Liborio G. (1992). The Val Biandino composite pluton: a Late Hercynian intrusion into the South Alpine metamorphic basement of the Alps (Italy). Neues Jahrbuch für Mineralogie Monatshefte, 12, 545-554.

Tichomirowa M., Köhler R. (2013). Discrimination of protolithic versus metamorphic zircon ages in eclogites: Constraints from the Erzgebirge metamorphic core complex (Germany). Lithos, 177, 436-450.

Tiepolo M., Tribuzio R., Langone A. (2011). High-Mg andesite petrogenesis by amphibole crystallization and ultramafic crust assimilation: evidence from Adamello hornblendites (Central Alps, Italy). Journal of Petrology, 52(5), 1011-1045.

Timmermann H., Dörr W., Krenn E., Finger F., Zulauf, G. (2006). Conventional and in situ geochronology of the Teplá Crystalline unit, Bohemian Massif: implications for the processes involving monazite formation. International Journal of Earth Sciences, 95(4), 629-647.

Timmermann H., Štědrá V., Gerdes A., Noble S.R., Parrish R.R., Dörr, W. (2004). The problem of dating high-pressure metamorphism: a U–Pb isotope and geochemical study on eclogites and related rocks of the Mariánské Lázně Complex, Czech Republic. Journal of Petrology, 45(7), 1311-1338.

Tomkins H.S., Powell R., Ellis D.J. (2007). The pressure dependence of the zirconium-in-rutile thermometer. Journal of Metamorphic Geology, 25, 703-713.

Török K. (1999). Pre-Alpine development of the andalusite sillimanite- biotite-schist from the Sopron Mountains (Eastern Alps, Western Hungary). Acta Geologica Hungarica, 42(2), 127-160.

Torsvik T.H. (1998). Palaeozoic palaeogeography: a North Atlantic viewpoint. GFF, 120(2), 109-118.

Torsvik T.H., Cocks L.R.M. (2009). The Lower Palaeozoic palaeogeographical evolution of the northeastern and eastern peri-Gondwanan margin from Turkey to New Zealand. Geological Society, London, Special Publications, 325(1), 3-21.

Torsvik T.H., Cocks L.R.M. (2019). The integration of palaeomagnetism, the geological record and mantle tomography in the location of ancient continents. Geological Magazine, 156(2), 242-260.

Torsvik T.H., Smethurst M., Meert J.G., Van der Voo R., McKerrow W., Brasier M., Sturt B., Walderhaug H. (1996). Continental break-up and collision in the Neoproterozoic and Palaeozoic-a tale of Baltica and Laurentia. Earth Science Reviews, 40, 229-258.

Torsvik T.H., Smethurst M.A., Briden J.C., Sturt B.A. (1990). A review of Paleozoic paleomagnetic data from Europe and their paleogeographic implications. In: Palaeozoic Palaeogeography and Biogeography 12. Geological Society Publishing House, Bath, 25-41.

Traversa G., Ronca S., Del Moro A., Pasquali C., Buraglini N., Barabino G. (2003). Late to post-Hercynian dyke activity in the Sardinia-Corsica domain: a transition from orogenic calc-alkaline to anorogenic alkaline magmatism. Bollettino della Società Geologica Italiana, 2, 131-152.

Tricart P. (1984). From passive margin to continental collision: a tectonic scenario for the Western Alps. American Journal of Sciences, 284, 97-120.

Tricart P., Schwartz S., Sue C., Lardeaux J.M. (2004). Evidence of synextension tilting and doming during final exhumation from analysis of multistage faults (Queyras Schistes lustrés, Western Alps). Journal of Structural Geology, 26(9), 1633-1645.

Tumiati S, Thöni M, Nimis P, Martin S, Mair V (2003) Mantle-crust interactions during Variscan subduction in the Eastern Alps (Nonsberg-Ulten zone): Geochronology and new petrological constraints. Earth and Planetary Science Letters 210(3-4), 509–526.

Ubide T., Gale C., Arranz E., Lago M., Larrea P. (2014). Clinopyroxene and amphibole crystal populations in a lamprophyre sill from the Catalonian Coastal Ranges (NE Spain): a record of magma history and a window to mineral-melt partitioning. Lithos, 184, 225-242.

Van Achterbergh E., Ryan C.G., Jackson S.E., Griffin W.L. (2001). Data reduction software for LA-ICP-MS: Appendix. Laser Ablation-ICP Mass Spectrometry in the Earth Sciences: Principles and Applications; Sylvester, PJ, Ed, 239-243.

van Hinsbergen D.J.J., Torsvik T.H., Schmid S.M., Maţenco L.C., Maffione M., Vissers R.L.M., Gürer D., Spakman, W. (2020). Orogenic architecture of the Mediterranean region and kinematic reconstruction of its tectonic evolution since the Triassic. Gondwana Research, 81, 79–229.

Van Roermund H., Boland J.N. (1983). Mechanisms of exsolution in omphacites from high-temperature, type-B, eclogites. Journal of the Geological Society, 140, 975-977.

van Staal C.R., Whalen J.B., Valverde-Vaquero P., Zagorevski A., Rogers N. (2009). Pre-Carboniferous, episodic accretion-related, orogenesis along the Laurentian margin of the northern Appalachians. Geological Society, London, Special Publications, 327(1), 271-316.

Vatin-Périgno N., Aumaitre R., Buffet G. (1974). La spilitisation dans le massif des Écrins-Pelvoux Un cortège intrusif et effusif dolérito-spilitique. Géologie Alpine, 50, 153-194.

Vatin-Périgno N., Juteau T., Le Fort P. (1972). Les filons du massif du Pelvoux (Alpes occidentales françaises). Géologie Alpine 48, 207-227.

Vernon RH. (2004, 2018). A Practical Guide to Rock Microstructures, second edition. Cambridge: Cambridge University Press, p. 432.

Vigano A., Tumiati S., Recchia S., Martin S., Marelli M., Rigon R. (2011). Carbonate pseudotachylytes: evidence for seismic faulting along carbonate faults. Terra Nova, 23(3), 187-194.

Vilà M., Fernández M., Jiménez-Munt I. (2010). Radiogenic heat production variability of some common lithological groups and its significance to lithospheric thermal modeling. Tectonophysics, 490, 152-164.

Visonà D. (1995). Polybaric evolution of calc-alkaline magmas: the dioritic belt of the Bressanone-Chiusa igneous complex (NE Italy), Memorie di Scienze Geologiche, Padova, 47, 11-124.

von Quadt A. (1992). U-Pb zircon and Sm—Nd geochronology of mafic and ultramafic rocks from the central part of the Tauern Window (eastern Alps). Contributions to Mineralogy and Petrology, 110(1), 57-67.

von Quadt A., Günther D., Frischknecht R., Zimmermann R., Franz G. (1997). The evolution of pre-Variscan eclogites of the Tauern Window (Eastern Alps): A Sm/Nd-, conventional and Laser ICP-MS zircon U-Pb study. Schweizerische Mineralogische und Petrographische Mitteilungen, 77(3), 265-279.

von Raumer J.F. (1998). The Palaeozoic evolution in the Alps: from Gondwana to Pangea. Geologische Rundschau, 87(3), 407-435.

von Raumer J.F. (1984). The External Massifs, relics of Variscan basement in the Alps, Geologische Rundschau, 73, 1-31.

von Raumer J.F. (1987). Les Massifs du Mont Blanc et des Aiguilles Rouges temoins de la formation de croute Varisque dans les Alpes Occidentales. Géologie Alpine, 63, 7-24.

von Raumer J.F. (1998). The Palaeozoic evolution in the Alps: from Gondwana to Pangea. Geologische Rundschau, 87(3), 407-435.

von Raumer J.F., Abrecht J., Bussy F., Lombardo B., Menot R.P., Schaltegger U. (1999). The Paleozoic metamorphic evolution of the Alpine external massifs. Schweizerische Mineralogische und Petrographische Mitteilungen, 79, 5-22.

von Raumer J.F., Bussy F., Schaltegger U., Schulz B., Stampfli G.M. (2013). Pre Mesozoic-Alpine basements – their place in the European Paleozoic framework. GSA Bulletin, 125, 89–108.

von Raumer J.F., Bussy F., Stampfli G.M. (2009). The Variscan evolution in the External massifs of the Alps and place in their Variscan framework. Comptes Rendus Geoscience 341(2-3), 239-252..

von Raumer J.F., Finger F., Veselà P., Stampfli G.M. (2014). Dubrachites-Vaugnerites - a geodynamic marker in the central European Variscan orogen. Terra Nova 26(2), 85-95.

von Raumer J.F., Ménot R.P., Abrecht J., Biino G. (1993). The Pre-Alpine evolution of the External massifs, in: von Raumer, J.F., Neubauer F. (Eds.), Pre-Mesozoic geology in the Alps. Springer, Berlin, Heidelberg, pp. 221-240.

von Raumer J.F., Stampfli G.M. (2008). The birth of the Rheic Ocean: Early Palaeozoic subsidence patterns and subsequent tectonic plate scenarios. Tectonophysics, 461, 9-20.

von Raumer J.F., Stampfli G.M., Arenas R., Martínez S.S. (2015). Ediacaran to Cambrian oceanic rocks of the Gondwana margin and their tectonic interpretation. International Journal of Earth Sciences, 104(5), 1107-1121.

von Raumer J.F., Stampfli G.M., Borel G., Bussy F. (2002). Organization of pre-Variscan basement areas at the north-Gondwanan margin. International Journal of Earth Sciences, 91(1), 35-52.

von Raumer J.F., Stampfli G.M., Bussy F. (2003). Gondwana-derived microcontinents — the constituents of the Variscan and Alpine collisional orogens. Tectnophysics 365:7-22.

Watson E.B., Wark D.A., Thomas J.B. (2006). Crystallization thermometers for zircon and rutile. Contributions to Mineralogy and Petrology, 151, 413–433.

Weber K., Behr H.J. (1983). Geodynamic interpretation of the mid-European Variscides. In Intracontinental Fold Belts. Springer, Berlin, Heidelberg, pp. 427-469.

Wennekers J.H.L. (1932). The structure of the Bergamo Alps compared with that of the Highlands of Scotland. Leidse Geologische Mededelingen, 4, 83 93.

White R.W., Powell R., Clarke G.L. (2002). The interpretation of reaction textures in Fe-rich metapelitic granulites of the Musgrave Block, central Australia: constraints from mineral equilibria calculations in the system K2O–FeO–MgO–Al2O3–SiO2–H2O–TiO2–Fe2O3. Journal of Metamorphic Geology, 20, 41-55.

White R.W., Powell R., Holland T.J.B. (2007). Progress relating to calculation of partial melting equilibria for metapelites. Journal of Metamorphic Geology, 25(5), 511-527.

White R.W., Powell R., Holland T.J.B. (2007). Progress relating to calculation of partial melting equilibria for metapelites. Journal of Metamorphic Geology, 25, 511-527.

White R.W., Powell R., Holland T.J.B., Johnson T.E., Green E.C.R., (2014). New mineral activity-composition relations for thermodynamic calculations in metapelitic systems. Journal of Metamorphic Geology, 32, 261-286.

White R.W., Powell R., Holland T.J.B., Worley B.A. (2000). The effect of TiO2 and Fe2O3 on metapelitic assemblages at greenschist and amphibolite facies conditions: mineral equilibria calculations in the system: K2O–FeO–MgO–Al2O3–SiO2–H2O–TiO2–Fe2O3. Journal of Metamorphic Geology, 18, 497-511.

White R.W., Powell R., Johnson T.E. (2014). The effect of Mn on mineral stability in metapelites revisited: new a-x relations for manganese-bearing minerals. Journal of Metamorphic Geology, 32, 809-828.

Whitney D.L., Evans B.W. (2010). Abbreviations for names of rock-forming minerals. American Mineralogist 95(1), 185-187.

Whitney D.L., Roger F., Teyssier C., Rey P.F., Respaut J.P. (2015). Syn-collapse eclogite metamorphism and exhumation of deep crust in a migmatite dome: the P–T–t record of the youngest Variscan eclogite (Montagne Noire, French Massif Central). Earth and Planetary Science Letters, 430, 224-234.

Wiedenbeck M., Alle P., Corfu F., Griffin W.L., Meier M., Oberli F., von Quadt A., Roddick J.C., Spiegel W. (1995). Three natural zircon standards for U-Th-Pb, Lu-Hf, trace element and REE analyses. Geostandards newsletter, 19(1), 1-23.

Wiedenbeck M., Hanchar J.M., Peck W.H., Sylvester P., Valley J., Whitehouse M., et al., (2004). Further characterization of the 91500 zircon crystal. Geostandards and Geoanalytical Research, 28(1), 9-39.

Wilks K.R., Carter N.L. (1990). Rheology of some continental lower crustal rocks. Tectonophysics, 182, 57–77.

Will T.M., Schmädicke E., Ling X.X., Li X.H., Li Q.L. (2018). New evidence for an old idea: Geochronological constraints for a paired metamorphic belt in the central European Variscides. Lithos, 302, 278-297.

Williams P.F. (1985). Multiply deformed terrains - problems of correlation. Journal of Structural Geology, 7(3-4), 269-280.

Winchester J.A., Floyd P.A. (1977). Geochemical discrimination of different magma series and their differentiation products using immobile elements. Chemical geology, 20, 325-343.

Wood B.J., Blundy J.D. (1997). A predictive model for rare earth element partitioning between clinopyroxene and anhydrous silicate melt. Contributions to Mineralogy and Petrology, 129(2-3), 166-181.

Workman R.K., Hart S.R. (2005). Major and trace element composition of the depleted MORB mantle (DMM). Earth and Planetary Science Letters, 231(1-2), 53-72.

Wu C.M. (2020). Calibration of the biotite-muscovite geobarometer for metapelitic assemblages devoid of garnet or plagioclase. Lithos, 372, 105668.

Wu C.M., Chen H.X. (2015). Revised Ti-in-biotite geothermometer for ilmenite-or rutile-bearing crustal metapelites. Science Bulletin, 60(1), 116-121.

Wyhlidal S., Thöny W.F., Tropper P., Kaindl R., Hauzenberger C., Mair V., 2012. Petrology of contact metamorphic metapelites from the southern rim of the Permian Brixen Granodiorite (South Tyrol, Italy). Mineralogy and Petrology, 106(3-4), 173-191.

Zack T., Brumm R. (1998). Ilmenite/liquid partition coefficients of 26 trace elements determined through ilmenite/clinopyroxene partitioning in garnet pyroxenites. In International Kimberlite Conference: Extended Abstracts (Vol. 7, pp. 986-988).

Zanchetta S., D'Adda P., Zanchi A., Barberini V., Villa I.M. (2011). Cretaceous-Eocene compression in the central Southern Alps (N Italy) inferred from 40Ar/39Ar dating of pseudotachylytes along regional thrust faults. Journal of Geodynamics, 51(4), 245-263.

Zanchetta S., Garzanti E., Doglioni C., Zanchi A. (2012). The Alps in the Cretaceous: a doubly vergent pre-collisional orogen. Terra Nova, 24(5), 351-356.

Zanchetta S., Malusà M.G., Zanchi A. (2015). Precollisional development and Cenozoic evolution of the Southalpine retrobelt (European Alps). Lithosphere, 7(6), 662-681.

Zanchi A., Zanchetta S., Berio L., Berra F., Felletti F. (2019). Low-angle normal faults record Early Permian extensional tectonics in the Orobic Basin (Southern Alps, N Italy). Italian Journal of Geosciences, 138(2), 184-201.

Zanoni D., Rebay G., Spalla M.I. (2016). Ocean floor and subduction record in the Zermatt-Saas rodingites, Valtournanche, Western Alps. Journal of Metamorphic Geology, 34, 941-961..

Zanoni D., Spalla M.I., 2018. The Variscan evolution in basement cobbles of the Permian Ponteranica Formation by microstructural and petrologic analysis. Italian Journal of Geosciences, 137(2), 254-271.

Zanoni D., Spalla M.I., Gosso G. (2010). Vestiges of lost tectonic units in conglomerate pebbles? A test in Permian sequences of the Southalpine Orobic Alps. Geological Magazine, 147(1), 98-122.

Zheng J.S., Mermet J.F., Toutin-Morin N., Hanes J., Gondolo A., Morin R., Féraud, G. (1992). Datation 40Ar-39Ar du magmatisme et de filons minéralisés permiens en Provence orientale (France). Geodinamica Acta, 5(3), 203-215.

Ziegler P. (1986). Geodynamic model for the Paleozoic crustal consolidation of Western and Central Europe. Tectonophysics, 126, 303-328.

Zimmermann V.R., Franz G. (1989). Die Eklogite der Unteren Schieferhülle; Frosnitztal/Südvenediger (Tauern, Österreich). Mittelungen der Östereichischen Geologischen Gesellschaft, 81, 167–188.

Zucali M. (2004). jPT java Mineral Formula Calculation and Pressure-Temperature tool.

Zurbriggen R. (2015). Ordovician orogeny in the Alps: a reappraisal. International Journal of Earth Sciences, 104(2), 335-350.

Chapter 6

Supplementary data

6 supplementary data files are attached in .xls format, complemented by 82 tables of BSE images.

Ringraziamenti

Ringrazio i miei tutor, Iole e Jean-Marc, che tanto hanno fatto per me, non solo in quest'ultimo triennio. Ringrazio Davide, Gisella; Manuel, e Michele per avermi aiutato e sostenuto nel lavoro, con gentilezza e infinita pazienza.
Ringrazio Luca, Pietro, Sara, Alexiane, e Maria José con i quali ho condiviso le stanze, spesso rumorose e me ne scuso, di Milano e Valbonne, Chiara, con la quale ho trascorso infinite ore serali in dipartimento, e Carlo e Jean per le scalate, le biciclettate, e le feste sulla riviera francese.

Durante quest'ultimo anno sono stato ospite di Guido ed Iole ad Antibes. Gliene sono infinitamente grato e non lo dimenticherò mai.

Ringrazio gli insostituibili amici che più hanno condiviso con me le gioie di questa gioventù spensierata, tra la Val Vigezzo, Milano, e il lago Maggiore. Grazie Laura per essermi vicina.

Tutto ciò è stato possibile solo grazie alla mia famiglia, che sempre mi sostiene e mi fa sentire fortunato.

Riassunto / Résumé

L'evoluzione tettonica della catena varisica meridionale è poco vincolata rispetto a quella della catena varisica centro-europea. La causa principale è l'intensa ristrutturazione alpina, particolarmente pervasiva nella zona assiale delle Alpi. Al contrario, il basamento varisico dei domini esterni delle Alpi è poco interessato da riequilibrazione alpina e la memoria varisica è ben preservata. Per questo motivo, lo studio dei domini esterni è fondamentale per comprendere la catena varisica meridionale.
La tesi ha come argomento le rocce di basamento varisico del massiccio dell'Argentera-Mercantour (dominio Elvetico), del basamento orobico (dominio Sudalpino), e del massiccio Maures-Tanneron. Quest'ultimo segmento è qui considerato in quanto porzione di catena varisica europea più prossima alle Alpi e, di conseguenza, ottimo termine di paragone nel tentativo di correlare il varisico "alpino" al varisico europeo. L'obiettivo è meglio vincolare l'evoluzione tettonica varisica e alpina di questi basamenti.

Questo studio comprende rilevamento geologico-strutturale multi-scala, integrato con analisi microstrutturale, mesostrutturale, e analisi chimiche e minerochimiche. Le condizioni metamorfiche che hanno interessato il basamento varisico sono stimate in termini di pressione e temperature e vincolate nel tempo da datazioni relative ed assolute. In questo modo, è stato posssibile discutere diverse fasi tettoniche varische ed alpine, dall'inizio del Cambriano al Terziario, nel contesto geodinamico e paleogeografico delle due catene. I risultati si riferiscono a quattro principali stadi tettonici, dalla subduzione dell'oceano varisico fino alla collisione alpina.

Come primo risultato è stata ricostruita l'evoluzione strutturale e metamorfica dei resti di listosfera oceanica di età cambriana presenti nel massiccio dell'Argentera-Mercantour. Queste rocce registrano un'evoluzione metamorfica prograda da condizioni di facies prenite-pumpellite fino al picco eclogitico (T = 610 – 660°C, P = 1.90 – 2.30 GPa) prima di essere esumate nel Carbonifero. Per la prima volta una suduzione "fredda" è descritta del dominio elvetico delle Alpi, che è quindi una zona assiale della catena varisica meridionale.

La seconda parte è dedicata al confronto dell'evoluzione tettonica di due domini esterni della catena varisica meridionale, il basamento orobico e il massiccio Maures-Tanneron occidentale. Questi due basamenti registrano un'evoluzione varisca sorprendentemente simile, con analoghe condizioni di picco metamorfico durante la collisione carbonifera (T = 550 – 650°C, P = 0.6 – 0.8 GPa). E' dunque suggerita una correlazione tra questi due domini, oggi posti in posizione inversa rispetto alla zona assiale della catena varisica meridionale rinvenuta nel dominio elvetico.

Come terzo punto, abbiamo cercato il segnale dell'assottigliamento litosferico permo-triassico su entrambi i lati del futuro oceano alpino, nel massiccio dell'Argentera-Mercantour e nel basamento orobico. In entrambi i casi sono presenti filoni lamprofirici calc-alcalini ed alcalini intrusi a bassa profondità nel basamento varisico esumato. Dal momento che la produzione di questi fusi di mantello alla fine del ciclo varisico richiede estensione frozata che non può rsultare dal solo collasso gravitazionale della catena, interpretiamo questi filoni tra le prime evidenze dell'inizio del ciclo alpino responsabile della rottura della catena varisica meridionale.

Da ultimo, è stata caratterizzata l'evoluzione alpina del basamento varisico nei domini esterni delle Alpi, considerando i lamprofiri come marker strutturali e metamorfici. Sono quindi state stimate simili condizioni di picco metamorpfico (T = 420 – 450°C and P = 0.15 – 0.40 GPa) sia nel dominio elvetico sia nel sudalpino, ovvero su entrambi i lati della catena alpina.

L'évolution tectonique de la chaine varisque méridionale est certainement moins comprise que celle de la chaine varisque de l'Europe centrale. La raison la plus importante est la rééquilibration alpine des roches varisques, qui a été particulièrement puissante dans la zone axiale des Alpes. Au contraire, la

rééquilibration alpine des socles varisques dans les domaines externes des Alpes n'est pas omniprésente et ces domaines bien préservent l'héritage varisque. Pour cette raison, les domaines externes des Alpes sont importants pour mieux comprendre la chaine varisque méridionale.

Les sujets de cette Thèse sont les roches varisques du socle de l'Argentera-Mercantour (domaine helvétique), du domaine Sud-Alpin, et du Massif des Maures-Tanneron. Ce dernier a été ici considéré parce que il est le segment de chaine varisque le plus proche des Alpes et donc une excellente référence pour établir une corrélation entre le varisque "alpine" et le varisque européen. L'objectif de ce projet est la description quantitative de l'évolution tectonique varisque et alpine de ces socles.

Le projet a prévu l'étude géologique-structurale du terrain à différentes échelles, intégré avec des analyses micro-structurelles et chimiques des roches et des minéraux. Les conditions métamorphiques des roches sont estimées par les méthodes de la thermo-barométrie et de la modélisation pétrologique et intégrées par des datations relatives et numériques. Ce faisant, il a été possible de examiner les différentes phases tectoniques varisques et alpines, depuis le début du Cambrien jusqu'à le Tertiaire, dans le cadre géodynamique et paléogéographique des deux chaines. Les résultats se réfèrent à quatre phases tectoniques principales, depuis la subduction de l'océan varisque jusqu'à la collision alpine.

Le premier résultat est la reconstruction de l'évolution structurelle et métamorphique des vestiges de croûte océanique du Cambrien inferieur dans le massif de l'Argentera-Mercantour. Ces roches enregistrent une évolution métamorphique prograde, depuis le facies à prehnite-pumpellyite jusqu'à le facies des éclogites (T = 610 – 660°C, P = 1.90 – 2.30 GPa), avant l'exhumation au cours du Carbonifère. Pour la première fois, une zone de subduction "froide" est décrite dans le domaine helvétique des Alpes, qui comprend donc le domaine axial de la chaine varisque méridionale.

La deuxième partie est dédiée à la comparaison de l'évolution tectonique des domaines externes de la chaine varisque méridionale, le Sud-Alpin et la parte occidentale du massif des Maures-Tanneron. Ces socles enregistrent une évolution tectonique varisque étonnamment similaire et les mêmes conditions métamorphiques pendant la collision varisque dans le Carbonifère (T = 550 – 650°C, P = 0.6 – 0.8 GPa). Il a été donc suggéré une corrélation entre ces domaines qui, aujourd'hui, sont en position inverse par rapport à le domaine axial de la chaine varisque méridionale dans le domaine helvétique des Alpes.

En troisième lieu, le signal d'amincissement lithosphérique du Permien-Trias sur les deux côtes de l'ocean alpin a été identifié dans le massif de l'Argentera-Mercantour et dans le domaine Sud-Alpin. Dans tous les cas, il y a des filons lamprophyriques calco-alcalines et alcalines qui se sont mises en place à faible profondeur dans le socle varisque exhumé. Étant donné que la fusion du manteau à la fin de l'orogenèse varisque a besoin d'extension forcée que ne peut pas résulter seulement par

l’effondrement gravitationnel de la chaine, ces filons sont parmi les premières évidences de la rupture de la chaine varisque méridionale et du début du cycle alpin.

Enfin, l’évolution alpine des domaines externes des Alpes a été quantifiée par les lamprophyres, qui sont des marqueurs structuraux et métamorphiques de premier plan. Conditions métamorphiques similaires (T = 420 – 450°C and P = 0.15 – 0.40 GPa) ont été reconnues dans le domaine helvétique et le Sud-Alpin, c’est-à-dire sur les deux faces externes de la chaine alpine.